SMALL-MOLECULE SEMICONDUCTORS FOR HIGH-EFFICIENCY ORGANIC SOLAR CELLS

EDITED BY: Chuanlang Zhan and Donghong Yu
PUBLISHED IN: Frontiers in Chemistry

frontiers Research Topics

frontiers

ISSN 1664-8714
ISBN 978-2-88945-980-3
DOI 10.3389/978-2-88945-980-3

About Frontiers

Frontiers is more than just an open-access publisher of scholarly articles: it is a pioneering approach to the world of academia, radically improving the way scholarly research is managed. The grand vision of Frontiers is a world where all people have an equal opportunity to seek, share and generate knowledge. Frontiers provides immediate and permanent online open access to all its publications, but this alone is not enough to realize our grand goals.

Frontiers Journal Series

The Frontiers Journal Series is a multi-tier and interdisciplinary set of open-access, online journals, promising a paradigm shift from the current review, selection and dissemination processes in academic publishing. All Frontiers journals are driven by researchers for researchers; therefore, they constitute a service to the scholarly community. At the same time, the Frontiers Journal Series operates on a revolutionary invention, the tiered publishing system, initially addressing specific communities of scholars, and gradually climbing up to broader public understanding, thus serving the interests of the lay society, too.

Dedication to Quality

Each Frontiers article is a landmark of the highest quality, thanks to genuinely collaborative interactions between authors and review editors, who include some of the world's best academicians. Research must be certified by peers before entering a stream of knowledge that may eventually reach the public - and shape society; therefore, Frontiers only applies the most rigorous and unbiased reviews.
Frontiers revolutionizes research publishing by freely delivering the most outstanding research, evaluated with no bias from both the academic and social point of view. By applying the most advanced information technologies, Frontiers is catapulting scholarly publishing into a new generation.

What are Frontiers Research Topics?

Frontiers Research Topics are very popular trademarks of the Frontiers Journals Series: they are collections of at least ten articles, all centered on a particular subject. With their unique mix of varied contributions from Original Research to Review Articles, Frontiers Research Topics unify the most influential researchers, the latest key findings and historical advances in a hot research area! Find out more on how to host your own Frontiers Research Topic or contribute to one as an author by contacting the Frontiers Editorial Office: researchtopics@frontiersin.org

SMALL-MOLECULE SEMICONDUCTORS FOR HIGH-EFFICIENCY ORGANIC SOLAR CELLS

Topic Editors:
Chuanlang Zhan, Institute of Chemistry (CAS), China
Donghong Yu, Aalborg University, Denmark

Citation: Zhan, C., Yu, D., eds. (2019). Small-Molecule Semiconductors for High-Efficiency Organic Solar Cells. Lausanne: Frontiers Media.
doi: 10.3389/978-2-88945-980-3

Table of Contents

frontiers in Chemistry

ORIGINAL RESEARCH
published: 10 December 2018
doi: 10.3389/fchem.2018.00613

Comparison Study of Wide Bandgap Polymer (PBDB-T) and Narrow Bandgap Polymer (PBDTTT-EFT) as Donor for Perylene Diimide Based Polymer Solar Cells

Tengling Ye[1], Shan Jin[1], Cong Kang[1], Changhao Tian[1], Xin Zhang[3], Chuanlang Zhan[3]*, Shirong Lu[2] and Zhipeng Kan[2]**

[1] MIIT Key Laboratory of Critical Materials Technology for New Energy Conversion and Storage, School of Chemistry and Chemical Engineering, Harbin Institute of Technology, Harbin, China, [2] Organic Semiconductor Research Center, Chongqing Institute of Green and Intelligent Technology, Chinese Academy of Sciences, Chongqing, China, [3] Beijing National Laboratory for Molecular Sciences, CAS Key Laboratory of Photochemistry, Institute of Chemistry, Chinese Academy of Sciences, Beijing, China

OPEN ACCESS

Edited by:
Iwao Ojima,
Stony Brook University, United States

Reviewed by:
Gregory C. Welch,
University of Calgary, Canada
Liming Ding,
National Center for Nanoscience and Technology (CAS), China
Jonathan G. Rudick,
Stony Brook University, United States

***Correspondence:**
Tengling Ye
ytl@hit.edu.cn
Zhipeng Kan
kanzhipeng@cigit.ac.cn
Chuanlang Zhan
clzhan@iccas.ac.cn

Specialty section:
This article was submitted to Organic Chemistry, a section of the journal Frontiers in Chemistry

Received: 18 June 2018
Accepted: 28 November 2018
Published: 10 December 2018

Citation:
Ye T, Jin S, Kang C, Tian C, Zhang X, Zhan C, Lu S and Kan Z (2018) Comparison Study of Wide Bandgap Polymer (PBDB-T) and Narrow Bandgap Polymer (PBDTTT-EFT) as Donor for Perylene Diimide Based Polymer Solar Cells. Front. Chem. 6:613. doi: 10.3389/fchem.2018.00613

Perylene diimide (PDI) derivatives as a kind of promising non-fullerene-based acceptor (NFA) have got rapid development. However, most of the relevant developmental work has focused on synthesizing novel PDI-based structures, and few paid attentions to the selection of the polymer donor in PDI-based solar cells. Wide bandgap polymer (PBDB-T) and narrow bandgap polymer (PBDTTT-EFT) are known as the most efficient polymer donors in polymer solar cells (PSCs). While PBDB-T is in favor with non-fullerene acceptors achieving power conversion efficiency (PCE) more than 12%, PBDTTT-EFT is one of the best electron donors with fullerene acceptors with PCE up to 10%. Despite the different absorption profiles, the working principle of these benchmark polymer donors with a same electron acceptor, specially PDI-based acceptors, was rarely compared. To this end, we used PBDB-T and PBDTTT-EFT as the electron donors, and 1,1′-bis(2-methoxyethoxyl)-7,7′-(2,5-thienyl) bis-PDI (Bis-PDI-T-EG) as the electron acceptor to fabricate PSCs, and systematically compared their differences in device performance, carrier mobility, recombination mechanism, and film morphology.

Keywords: polymer solar cells, perylene diimide, charge transport, charge recombination, non-fullerene, wide bandgap, narrow bandgap

INTRODUCTION

Polymer solar cells (PSCs) have been attracting more and more attention in both research and industrial applications due to their unique properties such as solution processability, light weight, low cost, and high mechanical flexibility. High-efficiency PSCs typically employ the bulk heterojunction structures composed of a p-type polymer material and an n-type small molecular material. The most studied combination was a polymer semiconductor donor and a fullerene-based small molecule acceptor, reaching a power conversion efficiency (PCE) of 11.7% (Zhao et al., 2016a). Due to the drawbacks of fullerene-based materials, such as weak absorption in visible and near infrared region, limited tunability of energy levels, and poor morphology stability, further

improvement of the PCE in such traditional donor/acceptor combinations is hindered (Eftaiha et al., 2014; Cheng and Zhan, 2016). To overcome these limiting factors, efficient non-fullerene-based acceptors (NFA) have been developed for decades. Yuze Lin (Lin et al., 2015a,b) and co-authors reported a series of NFAs based on highly electron-deficient (3-ethylhexyl-4-oxothiazolidine-2-yl) dimalononitrile (RCN) groups, such as ITIC IEIC and SFBRCN, getting PCE comparable to their fullerene counterparts and opening a new era of PSCs. After that, the first single cell with PCE more than 11% based on polymer/NFA was reported by Wenchao Zhao etc. (Zhao et al., 2016b). The RCN-based NFAs has been also introduced into ternary PSCs and tandem PSCs. The best PCE of single PSCs based on these acceptors has already exceeded 14% up to date (Xiao et al., 2017a; Li et al., 2018) and the optimal efficiency of tandem organic solar cells is up to 17.3% (Cui et al., 2018; Meng et al., 2018). The perylene diimide (PDI)-based small molecules as another kind of promising NFAs have been intensively studied. However, the development of PDI-based NFAs in efficiency is lagging. The main factor preventing PDI-based NFAs to get higher efficiency is that PDI moleculars have the intrinsic tendency to aggregate in solid thin film, where excimers are formed and the process of exciton diffusion/separation is severely limited (Ye et al., 2013). To overcome the aggregation, the design of twist PDI dimer derivatives linked at the imide positions or bay positions were designed. Bis-PDI-T-EG is an example of PDI dimmer linked by a thiophene group at bay position with a bandgap of 1.81 eV. A PCE of 6.1% was achieved when it was blended with PBDTTT-C-T by finely tuning the active layer morphology (Zhang et al., 2013, 2015). Recently, various linkers in PDI–π-linker–PDI type systems were reported, giving PCEs up to 9.5% (Liu et al., 2016; McAfee et al., 2017; Welsh et al., 2018a,b). In addition, the introduction of annulation to PDI molecular is another strategy to significantly improve performance giving PCEs in the range of 7–8% (Sun et al., 2015; Hendsbee et al., 2016; Meng et al., 2016; Dayneko et al., 2018). Although a great amount of work has been done in developing new PDI derivatives to restrict their intrinsic aggregation tendency, little work paid attention to the effect of the polymer donor selection on PDI-based on PSCs. PBDB-T, also named as PCE12, worked modest with PCBM, but performed amazingly high PCE with NFAs (Zhao et al., 2016b). PBDTTT-EFT, also named as PCE10 was found to be efficient with both fullerene-based acceptors and NFAs (Chen et al., 2015; Zhang et al., 2017). Despite the different absorption profiles, the working principle of these benchmark polymer donors with one PDI acceptor was rarely compared. To this end, we compared the PSCs made with PCE12 and PCE10 as the electron donors, and 1,1′-bis(2-methoxyethoxyl)-7,7′-(2,5-thienyl) bis-PDI (Bis-PDI-T-EG) as the electron acceptor. If not otherwise mentioned, we will refer PCE10 to PBDTTT-EFT, PCE12 to PBDB-T, and PDI to Bis-PDI-T-EG. The chemical structures of the PCE10, PCE12 and Bis-PDI-T-EG were shown in **Figure 1A**. Herein, we compared their differences in device performance, charge carrier mobility, recombination mechanism, and film morphology. The PSCs of PCE12/PDI and PCE10/PDI can give a PCE of 3 and 5.3%, respectively, both with FF about ∼50–60%. The hole mobilities of both devices were similar, 3.4×10^{-4} and 6.4×10^{-4} cm^2/V s for PCE12/PDI and PCE10/PDI, respectively. However, the electron mobilities were 2.3×10^{-6} and 1.2×10^{-5} cm^2/V s, which were much lower than the hole mobilities. The low and unbalanced charge carrier mobilities should be one of the limiting factors for the low FF of these PSCs. By combining photoluminescence (PL) quenching efficiency, light intensity dependent J-V measurements, transient photocurrent and transient photovoltage, we systematically studied the recombination profiles in two systems. Both systems showed a similar extent of bimolecular recombination, while the PCE10/PDI device suffered a severe trap-assisted recombination. The high electron mobility should be the key factor for efficient charge extraction and thus the high performance in PCE10/PDI devices. The mobility was resulted from the morphological difference, i.e., the distinct aggregation and phase separation in the blends. The results indicate that it is important to examine the donor and acceptor aggregation nature when we make choice of donors for Bis-PDI-T-EG based PSCs.

RESULTS AND DISCUSSION

Optical Properties and Photovoltaic Device Performance

Figure 1B shows the normalized UV-Vis absorption spectra of PCE10, PCE12, Bis-PDI-T-EG and their blend films. In the spectra, there are two distinguished features: (1) the absorption spectra of PCE12 and PDI substantially overlap with each other in the visible range from 450 to 700 nm; (2) the absorption spectra of PCE10 and PDI are well complementary to each other, covering the wavelength range from 300 to 800 nm. Thus, the PCE10/PDI blend film has the potential to harvest more photon energy compared with that of PCE12/PDI, which may result in higher short circuit current (J_{SC}) in the devices (Xiao et al., 2017b).

The lowest unoccupied molecular orbital (LUMO) and the highest occupied molecular orbital (HOMO) offsets between the donor and the acceptor are shown in **Figure 1C** (Zhang et al., 2014, 2015; Zhao et al., 2016b). It is noticeable that the existing energy offsets for electron transfer from donor to acceptor and the hole transfer from acceptor to donor are sufficient in both PCE10/PDI and PCE12/PDI systems. We also notice the HOMO energy difference in PCE10 and PCE12, i.e., the HOMO of PCE12 is about 0.1 eV deeper compared with that of PCE10, which may lead to a higher device open circuit voltage (V_{OC}). Proper device performance is expected for both polymer/PDI blends.

We fabricated solar cells in inverted device architecture to check the photovoltaic properties of the two blends. The device performance of optimized PSCs are listed in **Table 1**, and the optimal current density-voltage (J–V) curves and the corresponding external quantum efficiency (EQE) spectra are displayed in **Figures 1D,E**. As shown in **Table 1**, the device made with PCE12/PDI can yield PCEs of 3% in average, with a modest JSC and FF value of 6.15 mA cm^{-2} and 52%, respectively. As predicted from the energy alignment, the VOC is quite high with a value of 0.94 V. On the other hand, the device made with PCE10/PDI can yield markedly better PCEs of 5.3% in average,

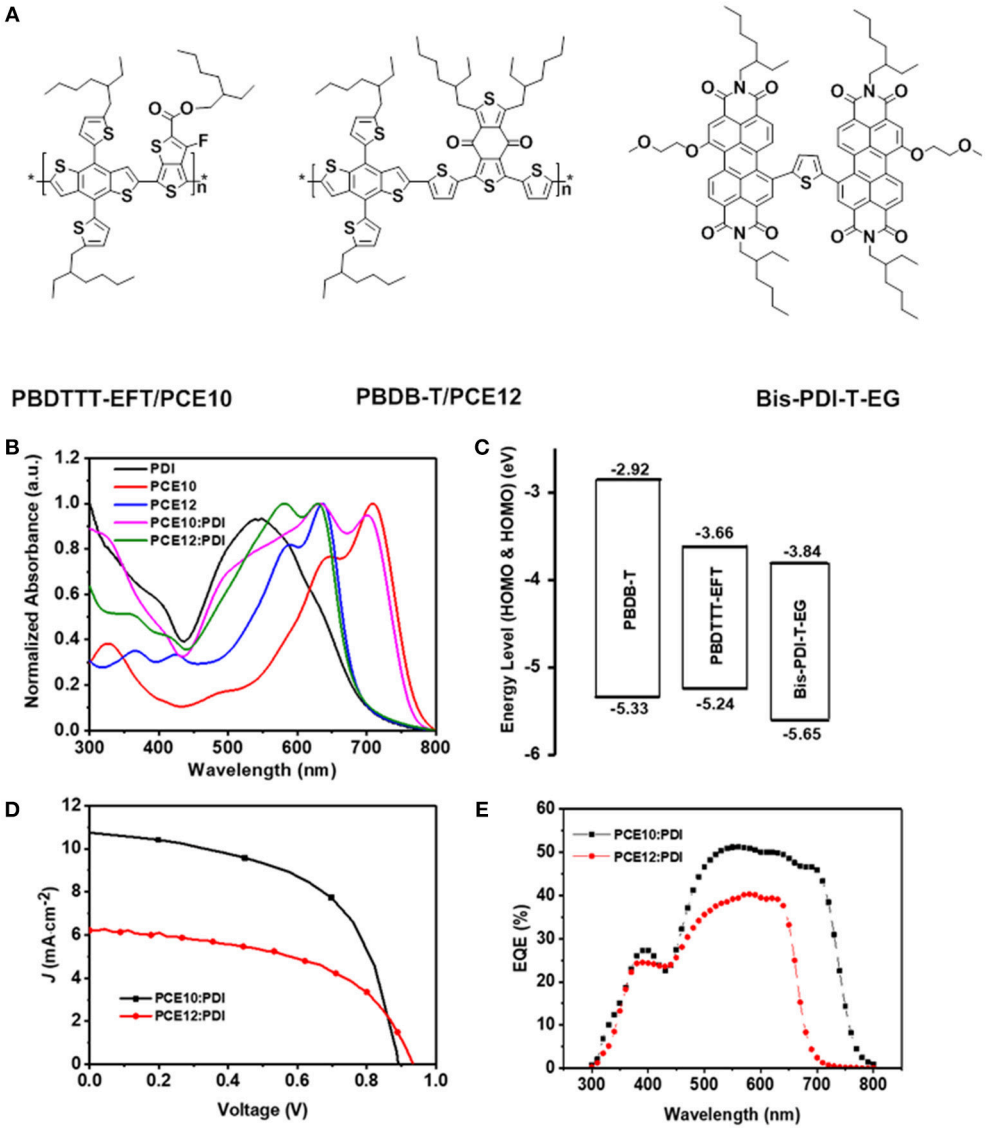

FIGURE 1 | (A) The chemical structures of the PBDTTT-EFT/PCE10, PBDB-T/PCE12 and Bis-PDI-T-EG, **(B)** Normalized UV-Vis absorption spectra, **(C)** Energy-level diagrams, **(D)** J–V characteristics and **(E)** EQE spectra of the PSCs based on PCE10/PDI and PCE12/PDI.

with a JSC value of 10.61 mA cm^{-2}, a FF value of 56% and a VOC value of 0.89 V. The apparent difference in the value of JSC is also observed in the EQE spectra plotted in **Figure 1E**. The EQE spectra of devices made with PCE10/PDI cover the range from 300 to 800 nm, while the PCE12/PDI devices only cover the spectra range from 300 to 750 nm. Furthermore, the maximum EQE in PCE10/PDI devices is about 10% higher than that of the PCE12/PDI devices. One should note that the integrated J_{SC} from the EQE spectra was within 5% deviation compared to the one measured under solar simulator.

To further understand the differences in J_{SC}, we performed optical simulation on the maximum J_{SC} in the two blends by considering the internal quantum efficiency (IQE) to be 100% and only relating with absorption. As shown in **Figures S1A,B** (Margulis et al., 2013), we found that the values of $J_{SC,max}$ of PCE12/PDI and PCE10/PDI were 12.80 and 15.70 mA cm^{-2} at the optimized film thickness and the difference of the calculated Jsc (12.8/15.7 = 0.815) was much closer compared with the measured values (6.15/10.61 = 0.579). The averaged IQE can be estimated as a ratio of measured J_{SC} to maximum theoretical $J_{SC,max}$ obtained as mentioned above by optical

TABLE 1 | Device performance of PSCs based on different donors.

Active layer	J_{SC}(mA cm^{-2})	V_{OC}(V)	FF	PCE (%)
PCE12/PDI	6.15	0.94	0.52	3.00
PCE10/PDI	10.61	0.89	0.56	5.29

Values were averaged from 10 working devices.

simulation. In addition, the IQE can be separated into two contributions which are charge generation efficiency (η_{gen}) and charge collection (and transport) efficiency (η_{coll}) (Benten et al., 2016):

$$IQE = \frac{J_{sc}}{J_{sc,max}} = \frac{\eta_{gen}}{\eta_{coll}} \quad (1)$$

The average IQE with value of 48% (PCE12/PDI) and 68% (PCE10/PDI) were obtained. We attribute the larger current density deviation of measured J_{SC} and the non-unity IQE to not only the different absorption but also great related with recombination, and charge transport.

TABLE 2 | The parameters in the equation of the measured dark current density.

Definition	Variable	Units
Zero-field mobility	μ_0	$cm^2\ V^{-1}\ s^{-1}$
Film thickness	L	cm
Dark current density	J	$mA\ cm^{-2}$
Voltage	V	V
Vacuum permittivity	ε_0 (88.54×10^{-12})	$mA\ s\ V^{-1}\ cm^{-1}$
Dielectric constant	ε_r (3)	
Field activation factor	β	$cm^{1/2}\ V^{-1/2}$

Charge Transport and Recombination

Before examining the charge recombination happened in the devices, we first checked the charge transport by space charge limited current (SCLC) model (Blakesley et al., 2014). The measured dark current density was fitted with the following equation and the parameters are listed in **Table 2**:

$$J(V) = \frac{9}{8}\varepsilon_0\varepsilon_r\mu_0 \exp\left(0.89\beta\sqrt{\frac{V}{L}}\right)\frac{(V)^2}{L^3} \quad (2)$$

The dark current density and fitting curve are shown in **Figures S2A,B**. The hole mobilities of 3.4×10^{-4} and 6.4×10^{-4} $cm^2/V\ s$ were obtained for the blends of PCE12/PDI and PCE10/PDI. The electron mobilities of PCE12/PDI and PCE10/PDI were 2.3×10^{-6} and 1.2×10^{-5} $cm^2/V\ s$, respectively, which were much lower than the hole mobilities. It is worth noting that the imbalance of hole and electron mobilities is likely the origin of significant space charge build-up in the optimized polymer/PDI solar cells, which in turn limits the photovoltaic performance.

The photoluminescence (PL) quenching efficiency is one of the methods to check whether the donor/acceptor combination may work or not. Low quenching efficiency usually relates to large domain size of the donor and acceptor and can translate to severe geminate recombination and poor exciton dissociation efficiency, resulting in bad device performance (Ye et al., 2013; Liu

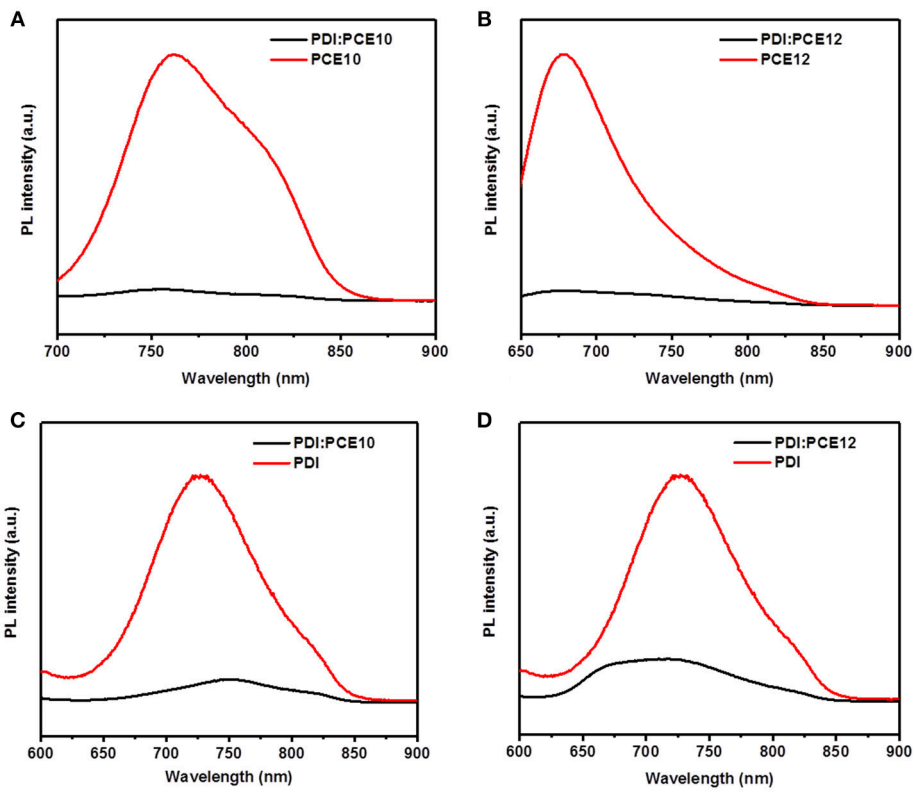

FIGURE 2 | The PL spectra of **(A)** PCE10, PCE10/PDI, **(B)** PCE12, PCE12/PDI, **(C)** PDI, PCE10/PDI, and **(D)** PDI, PCE12/PDI.

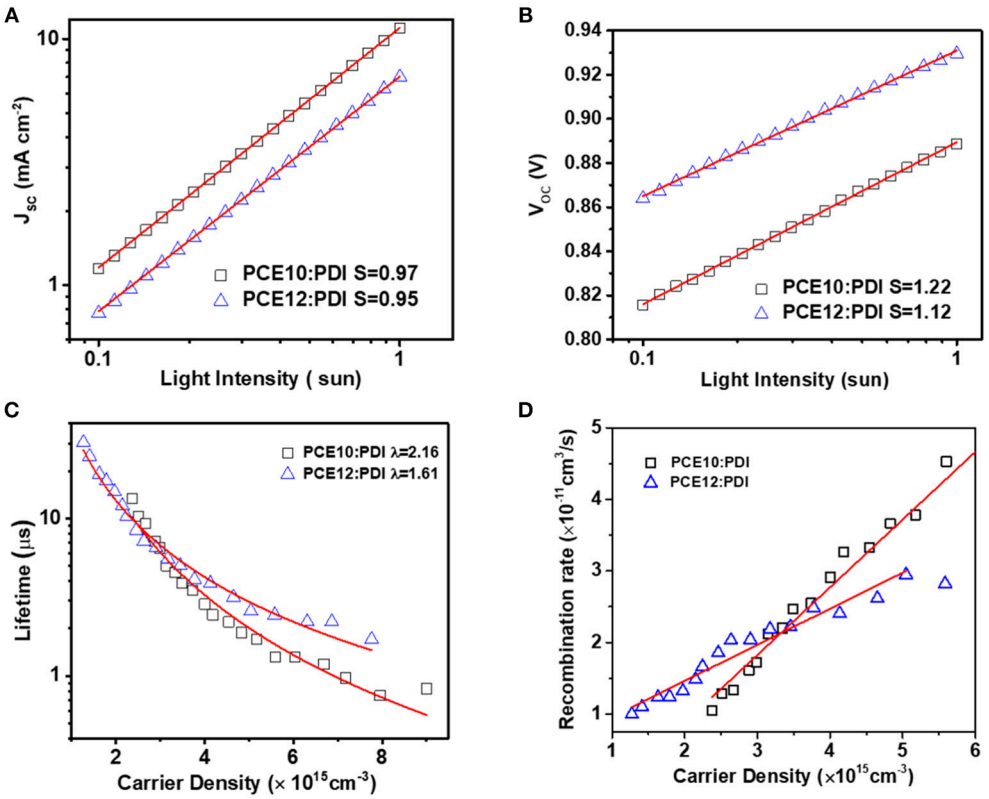

FIGURE 3 | (A) J_{SC} vs. light intensity curves, and **(B)** V_{OC} vs. light intensity measurements **(C)** Carrier lifetime as a function of carrier density and **(D)** Recombination rate as a function of charge carrier density. Obtained from TPC and TPV based on PCE10/PDI and PCE12/PDI.

et al., 2016). When the donors and acceptor were photoexcited individually, the PL quenching were shown in **Figures 2A–D**. As depicted in the **Figures 2A,B**, PL quenching efficiencies of 95% and 92% were achieved when the donor materials were excited at 680 nm and 620 nm, respectively. The PL quenching efficiencies larger than 90% suggest that the energy loss of geminate recombination in donor materials is secondary. When the acceptor was excited at 550 nm, PL quenching efficiencies of 89% and 77% were obtained as shown in **Figures 2C,D**. The lower PL quenching efficiencies indicate that the energy loss of geminate recombination in the blends is severe when the acceptor was excited. As presented in **Figures 2B,D**, PCE12/PDI system behaves lower PL quenching efficiency and more severe geminate recombination when both the donor material and acceptor were excited (Ye et al., 2013).

Light intensity dependent J_{SC} and V_{OC} were reported as an easy way to probe the recombination patterns in PSCs. In general, the J_{SC} was plotted against incident light intensity in a log-log scale, following a relationship: $J_{SC} \propto I^{\alpha}$, whereby 1) $\alpha = 1$ indicates that all dissociated free carriers are swept out of the device prior to the bimolecular recombination and 2) $\alpha < 1$ implies a dependence of J_{SC} on bimolecular recombination. As shown in **Figure 3A** and **S3**, the α was fitted with a value of 0.95 (±0.01) and 0.97 (±0.01) for PCE12/PDI and PCE10/PDI devices, respectively, suggesting that there was a certain extent of bimolecular recombination in both devices. The comparable α value means that bimolecular recombination was similar in both devices (Cowan et al., 2010; Koster et al., 2011). Next, we fitted the V_{OC}/incident light intensity in a natural-log scale to a relationship: $V_{OC} \propto nkT/q \ln(I)$, where k, T, and q are the Boltzmann constant, temperature in Kelvin, and the elementary charge, respectively. The parameter n (usually in the range of 1–2) reflects the presence/absence of carrier traps across the active layers or at interfaces with the electrodes. Any deviations from $n = 1$ (trap-free condition) point to the existence of the effect of trap-assisted recombination. As presented in **Figure 3B** and **S3**, the n-values for PCE12/PDI and PCE10/PDI are 1.12 (±0.02) and 1.22 (±0.10), respectively. The n value larger than 1 indicates that trap-assisted recombination is in both devices and the relatively larger n value of PCE10/PDI implies that trap-assisted recombination is more severe in the PCE10/PDI devices (Koster et al., 2005).

To have a deeper understand on the recombination profiles and quantitatively recombination characteristics, we then performed transient photocurrent (TPC) and transient photovoltage (TPV) characteristics (Li et al., 2011). From **Figures S4A,B**, we noticed that in both systems, the current reached to steady state current within 2 μs without current spike, in both systems, resulting from proper charge generation. By integrating the current after the pulse lights off, the total

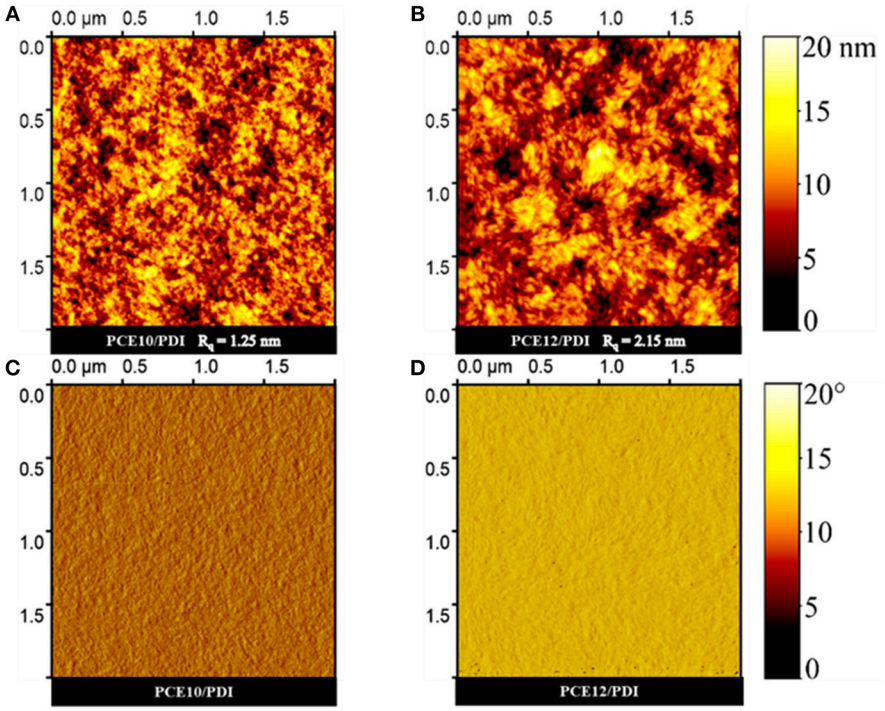

FIGURE 4 | AFM topographical height **(A,B)** and phase images **(C,D)** of PCE10/PDI and PCE12/PDI films.

generated charges can be estimated as discussed later in this part. We further compared the normalized TPC of the two systems at 1 sun condition, and it was found that the current decay in the system of PCE10/PDI was faster than that of the PCE12/PDI system shown in **Figure S6**, implying that the charge extraction in PCE10/PDI was better, in agreement with the results we made on the mobility measurement. While TPC provides the information on charge generation and extraction at short circuit condition, TPV gives the information on charge carrier lifetime and recombination at open circuit condition. The carrier life time was 1.7 and 0.9 μs for PCE12/PDI and PCE10/PDI systems at V_{OC} condition, respectively. The longer carrier life time of PCE12/PDI indicating reduced recombination loss. As fitted in **Figure 3C** and **S5**, the charge carrier lifetime changes with the charge carrier density following the relationship of $\tau = \tau_0 n^{-\lambda}$, where τ is the carrier lifetime, n is the carrier density, λ is the recombination order. The recombination order $\lambda = 2$ implies pure bimolecular recombination in the deceives, and other λ value implies both bimolecular recombination and trap-assisted recombination. We found that $\lambda = 1.61$ (±0.04) and $\lambda = 2.16$ (±0.10) were obtained from PCE12/PDI and PCE10/PDI systems. Based on the recombination order, the recombination rate then can be calculated as $k_{rec} = \frac{1}{(1+\lambda)n\tau}$ (shown in **Figure 3D**) (Guo et al., 2013; Li et al., 2016). We can find that the k_{rec} of PCE12/PDI is lower than that of PCE10/PDI when charge carrier density is larger than 3.3×10^{15} cm^{-3}. While close to the 1 sun condition, the charge carrier density is far larger than 3.3×10^{15} cm^{-3}, and then k_{rec} of PCE12/PDI is far lower than that of PCE10/PDI. Overall, light intensity dependent J_{SC} and TPC indicate the bimolecular recombination was comparable and the charge extraction in PCE10/PDI was better; the light intensity dependent V_{oc} and TPV study suggest that the dominating recombination route in PCE10/PDI device was trap-assisted recombination which leads to a severe recombination rate. One may argue that the recombination rate of PCE12/PDI system was lower than that of the PCE10/PDI thus, it appears to contradict with the better device performance of PCE10/PDI. Here we remind our readers that the electron mobility of PCE12/PDI device is about 5 times slower than that of PCE10/PDI device, so we conclude that the high electron mobility should be a very important factor to give an efficient charge extraction and then the device performance in PCE10/PDI devices.

Morphology Characterization

Finally, we studied the morphological properties of the PCE12/PDI and PCE10/PDI blend films using tapping-mode atomic force microscopy (AFM). The PCE12/PDI film shows a rougher surface (Rq = 1.25 nm) than that of PCE10/PDI (Rq = 1.25 nm, see **Figures 4A,B**). What's more, larger extend of the phase separation with granular aggregate sizes was observed for PCE12/PDI blend films, as shown in **Figures 4C,D** and **Figure S7**. Due to the limited exciton dissociation length (10–20 nm), smaller extent of phase-separation is beneficial for realizing efficient exciton dissociations in the device, suggesting that PCE10/PDI film has a more favourable morphology than that of the PCE12/PDI film. The morphology results well explained the low PL quenching efficiency of PCE12/PDI owing to the strong geminate recombination. The low carrier

mobility of PCE12/PDI can also be attributed to the large phase-separation, breaking the continuous pathway for electron transport. Therefore, we can conclude that the PCE12 is tending to form large size aggregations with Bis-PDI-T-EG, which is unfavorable to device performance. While PCE10 presents better compatibility with Bis-PDI-T-EG, favorable phase separation can be expected in the blend. As reported, PCE12 tends to aggregate in films and PCE10 has the tendency of forming amorphous films (Zhao et al., 2016b; Baran et al., 2017, 2018). The differences in the chemical structure of PCE12 and PCE10 should be responsible for the significant difference in thin film morphology, and it is important to check the donor materials' aggregation nature when those were chosen for PSCs with Bis-PDI-T-EG as the acceptor.

CONCLUSION

In this work, we systematically compared two polymer/PDI blends on their optical properties, photovoltaic performance, charge carrier transport and recombination, and the thin film morphology. We found that the PCE10/PDI and PCE12/PDI can give a PCE of 5.3 and 3%, respectively, both with FF about ∼50–60%. The hole mobilities of both devices are comparable, 3.4×10^{-4} and 6.4×10^{-4} cm^2/V s were obtained for PCE12/PDI and PCE10/PDI, respectively. However, the electron mobilities behave 5 times difference, 2.3×10^{-6} and 1.2×10^{-5} cm^2/V s were obtained for PCE12/PDI and PCE10/PDI, respectively. The obvious unbalanced charge carrier mobility resulted in low FF of these PSCs. By combining PL quenching efficiency, light intensity dependent J-V measurements, transient photocurrent and transient photovoltage, we noticed that both systems showed a similar extend of bimolecular recombination and PCE10/PDI behaved a severe trap-assisted recombination. Although the recombination rate of PCE10/PDI system was stronger than that of the PCE12/PDI, the high electron mobility and the wide absorption spectrum of PCE10/PDI film result in better device performance in PCE10/PDI devices. The mobility was determined by the distinct aggregation and phase-distribution in the blend. Our findings suggest that it is important to check the aggregation nature of donor materials for Bis-PDI-T-EG based PSCs, and a proper choice is that donor material doesn't tend to aggregate, leading to favorable phase separation.

AUTHOR CONTRIBUTIONS

TY, ZK, CZ, and SL proposed the idea of this paper and contributed to analize the experiment results and wring the paper. ZK, TY, and XZ contributed to the fabrication of the solar cells and characterization. SJ, CK, and CT contributed to the synthesis of the Bis-PDI-T-EG acceptor.

FUNDING

This work was supported by the National Science Foundation of China (Grant No. 51502058, 61504041), CAS Pioneer Hundred Talents Program (Y82A060Q10), the China Postdoctoral Science Foundation (Grant No. 2015M570284), the Postdoctoral Foundation of Heilongjiang Province (LBH-TZ0604), and the Special Fund of Technological Innovation Talents in Harbin City (Grant No. 2017RAQXJ085).

SUPPLEMENTARY MATERIAL

The Supplementary Material for this article can be found online at: https://www.frontiersin.org/articles/10.3389/fchem.2018.00613/full#supplementary-material

REFERENCES

Baran, D., Ashraf, R. S., Hanifi, D. A., Abdelsamie, M., Gasparini, N., Röhr, J. A., et al. (2017). Reducing the efficiency-stability-cost gap of organic photovoltaics with highly efficient and stable small molecule acceptor ternary solar cells. *Nat. Mater.* 16, 363–369. doi: 10.1038/nmat4797

Baran, D., Gasparini, N., Wadsworth, A., Tan, C. H., Wehbe, N., Song, X., et al. (2018). Robust nonfullerene solar cells approaching unity external quantum efficiency enabled by suppression of geminate recombination. *Nat. Commun.* 9:2059. doi: 10.1038/s41467-018-04502-3

Benten, H., Nishida, T., Mori, D., Xu, H., Ohkita, H., and Ito, S. (2016). High-performance ternary blend all-polymer solar cells with complementary absorption bands from visible to near-infrared wavelengths. *Energy Environ. Sci.* 9, 135–140. doi: 10.1039/c5ee03460d

Blakesley, J. C., Castro, F. A., Kylberg, W., Dibb, G. F. A., Arantes, C., Valaski, R., et al. (2014). Towards reliable charge-mobility benchmark measurements for organic semiconductors. *Org. Electron. Phys. Mater. Appl.* 15, 1263–1272. doi: 10.1016/j.orgel.2014.02.008

Chen, J. D., Cui, C., Li, Y. Q., Zhou, L., Ou, Q. D., Li, C., et al. (2015). Single-junction polymer solar cells exceeding 10% power conversion effi ciency. *Adv. Mater.* 27, 1035–1041. doi: 10.1002/adma.201404535

Cheng, P., and Zhan, X. (2016). Stability of organic solar cells: challenges and strategies. *Chem. Soc. Rev.* 45, 2544–2582. doi: 10.1039/C5CS00593K

Cowan, S. R., Roy, A., and Heeger, A. J. (2010). Recombination in polymer-fullerene bulk heterojunction solar cells. *Phys. Rev. B* 82:245207. doi: 10.1103/PhysRevB.82.245207

Cui, Y., Yao, H., Yang, C., Zhang, S., and Hou, J. (2018). Organic solar cells with an efficiency approaching 15%. *Acta Polym. Sin.* 2, 223–230. doi: 10.11777/j.issn1000-3304.2018.17297

Dayneko, S. V., Hendsbee, A. D., Welch, G. C., Dayneko, S. V., Hendsbee, A. D., and Welch, G. C. (2018). Combining facile synthetic methods with greener processing for efficient polymer-perylene diimide based organic solar cells. *Small Methods 2*:1800081. doi: 10.1002/smtd.201800081

Eftaiha, A. F., Sun, J.-P., Hill, I. G., and Welch, G. C. (2014). Recent advances of non-fullerene, small molecular acceptors for solution processed bulk heterojunction solar cells. *J. Mater. Chem. A* 2, 1201–1213. doi: 10.1039/C3TA14236A

Guo, X., Zhou, N., Lou, S. J., Smith, J., Tice, D. B., Hennek, J. W., et al. (2013). Polymer solar cells with enhanced fill factors. *Nat. Photonics* 7, 825–833. doi: 10.1038/nphoton.2013.207

Hendsbee, A. D., Sun, J. P., Law, W. K., Yan, H., Hill, I. G., Spasyuk, D. M., et al. (2016). Synthesis, self-assembly, and solar cell performance of N-annulated perylene diimide non-fullerene acceptors. *Chem. Mater.* 28, 7098–7109. doi: 10.1021/acs.chemmater.6b03292

Koster, L. J., Kemerink, M., Wienk, M. M., Maturová, K., and Janssen, R. A. J. (2011). Quantifying bimolecular recombination losses in organic bulk heterojunction solar cells. *Adv. Mater.* 23, 1670–1674. doi: 10.1002/adma.201004311

Koster, L. J. A., Mihailetchi, V. D., Ramaker, R., and Blom, P. W. M. (2005). Light intensity dependence of open-circuit voltage of polymer:fullerene solar cells. *Appl. Phys. Lett.* 86:123509. doi: 10.1063/1.1889240

Li, H., Xiao, Z., Ding, L., and Wang, J. (2018). Thermostable single-junction organic solar cells with a power conversion efficiency of 14.62%. *Sci. Bull.* 63, 340–342. doi: 10.1016/j.scib.2018.02.015

Li, J., Jiu, T., Li, B., Kuang, C., Chen, Q., Ma, S., et al. (2016). Inverted polymer solar cells with enhanced fill factor by inserting the potassium stearate interfacial modification layer. *Appl. Phys. Lett.* 108:181602. doi: 10.1063/1.4948585

Li, Z., Gao, F., Greenham, N. C., and McNeill, C. R. (2011). Comparison of the operation of polymer/fullerene, polymer/polymer, and polymer/nanocrystal solar cells: a transient photocurrent and photovoltage study. *Adv. Funct. Mater.* 21, 1419–1431. doi: 10.1002/adfm.201002154

Lin, Y., Wang, J., Zhang, Z.-G., Bai, H., Li, Y., Zhu, D., et al. (2015a). An electron acceptor challenging fullerenes for efficient polymer solar cells. *Adv. Mater.* 27, 1170–1174. doi: 10.1002/adma.201404317

Lin, Y., Zhang, Z.-G., Bai, H., Wang, J., Yao, Y., Li, Y., et al. (2015b). High-performance fullerene-free polymer solar cells with 6.31% efficiency. *Energy Environ. Sci.* 8, 610–616. doi: 10.1039/C4EE03424D

Liu, J., Chen, S., Qian, D., Gautam, B., Yang, G., Zhao, J., et al. (2016). Fast charge separation in a non-fullerene organic solar cell with a small driving force. *Nat. Energy* 1:16089. doi: 10.1038/nenergy.2016.89

Margulis, G. Y., Hardin, B. E., Ding, I. K., Hoke, E. T., and McGehee, M. D. (2013). Parasitic absorption and internal quantum efficiency measurements of solid-state dye sensitized solar cells. *Adv. Energy Mater.* 3, 959–966. doi: 10.1002/aenm.201300057

McAfee, S. M., Dayneko, S. V., Josse, P., Blanchard, P., Cabanetos, C., and Welch, G. C. (2017). Simply complex: the efficient synthesis of an intricate molecular acceptor for high-performance air-processed and air-tested fullerene-free organic solar cells. *Chem. Mater.* 29, 1309–1314. doi: 10.1021/acs.chemmater.6b04862

Meng, D., Sun, D., Zhong, C., Liu, T., Fan, B., Huo, L., et al. (2016). High-performance solution-processed non-fullerene organic solar cells based on selenophene-containing perylene bisimide acceptor. *J. Am. Chem. Soc.* 138, 375–380. doi: 10.1021/jacs.5b11149

Meng, L., Zhang, Y., Wan, X., Li, C., Zhang, X., Wang, Y., et al. (2018). Organic and solution-processed tandem solar cells with 17.3% efficiency. *Science* 361, 1094–1098. doi: 10.1126/science.aat2612

Sun, D., Meng, D., Cai, Y., Fan, B., Li, Y., Jiang, W., et al. (2015). Non-fullerene-acceptor-based bulk-heterojunction organic solar cells with efficiency over 7%. *J. Am. Chem. Soc.* 137, 11156–11162. doi: 10.1021/jacs.5b06414

Welsh, T. A., Laventure, A., Baumgartner, T., and Welch, G. C. (2018a). Dithienophosphole-based molecular electron acceptors constructed using direct (hetero)arylation cross-coupling methods. *J. Mater. Chem. C* 6, 2148–2154. doi: 10.1039/c7tc05631a

Welsh, T. A., Laventure, A., and Welch, G. (2018b). Direct (Hetero)arylation for the synthesis of molecular materials: coupling Thieno[3,4-c]pyrrole-4,6-dione with Perylene Diimide to yield novel non-fullerene acceptors for organic solar cells. *Molecules* 23:931. doi: 10.3390/molecules23040931

Xiao, Z., Jia, X., and Ding, L. (2017a). Ternary organic solar cells offer 14% power conversion efficiency. *Sci. Bull.* 62, 1562–1564. doi: 10.1016/j.scib.2017.11.003

Xiao, Z., Jia, X., Li, D., Wang, S., Geng, X., Liu, F., et al. (2017b). 26 mA cm $^{-2}$ Jsc from organic solar cells with a low-bandgap nonfullerene acceptor. *Sci. Bull.* 62, 1494–1496. doi: 10.1016/j.scib.2017.10.017

Ye, T., Singh, R., Butt, H. J., Floudas, G., and Keivanidis, P. E. (2013). Effect of local and global structural order on the performance of perylene diimide excimeric solar cells. *ACS Appl. Mater. Interfaces* 5, 11844–11857. doi: 10.1021/am4035416

Zhang, G., Yang, G., Yan, H., Kim, J. H., Ade, H., Wu, W., et al. (2017). Efficient nonfullerene polymer solar cells enabled by a novel wide bandgap small molecular acceptor. *Adv. Mater.* 29:1606054. doi: 10.1002/adma.201606054

Zhang, S., Ye, L., Zhao, W., Liu, D., Yao, H., and Hou, J. (2014). Side chain selection for designing highly efficient photovoltaic polymers with 2D-conjugated structure. *Macromolecules* 47, 4653–4659. doi: 10.1021/ma500829r

Zhang, X., Lu, Z., Ye, L., Zhan, C., Hou, J., Zhang, S., et al. (2013). A potential perylene diimide dimer-based acceptor material for highly efficient solution-processed non-fullerene organic solar cells with 4.03% efficiency. *Adv. Mater.* 25, 5791–5797. doi: 10.1002/adma.201300897

Zhang, X., Zhan, C., and Yao, J. (2015). Non-fullerene organic solar cells with 6.1% efficiency through fine-tuning parameters of the film-forming process. *Chem. Mater.* 27, 166–173. doi: 10.1021/cm504140c

Zhao, J., Li, Y., Yang, G., Jiang, K., Lin, H., Ade, H., et al. (2016a). Efficient organic solar cells processed from hydrocarbon solvents. *Nat. Energy.* 1:15027. doi: 10.1038/NENERGY.2015.27

Zhao, W., Qian, D., Zhang, S., Li, S., Inganäs, O., Gao, F., et al. (2016b). Fullerene-free polymer solar cells with over 11% efficiency and excellent thermal stability. *Adv. Mater.* 28, 4734–4739. doi: 10.1002/adma.201600281

Conflict of Interest Statement: The authors declare that the research was conducted in the absence of any commercial or financial relationships that could be construed as a potential conflict of interest.

frontiers in Chemistry

ORIGINAL RESEARCH
published: 28 November 2018
doi: 10.3389/fchem.2018.00578

Pyrene-Imidazole Based Aggregation Modifier Leads to Enhancement in Efficiency and Environmental Stability for Ternary Organic Solar Cells

*Hui Lin†, Xiaoyang Du†, Lijuan Li, Caijun Zheng and Silu Tao**

School of Optoelectronic Science and Engineering, University of Electronic Science and Technology of China, Chengdu, China

OPEN ACCESS

Edited by:
Chuanlang Zhan, Institute of Chemistry (CAS), China

Reviewed by:
Zhan'Ao Tan, North China Electric Power University, China
In Hwan Jung, Kookmin University, South Korea

***Correspondence:**
Silu Tao
silutao@uestc.edu.cn

†These authors have contributed equally to this work

Specialty section:
This article was submitted to Organic Chemistry, a section of the journal Frontiers in Chemistry

Received: *14 September 2018*
Accepted: *06 November 2018*
Published: *28 November 2018*

Citation:
Lin H, Du X, Li L, Zheng C and Tao S (2018) Pyrene-Imidazole Based Aggregation Modifier Leads to Enhancement in Efficiency and Environmental Stability for Ternary Organic Solar Cells. Front. Chem. 6:578. doi: 10.3389/fchem.2018.00578

A novel pyrene-imidazole derivative (PyPI), which can form effcient π-π stacking in solid film, has been utilized in organic solar cells (OSCs). The stacking of small a molecule PyPI can facilitate a charge transfer and suppress fullerene aggregation. As a result, PTB7-Th: PyPI: $PC_{71}BM$ based ternary OSC exhibits a high power conversion efficiency (PCE) of 10.36%, which presents a 15.88% increase from the binary device (8.94%). Concurrently, the ternary OSC shows a much better thermal and light illumination stability. Under continuous 60°C annealing for 3 h, in atmosphere, the device still remains at 94.13% efficiency more than the pristine state, while the control device remains at 52.47% PCE. Constant illumination under Air Mass (AM) 1.5G irradiation (100 mW cm^{-2}) in atmosphere, the PCE of OSC remains at 72.50%. The high conversion efficiency and excellent environmental stability of the PyPI based ternary OSC, has narrowed the gap between laboratory investigation and industrial production.

Keywords: pyrene-imidazole, π-π stacking, organic solar cells, fullerene aggregation, environmental stability

INTRODUCTION

Solvent processed organic solar cells (OSCs) have attracted extensive attention for their superiority in achieving high power conversion efficiency (PCE), low fabrication cost and fascinating potential application in flexible electronics (Kaltenbrunner et al., 2012; Chen et al., 2014; Cui et al., 2017; Bergqvist et al., 2018; Cheng et al., 2018; Zhang H. et al., 2018). Generally, existing OSCs can be classified as binary, tandem, and ternary structures. In a traditional bulk heterojunction binary system, although the matched donor and acceptor can form a bicontinuous network interpenetrating structure to accelerate exciton dissociation and charge collection, the narrowed absorption bonds limited the further optimization on the device efficiency (Huang et al., 2017; Xu and Gao, 2018) (Li et al., 2018; Liu et al., 2018). To compensate for the shortcomings of the absoption spectrum, tandem OSCs composed of two or more subcells were fabricated to capture more photons and yielded more photon-generated carriers than conventional single-junction OSCs (Chen S. et al., 2017; Che et al., 2018; Zhang Y. et al., 2018). However, the complexity of the device

structure and intricate interface,caused an increase in the device fabrication cost (Ameri et al., 2009; Kumari et al., 2017).

Compared with tandem OSCs, ternary strategy, which adds a third component to a binary system to broaden the absorption spectrum and promotes an interaction between the donor and acceptor, is an emerging and promising candidate for high performance OSCs with a simple device structure (Lu et al., 2015; Liu et al., 2016; Nian et al., 2016; Chen Y. et al., 2017; Xu et al., 2017). For ternary OSCs, the screening of the third component (either polymers or small molecules) is crucial. Challenges still remain in polymer materials as their purification and reproducibility are poor, further more, the chemical structure of polymers difficult hard to confirm. Other than polymer materials, small molecule materials have a simpler synthetic route and it is easy to obtain high purity. Additionally, the small molecules always have a mono-dispersed structure, with controlled energy levels and negligible batch to-batch variations (Chen et al., 2013; Roncali et al., 2014). Therefore, ternary OSCs using a small molecule as the third component have attracted increasing attention and have a great potential for achieving high-performance OSCs (Park et al., 2016; Chen Y. et al., 2017; Kumari et al., 2017; Zhang et al., 2017). As for the current ternary OSCs, the short-circuit current density's (J_{SC}s) are still limited by the narrowed absorption strength, which is because of the thickness of active layers are confined to about 100 nm (Yang et al., 2015; Zhang J. et al., 2015; Zhang Y. et al., 2015; Zhang et al., 2017; Gasparini et al., 2016). That is to say, finding a way to enhance the J_{SC}s of current OSCs is essential.

In this work, a novel small molecule PyPI (9,10-diphenyl-9H-pyreno[4, 5-d]imidazole) has been utilized to construct ternary organic solar cells. The small molecule PyPI can form efficient π-π stacking in a solid film, which is beneficial to accelerate a charge transfer in an active layer. Furthermore, the addition of PyPI can suppress fullerene aggregation and enhance device stability. For device fabrication, polymer PTB7-Th (poly(4,8-bis(5-(2-ethylhexyl)thiophen-2-yl)benzo[1,2-b;4,5-b0] dithiophene-2,6-diylalt-(4-(2-ethylhexyl)-3-fluorothieno[3,4-b]thiophene-)-2-carboxylate-2-6-diyl), and fullerene $PC_{71}BM$ ([6,6]-phenyl-C_{71}-butyric acid methyl ester) was respectively used as a donor and acceptor. This polymer-fullerene system has great compatibility and is widely used in the field of organic solar cells. After precise modulation, 10% PyPI doped ternary OSC showed a high PCE of 10.36% with an optimized J_{SC} of 19.26 mA/cm^2, which exhibited a 15.88% enhancement from the control device. In addition, after continuous thermal annealling at 60 or 80°C in atmosphere for 180 min, the PCE of the device can also be kept above 89.01%, while the control device remained at 36.96% PCE. The remarkable thermal stability is among the best of fullerene based OSCs. After continuous light illumination under 100 mW/cm^2, the PyPI-containing ternary device also reveals optimized stability with a small efficiency roll-off of 27.23%, while the control device exhibits a huge PCE roll-off of 58.79%. The improvement in environmental stability demonstrates that the addition of the small molecule PyPI indeed supprsses the aggregation of fullerene.

EXPERIMENTAL SECTION

General Information

The materials and solvents utilized in the device fabrication and measurements were received from commercial suppliers without further purification. PTB7-Th (wt. 145,000) and $PC_{71}BM$ was purchased from 1-Material and American Dye Source. PEDOT:PSS was purchased from Xi'an p-OLED Technology Corp. MoO_3 and LiF received from Luminescence Technology Corp. All solvents used in the device fabrication process originated from Sigma-Aldrich or Alfa Chemical.

Device Fabrication and Measurement

Conventional inverted device structures were used for the binary and ternary OSCs. ITO covered glasses with a sheet resistance of 15 Ohm per square was utilized as the substrates for these devices. The substrates were ultrasonically cleaned, in the order of deionized water, ethyl alcohol, acetone and ethyl alcohol. Before transport layers were deposited, the substrates were dried by a nitrogen blow. For the transport layer, ZnO precursor solution was formed by dissolving 110 mg of zinc acetate ($Zn(CH_3COO)_2{\bullet}2H_2O$) and 31 mg of ethanolamine ($NH_2CH_2CH_2OH$) in 1 ml of 2-methoxyethanol ($CH_3OCH_2CH_2OH$) and stirring at room temperature over night. As for the active layers, Donor and acceptor were blended with the ratio of 1:1.5, where the donor contained PTB7-Th and the small molecule PyPI, with varying proportions and maintained at a total concentration of 10 mg/ml. Chlorobenzene (CB) was used as the solvent for each of the devices. 3.0 vol% 1,8-diiodooctane (DIO) was added in the mixture as an additive. The active layer precursor solution was stirred in a nitrogen filled glove box for 24 h. For OSC fabrication, ZnO nano-particles were formed by spin-coating the precursor solution with 5,000 rpm for 30 s, after which the substrates were transferred to a heating stage and annealed immediately at 200°C for 1 h in atmosphere. The substrates were the transferred to the glove box and the active layer precursor solutions were spin-coated onto the ZnO buffer layer to yield an uniform film (∼120 nm). After that, the substrates were transferred to a vacuum deposition chamber and when the pressure of the chamber reached 5×10^{-4} Pa, 10 nm MoO_3 and 150 nm, Ag were evaporated at a rate of 0.5 and 3 Å/s, subsequently. An active area of 2.3 mm^2 was formed by a shadow mask.

Experimental Measurements

UV absorption spectra and photoluminescence spectra of monomeric and blend films were recorded by a Hitachi U-3010 UV-VS spectrophotometer and a Perkin-Elmer LS50B Luminescence spectrophotometer, respectively. The HOMO/LUMO energy level was determined by cyclic voltammetry with a CHI600E electrochemical analyzer. Nitrogen saturated DCM was used as a solvent with 0.1 mol/L tetrabutylammonium hexa?uorophosphate as the supporting electrolyte.

The performance of the solar cells were measured by AM 1.5G simulated sunlight (Newport Oriel Sol3A Simulator, 100 mW/cm^2) with a Keithley 2,400 source meter instrument. EQE

properties were determined by a QEX10 Quantum Efficiency Measurement System (PV Measurements, Inc.). The thicknesses were calibrated by a AMBIOS-XP2 step profilometer. The surface morphologies of the binary and ternary blend films were determained by an atomic force microscope (AFM) under ambient conditions. All the films were formed on ZnO coved substrates. The molecule aggregation and formed domain size were observed by a transmission electron microscopy (TEM) scanning-probe SPM system (Hitachi TEM system) under 100 kV in "Ceshigo Research Service, www.ceshigo.com."

RESULTS AND DISCUSSIONS

Characterization and Optical Properties

The chemical structures of used materials in the device as well as device structure are shown in **Figure 1**. It is well-known that the fullerene aggregates in the interspace between the stacked clearances of polymers, while the small molecule PyPI can form efficient π-π stacking in the clearance in a polymer, which can suppress this inferior phenomenon as indicated in the diagram of **Figure 1A** (Liu et al., 2017).We tested through cyclic voltammetry, that the LOMO and HOMO levels of the small molecule PyPI was −2.37 and −5.42. **Figure 2A** reveals the absorption spectra of PTB7-Th, $PC_{71}BM$ and the small molecule PyPI, the maximum absorption peak for PTB7-Th centered at 704 nm and that of PyPI film was located at 355 and 391 nm. As in the blend films, the increase of small molecule contents along with the absorption intensity, gradually increased in the range of short wavelength, while the intensity declined in turn around long wavelengths of 600–800 nm as shown in **Figure 2B**. This is because the contents of PTB7-Th have been decreased along with the increase of PyPI. Furthermore, PyPI contained films shows a small red-shift in long wavelength absorption, suggesting an enhanced stacking order in polymers, which may be caused by the positive interaction between the small molecule and PTB7-Th.

Photovoltaic Performance

To evaluate the contribution of the π-π stacking effect on the device performance, the small molecule PyPI was utilized as the third component to fabricated ternary OSCs. Device structure was performed as follows: ITO/ ZnO (20 nm) /active layer (120 nm) /MoO_3 (10 nm)/Ag (150 nm) and is shown in **Figure 1A**, a ZnO transport layer was formed with 20 nm thickness and the active layer was prepared in a glove box with

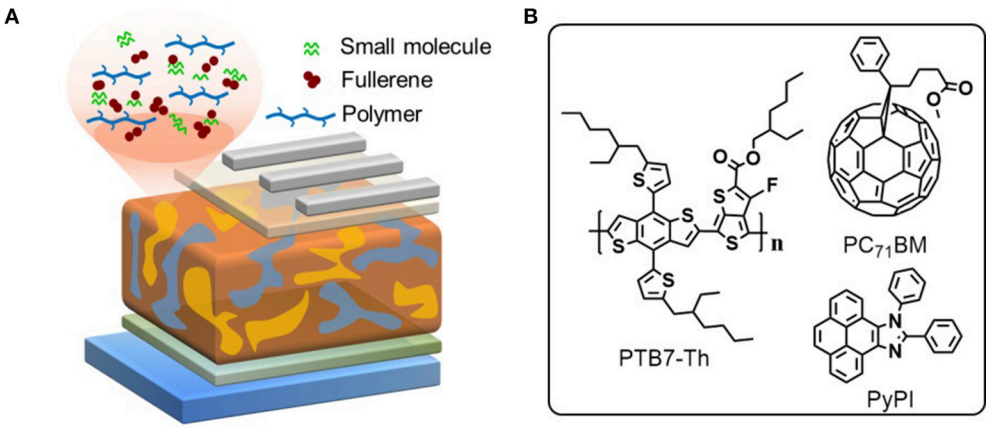

FIGURE 1 | (A) device structure and schematic diagram of the ternary OSC; **(B)** materials structure of the used materials.

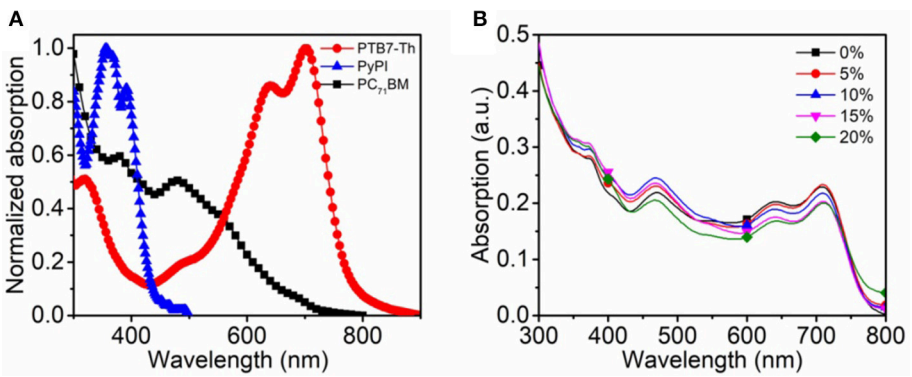

FIGURE 2 | (A) normalized absorption spectra of PTB7-Th, $PC_{71}BM$, and PyPI in neat film; **(B)** absorption spectra of the control and ternary blend films with different components of PyPI.

120 nm thickness. The total donor concentration was kept at 10 mg/ml in CB solvent, where the doping ratio of PyPI was tuned from 0 to 20% in donors. The weight ratio of donor: acceptor was maintained at 1:1.5. DIO was used as a solution additive with a volume ratio of 3%. To estimate the average OSC performance, about 20 samples were fabricated for each parameter.

The current density-voltage (J-V) characteristics of the binary and ternary OSCs are shown in **Figure 3A**, the corresponding

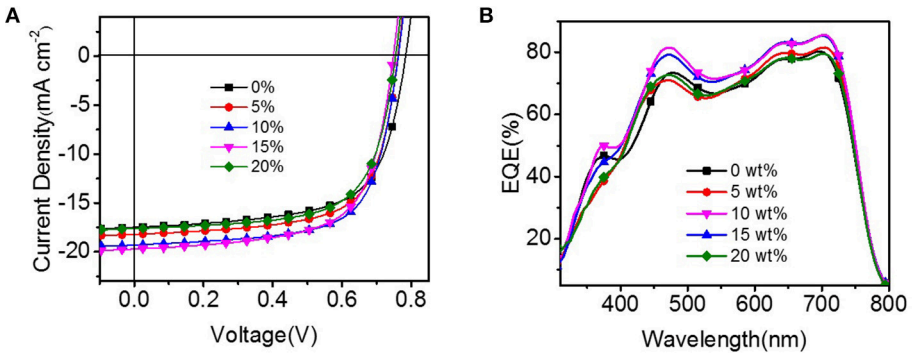

FIGURE 3 | (A) J-V curves of the binary and ternary OSCs under AM 1.5G irradiation at 100 mW cm^{-2}; **(B)** The EQE curves the binary and ternary OSCs.

TABLE 1 | Performance summaries of PTN based ternary OSCs.

PTB7-Th:PyPI:$PC_{71}BM$	V_{oc} (V)	J_{sc} (mA/cm^2)	J_{calc}[a](mA/cm^2)	FF(%)	PCE(average)[b](%)
100:0:150	0.78	17.46	17.22	65.38	9.11 (8.94)
95:5:150	0.77	18.17	17.96	67.50	9.69 (9.34)
90:10:150	0.77	19.26	18.94	67.90	10.36 (9.97)
85:15:150	0.76	19.06	18.62	67.22	10.02 (9.72)
80:20:150	0.76	17.59	17.13	66.81	9.07 (8.87)

[a] *J_{calc} is calculated from EQE spectra.*
[b] *Statistical data obtained from 20 devices.*

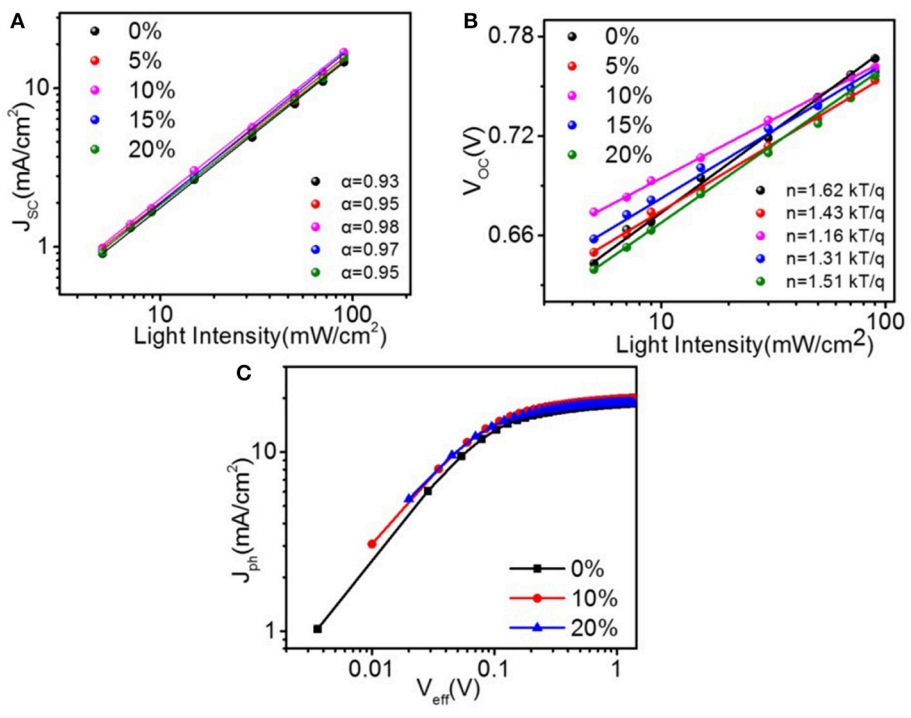

FIGURE 4 | Light-intensity dependence of **(A)** J_{SC} and V_{OC} **(B)** for ternary OSCs with different amounts of PyPI. **(C)**J_{ph}-V_{eff} curves of binary and ternary devices.

device parameters are listed in **Table 1**. After rigorously optimizing the fabrication conditions, the binary OSC obtained a maximum PCE of 9.11%, along with a short-circuit current density (J_{SC}) of 17.46 mA/cm^2, an open-circuit voltage (V_{OC}) of 0.78 V and a fill factor (FF) of 65.38%. Upon adding 5% to 20% PyPI into the binary systems, the device performances were observably improved. The highest PCE of 10.36% was achieved for PTB7-Th: 10% PyPI: $PC_{71}BM$, which exhibited a maximum enhancement of 15.88% more than the control device. Concurrently, the J_{SC} value was enhanced from 17.46 to 19.26 mA/cm^2, suggesting that the charge transfer was greatly improved when PyPI was doped in the binary system. The enhancement in current density is attributed to the stacking effect of PyPI that accelerates the charge transfer in the active layer. The FF improvement of ternary OSCs can be attributed to the optimizing film morphology as discussed below. When the concentration of the small molecule increased to 20%, the PCE decreased along with the degradation on J_{SC} and FF, which was mainly dominated by the overlarge domain size of the ternary OSC. EQE properties of the binary and ternary OSCs were measured to calibrate the high J_{SC}s, and more detailed data are listed in **Table 1**. **Figure 3B** shows the EQE curves with a different PyPI component, and all devices exhibit a prominent photo-generated current response in the whole visible absorption region from 300 to 800 nm. Along with the doping ratio of PyPI increasing from 0 to 10%, EQEs present a remarkable enhancement both in short wavelength (300–400 nm) and long wavelength (500–800 nm). The improvement in a 300–400 nm absorption bond is attributed to the contribution of PyPI, while the enhancement in the long wave range of polymer (500–800 nm) may be attributed to the optimization of polymer crystallinity. Further added the doping ratio of PyPI to 20%, the device EQE showed huge degeneration, and device performance also decreased, as the excess added PyPI reduced the content of the polymer and decreased the donor/acceptor connections. As a result, the ternary OSC shows a reduced J_{SC} and FF.

Recombination Dynamics

The charge generation and recombination dynamics' behavior in these solar cells were studied. J_{SC} and V_{OC} vs. light intensity (P_L) plotted on logarithm coordinate with the linear fittings are shown in **Figures 4A,B**, respectively. In J_{SC}-P_L measurements,

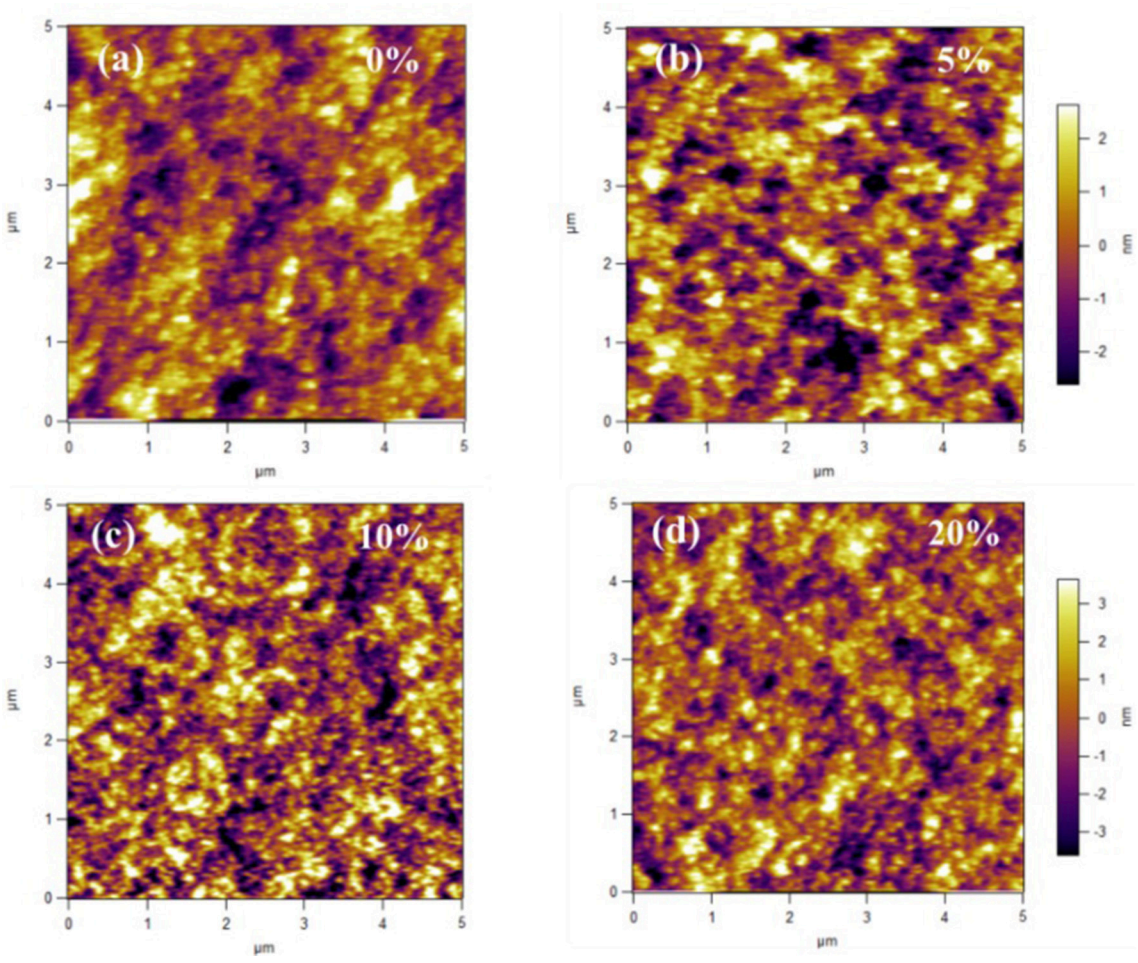

FIGURE 5 | AFM images for **(a)** PTB7-Th:$PC_{71}BM$; **(b)** PTB7-Th: 5%PyPI: $PC_{71}BM$; **(c)** PTB7-Th:10%PyPI: $PC_{71}BM$; **(d)** PTB7-Th:20%PyPI: $PC_{71}BM$ based film.

the variation in J_{SC} as a function of P_L can be concluded as $J_{SC} \propto P_0^{\alpha}$, where $\alpha = 1$ is indicative of the inexistence of bimolecular recombination in the film under short-circuit conditions. The α values of the solar cells with 0, 5, 10, 15, and 20 % PyPI were 0.93, 0.95, 0.98, 0.97, and 0.95, respectively, indicating very weak bimolecular recombination in these devices. Additionally, as shown in **Figure 4B**, the Voc of optimal device based on PTB7-Th:10 % PyPI: $PC_{71}BM$ shows a logarithmic dependence on P_L with a slope of 1.16 kT/q compared to that of 1.62 kT/q in the binary system. The slope value for the cells containing 5, 15, and 20 % PyPI were 1.43, 1.31, and 1.51 kT/q, respectively. The results suggested that the trap-assisted recombination was effectively alleviated by adding 10% PyPI. The characteristics of the photocurrent density (J_{ph}) vs. the effective applied voltage (V_{eff}) were then measured to further understand the charge generation and dissociation process in the ternary OSCs with different contents of PyPI. In theory, J_{ph} is defined as $J_{ph} = J_L - J_D$, where J_L and J_D represent photocurrent density and dark current density, respectively. V_{eff} is defined as $V_{eff} = V_0 - V_{bias}$, where V_0 is the voltage at which J_L is equal to J_D and V_{bias} is the applied bias voltage. As shown in **Figure 4C**, the exciton dissociation probabilities (P_{diss}), which are determined by J_{SC}/J_{sat}, were calculated as 92.2, 95.4, and 93.1% for the PTB7-Th:$PC_{71}BM$ binary device and ternary devices with 10 % and 20% PyPI under the short-circuit condition, respectively. The higher P_{diss} demonstrates that the corresponding ternary device has more efficient exciton dissociation and charge extraction. These results indicated that the ternary blend system can restrain charge recombination and facilitate exciton dissociation when compared to the binary system, which corresponds to the device performance.

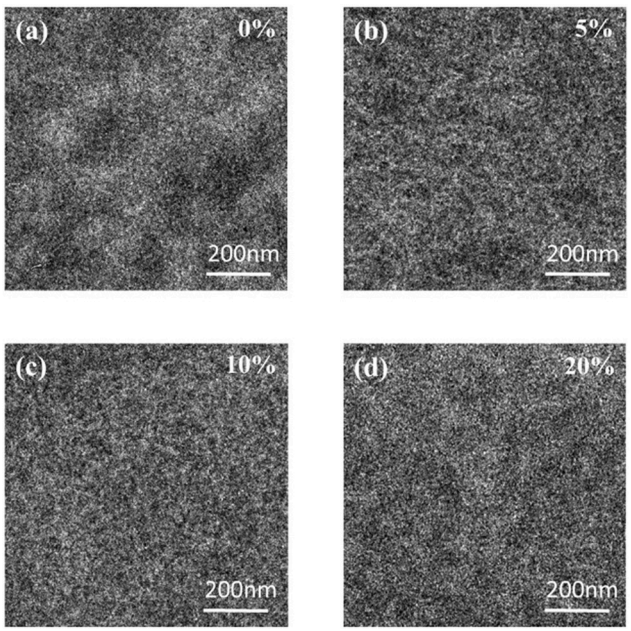

FIGURE 6 | TEM images for **(a)** PTB7-Th:$PC_{71}BM$; **(b)** PTB7-Th: 5%PyPI: $PC_{71}BM$; **(c)** PTB7-Th:10%PyPI: $PC_{71}BM$; **(d)** PTB7-Th:20%PyPI: $PC_{71}BM$ based film.

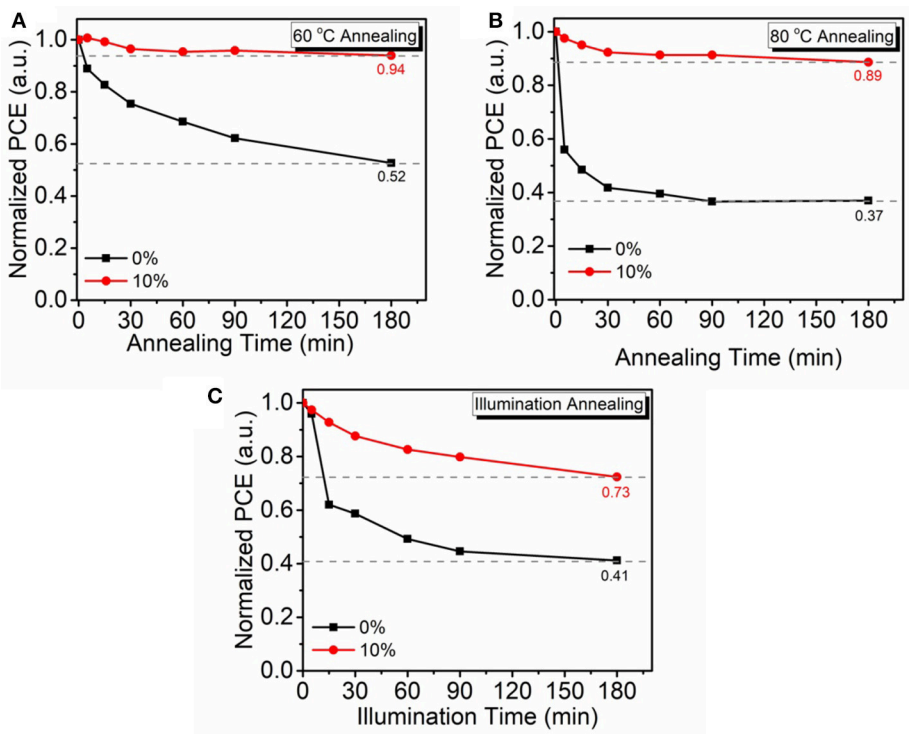

FIGURE 7 | Non-encapsulated device stability annealed at 60°C **(A)**, 80°C **(B)**, and under AM 1.5G irradiation (100 mW cm^{-2}), **(C)** in atmosphere.

Film Morphology and Molecule Distribution

To explore the reasons why the small molecule PyPI can improve the performance of conventional machines, the surface topography and potential of the active layers of the ternary devices were examined by an atomic force microscope (AFM). As shown in **Figure 5**, after addition of 5 and 10% PyPI, the ternary blend films remained homogeneous and smooth with similar root-mean-square (RMS) values of 1.53 and 1.29 nm, respectively, which is much better than that of the control film (1.78). Obviously, the RMS value decreases as the PyPI content increases, which means that a suitable amount of PyPI can be well-incorporated into the PTB7-Th:$PC_{71}BM$ based control device and the surface morphology of the membrane can be optimized. When the PyPI content exceeded 10 wt% and increased to 20 wt%, the RMS increased to 1.81 due to the lower solubility of the small molecules at such a high doping ratio, resulting in a larger domain size. The formation of large areas reduced the contact interface between the donor and acceptor, which is the main reason for the lower J_{SC} and PCE of these ternary OSCs.

Since the AFM image only reflects the surface information of the film layer, the phase distribution is studied by TEM, and the images are shown in **Figure 6**. It is well-known that bright and dark areas correspond to rich PTB7-Th and $PC_{71}BM$ regions, depending on the electron density. After the addition of 5% PyPI (**Figure 6b**) to prepare a ternary blend film, a better phase separation was observed compared to the binary film. The ternary device with a 10% PyPI content showed a fairly uniform membrane morphology with a rich donor/acceptor interface (**Figure 6c**), resulting in higher J_{SC} and FF. The nanofiber network of PTB7-Th can be observed in the PTB7-Th:$PC_{71}BM$ blend membrane. In addition, a large number of randomly distributed large regions are obtained in the active layer. For ternary blend membranes, the nanoscale network becomes more pronounced as the PyPI content increases. In the ternary blend membrane, PyPI can modulate the PTB7-Th molecular alignment and optimize phase separation and enhance photon collection of the active layer.

Environmental Stability

It is well-known that the aggregation of fullerene is the dominant reason of OSC performance degeneration in atmosphere. As small molecule PyPI can form a positive π-π stacking to suppress fullerene aggregation and we speculate that the intruding PyPI in the fullerene based OSC can improve the devices environmental stability. To verify this deduction, device stability of the non-encapsulated OSCs was investigated through thermal and light irradiation annealing in atmosphere. Thermal annealing temperatures were set at 60 to 80°C, which is a practical operation temperature range for OSCs under AM 1.5G irradiation (100 mW/cm^2). **Figure 7A** shows the thermal stability curves of control OSCs and 10% PyPI contained ternary OSCs that continuously annealed at 60 and 80°C in atmosphere for 180 min. After the annealing process, the PCE of ternary OSC remains at 94.13% of it pristine state, which is much higher than the control device (52.47%). Even more surprising, by further annealing the devices at 80°C for 180 min, PyPI based ternary OSCs also revealed a mild decay, as shown in **Figure 7B**, PyPI contained OSC still remained at 89.01% PCE, whereas the control binary device only processed 36.96%. The superior thermal stability of the ternary OSC is mainly ascribed to the addition of the small molecule which suppressed fullerene aggregation. **Figure 7C** shows the light illumination stability curves that were measured by continuously illuminating the PyPI based ternary device under 100 mW cm^{-2} AM 1.5G irradiation in atmosphere. The PyPI-containing ternary device revealed optimized stability with a small efficiency roll-off of 27.23%, while the control device exhibited a large PCE roll-off of 58.79%. The improvement in light illumination stability is mainly attributed to the introduction of the small molecule PyPI, restraining the aggregation of fullerene. The control device exhibited more severe efficiency degradation than PyPI based ternary OSC, which is attributed to the fact that fullerene can form dimers when exposed in light illumination (Fortunato et al., 2013; Wang et al., 2014; Heumueller et al., 2016). The dimeric fullerenes could significantly suppress charge transfer and deteriorate film morphology, resulting in declined device performance.

CONCLUSION

A novel ternary organic solar cell system containing PTB7-Th: PyPI as the donor and $PC_{71}BM$ as the acceptor has been fabricated to enhance device efficiency and environmental stability. The small molecule PyPI can form efficient π-π stacking in a solid film, which is beneficial to accelerate charge transfer and suppress fullerene aggregation in the active layer. After rigorous modulation, 10% PyPI contained ternary OSC exhibited a high PCE of 10.36%, which presented a 15.88% enhancement from the control device. Furthermore, the ternary OSC showed excellent thermal and light illumination stability. Under thermal annealing for 3 h in atmosphere, the device remain at 94.13% efficiency, over pristine state, while the control device only remained at 52.47% PCE. In the condition of constant illumination under AM 1.5G irradiation (100 mW cm^{-2}) in atmosphere, the PCE of OSC can remain at 72.50% PCE. The excellent performance of PyPI based OSC will stimulate the development of solar cells in practical production.

AUTHOR CONTRIBUTIONS

All authors listed have made a substantial, direct and intellectual contribution to the work, and approved it for publication.

ACKNOWLEDGMENTS

The work was supported by the National Natural Science Foundation of China (NSFC Grant Nos. 61775029, 61604035 and 51533005), the Fundamental Research Funds for the Central Universities (ZYGX2016Z010), International Cooperation and Exchange Project of Science and Technology Department of Sichuan Province (Grant 18GJHZ).

REFERENCES

Ameri, T., Dennler, G., Lungenschmied, C., and Brabec, C. J. (2009). Organic tandem solar cells: a review. *Energy Environ. Sci.* 2, 347–363. doi: 10.1039/B817952B

Bergqvist, J., Österberg, T., Melianas, A., Ever Aguirre, L., Tang, Z., Cai, W., et al. (2018). Asymmetric photocurrent extraction in semitransparent laminated flexible organic solar cells. *npj Flex. Electron.* 2:4. doi: 10.1038/s41528-017-0017-6

Che, X., Li, Y., Qu, Y., and Forrest, S. R. (2018). High fabrication yield organic tandem photovoltaics combining vacuum- and solution-processed subcells with 15% efficiency. *Nat. Energy* 3, 422–427. doi: 10.1038/s41560-018-0134-z

Chen, S., Zhang, G., Liu, J., Yao, H., Zhang, J., Ma, T., et al. (2017). An all-solution processed recombination layer with mild post-treatment enabling efficient homo-tandem non-fullerene organic solar cells. *Adv. Mater.* 29:1604231. doi: 10.1002/adma.201604231

Chen, Y., Wan, X., and Long, G. (2013). High performance photovoltaic applications using solution-processed small molecules. *Acc. Chem. Res.* 46, 2645–2655. doi: 10.1021/ar400088c

Chen, Y., Ye, P., Zhu, Z. G., Wang, X., Yang, L., Xu, X., et al. (2017). Achieving high-performance ternary organic solar cells through tuning acceptor alloy. *Adv. Mater.* 29:1603154. doi: 10.1002/adma.201603154

Chen, Y. H., Chen, C. W., Huang, Z. Y., Lin, W. C., Lin, L. Y., Lin, F., et al. (2014). Microcavity-embedded, colour-tuneable, transparent organic solar cells. *Adv. Mater.* 26, 1129–1134. doi: 10.1002/adma.201304658

Cheng, P., Li, G., Zhan, X., and Yang, Y. (2018). Next-generation organic photovoltaics based on non-fullerene acceptors. *Nat. Photonics* 12, 131–142. doi: 10.1038/s41566-018-0104-9

Cui, Y., Yang, C., Yao, H., Zhu, J., Wang, Y., Jia, G., et al. (2017). Efficient semitransparent organic solar cells with tunable color enabled by an ultralow-bandgap nonfullerene acceptor. *Adv. Mater.* 29:1703080. doi: 10.1002/adma.201703080

Fortunato, P., Giedrius, D., Sabine, B., Koen, V., Donato, S., Tim, V., et al. (2013). Influence of fullerene photodimerization on the PCBM crystallization in polymer: fullerene bulk heterojunctions under thermal stress. *J. Polym. Sci. B Polym. Phys.* 51, 1209–1214. doi: 10.1002/polb.23330

Gasparini, N., Jiao, X., Heumueller, T., Baran, D., Matt, G. J., Fladischer, S., et al. (2016). Designing ternary blend bulk heterojunction solar cells with reduced carrier recombination and a fill factor of 77%. *Nat. Energy* 1:16118. doi: 10.1038/nenergy.2016.118

Heumueller, T., Mateker, W. R., Distler, A., Fritze, U. F., Cheacharoen, R., Nguyen, W. H., et al. (2016). Morphological and electrical control of fullerene dimerization determines organic photovoltaic stability. *Energy Environ. Sci.* 9, 247–256. doi: 10.1039/C5EE02912K

Huang, H., Yang, L., and Sharma, B. (2017). Recent advances in organic ternary solar cells. *J. Mater. Chem. A* 5, 11501–11517. doi: 10.1039/c7ta00887b.

Kaltenbrunner, M., White, M. S., Głowacki, E. D., Sekitani, T., Someya, T., Sariciftci, N. S., et al. (2012). Ultrathin and lightweight organic solar cells with high flexibility. *Nat. Commun.* 3:770. doi: 10.1038/ncomms1772

Kumari, T., Lee, S. M., Kang, S. H., Chen, S., and Yang, C. (2017). Ternary solar cells with a mixed face-on and edge-on orientation enable an unprecedented efficiency of 12.1%. *Energy Environ. Sci.* 10, 258–265. doi: 10.1039/c6ee02851a

Li, J., Liu, H., Wang, Z., Bai, Y., Liu, L., Wang, F., et al. (2018). Broadening the photoresponse to near-infrared region by cooperating fullerene and nonfullerene acceptors for high performance ternary polymer solar cells. *Macromol. Rapid Commun.* 39:1700492. doi: 10.1002/marc.201700492

Liu, H., Li, J., Xia, L., Bai, Y., Hu, S., Liu, J., et al. (2018). Perfect complementary in absorption spectra with fullerene, nonfullerene acceptors and medium band gap donor for high-performance ternary polymer solar cells. *ACS Appl. Mater. Interf.* 10, 29831–29839. doi: 10.1021/acsami.8b07993

Liu, T., Guo, Y., Yi, Y., Huo, L., Xue, X., Sun, X., et al. (2016). Ternary Organic solar cells based on two compatible nonfullerene acceptors with power conversion efficiency >10%. *Adv. Mater.* 28, 10008–10015. doi: 10.1002/adma.201602570

Liu, Y. L., Lu, F., and Lu, P. (2017). Design, synthesis and electroluminescence of organic conjugated compounds based on pyrene-imidazole. *Chem. J. Chin. Univer.* 38, 583–590. doi: 10.7503/cjcu20170049

Lu, L., Chen, W., Xu, T., and Yu, L. (2015). High-performance ternary blend polymer solar cells involving both energy transfer and hole relay processes. *Nat. Commun.* 6:7327. doi: 10.1038/ncomms8327

Nian, L., Gao, K., Liu, F., Kan, Y., Jiang, X., Liu, L., et al. (2016). 11% efficient ternary organic solar cells with high composition tolerance via integrated near-IR sensitization and interface engineering. *Adv. Mater.* 28, 8184–8190. doi: 10.1002/adma.201602834

Park, K. H., An, Y., Jung, S., Park, H., and Yang, C. (2016). The use of an n-type macromolecular additive as a simple yet effective tool for improving and stabilizing the performance of organic solar cells. *Energy Environ. Sci.* 9, 3464–3471. doi: 10.1039/c6ee02255c

Roncali, J., Leriche, P., and Blanchard, P. (2014). Molecular materials for organic photovoltaics: small is beautiful. *Adv. Mater.* 26, 3821–3838. doi: 10.1002/adma.201305999

Wang, N., Tong, X., Burlingame, Q., Yu, J., and Forrest, S. R. (2014). Photodegradation of small-molecule organic photovoltaics. *Solar Energ. Mater. Solar Cells* 125, 170–175. doi: 10.1016/j.solmat.2014.03.005

Xu, W., and Gao, F. (2018). The progress and prospects of non-fullerene acceptors in ternary blend organic solar cells. *Mater. Horizons* 5, 206–221. doi: 10.1039/c7mh00958e

Xu, X., Bi, Z., Ma, W., Wang, Z., Choy, W. C. H., Wu, W., et al. (2017). Highly efficient ternary-blend polymer solar cells enabled by a nonfullerene acceptor and two polymer donors with a broad composition tolerance. *Adv. Mater.* 29:1704271. doi: 10.1002/adma.201704271

Yang, Y., Chen, W., Dou, L., Chang, W. H., Duan, H. S., Bob, B., et al. (2015). High-performance multiple-donor bulk heterojunction solar cells. *Nature Photonics* 9:190. doi: 10.1038/nphoton.2015.9

Zhang, G., Zhang, K., Yin, Q., Jiang, X.-F., Wang, Z., Xin, J., et al. (2017). High-Performance ternary organic solar cell enabled by a thick active layer containing a liquid crystalline small molecule donor. *J. Am. Chem. Soc.* 139, 2387–2395. doi: 10.1021/jacs.6b11991

Zhang, H., Yao, H., Hou, J., Zhu, J., Zhang, J., Li, W., et al. (2018). Over 14% efficiency in organic solar cells enabled by chlorinated nonfullerene small-molecule acceptors. *Adv. Mater.* 30:1800613. doi: 10.1002/adma.201800613

Zhang, J., Zhang, Y., Fang, J., Lu, K., Wang, Z., Ma, W., et al. (2015). Conjugated polymer–small molecule alloy leads to high efficient ternary organic solar cells. *J. Am. Chem. Soc.* 137, 8176–8183. doi: 10.1021/jacs.5b03449

Zhang, Y., Deng, D., Lu, K., Zhang, J., Xia, B., Zhao, Y., et al. (2015). Synergistic effect of polymer and small molecules for high-performance ternary organic solar cells. *Adv. Mater.* 27, 1071–1076. doi: 10.1002/adma.201404902

Zhang, Y., Kan, B., Sun, Y., Wang, Y., Xia, R., Ke, X., et al. (2018). Nonfullerene tandem organic solar cells with high performance of 14.11. *Adv. Mater.* 30:e1707508. doi: 10.1002/adma.201707508

Conflict of Interest Statement: The authors declare that the research was conducted in the absence of any commercial or financial relationships that could be construed as a potential conflict of interest.

frontiers in Chemistry

ORIGINAL RESEARCH
published: 09 October 2018
doi: 10.3389/fchem.2018.00473

Development of n-Type Porphyrin Acceptors for Panchromatic Light-Harvesting Fullerene-Free Organic Solar Cells

Un-Hak Lee[1†], Wisnu Tantyo Hadmojo[2†], Junho Kim[2], Seung Hun Eom[1], Sung Cheol Yoon[1], Sung-Yeon Jang[2*] and In Hwan Jung[2*]*

[1] Division of Advanced Materials, Korea Research Institute of Chemical Technology, Daejeon, South Korea, [2] Department of Chemistry, Kookmin University, Seoul, South Korea

OPEN ACCESS

Edited by:
Chuanlang Zhan, Institute of Chemistry (CAS), China

Reviewed by:
Francesca Di Maria, Istituto di Nanotecnologia (NANOTEC), Italy
Yongsheng Liu, Nankai University, China

****Correspondence:***
Sung Cheol Yoon
yoonsch@krict.re.kr
Sung-Yeon Jang
syjang@kookmin.ac.kr
In Hwan Jung
ihjung@kookmin.ac.kr

[†] These authors have contributed equally to this work

Specialty section:
This article was submitted to Organic Chemistry, a section of the journal Frontiers in Chemistry

Received: *16 June 2018*
Accepted: *18 September 2018*
Published: *09 October 2018*

Citation:
Lee U-H, Hadmojo WT, Kim J, Eom SH, Yoon SC, Jang S-Y and Jung IH (2018) Development of n-Type Porphyrin Acceptors for Panchromatic Light-Harvesting Fullerene-Free Organic Solar Cells. Front. Chem. 6:473. doi: 10.3389/fchem.2018.00473

The development of n-type porphyrin acceptors is challenging in organic solar cells. In this work, we synthesized a novel n-type porphyrin acceptor, P_{Zn}-TNI, via the introduction of the electron withdrawing naphthalene imide (NI) moiety at the meso position of zinc porphyrin (P_{Zn}). P_{Zn}-TNI has excellent thermal stability and unique bimodal absorption with a strong Soret band (300–600 nm) and weak Q-band (600–800 nm). The weak long-wavelength absorption of P_{Zn}-TNI was completely covered by combining the low bandgap polymer donor, PTB7-Th, which realized the well-balanced panchromatic photon-to-current conversion in the range of 300–800 nm. Notably, the one-step reaction of the NI moiety from a commercially available source leads to the cheap and simple n-type porphyrin synthesis. The substitution of four NIs in P_{Zn} ring induced sufficient n-type characteristics with proper HOMO and LUMO energy levels for efficient charge transport with PTB7-Th. Fullerene-free organic solar cells based-on PTB7-Th:P_{Zn}-TNI were investigated and showed a promising PCE of 5.07% without any additive treatment. To the best of our knowledge, this is the highest PCE in the porphyrin-based acceptors without utilization of the perylene diimide accepting unit.

Keywords: porphyrin acceptors, n-type porphyrins, organic solar cells, non-fullerene acceptors, panchromatic absorption

INTRODUCTION

For decades, organic solar cells (OSCs) have been studied as a portable and low-cost power generator due to their unique advantages: light-weight, use of earth-abundant organic materials, solution-processability and flexibility. The power conversion efficiency (PCE) of OSCs, an important parameter to determine the performance of the OSCs, has been continuously improved by optimization of light-harvesting in active layers and hole/electron charge transport pathways (Zhan et al., 2015; Zhao J. et al., 2016; Lin et al., 2017; Che et al., 2018; Hou et al., 2018). In the 2000s, low-bandgap polymer donors and n-type fullerene acceptors blended OSCs were developed to make broad absorption in the active layer. Polymer donors showing a strong absorption coefficient were responsible for light-harvesting and exciton generation, while the n-type fullerenes effectively separate and transfer the electrons to the electrode (Kim et al., 2006; Liang et al., 2010; Li et al., 2012; Liao et al., 2013). However, this was not enough to cover all the visible band by blending polymer

donors and fullerene acceptors. In the 2010s, new types of OSCs replaced the fullerenes with strong light-harvesting organic non-fullerene acceptors (NFAs). The active layer was composed of organic donors and NFAs, called fullerene-free OSCs (Cheng et al., 2017; Lin et al., 2017; Tang et al., 2018; Yan et al., 2018). Due to the strong absorption of both NFAs and organic donors in the visible area, their complementary absorption is important to achieve panchromatic photon-to-current conversion in the active layer. There are several successful strategies for panchromatic absorption in the visible and near infra-red area. The most common approach is mixing wide-bandgap donors and low-bandgap small-molecule NFAs such as ITIC (Zhao W. et al., 2016, 2017; Lin et al., 2017; Yao et al., 2017; Zhao F. et al., 2017). Another approach is mixing low-bandgap donors and wide-bandgap NFAs (e.g., blending of PTB7-Th and perylene-diimide (PDI)-based acceptor) (Wu et al., 2016; Duan et al., 2017; Liang et al., 2017; Eom et al., 2018). The red-dye PDIs enable a strong absorption in the short-wavelength area of 400–600 nm, while showing effective n-type characteristics.

As a new approach for panchromatic absorption in an active layer, utilization of a nature-inspired porphyrin dye has recently emerged in OSCs.(Gao et al., 2015; Li et al., 2016; Hadmojo et al., 2018) The porphyrin dyes have peculiar bimodal absorption characteristics composed of Soret and Q bands; strong transition from ground state (S0) to second excited state (S2) yields the Soret band, while the weak transition from S0 to first excited state (S1) provides the Q-band. Thus, the strong Soret absorption of porphyrin dyes enables efficient short-wavelength absorption in the 400–600 nm, which can be blended with low-bandgap donors having a dominant absorption in the 600–800 nm for panchromatic absorption. In addition, the long-wavelength absorption of the Q-band intensifies the light harvesting in the low bandgap area where abundant solar flux exists. However, most of the developed artificial porphyrin derivatives are p-type materials and only a few porphyrin derivatives currently show n-type characteristics with a promising PCEs over 5% (Hadmojo et al., 2017; Zhang et al., 2017). Exploring new structures for n-type porphyrin materials is challenging in fullerene-free OSCs.

In this study, we synthesized a novel porphyrin acceptor, P_{Zn}-TNI, via Sonogashira coupling of 5,10,15,20-tetrakis-ethynyl porphyrin Zinc (II) (P_{Zn}) and 4-bromo-N-(2-ethylhexyl)-1,8-naphthalimide (NI). NI is easily synthesized from the commercially available 4-bromo-1,8-naphthalic anhydride. This one-step reaction is beneficial in terms of time and cost for synthesizing the star-shape molecules that require an excess of NIs. Since the NI has n-type characteristics, the substitution of NIs to the four meso positions of P_{Zn} enables the excellent n-type properties as an electron acceptor. The ethyne π-bridge unit is incorporated between NI and P_{Zn} to increase the backbone planarity. The synthesized P_{Zn}-TNI showed excellent thermal stability with 5% weight loss temperature of 412°C and showed unique bimodal absorption behavior with maximum peaks at 479 nm and 719 nm. The uncovered UV-Vis absorption spectrum from P_{Zn}-TNI is completely covered by the blending of a polymer donor, PTB7-Th, which resulted in the panchromatic photon-to-current conversion from 300 to 800 nm in OSCs. The planar backbone structure of P_{Zn}-TNI assists the sizable face-on orientation in the PTB7-Th:P_{Zn}-TNI blend film without additive treatment, which resulted in the highest PCE of 5.07% (V_{OC} = 0.72 V, J_{SC} = 13.84 mA cm^{-2}, and fill factor = 0.51) in the additive-free OSCs. The excessive ordering of PTB7-Th:P_{Zn}-TNI film via pyridine additive rather reduced the photovoltaic performances. Our successful utilization of NI moiety in the P_{Zn} core will broaden and diversify the synthetic approaches for developing high-efficiency porphyrin acceptors.

EXPERIMENTAL

Synthesis

5,10,15,20-tetrakis-ethynyl porphyrin Zinc (II) (3): Macrocyclic porphyrin compound 1 was synthesized according to the reported general procedure (Yen et al., 2006). Compound 1 (0.90 g, 1.29 mmol) and zinc acetate (2.4 g, 13.1 mmol) were dissolved in the co-solvent (200 ml) of dichloromethane:methanol = 9:1 v/v%. The resulting mixture was refluxed at 65°C for 24 h. After removing the solvents, the remaining solid was rinsed with dichloromethane (300 mL) to give a purple solid compound 2 (0.65 g, yield: 62%). Without further purification, compound 2 was directly used to make compound 3. Compound 2 (0.60 g, 0.79 mmol) was dissolved in 100 mL anhydrous tetrahydrofuran (THF). Tetra-n-butylammonium fluoride solution 1.0 M in THF (3.6 ml, 3.6 mmol) was slowly added to the reaction mixture. The resulting mixture was stirred at room temperature for 4 h. After removing the solvents, the crude solid product was rinsed sequentially with methanol, dichloromethane, water and acetone. After drying the dark purple solid product 3 (180 mg, yield: 49%), it was immediately used in the next step to prevent the coupling reaction between the two terminal alkynes. ^{1}H NMR (THF-d_6, 400 MHz, ppm): δ 9.60 (s, 2H), 5.37 (s, 1H),

N,*N*'-(2-hexyldecyl) 4-bromo naphthalene imide (4): 2-Hexyldecyl amine (2.4 g, 9.93 mmol) was added to the suspension of 4-bromo-1,8-naphthalic anhydride (2.5 g, 9.03 mmol) in dry ethanol (50 mL). The reaction mixture was refluxed overnight at 110°C, and then cooled down to room temperature. After evaporating the solvents, the remaining crude solid was purified using column chromatography on silica gel with an eluent of CH_2Cl_2:n-hexane = 4:1 to give a yellow solid compound 4 (3.0 g, 66%). ^{1}H NMR ($CDCl_3$, 400 MHz, ppm): δ 8.65 (d, J = 6.4 Hz, 1H), 8.56 (d, J = 7.6 Hz, 1H), 8.40 (d, J = 8.0 Hz, 1H), 8.03 (d, J = 7.6 Hz, 1H), 7.82 (m, 1H), 4.14 (t, J = 8.0 Hz, 2H), 1.70 (m, 1H), 1.24 (br, 27H), 0.87 (t, J = 7.2 Hz, 3H).

P_{Zn}-TNI: Compound 3 (100 mg, 0.212 mmol), compound 4 (1.06 g, 2.12 mmol), $Pd_2(dba)_3$ (40 mg, 0.044 mmol) and $AsPh_3$ (100 mg, 0.33 mmol) were dissolved in dry THF (15 mL) and triethylamine (15 mL). The reaction mixture was stirred at 65°C for 4 days under N_2 atmosphere, and then quenched by distilled water. The organic layer was extracted using dichloromethane and water, and then the moisture in the organic solution was removed by Na_2SO_4. After evaporating the solvents, the solid residue was purified by column chromatography using an eluent of CH_2Cl_2:n-hexane = 4:1. Then it was further purified using recycling size exclusion chromatography to give a deep green solid P_{Zn}-TNI (290 mg, 75%). ^{1}H NMR (THF-d_6, 400 MHz,

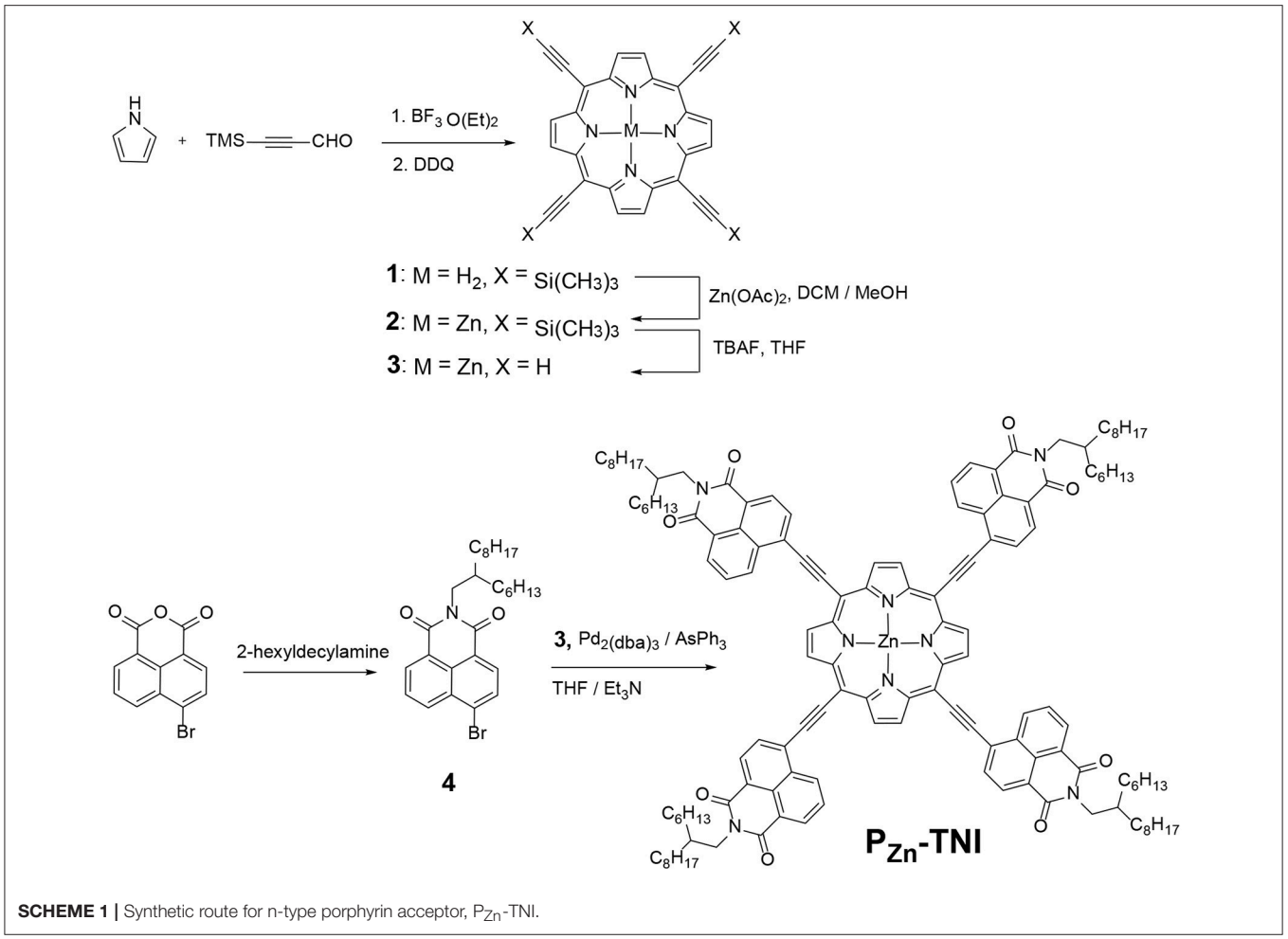

SCHEME 1 | Synthetic route for n-type porphyrin acceptor, P_{Zn}-TNI.

ppm): δ 9.02 (br, 2H), 8.85 (br, 1H), 8.40 (d, $J = 4.8$ Hz, 1H), 8.28 (d, $J = 5.6$ Hz, 1H), 8.19 (br, 1H), 7.88 (br, 1H), 4.24 (m, 2H), 1.92 (m, 1H), 1.39 (br, 27H), 0.96 (m, 3H). ^{13}C NMR (THF-d_6, 100 MHz, ppm): δ 163.58, 163.32, 149.75, 131.61, 131.49, 130.46, 130.18, 128.58, 128.35, 127.90, 124.02, 123.05, 102.08, 101.88, 96.30, 41.51, 33.14, 31.09, 31.05, 31.02, 30.99, 30.92, 30.87, 30.61, 29.22, 28.66, 23.82, 14.71. MALDI-TOF-MS: m/z: calcd. for $C_{140}H_{160}N_8O_8Zn$: 2145.17 $[M]^+$; found 2145.994.

RESULTS AND DISCUSSION

The synthetic procedure of P_{Zn}-TNI was recorded in **Scheme 1** and in the Supporting Information (SI) in detail. The porphyrin ring 1 was synthesized from pyrrole and 3-(trimethylsilyl)propiolaldehyde in the presence of $BF_3{\cdot}Et_2O$ followed by oxidation with 2,3-dichloro-5,6-dicyano-1,4-benzoquinone (DDQ). The zinc porphyrin (P_{Zn}) compound 2 was obtained using $Zn(OAc)_2$. The deprotection of TMS group by tetra-n-butylammonium fluoride (TBAF) was performed immediately before synthesizing the final acceptor, P_{Zn}-TNI. 4-Bromo-1,8-naphthalic anhydride purchased from Sigma-Aldrich was alkylated with 2-hexyldexylamine to give a compound 4. This one-step reaction to prepare the electron withdrawing NI unit is highly beneficial in terms of time and cost for achieving the n-type porphyrins. The final porphyrin acceptor, P_{Zn}-TNI, was achieved via Sonogashira coupling with P_{Zn} compound 3 and excess of NI compound 4, which was identified by ^{1}H-NMR and matrix assisted laser desorption/ionization time-of-flight mass spectrometry (MALDI-TOF-MS) (**Figures S1**–**S4**). The synthesized P_{Zn}-TNI showed excellent solubility in common organic solvents such as tetrahydrofuran (THF), dichloromethane (DCM), and chloroform (CF). In addition, it has excellent thermal stability, which was determined by thermal gravimetric analysis (TGA), with a 5% weight loss temperature (T_{5d}) of 412°C under an N_2 atmosphere (**Figure S5**).

Absorption spectra of P_{Zn}-TNI were measured in solution and the film state, as shown in **Figure 1**. P_{Zn}-TNI exhibited clear bimodal absorption composed of the Soret band (300 – 600 nm) and Q-bands (600–800 nm); the maximum absorption peaks of P_{Zn}-TNI were 479 and 713 nm in solution, and 478 and 719 nm in the film. The absorption of P_{Zn}-TNI was complementary to that of the low-bandgap donor polymer, PTB7-Th, which induced a well-balanced short- and long-wavelength absorption in the entire wavelength of 300–800 nm (**Figure 2B**). Notably, the film of P_{Zn}-TNI showed broadened

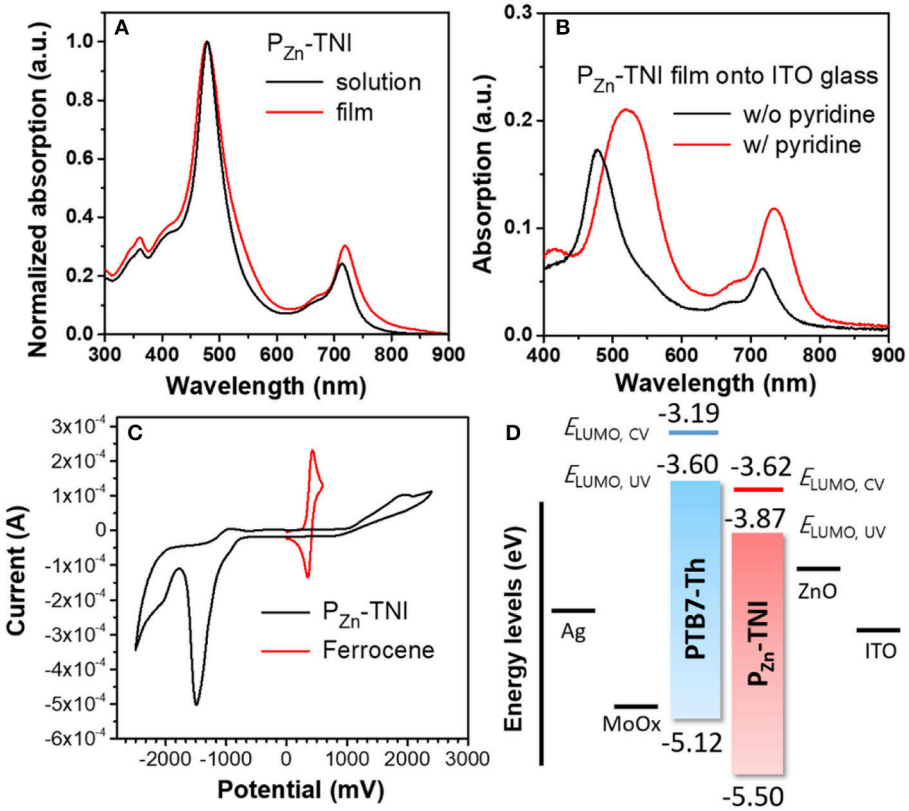

FIGURE 1 | Absorption spectra of PZn-TNI **(A)** in chloroform and in the film on the quartz plate, and **(B)** on ITO glass with or without pyridine additive. **(C)** Cyclic voltammogram of PZn-TNI, and **(D)** energy diagram of the PTB7-Th:PZn-TNI device.

and red-shifted Q-band absorption spectra compared to that in solution, indicating the enhanced intermolecular π-π stacking in the film state. Since the planar NIs and P_{Zn} are connected by an sp-hybridized ethyne π-bridge, P_{Zn}-TNI possesses a highly planar conjugated backbone for efficient intermolecular stacking. The optical bandgap (E_g^{opt}) of P_{Zn}-TNI was 1.63 eV, which was calculated from the absorption onset wavelength of 761 nm in the film. We previously reported the pyridine additive effect on the molecular ordering of porphyrin derivatives; pyridine enhances the intermolecular ordering of porphyrin derivatives via coordination to the zinc (Hadmojo et al., 2017). As shown in **Figure 1B**, the absorption of P_{Zn}-TNI was significantly broadened and red-shifted compared to that without pyridine treatment, resulting in the bathochromic shift of 42 nm in the Soret band and 15 nm in the Q-band. This supports our previous hypothesis for the pyridine effect on the molecular ordering and confirms that pyridine enhances the intermolecular ordering of P_{Zn}-TNI in the film states.

To evaluate the energy levels of P_{Zn}-TNI, the highest occupied molecular orbital (HOMO) energy levels and the lowest unoccupied molecular orbital (LUMO) energy levels were measured using cyclic voltammetry. The oxidation and reduction onset potentials of P_{Zn}-TNI were 1.07 and −0.80 V, respectively, which corresponds to HOMO levels ($E_{HOMO,CV}$) and LUMO levels ($E_{LUMO,CV}$) of −5.50 and −3.62 eV, respectively. The optical LUMO energy level ($E_{LUMO,UV}$) was calculated to be −3.87 eV from $E_{HOMO,CV}$ and E_g^{opt} of P_{Zn}-TNI. The energy diagram of the PTB7-Th and P_{Zn}-TNI was shown in **Figure 1D**, and the $E_{HOMO,CV}$, $E_{LUMO,CV}$, and $E_{LUMO,UV}$ of polymer donor (PTB7-Th) were taken from our previous measurement (Zhang et al., 2015; Hadmojo et al., 2016). The LUMO energy level of P_{Zn}-TNI is suitable for electron transport from PTB7-Th to P_{Zn}-TNI, while the HOMO of P_{Zn}-TNI is appropriate for hole transport from P_{Zn}-TNI to PTB7-Th (Marcus, 1963; Clarke and Durrant, 2010). The optical and electrochemical properties of P_{Zn}-TNI are summarized in **Table 1**.

Porphyrin acceptor-based fullerene-free OSCs were fabricated by blending PTB7-Th and P_{Zn}-TNI (**Figure 2A**). The current density-voltage (*J-V*) characteristic of PTB7-Th:P_{Zn}-TNI devices was investigated via changing the weight ratio between PTB7-Th and P_{Zn}-TNI, and the photovoltaic performance was optimized at the weight ratio of 1:1.5 w/w. The photovoltaic properties are summarized in **Figure 2C**, **Figure S6**, and **Table 2**. The best PCE of 5.07% was achieved with a V_{OC} of 0.72 V, a J_{SC} of 13.84 mA cm^{-2}, and FF of 0.51 (**Figure 2C**). As shown in **Figure 2D**, the external quantum efficiency (EQE) spectra of PTB7-Th:PZn-TNI devices cover the entire visible area of 300–800 nm and

TABLE 1 | Optical and electrochemical properties of P_{Zn}-TNI.

	UV-Vis absorption				Cyclic voltammetry				
	[a]Solution	[b]Film							
	λ_{max} (nm)	λ_{max} (nm)	λ_{onset} (nm)	[c]E_g^{opt} (eV)	E_{ox} (V)	E_{red} (V)	[d]$E_{HOMO, CV}$ (eV)	$E_{LUMO, CV}$ (eV)	[e]$E_{LUMO, UV}$ (eV)
P_{Zn}-TNI	479, 713	478, 719	761	1.63	1.07	−0.80	−5.50	−3.62	−3.87

[a]*Chloroform solution.*
[b]*Film on a quartz plate.*
[c]*Bandgap calculated from the film-state absorption onset wavelength (λ_{onset}).*
[d]*HOMO levels determined from E_{ox} of the first oxidation potential of P_{Zn}-TNI.*
[e]*LUMO levels calculated from $E_{HOMO, CV}$ and E_g^{opt}.*

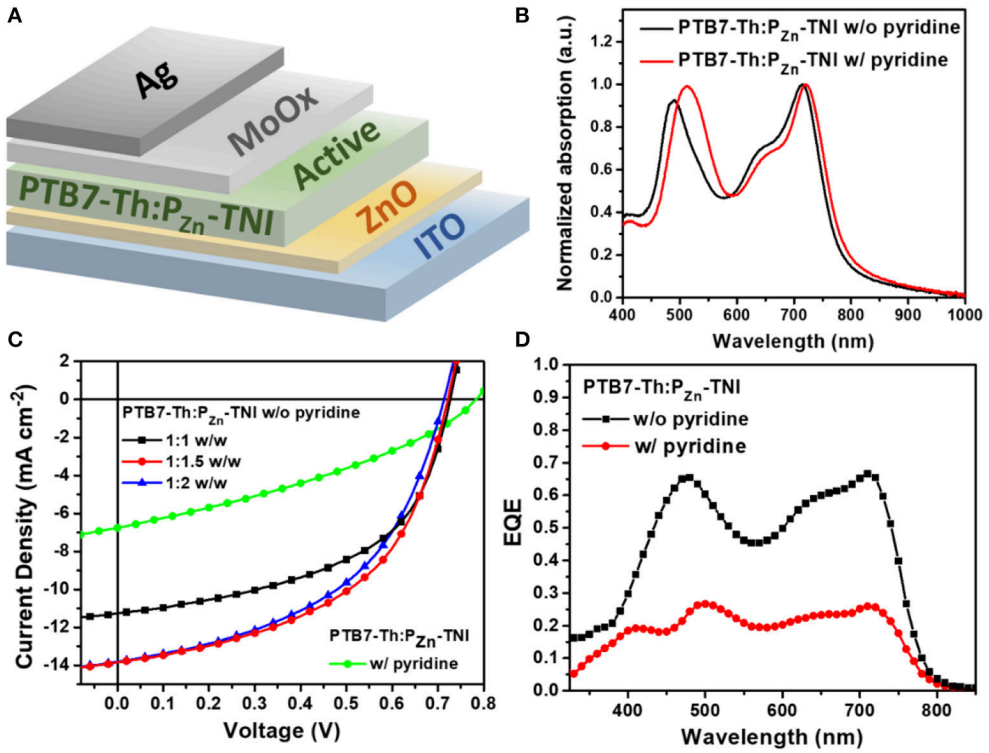

FIGURE 2 | (A) Device structure of PTB7-Th:P_{Zn}-TNI based OSCs, **(B)** absorption spectra of PTB7-Th:P_{Zn}-TNI active layer, **(C)** *J-V* characteristics of additive-free OSCs depending on the weight ratio between PTB7-Th and P_{Zn}-TNI, and the *J-V* curve of pyridine-treated OSCs at the weight ratio of PTB7-Th:PZn-TNI = 1:1.5 w/w. **(D)** the EQE spectra of PTB7-Th:P_{Zn}-TNI devices.

showed the panchromatic photon-to-current conversion due to the complementary solar flux absorption between PTB7-Th and PZn-TNI. Notably, the additive-free film-formation process provided superior photovoltaic performance compared to the pyridine-assisted one as shown in **Figure 2C**. As shown in **Figure 2D**, the EQE was increased in the entire wavelength, which indicates that hole/electron transport properties of both PTB7-Th and P_{Zn}-TNI are improved in the additive-free devices.

To understand the charge recombination mechanisms of PTB7-Th:P_{Zn}-TNI devices in the presence and absence of pyridine additive, the *J-V* characteristics were investigated as a function of the illumination intensity. The power law dependence of J_{SC} on the illumination intensity is generally expressed as $J_{SC} \propto I^{\alpha}$, where I is the light intensity and α is an exponential factor (**Figure 3A**) (Blom et al., 2007; Azmi et al., 2016). The α value of the PTB7-Th:P_{Zn}-TNI devices was close to unity regardless of additive treatment, indicating the negligible bimolecular recombination in PTB7-Th:P_{Zn}-TNI devices. However, the V_{OC} vs. illumination intensity was highly affected by the pyridine treatment. Assuming there is no trap-assisted recombination under an open-circuit condition, the slope of V_{OC} vs. the illumination intensity produces 1.00 kT/q (Mihailetchi et al., 2006). The higher value of kT/q indicates the more probability of trap-assisted recombination under an open-circuit condition (Mandoc et al., 2007; Azmi et al., 2016). As shown in **Figure 3B**,

TABLE 2 | Photovoltaic properties of PTB7-Th:P_{Zn}-TNI devices.

PTB7-Th:P_{Zn}-TNI		μ_h ($cm^2\ V^{-1}\cdot s^{-1}$)	μ_e ($cm^2\ V^{-1}\cdot s^{-1}$)	V_{OC} (V)	J_{SC} (mA cm^{-2})	FF	PCE (PCE_{ave})[a](%)
No additives	1:1	–	–	0.73	11.25	0.52	4.29 (3.97)
	1:1.5	2.9×10^{-4}	2.5×10^{-6}	0.72	13.84	0.51	5.07 (4.85)
	1:2	–	–	0.71	13.81	0.49	4.82 (4.59)
1% (v/v) pyridine	1:1.5	2.4×10^{-4}	1.3×10^{-6}	0.78	6.76	0.34	1.82 (1.61)

[a]*Average PCEs more than 10 devices.*

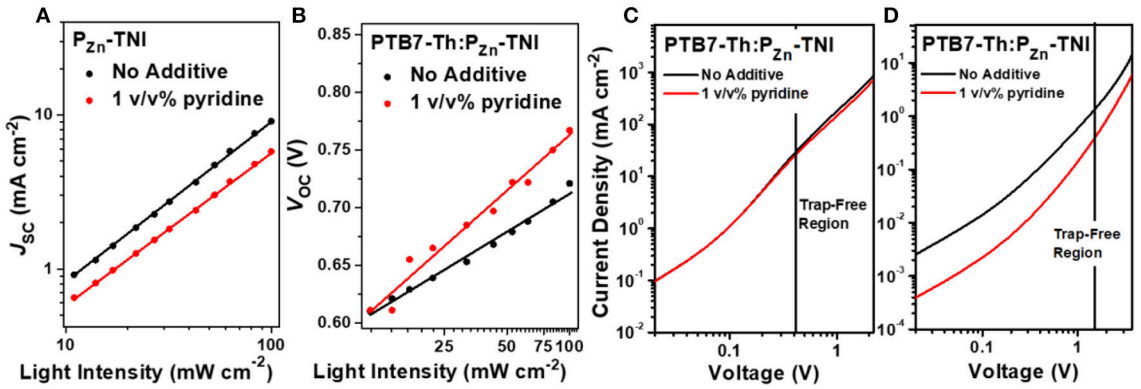

FIGURE 3 | (A) J_{SC} and **(B)** V_{OC} as a function of the illumination intensity. SCLC mobility of **(C)** hole-only and **(D)** electron-only devices.

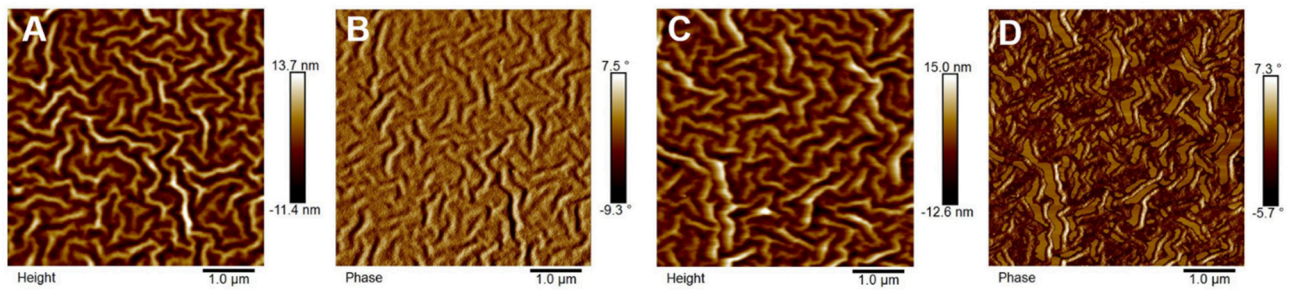

FIGURE 4 | AFM **(A,C)** height and **(B,D)** phase image of PTB7-Th:PZn-TNI; **(A,B)** in the absence of pyridine and **(C,D)** in the presence of pyridine.

PTB7-Th:P_{Zn}-TNI devices with and without additives show the slope of 2.63 and 1.93 kT/q, respectively. This implies that PTB7-Th:P_{Zn}-TNI devices in the absence of additives have the lowest trap-assisted recombination in anopen-circuit condition. The hole and electron transport properties of PTB7-Th:P_{Zn}-TNI devices were measured by a space-charge-limited-current (SCLC) analysis (**Figures 3C,D**) (Mihailetchi et al., 2005). The electron- and hole-only devices were fabricated with a structure of ITO/ZnO/PTB7-Th:P_{Zn}-TNI/ZnO/Al and ITO/PEDOT:PSS/PTB7-Th:P_{Zn}-TNI/MoO_x/Ag, respectively. In the presence of pyridine additive, the hole and electron mobilities of PTB7-Th:P_{Zn}-TNI were 2.4×10^{-4} and 1.3×10^{-6} $cm^2\ V^{-1}\cdot s^{-1}$, respectively, whereas, in the absence of additives, the hole and electron mobilities were increased to 2.9×10^{-4} and 2.5×10^{-6} $cm^2\ V^{-1}\cdot s^{-1}$, respectively. Thus, it is expected that the pyridine additive worsens the nanomorphology of PTB7-Th:P_{Zn}-TNI devices via excessive intermolecular aggregation.

The morphology of the PTB7-Th:P_{Zn}-TNI active layer was investigated by atomic force microscopy (AFM) (**Figure 4**) and two-dimensional grazing incidence X-ray diffraction (2D-GIXD) analyses (**Figure 5**). In AFM images, PTB7-Th:P_{Zn}-TNI blended film possesses bicontinuous crystalline domains in the absence of additives (**Figures 4A,B**), whereas the addition of pyridine additive intensifies the intermolecular ordering of P_{Zn}-TNI domains, leading to severe phase segregation between PTB7-Th and P_{Zn}-TNI (**Figures 4C,D**). The 2D-GIXD results also support the AFM analysis. Additive-free PTB7-Th:P_{Zn}-TNI film showed clear π-π stacking orientation (010) peak at ∼1.6 $Å^{-1}$ along the q_z axis, which indicates the face-on orientation with a d-spacing of ∼3.9 Å (**Figures 5B,C**). However, the pyridine-treated PTB7-Th:P_{Zn}-TNI film showed the increased π-π stacking

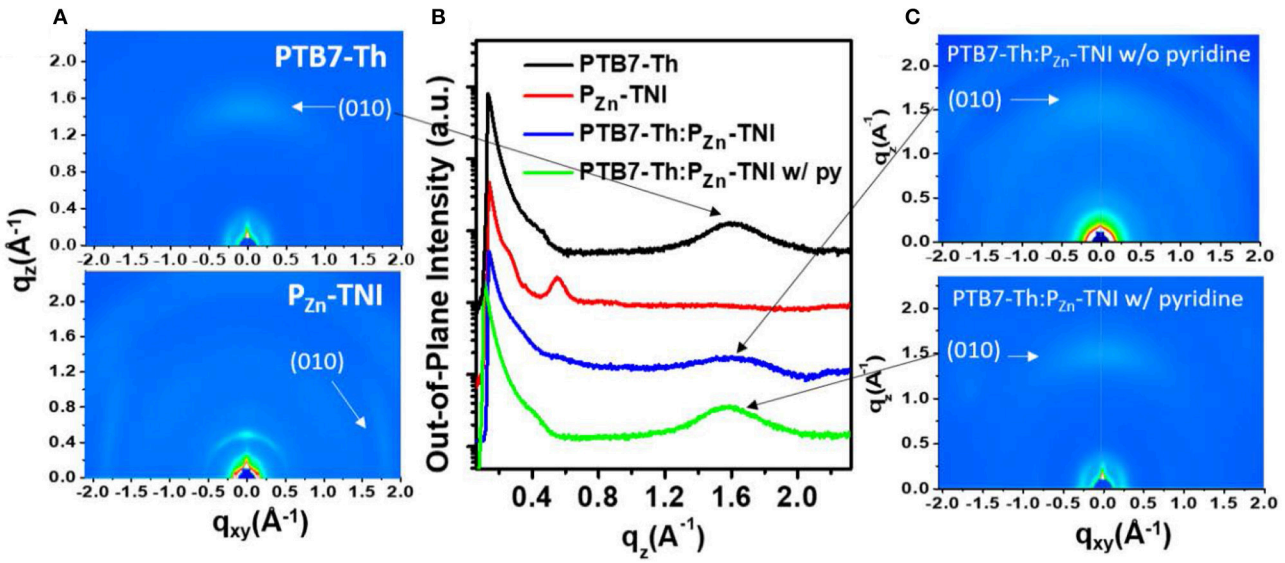

FIGURE 5 | (A) 2D-GIXD images of **(A)** pristine film of PTB7-Th and P_{Zn}-TNI, and **(C)** additive-free PTB7-Th:P_{Zn}-TNI blend film and pyridine-treated one. **(B)** Out-of-plane line-cut of PTB7-Th, P_{Zn}-TNI, and PTB7-Th:P_{Zn}-TNI film.

interaction and induced the phase aggregation (**Figure 5C**). The (010) peak in the blend film is assigned to the orientation of PTB7-Th domains (**Figure 5A**), which implies that the decrease in the photovoltaic performances in presence of pyridine is probably due to the aggregation of the PTB7-Th domains in the PTB7-Th:P_{Zn}-TNI blend film. As a result, the P_{Zn}-TNI having highly planar molecular structure possesses the sizable π-π intermolecular stacking and crystalline nanomorphology in the additive-free solvent system, which means that no more post-treatment is required in PTB7-Th:PZn-TNI blend system. In addition, the additive-free system can prevent undesirable morphological change and photo-oxidation degradation by additives in the active layer (Li et al., 2017).

CONCLUSIONS

We have synthesized a novel porphyrin acceptor, P_{Zn}-TNI, by incorporating four naphthalene imide (NI) units at the meso position of the P_{Zn} core. P_{Zn}-TNI showed unique bimodal absorption with a strong Soret band and a weak Q-band. The insufficient long-wavelength absorption of P_{Zn}-TNI was covered by a low-bandgap donor, PTB7-Th. As a result, bulk heterojunction fullerene-free OSCs composed of P_{Zn}-TNI and PTB7-Th showed panchromatic photon-to-current conversion covering entire area of 300–800 nm. The PTB7-Th:P_{Zn}-TNI devices exhibited a promising PCE of 5.07%, which is the highest and the first promising PCE in the porphyrin-based acceptors except for those utilizing the PDI units. Notably, the additive-free solution process provided the best photovoltaic performance, whereas the pyridine additive had a negative effect on the nanomorphology by the excessive molecular aggregation of the PTB7-Th:P_{Zn}-TNI film. The planar backbone structure of P_{Zn}-TNI assists the sizable molecular ordering in the PTB7-Th:P_{Zn}-TNI film without additive treatment, which is favorable for practical applications.

AUTHOR CONTRIBUTIONS

IJ and SY conceived the ideas and designed the PZn-TNI. U-HL synthesized all the materials and JK assisted the characterization of all the materials. S-YJ supervised all the device fabrication and optimization. WH fabricated all the OSC devices and SE assisted the device characterization.

ACKNOWLEDGMENTS

The authors gratefully acknowledge support from the New and Renewable Energy Core Technology Program of the Korea Institute of Energy Technology Evaluation and Planning (KETEP), granted financial resources from the Ministry of Trade, Industry and Energy, Republic of Korea (No. 20163030013960), the National Research Foundation (NRF) Grant funded by the Korean Government (MSIP, No. 2016R1A5A1012966 and No. 2017R1C1B2010694), and the Global Scholarship Program for Foreign Graduate Students at Kookmin University in Korea.

SUPPLEMENTARY MATERIAL

The Supplementary Material for this article can be found online at: https://www.frontiersin.org/articles/10.3389/fchem.2018.00473/full#supplementary-material

REFERENCES

Azmi, R., Oh, S. H., and Jang, S. Y. (2016). High-efficiency colloidal quantum dot photovoltaic devices using chemically modified heterojunctions. *ACS Energy Lett.* 1, 100–106. doi: 10.1021/acsenergylett.6b00070

Blom, P. W. M., Mihailetchi, V. D., Koster, L. J. A., and Markov, D. E. (2007). Device physics of polymer:fullerene bulk heterojunction solar cells. *Adv. Mater.* 19, 1551–1566. doi: 10.1002/adma.200601093

Che, X., Li, Y., Qu, Y., and Forrest, S. R. (2018). High fabrication yield organic tandem photovoltaics combining vacuum- and solution-processed subcells with 15% efficiency. *Nat. Energy* 3, 422–427. doi: 10.1038/s41560-018-0134-z

Cheng, P., Zhang, M., Lau, T. K., Wu, Y., Jia, B., Wang, J., et al. (2017). Realizing small energy loss of 0.55 eV, high open-circuit voltage >1 V and high efficiency >10% in fullerene-free polymer solar cells via energy driver. *Adv. Mater.* 29:1605216. doi: 10.1002/adma.201605216

Clarke, T. M., and Durrant, J. R. (2010). Charge photogeneration in organic solar cells. *Chem. Rev.* 110, 6736–6767. doi: 10.1021/cr900271s

Duan, Y., Xu, X., Yan, H., Wu, W., Li, Z., and Peng, Q. (2017). Pronounced effects of a triazine core on photovoltaic performance–efficient organic solar cells enabled by a PDI trimer-based small molecular acceptor. *Adv. Mater.* 29:1605115. doi: 10.1002/adma.201605115

Eom, S. H., Kim, H. S., Do, H. J., Lee, U. H., Wibowo, F. T. A., Hwang, D. H., et al. (2018). n-Type core effect on perylene diimide based acceptors for panchromatic fullerene-free organic solar cells. *Dyes Pigments* 156, 318–325. doi: 10.1039/C7PY00497D

Gao, K., Li, L., Lai, T., Xiao, L., Huang, Y., Huang, F., et al. (2015). Deep Absorbing porphyrin small molecule for high-performance organic solar cells with very low energy losses. *J. Am. Chem. Soc.* 137, 7282–7285. doi: 10.1021/jacs.5b03740

Hadmojo, W. T., Nam, S. Y., Shin, T. J., Yoon, S. C., Jang, S. Y., and Jung, I. H. (2016). Geometrically controlled organic small molecule acceptors for efficient fullerene-free organic photovoltaic devices. *J. Mater. Chem. A* 4, 12308–12318. doi: 10.1039/C6TA04344E

Hadmojo, W. T., Yim, D., Aqoma, H., Ryu, D. Y., Shin, T. J., Kim, H. W., et al. (2017). Artificial light-harvesting n-type porphyrin for panchromatic organic photovoltaic devices. *Chem. Sci.* 8, 5095–5100. doi: 10.1039/C7SC01275F

Hadmojo, W. T., Yim, D., Sinaga, S., Lee, W., Ryu, D. Y., Jang, W. D., et al. (2018). Near-infrared harvesting fullerene-free all-small-molecule organic solar cells based on porphyrin donors. *ACS Sustain. Chem. Eng.* 6, 5306–5313. doi: 10.1021/acssuschemeng.8b00010

Hou, J., Inganäs, O., Friend, R. H., and Gao, F. (2018). Organic solar cells based on non-fullerene acceptors. *Nat. Mater.* 17:119. doi: 10.1038/nmat5063

Kim, Y., Cook, S., Tuladhar, S. M., Choulis, S. A., Nelson, J., Durrant, J. R., et al. (2006). A strong regioregularity effect in self-organizing conjugated polymer films and high-efficiency polythiophene:fullerene solar cells. *Nat. Mater.* 5:197. doi: 10.1038/nmat1574

Li, G., Zhu, R., and Yang, Y. (2012). Polymer solar cells. *Nat. Photonics* 6:153. doi: 10.1038/nphoton.2012.11

Li, H., He, D., Mao, P., Wei, Y., Ding, L., and Wang, J. (2017). Additive-free organic solar cells with power conversion efficiency over 10%. *Adv. Energy Mater.* 7:1602663. doi: 10.1002/aenm.201602663

Li, N., Ke, G., Feng, L., Yuanyuan, K., Xiaofang, J., Linlin, L., et al. (2016). 11% efficient ternary organic solar cells with high composition tolerance via integrated near-IR sensitization and interface engineering. *Adv. Mater.* 28, 8184–8190. doi: 10.1002/adma.201602834

Liang, N., Jiang, W., Hou, J., and Wang, Z. (2017). New developments in non-fullerene small molecule acceptors for polymer solar cells. *Mater. Chem. Front.* 1, 1291–1303. doi: 10.1039/C6QM00247A

Liang, Y., Xu, Z., Xia, J., Tsai, S. T., Wu, Y., Li, G., et al. (2010). For the bright future—bulk heterojunction polymer solar cells with power conversion efficiency of 7.4%. *Adv. Mater.* 22, E135–E138. doi: 10.1002/adma.200903528

Liao, S. H., Jhuo, H. J., Cheng, Y. S., and Chen, S. A. (2013). Fullerene derivative-doped zinc oxide nanofilm as the cathode of inverted polymer solar cells with low-bandgap polymer (PTB7-Th) for high performance. *Adv. Mater.* 25, 4766–4771. doi: 10.1002/adma.201301476

Lin, Y., Zhao, F., Wu, Y., Chen, K., Xia, Y., Li, G., et al. (2017). Mapping polymer donors toward high-efficiency fullerene free organic solar cells. *Adv. Mater.* 29:1604155. doi: 10.1002/adma.201604155

Mandoc, M. M., Veurman, W., Koster, L. J. A., de Boer, B., and Blom, P. W. M., et al. (2007). Origin of the reduced fill factor and photocurrent in MDMO-PPV:PCNEPV all-polymer solar cells. *Adv. Funct. Mater.* 17, 2167–2173. doi: 10.1002/adfm.200601110

Marcus, R. A. (1963). On the theory of oxidation—reduction reactions involving electron transfer. v. comparison and properties of electrochemical and chemical rate constants. *J. Phys. Chem.* 67, 853–857. doi: 10.1021/j100798a033

Mihailetchi, V. D., Wildeman, J., and Blom, P. W. M. (2005). Space-charge limited photocurrent. *Phys. Rev. Lett.* 94:126602. doi: 10.1103/PhysRevLett.94.126602

Mihailetchi, V. D., Xie, H. X., de Boer, B., Koster, L. J. A., and Blom, P. W. M. (2006). Charge transport and photocurrent generation in poly(3-hexylthiophene): methanofullerene bulk-heterojunction solar cells. *Adv. Funct. Mater.* 16, 699–708. doi: 10.1002/adfm.200500420

Tang, A., Chen, F., Chen, B., Tan, Z. A., Yang, J., Li, J., et al. (2018). Utilizing benzotriazole and indacenodithiophene units to construct both polymeric donor and small molecular acceptors to realize organic solar cells with high open-circuit voltages beyond 1.2 V. *Front. Chem.* 6:147. doi: 10.3389/fchem.2018.00147

Wu, Q., Zhao, D., Schneider, A. M., Chen, W., and Yu, L. (2016). Covalently bound clusters of alpha-substituted pdi-rival electron acceptors to fullerene for organic solar cells. *J. Am. Chem. Soc.* 138, 7248–7251. doi: 10.1021/jacs.6b03562

Yan, C., Barlow, S., Wang, Z., Yan, H., Jen, A. K. Y., Marder, S. R., et al. (2018). Non-fullerene acceptors for organic solar cells. *Nat. Rev. Mater.* 3:18003. doi: 10.1038/natrevmats.2018.3

Yao, H., Ye, L., Hou, J., Jang, B., Han, G., Cui, Y., et al. (2017). Achieving highly efficient nonfullerene organic solar cells with improved intermolecular interaction and open-circuit voltage. *Adv. Mater.* 29:1700254. doi: 10.1002/adma.201700254

Yen, W. N., Lo, S. S., Kuo, M. C., Mai, C. L., Lee, G. H., Peng, S. M., et al. (2006). Synthesis, structure, and optical and electrochemical properties of star-shaped porphyrin–triarylamine conjugates. *Org. Lett.* 8, 4239–4242. doi: 10.1021/ol061478w

Zhan, C., Zhang, X., and Yao, J. (2015). New advances in non-fullerene acceptor based organic solar cells. *RSC Adv.* 5, 93002–93026. doi: 10.1039/C5RA17715D

Zhang, A., Li, C., Yang, F., Zhang, J., Wang, Z., Wei, Z., et al. (2017). An electron acceptor with porphyrin and perylene bisimides for efficient non-fullerene solar cells. *Angew. Chem. Int. Ed.* 56, 2694–2698. doi: 10.1002/anie.201612090

Zhang, Y., Wan, Q., Guo, X., Li, W., Guo, B., Zhang, M., et al. (2015). Synthesis and photovoltaic properties of an n-type two-dimension-conjugated polymer based on perylene diimide and benzodithiophene with thiophene conjugated side chains. *J. Mater. Chem. A* 3, 18442–18449. doi: 10.1039/C5TA05014F

Zhao, F., Dai, S., Wu, Y., Zhang, Q., Wang, J., Jiang, L., et al. (2017). Single-junction binary-blend nonfullerene polymer solar cells with 12.1% efficiency. *Adv. Mater.* 29:1700144. doi: 10.1002/adma.201700144

Zhao, J., Li, Y., Yang, G., Jiang, K., Lin, H., Ade, H., et al. (2016). Efficient organic solar cells processed from hydrocarbon solvents. *Nat. Energy* 1:15027. doi: 10.1038/nenergy.2015.27

Zhao, W., Li, S., Yao, H., Zhang, S., Zhang, Y., Yang, B., et al. (2017). Molecular optimization enables over 13% efficiency in organic solar cells. *J. Am. Chem. Soc.* 139, 7148–7151. doi: 10.1021/jacs.7b02677

Zhao, W., Qian, D., Zhang, S., Li, S., Inganäs, O., Gao, F., et al. (2016). Fullerene-free polymer solar cells with over 11% efficiency and excellent thermal stability. *Adv. Mater.* 28, 4734–4739. doi: 10.1002/adma.201600281

Conflict of Interest Statement: The authors declare that the research was conducted in the absence of any commercial or financial relationships that could be construed as a potential conflict of interest.

frontiers in Chemistry

REVIEW
published: 25 September 2018
doi: 10.3389/fchem.2018.00404

Recent Progress in Fused-Ring Based Nonfullerene Acceptors for Polymer Solar Cells

*Chaohua Cui**

Laboratory of Advanced Optoelectronic Materials, College of Chemistry, Chemical Engineering and Materials Science, Soochow University, Suzhou, China

The progress of bulk-heterojunction (BHJ) polymer solar cells (PSCs) is closely related to the innovation of photoactive materials (donor and acceptor materials), interface engineering, and device optimization. Especially, the development of the photoactive materials dominates the research filed in the past decades. Photoactive materials are basically classified as p-type organic semiconductor donor (D) and an n-type organic semiconductor acceptor (A). In the past two decades, fullerene derivatives are the dominant acceptors for high efficiency PSCs. Nevertheless, the limited absorption and challenging structural tunability of fullerenes hinder further improve the efficiency of PSCs. Encouragingly, the recent progresses of fused-ring based A-D-A type nonfullerene acceptors exhibit great potential in enhancing the photovoltaic performance of devices, driving the power conversion efficiency to over 13%. Such kind of nonfullerene acceptors is usually based on indacenodithiophene (IDT) or its extending backbone core and end-caped with strong electron-withdrawing group. Owing to the strong push-pulling effects, the acceptors possess strong absorption in the visible-NIR region and low-lying HOMO (highest occupied molecular orbital) level, which can realize both high open-circuit voltage and short-circuit current density of the devices. Moreover, the photo-electronic and aggregative properties of the acceptors can be flexibly manipulated via structural design. Many strategies have been successfully employed to tune the energy levels, absorption features, and aggregation properties of the fused-ring based acceptors. In this review, we will summarize the recent progress in developing highly efficient fused-ring based nonfullerene acceptors. We will mainly focus our discussion on the correlating factors of molecular structures to their absorption, molecular energy levels, and photovoltaic performance. It is envisioned that an analysis of the relationship between molecular structures and photovoltaic properties would contribute to a better understanding of this kind of acceptors for high-efficiency PSCs.

Keywords: polymer solar cells, nonfullerene acceptor, molecular design, power conversion efficiency, energy levels

OPEN ACCESS

Edited by:
Chuanlang Zhan,
Institute of Chemistry (CAS), China

Reviewed by:
Renqiang Yang,
Qingdao Institute of Bioenergy and Bioprocess Technology (CAS), China
Weiwei Li,
Institute of Chemistry (CAS), China

***Correspondence:**
Chaohua Cui
cuichaohua@suda.edu.cn

Specialty section:
This article was submitted to Organic Chemistry, a section of the journal Frontiers in Chemistry

Received: *12 June 2018*
Accepted: *20 August 2018*
Published: *25 September 2018*

Citation:
Cui C (2018) Recent Progress in Fused-Ring Based Nonfullerene Acceptors for Polymer Solar Cells. Front. Chem. 6:404. doi: 10.3389/fchem.2018.00404

INTRODUCTION

Typically, bulk-heterojunction (BHJ) polymer solar cells (PSCs) are composed of a photoactive layer sandwiched between a transparent anode and a low work function metal cathode (Li, 2012; Li et al., 2012; Nielsen et al., 2012; Chen et al., 2013; Heeger, 2013; Janssen and Nelson, 2013; Zhan et al., 2015; Elumalai and Uddin, 2016; Zhan and Yao, 2016; Zhang et al., 2017). The PCE of PSC is proportional to open-circuit voltage (V_{oc}), short-circuit current density (J_{sc}), and fill factor (FF). The progress of PSCs is closely related to the innovation of photoactive materials (donor and acceptor materials) (He and Li, 2011; Li, 2013; Cui et al., 2014, 2016; Ye et al., 2014; Lu et al., 2015; Cui and Wong, 2016; Cui Y. et al., 2017; Hu et al., 2017; Lopez et al., 2017; Osaka and Takimiya, 2017; Zou et al., 2017; Gupta et al., 2018; Liu et al., 2018; Sun et al., 2018), interface engineering (He et al., 2012; Duan et al., 2013; Chueh et al., 2015; Wang et al., 2015; Chen et al., 2016; Street, 2016), and device optimization (Ameri et al., 2009, 2013; Meillaud et al., 2015; Cui C. et al., 2017; Li W. et al., 2017; Zhao et al., 2018). Especially, the development of PSCs is always accompanied by photoactive material innovations. As the key component, photoactive materials are basically classified as a p-type organic semiconductor donor (D) and an n-type organic semiconductor acceptor (A). Due to the unique advantages of strong electron-accepting and high electron-transport capabilities, fullerene derivatives were predominately used as the acceptor in PSCs in the past two decades, driving the power conversion efficiency (PCE) of PSCs to 11–12% (Liu et al., 2014; Zhao J. et al., 2016). Nevertheless, fullerenes based acceptors show critical shortcomings of weak absorption and limited structural modification, hindering further improve photovoltaic performance of devices. To overcome these obstacles of fullerenes based acceptors, many efforts have been devoted to developing new kind of nonfullerene acceptor materials (Hendriks et al., 2014; Cheng et al., 2018; Hou et al., 2018; Yan et al., 2018). Very recently, A-D-A conjugated fused-ring molecules based on indacenodithiophene (IDT, **Figure 1**) or DTIDT unit (**Figure 4**) were reported as excellent nonfullerene acceptors for high performance PSCs, leading the PCE of device to over 13% (Wang et al., 2016; Li S. et al., 2018). Very recently, the PCEs of nonfullerene based PSCs have been driven to a milestone of over 14% (Li S. et al., 2018; Zhang et al., 2018). Unlike fullerene derivatives, fused-ring based nonfullerene acceptor materials offer many molecular design strategies to tune their optoelectronic properties and thus photovoltaic performance. In this review, we will provide some representative cases of molecular manipulation on IDT and DTIDT based nonfullerene acceptors to fine-tune the physicochemical and photovoltaic properties. We hope that this review article would contribute to a better understanding of the design strategies of high performance fused-ring based acceptors for efficient nonfullerene PSCs.

IDT BASED FUSED-RING ACCEPTORS

IDT unit (**Figure 1**) which features phenylene ring fused to thiophene was firstly reported by Wong in 2006 (Wong et al., 2006) Such fused rings structure is beneficial to forming effective interchain π-π overlap and enhance the rigidity of the molecular backbone as well as the degree of conjugation. Zhan et al. innovatively used IDT as central core to develop an A-D-A (A = acceptor, D = donor) type acceptor material (NA1) with 2-(3-oxo-2,3-dihydroinden-1-ylidene)-malononitrile as terminal acceptor unit (Lin et al., 2016a). NA1 showed promising energy levels and absorption spectrum as acceptor material for PSCs. By using NA1 as acceptor and PDBT-T1 as donor to fabricate PSC device, a high PCE of 7.39% was obtained, with V_{oc} = 0.92 V, J_{sc} = 13.39 mA cm^{-2}, and FF = 0.60 (**Table 2**) (Lin et al., 2016a). Molecular optimization based on NA1 greatly affects the photovoltaic performance. In the following, we will discuss the molecular design strategies including extension of conjugated backbone, substituted side chains, and end-capped group were conducted on NA1.

Extension of Conjugated Backbone With Donor Unit

The V_{oc} of PSCs device is tightly correlated with the energy level difference between the HOMO of the donor and the LUMO of the acceptor. Therefore, high LUMO level of acceptor material is essential for achieving high V_{oc} value. In D-A conjugated molecular system, the donor unit mainly determines the HOMO level. In other words, the optical bandgap (E_g) of D-A based molecules can be tuned by incorporating donor unit as conjugated extension while maintaining the similar LUMO level. For example, Zhan et al. employed one and two IDT units as conjugated extension block to develop two molecules NA2 and NA3 (Lin et al., 2016a). Due to the longer conjugated backbone, the absorption profiles of NA2 and NA3 are effectively red-shifted compared to NA1, and NA3 possesses the lowest E_g of 1.53 eV (**Table 1**). On the other hand, NA2 and NA3 showed up-shifted HOMO levels while similar LUMO levels. Due to the weaker molecular π-π stacking compared to NA1, the NA2 based device exhibited a low PCE of 2.58%, while no photovoltaic response was observed from the NA3 based device. In comparison with NA1, NA4 with thiophene units as π-bridge for conjugated extension showed slightly red-shifted absorption spectrum (E_g = 1.55 eV), up-shifted HOMO level of −5.42 eV, and similar LUMO level of −3.85 eV (Bai et al., 2015a). The device based on PBDTTT-C-T:NA4 exhibited a PCE of 3.93%, with a V_{oc} of 0.90 V, J_{sc} of 8.33 mA cm^{-2}, and FF of 0.523 (**Table 2**). Presumably owing to the conjugated twists, the E_g was increased to 1.57 eV when attaching 2-ethylhexyl chains in thiophene π-bridge of NA1 (IEIC, **Figure 1**) (Lin et al., 2015b). By using IEIC as acceptor and PTB7-Th as donor to fabricate device, a promising PCE of 6.31% was obtained, with V_{oc} = 0.97 V, J_{sc} = 13.55 mA cm^{-2}, and FF = 0.48 (**Table 2**). To reduce the E_g of IEIC, Hou et al. replaced the 2-ethylhexyl chains of IEIC with alkoxy chains to develop a new acceptor IEICO (Yao et al., 2016). Attributing to the strong electron-donating ability of alkoxy chains, IEICO exhibited a lower E_g of 1.34 eV than IEIC. Relative to IEIC, the density functional theory calculation result suggests that the introduction of alkoxy chains effectively up-shifted the HOMO level (∼0.19 eV) while

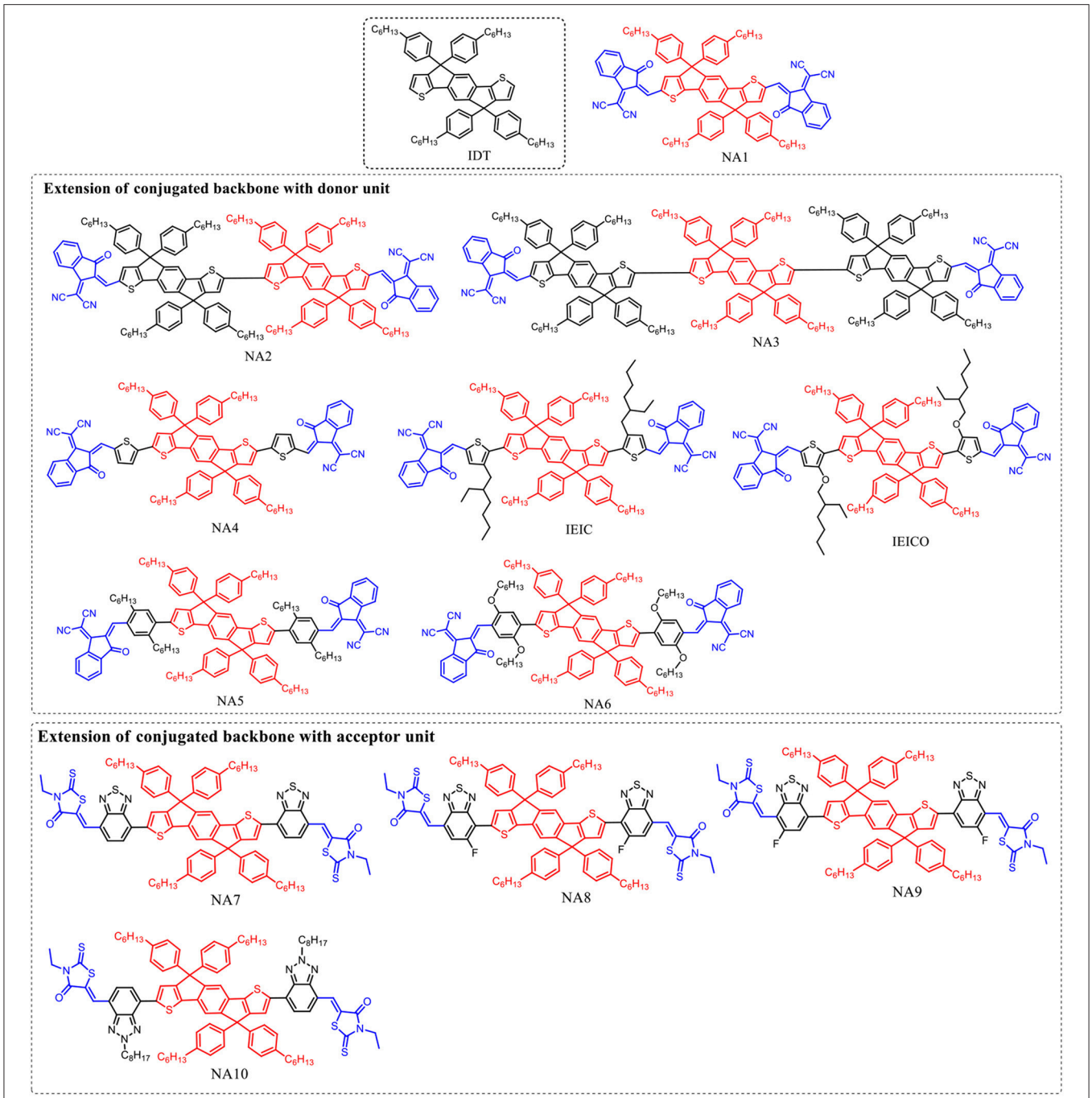

FIGURE 1 | IDT core based nonfullerene acceptors with different π conjugation extension.

maintaining the similar LUMO level (0.01 eV lower than IEIC). The PSCs using IEICO as acceptor yielded a high PCE of 8.4%, with a V_{oc} of 0.82 V and a J_{sc} of 17.7 mA cm^{-2}, while the control device with IEIC as acceptor exhibited a much lower PCE of 4.9% (**Table 2**) (Yao et al., 2016). In comparison with IEIC-based PSCs, the higher J_{sc} value of IEICO-based device should be resulted from the much broader photo-response spectrum with higher external quantum efficiency. Bo et al. used bis(alkoxy)-substituted or dialkyl-substituted benzene ring as π bridge for conjugated extension to develop two molecules NA5 and NA6 (**Figure 1**) (Liu Y. et al., 2017). Benefiting from the non-covalent S···O interaction locks, NA6 exhibited better planarity and broader absorption spectrum than NA5, with a lower E_g of 1.63 eV (**Table 1**). In addition, NA6 with locked conformation exhibited a higher quantum yield, which can effectively suppress the non-radiative energy loss and afford higher V_{oc} for devices.

TABLE 1 | Summary of absorption properties and energy levels of IDT core based nonfullerene acceptors shown in **Figure 1**.

Acceptor	Bandgap [eV]	HOMO [eV]	LUMO [eV]
NA1	1.70	−5.91	−3.83
NA2	1.57	−5.42	−3.80
NA3	1.53	−5.29	−3.79
NA4	1.55	−5.43	−3.85
IEIC	1.57	−5.42	−3.82
IEICO	1.34	−5.32	−3.95
NA5	1.75	−5.55	−3.82
NA6	1.63	−5.51	−3.78
NA7	1.68	−5.52	−3.69
NA8	1.67	−5.64	−3.73
NA9	1.71	−5.67	−3.74
NA10	1.87	−5.46	−3.57

TABLE 2 | Summary of photovoltaic properties of the nonfullerene acceptors shown in **Figure 1**.

Active layer	V_{oc} [v]	J_{sc} [mA cm^{-2}]	FF	PCE [%]	References
PDBT-T1:NA1	0.92	13.39	0.60	7.39	Lin et al., 2016a
PDBT-T1:NA2	1.02	5.28	0.48	2.58	Lin et al., 2016a
PDBT-T1:NA3	–	–	–	–	Lin et al., 2016a
PBDTTT-C-T:NA4	0.90	8.33	0.523	3.93	Bai et al., 2015b
PTB7-Th:IEIC	0.97	13.55	0.48	6.31	Lin et al., 2015b
PBDTTT-ET:IEICO	0.82	17.7	0.58	8.4	Yao et al., 2016
PBDTTT-ET:IEIC	0.90	11.7	0.47	4.90	Yao et al., 2016
PBDB-T:NA5	0.92	5.63	0.55	2.3	Liu Y. et al., 2017
PBDB-T:NA6	1.01	17.52	0.54	9.60	Liu F. et al., 2017
P3HT:NA7	0.84	8.91	0.681	5.12	Wu et al., 2015
PTzBI:NA8	1.00	11.6	0.623	7.44	Zhong et al., 2017
PTzBI:NA9	0.99	9.4	0.559	5.28	Zhong et al., 2017
J61:NA10	1.24	5.21	0.467	3.02	Tang et al., 2018

TABLE 3 | Summary of absorption properties and energy levels of IDT core based nonfullerene acceptors shown in **Figure 2**.

Acceptor	Bandgap [eV]	HOMO [eV]	LUMO [eV]
NA11	1.61	−5.37	−3.67
NA12	1.63	−5.51	−3.88
NA13	1.68	−5.58	−3.90

The device based on NA6 realized a promising PCE of 9.60%, with $V_{oc} = 1.01$ V, $J_{sc} = 17.52$ mA cm^{-2}, and FF = 0.54, while the NA5 based device showed a much lower PCE of 2.3% (**Table 2**).

As demonstrated above, using electron rich unit as conjugated backbone extension for NA1 is an effective strategy to broaden absorption spectrum, rise up HOMO levels while maintain similar LUMO levels of resulting molecules.

Extension of Conjugated Backbone With Acceptor Unit

Since the LUMO distribution is mainly located at the acceptor unit in D-A conjugated molecular system, using acceptor unit as building block can simultaneously manipulate the LUMO level and E_g of the molecules. Zhan et al. develop a nonfullerene acceptor NA7 (**Figure 1**) using benzothiadiazole as π-bridge (Wu et al., 2015). NA7 shows flat backbone configuration which is beneficial for charge transport, and a large dihedral angle between the hexylphenyl group and backbone plane which can prevent the over self-aggregation when blending with P3HT. Due to the relatively high LUMO level of NA7, the device based on P3HT:NA7 exhibited a high V_{oc} of 0.84 V, with a high PCE of 5.12% (**Table 2**) (Wu et al., 2015). Bazan et al. developed two NA7 analogs, NA8 and NA9 (**Figure 1**), with different positions of the fluorine atom in benzothiadiazole unit (Zhong et al., 2017). Relative to NA7 ($E_g = 1.68$ eV), NA8 exhibited a similar E_g of 1.67 eV, while NA9 showed a slightly larger E_g of 1.71 eV. The orientations of the fluorine atoms show little influence in the HOMO and LUMO levels but affect the calculated conformational diversity and the electrostatic potential of the molecules. The device based on PTzBI:NA8 exhibited a PCE of 7.44%, higher than that of PTzBI:NA9 based device (PCE = 5.28%). The photovoltaic performance of NA9 based device is poorer than that of NA8 based device, which should be resulted from the less optimal BHJ morphology. Zhou et al. replaced the benzothiadiazole units of NA7 by benzotriazole units to develop NA10 (**Figure 1**) (Tang et al., 2018). Due to the weaker electron-accepting ability of benzotriazole than benzothiadiazole, NA10 showed a higher LUMO level than NA7. Therefore, the J61:NA10 based device achieved an encouraging V_{oc} of 1.24 V, with a PCE of 3.02% (**Table 2**).

In short, the extension of conjugated backbone with donor or acceptor units will generally broaden absorption spectra and reduce E_g of the resulting molecules, and the introduction of donor units as π-bridge is more effective to reduce the E_g than acceptor units. On the other hand, the LUMO levels will be up-shifted when using donor units as π-bridge, while the incorporation of acceptor units will lead to higher LUMO levels.

Side Chains Engineering

The conjugated side chains substituents on the IDT unit will increase steric hindrance, reduce intermolecular interactions, and prevent over self-aggregation and large phase separation in blend film. Herein, the physicochemical and photovoltaic properties of IDT based acceptors can easily tune via side chains engineering in IDT unit. Zhan et al. developed an acceptor with non-conjugated alkyl chains in IDT unit (NA11, **Figure 2**) (Jia et al., 2017). NA11 exhibited a nearly flat molecular backbone configuration, with a lower E_g, higher HOMO level, and higher electron mobility than NA7 (**Table 3**). The device based on PTB7-Th:NA11 yielded a higher PCE of 8.7% than that of PTB7-Th:NA7 based device (**Table 4**). Furthermore, the NA11 based device exhibited better thermal stability and photo stability in comparison with NA7 based device. McCulloch et al. reported two alkyl chains substituted IDT based nonfullerene acceptors

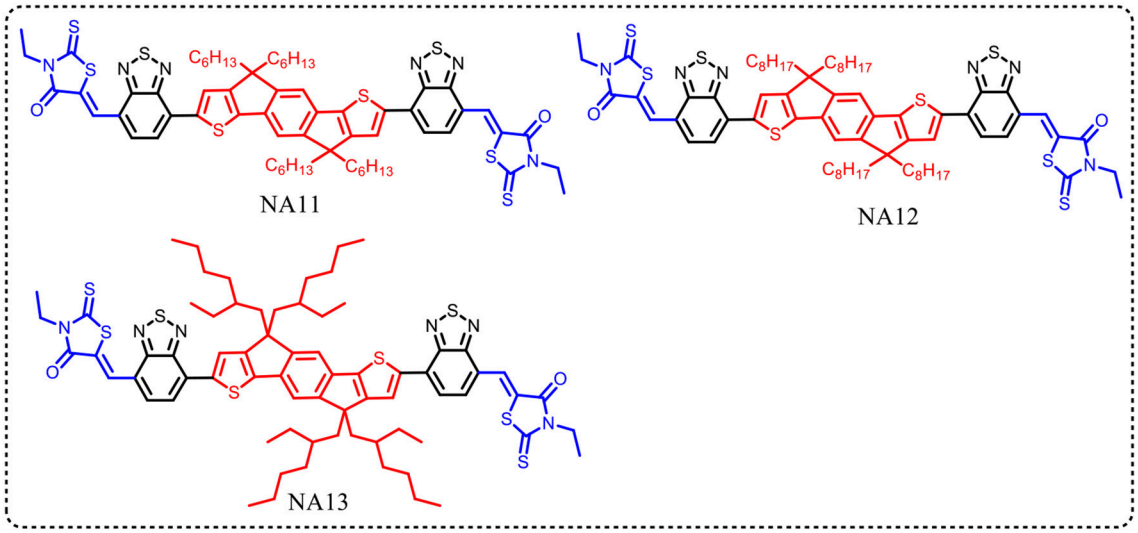

FIGURE 2 | Alkyl chains substituted IDT core based nonfullerene acceptors.

TABLE 4 | Summary of photovoltaic properties of the nonfullerene acceptors shown in **Figure 2**.

Active layer	V_{oc} [v]	J_{sc} [mA cm^{-2}]	FF	PCE [%]	References
PTB-Th:NA7	0.99	13.0	0.60	7.7	Jia et al., 2017
PTB-Th:NA11	0.95	15.2	0.60	8.7	Jia et al., 2017
P3HT:NA12	0.72	13.9	0.60	6.30	Holliday et al., 2016
P3HT:NA13	0.76	12.1	0.62	6.00	Holliday et al., 2016

NA12 and NA 13 (**Figure 2**) (Holliday et al., 2016). NA12 with linear alkyl chains showed a stronger crystallinity and a narrower E_g relative to NA13 with branched chains, resulting in higher J_{sc} and PCE values (**Tables 3**, **4**). In addition, the oxidative stability of these devices is superior to the benchmark P3HT:$PC_{60}BM$ device.

Effects of End-Capped Groups

The end-capped groups also affect the optical and electrochemical properties of this kind of nonfullerene acceptors. Hou et al. extended the π-conjugation area of the end group of NA1 to develop a new acceptor IDTN (as shown in **Figure 3**) (Li S. et al., 2017). The enlarged π-conjugation by phenyl unit in the end group effectively leads to red-shifted absorption and slightly lower LUMO and HOMO levels compared with NA1 (**Table 5**). Due to the enhanced intermolecular interactions and molecular ordering, IDTN shows a better molecular planarity and higher electron mobility than NA1. Therefore, an outstanding PCE of 12.2% was achieved from the PBDB-TF:IDTN based device, which is significantly higher than that of the NA1 based device (PCE = 7.4%). Zhan et al. used 2-(benzo[c][1,2,5]-thiadiazol-4-ylmethylene)-malononitrile as end-capped groups to develop a new acceptor NA14 (**Figure 3**) (Bai et al., 2015b). Relative to NA7, the stronger electron-withdrawing ability of end-capped units of NA14 leads to a lower E_g of 1.60 eV, lower LUMO of −3.8 eV, and lower HOMO of −5.6 eV (**Table 5**). The PBDTTT-C-T:NA14 based device afforded a relatively high PCE of 4.26%. Zhou et al. systematically engineered the end-capped units of three nonfullerene acceptors to carefully tune the driving force for high V_{oc} and J_{sc} values (Tang et al., 2018). With the increase of the electron-withdrawing ability of the end-capped units from NA15, NA10, to NA16, the LUMO levels and E_g simultaneously decrease (**Table 5**). By fine-tune the LUMO level of acceptor via end-capped unit, NA16 exhibited sufficient energy offset with J61 for efficient charge generation. The device based on J61:NA16 obtained a high PCE of 8.25%, with a high V_{oc} of 1.15 V (**Table 6**). Zhu et al. developed two thieno[3,4-b]thiophene-based acceptor, NA17 and NA18, with different end-capped groups (**Figure 3**) (Liu et al., 2016; Liu F. et al., 2017) NA17 exhibited an E_g of 1.54 eV, HOMO level of −5.50 eV, and LUMO level of −3.63 eV. Relative to NA 17, NA18 with stronger electron-withdrawing terminal group possesses lower E_g of 1.32 eV and deeper LUMO of −3.90 (**Table 5**). Device based on PTB7-Th:NA17 yielded a high PCE of 10.07%, with V_{oc} = 0.87 V, J_{sc} = 16.48 mA cm^{-2}, and FF = 0.70 (**Table 6**). Attributing to the deeper LUMO and broader absorption spectrum of NA18, PTB7-Th:NA18 based device exhibited a lower V_{oc} of 0.73 V and a higher J_{sc} of 16.48 mA cm^{-2}, leading to a promising PCE of 9.58% (**Table 6**). Yang et al. changed the end-capped unit of IEIC and IEICO to develop two analogs IDTC and IDTO (**Figure 3**) (Luo et al., 2017). Unexpectedly, IDTO showed slightly blue-shifted absorption range relative to IDTC. Nevertheless, the introduction of alkoxy groups effectively improved the intermolecular interactions and up-shifted the LUMO level of IDTO. The device based on PBDB-T:IDTC exhibited a PCE of 9.35%, with a V_{oc} of 0.917 V, while the PBDB-T:IDTO based device showed a higher PCE of 10.02% and a higher V_{oc} of 0.943 V (**Table 6**). Hou et al. introduced fluorine atoms onto the end group of IEICO (IEICO-4F, **Figure 3**) to

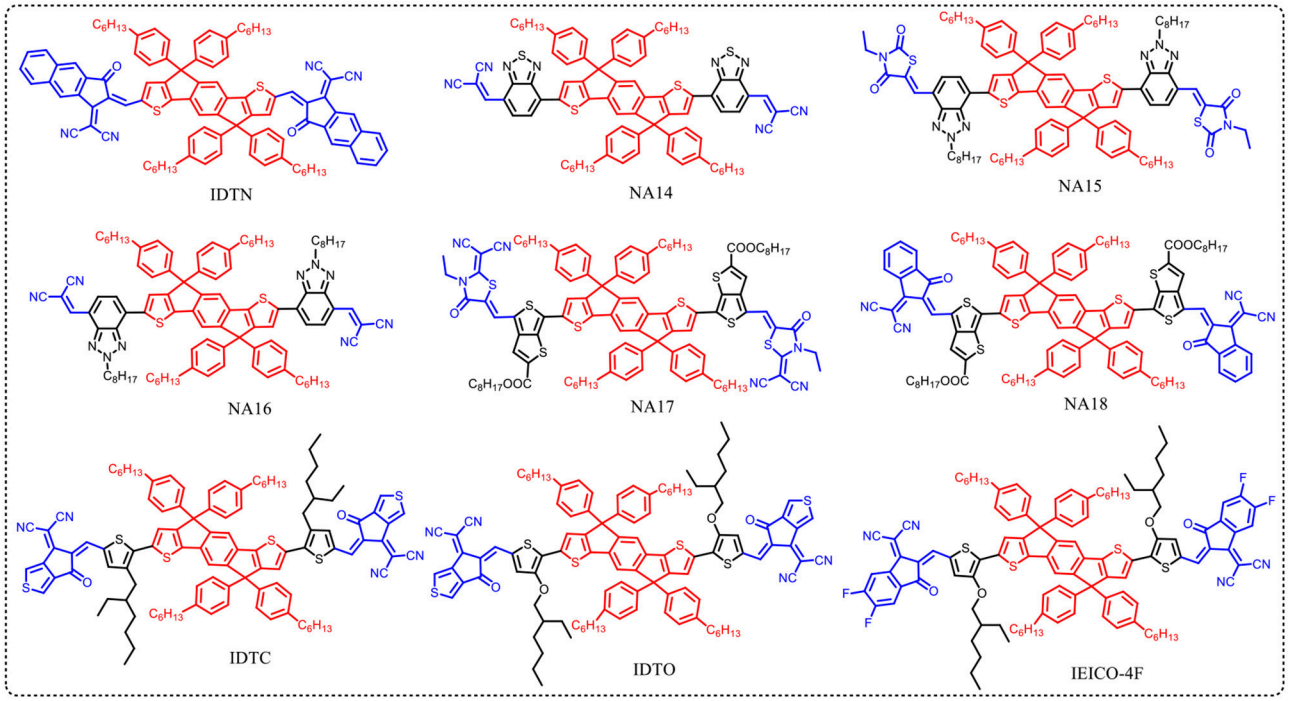

FIGURE 3 | IDT core based nonfullerene acceptors with different end group.

TABLE 5 | Summary of absorption properties and energy levels of IDT core based nonfullerene acceptors shown in **Figure 3**.

Acceptor	Bandgap [eV]	HOMO [eV]	LUMO [eV]
NA1	1.70	−5.81	−3.94
IDTN	1.59	−5.79	−3.98
NA14	1.60	−5.6	−3.8
NA15	2.00	−5.43	−3.46
NA16	1.76	−5.49	−3.61
NA17	1.54	−5.50	−3.63
NA18	1.32	−5.50	−3.90
IDTC	1.51	−5.57	−3.96
IDTO	1.53	−5.52	−3.84
IEICO-4F	1.24	−5.44	−4.19

TABLE 6 | Summary of photovoltaic properties of the nonfullerene acceptors shown in **Figure 3**.

Active layer	V_{oc} [v]	J_{sc} [mA cm^{-2}]	FF	PCE [%]	References
PBDB-TF:IDTN	0.946	16.58	0.78	12.2	Li S. et al., 2017
PBDB-TF:NA1	0.993	13.01	0.57	7.4	Li S. et al., 2017
PBDTTT-C-T:NA14	0.766	10.10	0.551	4.26	Bai et al., 2015b
J61:NA15	1.29	0.84	0.239	0.26	Tang et al., 2018
J61:NA16	1.15	10.84	0.662	8.25	Tang et al., 2018
PTB7-Th:NA17	0.87	16.48	0.70	10.07	Liu et al., 2016
PTB7-Th:NA18	0.73	20.75	0.63	9.58	Liu F. et al., 2017
PBDB-T:IDTC	0.917	16.56	0.616	9.35	Luo et al., 2017
PBDB-T:IDTO	0.943	16.25	0.654	10.02	Luo et al., 2017
PBDTTT-EFT:IEICO-4F	0.739	22.8	0.594	10.0	Yao et al., 2017a
J52:IEICO-4F	0.734	21.9	0.585	9.4	Yao et al., 2017a

enhance the intramolecular charge transfer effect. IEICO-4F showed lower *E*g of 1.24 eV and higher LUMO level of −4.19 eV than IEICO. Using IEICO-4F as acceptor, PBDTTT-EFT or J52 as donor, high J_{sc} values over 20 mA cm^{-2} were both recorded in the corresponding devices (**Table 6**).

IDTT BASED FUSED-RING ACCEPTORS

IDTT unit with two additional extended thiophene rings than IDT exhibits excellent planarity (Wong et al., 2006). The pioneering work for IDTT-based nonfullerene acceptor is the development of ITIC which was firstly reported by Lin et al. (2015a) and Zhan et al. (2015). ITIC possesses strong absorption, suitable energy level, good electron transport ability, and good miscibility with various polymer donors. A promising PCE of 6.80% was achieved from the PTB7-Th:ITIC based device (**Table 8**) (Lin et al., 2015a). Later on, many state-of-the-art ITIC-based PSCs with excellent photovoltaic performance have been reported (Bin et al., 2016; Gao et al., 2016; Qin et al., 2016; Zhao W. et al., 2016; Yang et al., 2017a,b; Xu et al., 2018), and ITIC has been regarded as excellent acceptor for high performance

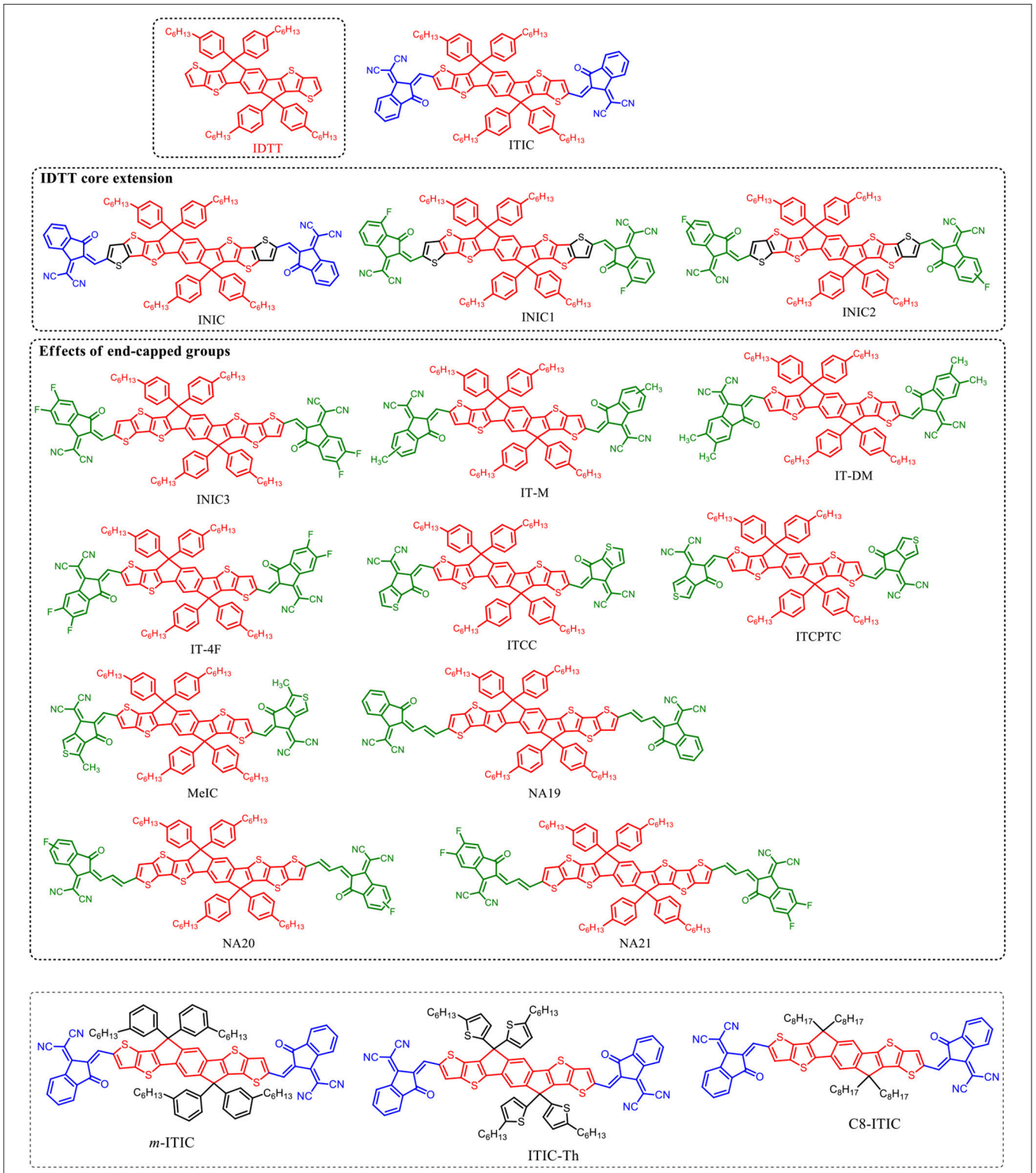

FIGURE 4 | IDTT core based nonfullerene acceptors.

TABLE 7 | Summary of absorption properties and energy levels of IDT core based nonfullerene acceptors shown in **Figure 3**.

Acceptor	Bandgap [eV]	HOMO [eV]	LUMO [eV]
ITIC	1.59	−5.48	−3.83
INIC	1.57	−5.45	−3.88
INIC1	1.56	−5.54	−3.97
INIC2	1.52	−5.52	−3.98
INIC3	1.48	−5.52	−4.02
IT-M	1.60	−5.58	−3.98
IT-DM	1.63	−5.56	−3.93
IT-4F	1.53	−5.66	−4.14
ITCC	1.67	−5.47	−3.76
ITCPTC	1.58	−5.62	−3.96
MeIC	1.58	−5.57	−3.92
NA19	1.40	−5.46	−3.97
NA20	1.37	−5.56	−4.01
NA21	1.35	−5.58	−4.04
m-ITIC	1.58	−5.52	−3.82
ITIC-Th	1.60	−5.66	−3.93
C8-ITIC	1.55	−5.63	−3.91

TABLE 8 | Summary of photovoltaic properties of the nonfullerene acceptors shown in **Figure 4**.

Active layer	V_{oc} [v]	J_{sc} [mA cm^{-2}]	FF	PCE [%]	References
PTB7-Th:ITIC	0.766	10.10	0.551	4.26	Bai et al., 2015b
FTAZ:INIC	0.957	13.51	0.579	7.7	Dai et al., 2017
FTAZ:INIC1	0.929	16.63	0.643	10.1	Dai et al., 2017
FTAZ:INIC2	0.903	17.56	0.668	10.8	Dai et al., 2017
FTAZ:INIC3	0.857	19.44	0.674	11.5	Dai et al., 2017
PBDB-T:ITIC	0.90	16.80	0.742	11.22	Li et al., 2016
PBDB-T:IT-M	0.94	17.44	0.735	12.05	Li et al., 2016
PBDB-T:IT-DM	0.97	16.48	0.706	11.29	Li et al., 2016
PBDB-T-SF:IT-4F	0.88	20.88	0.713	13.10	Zhao et al., 2017
PBDB-T-2Cl:IT-4F	0.86	21.80	0.77	14.4	Zhang et al., 2018
P2:IT-4F	0.90	20.73	0.76	14.2	Li W. et al., 2018
PBDB-T:ITCC	1.01	15.9	0.71	11.4	Yao et al., 2017b
PBT1-EH:ITCPTC	0.95	16.5	0.751	11.8	Dongjun et al., 2017
J71:MeIC	0.918	18.41	0.742	12.54	Luo et al., 2018
J71:NA19	0.89	14.47	0.576	7.34	Li X et al., 2017
J71:NA20	0.84	19.73	0.587	9.72	Li X et al., 2017
J71:NA21	0.81	20.60	0.632	10.54	Li X et al., 2017
J61:ITIC	0.898	17.97	0.655	10.57	Yang et al., 2016
J61:m-ITIC	0.912	18.31	0.755	11.77	Yang et al., 2016
PTB7-Th:ITIC-Th	0.80	15.93	0.680	8.7	Lin et al., 2016b
PDBT-T1:ITIC-Th	0.88	15.80	0.671	9.6	Lin et al., 2016b
PFBDB-T:ITIC	0.95	18.5	0.66	11.71	Fei et al., 2018
PFBDB-T:C8-ITIC	0.94	19.6	0.72	13.2	Fei et al., 2018

PSCs. To further improve the photovoltaic performance, plenty of molecular design strategies have been carried out to optimize the physicochemical of ITIC. Zhan et al. extended the fused-ring core of ITIC and end-capped with different acceptor unit to develop a series of ITIC derivatives INIC, INIC1, INIC2, and INIC3 (**Figure 4**) (Dai et al., 2017). Relative to ITIC, INIC with extended conjugated core showed red-shifted absorption spectrum (E_g = 1.57 eV), slightly higher HOMO level, and slightly lower LUMO level (**Table 7**). The introduction of fluorine atom onto the end-capped group of INIC effectively red-shifted the absorption and down-shifted the HOMO and LUMO levels (**Table 7**). The device based on INIC:FTAZ showed a high V_{oc} of 0.957 V, with moderate PCE of 7.7%. The fluorination in INIC leads to lower V_{oc} values, while significantly improves the FF and J_{sc} of the corresponding devices, delivering a higher PCE values (**Table 7**). The end-capped groups of ITIC show great impact in its photovoltaic performance. Variations of end-capped groups have been conducted onto ITIC to optimize its photovoltaic properties. To up-shift the LUMO level of ITIC without causing too much steric hindrance for intermolecular packing, Hou et al. modulated the LUMO levels of ITIC by incorporating one and two methyls in the end-capped groups (IT-M and IT-DM, **Figure 3**). Benefited from the weak electron-donating property of methyl, the LUMO levels of IT-M and IT-DM were elevated by 0.04 and 0.09 eV relative to ITIC, respectively (**Table 7**) (Li et al., 2016). Therefore, higher V_{oc} values of 0.94 V and 0.97 V were achieved from the PBDB-T:IT-M and PBDB-T:IT-DM based device, respectively. Encouragingly, a remarkable PCE of 12.05% was realized from the PBDB-T:IT-M based device, with J_{sc} = 17.44 mA cm^{-2}, and FF = 0.735 (**Table 8**). One successful molecular optimization on ITIC is the incorporated F-atoms into the end-capping groups to develop IT-4F (**Figure 4**) (Zhao et al., 2017). Due to the electron-pulling effect of the fluorine atom, IT-4F showed reduced LUMO level, red-shifted absorption spectrum, and enhanced intramolecular charge transfer effects than ITIC. By rational selection of polymer donor with matching energy level, over 13% PCEs have been achieved from IT-4F based PSCs (Cui Y. et al., 2017; Li S. et al., 2018; Zhang et al., 2018). Other end groups engineering such as the replacement of phenyl-fused indanone of ITIC by thienyl-fused indanone as end-groups (ITCC) also affects the electronic properties and enhances intermolecular interactions (Yao et al., 2017b). ITCC possesses larger E_g of 1.67 eV and up-shifted HOMO and LUMO levels (**Table 7**) than ITIC. In combination with the improved electron-transport properties and high-lying LUMO level of ITCC, an impressive V_{oc} of 1.01 V and a high PCE of 11.4% was achieved from the ITCC based PSC device (**Table 8**). Changing the orientation of end-capped thiophene of ITCC (ITCPTC, **Figure 4**) leads to reduced E_g of 1.58 eV and deeper energy levels (**Table 7**) (Dongjun et al., 2017). Furthermore, such thiophene-fused ending group can promote the molecular interactions and crystallization compared to ITIC with a benzene-fused end-capped group. The PSCs device using ITCPTC as acceptor and PBT1-EH as donor demonstrated a high PCE of 11.8%, with a remarkable FF of 0.751 (**Table 8**). Further molecular optimization of ITCPTC is the introduction of methyl onto the thiophene-fused end groups (MeIC, **Figure 4**) (Luo et al., 2018). Due to the weak electron-donating ability

of methyl group, MeIC showed slightly up-shifted LUMO level than ITCPTC and maintained the intramolecular interaction and crystallization. The MeIC-based PSC achieved a high PCE of 12.54%, with a V_{oc} of 0.918, a J_{sc} of 18.41 mA cm^{-2}, and FF of 0.742% (**Table 8**). Li et al. introduced double bond π-bridges into ITIC to develop three acceptor materials (NA19, NA20, and NA21, as shown in **Figure 4**) (Li X et al., 2017). The insertion of vinylene π-bridge reduces the E_g, and the fluorine substitution down-shifts the HOMO and LUMO levels of the molecules (**Table 7**). The PSC device based on J71:NA19 showed a moderate PCE of 7.34%. Significantly enhanced J_{sc} of 19.73 mA cm^{-2} was obtained from J71:NA20 based device, with a high PCE of 9.72%. In comparison with the NA19 and NA20 based devices, the devices based on J71:NA21 exhibited the highest PCE of 10.54%, with a notable J_{sc} of 20.60 mA cm^{-2}.

Similar to IDT unit, the steric effect of tetrahexylphenyl substituents on the IDTT unit also can reduce intermolecular interactions and prevent the acceptor from forming excessively large crystalline domains when blending with donor material. Thus, the electronic and intramolecular properties can be fine-tuned via the side chains manipulation on IDTT unit. Li et al. developed an analog (*m*-ITIC, **Figure 4**) by side chain isomerism engineering on the alkyl-phenyl substituents of ITIC (Yang et al., 2016). *m*-ITIC exhibited slightly reduced E_g and up-shifted LUMO and HOMO levels, while more crystalline and stronger film absorption coefficient than ITIC. In comparison with J61:ITIC based device, overall better photovoltaic performance was realized in J71:*m*-ITIC based device (**Table 8**). The replacement of phenyl side chains on ITIC by thienyl side chains leads to lower energy levels and increased intermolecular interactions of resulting molecule (ITIC-Th) (Lin et al., 2016b). The enhanced intermolecular interaction of ITIC-Th relative to ITIC should be attributed to the easy polarization of sulfur atom and sulfur-sulfur interaction. A high PCE of 9.6% was obtained from the PDBT-T1:ITIC-Th based device (**Table 8**). Consider the fact that linear alkyl chains could potentially improve the packing ability and the charge transport mobility of resulting molecules over bulky side chains, Heeney et al. developed an IDTT-based acceptor with linear alkyl side chains (C8-ITIC) (Fei et al., 2018). C8-ITIC showed reduced E_g, higher absorptivity, and increased propensity to crystallize than ITIC. The device based on C8-ITIC recorded an impressive PCE of 13.2%, which is higher than that of ITIC based device (PCE = 11.71%, **Table 8**).

Summary and Perspective

In summary, we have reviewed the recent progress of IDT and IDTT based nonfullerene acceptors for PSCs. Compared with fullerene acceptors, IDT and IDTT based nonfullerene acceptors offer plenty of molecular design possibilities to tune the physicochemical properties. With the purpose to well-match with the specific donor material, the absorption feature and energy levels of IDT and IDTT based acceptors can be easily and effectively manipulated by rational selection of π-bridge and end-capped groups. Moreover, the intermolecular packing, molecular orientation, as well as crystallinity can be optimized by side-chains engineering to form good morphology with donor materials. Benefiting from the diversification of chemical modification on acceptors and donors, significant progress has been achieved from the nonfullerene acceptors based PSCs. Obviously, the emerging of nonfullerene acceptors brings a bright future for PSCs field. Nevertheless, nonfullerene acceptors still confront challenges. Firstly, although it is straightforward to manipulate the optical absorption and energy level of the IDT and IDTT based molecules, the anisotropic conjugated structures of nonfullerene acceptors make it more complicate to tune the miscibility between donor and acceptor for well-developed morphology. The deep insight into the relationship between molecular structure and photovoltaic should be further exploited. In particularly, various nonfullerene acceptors with different photo-electronic and molecular packing properties have been developed, the rational selection of acceptor material to well-match with polymer donor is essential. Secondly, to further improve the photovoltaic performance, much effort should be devoted to manipulate the energy levels of donor and acceptors for minimizing the energy loss of the devices. Finally, the stability of nonfulleren based device should also be fully investigated.

AUTHOR CONTRIBUTIONS

The author confirms being the sole contributor of this work and approved it for publication.

ACKNOWLEDGMENTS

This work is supported by National Natural Science Foundation of China (51603136), Jiangsu Provincial Natural Science Foundation (BK20150327), and China Postdoctoral Science Foundation (2015M581855 and 2017T100395).

REFERENCES

Ameri, T., Dennler, G., Lungenschmied, C., and Brabec, C. J. (2009). Organic tandem solar cells: a review. *Energy Environ. Sci.* 2, 347–363. doi: 10.1039/B817952B

Ameri, T., Li, N., and Brabec, C. J. (2013). Highly efficient organic tandem solar cells: a follow up review. *Energy Environ. Sci.* 6, 2390–2413. doi: 10.1039/C3EE40388B

Bai, H., Wang, Y., Cheng, P., Wang, J., Wu, Y., Hou, J., et al. (2015a). An electron acceptor based on indacenodithiophene and 1,1-dicyanomethylene-3-indanone for fullerene-free organic solar cells. *J. Mater. Chem. A* 3, 1910–1914. doi: 10.1039/C4TA06004K

Bai, H., Wu, Y., Wang, Y., Wu, Y., Li, R., Cheng, P., et al. (2015b). Nonfullerene acceptors based on extended fused rings flanked with benzothiadiazolylmethylenemalononitrile for polymer solar cells. *J. Mater. Chem. A* 3, 20758–20766. doi: 10.1039/C5TA05901A

Bin, H., Gao, L., Zhang, Z.-G., Yang, Y., Zhang, Y., Zhang, C., et al. (2016). 11.4% Efficiency non-fullerene polymer solar cells with trialkylsilyl substituted 2D-conjugated polymer as donor. *Nat. Commun.* 7:13651. doi: 10.1038/ncomms13651

Chen, Y., Wan, X., and Long, G. (2013). High performance photovoltaic applications using solution-processed small molecules. *Acc. Chem. Res.* 46, 2645–2655. doi: 10.1021/ar400088c

Chen, Y., Zhan, C., and Yao, J. (2016). Understanding solvent manipulation of morphology in bulk-heterojunction organic solar cells. *Chem. Asian J.* 11, 2620–2632. doi: 10.1002/asia.201600374

Cheng, P., Li, G., Zhan, X., and Yang, Y. (2018). Next-generation organic photovoltaics based on non-fullerene acceptors. *Nat. Photon*. 12, 131–142. doi: 10.1038/s41566-018-0104-9

Chueh, C.-C., Li, C.-Z., and Jen, A. K. Y. (2015). Recent progress and perspective in solution-processed Interfacial materials for efficient and stable polymer and organometal perovskite solar cells. *Energy Environ. Sci.* 8, 1160–1189. doi: 10.1039/C4EE03824J

Cui, C., He, Z., Wu, Y., Cheng, X., Wu, H., Li, Y., et al. (2016). High-performance polymer solar cells based on a 2D-conjugated polymer with an alkylthio side-chain. *Energy Environ. Sci.* 9, 885–891. doi: 10.1039/C5EE03684D

Cui, C., Li, Y., and Li, Y. (2017). Fullerene derivatives for the applications as acceptor and cathode buffer layer materials for organic and perovskite solar cells. *Adv. Energy Mater.* 7:1601251. doi: 10.1002/aenm.201601251

Cui, C., and Wong, W.-Y. (2016). Effects of alkylthio and alkoxy side chains in polymer donor materials for organic solar cells. *Macromol. Rapid Commun.* 37, 287–302. doi: 10.1002/marc.201500620

Cui, C., Wong, W.-Y., and Li, Y. (2014). Improvement of open-circuit voltage and photovoltaic properties of 2D-conjugated polymers by alkylthio substitution. *Energy Environ. Sci.* 7, 2276–2284. doi: 10.1039/C4EE00446A

Cui, Y., Yao, H., Gao, B., Qin, Y., Zhang, S., Yang, B., et al. (2017). Fine-tuned photoactive and interconnection layers for achieving over 13% efficiency in a fullerene-free tandem organic solar cell. *J. Am. Chem. Soc*. 139, 7302–7309. doi: 10.1021/jacs.7b01493

Dai, S., Zhao, F., Zhang, Q., Lau, T.-K., Li, T., Liu, K., et al. (2017). Fused nonacyclic electron acceptors for efficient polymer solar cells. *J. Am. Chem. Soc*. 139, 1336–1343. doi: 10.1021/jacs.6b12755

Dongjun, X., Tao, L., Wei, G., Cheng, Z., Lijun, H., Zhenghui, L., et al. (2017). A novel thiophene-fused ending group enabling an excellent small molecule acceptor for high-performance fullerene-free polymer solar cells with 11.8% efficiency. *Sola RRL* 1:1700044. doi: 10.1002/solr.201700044

Duan, C., Zhang, K., Zhong, C., Huang, F., and Cao, Y. (2013). Recent advances in water/alcohol-soluble [small pi]-conjugated materials: new materials and growing applications in solar cells. *Chem. Soc. Rev*. 42, 9071–9104. doi: 10.1039/C3CS60200A

Elumalai, N. K., and Uddin, A. (2016). Open circuit voltage of organic solar cells: an in-depth review. *Energy Environ. Sci.* 9, 391–410. doi: 10.1039/C5EE02871J

Fei, Z., Eisner, F. D., Jiao, X., Azzouzi, M., Röhr, J. A., Han, Y., et al. (2018). An alkylated indacenodithieno[3,2-b]thiophene-based nonfullerene acceptor with high crystallinity exhibiting single junction solar cell efficiencies greater than 13% with low voltage losses. *Adv. Mater*. 30:1705209. doi: 10.1002/adma.201705209

Gao, L., Zhang, Z.-G., Bin, H., Xue, L., Yang, Y., Wang, C., et al. (2016). High-efficiency nonfullerene polymer solar cells with medium bandgap polymer donor and narrow bandgap organic semiconductor acceptor. *Adv. Mater*. 28, 8288–8295. doi: 10.1002/adma.201601595

Gupta, M., Yan, D., Shen, F., Xu, J., and Zhan, C. (2018). Perylenediimide: phosphonium-based binary blended small-molecule cathode interlayer for efficient fullerene-free polymer solar cells with open circuit voltage to 1.0 V. *Acta Phys.-Chim. Sin.* 34. doi: 10.3866/PKU.WHXB201805101

He, Y., and Li, Y. (2011). Fullerene derivative acceptors for high performance polymer solar cells. *Phys. Chem. Chem. Phys*. 13, 1970–1983. doi: 10.1039/c0cp01178a

He, Z., Zhong, C., Su, S., Xu, M., Wu, H., and Cao, Y. (2012). Enhanced power-conversion efficiency in polymer solar cells using an inverted device structure. *Nat. Photon*. 6, 591–595. doi: 10.1038/nphoton.2012.190

Heeger, A. J. (2013). 25th anniversary article: bulk heterojunction solar cells: understanding the mechanism of operation. *Adv. Mater*. 26, 10–27. doi: 10.1002/adma.201304373

Hendriks, K. H., Li, W., Heintges, G. H., van Pruissen, G. W., Wienk, M. M., and Janssen, R. A. (2014). Homocoupling defects in diketopyrrolopyrrole-based copolymers and their effect on photovoltaic performance. *J. Am. Chem. Soc.* 136, 11128–11133. doi: 10.1021/ja505574a

Holliday, S., Ashraf, R. S., Wadsworth, A., Baran, D., Yousaf, S. A., Nielsen, C. B., et al. (2016). High-efficiency and air-stable P3HT-based polymer solar cells with a new non-fullerene acceptor. *Nat. Commun*. 7:11585. doi: 10.1038/ncomms11585

Hou, J., Inganäs, O., Friend, R. H., and Gao, F. (2018). Organic solar cells based on non-fullerene acceptors. *Nat. Mater*. 17, 119–128. doi: 10.1038/nmat5063

Hu, H., Chow, P. C. Y., Zhang, G., Ma, T., Liu, J., Yang, G., et al. (2017). Design of donor polymers with strong temperature-dependent aggregation property for efficient organic photovoltaics. *Acc. Chem. Res.* 50, 2519–2528. doi: 10.1021/acs.accounts.7b00293

Janssen, R. A. J., and Nelson, J. (2013). Factors limiting device efficiency in organic photovoltaics. *Adv. Mater*. 25, 1847–1858. doi: 10.1002/adma.201202873

Jia, B., Wu, Y., Zhao, F., Yan, C., Zhu, S., Cheng, P., et al. (2017). Rhodanine flanked indacenodithiophene as non-fullerene acceptor for efficient polymer solar cells. *Sci. China Chem*. 60, 257–263. doi: 10.1007/s11426-016-0336-6

Li, G., Zhu, R., and Yang, Y. (2012). Polymer solar cells. *Nat. Photon*. 6, 153–161. doi: 10.1038/nphoton.2012.11

Li, S., Ye, L., Zhao, W., Liu, X., Zhu, J., Ade, H., et al. (2017). Design of a new small-molecule electron acceptor enables efficient polymer solar cells with high fill factor. *Adv. Mater.* 26:1704051. doi: 10.1002/adma.201704051

Li, S., Ye, L., Zhao, W., Yan, H., Yang, B., Liu, D., et al. (2018). A wide band gap polymer with a deep highest occupied molecular orbital level enables 14.2% efficiency in polymer solar cells. *J. Am. Chem. Soc.* 140, 7159–7167. doi: 10.1021/jacs.8b02695

Li, S., Ye, L., Zhao, W., Zhang, S., Mukherjee, S., Ade, H., et al. (2016). Energy-level modulation of small-molecule electron acceptors to achieve over 12% efficiency in polymer solar cells. *Adv. Mater*. 28, 9423–9429. doi: 10.1002/adma.201602776

Li, W., Yan, D., Liu, W., Chen, J., Xu, W., Zhan, C., et al. (2017). A new function of N719: N719 based solution-processible binary cathode buffer layer enables high-efficiency single-junction polymer solar cells. *Solar RRL* 1:1700014. doi: 10.1002/solr.201700014

Li, W., Ye, L., Li, S., Yao, H., Ade, H., and Hou, J. (2018). A high-efficiency organic solar cell enabled by the strong intramolecular electron push–pull effect of the nonfullerene acceptor. *Adv. Mater*. 30:1707170. doi: 10.1002/adma.201707170

Li, X., Huang, H., Bin, H., Peng, Z., Zhu, C., Xue, L., et al. (2017). Synthesis and photovoltaic properties of a series of narrow bandgap organic semiconductor acceptors with their absorption edge reaching 900 nm. *Chem. Mater*. 29, 10130–10138. doi: 10.1021/acs.chemmater.7b03928

Li, Y. (2012). Molecular design of photovoltaic materials for polymer solar cells: toward suitable electronic energy levels and broad absorption. *Acc. Chem. Res.* 45, 723–733. doi: 10.1021/ar2002446

Li, Y. (2013). Fullerene-bisadduct acceptors for polymer solar cells. *Chem. Asian J.* 8, 2316–2328. doi: 10.1002/asia.201300600

Lin, Y., Li, T., Zhao, F., Han, L., Wang, Z., Wu, Y., et al. (2016a). Structure evolution of oligomer fused-ring electron acceptors toward high efficiency of as-cast polymer solar cells. *Adv. Energy Mater*. 6:1600854. doi: 10.1002/aenm.201600854

Lin, Y., Wang, J., Zhang, Z.-G., Bai, H., Li, Y., Zhu, D., et al. (2015a). An electron acceptor challenging fullerenes for efficient polymer solar cells. *Adv. Mater.* 27, 1170–1174. doi: 10.1002/adma.201404317

Lin, Y., Zhang, Z.-G., Bai, H., Wang, J., Yao, Y., Li, Y., et al. (2015b). High-performance fullerene-free polymer solar cells with 6.31% efficiency. *Energy Environ. Sci.* 8, 610–616. doi: 10.1039/C4EE03424D

Lin, Y., Zhao, F., He, Q., Huo, L., Wu, Y., Parker, T. C., et al. (2016b). High-performance electron acceptor with thienyl side chains for organic photovoltaics. *J. Am. Chem. Soc.* 138, 4955–4961. doi: 10.1021/jacs.6b02004

Liu, F., Zhou, Z., Zhang, C., Vergote, T., Fan, H., Liu, F., et al. (2016). A Thieno[3,4-b]thiophene-based non-fullerene electron acceptor for high-performance bulk-heterojunction organic solar cells. *J. Am. Chem. Soc*. 138, 15523–15526. doi: 10.1021/jacs.6b08523

Liu, F., Zhou, Z., Zhang, C., Zhang, J., Hu, Q., Vergote, T., et al. (2017). Efficient semitransparent solar cells with high NIR responsiveness enabled by a small-bandgap electron acceptor. *Adv. Mater*. 29:1606574. doi: 10.1002/adma.201606574

Liu, W., Li, W., Yao, J., and Zhan, C. (2018). Achieving high short-circuit current and fill-factor via increasing quinoidal character on nonfullerene small molecule acceptor. *Chin. Chem. Lett.* 29, 381–384. doi: 10.1016/j.cclet.2017.11.018

Liu, Y., Zhang, Z., Feng, S., Li, M., Wu, L., Hou, R., et al. (2017). Exploiting noncovalently conformational locking as a design strategy for high performance fused-ring electron acceptor used in polymer solar cells. *J. Am. Chem. Soc*. 139, 3356–3359. doi: 10.1021/jacs.7b00566

Liu, Y., Zhao, J., Li, Z., Mu, Z., Ma, W., Hu, H., et al. (2014). Aggregation and morphology control enables multiple cases of high-efficiency polymer solar cells. *Nat. Commun*. 5:5293. doi: 10.1038/ncomms6293

Lopez, S. A., Sanchez-Lengeling, B., de Goes Soares, J., and Aspuru-Guzik, A. (2017). Design principles and top non-fullerene acceptor candidates for organic photovoltaics. *Joule* 1, 857–870. doi: 10.1016/j.joule.2017.10.006

Lu, L., Zheng, T., Wu, Q., Schneider, A. M., Zhao, D., and Yu, L. (2015). Recent advances in bulk heterojunction polymer solar cells. *Chem. Rev*. 115, 12666–12731. doi: 10.1021/acs.chemrev.5b00098

Luo, Z., Bin, H., Liu, T., Zhang, Z.-G., Yang, Y., Zhong, C., et al. (2018). Fine-tuning of molecular packing and energy level through methyl substitution enabling excellent small molecule acceptors for nonfullerene polymer solar cells with efficiency up to 12.54%. *Adv. Mater*. 30:1706124. doi: 10.1002/adma.201706124

Luo, Z., Zhao, Y., Zhang, Z.-G., Li, G., Wu, K., Xie, D., et al. (2017). Side-chain effects on energy-level modulation and device performance of organic semiconductor acceptors in organic solar cells. *ACS Appl. Mater. Interfaces* 9, 34146–34152. doi: 10.1021/acsami.7b10275

Meillaud, F., Boccard, M., Bugnon, G., Despeisse, M., Hänni, S., Haug, F.-J., et al. (2015). Recent advances and remaining challenges in thin-film silicon photovoltaic technology. *Mater. Today* 18, 378–384. doi: 10.1016/j.mattod.2015.03.002

Nielsen, C. B., Turbiez, M., and McCulloch, I. (2012). Recent advances in the development of semiconducting dpp-containing polymers for transistor applications. *Adv. Mater*. 25, 1859–1880. doi: 10.1002/adma.201201795

Osaka, I., and Takimiya, K. (2017). Naphthobischalcogenadiazole conjugated polymers: emerging materials for organic electronics. *Adv. Mater*. 29:1605218. doi: 10.1002/adma.201605218

Qin, Y., Uddin, M. A., Chen, Y., Jang, B., Zhao, K., Zheng, Z., et al. (2016). Highly efficient fullerene-free polymer solar cells fabricated with polythiophene derivative. *Adv. Mater*. 28, 9416–9422. doi: 10.1002/adma.201601803

Street, R. A. (2016). Electronic structure and properties of organic bulk-heterojunction interfaces. *Adv. Mater*. 28, 3814–3830. doi: 10.1002/adma.201503162

Sun, C., Pan, F., Bin, H., Zhang, J., Xue, L., Qiu, B., et al. (2018). A low cost and high performance polymer donor material for polymer solar cells. *Nat. Commun*. 9:743. doi: 10.1038/s41467-018-03207-x

Tang, A., Xiao, B., Wang, Y., Gao, F., Tajima, K., Bin, H., et al. (2018). Simultaneously achieved high open-circuit voltage and efficient charge generation by fine-tuning charge-transfer driving force in nonfullerene polymer solar cells. *Adv. Funct. Mater*. 28:1704507. doi: 10.1002/adfm.201704507

Wang, F., Tan, Z. A., and Li, Y. (2015). Solution-processable metal oxides/chelates as electrode buffer layers for efficient and stable polymer solar cells. *Energy Environ. Sci*. **8**, 1059–1091. doi: 10.1039/C4EE03802A

Wang, J., Shi, K., Suo, Y., Lin, Y., Yu, G., and Zhan, X. (2016). Monodisperse macromolecules based on benzodithiophene and diketopyrrolopyrrole with strong NIR absorption and high mobility. *J. Mater. Chem. C* 4, 3781–3791. doi: 10.1039/C5TC03589A

Wong, K.-T., Chao, T.-C., Chi, L.-C., Chu, Y.-Y., Balaiah, A., Chiu, S.-F., et al. (2006). Syntheses and structures of novel heteroarene-fused coplanar π-conjugated chromophores. *Organ. Lett*. 8, 5033–5036. doi: 10.1021/ol061791y

Wu, Y., Bai, H., Wang, Z., Cheng, P., Zhu, S., Wang, Y., et al. (2015). A planar electron acceptor for efficient polymer solar cells. *Energy Environ. Sci*. 8, 3215–3221. doi: 10.1039/C5EE02477C

Xu, X., Yu, T., Bi, Z., Ma, W., Li, Y., and Peng, Q. (2018). Realizing over 13% efficiency in green-solvent-processed nonfullerene organic solar cells enabled by 1,3,4-Thiadiazole-based wide-bandgap copolymers. *Adv. Mater*. 30:170397. doi: 10.1002/adma.201703973

Yan, C., Barlow, S., Wang, Z., Yan, H., Jen, A. K. Y., Marder, S. R., et al. (2018). Non-fullerene acceptors for organic solar cells. *Nat. Rev. Mater*. 3:18003. doi: 10.1038/natrevmats.2018.3

Yang, F., Li, C., Lai, W., Zhang, A., Huang, H., and Li, W. (2017a). Halogenated conjugated molecules for ambipolar field-effect transistors and non-fullerene organic solar cells. *Mater. Chem. Front*. 1, 1389–1395. doi: 10.1039/C7QM00025A

Yang, F., Qian, D., Balawi, A., Wu, Y., Ma, W., Laquai, F., et al. (2017b). Performance limitations in thieno[3,4-c]pyrrole-4,6-dione-based polymer:ITIC solar cells. *Phys. Chem. Chem. Phys*. 19, 23990–23998. doi: 10.1039/C7CP04780K

Yang, Y., Zhang, Z.-G., Bin, H., Chen, S., Gao, L., Xue, L., et al. (2016). Side-chain isomerization on an n-type organic semiconductor itic acceptor makes 11.77% high efficiency polymer solar cells. *J. Am. Chem. Soc*. 138, 15011–15018. doi: 10.1021/jacs.6b09110

Yao, H., Chen, Y., Qin, Y., Yu, R., Cui, Y., Yang, B., et al. (2016). Design and synthesis of a low bandgap small molecule acceptor for efficient polymer solar cells. *Adv. Mater*. 28, 8283–8287. doi: 10.1002/adma.201602642

Yao, H., Cui, Y., Yu, R., Gao, B., Zhang, H., and Hou, J. (2017a). Design, synthesis, and photovoltaic characterization of a small molecular acceptor with an ultra-narrow band gap. *Angew. Chem. Int. Ed*. 56, 3045–3049. doi: 10.1002/anie.201610944

Yao, H., Ye, L., Hou, J., Jang, B., Han, G., Cui, Y., et al. (2017b). Achieving highly efficient nonfullerene organic solar cells with improved intermolecular interaction and open-circuit voltage. *Adv. Mater*. 29:1700254. doi: 10.1002/adma.201700254

Ye, L., Zhang, S., Huo, L., Zhang, M., and Hou, J. (2014). Molecular design toward highly efficient photovoltaic polymers based on two-dimensional conjugated benzodithiophene. *Acc. Chem. Res*. 47, 1595–1603. doi: 10.1021/ar5000743

Zhan, C., and Yao, J. (2016). More than conformational "Twisting" or "Coplanarity": molecular strategies for designing high-efficiency nonfullerene organic solar cells. *Chem. Mater*. 28, 1948–1964. doi: 10.1021/acs.chemmater.5b04339

Zhan, C., Zhang, X., and Yao, J. (2015). New advances in non-fullerene acceptor based organic solar cells. *RSC Adv*. 5, 93002–93026. doi: 10.1039/C5RA17715D

Zhang, J., Zhu, L., and Wei, Z. (2017). Toward over 15% power conversion efficiency for organic solar cells: current status and perspectives. *Small Methods* 1:1700258. doi: 10.1002/smtd.201700258

Zhang, S., Qin, Y., Zhu, J., and Hou, J. (2018). Over 14% efficiency in polymer solar cells enabled by a chlorinated polymer donor. *Adv. Mater*. 30:e1800868. doi: 10.1002/adma.201800868

Zhao, F., Wang, C., and Zhan, X. (2018). Morphology control in organic solar cells. *Adv. Energy Mater*. 1703147. doi: 10.1002/aenm.201703147

Zhao, J., Li, Y., Yang, G., Jiang, K., Lin, H., Ade, H., et al. (2016). Efficient organic solar cells processed from hydrocarbon solvents. *Nat. Energy* 1:15027. doi: 10.1038/nenergy.2015.27

Zhao, W., Li, S., Yao, H., Zhang, S., Zhang, Y., Yang, B., et al. (2017). Molecular optimization enables over 13% efficiency in organic solar cells. *J. Am. Chem. Soc*. 139, 7148–7151. doi: 10.1021/jacs.7b02677

Zhao, W., Qian, D., Zhang, S., Li, S., Inganäs, O., Gao, F., et al. (2016). Fullerene-free polymer solar cells with over 11% efficiency and excellent thermal stability. *Adv. Mater*. 28, 4734–4739. doi: 10.1002/adma.201600281

Zhong, W., Fan, B., Cui, J., Ying, L., Liu, F., Peng, J., et al. (2017). Regioisomeric non-fullerene acceptors containing fluorobenzo[c][1,2,5]thiadiazole unit for polymer solar cells. *ACS Appl. Mater. Interfaces* 9, 37087–37093. doi: 10.1021/acsami.7b12902

Zou, Y., Wu, Y., Yang, H., Dong, Y., Cui, C., and Li, Y. (2017). The effect of alkylthio side chains in oligothiophene-based donor materials for organic solar cells. *Mol. Syst. Des. Eng*. 3, 131–141. doi: 10.1039/C7ME00075H

Conflict of Interest Statement: The author declares that the research was conducted in the absence of any commercial or financial relationships that could be construed as a potential conflict of interest.

The reviewer WL and handling Editor declared their shared affiliation.

frontiers in Chemistry

ORIGINAL RESEARCH
published: 24 September 2018
doi: 10.3389/fchem.2018.00427

Dithienonaphthalene-Based Non-fullerene Acceptors With Different Bandgaps for Organic Solar Cells

Meiqi Zhang[1,2], *Yunlong Ma*[1] *and Qingdong Zheng*[1]*

[1] State Key Laboratory of Structural Chemistry, Fujian Institute of Research on the Structure of Matter, Chinese Academy of Sciences, Fuzhou, China, [2] University of Chinese Academy of Sciences, Beijing, China

Compared to the traditional fullerene derivatives, non-fullerene acceptors show more tunable absorption bands as well as adjustable energy levels which are favorable for further PCE enhancement of organic solar cells. In order to enhance light-harvesting property of dithienonaphthalene (DTN)-based acceptors, we designed and synthesized two novel non-fullerene acceptors (DTNIF and DTNSF) based on a ladder-type DTN donor core flanked with two different acceptor units. In combination with a benchmark wide bandgap copolymer (PBDB-T), the best performance device based on DTNIF displayed a high PCE of 8.73% with a short-circuit current (J_{SC}) of 13.26 mA cm^{-2} and a large fill factor (FF) of 72.77%. With a reduced bandgap of DTNSF, the corresponding best performance device showed an increased J_{SC} of 14.49 mA cm^{-2} although only a moderate PCE of 7.15% was achieved. These findings offer a molecular design strategy to control the bandgap of DTN-based non-fullerene acceptors with improved light-harvesting.

Keywords: organic solar cell, non-fullerene, ladder-type structure, power conversion efficiency, bandgap

OPEN ACCESS

Edited by:
Chuanlang Zhan,
Institute of Chemistry (CAS), China

Reviewed by:
Chaohua Cui,
Soochow University, China
Jianhua Huang,
Huaqiao University, China

***Correspondence:**
Qingdong Zheng
qingdongzheng@fjirsm.ac.cn

Specialty section:
This article was submitted to Organic Chemistry, a section of the journal Frontiers in Chemistry

Received: *07 July 2018*
Accepted: *30 August 2018*
Published: *24 September 2018*

Citation:
Zhang M, Ma Y and Zheng Q (2018) Dithienonaphthalene-Based Non-fullerene Acceptors With Different Bandgaps for Organic Solar Cells. Front. Chem. 6:427. doi: 10.3389/fchem.2018.00427

INTRODUCTION

Organic solar cells (OSCs) have attracted increasing attention over the past decade due to their light-weight, mechanical flexibility, and potential low-cost (Facchetti, 2011; Liu et al., 2014; Rong et al., 2015). Bulk heterojunction (BHJ) OSCs featuring with an active layer of an electron acceptor material blended with an electron donor material, are widely used (Wu et al., 2011; Chen et al., 2013; Wang et al., 2014; Xu et al., 2015). In the early years' research on OSCs, fullerene derivatives, such as [6,6]-phenyl-C71-butyric acid methyl ester ($PC_{71}BM$) and [6,6]-phenyl-C61-butyric acid methyl ester ($PC_{61}BM$) have been used as the dominant electron acceptors due to their high electron mobilities and unique phase separation property when blended with rod-like donor materials (You et al., 2013; Ma et al., 2016). Although power conversion efficiencies (PCEs) of fullerene-based OSCs have surpassed 10% in single-junction OSCs (Liu et al., 2014; Chen et al., 2015; He et al., 2015; Zhang et al., 2015), the poor absorption in the visible region and the limited tunability in energy levels of the fullerene derivatives prevent a further PCE improvement of fullerene-based OSCs (Zhan et al., 2011). To break these limitations, emerging efforts have thus been devoted to designing non-fullerene acceptors which could have broader absorption, more adjustable energy levels and structural flexibility in comparison with the fullerene derivatives (Li et al., 2015; Lin et al., 2015; Nielsen et al., 2015; Liu et al., 2016, 2018; Qin et al., 2016; Zhang et al., 2016; Tang et al., 2017; Shen et al., 2018). Among the non-fullerene acceptors, small molecules with

acceptor-donor-acceptor (A-D-A) configuration are popular in organic photovoltaic field because the HOMO and LUMO energy levels of A-D-A type molecules can be separately tuned by selecting suitable donor cores and acceptor terminals (Lin et al., 2015; Wu et al., 2015; Zhao et al., 2017). Using ladder-type angular-shaped dithienonaphthalene (DTN) as the donor unit and 2-(3-oxo-2,3-dihydro-1H-inden-1-ylidene)malononitrile (INCN) as the strong electron-withdrawing unit, we reported an A-D-A type non-fullerene acceptor (DTNIC8), recently, which exhibited a bandgap of 1.73 eV and a decent PCE of 9.03% (Ma et al., 2017b). In order to obtain DTN-based non-fullerene acceptors with an up-shifted LUMO energy level, we further used 5-(benzo[c][1,2,5]thiadiazol-4-ylmethylene)-3-ethyl-2-thioxothiazolidin-4-one as the weak electron-deficient group (Ma et al., 2017a). The resulting non-fullerene acceptor (DTNR) exhibited a similar bandgap of 1.72 eV but a much high-lying LUMO energy level of −3.75 eV which is beneficial for achieving a large V_{oc} for the corresponding PSC. Both the DTN-based acceptors showed relatively wide bandgaps with intense absorption bands in the range of 500–750 nm (Ma et al., 2017a,b). In order to improve the PCEs of OSCs based on wide bandgap donor materials, the bandgaps of non-fullerene acceptors based on DTN should be reduced further. For the A-D-A type non-fullerene acceptors, their bandgaps can be reduced by using stronger electron withdrawing groups as terminals (Zhao et al., 2017) and by extending π-conjugation length of the molecular backbone (Dai et al., 2017).

In this context, two novel DTN-based non-fullerene acceptors, DTNIF and DTNSF, were designed and synthesized by using a stronger electron withdrawing group of 2-(6-fluoro-3-oxo-2,3-dihydro-1H-inden-1-ylidene)malononitrile (INCNF), or by inserting two additional thiophene bridges in molecular backbone (shown in **Figure 1**). Inverted OSCs were fabricated by blending a typical wide bandgap copolymer (PBDB-T in **Figure 1**) with the DTN-based non-fullerene acceptors. The PBDB-T:DTNIF-based devices exhibited a PCE of 8.73% with a high FF of 72.77%, and a short circuit current (J_{sc}) of 13.26 mA cm^{-2}. However, the PBDB-T:DTNSF-based devices showed a moderate PCE of 7.15% with an increased J_{sc} of 14.49 mA cm^{-2} and a low FF of 54.62%. Moreover, we also studied effects of the terminal units on the bandgap, energy level, and charge transporting property of the DTN-based non-fullerene acceptors.

RESULTS AND DISCUSSION

Synthesis and Characterization

The synthetic routes of DTNIF and DTNSF are shown in **Scheme 1** and the synthetic details are described in the Experimental section. Compounds **1** and **2** were synthesized according to our earlier published methods (Ma et al., 2013, 2017b).

Compound **3** was obtained in 96% yield by the Stille coupling reaction between Compound **2** and 5-bromothiophene-2-carbaldehyde using $Pd(PPh_3)_4$ as the catalyst. A Knoevenagel condensation reaction between Compound **3** and INCNF afforded DTNSF in 46% yield. DTNIF was synthesized in 60% yield by using the same condensation reaction between Compound **1** and INCNF. The chemical structures of DTNIF and DTNSF were determined by using ^1H NMR and high-resolution mass spectrometry. The purity of the acceptors was verified further by elemental analysis. All non-fullerene materials are soluble at room temperature in the traditional organic solvents, such as CH_2Cl_2, chlorobenzene, and $CHCl_3$ etc.

Optical and Electrochemical Properties

The absorption properties of DTNIF and DTNSF were investigated in $CHCl_3$ solution as well as in thin film. The obtained linear absorption spectra are shown in **Figure 2** and the specific optical data are shown in **Table 1**.

In chloroform solution, DTNIF displayed a strong absorption band in the wavelength region of 500–700 nm with a clear shoulder peak at 600 nm which can be attributed to the intramolecular charge transfer from the electron donating core to the electron withdrawing terminals. Compared to DTNIF, DTNSF showed a red-shifted absorption band in the wavelength region of 520–780 nm which can be ascribed to its extended conjugation with two additional thiophene bridges. The maximum extinction coefficient of DTNIF (1.8×10^5 M^{-1} cm^{-1} at 637 nm) was higher than that of DTNSF (1.4×10^5 M^{-1} cm^{-1} at 682 nm). From solution to thin film, both the non-fullerene acceptors showed broader and red-shifted absorptions. The optical bandgaps estimated from their absorption edges were 1.63 eV and 1.47 eV for DTNIF and DTNSF, respectively, both of which are lower than the bandgap of DTNIC8 (1.73 eV in **Table 1**). With the standard A-D-A configuration in the molecular backbone, DTNIF exhibits a deep HOMO energy level of −5.82 eV. However, with the insertion of two additional thiophene units in the A-D-A backbone, the HOMO energy level of DTNSF increases to −5.52 eV together with a significant reduced bandgap of 1.47 eV which is mainly attributed to its extended π-conjugation in comparison with DTNIF. As shown in **Figure 2B**, DTNSF in thin film exhibits a more complementary absorption spectrum with PBDB-T in comparison that with DTNIF, suggesting a possible enhanced J_{sc} value for the DTNSF-based OSC.

The electrochemical properties of the non-fullerene acceptors were tested by electrochemical cyclic voltammetry (CV). Here, ferrocene was used as an internal reference, which has a HOMO level of −4.80 eV. The cyclic voltammograms are shown in **Figure 3A** and the corresponding data are listed in **Table 1**. According to their onset potentials, the HOMO/LUMO energy levels of DTNIF and DTNSF were calculated to be −5.82/−3.92 and −5.52/−4.00 eV, respectively. PBDB-T has HOMO and LUMO energy levels of −5.33 and −2.92 eV, respectively, which energetically matched with those of the acceptors (**Figure 3B**).

Photoluminescence

In order to know the exciton dissociation as well as the charge transfer behaviors of donor/acceptor blends, photoluminescence (PL) quenching experiments were carried out and the results were shown in **Figure 4**. We selected 665 nm and 750 nm as the excitation wavelengths to respectively excite DTNIF and DTNSF in either pure or blend films. The donor/acceptor blend ratios were fixed at 1:1 by mol. As shown in **Figures 4A,C**, the

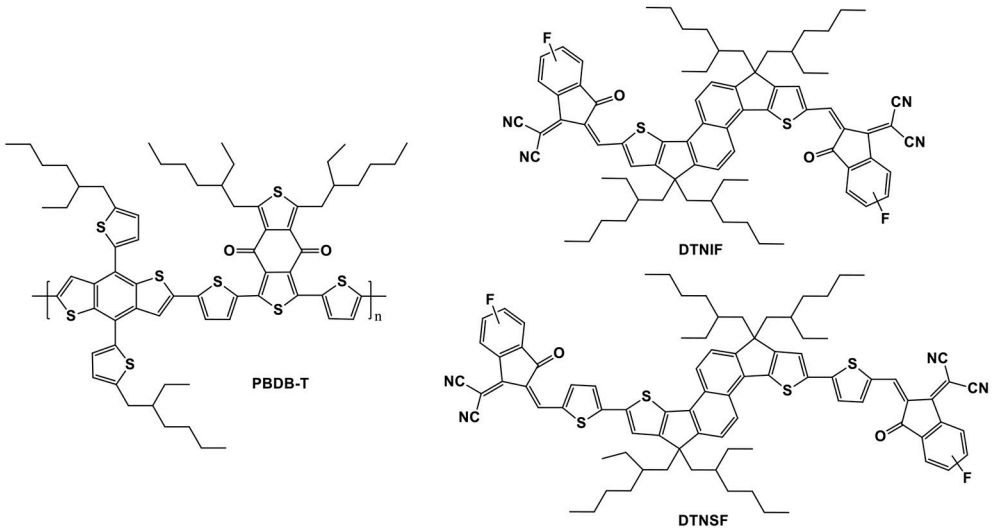

FIGURE 1 | Chemical structures of PBDB-T and the target non-fullerene acceptors.

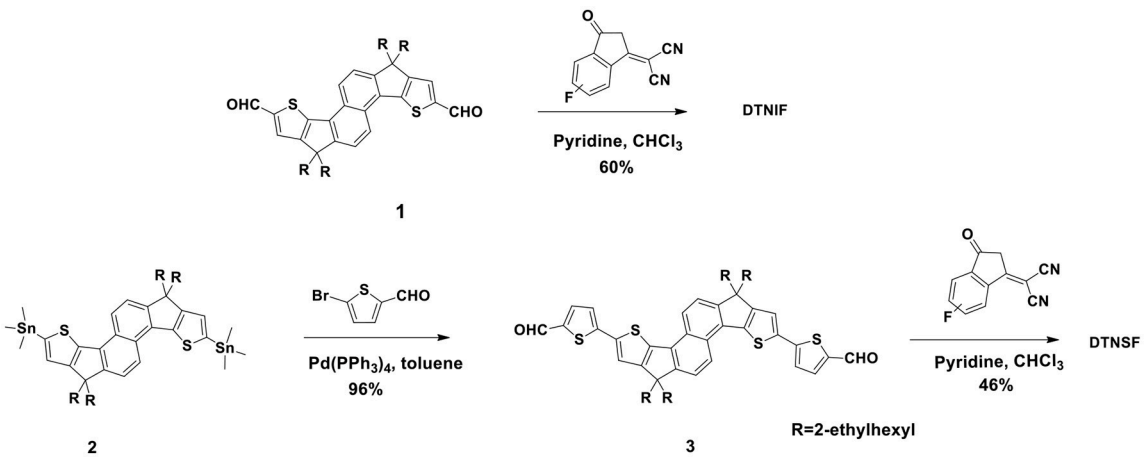

SCHEME 1 | Synthetic routes of the non-fullerene acceptors.

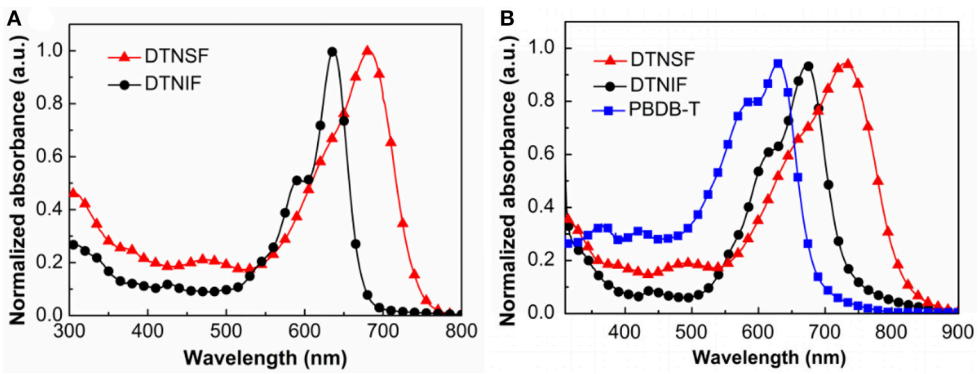

FIGURE 2 | (A) Normalized UV–Vis absorption spectra of DTNIF and DTNSF in $CHCl_3$. **(B)** Normalized UV–Vis absorption spectra of DTNIF, DTNSF, and PBDB-T in thin film.

TABLE 1 | Optical and electrochemical properties of DTNIF and DTNSF.

Molecules	ε [10^5 M^{-1} cm^{-1}]	$\lambda_{max}^{solution}$ [nm]	λ_{max}^{film} [nm]	E_g^{opt} [eV][a]	HOMO [eV][b]	LUMO [eV][c]	References
DTNIF	1.8	636	672	1.63	−5.82	−3.92	This work
DTNSF	1.4	682	731	1.47	−5.52	−4.00	This work
DTNIC8	2.1	634	660	1.73	−5.91	−3.93	Ma et al., 2017b

[a]*Estimated from the onset of the absorption spectra of thin films;* [b]$E_{HOMO} = -(\varphi_{ox} + 4.82)$ *eV;* [c]$E_{LUMO} = -(\varphi_{red} + 4.82)$ *eV.*

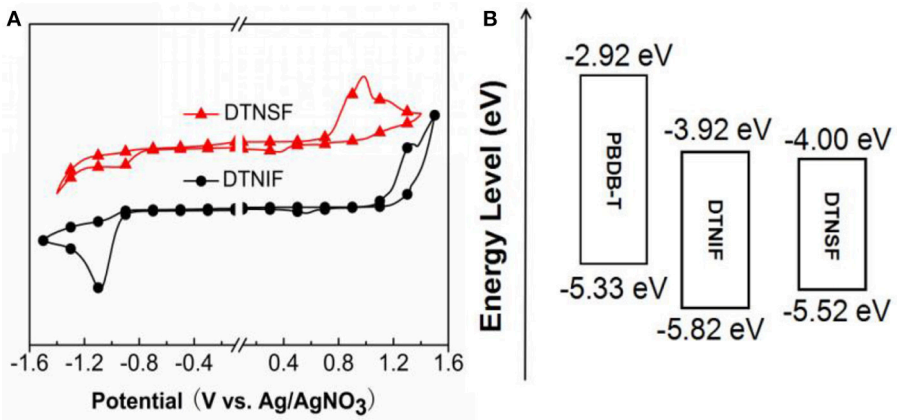

FIGURE 3 | (A) Cyclic voltammograms of DTNIF and DTNSF. **(B)** Estimated energy level diagram of DTNIF, DTNSF, and PBDB-T.

strong emission of DTNIF at 700 nm and 760 nm (DINSF at 825 nm) in the blend film apparently quenched when compared to that in the pure film, demonstrating the efficient hole transfer from both the acceptors to PBDB-T (donor). As for the PL emission of PBDB-T (shown in **Figures 4B,D**), the PL intensities of PBDB-T:DTNIF and PBDB-T:DTNSF blend films decreased significantly in comparison with those of the pure PBDB-T film when excited at 570 and 580 nm, respectively. It suggested that there is efficient electron transfer from the PBDB-T donor to both the acceptors. These results demonstrated that both the non-fullerene acceptors and the polymer donor contribute to the photocurrent generation of the OSCs.

Photovoltaic Performance

PBDB-T is a wide-bandgap polymer donor which has a strong absorption band in the wavelength range from 500 to 700 nm. The absorption bands of our non-fullerene acceptors generally match the absorption band of PBDB-T. Thus, we chose PBDB-T as donor to fabricate OSCs with an inverted device structure: indium tin oxide (ITO)/ZnO/donor:acceptor/MoO_3/Ag. The active layers were spin-coated by using PBDB-T:acceptor (w/w, 1:1) blend solution in chlorobenzene (18 mg/mL) without any additives and post-treatments. The *J*–*V* curves of the best performance devices are shown in **Figure 5A** and detailed device parameters are summarized in **Table 2**.

Under simulated AM 1.5 G, 100 mW cm^{-2} illumination and the optimal device fabrication condition, the best performance OSC based on PBDB-T:DTNIF showed a PCE of 8.73% with a V_{oc} of 0.90 V, a J_{sc} of 13.26 mA cm^{-2} and a FF of 72.77%. Nevertheless, the best performance DTNSF-based device exhibited a PCE of 7.15% with a V_{oc} of 0.92 V and a lower FF of 54.62%. The lower FF was mainly resulted from the lower and less balanced hole and electron mobilities for the PBDB-T:DTNSF active layer. However, the J_{sc} of 14.49 mA cm^{-2} for the DTNSF-based device is larger than the PBDB-T:DTNIF-based counterpart owing to the red-shifted absorption of DTNSF. We noticed that the DTNSF-based device showed a slightly higher V_{oc} than the DTNIF-based device despite the fact that DTNIF possesses a higher LUMO level than DTNSF. Besides the energy gap (between HOMO of the donor and LUMO of the acceptor) which can affect the V_{oc} of corresponding device, other factors, such as recombination rate, reverse saturation current, carrier density, defect states and crystallinity, and charge-transfer states could also play an important role in influencing the V_{oc} (Elumalai and Uddin, 2016). Therefore, it is reasonable that the DTNIF-based device exhibited a relatively lower V_{oc} of 0.90 V.

As shown in **Figure 5B**, external quantum efficiency (EQE) spectra of the best performance devices were measured to ensure the accuracy of the PCE measurements. The device based on DTNIF has higher EQE values in the wavelength range of 300–750 nm with a maximum value of 78% at 660 nm. In contrast, the EQE spectrum edge of the best performance DTNSF-based device extended to 850 nm, which agrees with the absorption spectrum of the DTNSF blend film. The J_{sc} values obtained by integrating the EQE data with the solar spectrum (AM 1.5 G) were 13.26 and 14.21 mA cm^{-2} for DTNIF and DTNSF,

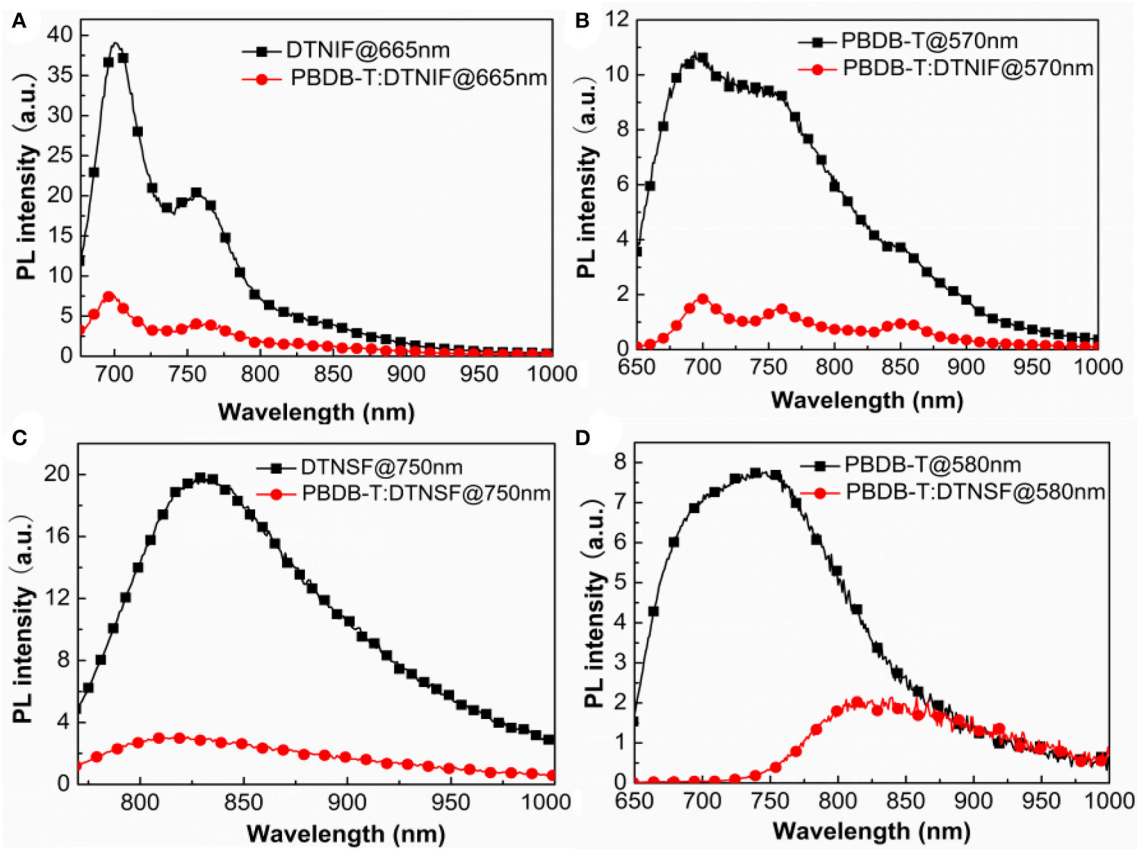

FIGURE 4 | Fluorescence quenching experiments of PBDB-T:DTNIF **(A,B)** and PBDB-T:DTNSF **(C,D)** excited mainly by the acceptor **(A,C)** and the donor **(B,D)**.

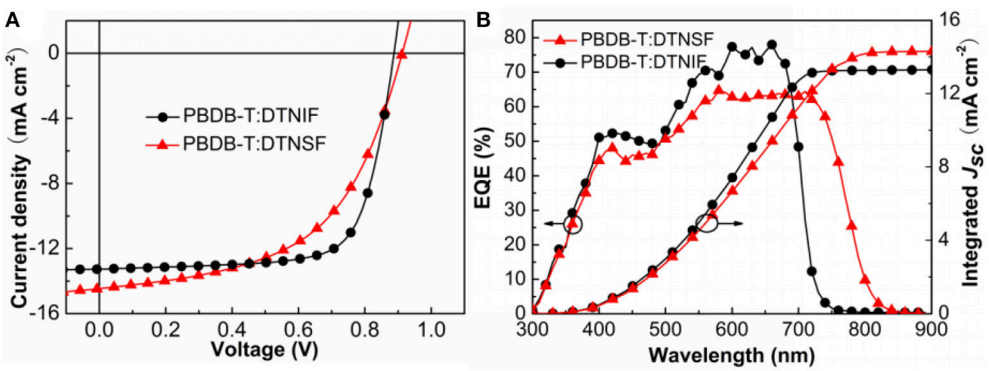

FIGURE 5 | (A) *J–V* characteristics of the non-fullerene OSCs. **(B)** EQE and the corresponding integrated J_{SC} curves for the OSCs.

respectively. The integrated values are in consistent with those from the *J-V* measurement within 2% error.

Film Morphology Analysis

Tapping-mode atomic force microscopy (AFM) was used to characterize the morphology of active layer that has an important influence on the performance of OSCs. The film samples for AFM analysis were prepared in identical fashion to those prepared for device fabrication in which the donor/acceptor blend ratios were fixed at 1:1 by mol. The obtained AFM images were presented in **Figure 6**. The AFM height images of the DTNIF and DTNSF-based blend films showed similar and apparently fibrillar structures (**Figures 6A,B**). However, the DTNSF-based blend shows smoother root-mean-square (RMS) roughness (R_q) than the DTNIF-based blend. Compared to PBDB-T:DTNIF film with a R_q of 3.25 nm, the RMS roughness of PBDB-T:DTNSF film

decreased to 2.09 nm which could be attributed to the smaller intramolecular twisted angel and greater coplanarity of DTNSF. As shown in the phase images (**Figures 6C,D**), fibrillar structure can also be observed in both the blend films. In comparison with PBDB-T:DTNSF blend film, PBDB-T:DTNIF film revealed fibrillar structures with larger sizes which will be favorable for efficient charge transport in the DTNIF-based devices as confirmed by their higher hole and electron mobilities.

As mentioned above, the optimal morphology can enhance charge transport efficiency that will further affect the J_{sc} and FF of OSCs. We measured the electron (μ_e) and hole (μ_h) mobilities using the space charge limited current (SCLC) method with the device structures of ITO/ZnO/PBDB-T:acceptor/Ca/Al and ITO/PEDOT:PSS/PBDB-T:acceptor/Au, respectively. For both the hole- and electron-only devices, the donor/acceptor ratios for are fixed at 1:1 by mol. The *J-V* characteristics of the hole-only and electron-only devices are shown in **Figure 7** and the mobility data are shown in **Table 3**. The μ_e and μ_h for the PBDB-T:DTNIF blend film were calculated to be 1.79×10^{-5} and 1.87×10^{-5} cm^2 V^{-1} s^{-1}, respectively, which far exceeded those for the PBDB-T:DTNSF film ($\mu_e = 6.70 \times 10^{-6}$ and $\mu_h = 1.35 \times 10^{-5}$ cm^2 V^{-1} s^{-1}). More balanced μ_h/μ_e ratio of 1.04 was observed for the PBDB-T:DTNIF blend film when compared to a larger μ_h/μ_e ratio of 2.01 for the PBDB-T:DTNSF blend. Thus, the higher and more balanced hole and electron mobilities of the PBDB-T:DTNIF blend can explain the higher FF of the resulting solar cell.

TABLE 2 | Photovoltaic properties of OSCs (under AM 1.5 G, 100 mW cm^{-2}).

Active layer	V_{oc} (V)	J_{sc} (mA cm^{-2})	FF (%)	PCE (%)
PBDB-T:DTNIF	0.90	13.26	72.77	8.73 (8.65 ± 0.23)
PBDB-T:DTNSF	0.92	14.49	54.62	7.15 (6.94 ± 0.20)

CONCLUSIONS

In summary, we have developed two novel non-fullerene acceptors, DTNIF and DTNSF, with different bandgaps. The introduction of F atom into the terminal group leads to a slightly narrow bandgap and a red-shifted absorption in the 500–750 nm region. To achieve a more complementary spectrum of non-fullerene acceptor with wide bandgap donor materials, such as PBDB-T, we further introduced two thiophenes as bridge units which lead to a more planar molecular configuration with an extended conjugation. Without any additive and post-treatment, the best performance DTNIF-based device exhibited a PCE of 8.73% with V_{oc} of 0.90 V, FF of 72.77% and J_{sc} of 13.26 mA cm^{-2}. The best performance device based on DTNSF afforded an enhanced J_{sc} of 14.49 mA cm^{-2} although only a moderate PCE of 7.15% was obtained due to the decreased and unbalanced hole and electron mobilities of the DTNSF-based active layer. It should be noted that the device performance of DTNIF-based

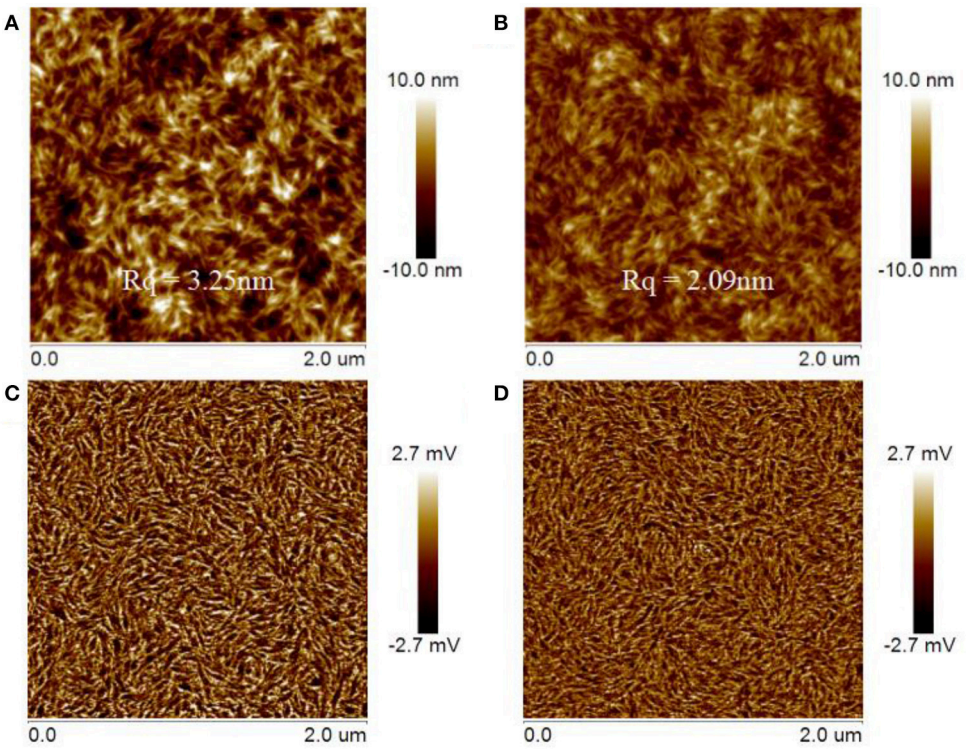

FIGURE 6 | Tapping-mode AFM topography images **(A,B)** and phase **(C,D)** images of the PBDB-T:DTNIF **(A,C)** and PBDB-T:DTNSF **(B,D)** films.

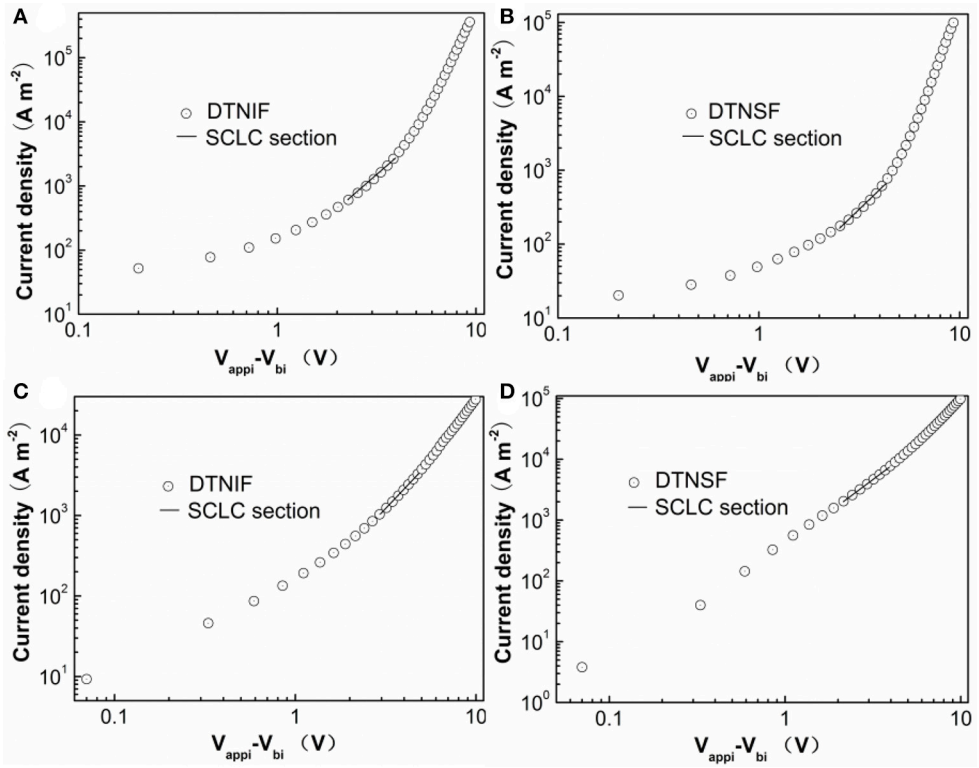

FIGURE 7 | *J–V* characteristic for **(A,C)** DTNIF and **(B,D)** DTNSF-based **(A,B)** electron-only and **(C,D)** hole-only devices.

TABLE 3 | Hole and electron mobilities of the SCLC devices based on two different active layers.

Active layer	μ_e [cm^2 V^{-1} s^{-1}]	μ_h [cm^2 V^{-1} s^{-1}]	μ_h/μ_e
PBDB-T:DTNIF	1.79×10^{-5}	1.87×10^{-5}	1.04
PBDB-T:DTNSF	6.70×10^{-6}	1.35×10^{-5}	2.01

OSCs might be improved by selecting other donor polymers of more complementary absorption spectra.

EXPERIMENTAL SECTION

Materials and Characterization

All the solvents were purified and dried according to standard procedures. The donor polymer PBDB-T (99.9%) was bought from Solarmer Materials, Inc. Compounds **1** and **2** were prepared by using the reported procedure (Ma et al., 2013, 2017b).

Synthesis of **3**: Compound **2** (0.6 g, 0.56 mmol), 5-bromothiophene-2-carbaldehyde (0.32 g, 1.6 mmol) and $Pd(PPh_3)_4$ (30 mg, 0.03 mmol) were dissolved in 30 mL of degassed toluene in a two neck flask. After refluxing for 24 h under nitrogen, the mixture was cooled down to room temperature. Then the solvent was removed by evaporation, and the remaining residue was purified by column chromatography (silica gel) using petroleum ether/CH_2Cl_2 (3:1) as eluent. Finally, a dark brown solid (0.47 g, 96%) was obtained. ^{1}H NMR ($CDCl_3$, 400 MHz, ppm): 9.91 (s, 2H), 8.04 (d, J = 8.0 Hz, 2H), 7.75 (d, J = 8.0 Hz, 2H), 7.67 (d, J = 8.0 Hz, 2H), 7.43 (s, 2H), 7.37 (s, 2H), 2.17–2.04 (m, 8H), 1.01–0.52 (m, 60H). HRMS (MALDI) m/z: calc. for $C_{62}H_{80}O_2S_4$: 984.5017; found: 984.5027. Elemental analysis (%) calc. for $C_{62}H_{80}O_2S_4$: C, 75.56; H, 8.18; found: C, 75.79; H, 8.09.

Synthesis of **DTNSF**: To a solution of Compound **3** (200 mg, 0.2 mmol) in dry $CHCl_3$ (30 mL), 2-(6-fluoro-3-oxo-2,3-dihydro-1H-inden-1-ylidene)malononitrile (340 mg, 1.6 mmol) were added. After degassing with nitrogen for 30 min, 0.15 mL of pyridine was added. The mixture was stirred at reflux for 24 h under nitrogen atmosphere. After the mixture was cooled to room temperature, it was poured into 100 mL of methanol. A precipitate was formed and filtered off which was further purified by using column chromatography (silica gel) with petroleum ether/CH_2Cl_2 (1:1) as the eluent. A dark green solid (130 mg, 46%) was obtained. ^{1}H NMR ($CDCl_3$, 400 MHz, ppm): 8.91 (d, J = 8.0 Hz, 2H), 8.42 (d, J = 8.0 Hz, 2H), 8.10 (d, J = 8.0 Hz, 2H), 8.01–7.97 (m, 2H), 7.86 (d, J = 8.0 Hz, 2H), 7.73–7.70 (m, 2H), 7.68 (d, J = 8.0 Hz, 2H), 7.50–7.45 (m, 4H), 2.20–2.09 (m, 8H), 1.05–0.54 (m, 60H). HRMS (MALDI) m/z: calc. for $C_{86}H_{86}F_2N_4O_2S_4$: 1,373.5689; found: 1,373.5674. Elemental analysis (%) calc. for $C_{86}H_{86}F_2N_4O_2S_4$: C, 75.18; H, 6.31; N, 4.08; found: C, 75.47; H, 6.20; N, 3.77.

Synthesis of **DTNIF**: To a solution of Compound **1** (174 mg, 0.2 mmol) in dry $CHCl_3$ (30 mL), 2-(6-fluoro-3-oxo-2,3-dihydro-1H-inden-1-ylidene)malononitrile (337 mg, 1.6 mmol) were added. After degassing with nitrogen for 30 min, 1 mL of pyridine was added into the mixture which was further stirred at reflux for 24 h under nitrogen atmosphere. Then the mixture was cooled down to room temperature. The reaction mixture was poured into 100 mL of methanol. A precipitate was formed and filtered off which was further purified by using column chromatography (silica gel) with petroleum ether/CH_2Cl_2 (1:1) as the eluent. A dark metallic luster solid (126 mg, 60%) was obtained. ^{1}H NMR ($CDCl_3$, 400 MHz, ppm): 9.07 (d, J = 8.0 Hz, 2H), 8.79–8.76 (m, 0.8H), 8.46–8.43 (m, 3.2H), 8.04–8.00 (m, 1.3H), 7.93–7.88 (m, 2H), 7.85–7.80 (m, 2H), 7.67–7.64 (m, 0.7H), 7.51–7.46 (m, 2H), 2.23–2.11 (m, 8H), 1.00–0.52 (m, 60H). HRMS (MALDI) m/z: calc. for $C_{78}H_{82}F_2N_4O_2S_2$: 1,209.5891; found: 1,209.5920. Elemental analysis (%) calc. for $C_{78}H_{82}F_2N_4O_2S_2$: C, 77.45; H, 6.83; N, 4.63; found: C, 77.50; H, 7.26; N, 4.24.

OSC Fabrication and Characterization

PSCs were fabricated by using a device configuration of indium tin oxide (ITO)/ZnO/active layer/MoO_3/Ag. The ITO glass was cleaned by sequentially in detergent, deionized water, acetone, and isopropanol for half an hour each and dried for more than 12 h in an oven. Then, the ITO glass was subjected to ultraviolet/ozone treatment for 15 min. Later on, a ZnO precursor solution (0.23 M in 2-methoxyethanol) was spin-coated on the ITO glass at 3,000 rpm for 50 s. On a hot plate (130°C), the obtained films were heated for 10 min first, then they were annealed by an oven (200°C) for 1 h. The blend ratios of the active layer (PBDB-T:acceptor) were fixed at 1:1 by weight. The donor/acceptor blends were dissolved in chlorobenzene with a total concentration of 18 mg/mL and spin-coated on top of the ZnO film (ca. 30 nm) in the glovebox. Finally, on the active layer, 10 nm of MoO_3 film was deposited followed by a further deposition of Ag film (100 nm). The active area of OSC devices was 6 mm^2.

Solar cell characterization was tested under AM 1.5 G irradiation (100 mW cm^{-2}) from an Oriel Sol3A simulator (Newport) with a NREL-certified silicon reference cell. J–V measurements were carried out in air using a Keithley 2440 source measurement unit. External quantum efficiency (EQE) data were collected by a Newport EQE measuring system.

Instruments and Measurements

^{1}H NMR was measured in $CDCl_3$ on a Bruker AVANCE-spectrometer. Elemental analysis of the non-fullerene acceptors was obtained on an Elementar Vario EL Cube analyzer. UV–Vis absorption spectra for all the samples were performed on a Perkin-Elmer Lambda 365 spectrophotometer. Linear emission spectra for pure films or blended films were obtained by using a FLS920 spectrophotometer. Atomic force microscopy (AFM) was conducted in a tapping mode with a Bruker Nanoscale V station. A Bruker Dektak XT surface profilometer was used to test the thickness of thin films in this work. A three-electrode CHI 604E electrochemical workstation was used to run the cyclic voltammetry (CV) using Bu_4NPF_6 solution (0.1 M in acetonitrile) and a scan rate of 100 mV s^{-1}. The solid films were precipitated on a Pt plate through dipping the Pt plate into the corresponding chloroform solutions and then took out for drying. $Ag/AgNO_3$ and a Pt wire were chosen as the reference electrode and the counter electrode, respectively. The LUMO and HOMO energy levels of films made by the small molecule were calculated by using the following equations:

$$E_{HOMO} = -(\varphi_{ox} + 4.82)\ (eV)$$
$$E_{LUMO} = -(\varphi_{RED} + 4.82)\ (eV)$$

Agilent 4155C semiconductor parameter analyzer was used to conduct the mobility measurements. Electron and hole mobilities were determined by using the space charge limited current model (SCLC) with an electron-only diode configuration of ITO/ZnO/active layer/Ca/Al and an hole-only diode configuration of ITO/PEDOT:PSS/active layer/Au, using current-voltage measurements in the range of –(3–10) V in the dark. The SCLC mobility was calculated by fitting the J-V curves to the Mott-Gurney relationship:

$$J = \frac{9}{8}\varepsilon_r\varepsilon_0\mu\frac{V^2}{L^3}$$

Where ε_0 is the permittivity of free space (8.85 × 10^{-12} F m^{-1}), ε_r is the dielectric constant of the active layer material (assumed to be 3), μ is the electron or hole mobility, L is the active layer thickness, V is the voltage drop across the electron- or hole-only device (V_{appl} – V_{bi}, where V_{appl} is the applied voltage, and V_{bi} is the built-in voltage induced by the work function difference of the two electrodes). The electron/hole mobilities can be determined according to the slope of the $J^{1/2}$–V curves.

AUTHOR CONTRIBUTIONS

QZ conceived the experiments. MZ and YM were primarily responsible for the experiments. MZ and QZ wrote the manuscript. All authors discussed the results.

FUNDING

This work was supported by the National Natural Science Foundation of China (Nos. U1605241, 51703226, 51561165011), the Key Research Program of Frontier Sciences, CAS (No. QYZDB-SSW-SLH032), the CAS/SAFEA International Partnership Program for Creative Research Teams, and the Strategic Priority Research Program of the Chinese Academy of Sciences, Grant No. XDB20000000.

REFERENCES

Chen, J. D., Cui, C., Li, Y. Q., Zhou, L., Ou, Q. D., Li, C., et al. (2015). Polymer solar cells: single-junction polymer solar cells exceeding 10% power conversion efficiency. *Adv. Mater. Weinheim.* 27, 1035–1041. doi: 10.1002/adma.201404535

Chen, Y., Wan, X., and Long, G. (2013). High performance photovoltaic applications using solution-processed small molecules. *Acc. Chem. Res.* 46, 2645–2655. doi: 10.1021/ar400088c

Dai, S., Zhao, F., Zhang, Q., Lau, T. K., Li, T., Liu, K., et al. (2017). Fused nonacyclic electron acceptors for efficient polymer solar cells. *J. Am. Chem. Soc.* 139, 1336–1343. doi: 10.1021/jacs.6b12755

Elumalai, N. K., and Uddin, A. (2016). Open circuit voltage of organic solar cells: an in-depth review. *Energy Environ. Sci.* 9, 391–410. doi: 10.1039/c5ee02871j

Facchetti, A. (2011). π-Conjugated polymers for organic electronics and photovoltaic cell applications. *Chem. Mater.* 23, 733–758. doi: 10.1021/cm102419z

He, Z., Xiao, B., Liu, F., Wu, H., Yang, Y., Xiao, S., et al. (2015). Single-junction polymer solar cells with high efficiency and photovoltage. *Nat. Photonics* 9, 174–179. doi: 10.1038/nphoton.2015.6

Li, H., Earmme, T., Subramaniyan, S., and Jenekhe, S. A. (2015). Bis(Naphthalene Imide)diphenylanthrazolines: a new class of electron acceptors for efficient nonfullerene organic solar cells and applicable to multiple donor polymers. *Adv. Energy Mater.* 5:1402041. doi: 10.1002/aenm.201402041

Lin, Y., Wang, J., Zhang, Z. G., Bai, H., Li, Y., Zhu, D., et al. (2015). An electron acceptor challenging fullerenes for efficient polymer solar cells. *Adv. Mater.* 27, 1170–1174. doi: 10.1002/adma.201404317

Liu, F., Zhou, Z., Zhang, C., Vergote, T., Fan, H., Liu, F., et al. (2016). A thieno[3,4-b]thiophene-based non-fullerene electron acceptor for high-performance bulk-heterojunction organic solar cells. *J. Am. Chem. Soc.* 138, 15523–15526. doi: 10.1021/jacs.6b08523

Liu, W., Li, W., Yao, J., and Zhan, C. (2018). Achieving high short-circuit current and fill-factor via increasing quinoidal character on nonfullerene small molecule acceptor. *Chin. Chem. Lett.* 29, 381–384. doi: 10.1016/j.cclet.2017.11.018

Liu, Y., Zhao, J., Li, Z., Mu, C., Ma, W., Hu, H., et al. (2014). Aggregation and morphology control enables multiple cases of high-efficiency polymer solar cells. *Nat. Commun.* 5:5293. doi: 10.1038/ncomms6293

Ma, Y., Kang, Z., and Zheng, Q. (2016). Recent advances in wide bandgap semiconducting polymers for polymer solar cells. *J. Mater. Chem. A* 5, 1860–1872. doi: 10.1039/c6ta09325f

Ma, Y., Zhang, M., Tang, Y., Ma, W., and Zheng, Q. (2017a). Angular-Shaped dithienonaphthalene-based non-fullerene acceptor for high-performance polymer solar cells with large open-circuit voltages and minimal energy losses. *Chem. Mater.* 22, 9775–9785. doi: 10.1021/acs.chemmater.7b03770

Ma, Y., Zhang, M., Yu, Y., Xin, J., Wang, T., Ma, W., et al. (2017b). Ladder-type dithienonaphthalene-based small-molecule acceptors for efficient nonfullerene organic solar cells. *Chem. Mater.* 29, 7942–7952. doi: 10.1021/acs.chemmater.7b02887

Ma, Y., Zheng, Q., Yin, Z., Cai, D., Chen, S. C., and Tang, C. (2013). Ladder-type dithienonaphthalene-based donor–acceptor copolymers for organic solar cells. *Macromolecules* 46, 4813–4821. doi: 10.1021/ma400696e

Nielsen, C. B., Holliday, S., Chen, H. Y., Cryer, S. J., and Mcculloch, I. (2015). Non-fullerene electron acceptors for use in organic solar cells. *Acc. Chem. Res.* 48, 2803–2812. doi: 10.1021/acs.accounts.5b00199

Qin, Y., Uddin, M. A., Chen, Y., Jang, B., Zhao, K., Zheng, Z., et al. (2016). Highly efficient fullerene-free polymer solar cells fabricated with polythiophene derivative. *Adv. Mater.* 28, 9416–9422. doi: 10.1002/adma.201601803

Rong, Z., Deng, Y., Xie, Z., Geng, Y., and Wang, F. (2015). Dithienocarbazole- and benzothiadiazole-based donor-acceptor conjugated polymers for bulk heterojunction polymer solar cells. *Sci. China Chem.* 58, 294–300. doi: 10.1007/s11426-014-5221-9

Shen, F., Xu, J., Li, X., and Zhan, C. (2018). Nonfullerene small-molecule acceptors with perpendicular side-chains for fullerene-free solar cells. *J. Mater. Chem. A* 6, 15433–15455. doi: 10.1039/C8TA04718A

Tang, C., Chen, S. C., Shang, Q., and Zheng, Q. (2017). Asymmetric indenothiophene-based non-fullerene acceptors for efficient polymer solar cells. *Sci. China Mater.* 60, 707–715. doi: 10.1007/s40843-017-9059-3

Wang, E., Mammo, W., and Andersson, M. R. (2014). 25th anniversary article: isoindigo-based polymers and small molecules for bulk heterojunction solar cells and field effect transistors. *Adv. Mater.* 26, 1801–1826. doi: 10.1002/adma.201302652

Wu, J. L., Chen, F. C., Hsiao, Y. S., Chien, F. C., Chen, P., Kuo, C. H., et al. (2011). Surface plasmonic effects of metallic nanoparticles on the performance of polymer bulk heterojunction solar cells. *ACS Nano* 5, 959–967. doi: 10.1021/nn102295p

Wu, J. S., Cheng, S. W., Cheng, Y. J., and Hsu, C. S. (2015). Donor-acceptor conjugated polymers based on multifused ladder-type arenes for organic solar cells. *Chem. Soc. Rev.* 44, 1113–1154. doi: 10.1039/c4cs00250d

Xu, X., Wang, C., Bäcke, O., James, D. I., Bini, K., Olsson, E., et al. (2015). Pyrrolo[3,4-g]quinoxaline-6,8-dione-based conjugated copolymers for bulk heterojunction solar cells with high photovoltages. *Polym. Chem.* 6, 4624–4633. doi: 10.1039/c5py00394f

You, J., Dou, L., Yoshimura, K., Kato, T., Ohya, K., Moriarty, T., et al. (2013). A polymer tandem solar cell with 10.6% power conversion efficiency. *Nat. Commun.* 4:1446. doi: 10.1038/ncomms2411

Zhan, X., Facchetti, A., Barlow, S., Marks, T. J., Ratner, M. A., Wasielewski, M. R., et al. (2011). Rylene and related diimides for organic electronics. *Adv. Mater.* 23, 268–284. doi: 10.1002/adma.201001402

Zhang, S., Ye, L., Zhao, W., Yang, B., Wang, Q., and Hou, J. (2015). Realizing over 10% efficiency in polymer solar cell by device optimization. *Sci. China Chem.* 58, 248–256. doi: 10.1007/s11426-014-5273-x

Zhang, X., Yao, J., and Zhan, C. (2016). Synthesis and photovoltaic properties of low bandgap dimeric perylene diimide based non-fullerene acceptors. *Sci. China Chem.* 59, 209–217. doi: 10.1007/s11426-015-5485-8

Zhao, F., Dai, S., Wu, Y., Zhang, Q., Wang, J., Jiang, L., et al. (2017). Single-junction binary-blend nonfullerene polymer solar cells with 12.1% efficiency. *Adv. Mater.* 29, 1604059. doi: 10.1002/adma.201700144

Conflict of Interest Statement: The authors declare that the research was conducted in the absence of any commercial or financial relationships that could be construed as a potential conflict of interest.

frontiers in Chemistry

REVIEW
published: 18 September 2018
doi: 10.3389/fchem.2018.00414

Small-Molecule Electron Acceptors for Efficient Non-fullerene Organic Solar Cells

*Zhenzhen Zhang, Jun Yuan, Qingya Wei and Yingping Zou**

College of Chemistry and Chemical Engineering, Central South University, Changsha, China

The development of organic electron acceptor materials is one of the key factors for realizing high performance organic solar cells. Compared to traditional fullerene acceptor materials, non-fullerene electron acceptors have attracted much attention due to their better optoelectronic tunabilities and lower cost as well as higher stability. Non-fullerene organic solar cells have recently experienced a rapid increase with power conversion efficiency of single-junction devices over 14% and a bit higher than 15% for tandem solar cells. In this review, two types of promising small-molecule electron acceptors are discussed: perylene diimide based acceptors and acceptor(A)-donor(D)-acceptor(A) fused-ring electron acceptors, focusing on the effects of structural modification on absorption, energy levels, aggregation and performances. We strongly believe that further development of non-fullerene electron acceptors will hold bright future for organic solar cells.

Keywords: organic solar cells, efficiency, small molecule, fused ring, perylene diimide

OPEN ACCESS

Edited by:
Chuanlang Zhan,
Institute of Chemistry (CAS), China

Reviewed by:
Qingdong Zheng,
Fujian Institute of Research on the Structure of Matter (CAS), China
Francesca Di Maria,
Istituto di Nanotecnologia (NANOTEC), Italy
Lei Ying,
South China University of Technology, China

****Correspondence:***
Yingping Zou
yingpingzou@csu.edu.cn

Specialty section:
This article was submitted to Organic Chemistry, a section of the journal Frontiers in Chemistry

Received: *17 June 2018*
Accepted: *23 August 2018*
Published: *18 September 2018*

Citation:
Zhang Z, Yuan J, Wei Q and Zou Y (2018) Small-Molecule Electron Acceptors for Efficient Non-fullerene Organic Solar Cells. Front. Chem. 6:414. doi: 10.3389/fchem.2018.00414

INTRODUCTION

Energy is the important foundation of human survival and economic development. With the rapid development of the global economy, the traditional non-renewable fossil energy such as coal, petroleum, and natural gas appears to be decreasing, and the burning of fossil fuels brings about greenhouse gases such as carbon dioxide and other chemical pollutants. At the background of energy crisis and environmental pollution, the development of clean and renewable energy has become the world's urgent requirements (Zhan et al., 2015). The emerging new energy sources include nuclear, solar, wind, hydro, and tidal energy. Among them, solar energy has the advantages of being clean, non-polluting, widely distributed, and non-exhaustive. It meets the requirements of sustainable development in the world today. There are three main ways to use solar energy: solar to thermal energy conversion, photoelectric conversion and photochemical conversion. Presently, the photoelectric conversion is one of the world focuses. The development of photovoltaic cells has become a promising solution for transforming solar energy into electricity. The first photovoltaic cell based on monocrystalline silicon materials was invented by Bell Laboratories (Chapin et al., 1954). Since then, the performance based on inorganic semiconductor solar cells began to get improved. However, the shortcomings of the complicated preparation process, high production cost, inflexibility in processing limited the preparation and application of large-area inorganic solar cells. On the contrary, organic solar cells (OSCs) have some merits of light weight, low cost, mechanical flexibility (Sariciftci et al., 1992; Li and Zou, 2008; Krebs, 2009; Li, 2011; Li et al., 2012; Heeger, 2014). More importantly, organic raw materials are abundant and the photoelectric properties can be modified by simple and feasible organic synthesis.

Nowadays, the typical OSCs active layers are bulk heterojunction (BHJ) structures, which are based on percolate and continuous electron donor (D) and electron acceptor (A) blend films. The working mechanism of OSCs is generally divided into four steps: (1) The active layer absorbs photons and then forms excitons (electron-hole pairs); (2) Exciton diffuses to D/A interface; (3) Exciton dissociates into free holes and electrons; (4) Free holes and electrons transport to the corresponding electrodes through the donor and acceptor channels, and subsequently are collected by electrodes. Finally, the photocurrent is formed in the external circuit (Lin and Zhan, 2014). To achieve high efficiency, an amount of small molecule/polymer donor materials have been developed, the power conversion efficiency (PCE) of fullerene OSCs had made a dramatic progress with values over 10% after decades of the tireless efforts by scientific community (Zhao et al., 2016b). However, the further development of fullerene-based OSCs encounters bottlenecks due to the inherent defects of fullerene derivatives, such as limited tunability of absorption and energy level, costly preparation and purification as well as poor stability.

In contrast to fullerene derivatives, non-fullerene acceptors (NFAs) can be modified by classical synthesis strategies, for example donor (D)-acceptor (A) conjugation, conformation locked and incorporation of functional groups, which is beneficial to adjusting crystallinity, electrical and optical properties. Although the first bilayered OSC is based on non-fullerene acceptor, the development of the electron acceptor lagged far behind of the donor materials in early studies (Kallmann and Pope, 1959). Early stage, rylene diimides derivatives, including perylene diimide (PDI) and naphthalene diimide (NDI), occupied the forefront of the non-fullerene materials. Before 2013, the PCEs were only about 1–3% (Bloking et al., 2011). After decades of mediocrity, Yao's group reported a novel acceptor (bis-PDI-T-EG), the performance achieved first breakthrough with PCE of 4.03% (Zhang et al., 2013). The second progress was the discovery of the ITIC, when blended with PTB7-Th, the device delivered a PCE of 6.8%, which is higher than 6.05% efficiency of PTB7-Th: $PC_{61}BM$ based devices (Lin et al., 2015b). This inspiring study showed that the performance of non-fullerene solar cells is expected to catch up or even be superior to fullerene based solar cells. In recent years, non-fullerene solar cells have once again revived and become a hot topic in photovoltaic researches (Liang et al., 2017; Zhang et al., 2018a). Currently, the highest efficiency has exceeded 14% for single-junction NF-OSCs and 15% for tandem NF-OSCs (Che et al., 2018; Zhang et al., 2018b).

To achieve high performance NF-OSCs, the primary factor to consider is the design and synthesis of acceptor materials. Generally, a promising acceptor should meet the following criteria:

a) The acceptor should have complementary absorption with the donor as much as possible to increase photon utilization, which is beneficial for achieving high external quantum efficiency (EQE) and short-circuit current density (J_{sc}). For example, to better match high performance narrow bandgap donors, wide or ultra-narrow bandgap acceptors should be designed. Narrow bandgap acceptors are likely to work well with wide or medium bandgap donors. In addition, the photocurrent can be formed by generation of excitons from both donor (channel 1) and acceptor (channel 2). Thus, apart from the complementary absorption with donors, the optical absorptivity of the NFA is also important (Nielsen et al., 2015; Cheng et al., 2018; Wadsworth et al., 2018).
b) Besides the absorption, the energy levels matching with the donor material facilitates high open circuit voltage (V_{oc}) and low energy loss (E_{loss}). For fullerene OSCs, the highest occupied molecular orbital (HOMO) or the lowest unoccupied molecular orbital (LUMO) energy offset should be larger than 0.3 eV. However, recent investigations showed that the efficient exciton seperation and charge transfer for most non-fullerene system still can take place under less than 0.3 eV energy level offset (Liu et al., 2016b). Therefore, NF solar cells have unexpected potential in improving V_{oc} and decreasing E_{loss} through the appropriate regulation of the energy level of NFAs and donors.
c) Another complicated but important factor is nanoscale interpenetrating morphology while blended with donor materials. The ideal morphology should be moderately aggregations. Too small aggregate domains will reduce the optical absorption and charge transport, but excessive aggregations will reduce the excitons separation efficiency and cause geminate recombination losses. Modulating the crystallinity of molecules by changing their conformations or structures seemed to be a useful strategy (Liu et al., 2014; Li et al., 2017a). Enhanced noncovalent forces, such as π-π stacking, van der waals, hydrogen-bonding interaction, help to increase the crystallinity and thus improve the carrier mobility. On the contrary, reducing inter- and intramolecular forces and twisting the conformation of molecules as well as introduction of side chains helps to improve solubility and reduce aggregations (Zhan and Yao, 2016).

Except for the above mentioned prerequisites, simple synthesis and low cost NFAs are beneficial for practical applications.

NFAs are classified into two major classes of polymers and small molecules. Small molecule NFAs have been intensively investigated by blending with polymer and small molecule donor materials (**Figure 1**) owing to their features over their polymeric counterparts, which include clear molecular structures, high purity and batch-to-batch stability (Roncali, 2009). In this review, we will focus on discussing the small molecule NFAs developed for high efficiency OSCs in recent years. **Figure 1** listed chemical structures of the polymer donors referred herein.

PDI BASED SMALL MOLECULE ELECTRON ACCEPTORS

PDI derivatives have attracted considerable attention as NFAs since they possess excellent optical absorption, similar energy levels to fullerenes, high electron mobility as well as good stability. Moreover, these properties can be easily tailored through the substituent groups on the bay region or on the nitrogen atoms (Zhao et al., 2013). The major problem is that PDI

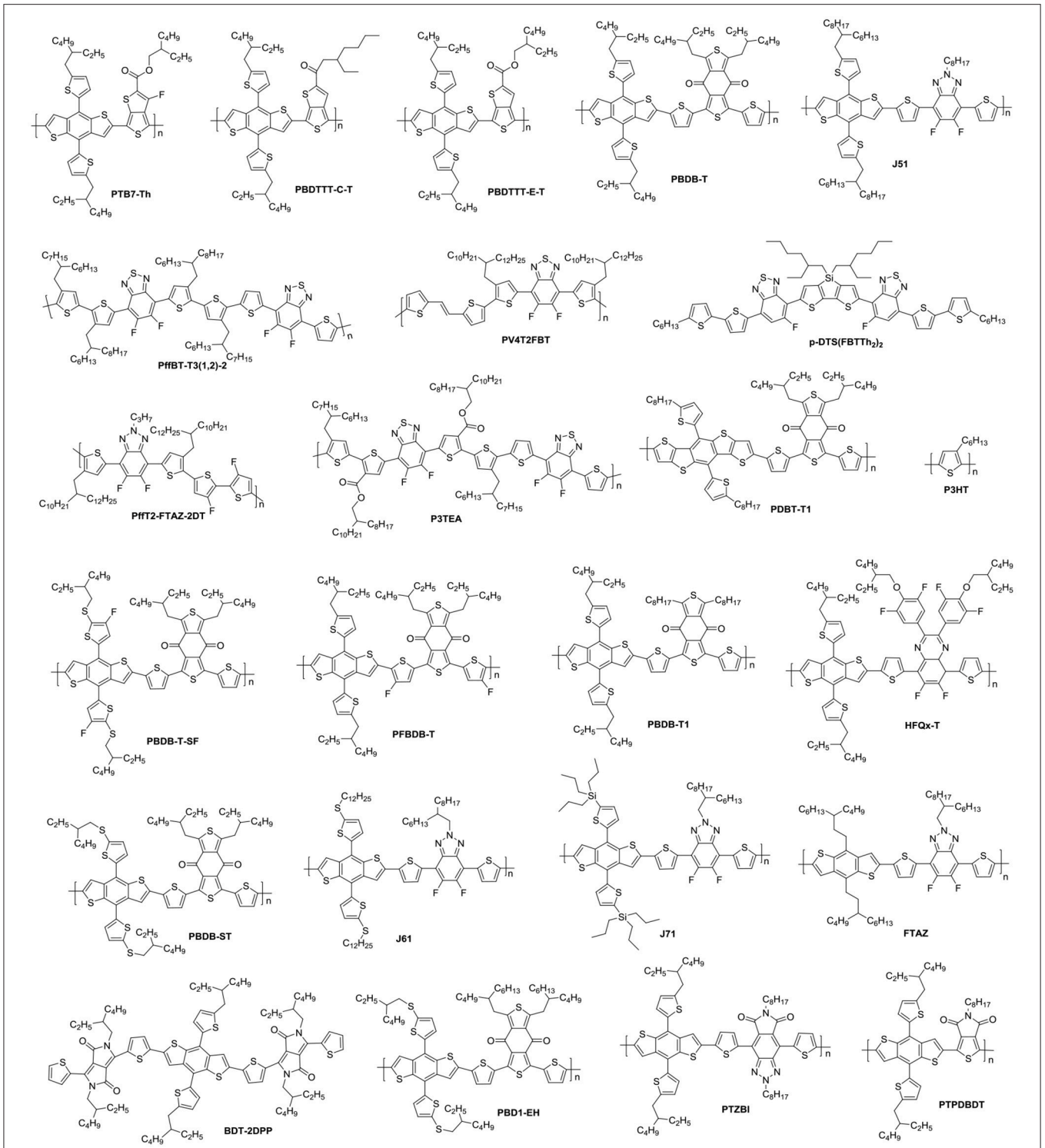

FIGURE 1 | Chemical structures of the organic molecule/polymer donors referred in this review.

units tend to form large aggregates domains, which is more than the exciton diffusion length, led to less exciton separation and poor performance (Zhang et al., 2012). Therefore, it's essential to design and synthesize high performance PDI derivatives with moderate aggregations for effective exciton separation and charge transport.

Until now, several chemical modification methods have been used to reduce the self-aggregation of PDI and achieve good

results (**Figure 2** and **Table 1**). The initial design strategy is to introduce alkyl side chains on the nitrogen position or the ortho position. A series of alkyl-substituted PDI acceptor (PDI-1, PDI-2, PDI-3) was reported and studied, with improved solubility during solution processing and weakening the crystallinity to some extent. When blending with P3HT, the performance was poor (Kamm et al., 2011). But mapping other donors and optimizing the conditions for device fabrications, the OSCs based on p-DTS(FBTTh$_2$)$_2$: PDI-2 blend film showed the PCE of 5.13% (Chen et al., 2015). TP-PDI was a bay-substituted tetraphenyl functionalized PDI derivative, which suppressed the strong aggregation tendency due to steric hindrance effects. While blended with PTB7-Th, a PCE of 4.1% was achieved (Cai et al., 2015).

Moreover, PDI dimers can also reduce their crystallization tendency. Two PDI units were brought together using hydrazine as a linker, giving H-di-PDI. The perylene units are oriented perpendicular to each other, alleviated the aggregation. A PCE of 2.78% has been achieved when PBDTTT-C-T was used as donor material (Rajaram et al., 2012). Wang designed three PDI dimers (s-diPBI, d-diPBI, and t-diPBI), with singly-linked, chiral doubly-linked, and graphene like triply-linked between two PDI units, respectively. Blended with PBDTTT-C-T, s-diPBI delivered the best photovoltaic performance up to 3.63%, which is the result of a flexible structure with a twist angle of about 70° (Jiang et al., 2014). Subsequently, s-diPBI was modified by inserting thiophene and selenophene units in the bay positions, affording two new acceptors (SdiPBI-S and SdiPBI-Se). Both acceptors have a more twisted configuration and higher LUMO energy levels due to big and loose outmost electron clouds of sulfur and selenium. Moreover, the selenium is more polarized than sulfur, which is helpful to improving intramolecular interactions and carrier mobility. Thus, SdiPBI-Se exhibited a higher performance with PCE of 8.42 vs. 7.16% for SdiPBI-S when blended with same donor PDBT-T1 (Sun et al., 2015; Meng et al., 2016b). 7b was obtained by incorporating nitrogen heteroatom in the bay position of PDI to further study the potential of bay-linked PDI dimers. By modulating the N-R functional group, the self-assembly of acceptor would be changed. When the alkyl chain of the bay position is ethyl, the device demonstrated a best PCE of 7.55% with P3TEA as donor. More significantly, N-annulation of the PDI derivative can be synthesized in gram scale without the need for purification using column chromatography (Hendsbee et al., 2016).

Aside from direct linking two PDI units, twisted structure can be also achieved by using functional groups as the linkage. Bis-PDI-T-EG produced small phase domains with a size of ∼30 nm. A promising PCE of 4.03% was obtained due to significant reduction of the aggregation (Zhang et al., 2013). This is the first time the PCE more than 4% in non-fullerene OSCs, demonstrated that the introduction of the π linkage is an effective method to improve photovoltaic performance, the synthetic steps of Bis-PDI-T-EG were shown in **Scheme 1**. Almost at the same time, another acceptor (SF-PDI$_2$) featuring spirobifluorene linker was developed. When P3HT was used as donor, the PCE of 2.35% was achieved. The results demonstrated that steric-demanding substituents on PDI units was able to suppress self-aggregation and crystallization (Yan et al., 2013). Moreover, donor material PffBT4T-2DT can match particularly well with SF-PDI$_2$ with complementary absorption and small driving force. The NF-OSCs possessed a high PCE of 6.3% (Zhao et al., 2015). After that, another NF-OSCs based on P3TEA: SF-PDI$_2$ were fabricated, exhibiting ultrafast and efficient charge separation despite of a negligible driving force, with an excellent PCE of 9.5% (Liu et al., 2016b). A twisted PDI dimers (IDT-2PDI) with bulky indacenodithiophene as a bridge is developed as an electron acceptor. The OSCs based on BDT-2DPP: IDT-2PDI blend film showed a PCE of 3.12% (Lin et al., 2014a).

Undoubtedly, both approaches to reduce the strong π-stacking aggregation by connecting two PDI units with single bond or linker have been efficient and shown improved photovoltaic performance, compared to traditional PDI derivatives. However, It must be admitted that the twisting of the structure will hinder the effective π-π stacking and diminish the charge transport. Thus, the trade-off between high electron mobility and effective exciton dissociation need to be solved in order to achieve excellent performance (**Figure 3** and **Table 2**). Based on these considerations, two PDI dimers substituted at the α position (αPBDT) and β position (βPBDT) with benzodithiophene (BDT) unit were synthesized. The absorption revealed αPBDT have stronger intermolecular π-π stacking and higher packing order than βPBDT due to good planarity. The OSCs based on αPBDT as acceptor demonstrated a PCE of 4.92%, which is 39% higher than that of βPBDT counterparts, which is consequence of higher electron mobility and more efficient exciton dissociation in the αPBDT-based devices (Zhao et al., 2016a). A class of fused but helical PDI oligomers (hPDI, hPDI3, hPDI4) with ethylene group as bridges were designed and studied, which all possess strong light absorption, weak aggregation trendency and both hole and electron can be generated in both the donor and acceptor phases. The device based on PTB7-Th: hPDI4 reached a highest PCE of 8.3% (Zhong et al., 2014, 2015). A series of fused heterocycle PDI derivatives with different chalcogen atoms of O, S and Se (FPDI-F, FPDI-T, FPDI-Se,) were reported. Compared to unfused PDIs, fused PDIs increased effective conjugation and reduced reorganization energy helpful for high charge mobility, while maintaining nonplanar structure for suppress the strong aggregation. Moreover, the device based on FPDI-T showed a best photovoltaic performance with a PCE of 6.72% because of smallest twist angle leading to high packing order and close π-π stacking (Zhong et al., 2016). The first triplet tellurophene-PDI based acceptor (BFPTP) possessed long exciton lifetime and diffusion distances for efficient exciton dissociation rather than recombination. Thus, the PBDB-T: BFPTP blended films delivered a PCE of 7.52% (Yang et al., 2018a). A fused and twisted PDI derivative with twisted thieno[2,3-b]thiophene (TT) as linker (cis-PBI) was reported. When blended with PBDB-T, the OSCs demonstrated a high PCE of 7.6% as a result of high electron mobility and isotropic crystalline properties of electron acceptor (Jiang et al., 2017). A fused PDI derivative with indacenodithieno [3,2-*b*]thiophene (IDTT) as central core (FITP) maintaining rigid conjugated skeleton and hexylphenyl side chains of IDTT hindered the large crystallites. The devices

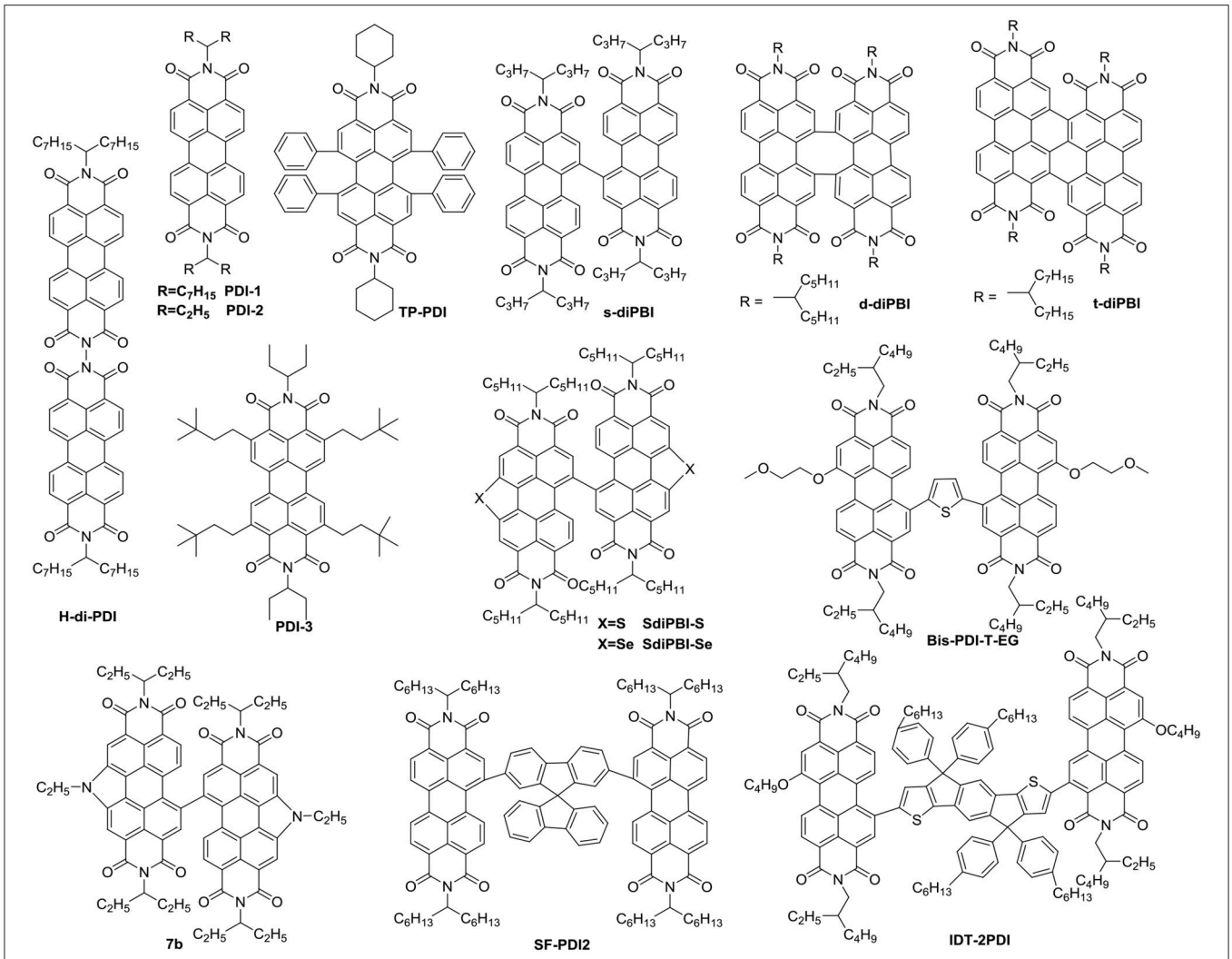

FIGURE 2 | Chemical structures of selected perylene diimide-based electron acceptors from PDI-1 to IDT-2PDI.

based PTB7-Th: FITP exhibited a high PCE of 7.33% due to elevated LUMO and superior electron mobility (Li et al., 2016b). Compound 3 with a planar conformation utilized weak electron acceptor (thieno-pyride-thieno-isoquinoline-dione) bridge for the lateral PDIs. When blended with PTB7-Th, the devices delivered a PCE of 5.03% (Carlotti et al., 2018).

In general, the three-dimensional (3D) or quasi-3D PDI derivatives have good compatibility with polymer donors and 3D charge-transporting channel. A star-shaped PDI acceptor (S(TPA-PDI)) with a triphenylamine (TPA) core displayed weak molecular aggregation and strong absorption as well as matched energy levels with PBDTTT-C-T. A PCE of 3.22% was achieved with 5% 1,8-diiodooctane (DIO) solvent additive (Lin et al., 2014b). A pyrene-fused PDI derivative (TPAPPDI) possessed upshifting LUMO energy level and low bandgap. The devices exhibited a PCE of 5.10% with ultra-high V_{oc} of up to 1.21V (Zhan et al., 2017). Two twisted propeller configuration PDI derivatives (TPH and TPH-Se) were developed. The investigations indicated that TPH-Se possessed more compact 3D network assembly due to the Se…O interactions. The PDBT-T1: TPH-Se solar cell showed a relatively high PCE of 9.28% while 8.28% for TPH based polymer solar cells (PSCs) (Meng et al., 2016a). Three PDI tetramers (TPC-PDI_4, TPE-PDI_4, and TPPz-PDI_4) with twisted 3D structure were systematically studied through the relationship between structure and performance of 3D acceptor. The results revealed that intramolecular twist angle changed as the sequence of TPPz-PDI_4 < TPE-PDI_4 < TPC-PDI_4. Although TPPz-PDI_4 showed the strongest aggregation, it still had fine phase separation and effective charge transfer, and therefore, the highest PCE of 7.1% was obtained ascribed to high electron mobility (Lin et al., 2016a). Further transformed planar SF-PDI_2 into a 3D molecular conformation created SF-PDI_4. SF-PDI_4 demonstrated a 3D interlocking geometry, which prevented excessive rotation and reinforcing conformational uniformity. The PCE of the PV4T2FBT: SF-PDI_4 based devices was 5.98% (Lee et al., 2016). A PDI acceptor (TPB) exhibited cross-like

TABLE 1 | Summary of the photophysical and photovoltaic properties of selected perylene diimide-based electron acceptors from PDI-1 to IDT-2PDI.

Acceptor	Donor	E_g (eV)	LUMO/ HOMO (eV)	μ_e ($cm^2 \cdot V^{-1} \cdot s^{-1}$)	V_{oc} (V)	J_{sc} (mA cm^{-2})	FF (%)	PCE (%)
PDI-1	P3HT	–	–	–	0.25	0.21	22	0.01
PDI-2	P3HT	–	–	–	0.48	1.49	35	0.25
PDI-2	p-DTS($FBTTh_2$)$_2$	1.91	−3.82/−5.87	4.5×10^{-4} (S,B)	0.80	10.07	64	5.13
PDI-3	P3HT	–	–	–	0.45	2.05	31	0.29
TP-PDI	PTB7-Th	1.85	−3.82/−5.69	–	0.87	10.1	46	4.1
H-di-PDI	PBDTTT-C-T	–	−4.1/−5.9	8×10^{-3} (O,B)	0.76	9.5	46	2.78
s-diPBI	PBDTTT-C-T	2.08	−3.87/−5.95	3.21×10^{-5}(O,B)	0.76	10.58	47	3.63
d-diPBI	PBDTTT-C-T	2.22	−3.79/−6.01	–	0.74	5.76	36	1.51
t-diPBI	PBDTTT-C-T	1.69	−4.09/−5.78	1.84×10^{-4}(O,B)	0.46	5.77	51	1.36
SdiPBI-S	PDBT-T1	2.20	−3.85/−6.05	3.20×10^{-3}(S,B)	0.90	11.98	66	7.16
SdiPBI-Se	PDBT-T1	2.22	−3.87/−6.09	6.40×10^{-3}(S,B)	0.96	12.49	70	8.42
7b	P3TEA	–	−3.8/–	10×10^{-7}(S,B)	1.13	11.03	61	7.55
Bis-PDI-T-EG	PBDTTT-C-T	1.88	−3.84/−5.65	3.9×10^{-4}(O,B)	0.85	8.86	54	4.03
SF-PDI_2	P3HT	2.00	−3.71/−5.71	7.1×10^{-5}(S,B)	0.61	5.92	65	2.35
SF-PDI_2	PffBT4T-2DT	–	−3.83/−5.90	1.80×10^{-4}(S,B)	0.98	11.10	58	6.30
SF-PDI_2	P3TEA	–	–	–	1.11	13.27	64	9.5
IDT-2PDI	BDT-2DPP	1.54	−3.83/−5.53	2.3×10^{-6} (S,B)	0.95	7.75	42	3.12

S stands for the mobility measured by the space charge limited current (SCLC) method and O for the organic field effect transistor (OFET)method; N stands for the neat film and B for the blended film.

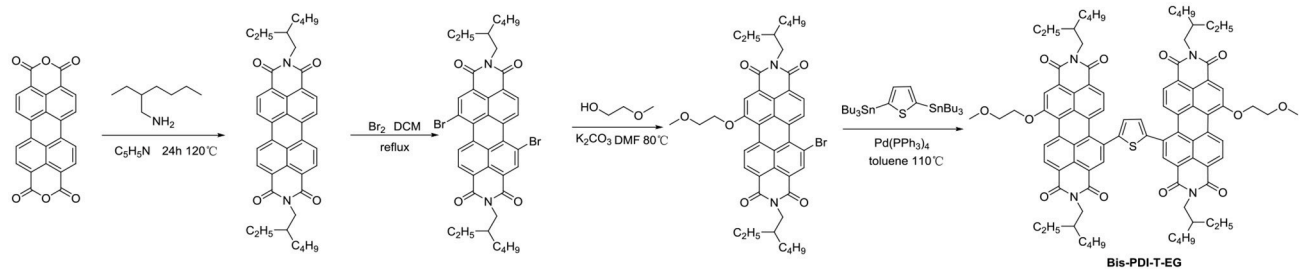

SCHEME 1 | Synthetic route of Bis-PDI-T-EG.

molecular conformation but still partially conjugated with the BDTTh core. The PTB7-Th: TPB based solar cells achieved a PCE of 8.47% due to better conjugation and planarity (Wu et al., 2016). A star-shaped PDI derivative (PBI-Por) with porphyrin as central core was studied. Because porphyrin showed the large conjugated macrocycle and three characteristic absorption bands in the visible and NIR regions, the non-fullerene PSCs based on PBDB-T: PBI-Por blend films achieved a PCE of 7.4% (Zhang et al., 2017a).

ACCEPTOR-DONOR-ACCEPTOR (A-D-A) FUSED-RING ELECTRON ACCEPTORS

In recent years, A-D-A conjugated structures seem to be the most promising class of NFAs. The conjugated push-pull structure containing electron-rich and electron-poor units induces strong intramolecular charge transfer, which is beneficial to reducing the optical band gap. Moreover, variation of the donor or acceptor units can be used to regulate the HOMO or LUMO energy levels. The fused ring backbone facilitates electron delocalization and broadens absorption, and it can prevent the torsion or conformational transition of the molecular skeleton and enhance carrier mobility. The presence of the side chains on the conjugated backbone firstly ensures solution processing, in addition, and reduces molecular stacking, inhibits strong self-assembly and large phase separations.

Fused Tricyclic Small Molecule Acceptors

The three-membered ring is fused ring structure with the smallest size (**Figure 4** and **Table 3**). Dibenzosilole (DBS) unit was the firstly to be used in A-D-A type NFAs, due to good electron-transporting properties, in addition to low-lying LUMO energy levels of silole moiety deriving from effective interactions between σ*-orbital of the silicon-carbon bond and π*-orbital of the butadiene. Diketopyrrolopyrrole (DPP) exhibits excellent

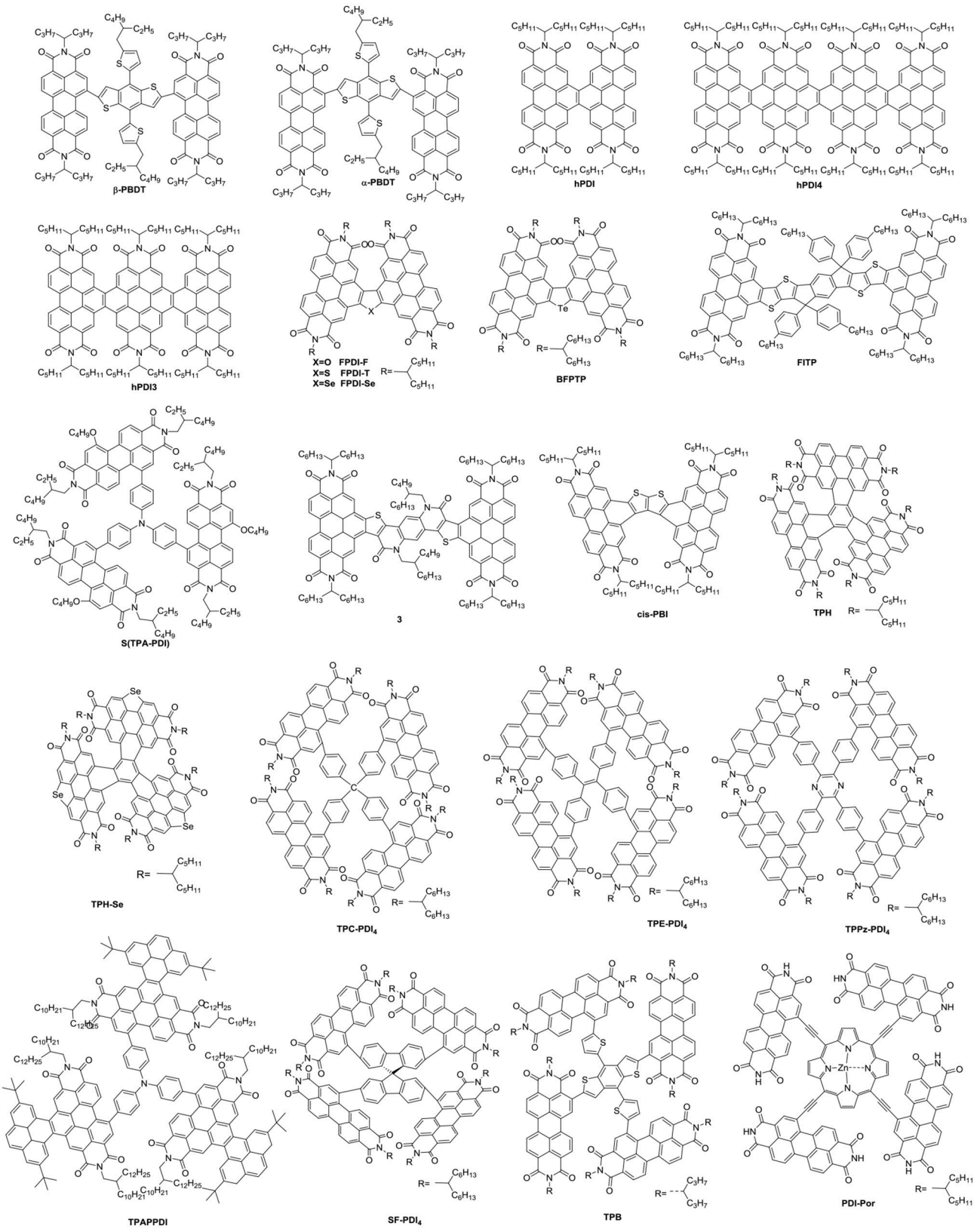

FIGURE 3 | Chemical structures of selected perylene diimide-based electron acceptors from β-PBDT to PBI-Por.

TABLE 2 | Summary of the photophysical and photovoltaic properties of selected perylene diimide-based electron acceptors from β-PBDT to PBI-Por.

Acceptor	Donor	E_g (eV)	LUMO /HOMO (eV)	μ_e ($cm^2 \cdot V^{-1} \cdot s^{-1}$)	V_{oc} (V)	J_{sc} (mA cm^{-2})	FF (%)	PCE (%)
α-PBDT	PTB7-Th	1.58	−3.78/−5.60	8×10^{-4}(S,B)	0.81	12.74	46	4.76
β-PBDT	PTB7-Th	1.58	−3.76/−5.64	4.81×10^{-4}(S,B)	0.81	9.80	44	3.49
hPDI	PBDTT-TT	–	−3.77/−6.04	3.4×10^{-4}(S,B)	0.80	13.3	57	6.05
hPDI3	PTB7-Th	–	−3.86/−6.23	1.5×10^{-4}(S,B)	0.81	14.5	67	7.9
hPD4	PTB7-Th	–	−3.92/−6.26	1.5×10^{-5}(S,B)	0.80	15.2	68	8.3
FPDI-F	PTB7-Th	2.20	−3.80/−6.01	3.17×10^{-7}(S,B)	0.94	8.79	40	3.29
FPDI-T	PTB7-Th	2.22	−3.77/−5.98	1.63×10^{-4}(S,B)	0.94	12.28	59	6.72
FPDI-Se	PTB7-Th	2.22	−3.76/−5.96	1.21×10^{-4}(S,B)	0.92	11.36	56	5.77
BFPTP	PBDB-T	2.12	−3.88/−6.00	3.06×10^{-4}(S,B)	0.94	12.83	62	7.52
cis-PBI	PBDB-T	2.19	−3.74/−5.93	3.2×10^{-3}(O,B)	1.00	11.9	64	7.6
FITP	PTB7-Th	–	−3.75/−5.48	3.66×10^{-4}(S,B)	0.99	13.24	56	7.33
3	PTB7-Th	–	−3.05/−5.84	3.9×10^{-6}(S,B)	0.94	12.12	46	5.03
S(TPA-PDI)	PBDTTT-C-T	1.76	−3.70/−5.40	3.0×10^{-5}(S,B)	0.87	11.27	33	3.22
TPAPPDI	PBT1-EH	1.88	−3.59/−5.47	2.0×10^{-3}(S,B)	1.21	6.83	62	5.10
TPH	PDBT-T1	2.19	−3.83/−6.02	1.5×10^{-3}(S,B)	0.97	12.40	70	8.28
TPH-Se	PDBT-T1	2.17	−3.80/−5.97	2.2×10^{-3}(S,B)	1.00	12.72	72	9.28
TPC-PDI_4	PffBT-T3(1,2)-2	2.25	−3.75/−6.00	2.8×10^{-4}(S,B)	1.04	8.8	61	4.7
TPE-PDI_4	PffBT-T3(1,2)-2	2.05	−3.72/−5.77	1.2×10^{-3}(S,B)	1.03	11.1	55	6.0
TPPz-PDI_4	PffBT-T3(1,2)-2	2.10	−3.76/−5.86	2.5×10^{-3}(S,B)	0.99	12.7	57	7.1
SF-PDI_4	PV4T2FBT	2.05	−3.78/−5.97	1.93×10^{-5}(S,B)	0.90	12.02	54	5.98
TPB	PTB7-Th	1.82	−3.89/−5.71	6.10×10^{-6}(S,B)	0.79	18.20	59	8.47
PBI-Por	PBDB-T	1.48	−3.68/−5.46	1.0×10^{-2}(O,B)	0.78	14.5	66	7.4

S stands for the mobility measured by the space charge limited current (SCLC) method and O for the organic field effect transistor (OFET)method; N stands for the neat film and B for the blended film.

light absorption and strong electron-withdrawing properties. A novel linear NFA (DBS-2DPP) based on DBS as central core and DPP as end group was reported in 2013, which possesses strong and broad absorption and moderate electron mobility. When P3HT was used as donor, the blended film formed fibrous nano-interpenetrating network, leading to a PCE of 2.05% (Lin et al., 2013). Based on this strategy, another DPP derivative ($F(DPP)_2B_2$) was developed. Consisting of fluorene as the core and two benzene end-capped DPP as the terminal, $F(DPP)_2B_2$ possessed excellent light-harvesting capability, moderate energy levels and good charge-transporting with the value of 2.8×10^{-4} $cm^2 \cdot V^{-1} \cdot s^{-1}$. While P3HT was also used as a donor material, the devices delivered a PCE of 3.1% with an extremely high V_{oc} (Shi et al., 2015). Because of concise synthesis and ready availability of fluorene, two isomeric acceptors (F8IDT and FEHIDT) using 2,3-dihydro-1*H*-indene-1,3-dione (ID) as end group were synthesized. The density functional theory calculations have shown that the LUMO energy of FxIDT were similar to that of fullerene derivatives, demonstrating FxIDT can be potentially used as acceptor materials. The devices based on P3HT: FxIDT blend films showed different performance (1.67% for F8IDT; 2.43% for FEHIDT). The main reason can be attributed to the difference of LUMO energy levels and the degree of electronic coupling between molecules, leading to various and low V_{oc} (Winzenberg et al., 2013). To reach a higher V_{oc}, 3-ethylrhodanine is a reasonable choice as end group relative to ID due to weaker electron-withdrawing nature. Two rhodanine-based acceptors (Cz-RH and Flu-RH) were obtained. Cz-RH and Flu-RH possessed high-lying LUMO energy levels of −3.50 and −3.53 eV, respectively, compared to F8IDT, resulting in an excellent V_{oc} of 1.03 V. The devices exhibited a good photovoltaic performance with PCE of 3.08% for P3HT: Flu-RH and 2.56% for P3HT: Cz-RH. The difference was mostly attributed to the J_{sc}, which originated from the maximum EQE intensity of 40% and a more efficient charge transfer from donor to acceptor in P3HT: Flu-RH blend films with higher photoluminescence (PL) quenching efficiencies of 86.7% (Kim et al., 2014). Subsequently, another acceptor FBR, bearing fluorene core and 3-ethylrhodanine end group but flanked by electron-deficient benzothiadiazole (BT) rather than thiophene spacer, was reported. BT as linker extends the conjugation and enhances charge transport. FBR exhibited a nonplanar 3D molecular structure, which is helpful to suppressing large aggregation and achieve efficient exciton separation confirmed by PL quenching efficiencies of over 90%. When blended with P3HT, the device showed a PCE of 4.11% with high V_{oc} of 0.82 V as a result of high LUMO energy level compared to $PC_{60}BM$. It is a pity that the J_{sc} and FF of P3HT: FBR is inferior to those of P3HT: $PC_{60}BM$, which can be caused by the difference of devices thickness and faster geminate

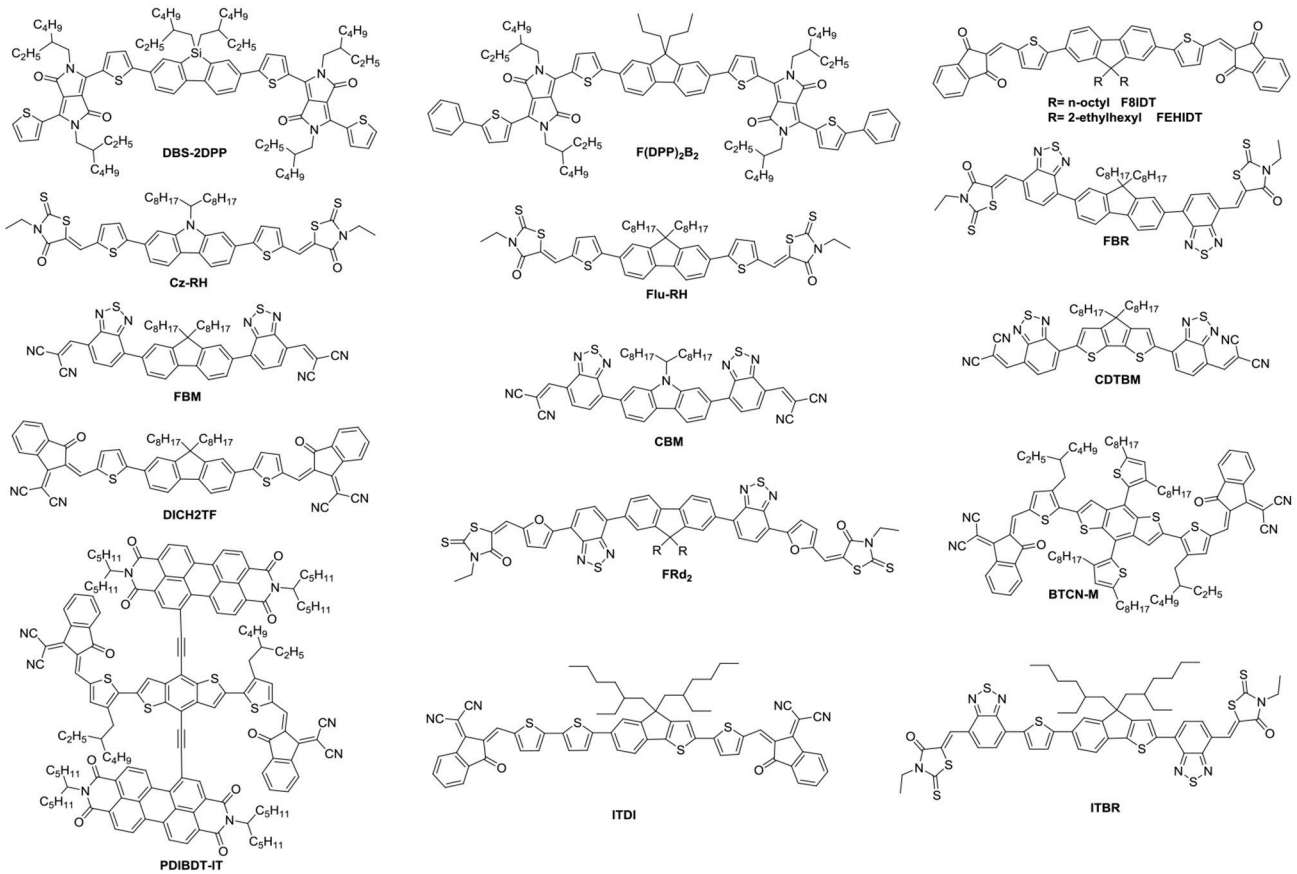

FIGURE 4 | Chemical structures of fused tricyclic small molecule acceptors.

recombination. Moreover, large overlapping absorption in P3HT: FBR blend films limited the more photocurrent generation. To harvest more photons across the solar spectrum, a low bandgap polymer PffBT4T-2DT was used to replace wide bandgap P3HT as donor, the device achieved PCE up to 7.8% with improved J_{sc}. The increase of V_{oc} is originated from deep HOMO energy levels of donor (Holliday et al., 2015; Baran et al., 2016). Except for the optimization of donor materials, modification of acceptor materials also play an important role in improving the light absorption properties. FRd_2 was developed based on FBR, but incorporation of furan spacer between BT and rhodanine end group, which help extending π-conjugation and reducing optical ban gaps. Employing PTB7-Th as donor, the device exhibited a PCE of 9.4% with J_{sc} of 15.7 mA cm^{-2}, which is the reported highest performance for fluorene-based acceptors so far (Suman et al., 2017). Dicyanovinyl (DCV) unit was also an excellent electron-accepting motif to build A-D-A NFAs, because target molecules containing DCV can induce intramolecular charge transfer and promote planarity, which tends to achieve improved carrier mobilities. A set of acceptors (FBM, CBM and CDTBM) flanked by BT as spacer and DCV as end group were systematic studied. FBM and CBM possessed similar electronic properties, but CDTBM exhibited res-shifted absorption and deep LUMO level. Thus, CDTBM obtained higher J_{sc} and FF but lower $V_{oc,}$ leading to similar performance with PCE of ∼5% (Wang et al., 2016). Another stronger electron-withdrawing end-capping group, 2-(6-oxo-5,6-dihydro-4*H*-cyclopenta[c]thiophen-4-ylidene)malononitrile (IC), built upon the structure of DC, could lower the band gap of the acceptor. A easily synthesized and high yield acceptor DICTF, bearing fluorene central block and thiophene spacers as well as IC terminal group, was reported in 2016. DICTF has strong and complementary absorption in the visible region and matched energy levels with PTB7-Th. The devices delivered a PCE near 8% (Li et al., 2016a). Benzo[1,2-*b*:4,5-*b*′]dithiophene (BDT) and its derivatives as electron-rich units in conjugated polymers have been well studied and have demonstrated outstanding results. Recently, BTCN-M, in which 4,8-bis-thiophene-substituted benzo[1,2-*b*:4,5-*b*′]dithiophene (BDT-T) as central block and IC as end group linking with BDT-T by thiophene spacer, was synthesized. Due to high steric hindrance caused by alkyl side groups in the BDT unit, BTCN-M showed weak π-π stacking, tending to act as acceptor material. Therefore, the devices based on BTCN-M: PBDB-T blended films exhibited a outperforming PCE of 5.89% whereas only 0.29% for that of BTCN-M: $PC_{71}BM$ blended films (Liu et al., 2018b). Cross-conjugated small

TABLE 3 | Summary of the photophysical and photovoltaic properties of fused tricyclic small molecule acceptors.

Acceptor	Donor	E_g (eV)	LUMO/HOMO (eV)	μe ($cm^2 \cdot V^{-1} \cdot s^{-1}$)	V_{oc} (V)	J_{sc} (mA cm^{-2})	FF (%)	PCE (%)
DBS-2DPP	P3HT	1.83	−3.28/−5.30	3.3×10^{-4}(S,B)	0.97	4.91	43	2.05
$F(DPP)_2B_2$	P3HT	1.82	−3.39/−5.21	2.8×10^{-4}(S,B)	1.18	5.35	50	3.17
F8IDT	P3HT	2.10	−3.75/−5.85	–	0.72	4.82	48	1.67
FEHIDT	P3HT	2.00	−3.95/−5.95	–	0.95	3.82	67	2.43
Cz-RH	P3HT	2.05	−3.50/−5.53	–	1.03	4.69	53	2.56
Flu-RH	P3HT	2.10	−3.53/−5.58	–	1.01.3	5.70	52	3.08
FBR	P3HT	2.14	−3.57/−5.70	2.6×10^{-5}(S,B)	0.82	7.95	63	4.11
FBR	Pff4TBT-2DT	2.14	−3.75/−5.83	3.8×10^{-4}(S,B)	1.12	11.5	61	7.80
FRd_2	PTB7-Th	2.09	−3.58/−5.67	4.3×10^{-4}(S,B)	0.83	15.7	72	9.40
FBM	PTB7-Th	2.11	−3.67/−6.18	1.0×10^{-6}(S,B)	0.88	11.2	51	5.10
CBM	PTB7-Th	2.02	−3.64/−6.10	1.9×10^{-6}(S,B)	0.88	10.6	53	5.30
CDTBM	PTB7-Th	1.45	−3.90/−5.79	1.8×10^{-6}(S,B)	0.66	11.9	60	5.00
DICTF	PTB7-Th	1.88	−3.79/−5.67	5.85×10^{-5}(S,B)	0.86	16.6	56	7.93
BTCN-M	PBDB-T	1.63	−3.95/−5.69	2.91×10^{-5}(S,N)	0.98	12.3	50	5.89
PDIBDT-IT	PTB7-Th	1.69	−3.97/−5.95	3.51×10^{-5}(S,B)	0.74	13.6	61	6.06
ITDI	PBDB-T	1.53	−4.18/−5.89	9.15×10^{-6}(S,N)	0.94	14.23	60	8.00
ITBR	PTB7-Th	1.71	−3.71/−5.55	1.51×10^{-5}(S,B)	1.02	14.46	51	7.49

S stands for the mobility measured by the space charge limited current (SCLC) method and O for the organic field effect transistor (OFET)method; N stands for the neat film and B for the blended film

molecular acceptor PDIBDT-IT, which combined the advantages of both the A-D-A and PDI type acceptors, exhibited broad absorption band ranging from 300 to 700 nm. The devices based on PDIBDT-IT: PTB7-Th blended films exhibited a PCE of 6.06% (Liu et al., 2018e). It is worth noting that these electron-rich central core were based on symmetrical units, however, NFAs based on asymmetrical cores were promising acceptor materials. Such as, ITDI and ITBR incorporating indenothiophene as core delivered PCEs of 8.00 and 7.49% when blended with PBDB-T and PTB7-Th, respectively (Kang et al., 2017; Tang et al., 2017). Although this type of fused-ring acceptor has made some progress, most of acceptors exhibited wide or medium band gaps absorption with poor spectral coverage and encountered sub-optimal morphologies, therefore, relatively low J_{sc} and FF were obtained.

Fused Pentacyclic Small Molecule Acceptors

Indacenodithiophene (IDT) is the most representative fused pentacyclic donor unit in A-D-A acceptors due to rigid and coplanar structure for good absorption and excellent charge mobility. Moreover, the side chain substituents of the conjugated block can ensure the solution processability and inhibit strong self-assembly of molecules (**Figure 5** and **Table 4**).

IEIC with IDT as the core flanked by thiophene spacers and IC end groups was studied (**Scheme 2**). IEIC showed strong absorption in the 500–750 nm region with an extinction coefficient of 1.1×10^5 M^{-1} cm^{-1} at 672 nm and relatively high electron mobility of 2.1×10^{-4} cm^2 V^{-1} S^{-1}. The blend films of PTB7-Th as donor and IEIC as acceptor showed nanoscale interpenetrating morphology, thereby a PCE of 6.31% was achieved (Lin et al., 2015c). The limitation of the PCE was poor FF and J_{sc}, which mainly came from the big overlapped absorption profiles and imbalanced charge mobility of active layer. With this in mind, when IEIC was laterly blended with a large bandgap donor polymer PffT2-FTAZ-2DT, the PCE reached 7.30%. The improved PCE can be attributed to complementary absorption and balanced charge mobility as well as moderate phase domain size (Lin et al., 2015a). IEIC was the first acceptor material using IDT as central core, and exhibited good performance at that time, providing a good theoretical basis for the later fused pentacyclic small molecule acceptors. The synthetic steps of ITIC were shown in **Scheme 2**. Using larger and looser outermost electron cloud, selenium atoms to replace sulfur atoms afford IDSe-T-IC, which possessed decreased bandgap of 1.52 eV and improved LUMO energy level as well as increased carrier mobility. Thus a high PCE of 8.58% was obtained with a large bandgap polymer J51 as donor (Li et al., 2016d). Designing and synthesizing low bandgap acceptor materials can also make better use of solar spectrum to absorb larger fractions of photons. IEICO, replacing alkyl groups with alkoxy groups, was reported with E_g of 1.34 eV. Introduction of alkoxyl chains increased the HOMO energy level but had little effect on the LUMO level. By employing PBDTTT-E-T as the donor, the IEICO-based devices delivered a high PCE of 8.4% with an increased J_{sc} of 17.70 mA cm^{-2} (Yao et al., 2016). A further development of IEICO obtained IEICO-4F by introducing F atoms in the IC end groups. When blended with a narrow bandgap polymer PTB7-Th, a PCE of 12.8% was achieved (Wang et al., 2018a). i-IEICO-4F, an isomer of IEICO-4F by attaching the end groups in the 4-position instead of 5-position at the neighboring spacers, is a twisted configuration, resulting in blue shifts and complementary absorption with the wide-bandgap polymer J52. The devices based on i-IEICO-4F delivered an excellent PCE of 13.18%

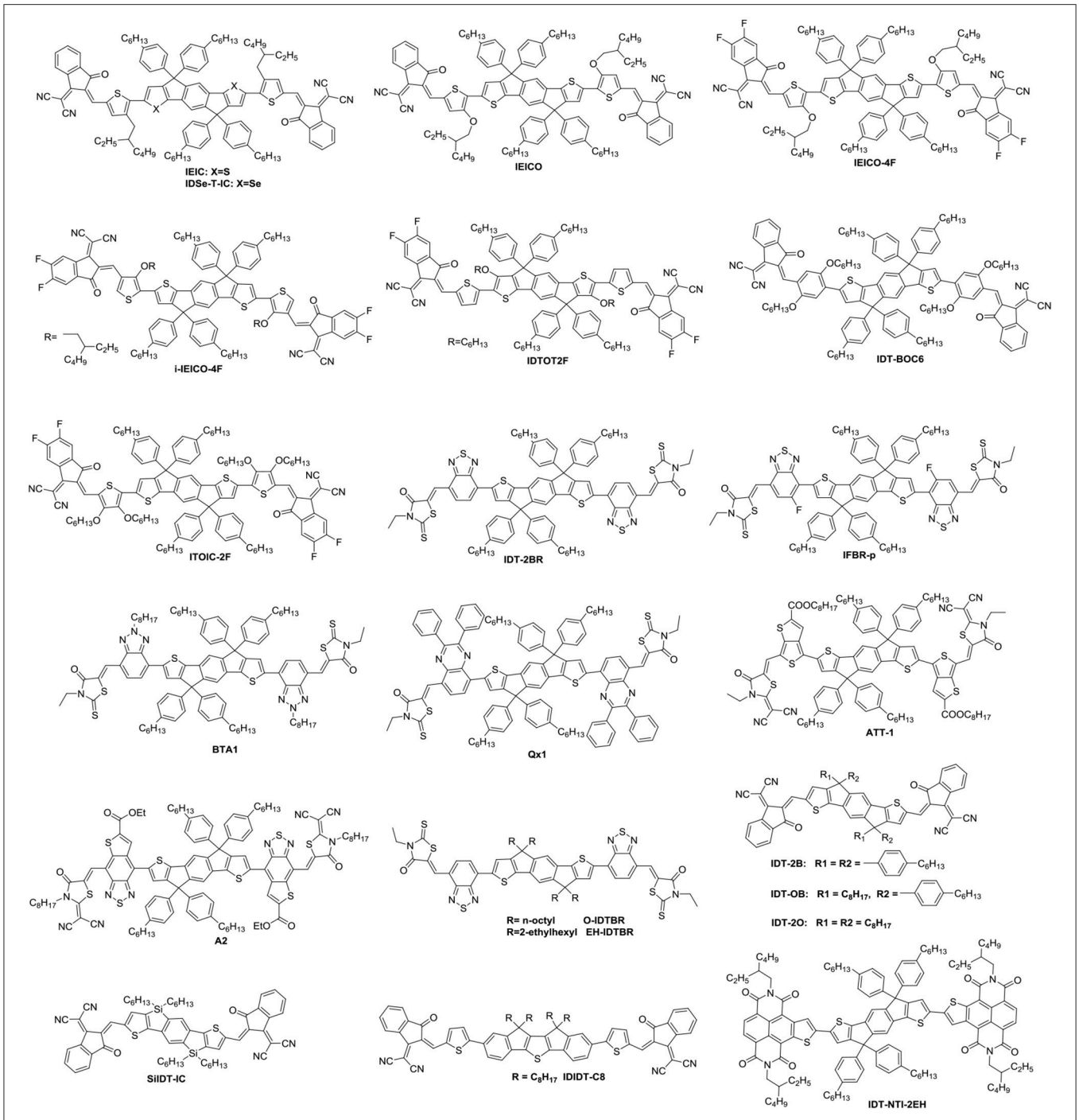

FIGURE 5 | Chemical structures of fused pentacyclic small molecule acceptors.

(Song et al., 2018). Introducing alkoxyl side chains at the central core rather than thiophene spacer provided IDTT2F, which exhibited excellent solubility and ordered molecular packing, resulting in a PCE of 12.79% blended with PBDB-T (Liu et al., 2018d). IDT-BOC6 was also synthesized by using IDT as central core and IC as end groups, but bis(alkoxy)-substituted benzene ring as spacer. Incorporation of alkoxyl groups not only increased the LUMO energy levels but also induced conformational control and enhanced the planarity. IDT-BOC6 locked by intramolecular noncovalent interactions displayed a broad absorption spectrum, high electron mobility and weak nonradiative recombination. The devices based IDT-BOC6 afforded a PCE of 9.6% with PBDB-T as donor (Liu et al., 2017b). ITOIC-2F was also included noncovalently

TABLE 4 | Summary of the photophysical and photovoltaic properties of fused pentacyclic small molecule acceptors.

Acceptor	Donor	E_g (eV)	LUMO/HOMO (eV)	μe ($cm^2 \cdot V^{-1} \cdot s^{-1}$)	V_{oc} (V)	J_{sc} (mA cm^{-2})	FF (%)	PCE (%)
IEIC	PTB7-Th	1.57	−3.82/−5.42	1.00×10^{-4}(S,B)	0.97	13.55	48	6.31
IEIC	PffT2-FTAZ-2DT	1.57	−3.88/−5.45	2.10×10^{-4}(S,B)	1.00	12.70	62	7.30
IDSe-T-IC	J51	1.52	−3.79/−5.45	7.72×10^{-5}(S,B)	0.91	15.20	62	8.58
IEICO	PBDTTT-E-T	1.34	−3.95/−5.32	1.50×10^{-3}(S,B)	0.82	17.70	58	8.40
IEICO-4F	PTB7-Th	1.29	−4.19/−5.44	1.48×10^{-4}(S,B)	0.71	27.3	66	12.1
i-IEICO-4F	J52	1.56	−3.33/−5.01	3.83×10^{-4}(S,B)	0.85	22.86	68	13.18
IDTOT-2F	PBDB-T	1.44	−3.94/−5.54	4.99×10^{-4}(S,B)	0.85	20.87	72	12.79
IDT-BOC6	PBDB-T	1.63	−3.78/−5.51	4.00×10^{-5}(S,B)	1.01	17.52	54	9.60
ITOIC-2F	PBDB-T	1.45	−3.87/−5.57	6.02×10^{-4}(S,B)	0.90	21.04	65	12.17
IDT-2BR	P3HT	1.68	−3.69/−5.52	2.60×10^{-4}(S,B)	0.84	8.91	68	5.12
IFBR-p	PTzBI	1.67	−3.73/−5.64	1.50×10^{-4}(S,B)	1.00	11.9	63	7.44
BTA1	P3HT	1.85	−3.55/−5.51	3.20×10^{-5}(S,B)	1.02	9.93	57	5.24
Qx1	P3HT	1.74	−3.60/−5.42	3.20×10^{-5}(S,B)	1.00	6.02	67	4.03
ATT-1	PTB7-Th	1.54	−3.63/−5.50	2.40×10^{-4}(S,B)	0.87	16.48	70	10.07
A2	PTB7-Th	1.36	−3.78/−5.70	2.30×10^{-4}(S,B)	0.71	20.33	63	9.07
O-IDTBR	P3HT	1.63	−3.88/−5.51	4.70×10^{-6}(S,B)	0.73	14.10	63	6.40
EH-IDTBR	P3HT	1.68	−3.90/−5.58	6.10×10^{-6}(S,B)	0.77	12.2	64	6.05
IDT-2B	PBDB-T	1.73	−3.84/−5.80	1.26×10^{-5}(S,B)	0.89	13.30	54	6.42
IDT-OB	PBDB-T	1.66	−3.87/−5.77	2.71×10^{-4}(S,B)	0.88	16.18	71	10.12
IDT-2O	PBDB-T	1.64	−3.85/−5.73	7.12×10^{-5}(S,B)	0.86	15.64	72	9.68
SiIDT-IC	PBDB-T	1.69	−3.78/−5.47	1.02×10^{-4}(S,B)	0.92	13.53	66	8.16
IDIDT-C8	PBDB-T	1.63	−3.86/−5.50	2.41×10^{-5}(S,B)	0.97	15.81	66	10.10
IDT-NTI-2EH	PBDB-T	1.59	−3.90/−5.40	1.40×10^{-3}(S,B)	0.92	14.48	69	9.07

S stands for the mobility measured by the space charge limited current (SCLC) method and O for the organic field effect transistor (OFET)method; N stands for the neat film and B for the blended film.

conformational locking, the corresponding devices delivered a PCE of 12.17% when blended with PBDB-T (Liu et al., 2018f).

A planar electron acceptor IDT-2BR was synthesized, which IDT was as core flanked by BT as the first electron-withdrawing group and the second electron-deficient 3-ethylrhodanine units on the periphery. The P3HT: IDT-2BR blended films exhibited clear interpenetrating networks and moderate phase separation with the addition of 3% CN. The devices achieved a PCE of 5.12% with a high FF of 68% due to balanced charge mobilities (Wu et al., 2015). IFBR-p was synthesized by incorporating fluorine atoms on the BT unit of IBT-2BR.The OSCs based on PTzBI: IFBR-p blend film showed a PCE as high as 7.44% as result of intermolecular and intramolecular interactions induced by C–H…F non-covalent force (Zhong et al., 2017). BTA1, containing benzo[d][1,2,3]triazole (BTA) as spacer, is analogous to the IBT-2BR acceptor. BTA was a weaker electron-deficient unit than BT, which would make it possess a higher LUMO energy level. Also while blended with P3HT, the device gives the PCE of 5.24% with a high V_{oc} of 1.02 V (Xiao et al., 2017a). Meanwhile, quinoxaline (Qx) is the other weak electron-drawing unit and has been copolymerized with different electron-rich building block to get high performance D-A polymers (Yuan et al., 2017). Qx1, using Qx as bridge, was synthesized and explored. The devices based on P3HT: Qx1 blend films achieved a PCE of 4.03% with a V_{oc} of 1.00 V (Xiao et al., 2018). ATT-1 can be considered as a IDT-2BR derivative, which used ester-substituted thieno[3,4-b]thiophene as spacer and 2-(1,1-dicyanomethylene) rhodanine as end group. ATT-1, adopting quinoidal resonance to extend the π-conjugation and enhance the absorption, exhibits a broad absorption with a high absorption coefficient of 1.2×10^5 L mol^{-1} $cm^{-1}$and slightly high LUMO energy level. When blended with PTB7-Th, the devices achieved a PCE of 10.07% after the addition of DIO. It's worthy to note that the PCE was only 4.46% without any post-treatment,. The investigations indicated that the addition of DIO provided an ideal morphology for efficient charge transport (Liu et al., 2016a). The design of ATT-1 was further developed by substituting the thieno[3,4-b]thiophene spacer with thiophene-fused benzothiadiazole (BTT) unit as p-bridge to obtain A2. The BTT unit connecting on the IDT core not only extend the conjugation length, but also stabilize the quinoid conjugation system, which resulted in red-shift absorption and low bandgap of 1.36 eV. Ultimately, the PCE of 9.07% was reached with an excellent J_{sc} of 20.33 mA cm^{-2} (Xu et al., 2018a). IDT-BR with IDT core was designed and synthesized to solve the issues of FBR, including the large spectra overlap and poor charge percolation pathway. IDTBR had significantly red-shift absorption and tended to crystallize on length scales, meanwhile, O-IDTBR with linear alkyl chains was a more crystalline acceptor and had a further red-shift absorption. The resulting OSCs based on O-IDTBR achieved a

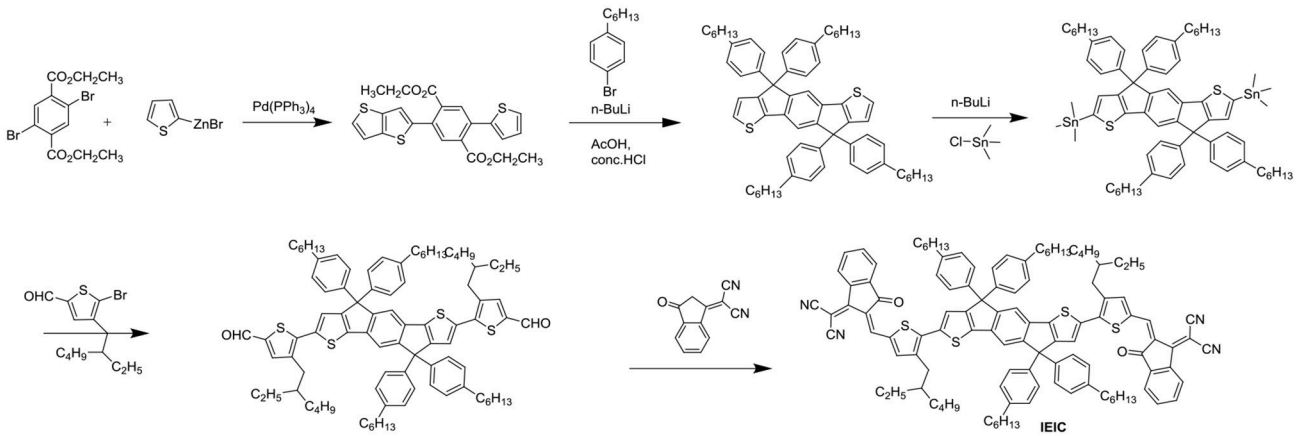

SCHEME 2 | Synthetic route of IEIC.

PCE of 6.4% while 6.05% for EH-IDTBR (Holliday et al., 2016). Alkyl and alkylaryl groups have been widely used as side chains of IDT to ensure solubility and suppress strong aggregations. Compared with alkylaryl units, alkyl substituents enable π-π stacking. However, alkyl substituted acceptor usually formed large domains, leading to incomplete exciton separation. Thus a new acceptor IDT-OB with asymmetric side chains was reported, which reduced strong self-assembly but still had close packing in film due to the existence of more configurationally isomers. As a result, 10.12% was reached for IDT-OB based devices without any post-treatment, while the PCE of 9.68% for IDT-2O, the performance based on IDT-2B was the worst, with only 6.42% efficiency (Feng et al., 2017c). By the replacement of the C-bridge of IDT with the Si-bridge, SiIDT-IC was obtained. Introduction of Si atom can result in a high-lying LUMO energy level to achieve a high V_{oc}. When blended with PBDB-T, the devices delivered a PCE of 8.16% with high V_{oc} of 0.92 V, but the performance is lower than the corresponding C-bridge acceptor (8.83%) due to inferior J_{sc} (Nian et al., 2018). Most of the reported NFAs are trans-arranged side chains linked with the central core. However, IDIDT-C8 with cis-arranged alkyl side chains had weaker π-π stacking than that of trans-arranged one. The blend films with PBDB-T as donor exhibited moderate molecular packing and film morphology, especially, IDIDT-C8 showed a good crystallinity and face-on orientation, resulting in an excellent PCE of 10.10% (Hou et al., 2018). Naphthalene diimide (NDI) was broadly used as acceptor unit due to their strong electron affinity and excellent electron transport properties. Naphtho[2,3-*b*]thiophene diimide (NTI) was connected on the IDT core to give a new acceptor IDT-NTI-2EH, which had red-shifted absorption and strong π-π stacking due to planar conjugated structure. The corresponding devices showed a PCE of 9.07% with PBDB-T as donor (Hamonnet et al., 2017).

Fused Heptacyclic Small Molecule Acceptors

Indacenodithieno[3,2-*b*]thiophene (IDTT) was a further development of the IDT, from a fused pentacyclic to a fused heptacyclic structure (**Figure 6** and **Table 5**). The first A-D-A acceptor based on IDTT was ITIC, which IDTT was used as core directly flanked by IC. ITIC possessed strong and broad absorption in the visible and even NIR region, matched energy levels and good miscibility with PTB7-Th. The resulting OSCs based on PTB7-Th: ITIC blend films exhibited a promising PCE of 6.8%, which was better than that of the devices based on PTB7-Th: $PC_{61}BM$ (Lin et al., 2015b). Since then, the ITIC-based OSCs have shown high photovoltaic performance with multiple polymer donors (Bin et al., 2016; Xia et al., 2016; Yuan et al., 2016; Yu et al., 2017; Hu et al., 2018; Liu et al., 2018a; Xu et al., 2018b). ITIC was the first and a successful fused heptacyclic small molecule acceptors. The synthetic steps of ITIC were shown in **Scheme 3**. After that, much effort has been devoted to the modifications of ITIC structure, for example, by manipulating the aromatic core and changing the side chains as well as substituting the electron deficient end-capping groups (Wei et al., 2017; Alamoudi et al., 2018; Yang et al., 2018b).

It is well-established that the length, type and branch position of side chains play an important role in electronic properties and intermolecular self-assembly. C8-ITIC with four linear octyl side chains was reported for comparison with ITIC. C8-ITIC possessed a lower optical band gap, higher absorption coefficient and increased crystallinity. Blending with PFBDB-T, the devices delivered a PCE up to 13.2% while the devices based on ITIC showed only 11.71% efficiency (Fei et al., 2018). A new acceptor m-ITIC with meta-alkyl-phenyl side groups was synthesized to investigate the effects of side-chain isomerism. This work showed that m-ITIC had higher absorption coefficient, more crystallinity, and increased electron mobilities in comparison with ITIC. The resulting OSCs based on m-ITIC demonstrated a higher PCE of 11.77% than 10.57% for ITIC with a medium bandgap polymer J61 as donor (Yang et al., 2016). Actually, alkoxyphenyl side chains seemed more easily synthesized *via* simple etherification, which is beneficial for large scale production. The m-ITIC-OR bearing IDTT core with meta-alkoxyphenyl side chains and IC as end groups was reported. The HFQx-T: m-ITIC-OR blend films possessed

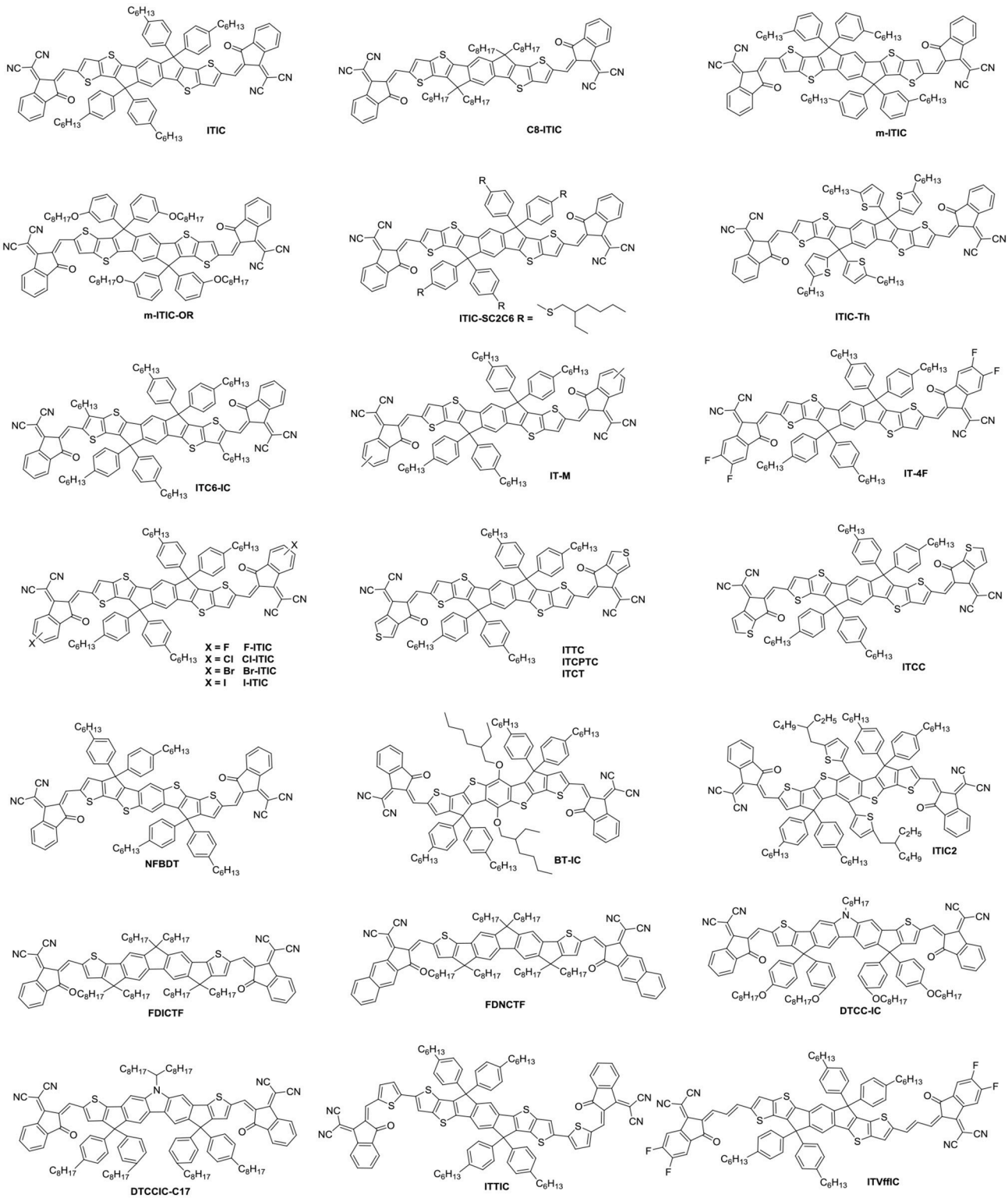

FIGURE 6 | Chemical structures of fused heptacyclic small molecule acceptors.

TABLE 5 | Summary of the photophysical and photovoltaic properties of fused heptacyclic small molecule acceptors.

Acceptor	Donor	E_g (eV)	LUMO/HOMO (eV)	μ_e ($cm^2 \cdot V^{-1} \cdot s^{-1}$)	V_{oc} (V)	J_{sc} (mA cm^{-2})	FF (%)	PCE (%)
ITIC	PTB7-Th	1.59	−3.83/−5.48	1.10×10^{-4}(S,B)	0.81	14.21	59	6.80
C8-ITIC	PFBDB-T	1.53	−3.91/−5.63	–	0.94	19.6	72	13.2
m-ITIC	J61	1.58	−3.82/−5.52	2.45×10^{-4}(S,N)	0.91	18.31	71	11.77
m-ITIC-OR	HFQx-T	1.65	−3.97/−5.65	2.02×10^{-4}(S,B)	0.90	16.15	64	9.30
ITIC-SC2C6	PBDB-ST		−3.86/−5.74	5.43×10^{-4}(S,B)	0.92	15.81	63	9.16
ITIC-Th	PTB7-Th	1.60	−3.93/−5.66	4.50×10^{-4}(S,B)	0.80	15.93	68	8.7
ITIC-Th	PDBT-T1	1.60	−3.93/−5.66	4.20×10^{-4}(S,B)	0.88	16.24	67	9.6
ITC6-IC	PBDB-T	1.60	−3.92/−5.73	–	0.97	16.41	73	11.61
IT-M	PBDB-T	1..60	−3.98/−5.58	1.10×10^{-4}(S,B)	0.94	17.44	74	12.05
IT-4F	PBDB-T-SF	1.51	−4.14/−5.66	4.20×10^{-4}(S,B)	0.88	20.88	71	13.10
F-ITIC	PTPDBDT	1.56	−4.09/−5.65	3.10×10^{-4}(S,B)	0.94	14.1	66	8.8
Cl-ITIC	PTPDBDT	1.56	−4.14/−5.70	5.20×10^{-4}(S,B)	0.94	15.6	65	9.5
Br-ITIC	PTPDBDT	1.53	−4.20/−5.73	5.10×10^{-4}(S,B)	0.93	15.4	66	9.4
I-ITIC	PTPDBDT	1.55	−4.14/−5.68	4.10×10^{-4}(S,B)	0.95	14.5	65	8.9
ITTC	HFQx-T	1.61	−3.85/−5.49	1.44×10^{-4}(S,B)	0.88	16.49	71	10.4
ITCPTC	PBT1-EH	1.58	−3.96/−5.62	2.69×10^{-3}(S,B)	0.95	16.5	75	11.8
ITCT	PBDB-T	1.59	−4.02/−5.66	5.10×10^{-4}(S,B)	0.86	18.1	73	11.27
ITCC	PBDB-T	1.67	3.76/−5.47	6.74×10^{-4}(S,B)	1.01	15.9	71	11.4
NFBDT	PBDB-T	1.56	−3.83/−5.40	1.38×10^{-4}(S,B)	0.87	17.85	67	10.42
BT-IC	J71	1.43	−3.85/−5.32	3.53×10^{-4}(S,B)	0.90	17.75	66	10.46
ITIC2	FTAZ	1.53	−3.80/−5.43	4.10×10^{-4}(S,B)	0.93	18.88	63	11.0
FDICTF	PBDB-T	1.63	−3.71/−5.43	3.79×10^{-5}(S,N)	0.95	16.0	67	10.0
FDNCTF	PBDB-T	1.60	−3.73/−5.42	2.83×10^{-4}(S,N)	0.94	16.5	73	11.2
DTCC-IC	PTB7-Th	1.59	−3.87/−5.50	1.86×10^{-3}(S,B)	0.95	11.23	56	6.0
DTCCIC-C17	PBDB-T	1.60	−3.65/−5.46	-	0.97	14.27	68	9.48
ITTIC	PBDB-T1	1.46	−3.82/−5.28	1.08×10^{-4}(S,B)	0.92	15.93	62	9.12
ITVffIC	J71	1.35	−4.04/−5.58	2.15×10^{-4}(S,B)	0.81	2.60	63	10.54

S stands for the mobility measured by the space charge limited current (SCLC) method and O for the organic field effect transistor (OFET)method; N stands for the neat film and B for the blended film.

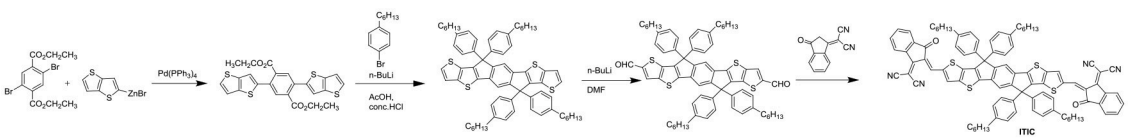

SCHEME 3 | Synthetic route of ITIC.

high and balanced charge transport, negligible bimolecular recombination resulting in a promising PCE of 9.3%, which was higher than 9.07% efficiency of ITIC based devices under the same conditions (Zhang et al., 2017c). ITIC-SC2C6 based on branched 4-(alkylthio)-phenyl side chains was systematically explored. The investigations indicated that this acceptor had improved solubility, which is helpful for polymer donor to form nanofibrils. Consequently, the OSCs exhibited a PCE of 9.16% with PBDB-ST as donor (Zhang et al., 2017b). ITIC-Th, replacing phenyl side chains of ITIC with thienyl side groups, exhibited low LUMO energy levels, which can match with low bandgap and wide bandgap polymer donor. Additionally, ITIC-Th possessed high electron mobility owing to enhanced intermolecular interactions induced by S…S interaction. The OSCs were fabricated by blending ITIC-Th with low bandgap polymer PTB7-Th and wide bandgap polymer PBDB-T1, the PCE reached 8.7 and 9.6%, respectively (Lin et al., 2016b). ITIC and its derivatives has inevitable steric isomers between donor units and end groups linking by C = C covalent bond. To solve this defect, a definite molecular conformation ITC6-IC, which long alkyl chains were introduced into the terminal of IDTT, was synthesized and discussed. ITC6-IC exhibited planar structure, good solubility, high-lying LUMO energy levels and enhanced compatibility with donor materials. The blend films with PBDB-T as polymer donor and ITC6-IC as acceptor showed a fibril crystallization with bicontinuous network morphology

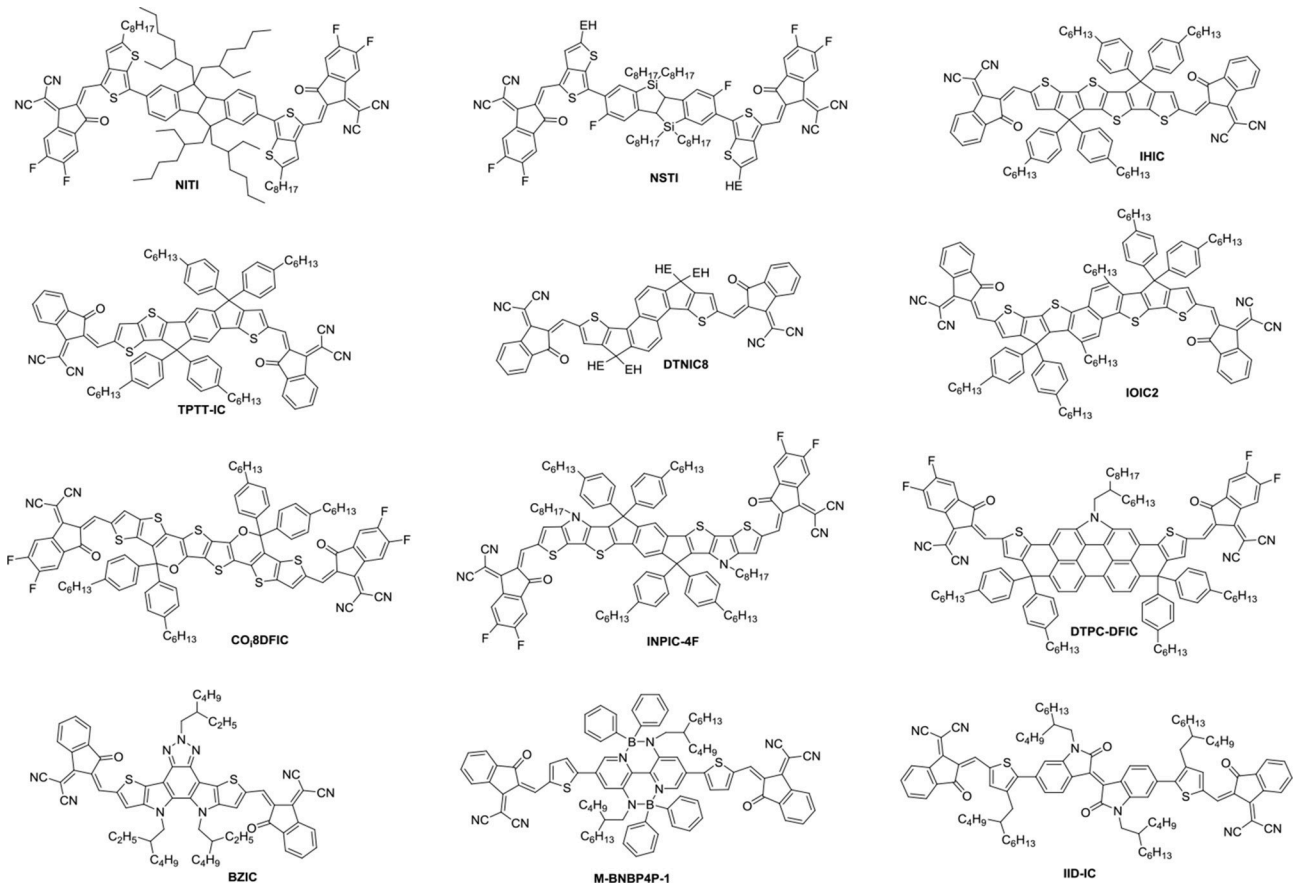

FIGURE 7 | Chemical structures of other fused-ring small molecule acceptors.

after thermal annealing. Consequently, the OSCs revealed a promising PCE of 11.61% with a high V_{oc} of 0.97 V (Zhang et al., 2018d).

Density functional theory calculations reveal that the LUMO mainly delocalizes at the end groups of the ITIC derivatives. Furthermore, the side chains on the central donor units would hinder the tight stacking of the molecules, thus, the stacking of the end groups are likely to provide the main electron transport pathway. Indeed, atomistic molecular dynamic simulations referred that local intermolecular π-π stacking between the acceptor units of the ITIC film led to 3D molecular packing (Han et al., 2017; Yan et al., 2018). As a consequence, the reasonable regulation of ITIC terminal units is excepted to obtain higher LUMO energy level and better isotropic electron transport characteristics. A methyl group was introduced onto the phenyl of the IC to give IT-M, which elevates the LUMO energy levels due to the weak electron-rich properties of methyl. The devices demonstrated a high PCE of 12.05% with V_{oc} of 0.94 V when blended with PBDB-T donor, which is the highest value for single-junction OSCs at that time (Li et al., 2016c). Then, replacing the methyl groups with the most electronegative fluorine atoms provided the new acceptor IT-4F. Although the fluorine atom resulted in low LUMO level, it had good crystallinity and high electron transport properties from noncovalent interactions of F…H,S…F and so on. The resulting OSCs based on PBDB-T-SF: IT-4F achieved a high PCE of 13.1% (Zhao et al., 2017). A similar effect of good crystallinities and noncovalent interactions can be found in other halogenated non-fullerene small molecular Cl-ITIC, Br-ITIC, and I-ITIC. The devices based on these halogenated acceptors showed PCEs of 9.5, 9.4, and 8.9%, respectively, which are higher than that of F-ITIC (8.8%) under the same circumstances (Yang et al., 2017). There are similar phenomena in other systems (Li et al., 2017c; Wang et al., 2018b). Apart from changing the substituents of the end groups, the modification of aromatic structure also attracted attention. Replacing the benzene of the IC with thiophene units gave isomers ITTC, ITCPTC, ITCT, and ITCC, which all show good potential in OSCs due to enhanced intermolecular π-π interaction induced by S…S interactions. When ITTC (or ITCPTC) as acceptor, the OSCs based on HFQx-T donor achieved a PCE of 10.4% (Zhang et al., 2017d) and 11.8% with PBT1-EH as donor (Xie et al., 2017). When PBDB-T as donor, the device based on ITCC delivered a PCE of 11.4% (Yao et al., 2017) and 11.27% for ITCT based devices (Liu et al., 2018c). Introducing methyl group onto the thiophene unit can also increase the V_{oc} (Cui et al., 2017; Luo et al., 2018).

TABLE 6 | Summary of the photophysical and photovoltaic properties of fused eptacyclic small molecule acceptors.

Acceptor	Donor	E_g (eV)	LUMO/HOMO (eV)	μe ($cm^2 \cdot V^{-1} \cdot s^{-1}$)	V_{oc} (V)	J_{sc} (mA cm^{-2})	FF (%)	PCE (%)
NITI	PBDB-T	1.49	−3.84/−5.68	1.19×10^{-4}(S,B)	0.86	20.67	71	12.74
NSTI	PBDB-T	1.58	−3.87/−5.54	1.06×10^{-4}(S,B)	0.83	16.47	75	10.33
IHIC	PTB7-Th	1.38	−3.93/−5.45	1.20×10^{-3}(S,B)	0.75	19.01	68	9.77
TPTT-IC	PBT1-C	1.63	−3.95/−5.78	3.23×10^{-4}(S,B)	0.96	15.6	70	10.5
DTNIC8	PBDB-T	1.73	−3.93/−5.91	2.80×10^{-5}(S,B)	0.96	12.92	73	9.03
IOIC2	FTAZ	1.55	−3.78/−5.41	3.23×10^{-4}(S,B)	0.90	19.7	69	12.3
CO_i8DFIC	PTB7-Th	1.26	−3.88/−5.50	3.91×10^{-5}(S,B)	0.68	26.12	68	12.16
INPIC-4F	PBDB-T	1.39	−3.94/−5.42	5.00×10^{-4}(S,B)	0.85	21.61	72	13.13
DTPC-DFIC	PTB7-Th	1.21	−4.10/−5.31	3.60×10^{-4}(S,B)	0.76	21.92	61	10.21
BZIC	HFQx-T	1.45	−3.88/−5.42	8.97×10^{-5}(S,B)	0.84	12.67	59	6.3
M-BNBP4P-1	PTB7-Th	1.40	−3.93/−5.34	1.47×10^{-4}(S,B)	0.78	14.62	62	7.06
IID-IC	J61	1.71	−3.95/−5.99	4.15×10^{-5}(S,B)	0.83	6.36	53	2.82

S stands for the mobility measured by the space charge limited current (SCLC) method and O for the organic field effect transistor (OFET)method; N stands for the neat film and B for the blended film.

NFBDT is an isomer of ITIC, which based on a heptacyclic benzodi(cyclopentadithiophene) (FBDT) unit as core and IC as end groups. Due to symmetric and planar conjugated structure of BDT unit, the NFBDT possessed low bandgap of 1.56 eV. When blended with PBDB-T, the devices showed a PCE of 10.42% (Kan et al., 2017). Introducing 2-ethylhexyloxy on the BDT unit obtained BT-IC to further reduce E_g (1.43 eV) by elevating the HOMO energy levels. The OSC fabricated by blending J71 and BT-IC achieved a PCE of 10.5% (Li et al., 2017d). ITIC2 with 5-(2-ethylhexyl) thiophene as side chains was a further development of NFBDT. The conjugated side chains is helpful for enhancing the absorption, intermolecular interaction and π-π stacking. Thus a high PCE of 11.0% was obtained while blended with FTAZ donor (Wang et al., 2017a). Fusing the thiophene spacers to the fluorene of DICTF afforded ladder acceptor FDICTF, leading to narrow bandgap, higher extinction coefficient and slightly higher LUMO energy level. In addition to extending the central core to enhanced absorption and intermolecular overlaps, extending conjugation end groups was also an effective strategy. For example, FDNCTF was obtained by replacing the benzene units of FDICTF with naphthalene units. The devices based on FDNCTF blended with PBDB-T delivered a higher PCE of 11.2% compared to 10.0% for FDICTF (Feng et al., 2017a; Qiu et al., 2017). Two acceptors DTCC-IC and DTCCIC-C17 based on dithienocyclopentacarbazole (DTCC) with different side chains were reported. Due to strong electron-donating properties and coplanar conjugated skeleton, both of them possessed strong absorption and good performance with PCE of 6.0% for DTCC-IC and 9.48% for DTCCIC-C17 (Cao et al., 2017; Hsiao et al., 2017). Two narrow bandgap acceptors ITTIC (1.46 eV) and ITVffIC (1.35 eV) were synthesized by incorporating thiophene units and double-bond as spacers, respectively. The PSCs based on PBDB-T1: ITTIC showed a PCE of 9.12% without any additives, and 10.54% for J71: ITVffIC blend films (Li et al., 2017b; Zhang et al., 2017e).

Other Fused-Ring Small Molecule Acceptors

NITI, bearing an indenoindene core which is a carbon-bridged E-stilbene with a centrosymmetry, exhibited a low optical bandgap of 1.49 eV and high extinction coefficient of 1.90×10^5 cm^{-1} (**Figure 7** and **Table 6**). The corresponding devices delivered an excellent PCE of 12.74% by blending a large bandgap polymer PBDB-T due to the good charge transport property and proper phase separation (Xu et al., 2017). A further development of NITI was by replacing carbon-bridge with silicon-bridge to give NSTI. Bis-silicon-bridged stilbene (BSS) has rigid and coplanar structure and four side chains can suppress the strong aggregations. When blended with PBDB-T, the OSCs obtained a PCE of 10.33% with CN as additive (Zhang and Zhu, 2018). IHIC was a fused hexacyclic small molecule acceptor and the central core consisted of thieno[3,2-*b*]thiophene ring and two terminal thiophene. The thiophene-rich cores possessed symmetrical, rigid and coplanar structure, IC was used as the end group to construct push-pull structure, which is beneficial to inducing ICT and shifting the absorption spectrum to the NIR region. The IHIC showed strong NIR absorption with a narrow bandgap of 1.38 eV and a high electron mobility of 2.4×10^{-3} cm^2 V^{-1} s^{-1}. The semitransparent OSCs achieved a PCE of 9.77% with a visible transmittance of 36% when blended with PTB7-Th (Wang et al., 2017b). Other similar thiophene-rich acceptors had strong NIR absorption and showed excellent performance (Jia et al., 2017; Dai et al., 2018; Li et al., 2018b). TPTT-IC was synthesized with a asymmetric thiophene-phenylene-thieno[3,2-*b*]thiophene-fused central core. Dipole-dipole interactions of asymmetric molecules tend to form strong π-π stacking on the face on orientation and achieved high FF (Li et al., 2018a). The OSCs achieved a PCE of 10.5% while blended with wide bandgap polymer PBT1-C (Li et al., 2018a). DTNIC8 can be considered as a further development of the IHIC by replacing thieno[3,2-*b*]thiophene with naphthalene. The angular-shaped central core dithienonaphthalene (DTN) had a more extended

π-conjugation system in comparison with IDT (Ma et al., 2017a). The devices based on PBDB-T: DTNIC8 blend films delivered a PCE of 9.03% with high FF of 73% attributed to well-defined film morphology (Ma et al., 2017b). IOIC2 is a naphthodithiophene-based fused octacyclic acceptor. IOIC2 had larger π-conjugation and stronger electron-rich properties, leading to higher LUMO energy levels, lower bandgap and higher electron mobilities, compared to naphthalene-based fused hexacyclic acceptor. Thus, the devices based on FTAZ: IOIC2 exhibited an excellent PCE of up to 12.3% (Zhu et al., 2018a,b). Another representative fused octacyclic acceptor was CO_i8DFIC with carbon-oxygen-bridge, which had lower bandgap, higher electron transport properties due to higher electron-donating ability and more planar conjugated structure. When PTB7-Th was used as donor polymer, a high PCE of 12.16% was obtained with high J_{sc} of 26.12 mA cm^{-2} (Xiao et al., 2017b). Compared to carbon-bridge, the molecules with nitrogen-bridge usually exhibited stronger electron-donating properties and better solution processing. The INPIC-4F with nitrogen-bridge and fluorinated IC as end group possessed narrow bandgap of 1.39 eV and high electron mobility as well as strong crystallinity. A PCE of 13.13% was achieved with PBDB-T as donor (Sun et al., 2018). To improve electron-donating ability, in addition to increasing the conjugation length, dithienopicenocarbazole (DTPC) possessed strong electron-rich properties by broadening the central core to two-dimensional conjugation system. DTPC-DFIC possessed low band gap of 1.21 eV and exhibited a PCE of 10.21% with PTB7-Th as donor (Yao et al., 2018). A novel small molecular acceptor (BZIC) bearing a D-A-D type thieno [3,2-*b*] pyrrolo-fused pentacyclic benzotrizole core was reported. A broad absorption spectra with optical bandgap of 1.45 eV was achieved due to increased intramolecular electronic interactions from D-A-D conjugated structure. BZIC was the first acceptor material based on a weak electron-deficient unit flanking with electron rich ring as central core rather than electron-donating fused ring unit like IDTT as core. By using HFQx-T as polymer donor, the OSCs exhibited a PCE of 6.30% (Feng et al., 2017b). Most of the above-mentioned acceptor molecules exhibited only one strong absorption band due to strong intramolecular charge transfer. However, M-BNBP4P-1 was developed with two strong absorption bands due to its delocalized LUMO and localized HOMO. The devices showed a PCE of 7.06% with PTB7-Th as donor (Liu et al., 2017a). IID-IC was an A-D-A'-D-A type acceptor. Because of the partially suppressed intramolecular charge transfer effects with the introduction of additional electron-deficient isoindigo unit, IID-IC exhibited a full width at half maximum of 190 nm but only 95 nm for ITIC. The OSCs based on J61: IID-IC delivered a PCE of 2.82% with broad photoresponses from 320 to 780 nm (Miao et al., 2018).

SUMMARY AND OUTLOOK

In this review, two types of promising small-molecule electron acceptors were discussed: PDI based acceptors and A-D-A fused-ring electron acceptors. Traditional PDI units tended to form large aggregate domains leading to low exciton separation and highly torsional PDI derivatives could decrease the charge transport. Thus, a series of strategies, such as: forming PDI dimers and 3D PDI derivatives *etc.*, were used to find the balance toward a certain aggregations that exhibited efficient exciton separation without sacrificing charge transfer and mobility. A-D-A type acceptor materials have been developed rapidly and have made exciting progress with highest PCE over 14%. In general, from fused tricyclic to fused octacyclic system, larger central core possessed redshifted absorption and high electron mobilities. Side chains were used to ensure solubility in common solvents and to inhibit strong self-assembly as well as to regulate molecular orientation and morphology. Electron-deficient end groups were used to tuning the LUMO energy level and π-π stacking.

Although non-fullerene-based solar cells have made tremendous progress in recent few years, in order to meet practical applications, designing and synthesizing new acceptor materials, pairing with donor materials, together with technical progress in device fabrications are highly desirable. When designing new active layer materials, basic properties such as absorption, energy levels and charge transport should be carefully considered. Another needed to consider is the cost and stability. We believe that a bright future for realizing high-performance and practical non-fullerene OSCs can be expected.

AUTHOR CONTRIBUTIONS

ZZ collected the references, drew the structures, wrote the first draft of the manuscript; JY and QW helped with the revision of the manuscript and answered questions the reviewers raised; YZ supervised this project, revised the manuscript and helped all the submissions and giving the answers.

ACKNOWLEDGMENTS

This work has been financially supported by the National Natural Science Foundation of China (21875286, 51173206), National Key Research & Development Projects of China (2017YFA0206600), Science Fund for Distinguished Young Scholars of Hunan Province (2017JJ1029) and Project of Innovation-driven Plan in Central South University, China (2016CX035).

REFERENCES

Alamoudi, M. A., Khan, J. I., Firdaus, Y., Wang, K., Andrienko, D., Beaujuge, P. M., et al. (2018). Impact of nonfullerene acceptor core structure on the photophysics and efficiency of polymer solar cells. *ACS Energy Lett.* 3, 802–811. doi: 10.1021/acsenergylett.8b00045

Baran, D., Kirchartz, T., Wheeler, S., Dimitrov, S., Abdelsamie, M., Gorman, J., et al. (2016). Reduced voltage losses yield 10% efficient fullerene free organic solar cells with >1 V open circuit voltages. *Energy Environ. Sci.* 9, 3783–3793. doi: 10.1039/c6ee02598f

Bin, H., Zhang, Z. G., Gao, L., Chen, S., Zhong, L., Xue, L., et al. (2016). Non-Fullerene Polymer Solar Cells Based on Alkylthio and Fluorine Substituted

2D-Conjugated Polymers Reach 9.5% Efficiency. *J. Am. Chem. Soc.* 138, 4657–4664. doi: 10.1021/jacs.6b01744

Bloking, J. T., Han, X., Higgs, A. T., Kastrop, J. P., Pandey, L., Norton, J. E., et al. (2011). Solution-Processed Organic Solar Cells with Power Conversion Efficiencies of 2.5% using Benzothiadiazole/Imide-Based Acceptors. *Chem. Mater.* 23, 5484–5490. doi: 10.1021/cm203111k

Cai, Y., Huo, L., Sun, X., Wei, D., Tang, M., and Sun, Y. (2015). High performance organic solar cells based on a twisted bay-substituted tetraphenyl functionalized perylenediimide electron acceptor. *Adv. Energy Mater.* 5:1500032. doi: 10.1002/aenm.201500032

Cao, Q., Xiong, W., Chen, H., Cai, G., Wang, G., Zheng, L., et al. (2017). Design, synthesis, and structural characterization of the first dithienocyclopentacarbazole-based n-type organic semiconductor and its application in non-fullerene polymer solar cells. *J. Mater. Chem. A* 5, 7451–7461. doi: 10.1039/C7TA01143A

Carlotti, B., Cai, Z., Kim, H., Sharapov, V., Madu, I. K., Zhao, D., et al. (2018). Charge Transfer and aggregation effects on the performance of planar vs twisted nonfullerene acceptor isomers for organic solar cells. *Chem. Mater.* 30, 4263–4276. doi: 10.1021/acs.chemmater.8b01047

Chapin, D. M., Fuller, C. S., and Pearson, G. L. (1954). A new silicon p-n junction photocell for converting solar radiation into electrical power. *J. Appl. Phys.* 25, 676–677. doi: 10.1063/1.1721711

Che, X., Li, Y., Qu, Y., and Forrest, S. R. (2018). High fabrication yield organic tandem photovoltaics combining vacuum- and solution-processed subcells with 15% efficiency. *Nat. Energy* 3, 422–427. doi: 10.1038/s41560-018-0134-z

Chen, Y., Zhang, X., Zhan, C., and Yao, J. (2015). In-depth understanding of photocurrent enhancement in solution-processed small-molecule:perylene diimide non-fullerene organic solar cells. *Phys. Status Solidi.* 212, 1961–1968. doi: 10.1002/pssa.201532102

Cheng, P., Li, G., Zhan, X., and Yang, Y. (2018). Next-generation organic photovoltaics based on non-fullerene acceptors. *Nat. Photonics* 12, 131–142. doi: 10.1038/s41566-018-0104-9

Cui, Y., Yao, H., Gao, B., Qin, Y., Zhang, S., Yang, B., et al. (2017). Fine-Tuned Photoactive and Interconnection Layers for Achieving over 13% Efficiency in a Fullerene-Free Tandem Organic Solar Cell. *J. Am. Chem. Soc.* 139, 7302–7309. doi: 10.1021/jacs.7b01493

Dai, S., Li, T., Wang, W., Xiao, Y., Lau, T. K., Li, Z., et al. (2018). Enhancing the performance of polymer solar cells via core engineering of NIR-absorbing electron acceptors. *Adv. Mater. Weinheim.* 30:e1706571. doi: 10.1002/adma.201706571

Fei, Z., Eisner, F. D., Jiao, X., Azzouzi, M., Rohr, J. A., Han, Y., et al. (2018). An Alkylated Indacenodithieno[3,2-b]thiophene-Based nonfullerene acceptor with high crystallinity exhibiting single junction solar cell efficiencies greater than 13% with low voltage losses. *Adv. Mater.* 30:1705209. doi: 10.1002/adma.201705209

Feng, H., Qiu, N., Wang, X., Wang, Y., Kan, B., Wan, X., et al. (2017a). An A-D-A type small-molecule electron acceptor with end-extended conjugation for high performance organic solar cells. *Chem. Mater.* 29, 7908–7917. doi: 10.1021/acs.chemmater.7b02811

Feng, L., Yuan, J., Zhang, Z., Peng, H., Zhang, Z. G., Xu, S., et al. (2017b). Thieno[3,2-b]pyrrolo-fused pentacyclic benzotriazole-based acceptor for efficient organic photovoltaics. *ACS Appl. Mater. Interfaces* 9, 31985–31992. doi: 10.1021/acsami.7b10995

Feng, S., Zhang, C., Liu, Y., Bi, Z., Zhang, Z., Xu, X., et al. (2017c). Fused-ring acceptors with asymmetric side chains for high-performance thick-film organic solar cells. *Adv. Mater.* 29:1703527. doi: 10.1002/adma.201703527

Hamonnet, J., Nakano, M., Nakano, K., Sugino, H., Takimiya, K., and Tajima, K. (2017). Bis(naphthothiophene diimide)indacenodithiophenes as Acceptors for Organic Photovoltaics. *Chem. Mater.* 29, 9618–9622. doi: 10.1021/acs.chemmater.7b03733

Han, G., Guo, Y., Song, X., Wang, Y., and Yi, Y. (2017). Terminal π-π stacking determines three-dimensional molecular packing and isotropic charge transport in an A–π-A electron acceptor for non-fullerene organic solar cells. *J. Mater. Chem. C.* 5, 4852–4857. doi: 10.1039/c7tc01310h

Heeger, A. J. (2014). 25th anniversary article: bulk heterojunction solar cells: understanding the mechanism of operation. *Adv. Mater.* 26, 10–27. doi: 10.1002/adma.201304373

Hendsbee, A. D., Sun, J.-P., Law, W. K., Yan, H., Hill, I. G., Spasyuk, D. M., et al. (2016). Synthesis, Self-Assembly, and Solar Cell Performance of N-Annulated Perylene Diimide Non-Fullerene Acceptors. *Chem. Mater.* 28, 7098–7109. doi: 10.1021/acs.chemmater.6b03292

Holliday, S., Ashraf, R. S., Nielsen, C. B., Kirkus, M., Rohr, J. A., Tan, C. H., et al. (2015). A rhodanine flanked nonfullerene acceptor for solution-processed organic photovoltaics. *J. Am. Chem. Soc.* 137, 898–904. doi: 10.1021/ja5110602

Holliday, S., Ashraf, R. S., Wadsworth, A., Baran, D., Yousaf, S. A., Nielsen, C. B., et al. (2016). High-efficiency and air-stable P3HT-based polymer solar cells with a new non-fullerene acceptor. *Nat. Commun.* 7:11585. doi: 10.1038/ncomms11585

Hou, R., Li, M., Feng, S., Liu, Y., Wu, L., Bi, Z., et al. (2018). Fused pentacyclic electron acceptors with four cis-arranged alkyl side chains for efficient polymer solar cells. *J. Mater. Chem. A* 6, 3724–3729. doi: 10.1039/c7ta10026d

Hsiao, Y. T., Li, C. H., Chang, S. L., Heo, S., Tajima, K., Cheng, Y. J., et al. (2017). Heptacyclic carbazole-based ladder-type nonfullerene acceptor with side-chain optimization for efficient organic photovoltaics. *ACS Appl. Mater. Interfaces* 9, 42035–42042. doi: 10.1021/acsami.7b12612

Hu, Z., Zhang, F., An, Q., Zhang, M., Ma, X., Wang, J., et al. (2018). Ternary nonfullerene polymer solar cells with a power conversion efficiency of 11.6% by inheriting the advantages of binary cells. *ACS Energy Lett.* 3, 555–561. doi: 10.1021/acsenergylett.8b00100

Jia, B., Dai, S., Ke, Z., Yan, C., Ma, W., and Zhan, X. (2017). Breaking 10% efficiency in semitransparent solar cells with fused-undecacyclic electron acceptor. *Chem. Mater.* 30, 239–245. doi: 10.1021/acs.chemmater.7b04251

Jiang, W., Ye, L., Li, X., Xiao, C., Tan, F., Zhao, W., et al. (2014). Bay-linked perylene bisimides as promising non-fullerene acceptors for organic solar cells. *Chem. Commun.* 50, 1024–1026. doi: 10.1039/c3cc47204c

Jiang, X., Xu, Y., Wang, X., Yang, F., Zhang, A., Li, C., et al. (2017). Conjugated polymer acceptors based on fused perylene bisimides with a twisted backbone for non-fullerene solar cells. *Polym. Chem.* 8, 3300–3306. doi: 10.1039/c7py00444c

Kallmann, H., and Pope, M. (1959). Photovoltaic Effect in Organic Crystals. *J. Chem. Phys.* 30, 585–586. doi: 10.1063/1.1729992

Kamm, V., Battagliarin, G., Howard, I. A., Pisula, W., Mavrinskiy, A., Li, C., et al. (2011). Polythiophene:Perylene Diimide Solar Cells - the Impact of Alkyl-Substitution on the Photovoltaic Performance. *Adv. Energy Mater.* 1, 297–302. doi: 10.1002/aenm.201000006

Kan, B., Feng, H., Wan, X., Liu, F., Ke, X., Wang, Y., et al. (2017). Small-Molecule Acceptor Based on the Heptacyclic Benzodi(cyclopentadithiophene) unit for highly efficient nonfullerene organic solar cells. *J. Am. Chem. Soc.* 139, 4929–4934. doi: 10.1021/jacs.7b01170

Kang, Z., Chen, S. C., Ma, Y., Wang, J., and Zheng, Q. (2017). Push-Pull type non-fullerene acceptors for polymer solar cells: effect of the donor core. *ACS Appl. Mater. Interfaces* 9, 24771–24777. doi: 10.1021/acsami.7b05417

Kim, Y., Song, C. E., Moon, S. J., and Lim, E. (2014). Rhodanine dye-based small molecule acceptors for organic photovoltaic cells. *Chem. Commun. (Camb).* 50, 8235–8238. doi: 10.1039/c4cc01695e

Krebs, F. C. (2009). Fabrication and processing of polymer solar cells: a review of printing and coating techniques. *Sol. Energy Mater. Sol. Cells* 93, 394–412. doi: 10.1016/j.solmat.2008.10.004

Lee, J., Singh, R., Sin, D. H., Kim, H. G., Song, K. C., and Cho, K. (2016). A nonfullerene small molecule acceptor with 3D interlocking geometry enabling efficient organic solar cells. *Adv. Mater.* 28, 69–76. doi: 10.1002/adma.201504010

Li, C., Xie, Y., Fan, B., Han, G., Yi, Y., and Sun, Y. (2018a). A nonfullerene acceptor utilizing a novel asymmetric multifused-ring core unit for highly efficient organic solar cells. *J. Mater. Chem. C* 6, 4873–4877. doi: 10.1039/C8TC01229F

Li, G., Zhu, R., and Yang, Y. (2012). Polymer solar cells. *Nat. Photonics* 6, 153–161. doi: 10.1038/nphoton.2012.11

Li, M., Liu, Y., Ni, W., Liu, F., Feng, H., Zhang, Y., et al. (2016a). A simple small molecule as an acceptor for fullerene-free organic solar cells with efficiency near 8%. *J. Mater. Chem. A* 4, 10409–10413. doi: 10.1039/c6ta04358e

Li, S., Liu, W., Li, C.-Z., Lau, T.-K., Lu, X., Shi, M., et al. (2016b). A non-fullerene acceptor with a fully fused backbone for efficient polymer solar cells with a high open-circuit voltage. *J. Mater. Chem. A* 4, 14983–14987. doi: 10.1039/C6TA07368A

Li, S., Liu, W., Li, C. Z., Shi, M., and Chen, H. (2017a). Efficient organic solar cells with non-fullerene acceptors. *Small* 13:1701120. doi: 10.1002/smll.201701120

Li, S., Ye, L., Zhao, W., Zhang, S., Mukherjee, S., Ade, H., et al. (2016c). Energy-level modulation of small-molecule electron acceptors to achieve over 12% efficiency in polymer solar cells. *Adv. Mater.* 28, 9423–9429. doi: 10.1002/adma.201602776

Li, T., Dai, S., Ke, Z., Yang, L., Wang, J., Yan, C., et al. (2018b). Fused Tris(thienothiophene)-based electron acceptor with strong near-infrared absorption for high-performance as-cast solar cells. *Adv. Mater.* 30:1705969. doi: 10.1002/adma.201705969

Li, X., Huang, H., Bin, H., Peng, Z., Zhu, C., Xue, L., et al. (2017b). Synthesis and photovoltaic properties of a series of narrow bandgap organic semiconductor acceptors with their absorption edge reaching 900 nm. *Chem. Mater.* 29, 10130–10138. doi: 10.1021/acs.chemmater.7b03928

Li, Y. (2011). Molecular design of photovoltaic materials for polymer solar cells: toward suitable electronic energy levels and broad absorption. *Acc. Chem. Res.* 45, 723–733. doi: 10.1021/ar2002446

Li, Y., Lin, J. D., Che, X., Qu, Y., Liu, F., Liao, L. S., et al. (2017c). High efficiency near-infrared and semitransparent non-fullerene acceptor organic photovoltaic cells. *J. Am. Chem. Soc.* 139, 17114–17119. doi: 10.1021/jacs.7b11278

Li, Y., Zhong, L., Gautam, B., Bin, H.-J., Lin, J.-D., Wu, F.-P., et al. (2017d). A near-infrared non-fullerene electron acceptor for high performance polymer solar cells. *Energy Environ. Sci.* 10, 1610–1620. doi: 10.1039/c7ee00844a

Li, Y., Zhong, L., Wu, F.-P., Yuan, Y., Bin, H.-J., Jiang, Z.-Q., et al. (2016d). Non-fullerene polymer solar cells based on a selenophene-containing fused-ring acceptor with photovoltaic performance of 8.6%. *Energy Environ Sci* 9, 3429–3435. doi: 10.1039/c6ee00315j

Li, Y., and Zou, Y. (2008). Conjugated polymer photovoltaic materials with broad absorption band and high charge carrier mobility. *Adv. Mater.* 20, 2952–2958. doi: 10.1002/adma.200800606

Liang, N., Jiang, W., Hou, J., and Wang, Z. (2017). New developments in non-fullerene small molecule acceptors for polymer solar cells. *Mater. Chem. Front.* 1, 1291–1303. doi: 10.1039/c6qm00247a

Lin, H., Chen, S., Hu, H., Zhang, L., Ma, T., Lai, J. Y., et al. (2016a). Reduced intramolecular twisting improves the performance of 3D molecular acceptors in non-fullerene organic solar cells. *Adv. Mater.* 28, 8546–8551. doi: 10.1002/adma.201600997

Lin, H., Chen, S., Li, Z., Lai, J. Y., Yang, G., Mcafee, T., et al. (2015a). High-performance non-fullerene polymer solar cells based on a pair of donor-acceptor materials with complementary absorption properties. *Adv. Mater.* 27, 7299–7304. doi: 10.1002/adma.201502775

Lin, Y., Li, Y., and Zhan, X. (2013). A solution-processable electron acceptor based on dibenzosilole and diketopyrrolopyrrole for organic solar cells. *Adv. Energy Mater.* 3, 724–728. doi: 10.1002/aenm.201200911

Lin, Y., Wang, J., Dai, S., Li, Y., Zhu, D., and Zhan, X. (2014a). A twisted dimeric perylene diimide electron acceptor for efficient organic solar cells. *Adv. Energy Mater.* 4:1400420. doi: 10.1002/aenm.201400420

Lin, Y., Wang, J., Zhang, Z. G., Bai, H., Li, Y., Zhu, D., et al. (2015b). An electron acceptor challenging fullerenes for efficient polymer solar cells. *Adv. Mater.* 27, 1170–1174. doi: 10.1002/adma.201404317

Lin, Y., Wang, Y., Wang, J., Hou, J., Li, Y., Zhu, D., et al. (2014b). A star-shaped perylene diimide electron acceptor for high-performance organic solar cells. *Adv. Mater.* 26, 5137–5142. doi: 10.1002/adma.201400525

Lin, Y., and Zhan, X. (2014). Non-fullerene acceptors for organic photovoltaics: an emerging horizon. *Materials Horizons* 1:470. doi: 10.1039/c4mh00042k

Lin, Y., Zhang, Z.-G., Bai, H., Wang, J., Yao, Y., Li, Y., et al. (2015c). High-performance fullerene-free polymer solar cells with 6.31% efficiency. *Energy Environ. Sci.* 8, 610–616. doi: 10.1039/c4ee03424d

Lin, Y., Zhao, F., He, Q., Huo, L., Wu, Y., Parker, T. C., et al. (2016b). High-Performance Electron Acceptor with Thienyl Side Chains for Organic Photovoltaics. *J. Am. Chem. Soc.* 138, 4955–4961. doi: 10.1021/jacs.6b02004

Liu, D., Wang, J., Gu, C., Li, Y., Bao, X., and Yang, R. (2018a). Stirring up acceptor phase and controlling morphology via choosing appropriate rigid aryl rings as lever arms in symmetry-breaking benzodithiophene for high-performance fullerene and fullerene-free polymer solar cells. *Adv. Mater.*. 30:1705870. doi: 10.1002/adma.201705870

Liu, D., Yang, L., Wu, Y., Wang, X., Zeng, Y., Han, G., et al. (2018b). Tunable Electron Donating and Accepting Properties Achieved by Modulating the Steric Hindrance of Side Chains in A-D-A Small-Molecule Photovoltaic Materials. *Chem. Mater.* 30, 619–628. doi: 10.1021/acs.chemmater.7b03142

Liu, F., Ding, Z., Liu, J., and Wang, L. (2017a). An organoboron compound with a wide absorption spectrum for solar cell applications. *Chem. Commun.* 53, 12213–12216. doi: 10.1039/c7cc07494h

Liu, F., Zhou, Z., Zhang, C., Vergote, T., Fan, H., Liu, F., et al. (2016a). A Thieno[3,4-b]thiophene-Based Non-fullerene Electron Acceptor for High-Performance Bulk-Heterojunction Organic Solar Cells. *J. Am. Chem. Soc.* 138, 15523–15526. doi: 10.1021/jacs.6b08523

Liu, J., Chen, S., Qian, D., Gautam, B., Yang, G., Zhao, J., et al. (2016b). Fast charge separation in a non-fullerene organic solar cell with a small driving force. *Nat. Energy* 1:16089. doi: 10.1038/NENERGY.2016.89

Liu, W., Li, W., Yao, J., and Zhan, C. (2018c). Achieving high short-circuit current and fill-factor via increasing quinoidal character on nonfullerene small molecule acceptor. *Chin. Chem. Lett.* 29, 381–384. doi: 10.1016/j.cclet.2017.11.018

Liu, Y., Li, M., Zhou, X., Jia, Q.-Q., Feng, S., Jiang, P., et al. (2018d). Nonfullerene Acceptors with Enhanced Solubility and Ordered Packing for High-Efficiency Polymer Solar Cells. *ACS Energy Lett.* 3, 1832–1839. doi: 10.1021/acsenergylett.8b00928

Liu, Y., Liu, G., Xie, R., Wang, Z., Zhong, W., Li, Y., et al. (2018e). A rational design and synthesis of cross-conjugated small molecule acceptors approaching high-performance fullerene-free polymer solar cells. *Chem. Mater.* 30, 4331–4342. doi: 10.1021/acs.chemmater.8b01491

Liu, Y., Zhang, C. E., Hao, D., Zhang, Z., Wu, L., Li, M., et al. (2018f). Enhancing the Performance of Organic Solar Cells by Hierarchically Supramolecular Self-Assembly of Fused-Ring Electron Acceptors. *Chem. Mater.* 30, 4307–4312. doi: 10.1021/acs.chemmater.8b01319

Liu, Y., Zhang, Z., Feng, S., Li, M., Wu, L., Hou, R., et al. (2017b). Exploiting noncovalently conformational locking as a design strategy for high performance fused-ring electron acceptor used in polymer solar cells. *J. Am. Chem. Soc.* 139, 3356–3359. doi: 10.1021/jacs.7b00566

Liu, Y., Zhao, J., Li, Z., Mu, C., Ma, W., Hu, H., et al. (2014). Aggregation and morphology control enables multiple cases of high-efficiency polymer solar cells. *Nat. Commun.* 5:5293. doi: 10.1038/ncomms6293

Luo, Z., Bin, H., Liu, T., Zhang, Z. G., Yang, Y., Zhong, C., et al. (2018). Fine-Tuning of Molecular Packing and Energy Level through Methyl Substitution Enabling Excellent Small Molecule Acceptors for Nonfullerene Polymer Solar Cells with Efficiency up to 12.54%. *Adv. Mater.* 30:1706124. doi: 10.1002/adma.201706124

Ma, Y., Zhang, M., Tang, Y., Ma, W., and Zheng, Q. (2017a). Angular-shaped dithienonaphthalene-based nonfullerene acceptor for high-performance polymer solar cells with large open-circuit voltages and minimal energy losses. *Chem. Mater.* 29, 9775–9785. doi: 10.1021/acs.chemmater.7b03770

Ma, Y., Zhang, M., Yan, Y., Xin, J., Wang, T., Ma, W., et al. (2017b). Ladder-type dithienonaphthalene-based small-molecule acceptors for efficient nonfullerene organic solar cells. *Chem. Mater.* 29, 7942–7952. doi: 10.1021/acs.chemmater.7b02887

Meng, D., Fu, H., Xiao, C., Meng, X., Winands, T., Ma, W., et al. (2016a). Three-Bladed Rylene Propellers with Three-Dimensional Network Assembly for Organic Electronics. *J. Am. Chem. Soc.* 138, 10184–10190. doi: 10.1021/jacs.6b04368

Meng, D., Sun, D., Zhong, C., Liu, T., Fan, B., Huo, L., et al. (2016b). High-performance solution-processed non-fullerene organic solar cells based on selenophene-containing perylene bisimide acceptor. *J. Am. Chem. Soc.* 138, 375–380. doi: 10.1021/jacs.5b11149

Miao, J., Meng, B., Liu, J., and Wang, L. (2018). An A-D-A'-D-A type small molecule acceptor with a broad absorption spectrum for organic solar cells. *Chem. Commun.* 54, 303–306. doi: 10.1039/c7cc08497h

Nian, Y., Wang, Z., Jiang, H., Feng, S., Li, S., Zhang, L., et al. (2018). Silaindacenodithiophene-based fused-ring non-fullerene electron acceptor for efficient polymer solar cells. *Chin. J. Chem.* 36, 495–501. doi: 10.1002/cjoc.201700809

Nielsen, C. B., Holliday, S., Chen, H. Y., Cryer, S. J., and Mcculloch, I. (2015). Non-fullerene electron acceptors for use in organic solar cells. *Acc. Chem. Res.* 48, 2803–2812. doi: 10.1021/acs.accounts.5b00199

Qiu, N., Zhang, H., Wan, X., Li, C., Ke, X., Feng, H., et al. (2017). A New nonfullerene electron acceptor with a ladder type backbone

for high-performance organic solar cells. *Adv. Mater.* 29:1604964. doi: 10.1002/adma.201604964

Rajaram, S., Shivanna, R., Kandappa, S. K., and Narayan, K. S. (2012). Nonplanar perylene diimides as potential alternatives to fullerenes in organic solar cells. *J. Phys. Chem. Lett.* 3, 2405–2408. doi: 10.1021/jz301047d

Roncali, J. (2009). Molecular bulk heterojunctions: an emerging approach to organic solar cells. *Acc. Chem. Res.* 42, 1719–1730. doi: 10.1021/ar900041b

Sariciftci, N. S., Smilowitz, L., Heeger, A. J., and Wudl, F. (1992). Photoinduced electron transfer from a conducting polymer to buckminsterfullerene. *Science* 258, 1474–1476. doi: 10.1126/science.258.5087.1474

Shi, H., Fu, W., Shi, M., Ling, J., and Chen, H. (2015). A solution-processable bipolar diketopyrrolopyrrole molecule used as both electron donor and acceptor for efficient organic solar cells. *J. Mater. Chem. A* 3, 1902–1905. doi: 10.1039/C4TA06035K.

Song, X., Gasparini, N., Ye, L., Yao, H., Hou, J., Ade, H., et al. (2018). Controlling Blend Morphology for Ultrahigh Current Density in Nonfullerene Acceptor-Based Organic Solar Cells. *ACS Energy Lett* 3, 669–676. doi: 10.1021/acsenergylett.7b01266

Suman, Bagui, A., Datt, R., Gupta, V., and Singh, S. P. (2017). A simple fluorene core-based non-fullerene acceptor for high performance organic solar cells. *Chem. Commun.* 53, 12790–12793. doi: 10.1039/c7cc08237a

Sun, D., Meng, D., Cai, Y., Fan, B., Li, Y., Jiang, W., et al. (2015). Non-fullerene-acceptor-based bulk-heterojunction organic solar cells with efficiency over 7%. *J. Am. Chem. Soc.* 137, 11156–11162. doi: 10.1021/jacs.5b06414

Sun, J., Ma, X., Zhang, Z., Yu, J., Zhou, J., Yin, X., et al. (2018). Dithieno[3,2-b:2',3'-d]pyrrole fused nonfullerene acceptors enabling over 13% efficiency for organic solar cells. *Adv. Mater.* 30:e1707150. doi: 10.1002/adma.201707150

Tang, C., Chen, S.-C., Shang, Q., and Zheng, Q. (2017). Asymmetric indenothiophene-based non-fullerene acceptors for efficient polymer solar cells. *Sci. China Mater.* 60, 707–716. doi: 10.1007/s40843-017-9059-3

Wadsworth, A., Moser, M., Marks, A., Little, M. S., Gasparini, N., Brabec, C. J., et al. (2018). Critical review of the molecular design progress in non-fullerene electron acceptors towards commercially viable organic solar cells. *Chem. Soc. Rev.* doi: 10.1039/c7cs00892a

Wang, J., Wang, W., Wang, X., Wu, Y., Zhang, Q., Yan, C., et al. (2017a). Enhancing performance of nonfullerene acceptors via side-chain conjugation strategy. *Adv. Mater.* 29:1702125. doi: 10.1002/adma.201702125

Wang, K., Firdaus, Y., Babics, M., Cruciani, F., Saleem, Q., El Labban, A., et al. (2016). π-Bridge-Independent 2-(Benzo[c][1,2,5]thiadiazol-4-ylmethylene)malononitrile-Substituted Nonfullerene Acceptors for Efficient Bulk Heterojunction Solar Cells. *Chem. Mater.* 28, 2200–2208. doi: 10.1021/acs.chemmater.6b00131

Wang, W., Yan, C., Lau, T. K., Wang, J., Liu, K., Fan, Y., et al. (2017b). Fused hexacyclic nonfullerene acceptor with strong near-infrared absorption for semitransparent organic solar cells with 9.77% efficiency. *Adv. Mater.* 29:1701308. doi: 10.1002/adma.201701308

Wang, W., Zhao, B., Cong, Z., Xie, Y., Wu, H., Liang, Q., et al. (2018a). Nonfullerene polymer solar cells based on a main-chain twisted low-bandgap acceptor with power conversion efficiency of 13.2%. *ACS Energy Lett* 3, 1499–1507. doi: 10.1021/acsenergylett.8b00627

Wang, Y., Zhang, Y., Qiu, N., Feng, H., Gao, H., Kan, B., et al. (2018b). A Halogenation Strategy for over 12% Efficiency Nonfullerene Organic Solar Cells. *Adv. Energy Mater.* 8:1702870. doi: 10.1002/aenm.201702870

Wei, J., Tu, Q., and Zheng, Q. (2017). Heteroheptacene-cored semiconducting molecules for non-fullerene organic solar cells. *Dyes Pigm.* 144, 133–141. doi: 10.1016/j.dyepig.2017.05.026

Winzenberg, K. N., Kemppinen, P., Scholes, F. H., Collis, G. E., Shu, Y., Singh, T. B., et al. (2013). Indan-1,3-dione electron-acceptor small molecules for solution-processable solar cells: a structure-property correlation. *Chem. Commun.* 49, 6307–6309. doi: 10.1039/c3cc42293c

Wu, Q., Zhao, D., Schneider, A. M., Chen, W., and Yu, L. (2016). Covalently Bound Clusters of Alpha-Substituted PDI-Rival Electron Acceptors to Fullerene for Organic Solar Cells. *J. Am. Chem. Soc.* 138, 7248–7251. doi: 10.1021/jacs.6b03562

Wu, Y., Bai, H., Wang, Z., Cheng, P., Zhu, S., Wang, Y., et al. (2015). A planar electron acceptor for efficient polymer solar cells. *Energy Environ. Sci.* 8, 3215–3221. doi: 10.1039/c5ee02477c

Xia, D., Wu, Y., Wang, Q., Zhang, A., Li, C., Lin, Y., et al. and Li, W. (2016). Effect of Alkyl Side Chains of Conjugated Polymer Donors on the Device Performance of Non-Fullerene Solar Cells. *Macromolecules* 49, 6445–6454. doi: 10.1021/acs.macromol.6b01326

Xiao, B., Tang, A., Yang, J., Mahmood, A., Sun, X., and Zhou, E. (2018). Quinoxaline-Containing Nonfullerene Small-Molecule Acceptors with a Linear A2-A1-D-A1-A2 Skeleton for Poly(3-hexylthiophene)-Based Organic Solar Cells. *ACS Appl. Mater. Interfaces* 10, 10254–10261. doi: 10.1021/acsami.8b00216

Xiao, B., Tang, A., Zhang, J., Mahmood, A., Wei, Z., and Zhou, E. (2017a). Achievement of High Voc of 1.02 V for P3HT-Based Organic Solar Cell Using a Benzotriazole-Containing Non-Fullerene Acceptor. *Adv. Energy Mater.* 7:1602269. doi: 10.1002/aenm.201602269

Xiao, Z., Jia, X., Li, D., Wang, S., Geng, X., Liu, F., et al. (2017b). 26 mA cm^{-2} Jsc from organic solar cells with a low-bandgap nonfullerene acceptor. *Sci. Bull.* 62, 1494–1496. doi: 10.1016/j.scib.2017.10.017

Xie, D., Liu, T., Gao, W., Zhong, C., Huo, L., Luo, Z., et al. (2017). A Novel thiophene-fused ending group enabling an excellent small molecule acceptor for high-performance fullerene-free polymer solar cells with 11.8% Efficiency. *Solar RRL* 1:1700044. doi: 10.1002/solr.201700044

Xu, H., Yang, Y., Zhong, C., Zhan, X., and Chen, X. (2018a). Narrow bandgap non-fullerene acceptor based on a thiophene-fused benzothiadiazole unit with a high short-circuit current density of over 20 mA cm^{-2}. *J. Mater. Chem. A* 6, 6393–6401. doi: 10.1039/c8ta00704g

Xu, S., Wang, X., Feng, L., He, Z., Peng, H., Cimrov,á, V., et al. (2018b). Optimizing the conjugated side chains of quinoxaline based polymers for nonfullerene solar cells with 10.5% efficiency. *J. Mater. Chem. A* 6, 3074–3083. doi: 10.1039/c7ta10262c

Xu, S. J., Zhou, Z., Liu, W., Zhang, Z., Liu, F., Yan, H., et al. (2017). A Twisted Thieno[3,4-b]thiophene-Based Electron Acceptor Featuring a 14-pi-Electron Indenoindene Core for High-Performance Organic Photovoltaics. *Adv. Mater.* 29:1704510. doi: 10.1002/adma.201704510

Yan, C., Barlow, S., Wang, Z., Yan, H., Jen, A. K. Y., Marder, S. R., et al. (2018). Non-fullerene acceptors for organic solar cells. *Nat. Rev. Mater.* 3:18003. doi: 10.1038/natrevmats.2018.3

Yan, Q., Zhou, Y., Zheng, Y.-Q., Pei, J., and Zhao, D. (2013). Towards rational design of organic electron acceptors for photovoltaics: a study based on perylenediimide derivatives. *Chem. Sci.* 4:4389. doi: 10.1039/c3sc51841h

Yang, F., Li, C., Lai, W., Zhang, A., Huang, H., and Li, W. (2017). Halogenated conjugated molecules for ambipolar field-effect transistors and non-fullerene organic solar cells. *Mater. Chem. Front.* 1, 1389–1395. doi: 10.1039/c7qm00025a

Yang, L., Gu, W., Lv, L., Chen, Y., Yang, Y., Ye, P., et al. (2018a). Triplet tellurophene-based acceptors for organic solar cells. *Angew. Chem. Int. Ed Engl.* 57, 1096–1102. doi: 10.1002/anie.201712011

Yang, L., Zhang, S., He, C., Zhang, J., Yang, Y., Zhu, J., et al. (2018b). Modulating molecular orientation enables efficient nonfullerene small-molecule organic solar cells. *Chem. Mater.* 30, 2129–2134. doi: 10.1021/acs.chemmater.8b00287

Yang, Y., Zhang, Z. G., Bin, H., Chen, S., Gao, L., Xue, L., et al. (2016). Side-Chain Isomerization on an n-type Organic Semiconductor ITIC Acceptor Makes 11.77% High Efficiency Polymer Solar Cells. *J. Am. Chem. Soc.* 138, 15011–15018. doi: 10.1021/jacs.6b09110

Yao, H., Chen, Y., Qin, Y., Yu, R., Cui, Y., Yang, B., et al. (2016). Design and synthesis of a low bandgap small molecule acceptor for efficient polymer solar cells. *Adv. Mater.* 28, 8283–8287. doi: 10.1002/adma.201602642

Yao, H., Ye, L., Hou, J., Jang, B., Han, G., Cui, Y., et al. (2017). Achieving highly efficient nonfullerene organic solar cells with improved intermolecular interaction and open-circuit voltage. *Adv. Mater.* 29:1700254. doi: 10.1002/adma.201700254

Yao, Z., Liao, X., Gao, K., Lin, F., Xu, X., Shi, X., et al. (2018). Dithienopicenocarbazole-based acceptors for efficient organic solar cells with optoelectronic response over 1000 nm and an extremely low energy loss. *J. Am. Chem. Soc.* 140, 2054–2057.doi: 10.1021/jacs.7b13239

Yu, T., Xu, X., Zhang, G., Wan, J., Li, Y., and Peng, Q. (2017). Wide Bandgap Copolymers Based on Quinoxalino[6,5-f].quinoxaline for Highly Efficient Nonfullerene Polymer Solar Cells. *Adv. Funct. Mater.* 27:1701491. doi: 10.1002/adfm.201701491

Yuan, J., Ouyang, J., Cimrová, V., Leclerc, M., Najari, A., and Zou, Y. (2017). Development of quinoxaline based polymers for photovoltaic applications. *J. Mater. Chem. C* 5, 1858–1879. doi: 10.1039/c6tc05381e

Yuan, J., Qiu, L. X., Zhang, Z. G., Li, Y. F., Chen, Y. W., and Zou, Y. P. (2016). Tetrafluoroquinoxaline based polymers for non-fullerene polymer solar cells with efficiency over 9%. *Nano Energy* 30, 312–320. doi: 10.1016/j.nanoen.2016.10.008

Zhan, C., and Yao, J. (2016). More than Conformational "Twisting" or "Coplanarity": molecular strategies for designing high-efficiency nonfullerene organic solar cells. *Chem. Mater.* 28, 1948–1964. doi: 10.1021/acs.chemmater.5b04339

Zhan, C., Zhang, X., and Yao, J. (2015). New advances in non-fullerene acceptor based organic solar cells. *RSC Adv.* 5, 93002–93026. doi: 10.1039/c5ra17715d

Zhan, X., Xiong, W., Gong, Y., Liu, T., Xie, Y., Peng, Q., et al. (2017). Pyrene-fused perylene diimides: new building blocks to construct non-fullerene acceptors with extremely high open-circuit voltages up to 1.26 V. *Solar RRL* 1:1700123. doi: 10.1002/solr.201700123

Zhang, A., Li, C., Yang, F., Zhang, J., Wang, Z., Wei, Z., et al. (2017a). An Electron acceptor with porphyrin and perylene bisimides for efficient non-fullerene solar cells. *Angew. Chem. Int. Ed. Engl.* 56, 2694–2698. doi: 10.1002/anie.201612090

Zhang, C., Feng, S., Liu, Y., Hou, R., Zhang, Z., Xu, X., et al. (2017b). Effect of non-fullerene acceptors' side chains on the morphology and photovoltaic performance of organic solar cells. *ACS Appl. Mater. Interfaces* 9, 33906–33912. doi: 10.1021/acsami.7b09915

Zhang, G., Zhao, J., Chow, P. C. Y., Jiang, K., Zhang, J., Zhu, Z., et al. (2018a). Nonfullerene acceptor molecules for bulk heterojunction organic solar cells. *Chem. Rev.* 118, 3447–3507. doi: 10.1021/acs.chemrev.7b00535

Zhang, S., Qin, Y., Zhu, J., and Hou, J. (2018b). Over 14% Efficiency in Polymer Solar Cells Enabled by a Chlorinated Polymer Donor. *Adv. Mater. Weinheim.* 30:e1800868. doi: 10.1002/adma.201800868

Zhang, X., Lu, Z., Ye, L., Zhan, C., Hou, J., Zhang, S., et al. (2013). A potential perylene diimide dimer-based acceptor material for highly efficient solution-processed non-fullerene organic solar cells with 4.03% efficiency. *Adv. Mater.* 25, 5791–5797. doi: 10.1002/adma.201300897

Zhang, Z., Feng, L., Xu, S., Liu, Y., Peng, H., Zhang, Z. G., et al. (2017c). A new electron acceptor with meta-alkoxyphenyl side chain for fullerene-free polymer solar cells with 9.3% efficiency. *Adv. Sci.* 4:1700152. doi: 10.1002/advs.201700152

Zhang, Z., Feng, L., Xu, S., Yuan, J., Zhang, Z.-G., Peng, H., et al. (2017d). Achieving over 10% efficiency in a new acceptor ITTC and its blends with hexafluoroquinoxaline based polymers. *J. Mater. Chem. A* 5, 11286–11293. doi: 10.1039/c7ta02486j

Zhang, Z., Liu, W., Rehman, T., Ju, H.-X., Mai, J., Lu, X., et al. (2017e). Energy-level modulation of non-fullerene acceptors to achieve high-efficiency polymer solar cells at a diminished energy offset. *J. Mater. Chem. A* 5, 9649–9654. doi: 10.1039/C7TA01554B

Zhang, Z., Yu, J., Yin, X., Hu, Z., Jiang, Y., Sun, J., et al. (2018d). Conformation locking on fused-ring electron acceptor for high-performance nonfullerene organic solar cells. *Adv. Funct. Mater.* 28:1705095. doi: 10.1002/adfm.201705095

Zhang, Z., Zhan, C., Zhang, X., Zhang, S., Huang, J., Li, A. D., et al. (2012). A self-assembly phase diagram from amphiphilic perylene diimides. *Chemistry* 18, 12305–12313. doi: 10.1002/chem.201201352

Zhang, Z., and Zhu, X. (2018). Bis-silicon-bridged stilbene: a core for small-molecule electron acceptor for high-performance organic solar cells. *Chem. Mater.* 30, 587–591. doi: 10.1021/acs.chemmater.7b04930

Zhao, D., Wu, Q., Cai, Z., Zheng, T., Chen, W., Lu, J., et al. (2016a). Electron Acceptors Based on α-Substituted Perylene Diimide (PDI) for Organic Solar Cells. *Chem. Mater.* 28, 1139–1146. doi: 10.1021/acs.chemmater.5b04570

Zhao, J., Li, Y., Lin, H., Liu, Y., Jiang, K., Mu, C., et al. (2015). High-efficiency non-fullerene organic solar cells enabled by a difluorobenzothiadiazole-based donor polymer combined with a properly matched small molecule acceptor. *Energy Environ. Sci.* 8, 520–525. doi: 10.1039/c4ee02990a

Zhao, J., Li, Y., Yang, G., Jiang, K., Lin, H., Ade, H., et al. (2016b). Efficient organic solar cells processed from hydrocarbon solvents. *Nat. Energy* 1:15027. doi: 10.1038/NENERGY.2015.27

Zhao, W., Li, S., Yao, H., Zhang, S., Zhang, Y., Yang, B., et al. (2017). Molecular Optimization Enables over 13% Efficiency in Organic Solar Cells. *J. Am. Chem. Soc.* 139, 7148–7151. doi: 10.1021/jacs.7b02677

Zhao, Y., Guo, Y., and Liu, Y. (2013). 25th anniversary article: recent advances in n-type and ambipolar organic field-effect transistors. *Adv. Mater.* 25, 5372–5391. doi: 10.1002/adma.201302315

Zhong, H., Wu, C. H., Li, C. Z., Carpenter, J., Chueh, C. C., Chen, J. Y., et al. (2016). Rigidifying Nonplanar perylene diimides by ring fusion toward geometry-tunable acceptors for high-performance fullerene-free solar cells. *Adv. Mater.* 28, 951–958. doi: 10.1002/adma.201504120

Zhong, W., Fan, B., Cui, J., Ying, L., Liu, F., Peng, J., et al. (2017). Regioisomeric Non-Fullerene Acceptors Containing Fluorobenzo[c][1,2,5]thiadiazole Unit for Polymer Solar Cells. *ACS Appl. Mater. Interfaces* 9, 37087–37093. doi: 10.1021/acsami.7b12902

Zhong, Y., Trinh, M. T., Chen, R., Purdum, G. E., Khlyabich, P. P., Sezen, M., et al. (2015). Molecular helices as electron acceptors in high-performance bulk heterojunction solar cells. *Nat. Commun.* 6:8242. doi: 10.1038/ncomms9242

Zhong, Y., Trinh, M. T., Chen, R., Wang, W., Khlyabich, P. P., Kumar, B., et al. (2014). Efficient organic solar cells with helical perylene diimide electron acceptors. *J. Am. Chem. Soc.* 136, 15215–15221. doi: 10.1021/ja5092613

Zhu, J., Ke, Z., Zhang, Q., Wang, J., Dai, S., Wu, Y., et al. (2018a). Naphthodithiophene-based nonfullerene acceptor for high-performance organic photovoltaics: effect of extended conjugation. *Adv. Mater.* 30:1704713. doi: 10.1002/adma.201704713

Zhu, J., Xiao, Y., Wang, J., Liu, K., Jiang, H., Lin, Y., et al. (2018b). Alkoxy-induced near-infrared sensitive electron acceptor for high-performance organic solar cells. *Chem. Mater.* 30, 4150–4156. doi: 10.1021/acs.chemmater.8b01677

Conflict of Interest Statement: The authors declare that the research was conducted in the absence of any commercial or financial relationships that could be construed as a potential conflict of interest.

frontiers in Chemistry

ORIGINAL RESEARCH
published: 13 September 2018
doi: 10.3389/fchem.2018.00413

Effects of Alkoxy and Fluorine Atom Substitution of Donor Molecules on the Morphology and Photovoltaic Performance of All Small Molecule Organic Solar Cells

Beibei Qiu[1,2], *Shanshan Chen*[3], *Lingwei Xue*[1], *Chenkai Sun*[1,2], *Xiaojun Li*[1,2], *Zhi-Guo Zhang*[1], *Changduk Yang*[3] *and Yongfang Li*[1,2,4]*

[1] CAS Key Laboratory of Organic Solids, CAS Research/Education Center for Excellence in Molecular Sciences, Institute of Chemistry, Chinese Academy of Sciences, Beijing, China, [2] School of Chemical Science, University of Chinese Academy of Sciences, Beijing, China, [3] Department of Energy Engineering, Low Dimensional Carbon Materials Center, School of Energy and Chemical Engineering, Ulsan National Institute of Science and Technology, Ulsan, South Korea, [4] Laboratory of Advanced Optoelectronic Materials, College of Chemistry, Chemical Engineering and Materials Science, Soochow University, Suzhou, China

OPEN ACCESS

Edited by:
Donghong Yu,
Aalborg University, Denmark

Reviewed by:
Qiang Peng,
Sichuan University, China
Florenci Vicent González,
Universitat Jaume I, Spain

***Correspondence:**
Yongfang Li
liyf@iccas.ac.cn

Specialty section:
This article was submitted to Organic Chemistry, a section of the journal Frontiers in Chemistry

Received: 20 June 2018
Accepted: 23 August 2018
Published: 13 September 2018

Citation:
Qiu B, Chen S, Xue L, Sun C, Li X, Zhang Z-G, Yang C and Li Y (2018) Effects of Alkoxy and Fluorine Atom Substitution of Donor Molecules on the Morphology and Photovoltaic Performance of All Small Molecule Organic Solar Cells. Front. Chem. 6:413. doi: 10.3389/fchem.2018.00413

Two benzothiadiazole (BT)-based small-molecule donors, SM-BT-2OR with alkoxy side chain and SM-BT-2F with fluorine atom substitution, were designed and synthesized for investigating the effect of the substituents on the photovoltaic performance of the donor molecules in all small molecule organic solar cells (SM-OSCs). Compared to SM-BT-2OR, the film of SM-BT-2F exhibited red-shifted absorption and deeper HOMO level of −5.36 eV. When blending with *n*-type organic semiconductor (*n*-OS) acceptor IDIC, the as-cast devices displayed similar PCE values of 2.33 and 2.76% for the SM-BT-2OR and SM-BT-2F-based devices, respectively. The SM-BT-2OR-based devices with thermal annealing (TA) at 120°C for 10 min showed optimized PCE of 7.20%, however, the SM-BT-2F-based device displayed lower PCE after the TA treatment, which should be ascribed to the undesirable morphology and molecular orientation. Our results reveal that for the SM-OSCs, the substituent groups of small molecule donors have great impact on the film morphology, as well as the photovoltaic performance.

Keywords: benzothiadiazole, organic small molecule donors, fluorine substitution, alkoxy side chain, all small molecule organic solar cells

INTRODUCTION

Organic photovoltaics (OPV), as one of the most promising next generation technologies to utilize solar energy, have been extensively investigated during the past several decades, due to its attractive advantages of light-weight, low-cost and capability to be fabricated into flexible and semitransparent devices (Liang and Yu, 2010; Li, 2012; Li et al., 2012). In recent years, bulk-heterojunction (BHJ) organic solar cells (OSCs) that use small-molecule *n*-type organic semiconductor (*n*-OS) as acceptor have gained significant progress (Lin and Zhan, 2014; Nielsen et al., 2015). In particular, most recently, power conversion efficiencies (PCEs) over 14% for single-layer device and 15% for tandem device have been achieved, demonstrating great potential for the commercialization of OSCs (Che et al., 2018; Li et al., 2018; Zhang et al., 2018).

The rapid development of OSCs is a combination of the innovation of donor and acceptor photovoltaic materials, the methodology of morphology tuning and the optimization of device structures (Lee et al., 2008; Hau et al., 2010; Huang et al., 2014; Wang and Kyaw, 2014; Ye et al., 2014; Gao et al., 2015; Lin and Zhan, 2016; Zhang et al., 2016; Yan et al., 2017). Especially, the progress of photovoltaic materials plays a critical role in promoting the development of OSCs (Nielsen et al., 2015; Zhang and Zhu, 2017; Wadsworth et al., 2018). Especially, great improvement of the OSCs has been achieved by the development of wide bandgap conjugated polymer donors and narrow bandgap *n*-OS small-molecule acceptors (Bin et al., 2016a; Sun et al., 2018). Although small-molecule *p*-type organic semiconductor (*p*-OS) donors, compared with polymer donors, possess the advantages of well-defined chemical structures and easy purification, the photovoltaic performance of the all small molecules OSCs (SM-OSCs) is relatively lag behind, because of its more difficult morphology tuning than polymer donor/*n*-OS acceptor system (Yang et al., 2017; Shi et al., 2018). In order to further improve the performance of SM-OSCs, it is crucial to deeply investigate the relationship between the molecular structures and device performance of the SM-OSCs.

In the donor-acceptor (D-A) structured *p*-type semiconductor donor materials, benzothiadiazole (BT) unit is a widely used acceptor (A) building block, due to its superior advantages of planar structure and low-lying energy level (Lin and Zhan, 2016). Yan et al. adjusted alkyl chain lengths of BT-based polymer donor (PffBT4T-C_9C_{13}) and the PffBT4T-C_9C_{13}-based OSCs fabricated with a hydrocarbon solvents demonstrate a superior performance (Zhao et al., 2016). Then they designed another BT-based polymer donor P3TEA which demonstrated an efficient OSC with a negligible driving force when blending with a non-fullerene acceptor, SF-PDI_2 (Liu et al., 2016). Beside polymer donors, BT unit has been widely used in constructing small molecule semiconductor *p*-OS donors. Bazan et al. have systematically investigated BT-based donor-acceptor-donor-acceptor-donor (D-A-D-A-D) type small molecule donor materials (Coughlin et al., 2014). In addition, BT-unit also has been used to construct *n*-type organic semiconductor materials and desirable results have been obtained (Holliday et al., 2016; Baran et al., 2017).

Considering the effective role of side chain engineering in morphology tuning, in order to study the relationship between device performance of the SM-OSCs and molecular structures, herein two BT-based small-molecule donors, SM-BT-2OR and SM-BT-2F (see **Figure 1**), were designed and synthesized for comparison studies. By rationally introducing alkoxy substituent and fluorine atom (F) on the BT unit, the two small molecules exhibits different absorption characteristics, frontier molecular orbital energy levels, and energy bandgaps. When blending with *n*-type organic semiconductor (*n*-OS) acceptor IDIC, the as cast devices for both small molecules donors showed similar PCE values. The SM-BT-2OR-based devices after thermal annealing (TA) at 120°C for 10 min showed optimized PCE of 7.20% but lower open circuit voltage (V_{oc}), while the SM-BT-2F-based device displayed lower PCE but slightly higher V_{oc} after the TA treatment. Such opposite trends in the PCE and V_{oc} should be ascribed to the different effect of the thermal annealing on the morphology and crystallinity of the two small molecules with the different substituent groups. Our results reveal that for the SM-OSCs the substituent groups have great impact on the film morphology and the photovoltaic performance.

RESULTS AND DISCUSSION

Synthesis and Thermal Properties

Scheme 1 shows the synthetic routes of SM-BT-2OR and SM-BT-2F. Compounds **M1** and **M2** were synthesized according to the previously reported methods in high yields (Gu et al., 2012; Feng et al., 2013). Then, the two small molecules SM-BT-2OR and SM-BT-2F were synthesized through similar procedures by a Stille-coupling reaction between compound **M3** and compound **M1** or **M2** with toluene as the solvent and $Pd(PPh_3)_4$ as catalyst. Then, the two molecules were obtained through column chromatography. The two molecules show onset temperatures with 5% weight-loss of 331 and 377°C for SM-BT-2OR and SM-BT-2F, respectively, in the thermogravimetric analysis as shown in **Figure S1**, indicating that both molecules possess good thermal stability for application in OSCs.

Photophysical Properties and Electronic Energy Levels

Figure 2A shows the UV-vis absorption spectra of the two molecules in dilute $CHCl_3$ solutions and as thin films, and IDIC film. The specific absorption characteristics of the two molecules are summarized in **Table 1**. The two molecules in solution exhibit similar absorption profiles with the same maximum absorption wavelength at 542 nm besides the slightly higher absorption at short wavelength for SM-BT-2F solution. Whereas, in solid films, the maximum absorption wavelength of SM-BT-2F (606 nm) is red-shifted by ∼22 nm compared to that of SM-BT-2OR (584 nm), indicating that the introduction of fluorine (F) substituents could influence the stacking behavior of the molecules (Umeyama et al., 2013; Liu et al., 2014; Do et al., 2016). Because of the stronger intermolecular interactions in film state, the maximum absorption peaks of the two molecules show obvious bathochromic shifts of 42 and 64 nm for SM-BT-2OR and SM-BT-2F, respectively. The optical bandgaps (E_g^{opt}) estimated from the UV-vis absorption onsets (701 nm for SM-BT-2OR and 745 nm for SM-BT-2F) in the film state are determined to be 1.77 and 1.66 eV for SM-BT-2OR and SM-BT-2F, respectively.

The highest occupied molecular orbital (HOMO) and the lowest unoccupied molecular orbital (LUMO) levels of the two molecules were measured by electrochemical cyclic voltammetry with Ag/AgCl as reference electrode, as shown in **Figure 2B.** The HOMO/LUMO energy levels (E_{HOMO}/E_{LUMO}) were calculated from the onset oxidation / reduction potentials (ϕ_{ox}/ϕ_{red}) according to the equations of $E_{HOMO}/E_{LUMO} = -e(\phi_{ox}/\phi_{red} + 4.8 - \phi_{Fc/Fc+})$ (eV) (Bin et al., 2016a). $\phi_{Fc/Fc+}$ was measured to be 0.44 V vs. Ag/AgCl in this measurement system, and then the calculation equations are $E_{HOMO}/E_{LUMO} = -e(\phi_{ox}/\phi_{red} + 4.36)$ (eV). As shown in **Figure 2B**, the onset oxidation

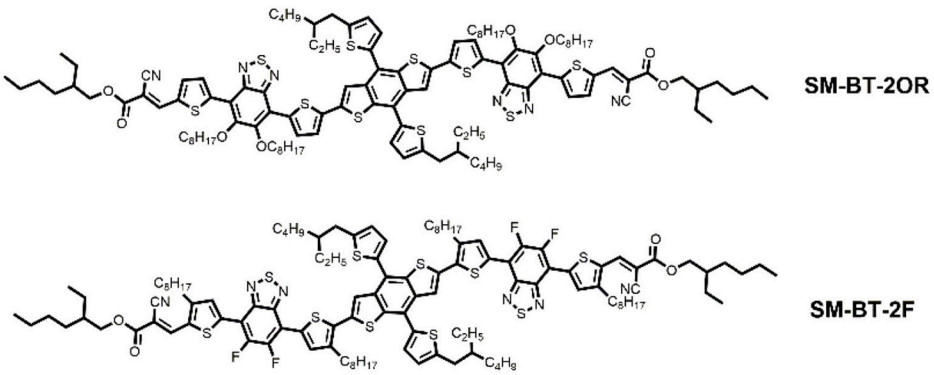

FIGURE 1 | Chemical structures of small molecule donors SM-BT-2OR and SM-BT-2F.

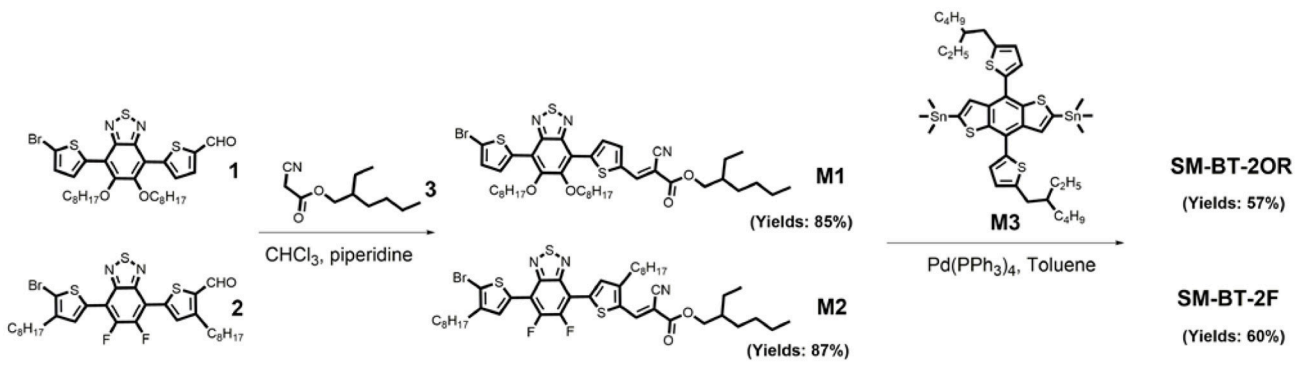

SCHEME 1 | Synthetic routes of small molecule donors SM-BT-2OR and SM-BT-2F.

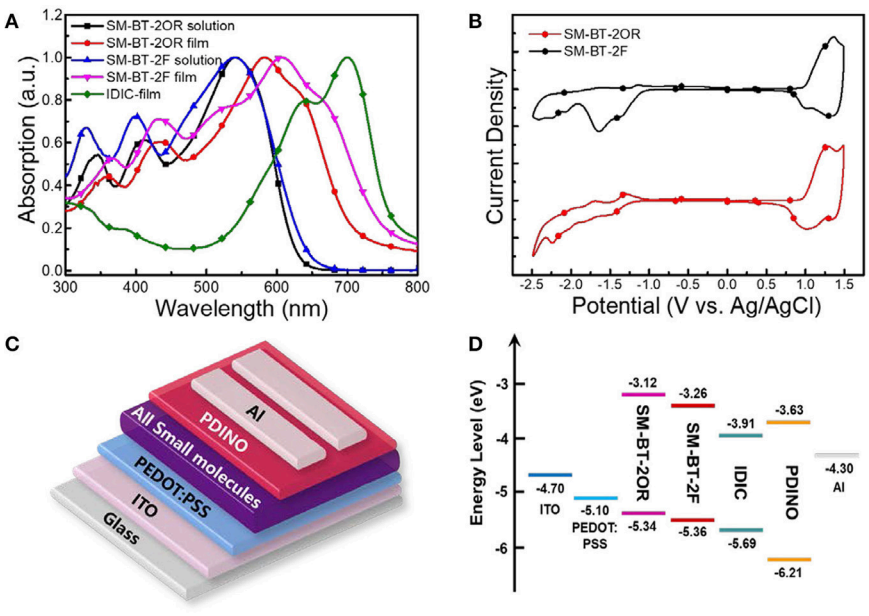

FIGURE 2 | (A) Absorption spectra of SM-BT-2OR, SM-BT-2F and IDIC. **(B)** Cyclic voltammograms of SM-BT-2OR and SM-BT-2F. **(C)** Device structure of the SM-OSCs. **(D)** Schematic energy diagram of the materials involved in the SM-OSCs.

TABLE 1 | Absorption properties and electronic energy levels of SM-BT-2OR and SM-BT-2F.

Small molecule	λ_{max} solution	λ_{max} film	λ_{onset} film	E_g^{opt}	E_{ox}	E_{re}	E_{HOMO}	E_{LUMO}
	(nm)	(nm)	(nm)	(eV)	(V)	(V)	(eV)	(eV)
SM-BT-2OR	542	584	701	1.77	0.98	−1.24	−5.34	−3.12
SM-BT-2F	542	606	745	1.66	1.00	−1.10	−5.36	−3.26

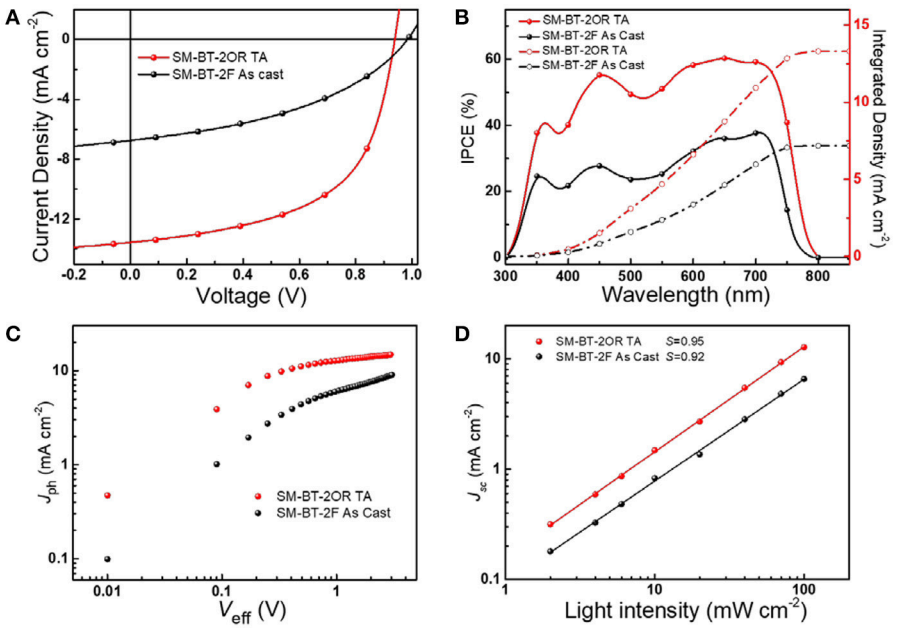

FIGURE 3 | (A) *J–V* characteristics of the best SM-OSCs with D/A weight ratio of 2:1 under the illumination of AM 1.5G, 100 mW cm^{-2}. **(B)** IPCE spectra of the corresponding devices. **(C)** J_{ph} vs. V_{eff} of the devices. **(D)** Light intensity dependence of J_{SC} of the devices.

TABLE 2 | Photovoltaic performance parameters of the optimized SM-OSCs based on SM-BT-2OR: IDIC and SM-BT-2F:IDIC.

Active layer	Condition	V_{oc} (V)	J_{sc} (mA cm^{-2})	FF (%)	PCE (%)[a]	Slope (J_{sc})[b]	Slope (V_{oc})[c]
SM-BT-2OR:IDIC	As cast	0.962	7.10	34.1	2.33 (2.20 ± 0.15)	0.926	1.20 kT/q
	120°C 10 min	0.939	13.57	56.5	7.20 (6.86 ± 0.18)	0.953	1.11 kT/q
SM-BT-2F:IDIC	As cast	0.983	6.74	41.7	2.76 (2.62 ± 0.15)	0.924	1.41 kT/q
	120°C 10 min	0.987	5.36	30.2	1.60 (1.54 ± 0.08)	0.914	1.78 kT/q

[a] *Average values with standard deviations were obtained from 10 devices.*
[b] *The slope of the dependence of J_{sc} on light intensity (P) on logarithmic coordinates.*
[c] *The dependence of V_{oc} on light intensity on semilogarithmic coordinate.*

potentials (ϕ_{ox}) / onset reduction potentials (ϕ_{red}) for SM-BT-2OR and SM-BT-2F are 0.98/−1.24 V and 1.00/−1.10 V vs. Ag/AgCl, respectively. The E_{LUMO}/E_{HOMO} of SM-BT-2OR and SM-BT-2F were calculated to be −3.12/−5.34 and −3.26/−5.36 eV, respectively. In comparison with SM-BT-2OR, the E_{HOMO} of SM-BT-2F with F atoms substitution is slightly down-shifted by 0.02 eV, which is beneficial for higher V_{oc} of the SM-OSCs. Compared with the energy level of IDIC, the LUMO energy level offsets (ΔE_{LUMO}) and HOMO energy level offsets (ΔE_{HOMO}) of SM-BT-2OR/IDIC and SM-BT-2F/IDIC are 0.71/0.35 and 0.57/0.33 eV, respectively, which is sufficient for charge separation (Hendriks et al., 2016).

Photovoltaic Performance

SM-OSCs were fabricated with a conventional device structure of ITO/PEDOT:PSS/*p*-OS:IDIC/PDINO/Al, and characterized to investigate the photovoltaic properties of the *p*-OS SM-BT-2OR and SM-BT-2F (Zhang et al., 2014). **Figure 3A** shows the typical current density-voltage (*J-V*) curves of the best devices based on SM-BT-2OR and SM-BT-2F under the illumination of AM 1.5G, 100 mW cm^{-2}, and the corresponding device performances, including V_{oc}, J_{sc}, FF and PCE, are summarized in **Table 2**. As shown in **Figure 3A**, for the as-cast devices, the device based on SM-BT-2OR: IDIC displayed an inferior PCE of 2.33%, with a high V_{oc} of 0.962 V, but a low J_{sc} and low FF. The SM-BT-2F-based device showed slightly higher PCE of 2.76%, with a higher V_{oc} of 0.983 V, which should be ascribed to the deeper HOMO level of SM-BT-2F. Thermal annealing (TA)

TABLE 3 | Hole and electron mobilities of the SM-BT-2OR: IDIC and SM-BT-2F: IDIC blend films with or without thermal annealing treatment at 120°C for 10 min.

Active layer	Treatment	Hole mobility (μ_h) ($cm^2\ V^{-1}\ s^{-1}$)	Electron mobility (μ_e) ($cm^2\ V^{-1}\ s^{-1}$)	μ_h/μ_e
SM-BT-2OR:IDIC	As cast	2.79×10^{-5} $cm^2\ V^{-1}\ s^{-1}$	1.26×10^{-4} $cm^2\ V^{-1}\ s^{-1}$	0.22
	120°C 10 min	7.37×10^{-5} $cm^2\ V^{-1}\ s^{-1}$	2.79×10^{-4} $cm^2\ V^{-1}\ s^{-1}$	0.26
SM-BT-2F:IDIC	As cast	0.37×10^{-5} $cm^2\ V^{-1}\ s^{-1}$	0.51×10^{-4} $cm^2\ V^{-1}\ s^{-1}$	0.07
	120°C 10 min	1.77×10^{-5} $cm^2\ V^{-1}\ s^{-1}$	2.19×10^{-4} $cm^2\ V^{-1}\ s^{-1}$	0.08

treatment has been proved to be an effective method to tune the morphology and phase separation of non-fullerene OSCs (Bin et al., 2016b; Chen et al., 2017). **Table S1** displays the photovoltaic parameters of the OSCs based on SM-BT-2OR: IDIC (w/w, 2:1) and SM-BT-2F: IDIC (w/w, 2:1) as cast or with TA treatment at different temperatures. Interestingly, for the devices based on SM-BT-2OR: IDIC, TA treatment leads to higher photovoltaic performance, however, for SM-BT-2F: IDIC, TA treatment leads to poorer efficiency. As shown in **Table 2**, when treated at 120°C for 10 min, the device based on SM-BT-2OR: IDIC demonstrated preferable PCE of 7.20%, with a slightly lower V_{oc} of 0.939 V, an enhanced J_{sc} of 13.57 mA cm^{-2} and a higher FF of 56.5%. However, the device based on SM-BT-2F: IDIC showed worse PCE of 1.82%, with a slightly higher V_{oc} of 0.987 V, but a lower J_{sc} of 5.36 mA cm^{-2} and a poorer FF of 30.2%. The reverse trends of the TA treatment on the PCE and V_{oc} of the devices could be related to the different substituents of the donor molecules.

The input photon to converted current efficiency (IPCE) spectra of the best devices are shown in **Figure 3B**. Both of the two small molecule-based devices demonstrate broad photoresponse from 300 to 800 nm, which indicates that both the small molecule donors and the IDIC acceptor make contributions to the photo current. Compared to the device based on SM-BT-2F, the SM-BT-2OR-based devices present higher photoresponse. Especially, the SM-BT-2OR-based device with the TA treatment present a broad plateau with IPCE values of around 50–60% in the wavelength range of *ca*. 420–740 nm, resulting in the relatively higher J_{sc} of 13.57 mA cm^{-2}. The J_{sc} values of the OSCs based on SM-BT-2OR and SM-BT-2F calculated from integration of the EQE spectra with the AM 1.5G reference spectrum are 13.31 and 7.17 mA cm^{-2}, respectively, which are in good agreement with J_{sc} values measured from *J-V* curves.

In order to investigate the charge dissociation of the SM-OSCs, the relationship between photocurrent density (J_{ph}, $J_{ph} = J_L - J_D$, where J_L and J_D represent the current densities under the illumination and in the dark, respectively) and effective applied voltage (V_{eff}) was analyzed (Mihailetchi et al., 2004; Wu et al., 2011). As can be seen from **Figure 3C**, when V_{eff} arrives at ∼3 V, J_{ph} value for the SM-BT-2OR-based device with the TA treatment reached saturation (J_{sat}). While for the SM-BT-2F-based device (with and without the TA treatment) and the SM-BT-2OR-based device without the TA treatment (**Figure S2**), the Jph values do not show a saturation trend within the whole measurement region, suggesting serious recombination process. The charge dissociation and charge collection probability [P(E, T)] in the devices could be estimated by calculating the value of J_{ph}/J_{sat}. Under the short circuit and maximal power output conditions, for the SM-BT-2OR-based devices, the P(E, T) values are 63% and 36% for the as-cast device, and 86 and 63% for the TA treated devices, suggesting a higher charge collection efficiency after TA treatment. However, the corresponding P(E, T) values of the SM-BT-2F-based devices are 68 and 44% for the as-cast device, and 53 and 30% for the TA treated devices, respectively, which means that the SM-BT-2F-based devices possess serious recombination whether with or without TA treatment, which could be ascribed to poorer morphology of the blend films of SM-BT-2F:IDIC.

To further study the charge recombination behavior in the SM-OSCs system, the dependence of J_{sc} on light intensity (P) was evaluated (**Figure 3D**; **Figure S3**). Generally, J_{sc} is known to follow a power-law dependence with respect to P_{light}, which can be described as $J_{ph} \propto P^{\alpha}$ (Schilinsky et al., 2002; Koster et al., 2005). For the SM-BT-2OR-based device, the exponential factor (α) is 0.926 for the as-cast device (**Figure S3A**) and 0.953 for the device with the TA treatment (**Figure 3D**), indicating that bimolecular recombination could be effectively suppressed by the TA treatment. However, for the SM-BT-2F-based device with the TA treatment (**Figure S3B**), the exponential factor (α) is only 0.914, which is slightly lower than that without the TA treatment (α = 0.924, **Figure 3D**), suggesting the existence of a certain amount of bimolecular recombination whether with or without the TA treatment. Compared to the SM-BT-2F-based device, the SM-BT-2OR-based device with the TA treatment shows higher α value, indicating better charge transport capacity, which agrees well with its better device performance. We also measured the dependence of V_{oc} on the light intensity to investigate the recombination mechanisms. As shown in **Figure S4**, for the SM-BT-2OR-based devices, the slopes are 1.20 and 1.11 kT/q for the devices as cast and with the TA treatment respectively, which means the recombination at open circuit is a bimolecular dominated process. While for the SM-BT-2F-based devices with or without the TA treatment, the slopes could be separated into two regions, as shown in **Figure S5**. Even under higher light intensity, the slopes are 1.41 kT/q and 1.78 kT/q for the devices as cast and with TA treatment, respectively, indicating a combination of monomolecular and bimolecular recombination processes. Besides, the larger value of 1.78 kT/q suggests a more undesirable morphology could be formed when the TA treatment was applied for the SM-BT-2F-based device.

The space-charge limited current models, using hole-only and electron-only devices with architectures of ITO/PEDOT:PSS/active layer/Au and ITO/ZnO/active

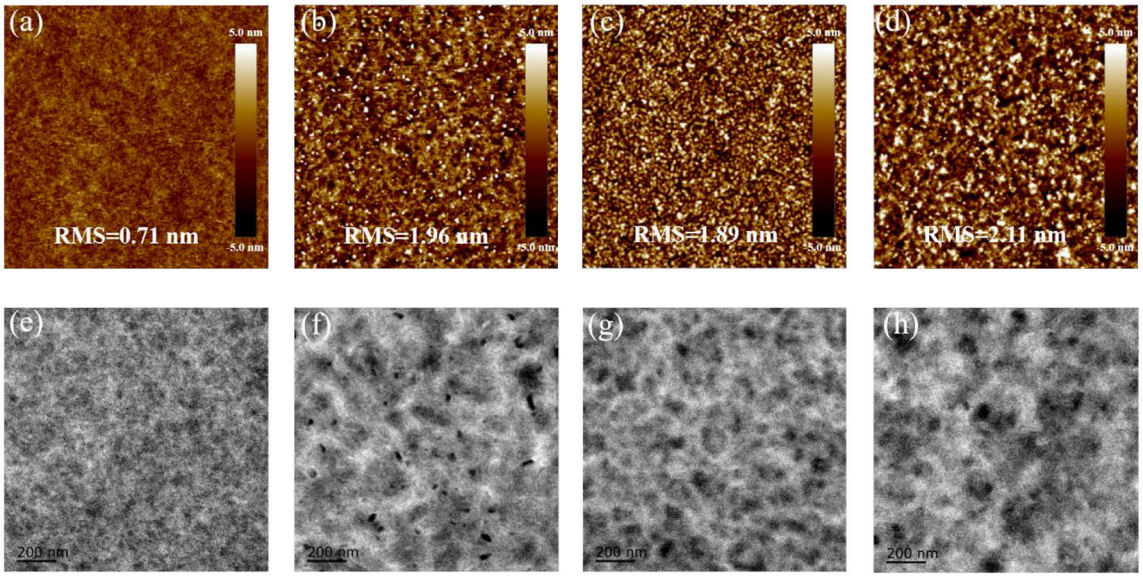

FIGURE 4 | AFM height images (size: 5 × 5 μm^2) of SM-BT-2OR: IDIC blends as cast **(a)** and TA treated **(b)**, SM-BT-2F: IDIC blends as cast **(c)** and TA treated **(d)**. Root-mean-square (RMS) roughness values are given to describe the smoothness of the morphology. TEM images of SM-BT-2OR: IDIC blends as cast **(e)** and TA treated **(f)**, SM-BT-2F: IDIC blends as cast **(g)** and TA treated **(h)**.

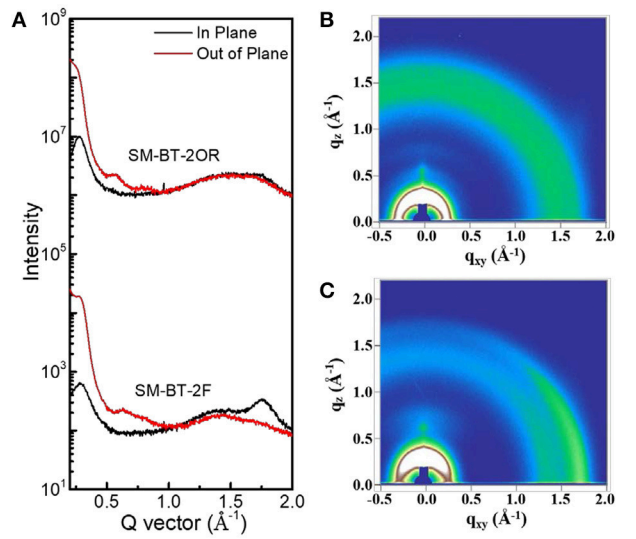

FIGURE 5 | (A) Line cuts of the GIWAXS images of neat SM-BT-2OR and SM-BT-2F film; The GIWAXS images of **(B)** neat SM-BT-2OR film and **(C)** neat SM-BT-2F film.

layer/PDINO/Al, respectively, were applied to measure the hole and electron mobilities of the blends before or after the TA treatment (**Figures S6**, **S7**). As shown in **Table 3**, for both blend films, after the thermal annealing treatment, the charge mobilities (electron and hole mobility) were higher than those of the as cast devices. The hole mobilities of the SM-BT-2OR-based devices were measured to be 2.79×10^{-5} and 7.37×10^{-5} cm^2 V^{-1} s^{-1} for the devices as cast and with TA treatment, respectively. Compared with the SM-BT-2OR-based devices, the hole mobility of the SM-BT-2F-based blends were rather low whether before (0.37×10^{-5} cm^2 V^{-1} s^{-1}) or after the TA treatment (1.77×10^{-5} cm^2 V^{-1} s^{-1}), leading to inferior FF and photovoltaic performance. For the SM-BT-2OR-based devices, after the TA treatment, the ratio of hole mobility/electron mobility was slightly balanced, which might benefit for obtaining higher FF of the SM-BT-2OR-based devices. Though the device performance of the SM-BT-2OR-based device with the TA treatment is fairly good, compared to previous results of the SM-OSCs (Qiu et al., 2017; Yang et al., 2018), the hole mobilites of the SM-BT-2OR-based blend is slightly lower, which limits its further improvement of photovoltaic performance.

Considering that the device performance is closely related to the blend morphology, detailed investigations on the morphological characteristics of the blend films were carried out (Li et al., 2005; Rivnay et al., 2012). Atomic force microscopy (AFM) was utilized to probe the surface morphologies of the blend films with or without the TA treatment. As shown in **Figure 4**, all the blends display homogeneous surfaces with a moderate root-mean-square (RMS) roughness. The SM-BT-2F: IDIC blend without the TA treatment presents higher RMS value than that of the SM-BT-2OR: IDIC blend, which should be ascribed to the better crystallinity of SM-BT-2F. Compared to the blend without the TA treatment, the blends with the TA treatment show larger RMS, indicating that the TA treatment could effectively tune the morphology of the active layers of the SM-OSCs. In order to clearly understand aggregation situation of both small molecules in the blend films, transmission electron microscope (TEM) was applied

to investigate the phase separation. As shown in **Figure 4**, the black and white regions in the TEM images of the as-cast blend of SM-BT-2OR: IDIC is uniformly distributed, indicating that SM-BT-2OR and IDIC can be well-mixed. For the as cast blend of SM-BT-2F: IDIC, the TEM image shows relatively large aggregation, which explains the rather low short circuit current density and photovoltaic performance. After thermal annealing, the phase separation of the SM-BT-2F: IDIC blend become even larger, resulting to the more severe recombination, thus leading to the poorer J_{sc} and device performance. While for the SM-BT-2OR: IDIC blend with the TA treatment, the TEM image shows enhanced phase separation with small fiber like aggregation, which is beneficial for effective exciton dissociation and charge transport, therefore, better device performance could be achieved. In addition, it should be noticed that, although the AFM and TEM images of the SM-BT-2F-based films seem rather uniform, the image of optical microscope presented obvious striped aggregation, as shown in **Figure S8**, indicating the inferior blend morphology on micrometer scale.

To gain deep insight into the molecular stacking differences between SM-BT-2OR and SM-BT-2F, grazing incidence wide-angle X-ray scattering (GIWAXS) measurements were employed (Lilliu et al., 2011; Rivnay et al., 2012; Huang et al., 2014). The 2D GIWAXS patterns and corresponding cut-line profiles in the in-plane and out-of-plane directions are shown in **Figure 5** (neat films) and **Figure 6** (blend films). The neat SM-BT-2OR films showed amorphous feature with π-π stacking peak at 1.74 $Å^{-1}$ (d-spacing: 3.61 Å) and coherence length of 25.4 Å. The neat SM-BT-2F film displayed edge-on orientations with π-π stacking peak at 1.76 $Å^{-1}$ (*d*-spacing: 3.56 Å) and coherence length of 36.0 Å. The smaller π-π stacking peak and longer coherence length of neat SM-BT-2F film should be ascribed to the better molecular planarity and crystallinity caused by the introduction of F atoms on the BT unit, leading to rather large phase separation as discussed in TEM section.

When blending with IDIC, both films exhibits random orientation and disordered microstructure features with relatively weak peak intensities. After the thermal annealing treatment, significantly stronger peaks with more narrow width accompany by the appearance of new peaks. For both blends of SM-BT-2OR: IDIC and SM-BT-2F: IDIC, the 2D GIWAXS patterns exhibit strong lamellar (100) and (200) diffraction peaks in the out-of-plane direction, indicating a high degree of molecular ordering. Besides, the (010) diffraction peaks demonstrated in-plane preferred orientation, with enhanced coherence length of 47.0 and 52.1 Å, for the SM-BT-2OR: IDIC and SM-BT-2F: IDIC blends, respectively, resulting in better charge transport. Compared to the TA treated blend films of SM-BT-2OR, it can be observed that the SM-BT-2F-based blend film are more prone to adopt a predominant edge-on crystalline orientation, which suggests that it possesses less three-dimensional (3-D) charge pathways in the active layer (Bin et al., 2017; Kumari et al., 2017). Thus, although the molecular packing and phase separation was enhanced, carrier collection was hampered, resulting in lower FF, J_{sc} and photovoltaic performance. These results indicate that for both small molecules, TA treatment could effectively enhance the molecular packing and affect the molecular orientation in the blend film. In addition, we want to mention that the GIWAXS results show weak face-on stacking, which is also observed for other SM-OSCs based on small molecule donor and small molecule acceptor (Bin et al., 2017; Yang et al., 2017). In order to further improve photovoltaic performance of the SM-OSCs, we should do more work on the morphology optimization of the blend active layer of the p-type small molecule donor and n-type small molecule acceptor.

It should also be mentioned that differing from most other fluorine-containing donor materials SM-BT-2F based device

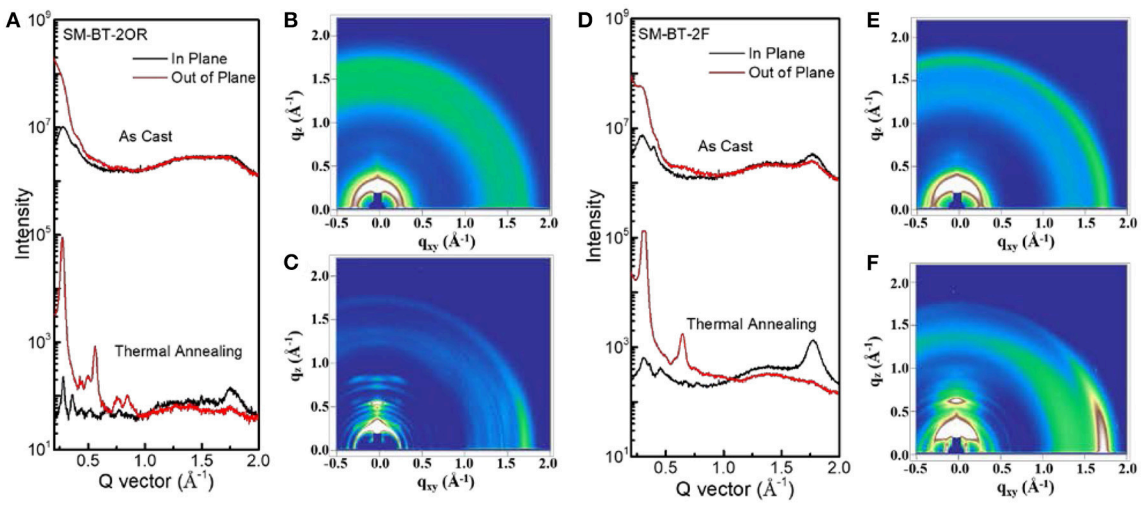

FIGURE 6 | (A) Line cuts of the GIWAXS images of SM-BT-2OR: IDIC blend. The GIWAXS images of SM-BT-2OR: IDIC blend **(B)** as cast, **(C)** TA treated. **(D)** Line cuts of the GIWAXS images of SM-BT-2F: IDIC blend. The GIWAXS images of SM-BT-2F: IDIC blend **(E)** as cast and **(F)** TA treated.

displayed inferior FF and photovoltaic performance, which could be ascribed to the too large phase separation and unsatisfactory molecular orientation of SM-BT-2F.

CONCLUSIONS

In summary, two benzothiadiazole based small-molecule donors, SM-BT-2OR and SM-BT-2F, were designed and synthesized for investigating the effect of the substituents on the photovoltaic performance of the molecules. Compared to SM-BT-2OR, because of the substitution of fluorine atom (F), SM-BT-2F presented red-shifted absorption profile in film state and deeper HOMO level of 5.36 eV. When blending with *n*-type organic semiconductor (*n*-OS) acceptor IDIC, the as-cast devices displayed similar PCE values of 2.33 and 2.76% for the SM-BT-2OR and SM-BT-2F-based devices, respectively. When TA treatment at 120°C for 10 min was applied, the SM-BT-2OR-based devices showed better performance of 7.20%, while the SM-BT-2F-based device displayed even lower PCE. The lower PCE of the SM-BT-2F-based device should be ascribed to the rather large phase separation and more in-plane preferred orientation of π-π stacking when the TA treatment was used, which decreased the exciton dissociation and charge transportation. Besides, the reduced V_{oc} of the SM-BT-2OR-based devices with the TA treatment should be due to the enhanced phase separation. Our results reveal that for the SM-OSCs the substituent groups have great impact on the film morphology, as well as the photovoltaic performance.

AUTHOR CONTRIBUTIONS

BQ and YL designed the two small molecules. BQ carried out the materials synthesis and device fabrication and photovoltaic performance studies. Z-GZ, CS, and XL participated in the discussion of the material synthesis. LX and Z-GZ provided the cathode buffer layer material. SC and CY measured the GIWAXS diffraction patterns. YL supervised the project. BQ and YL write the manuscript.

ACKNOWLEDGMENTS

The work was supported by the Ministry of Science and Technology of China (973 project, No. 2014CB643501) and NSFC (Nos. 91633301, 21734008, and 51673200) and the Strategic Priority Research Program of the Chinese Academy of Sciences, Grant No. XDB12030200.

SUPPLEMENTARY MATERIAL

The Supplementary Material for this article can be found online at: https://www.frontiersin.org/articles/10.3389/fchem.2018.00413/full#supplementary-material

REFERENCES

Baran, D., Ashraf, R. S., Hanifi, D. A., Abdelsamie, M., Gasparini, N., Rohr, J. A., et al. (2017). Reducing the efficiency-stability-cost gap of organic photovoltaics with highly efficient and stable small molecule acceptor ternary solar cells. *Nat. Mater.* 16, 363–369. doi: 10.1038/nmat4797

Bin, H., Gao, L., Zhang, Z. G., Yang, Y., Zhang, Y., Zhang, C., et al. (2016a). 11.4% Efficiency non-fullerene polymer solar cells with trialkylsilyl substituted 2d-conjugated polymer as donor. *Nat. Commun.* 7:13651. doi: 10.1038/ncomms13651

Bin, H., Yang, Y., Zhang, Z. G., Ye, L., Ghasemi, M., Chen, S., et al. (2017). 9.73% efficiency nonfullerene all organic small molecule solar cells with absorption-complementary donor and acceptor. *J. Am. Chem. Soc.* 139, 5085–5094. doi: 10.1021/jacs.6b12826

Bin, H., Zhang, Z. G., Gao, L., Chen, S., Zhong, L., Xue, L., et al. (2016b). Non-fullerene polymer solar cells based on alkylthio and fluorine substituted 2d-conjugated polymers reach 9.5% efficiency. *J. Am. Chem. Soc.* 138, 4657–4664. doi: 10.1021/jacs.6b01744

Che, X. Z., Li, Y. X., Qu, Y., and Forrest, S. R. (2018). High fabrication yield organic tandem photovoltaics combining vacuum- and solution-processed subcells with 15% efficiency. *Nat. Energy* 3, 422–427. doi: 10.1038/s41560-018-0134-z

Chen, S., Cho, H. J., Lee, J., Yang, Y., Zhang, Z.-G., Li, Y., et al. (2017). Modulating the molecular packing and nanophase blending via a random terpolymerization strategy toward 11% efficiency nonfullerene polymer solar cells. *Adv. Energy Mater.* 7:1701125. doi: 10.1002/aenm.201701125

Coughlin, J. E., Henson, Z. B., Welch, G. C., and Bazan, G. C. (2014). Design and synthesis of molecular donors for solution-processed high-efficiency organic solar cells. *Acc. Chem. Res.* 47, 257–270. doi: 10.1021/ar400136b

Do, K., Saleem, Q., Ravva, M. K., Cruciani, F., Kan, Z., Wolf, J., et al. (2016). Impact of fluorine substituents on pi-conjugated polymer main-chain conformations, packing, and electronic couplings. *Adv. Mater.* 28, 8197–8205. doi: 10.1002/adma.201601282

Feng, Q., Zhang, W., Zhou, G., and Wang, Z. S. (2013). Enhanced performance of quasi-solid-state dye-sensitized solar cells by branching the linear substituent in sensitizers based on thieno[3,4-C]Pyrrole-4,6-Dione. *Chem. Asian J.* 8, 168–177. doi: 10.1002/asia.201200720

Gao, F., Himmelberger, S., Andersson, M., Hanifi, D., Xia, Y., Zhang, S., et al. (2015). The effect of processing additives on energetic disorder in highly efficient organic photovoltaics: a case study on Pbdttt-C-T:Pc71 Bm. *Adv. Mater.* 27, 3868–3873. doi: 10.1002/adma.201405913

Gu, Z., Deng, L., Luo, H., Guo, X., Li, H., Cao, Z., et al. (2012). Synthesis and photovoltaic properties of conjugated side chains polymers with different electron-withdrawing and donating end groups. *J. Polym. Sci. Part A Polym. Chem.* 50, 3848–3858. doi: 10.1002/pola.26180

Hau, S. K., Yip, H.-L., and Jen, A. K. Y. (2010). A review on the development of the inverted polymer solar cell architecture. *Polym. Rev.* 50, 474–510. doi: 10.1080/15583724.2010.515764

Hendriks, K. H., Wijpkema, A. S., Van Franeker, J. J., Wienk, M. M., and Janssen, R. A. (2016). Dichotomous role of exciting the donor or the acceptor on charge generation in organic solar cells. *J. Am. Chem. Soc.* 138, 10026–10031. doi: 10.1021/jacs.6b05868

Holliday, S., Ashraf, R. S., Wadsworth, A., Baran, D., Yousaf, S. A., Nielsen, C. B., et al. (2016). High-efficiency and air-stable P3ht-based polymer solar cells with a new non-fullerene acceptor. *Nat. Commun.* 7, 11585. doi: 10.1038/ncomms11585

Huang, Y., Kramer, E. J., Heeger, A. J., and Bazan, G. C. (2014). Bulk heterojunction solar cells: morphology and performance relationships. *Chem. Rev.* 114, 7006–7043. doi: 10.1021/cr400353v

Koster, L. J. A., Mihailetchi, V. D., Xie, H., and Blom, P. W. M. (2005). Origin of the light intensity dependence of the short-circuit current of polymer/fullerene solar cells. *Appl. Phys. Lett.* 87:203502. doi: 10.1063/1.2130396

Kumari, T., Lee, S. M., Kang, S.-H., Chen, S., and Yang, C. (2017). Ternary solar cells with a mixed face-on and edge-on orientation enable an unprecedented efficiency of 12.1%. *Energy Environ. Sci.* 10, 258–265. doi: 10.1039/C6EE02851A

Lee, J. K., Ma, W. L., Brabec, C. J., Yuen, J., Moon, J. S., Kim, J. Y., et al. (2008). Processing additives for improved efficiency from bulk heterojunction solar cells. *J. Am. Chem. Soc.* 130, 3619–3623. doi: 10.1021/ja710079w

Li, G., Shrotriya, V., Huang, J., Yao, Y., Moriarty, T., Emery, K., et al. (2005). High-efficiency solution processable polymer photovoltaic cells by self-organization of polymer blends. *Nat. Mater.* 4, 864–868. doi: 10.1038/nmat1500

Li, G., Zhu, R., and Yang, Y. (2012). Polymer solar cells. *Nat. Photonics* 6, 153–161. doi: 10.1038/nphoton.2012.11

Li, S., Ye, L., Zhao, W., Yan, H., Yang, B., Liu, D., et al. (2018). A wide band gap polymer with a deep highest occupied molecular orbital level enables 14.2% efficiency in polymer solar cells. *J. Am. Chem. Soc.* 140, 7159–7167. doi: 10.1021/jacs.8b02695

Li, Y. (2012). Molecular design of photovoltaic materials for polymer solar cells: toward suitable electronic energy levels and broad absorption. *Acc. Chem. Res.* 45, 723–733. doi: 10.1021/ar2002446

Liang, Y., and Yu, L. (2010). Development of semiconducting polymers for solar energy harvesting. *Polym. Rev.* 50, 454–473. doi: 10.1080/15583724.2010.515765

Lilliu, S., Agostinelli, T., Pires, E., Hampton, M., Nelson, J., and Macdonald, J. E. (2011). Dynamics of crystallization and disorder during annealing of P3ht/Pcbm bulk heterojunctions. *Macromolecules* 44, 2725–2734. doi: 10.1021/ma102817z

Lin, Y., and Zhan, X. (2016). Oligomer molecules for efficient organic photovoltaics. *Acc. Chem. Res.* 49, 175–183. doi: 10.1021/acs.accounts.5b00363

Lin, Y. Z., and Zhan, X. W. (2014). Non-fullerene acceptors for organic photovoltaics: an emerging horizon. *Mater Horiz.* 1, 470–488. doi: 10.1039/C4MH00042K

Liu, J., Chen, S., Qian, D., Gautam, B., Yang, G., Zhao, J., et al. (2016). Fast charge separation in a non-fullerene organic solar cell with a small driving force. *Nat. Energy* 1, 16089. doi: 10.1038/nenergy.2016.89

Liu, P., Zhang, K., Liu, F., Jin, Y. C., Liu, S. J., Russell, T. P., et al. (2014). Effect of fluorine content in thienothiophene-benzodithiophene copolymers on the morphology and performance of polymer solar cells. *Chem. Mater.* 26, 3009–3017. doi: 10.1021/cm500953e

Mihailetchi, V. D., Koster, L. J., Hummelen, J. C., and Blom, P. W. (2004). Photocurrent generation in polymer-fullerene bulk heterojunctions. *Phys. Rev. Lett.* 93, 216601. doi: 10.1103/PhysRevLett.93.216601

Nielsen, C. B., Holliday, S., Chen, H. Y., Cryer, S. J., and Mcculloch, I. (2015). Non-fullerene electron acceptors for use in organic solar cells. *Acc. Chem. Res.* 48, 2803–2812. doi: 10.1021/acs.accounts.5b00199

Qiu, B. B., Xue, L. W., Yang, Y. K., Bin, H. J., Zhang, Y. D., Zhang, C. F., et al. (2017). All-small-molecule nonfullerene organic solar cells with high fill factor and high efficiency over 10%. *Chem. Mater.* 29, 7543–7553. doi: 10.1021/acs.chemmater.7b02536

Rivnay, J., Mannsfeld, S. C., Miller, C. E., Salleo, A., and Toney, M. F. (2012). Quantitative determination of organic semiconductor microstructure from the molecular to device scale. *Chem. Rev.* 112, 5488–5519. doi: 10.1021/cr3001109

Schilinsky, P., Waldauf, C., and Brabec, C. J. (2002). Recombination and loss analysis in polythiophene based bulk heterojunction photodetectors. *Appl. Phys. Lett.* 81, 3885. doi: 10.1063/1.1521244

Shi, J., Isakova, A., Abudulimu, A., Van Den Berg, M., Kwon, O. K., Meixner, A. J., et al. (2018). Designing high performance all-small-molecule solar cells with non-fullerene acceptors: comprehensive studies on photoexcitation dynamics and charge separation kinetics. *Energy Environ. Sci.* 11, 211–220. doi: 10.1039/C7EE02967E

Sun, C., Pan, F., Bin, H., Zhang, J., Xue, L., Qiu, B., et al. (2018). A low cost and high performance polymer donor material for polymer solar cells. *Nat. Commun.* 9, 743. doi: 10.1038/s41467-018-03207-x

Umeyama, T., Watanabe, Y., Douvogianni, E., and Imahori, H. (2013). Effect of fluorine substitution on photovoltaic properties of benzothiadiazole–carbazole alternating copolymers. *J. Phys. Chem. C* 117, 21148–21157. doi: 10.1021/jp407707u

Wadsworth, A., Moser, M., Marks, A., Little, M. S., Gasparini, N., Brabec, C. J., et al. (2018). Critical review of the molecular design progress in non-fullerene electron acceptors towards commercially viable organic solar cells. *Chem. Soc. Rev.* doi: 10.1039/C7CS00892A

Wang, D. H., and Kyaw, A. K. K. (2014). Roles of solvent additive in organic photovoltaic cells through intensity dependence of current-voltage characteristics and charge recombination. *Appl. Phys. Lett.* 105, 103301. doi: 10.1063/1.4895531

Wu, J. L., Chen, F. C., Hsiao, Y. S., Chien, F. C., Chen, P., Kuo, C. H., et al. (2011). Surface plasmonic effects of metallic nanoparticles on the performance of polymer bulk heterojunction solar cells. *ACS. Nano* 5, 959–967. doi: 10.1021/nn102295p

Yan, Y., Liu, X., and Wang, T. (2017). conjugated-polymer blends for organic photovoltaics: rational control of vertical stratification for high performance. *Adv. Mater.* 29:1601674. doi: 10.1002/adma.201601674

Yang, L., Zhang, S., He, C., Zhang, J., Yang, Y., Zhu, J., et al. (2018). Modulating molecular orientation enables efficient nonfullerene small-molecule organic solar cells. *Chem. Mater.* 30, 2129–2134. doi: 10.1021/acs.chemmater.8b00287

Yang, L., Zhang, S., He, C., Zhang, J., Yao, H., Yang, Y., et al. (2017). New wide band gap donor for efficient fullerene-free all-small-molecule organic solar cells. *J. Am. Chem. Soc.* 139, 1958–1966. doi: 10.1021/jacs.6b11612

Ye, L., Zhang, S., Huo, L., Zhang, M., and Hou, J. (2014). Molecular design toward highly efficient photovoltaic polymers based on two-dimensional conjugated benzodithiophene. *Acc. Chem. Res.* 47, 1595–1603. doi: 10.1021/ar5000743

Zhang, C., and Zhu, X. (2017). Thieno[3,4-B]thiophene-based novel small-molecule optoelectronic materials. *Acc. Chem. Res.* 50, 1342–1350. doi: 10.1021/acs.accounts.7b00050

Zhang, S., Qin, Y., Zhu, J., and Hou, J. (2018). Over 14% efficiency in polymer solar cells enabled by a chlorinated polymer donor. *Adv. Mater.* 30:e1800868. doi: 10.1002/adma.201800868

Zhang, S. Q., Ye, L., Zhang, H., and Hou, J. H. (2016). Green-solvent-processable organic solar cells. *Mater. Today* 19, 533–543. doi: 10.1016/j.mattod.2016.02.019

Zhang, Z. G., Qi, B. Y., Jin, Z. W., Chi, D., Qi, Z., Li, Y. F., et al. (2014). Perylene diimides: a thickness-insensitive cathode interlayer for high performance polymer solar cells. *Energy Environ. Sci.* 7, 1966–1973. doi: 10.1039/c4ee00022f

Zhao, J., Li, Y., Yang, G., Jiang, K., Lin, H., Ade, H., et al. (2016). Efficient organic solar cells processed from hydrocarbon solvents. *Nat. Energy* 1, 15027. doi: 10.1038/nenergy.2015.27

Conflict of Interest Statement: The authors declare that the research was conducted in the absence of any commercial or financial relationships that could be construed as a potential conflict of interest.

frontiers in Chemistry

ORIGINAL RESEARCH
published: 11 September 2018
doi: 10.3389/fchem.2018.00412

Comparison of the Solution and Vacuum-Processed Squaraine:Fullerene Small-Molecule Bulk Heterojunction Solar Cells

Guo Chen[1], Zhitian Ling[1], Bin Wei[1], Jianhua Zhang[1], Ziruo Hong[2], Hisahiro Sasabe[2]* and Junji Kido[2]*

[1] *Key Laboratory of Advanced Display and System Applications, Ministry of Education, Shanghai University, Shanghai, China,* [2] *Department of Organic Device Engineering, Graduate School of Engineering, Research Center for Organic Electronics, Yamagata University, Yonezawa, Japan*

OPEN ACCESS

Edited by:
Chuanlang Zhan, Institute of Chemistry (CAS), China

Reviewed by:
Kunpeng Guo, Taiyuan University of Technology, China
Chunhui Duan, South China University of Technology, China

***Correspondence:**
Guo Chen
chenguo@shu.edu.cn
Hisahiro Sasabe
h-sasabe@yz.yamagata-u.ac.jp

Specialty section:
This article was submitted to Organic Chemistry, a section of the journal Frontiers in Chemistry

Received: *17 June 2018*
Accepted: *22 August 2018*
Published: *11 September 2018*

Citation:
Chen G, Ling Z, Wei B, Zhang J, Hong Z, Sasabe H and Kido J (2018) Comparison of the Solution and Vacuum-Processed Squaraine:Fullerene Small-Molecule Bulk Heterojunction Solar Cells. Front. Chem. 6:412. doi: 10.3389/fchem.2018.00412

Squaraine dyes have shown promising properties for high performance organic solar cells owing to their advantages of intense absorption and high absorption coefficients in the visible and near-infrared (NIR) regions. In this work, to directly compare the photovoltaic performance of solution- and vacuum-processed small-molecule bulk heterojunction (SMBHJ) solar cells, we employed a squaraine small molecular dye, 2,4-bis[4-(N,N-diisobutylamino)-2,6-dihydroxyphenyl] squaraine (DIBSQ), as an electron donor combined with fullerene acceptors to fabricate SMBHJ cells either from solution or vacuum deposition process. The solution-processed SMBHJ cell possesses a power conversion efficiency (PCE) of ∼4.3%, while the vacuum-processed cell provides a PCE of ∼6.3%. Comparison of the device performance shows that the vacuum-processed SMBHJ cells possess higher short-circuit current density, fill factor and thus higher PCE than the solution-processed devices, which should be assigned to more efficient charge transport and charge extraction in the vacuum-processed SMBHJ cells. However, solution-processed SMBHJ cells demonstrate more pronounced temperature-dependent device performance and higher device stability. This study indicates the great potential of DIBSQ in photovoltaic application via both of solution and vacuum processing techniques.

Keywords: organic solar cells, bulk heterojunction, squaraine dye, solution-process, vacuum-process

INTRODUCTION

Organic solar cells (OSCs) have attracted much attention as a green solar energy technology for cost-effective, renewable energy sources because of their advantages of low-cost, light-weight, large-area manufacturing, and mechanical flexibility (Yu et al., 1995; Günes et al., 2007; Li et al., 2012; He et al., 2015; Duan et al., 2017). An efficient OSC must absorb over a broad spectral range from visible to near-infrared (NIR) wavelengths (350∼950 nm) and convert the incident light effectively into charges (Yu et al., 1995). Bulk heterojunction (BHJ) cell with broad spectral absorbing photoactive layer has great potential to realize high power conversion efficiency (PCE) because the donor/acceptor system in this kind of device can efficiently overcome the strong exciton

binding energy and thus achieve efficient charge generation (Lin et al., 2012; Chen et al., 2017b; Tang et al., 2017; Duan et al., 2018; Qi et al., 2018). Generally, there are two processing techniques to fabricate BHJ cells, i.e., solution processing and vacuum evaporation. These two deposition routes require the raw materials with much different properties, in particular solubility and thermal stability, respectively (Kronenberg et al., 2010; Hu et al., 2017). In general, the conjugated polymers with high solubility are deposited by solution process while small molecules (SMs) with high-thermal stability are deposited by vacuum evaporation. Solution processing is a relatively low-cost and fast method for depositing thin films. However, the stacking of multilayer layers becomes a great challenge because the interface erosion issue between the different solution-processed stacked layers (Hu et al., 2017). In comparison, vacuum deposition has several exceptive advantages such as accurate control of the thin film thickness and evaporation rate of the materials, and easy fabrication of multilayer devices by successive deposition of the materials. However, the vacuum conditions lead to high production costs (Kronenberg et al., 2010).

Recently, much effort has been dedicated to develop NIR absorbing polymer or small molecular donors combined with the fullerene acceptors to construct broad spectral absorbing BHJ layers (Li, 2012; Roncali et al., 2014; Chen et al., 2016b; Huang et al., 2016; Jiang et al., 2016; Du et al., 2018). Squaraine (SQ) dye is a kind of NIR absorbing small molecular donor material due to its advantages of simple synthetic route, high photochemical and thermal stability and high absorption coefficient in the NIR region (Ajayaghosh, 2005; Sasabe et al., 2014; Chen et al., 2015, 2017b). More recently, some NIR absorbing SQ donor materials with symmetric or asymmetrical molecular structures have been developed for high-performance BHJ cells by several groups: Silvestri et al. firstly introduced the hydrazine end-capped symmetric SQ donor into the BHJ system combined with [6,6]-phenyl-C61-butyric acid methyl ester (PCBM) acceptor and obtained a PCE of over 1% (Silvestri et al., 2008), and 2% of PCE was then obtained from the alkenyl-functionalized symmetric SQ and [6,6]-phenyl-C71-butyric acid methyl ester ($PC_{71}BM$) based BHJ cell (Bagnis et al., 2010). Würthner's group reported several symmetric SQs based BHJ cells and achieved a PCE of 1.8% with unusually high short circuit current (J_{sc}) of 12.6 mA/cm^2 (Mayerhöffer et al., 2009). Wei et al. reported PCEs of over 5% from symmetric SQ and $PC_{71}BM$ based BHJ cells (Wei et al., 2011). Chen et al. further promoted the PCE of symmetric SQ based BHJ up to over 6% by using co-evaporation technology (Chen et al., 2012a). Huang's group has synthesized a series of NIR absorbing asymmetric SQ donors combined with $PC_{71}BM$ acceptor to realize PCEs of over 6% (Wu et al., 2018).

Among all the above mentioned SQ dyes, the symmetric SQ dye 2,4-bis[4-(N,N-diisobutylamino)-2,6-dihydroxyphenyl] squaraine (DIBSQ) has shown promising properties for highly efficient BHJ cells (Chen et al., 2012a): DIBSQ has a wide absorption spectra in the NIR region with high absorption coefficient of over 3×10^5 cm^{-1}, and its highest occupied molecular orbital (HOMO) and lowest unoccupied molecular orbital (LUMO) levels are located at −5.3 and −3.5 eV, respectively (Chen et al., 2016a), which provides a higher photocurrent and higher V_{oc} for the BHJ cells. The most unique property of DIBSQ is that the DIBSQ thin film can be deposited by using both of vacuum evaporation and solution processing technologies because the DIBSQ has high thermal

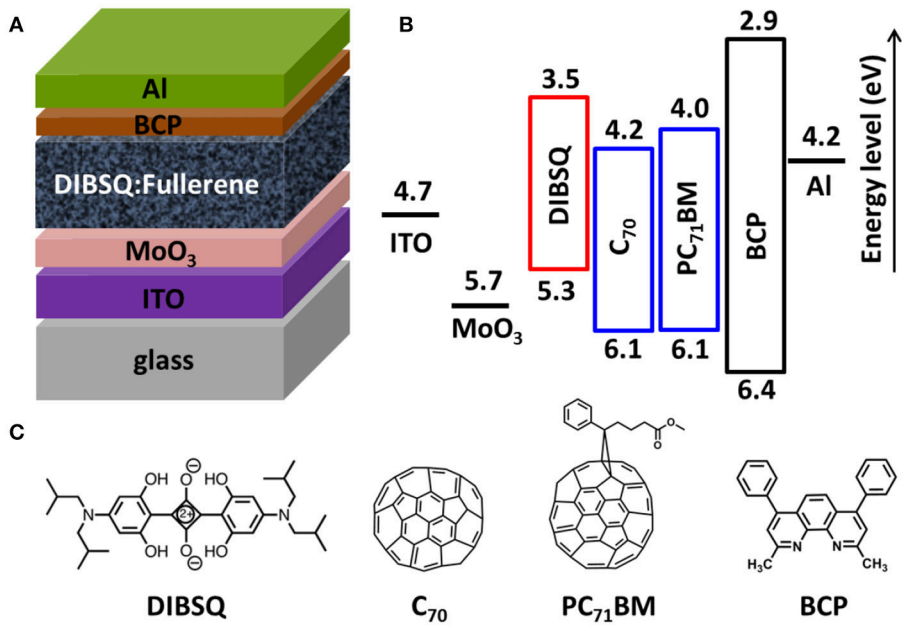

FIGURE 1 | (A) Device architecture of the DIBSQ:Fullerene bulk heterojunction photovoltaic cells, i.e., ITO/MoO_3 (5 nm)/DIBSQ:Fullerene (1:5, 60 nm)/BCP (10 nm)/Al (100 nm); **(B)** energy-level diagram, and **(C)** molecular structures of the materials under investigation.

stability and moderate solubility in organic solvents. To the best of our knowledge, it is rare that a small molecular thin film can be fabricated by using both of solution process and vacuum evaporation techniques (Chen et al., 2013). This unique property of DIBSQ indicates the photoactive layers of the DIBSQ:Fullerene based SMBHJ cells can be fabricated by spin-coating DIBSQ:$PC_{71}BM$ mixed solution or by vacuum co-evaporation of DIBSQ and C_{70}, which offers the possibility to directly compare the device performance of two processing techniques.

In this work, to directly compare the two processing techniques for BHJs, i.e., solution process and vacuum evaporation process, we fabricated a DIBSQ:$PC_{71}BM$ SMBHJ cell by using spin-coating processing and a DIBSQ:C_{70} SMBHJ cell by using vacuum co-evaporation processing. Then the device performance and film properties of the SMBHJ active layers were characterized and systematically compared.

EXPERIMENTAL SECTION

Materials

DIBSQ was synthesized according to the procedure reported by Tian et al. (2002), The purity of DIBSQ was proved to be over 99.9% by NMR and elemental analysis. MoO_3, bathocuproine (BCP) and $PC_{71}BM$ were commercially available and used as received. Commercially available C_{70} was sublimated 3 times before use. Patterned indium-tine-oxide (ITO) glass substrates were successively cleaned by using detergent, deionized water, acetone and isopropanol in ultrasonic bath, respectively, finally the cleaned ITO substrates were kept in an oven at 80°C for 12 h to be completely dried.

Film Characterization

UV-vis absorption spectra were carried out using a UV-vis-NIR spectrophotometer (SHIMADZU, UV-3150). Atomic force microscopy (AFM) images were performed in air on a scanning probe microscope (Nanonavi SPA-400SPM, Japan) using a tapping mode. X-ray diffraction (XRD) patterns were measured using a high-resolution XRD diffractometer (SmartLab, Rigaku Co.). The films for these measurements were prepared by using the same fabrication conditions for the devices to enable accurate comparisons.

Device Fabrication and Characterization

The DIBSQ:$PC_{71}BM$ BHJ cells with the structure of ITO/MoO_3 (5 nm)/DIBSQ:$PC_{71}BM$ (60 nm, 1:5)/BCP (10 nm)/Al (100 nm) (as shown in **Figure 1**) were fabricated as follows: the cleaned ITO substrates were exposed to UV ozone for 30 min and immediately transferred into a high-vacuum chamber for deposition of 5 nm-thick MoO_3 at a base pressure of 1×10^{-5} Pa. The substrates were then transferred into a nitrogen-filled glove box, 60 nm-thick photoactive layers were fabricated by spin-coating DIBSQ:$PC_{71}BM$ solution (20 mg mL^{-1} in chloroform with donor:acceptor weight ratio of 1:5) on the MoO_3 coated ITO surface at a rate of 4,000 revolutions per minute (rpm), then the DIBSQ:$PC_{71}BM$ blend films were thermally annealed at 70°C for 10 min. Finally, the substrates were transferred back to the high-vacuum chamber where 10 nm-thick BCP and 100 nm-thick Al cathode were successively deposited. The DIBSQ:C_{70} BHJ cells with the structure of ITO/MoO_3 (5 nm)/DIBSQ:C_{70} (60 nm, 1:5)/BCP (10 nm)/Al (100 nm) were fabricated in a high vacuum chamber with a pressure of 5×10^{-6} Pa, where 5 nm MoO_3 was deposited on the pre-cleaned ITO surface, then the 60 nm-thick DIBSQ:C_{70} photoactive layer were prepared by co-depositing DIBSQ and C_{70} with a blending ratio of 1:5, finally the devices were completed by evaporating 10 nm-thick BCP and 100 nm-thick Al cathode. The active area of solar cells is 0.04 cm^2. Hole-only devices with the structure of ITO/MoO_3 (5 nm)/DIBSQ:$PC_{71}BM$ (60 nm, 1:5) or DIBSQ:C_{70} (60 nm, 1:5)/MoO_3 (5 nm)/Al (100 nm) and electron-only devices with the structure of ITO/Cs_2CO_3 (1 nm)/DIBSQ:$PC_{71}BM$ (60 nm, 1:5) or DIBSQ:C_{70} (60 nm, 1:5)/BCP (10 nm)/Al (100 nm) were fabricated to characterize hole and electron mobility in photoactive blend films by using space-charge-limited current (SCLC) method (Shrotriya et al., 2006), respectively. The current density-voltage (J-V) and external quantum efficiency (EQE) of BHJ cells were measured on a CEP-2000 integrated system (Bunkou Keiki Co.) under standard measurement conditions. The device performance data were averaged from 16 individually fabricated BHJ cells.

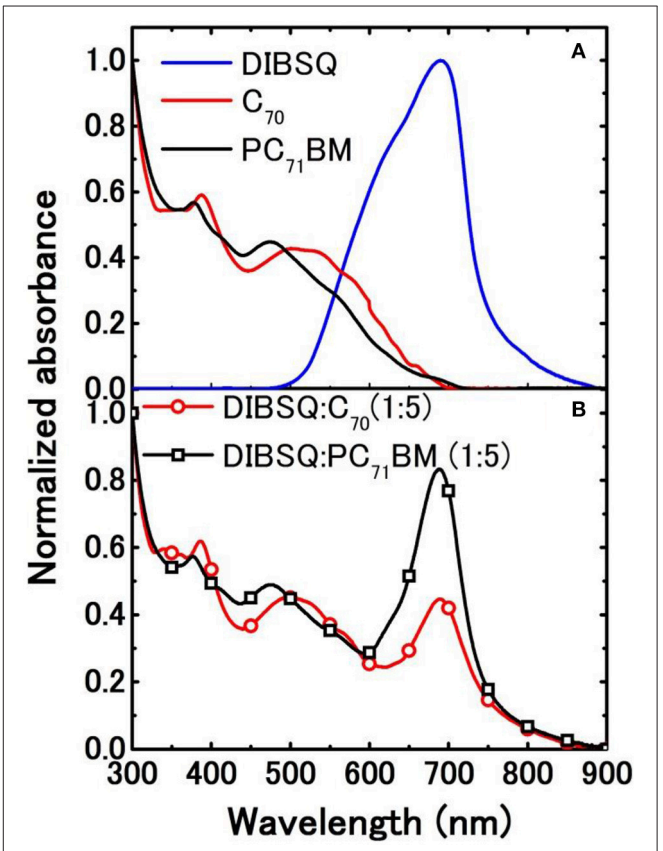

FIGURE 2 | Absorbance of **(A)** DIBSQ, C_{70} and $PC_{71}BM$ neat films and **(B)** DIBSQ:$PC_{71}BM$ and DIBSQ:C_{70} blend films with blend ratio of 1:5.

RESULTS AND DISCUSSION

Figure 1 represents the architectures of the DIBSQ:Fullerene SMBHJ cells (**Figure 1a**), the corresponding energy-level diagram (**Figure 1b**) and the molecular structures of the organic materials used in the device (**Figure 1c**). In the SMBHJ device, MoO_3 is adopted as hole-transporting layer. As demonstrated in our previous research (Chen et al., 2012b), the MoO_3 layer effectively deepened the work function of ITO to −5.7 eV, and thus delivered a larger open circuit voltage (V_{oc}) for the DIBSQ:Fullerene SMBHJ cells compared with those based on the typical ITO/PEDOT:PSS anode. The DIBSQ:Fullerene blend film is employed as the photoactive layer, while the bathocuproine (BCP) is used as electron-transporting layer. For comparison, the same ITO/MoO_3 (5 nm) cathode and BCP (10 nm)/Al (100 nm) anode were employed in all devices, as well as the film thickness and the blend ratio of DIBSQ and Fullerene for all the devices were also kept same as 60 nm and 1:5 ratio, respectively. The only difference is the fabrication processing and the corresponding acceptor materials used for the photoactive layers: the solution-processed DIBSQ:$PC_{71}BM$ SMBHJ cells were prepared by spin-coating the DIBSQ:$PC_{71}BM$ blend solution, while the vacuum-processed DIBSQ:C_{70} SMBHJ cells were fabricated by co-evaporating the DIBSQ and C_{70} in the vacuum condition.

The UV-Vis absorption spectra of the neat films of DIBSQ, C_{70}, $PC_{71}BM$ and the blend films of DIBSQ:$PC_{71}BM$ and DIBSQ:C_{70} were characterized. As shown in **Figure 2a**, the DIBSQ film displays an absorption band in the region of 500–800 nm with an absorption peak at 700 nm; the C_{70} and $PC_{71}BM$ film show wide absorption bands between 300 and 740 nm, thus the blend films of both DIBSQ:$PC_{71}BM$ and DIBSQ:C_{70} display strong and broad absorption covering the region from visible to NIR, which leads to larger light-harvesting, and thus potentially obtains higher J_{sc} of the DIBSQ:Fullerene SMBHJ cells (Chen et al., 2014).

Figure 3a exhibits the *J-V* curves of the SMBHJ cells under 100 mW/cm^2 AM 1.5 illumination. As shown in **Figure 3a**

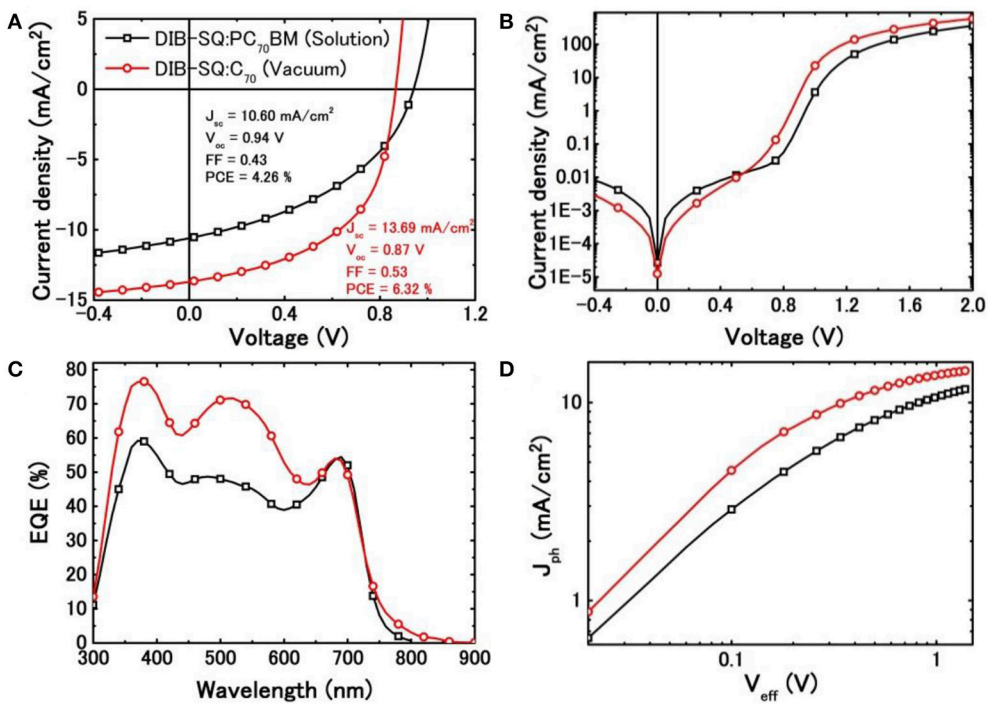

FIGURE 3 | (A) *J-V* curves under AM 1.5G solar spectrum at 100 mW/cm^2 illumination; **(B)** *J-V* curves under dark condition; **(C)** EQE spectra, and **(D)** J_{ph}-V_{eff} curves measured at the AM1.5G condition (100 mW/cm^2) of solution-processed DIBSQ:$PC_{71}BM$ and vacuum-processed DIBSQ:C_{70} SMBHJ cells.

TABLE 1 | Comparison of device performance of solution-processed DIBSQ:$PC_{71}BM$ and vacuum-processed DIBSQ:C_{70} SMBHJ cells.

Fabrication processing	J_{sc} (mA/cm^2)	V_{oc} (V)	FF	PCE (%)	μ_h (cm^2/Vs)[a]	μ_e (cm^2/Vs)[a]	R_s (Ω cm^2)	R_{sh} (Ω cm^2)
Solution	10.60	0.94	0.43	4.26	2.1×10^{-5}	3.7×10^{-4}	16.2	2.9×10^3
Vacuum	13.69	0.87	0.53	6.32	9.8×10^{-5}	6.8×10^{-4}	6.8	4.0×10^3

[a] *Carrier mobility data were originated from a space-charge-limited current (SCLC) model.*
The device performance data were averaged from 16 individually fabricated BHJ cells.

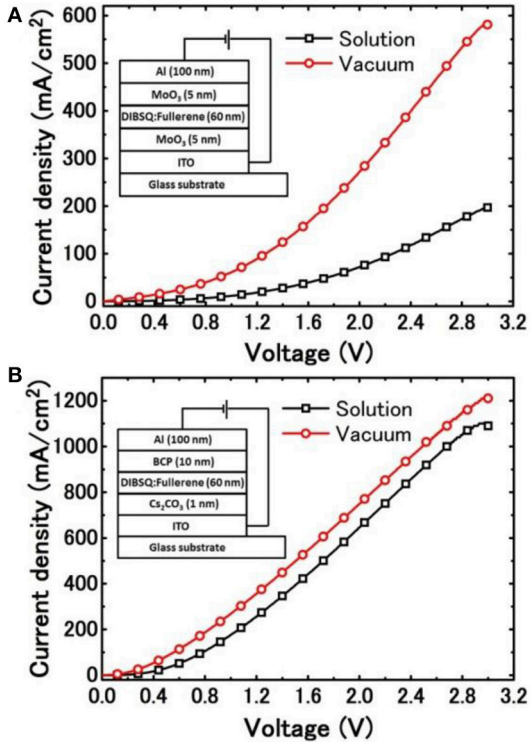

FIGURE 4 | *J-V* characteristics of **(A)** hole-only devices and **(B)** electron-only devices based on solution-processed DIBSQ:$PC_{71}BM$ and vacuum-processed DIBSQ:C_{70} blend films, inset show the schematic structures of the corresponding single carrier devices.

and **Table 1**, the solution-processed DIBSQ:$PC_{71}BM$ SMBHJ cell possesses a PCE of 4.26% with a J_{sc} of 10.60 mA/cm^2, a V_{oc} of 0.94 V and a fill factor (FF) of 0.43. While the vacuum-processed DIBSQ:C_{70} SMBHJ cell provides a PCE of 6.32% with a J_{sc} of 13.69 mA/cm^2, V_{oc} of 0.87 V and FF of 0.53. Comparison of the device performance shows that the vacuum-processed BHJ cells possess higher J_{sc} and FF and thus higher PCE than the solution-processed devices, which should be assigned to more efficient charge transport and charge extraction in the vacuum-processed SMBHJ cells owing to much higher and more balanced hole and electron mobilities in their active layers (**Table 1**) (Chen et al., 2017b), as discussed in a subsequent section. The lower V_{oc} in the vacuum-processed DIBSQ:C_{70} SMBHJ cells can be explained by the deeper LUMO level of C_{70} acceptor compared with that of $PC_{71}BM$ acceptor, as shown in **Figure 1b**. Normally, the V_{oc} of BHJs depends on the energy level difference between the HOMO of the donor (HOMO $_{Donor}$) and LUMO of the acceptor (LUMO $_{Acceptor}$) (Chen et al., 2017b), the deeper LUMO level of C_{70} leads to smaller |HOMO $_{Donor}$| – |LUMO $_{Acceptor}$| value and thus smaller V_{oc}. As shown in **Table 1**, comparing with the solution-processed DIBSQ:$PC_{71}BM$ SMBHJ cell, the series resistance (R_s) of the DBSQ:C_{70} SMBHJ cell obviously decreases from 16.2 to 6.8 Ω cm^2, whereas the shunt resistance (R_{sh}) increase from 2.9 × 10^3 to 4.0 × 10^3 Ω cm^2 in the same time. The decreased R_s and increased R_{sh} also contribute to higher FF of the vacuum-processed DIBSQ:C_{70} SMBHJ device (Chen et al., 2017b).

Figure 3b displays the *J-V* curves of the SMBHJ cells under dark condition. The solution-processed DIBSQ:$PC_{71}BM$ SMBHJ cell demonstrates a turn-on voltage of approximately 0.8–1.0 V while it is approximately 0.7–0.9 V for the vacuum-processed DIBSQ:C_{70} device, which indicates that the superior limit of the attainable V_{oc} in SMBHJ cell, i.e., the built-in potential (V_{bi}) across the SMBHJ cell, obviously decreases by using the vacuum-processed DIBSQ:C_{70} active layer (He et al., 2011; Chen et al., 2017b). This observation means that solution-processed DIBSQ:$PC_{71}BM$ SMBHJ device possesses larger V_{bi} than the vacuum-processed DIBSQ:C_{70} SMBHJ device, which should be ascribed to poorer charge-transporting properties in the solution-processed SMBHJ cells. As shown in **Figure 3c**, the EQE spectra of both devices consist of three major peaks at 370, 500, and 700 nm approximately. The first two peaks located at 370 and 500 nm correspond to the absorption of $PC_{71}BM$ or C_{70}, and the third peak at 700 nm is from the absorption of DIBSQ, which is consistent with the absorption spectra of the blend DIBSQ:$PC_{71}BM$ and DIBSQ:C_{70} films (**Figure 2b**). Even though the photo response in the longer wavelength region are almost same for the solution- and vacuum-processed SMBHJ cells, the photo response in the near ultraviolet and visible region for the vacuum-processed DIBSQ:C_{70} SMBHJ cell is significantly enhanced up to 76 and 72%, respectively, which explains that why the vacuum-processed SMBHJ cell possesses higher J_{sc} than that of solution-processed SMBHJ cell. The normalized EQE spectra (**Figure S1**) shows that the photo response in the longer wavelength region of the solution-processed DIBSQ:$PC_{71}BM$ SMBHJ cell is much stronger than that of the DIBSQ:C_{70} SMBHJ cell, which is consistent with the observation in the normalized absorption spectra of DIBSQ:Fullerene films (**Figure 2b**). Moreover, the obviously higher and longer photo response from 750 to 850 nm should be ascribed to the absorption of charge transfer states between DIBSQ and C_{70} (Wang et al., 2013), which also contributes to the higher J_{sc} in the DIBSQ:C_{70} SMBHJ cell.

To further study the effect of fabrication processing on the SMBHJ device performance, we also characterized the photocurrent density (J_{ph}) vs. effective voltage (V_{eff}) of the DIBSQ:$PC_{71}BM$ and DIBSQ:C_{70} SMBHJ cells, respectively, as demonstrated in **Figure 3d**. Here, J_{ph} and V_{eff} are defined by

$$J_{ph} = J_L - J_D \quad (1)$$

$$V_{eff} = V_0 - V_a \quad (2)$$

where J_L and J_D represent the current density measured under AM 1.5G illumination and in the dark at an applied bias voltage V_b, respectively. V_0 is the built-in potential, which can by identified as the voltage at $J_{ph} = 0$ (Wu et al., 2016). **Figure 3d** displays that the J_{ph} increases linearly with V_{eff} at low V_{eff} range (<0.1 V), and then gradually saturates at a high V_{eff}. In general, it is supposed that all photogenerated excitons are dissociated into free carriers and extracted by electrodes at high V_{eff} (Chen et al., 2017b). At lower V_{eff} region, higher J_{ph} can be found for the solution-processed SMBHJ device than that of the

vacuum-processed device, which reflects the charge collection in the vacuum-processed SMBHJ cells is more efficient than that in the solution-processed SMBHJ cells. The enhanced charge collection efficiency leads to improved device performance in the vacuum-processed devices, as discussed in the previous sections.

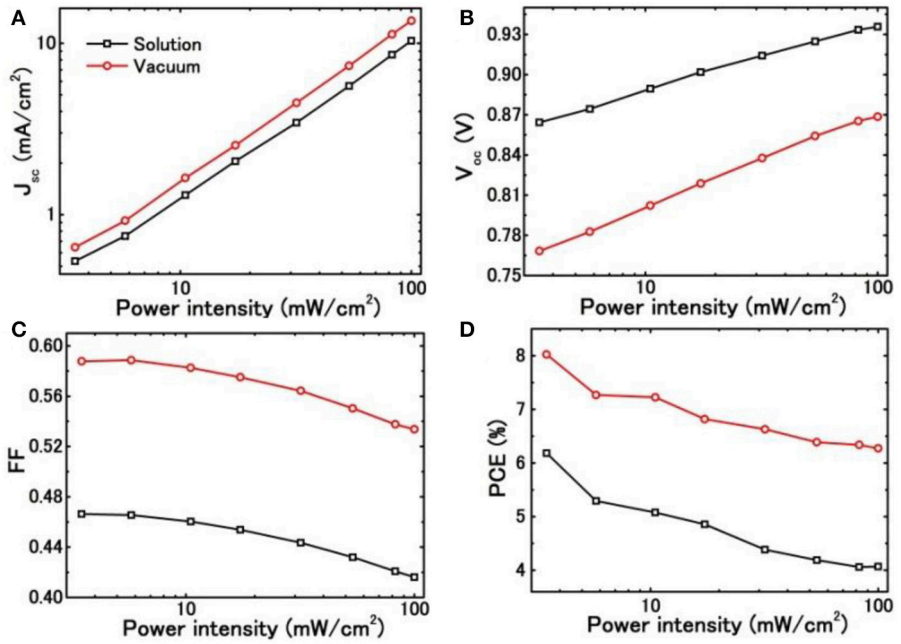

FIGURE 5 | (A) The short circuit current (J_{SC}); **(B)** open circuit voltage (V_{OC}); **(C)** fill factor (FF) and **(D)** power conversion efficiency (PCE) vs. power intensity for solution-processed DIBSQ:PC_{71}BM SMBHJ cells and vacuum-processed DIBSQ:C_{70} SMBHJ cells.

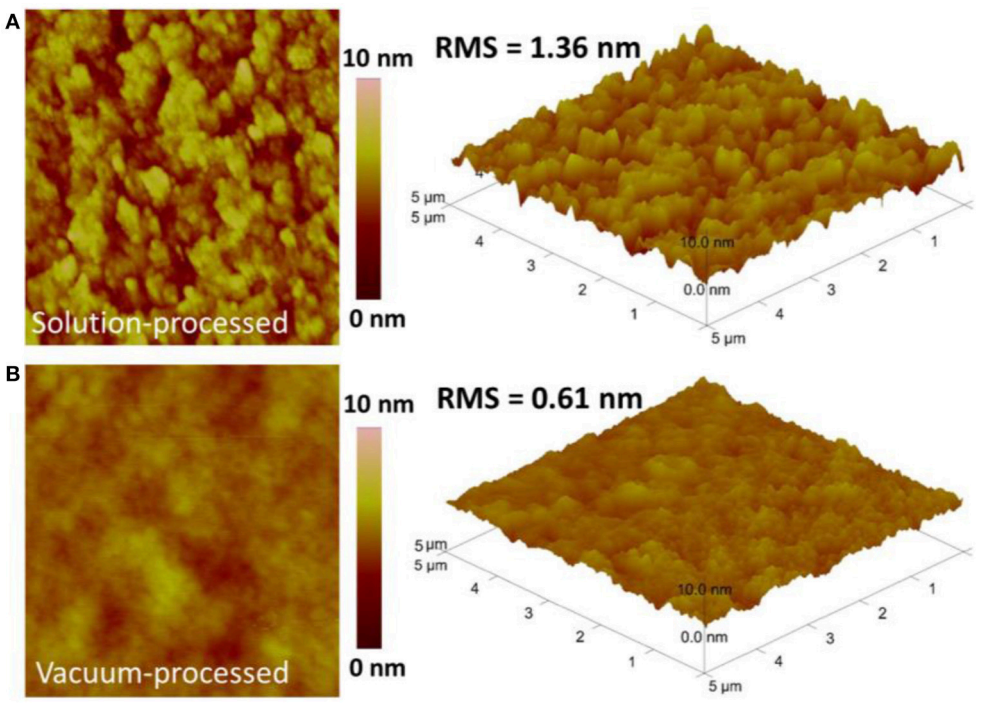

FIGURE 6 | AFM topographic and 3D images of **(A)** the solution-processed DIBSQ:PC_{71}BM (1:5, 60 nm) film and **(B)** the vacuum-processed DIBSQ:C_{70} (1:5, 60 nm) film.

Carrier mobilities in BSQ:Fullerene blend films deposited from different fabrication processing were also characterized and compared, as shown in **Figure 4**. Hole-only diodes were fabricated using the structure of ITO/MoO_3 (5 nm)/DIBSQ:$PC_{71}BM$ (60 nm, 1:5) or DIBSQ:C_{70} (60 nm, 1:5)/MoO_3 (5 nm)/Al (100 nm), while the electron-only diodes were prepared using the structure of ITO/Cs_2CO_3 (1 nm)/DIBSQ:$PC_{71}BM$ (60 nm, 1:5) or DIBSQ:C_{70} (60 nm, 1:5)/BCP (10 nm)/Al (100 nm) for electrons. Where the DIBSQ:$PC_{71}BM$ and DIBSQ:C_{70} blend films were prepared by using the same solution- and vacuum-processing, respectively, as those in the SMBHJ devices. The *J-V* curves of the hole- and electron-only diodes were characterized as shown in **Figure 4**, and then the carrier mobilities were calculated by fitting the *J-V* data using the SCLC method according to the following equation (3) (Wang et al., 2015):

$$J = \frac{9}{8}\mu\varepsilon_0\varepsilon_r\frac{V^2}{d^3} \quad (3)$$

where J represents the current density, μ represents effective carrier mobility, ε_0 and ε_r represent the absolute dielectric constant and relative dielectric constant, respectively, d represents the thickness of the DBSQ:$PC_{71}BM$ film and V is the applied voltage (Chen et al., 2017b). The SCLC-estimated hole and electron mobility data were summarized in **Table 1**. The hole and electron mobility in vacuum-processed DIBSQ:C_{70} films are about 4.7 and 1.8 times greater than that in the solution-processed DBISQ:$PC_{71}BM$ film, respectively, which shall be ascribed to the closer intermolecular distance in the denser vacuum-processed DIBSQ:C_{70} film. Meanwhile the hole and electron mobilities in vacuum-processed DIBSQ:C_{70} films are much more balanced than those in solution-processed DBISQ:$PC_{71}BM$ films. More balanced hole and electron mobilities leads to more efficient charge extraction and thus much higher device performance in the DIBSQ:C_{70} SMBHJ devices (Chen et al., 2017b).

The light-intensity dependence of device performance for the DIBSQ:Fullerene SMBHJ cell was also characterized and compared, as shown in **Figure 5**. For both of the solution- and vacuum SMBHJ cells, the J_{sc} is linearly proportional to the light intensity. The slope value (0.91) nears the ideal value (1.0) for OSC device. The V_{oc} of the device shows a sub-linear trend with saturation when the light intensity reaches 100 mW/cm^2. The slope is roughly close to kT/q, demonstrating that bimolecular recombination dominates, where k is Boltzmann's constant, T is the temperature, and q is elementary charge (Koster et al., 2005; Chen et al., 2017a). The FF decreases with increasing the light intensity, which indicates that the recombination loss of the device is sensitive to both carrier density and electrical field. The PCEs of the solution-processed DIBSQ:$PC_{71}BM$ cell and DIBSQ:C_{70} SMBHJ cell improve up to 6.21 and 8.06% at 3.5 mW cm^{-2}, respectively, respective to suppressed non-germinated recombination (Chen et al., 2012a), which is a strong indication of the great potential of the DIBSQ:Fullerene SMBHJ cell for the commercial application in the lower light intensity ambient.

To deeply understand the device performance of DIBSQ:Fullerene BHJ cells, we used AFM and XRD characterizations to study the film morphology of the BHJ active layer fabricated by using solution- or vacuum processing, as depicted in **Figure 6**, **Figure S2**. From the AFM images, a small root-mean-square (RMS) roughness of 1.36 and 0.61 nm for

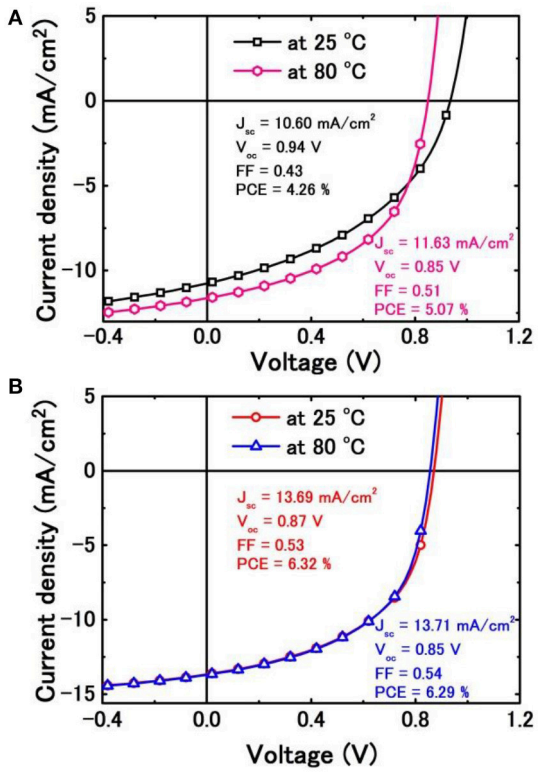

FIGURE 7 | (A) *J-V* characteristics of the solution-processed DIBSQ:$PC_{71}BM$ SMBHJ cells at 25 and 80°C; and **(B)** *J-V* characteristics of the vacuum-processed DIBSQ:C_{70} SMBHJ cells at 25 and 80°C.

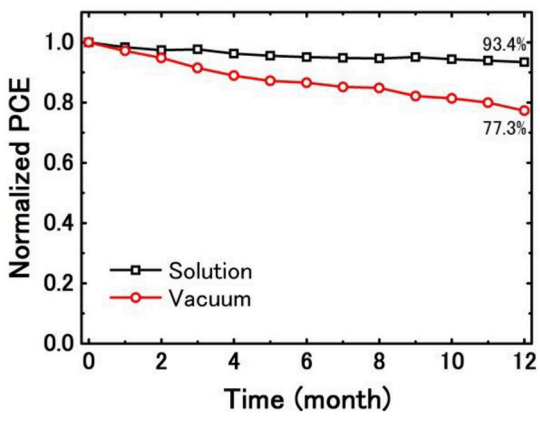

FIGURE 8 | Comparison of the degradation of normalized PCE of solution-processed DIBSQ:$PC_{71}BM$ SMBHJ cells and vacuum-processed DIBSQ:C_{70} SMBHJ cells.

the solution-processed DIBSQ:$PC_{71}BM$ and vacuum-processed DIBSQ:C_{70} films were determined, respectively. And no peaks can be observed in the XRD patterns. These observations indicate that both of the solution- and vacuum-processed photoactive layers are amorphous. Though the amorphous feature of the photoactive layers is not conducive to charge transport, the small roughness of the photoactive layers are critical to avoid leakage current (Chen et al., 2012b), as demonstrated in **Figure 3b**.

Considering DIBSQ:$PC_{71}BM$ SMBHJ cell has pronounced temperature-dependent performance, which has been systemically studied by our group (Chen et al., 2016a). In this work, we also test the device performance of vacuum-processed DIBSQ:C_{70} SMBHJ cell at higher temperature, and then compare the device performance with that of the solution-processed DIBSQ:$PC_{71}BM$ SMBHJ cell at the same testing temperature, as shown in **Figure 7**. For the solution-processed SMBHJ cell, the PCE will significantly increase up to 5.07% with increased J_{sc} and FF at a testing temperature of 80°C. While the V_{oc} decreases in the same time owing to the carrier recombination of the SMBHJ device (Chen et al., 2016a). As a result, the PCE is near 20% enhancement at 80°C comparing with the device performance at 25°C. However, we can not observe the similar temperature-dependent device performance from the vacuum-processed DIBSQ:C_{70} SMBHJ system. The DIBSQ:C_{70} SMBHJ cell at 80°C shows a slightly increased J_{sc} and FF while slightly decreased V_{oc} and thus a similar PCE compared with the device performance at 25°C, which can be explained by the almost unchanged carrier mobilities in the DIBSQ:C_{70} film compared with those at 25°C (**Table S1**). This observation is different from that in the DIBSQ:$PC_{71}BM$ SMBHJ cell, in which the carrier mobility will significant increase and thus the device performance will increase in the same time with increasing the testing temperature.

Besides PCE, stability is another important parameter to evaluate the performance of an OSC cell (Ecker et al., 2011). **Figure 8** shows the degradation of normalized PCE of the solution- and vacuum-processed BHJ cells in 1 year, and all the measurements were carried out with all devices kept in air with glass encapsulation. After keeping in air one year, the PCE of the solution-processed DIBSQ:$PC_{71}BM$ SMBHJ cell still remains 93.4% of the initial value, while the PCE of the vacuum-processed DIBSQ:C_{70} SMBHJ cell remains 77.3% of the initial number. The higher device stability of the solution-processed DIBSQ:$PC_{71}BM$ SMBHJ cell demonstrates that the stable DIBSQ and $PC_{71}BM$ materials employed in the device can efficiently resist the chemical and photochemical degradation inside the SMBHJ cells, which is a very important property for the commercial application because many OSC materials can realize higher PCE while short lifetime.

CONCLUSIONS

In summary, to directly compare the device performance of solution- and vacuum-processed SMBHJ solar cells, we employed a SQ dye, which can be deposited by using both of the solution and vacuum processing, as electron donor combined with fullerene as acceptor to construct solution- and vacuum-processed DIBSQ:Fullerene SMBHJ cells. Then the device performance were characterized and compared. The results demonstrates that the vacuum-processed cell provides a ∼47% higher PCE than that of the solution-processed SMBHJ cell due to more efficient charge transport and charge extraction in the vacuum-processed SMBHJ cells. However, solution-processed SMBHJ cells demonstrate more pronounced temperature-dependent device performance and higher device stability. The light intensity-dependent device performance for both of the solution- and vacuum-processed DIBSQ:Fullerene SMBHJ cell indicates their promising application in the lower light intensity ambient. This study indicates the great potential of DIBSQ in photovoltaic application via both of solution and vacuum processing techniques.

AUTHOR CONTRIBUTIONS

GC, HS, and JK designed experiments, GC and ZL carried out experiments, BW and ZH analyzed experimental results GC, JZ, and HS wrote the manuscript.

ACKNOWLEDGMENTS

This work is financially supported by the Shanghai Pujiang Program (16PJ1403300), the National Natural Scientific Foundation of China (61604093), the Natural Science Foundation of Shanghai (16ZR1411000), and the Science and Technology Commission of Shanghai Municipality Program (17DZ2281700).

SUPPLEMENTARY MATERIAL

The Supplementary Material for this article can be found online at: https://www.frontiersin.org/articles/10.3389/fchem.2018.00412/full#supplementary-material

REFERENCES

Ajayaghosh, A. (2005). Chemistry of squaraine-derived materials: near-IR dyes, low band gap systems, and cation sensors. *Acc. Chem. Res.* 38, 449–459. doi: 10.1021/ar0401000

Bagnis, D., Beverina, L., Huang, H., Silvestri, F., Yao, Y., Yan, H., et al. (2010). Marked alkyl- vs alkenyl-substitutent effects on squaraine dye solid-state structure, carrier mobility, and bulk-heterojunction solar cell efficiency. *J. Am. Chem. Soc.* 132, 4074–4075. doi: 10.1021/ja100520q

Chen, G., Sasabe, H., Igarashi, T., Hong, Z., and Kido, J. (2015). Squaraine dyes for organic photovoltaic cells. *J. Mater. Chem. A* 3, 14517–14534. doi: 10.1039/C5TA01879J

Chen, G., Sasabe, H., Sano, T., Wang, X. F., Hong, Z., Kido, J., et al. (2013). Chloroboron (III) subnaphthalocyanine as an electron donor in bulk heterojunction photovoltaic cells. *Nanotechnology* 24:484007. doi: 10.1088/0957-4484/24/48/484007

Chen, G., Sasabe, H., Wang, X.-F., Hong, Z., and Kido, J. (2014). A squaraine dye as molecular sensitizer for increasing light harvesting in

polymer solar cells. *Synthetic Met*. 192, 10–14. doi: 10.1016/j.synthmet.2014.02.018

Chen, G., Sasabe, H., Wang, Z., Wang, X., Hong, Z., Kido, J., et al. (2012b). Solution-processed organic photovoltaic cells based on a squaraine dye. *Phys. Chem. Chem. Phys*. 14, 14661–14666. doi: 10.1039/c2cp42445b

Chen, G., Sasabe, H., Wang, Z., Wang, X.-F., Hong, Z., Yang, Y., et al. (2012a). Co-evaporated bulk heterojunction solar cells with >6.0% efficiency. *Adv. Mater*. 24, 2768–2773. doi: 10.1002/adma.201200234

Chen, G., Si, C., Tang, Z., Guo, K., Wang, T., Zhang, J., et al. (2016a). Temperature-dependent device performance of organic photovoltaic cells based on a squaraine dye. *Synthetic Met*. 222, 293–298. doi: 10.1016/j.synthmet.2016.11.007

Chen, G., Si, C., Zhang, P., Guo, K., Pan, S., Zhu, W., et al. (2017a). Efficiency enhancement in DIBSQ:PC71BM organic photovoltaic cells by using Liq-doped Bphen as a cathode buffer layer. *Front. Mater. Sci*. 11, 233–240. doi: 10.1007/s11706-017-0384-x

Chen, G., Si, C., Zhang, P., Wei, B., Zhang, J., Hong, Z., et al. (2017b). The effect of processing solvent dependent film aggregation on the device performance of squaraine:PC71BM bulk heterojunction solar cells. *Org. Electroncis* 51, 62–69. doi: 10.1016/j.orgel.2017.09.015

Chen, G., Wang, T., Li, C., Yang, L., Xu, T., Zhu, W., et al. (2016b). Enhanced photovoltaic performance in inverted polymer solar cells using Li ion doped ZnO cathode buffer layer. *Org. Electronics* 36, 50–56. doi: 10.1016/j.orgel.2016.05.033

Du, Z., Bao, X., Li, Y., Liu, D., Wang, J., Yang, C., et al. (2018). Balancing high open circuit voltage over 1.0 V and high short circuit current in benzodithiophene-based polymer solar cells with low energy loss: a synergistic effect of fluorination and alkylthiolation. *Adv. Energy Mater*. 8:1701471. doi: 10.1002/aenm.201701471

Duan, C., Guzmán, D., Colberts, F. J. M., Janssen, R. A. J., and Torres, T. (2018). Subnaphthalocyanines as electron acceptors in polymer solar cells: improving device performance by modifying peripheral and axial substituents. *Chem. Eur. J*. 24, 6339–6343. doi: 10.1002/chem.201800596

Duan, C., Zango, G.,García Iglesias, M., Colberts, F. J., Wienk, M. M., Martínez-Díaz, M. V., et al. (2017). The role of the axial substituent in subphthalocyanine acceptors for bulk-heterojunction solar cells. *Angew. Chem.* 56, 148–152. doi: 10.1002/anie.201608644

Ecker, B., Nolasco, J. C., Pallarés, J., Marsal, L. F., Posdorfer, J., Parisi, J., et al. (2011). Degradation effects related to the hole transport layer in organic solar cells. *Adv. Funct. Mater*. 21, 2705–2711. doi: 10.1002/adfm.201100429

Günes, S., Neugebauer, H., and Sariciftci, N. S. (2007). Conjugated polymer-based organic solar cells. *Chem. Rev*. 107, 1324–1338. doi: 10.1021/cr050149z

He, Z., Xiao, B., Liu, F., Wu, H., Yang, Y., Xiao, S., et al. (2015). Single-junction polymer solar cells with high efficiency and photovoltage. *Nat. Photonics* 9, 174–179. doi: 10.1038/nphoton.2015.6

He, Z., Zhong, C., Huang, X., Wong, W. Y., Wu, H., Chen, L., et al. (2011). Simultaneous enhancement of open-circuit voltage, short-circuit current density, and fill factor in polymer solar cells. *Adv. Mater*. 23, 4636–4643. doi: 10.1002/adma.201103006

Hu, Z., Huang, F., and Cao, Y. (2017). Layer-by-layer assembly of multilayer thin films for organic optoelectronic devices. *Small Methods* 1:201700264. doi: 10.1002/smtd.201700264

Huang, J., Zhang, S., Jiang, B., Chen, Y., Zhang, X., Fan, Z., et al. (2016). Terminal moiety-driven electrical performance of asymmetric small-molecule-based organic solar cells. *J. Mater. Chem. A* 4, 15688–15697. doi: 10.1039/C6TA07450B

Jiang, B., Yao, J., and Zhan, C. (2016). Modulating PCBM-acceptor crystallinity and organic solar cell performance by judiciously designing small-molecule mainchain end-capping units. *ACS Appl. Mater. Interfaces* 8, 26058–26065. doi: 10.1021/acsami.6b08407

Koster, L. J. A., Mihailetchi, V. D., Ramaker, R., and Blom, P. W. M. (2005). Light intensity dependence of open-circuit voltage of polymer:fullerene solar cells. *Appl. Phys. Lett*. 86:123509. doi: 10.1063/1.1889240

Kronenberg, N. M., Steinmann, V., Bürckstümmer, H., Hwang, J., Hertel, D., Würthner, F., et al. (2010). Direct comparison of highly efficient solution- and vacuum-processed organic solar cells based on merocyanine dyes. *Adv. Mater*. 22, 4193–4197, doi: 10.1002/adma.201000800

Li, G., Zhu, R., and Yang, Y. (2012). Polymer solar cells. *Nat. Photonics* 6, 153–161. doi: 10.1038/nphoton.2012.11

Li, Y. (2012). Molecular design of photovoltaic materials for polymer solar cells: toward suitable electronic energy levels and broad absorption. *Acc. Chem. Res*. 45, 723–733. doi: 10.1021/ar2002446

Lin, Y., Li, Y., and Zhan, X. (2012). Small molecule semiconductors for high-efficiency organic photovoltaics. *Chem. Soc. Rev*. 41, 4245–4272. doi: 10.1039/c2cs15313k

Mayerhöffer, U., Deing, K., Gruss, K., Braunschweig, H., Meerholz, K., and Würthner, F. (2009). Outstanding short-circuit currents in BHJ solar cells based on NIR-absorbing acceptor-substituted squaraines. *Angew. Chem.* 48, 8776–8779. doi: 10.1002/anie.200903125

Qi, X., Lo, Y. -C., Zhao, Y., Xuan, L., Ting, H.-C., Wong, K.-T., et al. (2018). Two novel small molecule donors and the applications in bulk-heterojunction solar cells. *Front. Chem*. 6:260. doi: 10.3389/fchem.2018.00260

Roncali, J., Leriche, P., and Blanchard, P. (2014). Molecular materials for organic photovoltaics: small is beautiful. *Adv. Mater*. 26, 3821–3838. doi: 10.1002/adma.201305999

Sasabe, H., Igrashi, T., Sasaki, Y., Chen, G., Hong, Z., and Kido, J. (2014). Soluble squaraine derivatives for 4.9% efficient organic photovoltaic cells. *RSC Adv*. 4, 42804–42807. doi: 10.1039/c4ra08171d

Shrotriya, V., Li, G., Yao, Y., Chu, C. W., and Yang, Y. (2006). Transition metal oxides as the buffer layer for polymer photovoltaic cells. *Appl. Phys. Lett*. 88:073508. doi: 10.1063/1.2174093

Silvestri, F., Irwin, M. D., Beverina, L., Facchetti, A., Pagani, G. A., and Marks, T. J. (2008). Efficient squaraine-based solution processable bulk-heterojunction solar cells. *J. Am. Chem. Soc*. 130, 17640–17641. doi: 10.1021/ja8067879

Tang, A., Zhan, C., Yao, J., and Zhou, E. (2017). Design of diketopyrrolopyrrole (DPP)-based small molecules for organic-solar-cell applications. *Adv. Mater*. 29:1600013. doi: 10.1002/adma.201600013

Tian, M., Furuki, M., Iwasa, I., Sato, Y., Pu, L. S., and Tatsuura, S. (2002). Search for squaraine derivatives that can be sublimed without thermal decomposition. *J. Phys. Chem. B* 106, 4370–4376. doi: 10.1021/jp013698r

Wang, Y., Zhao, X., and Zhan, X. (2015). Layer by layer solution processed organic solar cells based on a small molecule donor and a polymer acceptor. *J. Mater. Chem. C* 3, 447–452. doi: 10.1039/C4TC02103G

Wang, Z., Yokoyama, D., Wang, X. F., Hong, Z., Yang, Y., and Kido, J. (2013). Highly efficient organic p–i–n photovoltaic cells based on tetraphenyldibenzoperiflanthene and fullerene C70. *Energy Environ. Sci*. 6, 249–255. doi: 10.1039/C2EE22952H

Wei, G., Wang, S., Sun, K., Thompson, M. E., and Forrest, S. R. (2011). Solvent-annealed crystalline squaraine: PC70BM (1:6) solar cells. *Adv. Energy Mater*. 1, 184–187. doi: 10.1002/aenm.201100045

Wu, B., Wu, Z., Yang, Q., Zhu, F., Ng, T. W., Lee, C. S., et al. (2016). Improvement of charge collection and performance reproducibility in inverted organic solar cells by suppression of ZnO subgap states. *ACS Appl. Mater. Interfaces* 8, 14717–14724. doi: 10.1021/acsami.6b03619

Wu, J., Si, C., Chen, Y., Yang, L., Hu, B., Chen, G., et al. (2018). Photovoltaic devices prepared through a trihydroxy substitution strategy on an unsymmetrical squaraine dye. *Chem. Eur. J*. 24, 3234–3240. doi: 10.1002/chem.201705140

Yu, G., Gao, J., Hummelen, J. C., Wudl, F., and Heeger, A. J. (1995). Polymer photovoltaic cells: enhanced efficiencies via a network of internal donor-acceptor heterojunctions. *Science* 270, 1789–1791. doi: 10.1126/science.270.5243.1789

Conflict of Interest Statement: The authors declare that the research was conducted in the absence of any commercial or financial relationships that could be construed as a potential conflict of interest.

frontiers in Chemistry

ORIGINAL RESEARCH
published: 07 September 2018
doi: 10.3389/fchem.2018.00398

Urea-Doped ZnO Films as the Electron Transport Layer for High Efficiency Inverted Polymer Solar Cells

Zongtao Wang[1], Zhongqiang Wang[1], Ruqin Zhang[1], Kunpeng Guo[1]*, Yuezhen Wu[1], Hua Wang[1], Yuying Hao[1] and Guo Chen[2]*

[1] Key Laboratory of Interface Science and Engineering in Advanced Materials, Ministry of Education, Research Center of Advanced Materials Science and Technology, Taiyuan University of Technology, Taiyuan, China, [2] Key Laboratory of Advanced Display and System Applications, Ministry of Education, Shanghai University, Shanghai, China

In this paper, urea-doped ZnO (U-ZnO) is investigated as a modified electron transport layer (ETL) in inverted polymer solar cells (PSCs). Using a blend of Poly{4,8-bis[(2-ethylhexyl)oxy] benzo [1,2-b:4,5-b'] dithiophene-2,6-diyl-alt-3-fluoro-2-[(2-ethylhexyl)carbonyl] thieno [3,4-b] thiophene-4,6-diyl}(PTB7), and [6,6]-phenyl-C71-butyric acid methyl ester ($PC_{71}BM$) as light absorber, a champion power conversion efficiency (PCE) of 9.15% for U-ZnO ETL based PSCs was obtained, which is 15% higher than that of the pure ZnO ETL based PSCs (7.76%). It was demonstrated that urea helps to passivate defects in ZnO ETL, resulting in enhanced exciton dissociation, suppressed charge recombination and efficient charge extraction efficiency. This work suggests that the utilization of the U-ZnO ETL offer promising potential for achieving highly efficient PSCs.

Keywords: polymer solar cells, ETL, ZnO, urea, PCE

OPEN ACCESS

Edited by:
Donghong Yu,
Aalborg University, Denmark

Reviewed by:
Xichang Bao,
Qingdao Institute of Bioenergy and Bioprocess Technology (CAS), China
Weiwei Li,
Institute of Chemistry (CAS), China

***Correspondence:**
Zhongqiang Wang
wangzhongqiang@tyut.edu.cn
Kunpeng Guo
guokunpeng@tyut.edu.cn

Specialty section:
This article was submitted to Organic Chemistry, a section of the journal Frontiers in Chemistry

Received: *30 May 2018*
Accepted: *20 August 2018*
Published: *07 September 2018*

Citation:
Wang Z, Wang Z, Zhang R, Guo K, Wu Y, Wang H, Hao Y and Chen G (2018) Urea-Doped ZnO Films as the Electron Transport Layer for High Efficiency Inverted Polymer Solar Cells. Front. Chem. 6:398. doi: 10.3389/fchem.2018.00398

INTRODUCTION

In past decades, the need of green and sustainable energy has become more and more pressing. Polymer solar cells (PSCs) as one of the most potential renewable energy technologies have attracted wide attention due to its merits, such as low cost, light weight, and the capability of fabricating flexible large-area modules (Zhang et al., 2016; Sun et al., 2017; Tran et al., 2017; Hou et al., 2018; Li et al., 2018). To improve the performance of PSCs, enormous efforts have been made by the worldwide researchers. Benefited from the progresses of new optoelectronic materials and interfacial engineering, the power conversion efficiency (PCE) have reached over 14% in single-junction PSCs (Gao et al., 2016; Liu et al., 2016; Wu et al., 2016; Li et al., 2017; Peng et al., 2017). Meantime, it was found the interfacial engineering plays key role in determining the efficiency and the stability of PSCs (Liu, Z. et al., 2017). For example, it has been demonstrated that the application of anode and electrode interlayer leads to 20% improvement compared to the reference device without electrode interlayer (Wu et al., 2016). The interfacial contact at the interface between active layer and electrode usually polished by inorganic and organic materials (such as graphene, carbon quantum dots, PEIE, PEI), which benefits the charge transport and extraction in PSCs, resulting in enhanced device performance (Bi et al., 2018).

In conventional structure devices, low work-function metal and air sensitive materials are widely used as electron extraction layer (Liu, D. et al., 2017; Huai et al., 2018), which limits the stability of devices. Hence, the inverted device structure is developed in PSCs, which switches the position of anode and cathode, preventing the interfacial deterioration and physical degradation of organic layers (Wang et al., 2012; Cheng et al., 2018). Therefore, the device stability can be significantly improved in inverted structure devices. In addition, the inverted PSCs showed excellent performance due to the efficient charge extraction and suppressed recombination loss compared to the conventional structure devices (Wang et al., 2017).

In inverted PSCs, the metal-oxide materials have been utilized as buffer layers to extract and transport charge carriers, such as TiO_x, CsO_x, SnO_2, ZnO (Tozlu et al., 2017; Tran et al., 2017; Wang et al., 2017; Jung et al., 2018). Due to the excellent electron extraction property, high electron mobility and easy processing, environment-friendly ZnO is widely used in the inverted PSCs (Vohra et al., 2015).. However, Sol-Gel processed ZnO films exhibit certain defects on the surface and inside, which limit the application as electron transport layer (ETL) in the highly efficient PSCs (Gu et al., 2014). These defects are apt to cause electron trap loss in PSCs, resulting in the severe charge carrier recombination loss. Additionally, poor contact between inorganic and organic materials also cause bad electrical contact, leading to recombination loss (Han et al., 2016).

To facilitate the electron extraction in PSCs, many attempts have been made to polish the interface between ZnO ETL and active layer (Zhang et al., 2018). The double-layer structure of ZnO/organic was developed to modify ZnO ETL and prevent direct contact of ZnO ETL with active layer (Zhang et al., 2018). Compared to pristine ZnO ETL, double-layer structure ZnO/organic ETL showed impressive enhancement in PCE. Following this principle, various materials, such as ionic liquids, polyelectrolytes, self-assembled monolayers, have been introduced to form double-layer structure ETL in PSCs (Dai et al., 2011; Zhang et al., 2018). However, new interfaces are introduced into the devices after the application of double-layer structure ETL, resulting in new interfacial contact. Thus, it is highly desirable but challenged to develop efficient and simple ETL in PSCs.

In order to address the above mentioned problems, we envisaging that modifying ZnO with suitable material would help to eliminate or passivate defects in ZnO films. To realize this, we noticed urea would be a good dopant candidate. This is because the possibility of formation of coordinate bonds between the lone pair of electrons on the two nitrogen atom of the amino groups and the Lewis acid sites of the ZnO surface would enable defects reducing.

In this work, urea-doped ZnO (U-ZnO) was investigated as an electron transport layer (ETL) in inverted PSCs with a blend of Poly{4,8-bis[(2-ethylhexyl)oxy]benzo[1,2-b:4,5-b']dithiophene-2,6-diyl-alt-3-fluoro-2-[(2-ethylhexyl)carbonyl]thieno[3,4-b]thiophene-4,6-diyl} (PTB7), and [6,6]-phenyl-C71-butyric acid methyl ester ($PC_{71}BM$) as active layer. With the device structure of ITO/ U-ZnO (40 nm)/PTB7:$PC_{71}BM$(95 nm)/MoO_3(5 nm)/Al (80 nm), an optimal PCE value of 9.15% was achieved, which is 15% higher than that of the pure ZnO ETL based reference device (7.76%). The performance enhancement of the U-ZnO ETL based PSCs may be attributed to the promotion of exciton dissociation, the suppression of charge recombination and the improvement of charge extraction capability. This investigation proves that the U-ZnO ETL offers promising potential for achieving high efficiency in PSCs.

EXPERIMENTAL

General Information

PTB7, $PC_{71}BM$, and MoO_3 were purchased from 1-Material Company of United States, Luminescence Technology Corporation of Taiwan and Rieke Company of China, respectively. Anhydrous zinc acetate [$Zn(CH_3COO)_2$] and 2-methoxyethanol ($CH_3OCH_2CH_2OH$) were obtained from Energy Chemical. Ethanolamine ($NH_2CH_2CH_2OH$) was purchased from Sigma-Aldrich Company. All materials and solvents were used as purchased without further purification.

Device Fabrication

To obtain the ZnO precursor solution, 0.836 g of $Zn(CH_3COO)_2$ and 0.28 g of $NH_2CH_2CH_2OH$ were dissolved in 10 mL of $CH_3OCH_2CH_2OH$. Different ratios of urea were added into $CH_3OCH_2CH_2OH$ to prepare the U-ZnO precursor. All the precursor solutions were stirred overnight in air. A blend of PTB7:$PC_{71}BM$ (1:1.5 *wt* %, 25 mg mL^{-1}) was dissolved in the mixed solvents of CB and DIO (97:3 *vol*%) and was stirred overnight at 50°C. Pre-patterned ITO substrates (15 Ω/square) were cleaned in detergent, acetone, and isopropanol for 30 min in sequence. Then the substrates were dried overnight in an oven with a temperature of 50°C. The ultraviolet-ozone treated ITO substrates were used to spin coat ZnO precursor or U-ZnO precursor at 4000 rpm in air. Then the ZnO-coated or ZnO-coated substrates were annealed at 200°C for 1 h in air. After that, the substrates were put into a N_2-filled glovebox for active layer spin-coating. Then the samples were quickly transfer into vacuum chamber for electrode deposition. Finally, 5 nm MoO_3 and 80 nm Al were deposited in a vacuum chamber with base press of 1×10^{-4} Pa.

Characterization

The current density-voltage (*J-V*) characteristics, PCE and external efficiency quantum (EQE) were recorded by a Newport solar simulator system. The *J-V* characteristics were recorded under AM 1.5G illumination with light intensity of 100 mW cm^{-2}. A calibrated silicon diode was set as the reference, which exhibited a response from 300 to 800 nm. The photoluminescence (PL) samples were measured by A Hitachi F-7000 spectrofluorophotometer.

RESULTS AND DISCUSSION

The device architecture of inverted PSCs was shown in **Figure 1A**, with a structure of ITO/U-ZnO(40 nm)/PTB7:$PC_{71}BM$(95 nm)/MoO_3(5 nm)/Al.
According to our previous study, the thicknesses of ETL

and active layer were set to the optimal values of 40 and 95 nm in the device fabrication, respectively(Zhang et al., 2018). The molecular structures of PTB7 and $PC_{71}BM$ were illustrated in **Figure 1B**.

As a ETL in PSCs, high transmittance is the priority, which is highly related to the photovoltaic performance. As shown in Supporting Information **Figure S1**, the U-ZnO ETLs show high transmittance, which is slightly lower than pure ZnO ETL. Moreover, Supporting Information **Figure S2** compares the light absorption in PTB7:$PC_{71}BM$ active layers. The light absorption spectra overlap each other, indicating good transmittance of U-ZnO ETL. To optimize the photovoltaic performance of PSCs, the urea doped concentration was tuned from 0 to 5 mg mL^{-1} in ZnO precursor solution. **Figure 2A** shows *J-V* characteristics and **Figure 2B** shows EQE photoresponse spectra of pure ZnO and U-ZnO ETLs based inverted PSCs. A summary of the corresponding photovoltaic parameters is listed in **Table 1**. The reference device exhibited an open circuit voltage(V_{oc}) of 0.73 V, a short circuit current density(J_{sc})of 15.38 mA/cm^2, a fill factor (FF) of 68.75%, and a PCE of 7.76%. In comparison with the reference device, the U-ZnO ETL based devices showed an obvious improvement in J_{sc} and FF, resulting in enhanced PCE. As a result of variations of J_{sc}, FF and V_{oc} in inverted PSCs, a champion efficiency of 9.15% was obtained with a V_{oc} of 0.74 V, a J_{sc} of 17.31 mA/cm^2, and a FF of 71.43% for the device using 3 mg mL^{-1} U-ZnO as the ETL. As listed in **Table 1**, the values of J_{sc}, FF and PCE were increased by increasing the concentration of urea from 0 to 3 mg mL^{-1} and then decreased at high concentration > 3 mg mL^{-1}. The increased J_{sc} was supported by the EQE profiles of the devices. The Supporting Information **Figure S3** plots the current density (16.86 mA/cm2) of champion cell calculated from EQE,

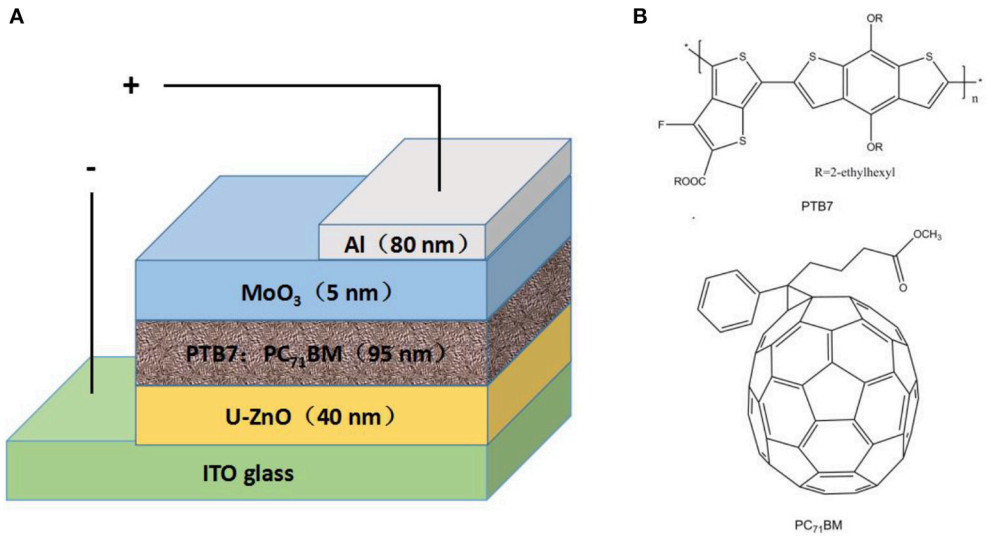

FIGURE 1 | (A) Device architecture of inverted polymer solar cells. **(B)** Molecular structures of PTB7 and $PC_{71}BM$.

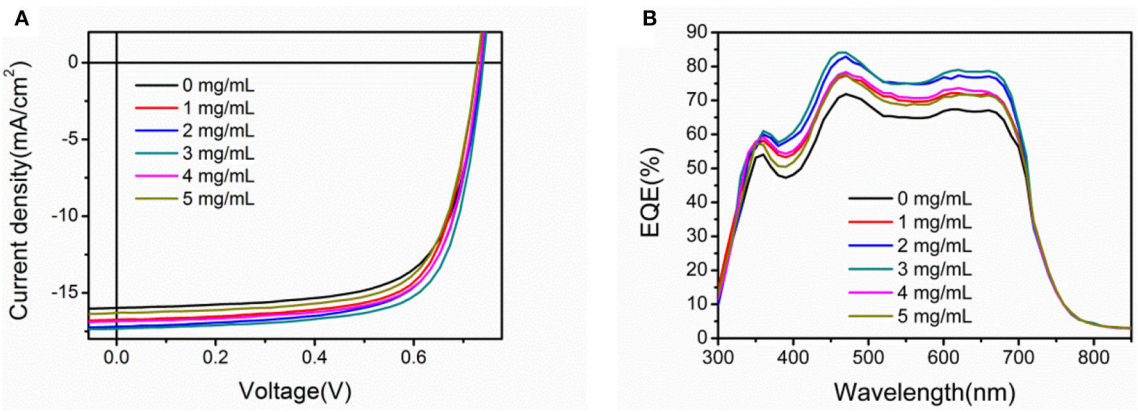

FIGURE 2 | (A) Illuminated *J-V* characteristics and **(B)** EQE spectra in inverted PSCs using different concentrations U-ZnO as the ETLs. The structure of PSCs is ITO/ETL(40 nm)/PTB7:$PC_{71}BM$(95 nm)/MoO_3(5 nm)/Al(80 nm).

showing lower discrepancy with the J_{sc} (17.31 mA/cm^2) extracted from *J-V* curve. The enhanced photovoltaic performance in PTB7:$PC_{71}BM$ based devices means the superior property of U-ZnO ETL in inverted PSCs.

To investigate the interface contact between U-ZnO ETL and active layer, the contact angle of water droplets on pure ZnO and U-ZnO ETLs were measured in this study (Zisman, 2008; Peng et al., 2017; Han et al., 2018). As shown in **Figure 3**, the contact angles of water on 0, 3, 5 mg mL^{-1} U-ZnO ETLs were 26, 31.5 and 29.5°, respectively. In comparison with pure ZnO ETL, the U-ZnO ETL show much higher hydrophobicity, resulting in better interface contact between ETLs and photoactive layers. Thus, the better interface contact is beneficial to the improved performance of U-ZnO ETL based inverted PSCs.

It is known that the morphology of ETL is critical in determining the performance of PSCs(Tran et al., 2017). Hence, the surfacemorphology of the ETLs without and with the urea-doping are studied by atomic force microscopy (AFM), and the top images are displayed in **Figure 4**. The Root-Mean-Square (RMS) roughness of ZnO ETL without urea-doping is 1.19 nm. The RMS roughness is decreased to 0.74 and 1.14 nm in U-ZnO with 3 mg mL^{-1} and 5 mg mL^{-1}, respectively. The smooth surface after urea-doping modifies the contact between ETLs and active layers, and infects the

TABLE 1 | Photovoltaic parameters of inverted PSCs based on PTB7:$PC_{71}BM$ using U-ZnO as the ETL under AM 1.5G irradiation (100 m W cm $^{-2}$). The values of J_{cal} are calculated from the related EQE spectra.

Concentration (mg mL^{-1})	V_{oc} (V)	$J_{sc}(J_{cal})$ (mA/cm^2)	*FF* (%)	*PCE* (%)	R_s (Ω cm^2)	R_{sh} (Ω cm^2)
0	0.73 ± 0.01	15.38 ± 0.22(14.95)	68.75 ± 1.0	7.76 ± 0.20	41	5470
1	0.73 ± 0.01	16.74 ± 0.13(16.26)	70.40 ± 0.2	8.59 ± 0.11	36	9627
2	0.73 ± 0.01	17.18 ± 0.16(16.81)	71.08 ± 0.8	8.67 ± 0.22	32	9932
3	0.73 ± 0.01	17.31 ± 0.09(16.86)	71.43 ± 0.6	9.00 ± 0.15	27	9785
4	0.73 ± 0.01	16.85 ± 0.11(16.57)	70.81 ± 0.8	8.76 ± 0.14	33	9404
5	0.73 ± 0.01	16.32 ± 0.10(15.97)	69.86 ± 0.7	8.29 ± 0.06	36	9501

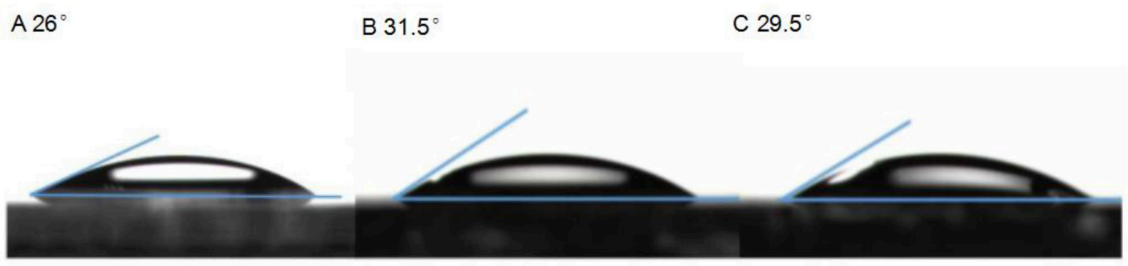

FIGURE 3 | The water contact angle (θ) of different ratios U-ZnO ETLs, **(A)** 0 mg mL^{-1}, **(B)** 3 mg mL^{-1}, **(C)** 5 mg mL^{-1}.

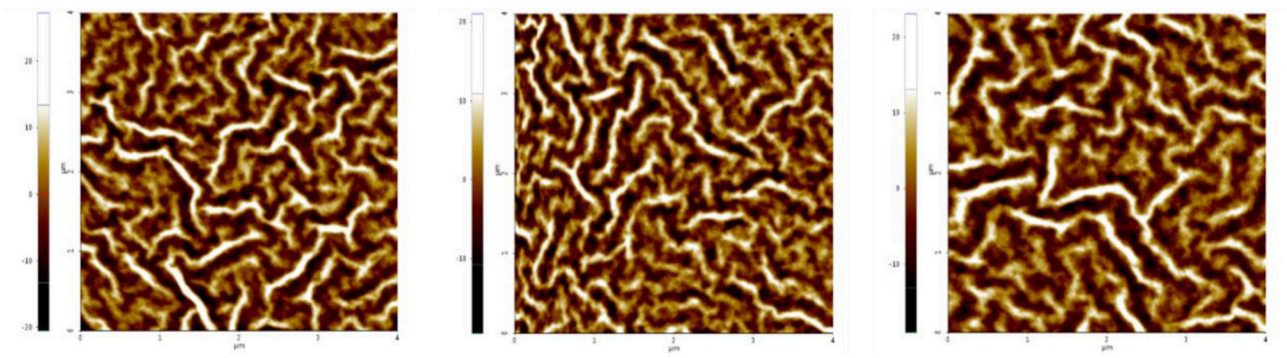

FIGURE 4 | AFM top images (4.0 × 4.0 μm^2) of the U-ZnO with different ratio of urea doping **(A)** 0 mg mL^{-1}, **(B)** 3 mg mL^{-1}, **(C)** 5 mg mL^{-1}. The structure of samples is ITO/U-ZnO (40 nm).

charge transport and collection in PSCs, leading to photocurrent improvement. On the other hand, the 2-D and 3-D images of PTB7:$PC_{71}BM$ active layers on U-ZnO ETLs are shown in Supporting Information **Figure S4**. AFM images of active layers reveal little morphology variation. The RMS surface roughness is slightly changed.

The space-charge-limited current (SCLC) method can be utilized to study the effect of urea on charge transport behavior inside the PSCs (Gupta et al., 2018). Hence, the electron mobility in ZnO and U-ZnO based devices were extracted by SCLC model. The electron-only device structures were ITO/ZnO or U-ZnO(40 nm)/PTB7:$PC_{71}BM$(95 nm)/BCP(8 nm)/Al. As shown in Supporting Information **Figure S5**, the electron-only device *J-V* characteristics were fitted by SCLC model. The electron mobility in PSCs based on 0, 3, 5 mg mL^{-1} urea-doping U-ZnO ETLs are 1.87×10^{-4}, 1.14×10^{-3}, and 3.84×10^{-4} cm^2 V^{-1} S^{-1}, respectively. The superior electron mobility after urea-doping is beneficial to the electrical properties in PSCs, leading to efficient charge transport and extraction.

To understand the contribution of U-ZnO ETL in PSCs, the dependence of *J-V* characteristics with incident light intensity were compared in U-ZnO ETL based devices (Xiao et al., 2018). The plots in **Figure 5A** were fitted with power law, then the values of α were obtained (Schilinsky et al., 2002). As shown in **Figure 5A**, each α value is close to unity, indicating efficient charge transport and collection in these inverted PSCs at short circuit condition (Huang et al., 2018). Slightly improved α was observed after introduction of urea in precursor solution, which means more efficient charge transport and collection in inverted PSCs using U-ZnO as the ETL.

Furthermore, photo generated charge carriers recombine again inside of cells under the open circuit condition, which directly reflects the recombination loss of cells. Therefore,the dependence of V_{oc} with incident light intensity was studied in this work. The V_{oc} shows linear dependence with semi logarithmic incident light intensity with a slope of $\frac{KT}{e}$ (Yang et al., 2018), where *K* is the Boltzmann constant, *T* is the temperature in Kelvin, and *e* is the elementary charge. **Figure 5B** shows the linear dependence of V_{oc} as a function with incident light intensity and the extracted slope. It can be seen from the extracted slope that the values of slope are decreased after adding urea into ZnO precursor. Compared to the slope of $1.23\frac{KT}{e}$ in PSCs using pure ZnO as the ETL, a smaller slope of $1.11\frac{KT}{e}$ is obtained when the concentration of urea in ZnO precursor solution is 3 mg mL^{-1}, indicating the suppressed interfacial trap defects of the U-ZnO ETL. Consequently, the introduction of urea in ZnO precursor solution could passivate the defects of Sol-Gel processed ZnO ETL, resulting in improved J_{sc} and FF in U-ZnO ETL based PSCs.

To further study the enhancement of J_{sc}, the maximum exciton generation rate (G_{max}) of PSCs was calculated in this study (Zhang et al., 2017). **Figure 6A** shows the dependence of photocurrent density (J_{ph}) with the effective voltage (V_{eff}). Apparently, two different regions were observed in J_{ph}-V_{eff} characteristics. Under low effective voltage, the J_{ph} shows linear dependence with V_{eff}. Then, it gradually approaches saturated value (J_{sat}) under high effective voltage. The values of G_{max} are showed in **Figure 6C**. An obvious improvement in G_{max} for U-ZnO ETL based PSCs is clearly seen in **Figure 6C**, which means efficient charge carrier transport and extraction. The enhanced G_{max} highly contributes to the enhanced J_{sc} in U-ZnO ETL based PSCs.

In organic PSCs, only a portion of excitons dissociate into free charge carriers due to the unique optoelectronic conversion behavior. The exciton dissociation probability *P* (*E*, *T*) is related to electric field (*E*) and temperature (*T*). Hence, the value of *P* (*E*, *T*) under zero bias is deduced from **Figure 6B**. The value of *P (E, T)* increased from 81.6% in the control device to 88.2% in the U-ZnO ETL based device, implying that U-ZnO ETL can promote excitons dissociation. The improved excitons dissociation probability also contributes to the enhancement of J_{sc}.

Due to the priority of exciton quenching in PSCs, photoluminescence (PL) spectra was used to analyze PL effect of pure ZnO and U-ZnO ETLs (Anger et al., 2006). **Figure 7A** shows the PL spectra of samples with a structure of ITO/ETL (40 nm)/PTB7 (50 nm)/MoO_3 (5 nm)/Al (10 nm). In comparison with pure ZnO ETL, significant enhancement of PL

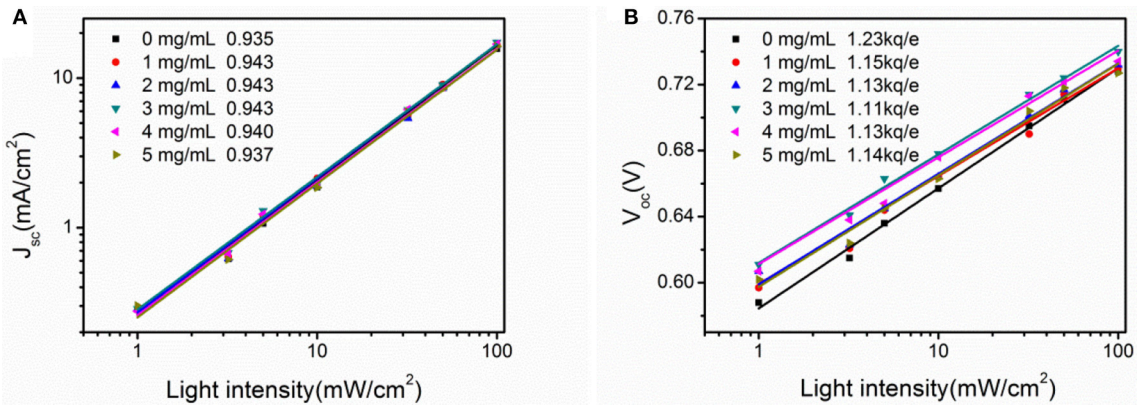

FIGURE 5 | (A) J_{SC} of inverted PSCs as a function incident light intensity and **(B)** V_{OC} of inverted PSCs as a function of incident light intensity.

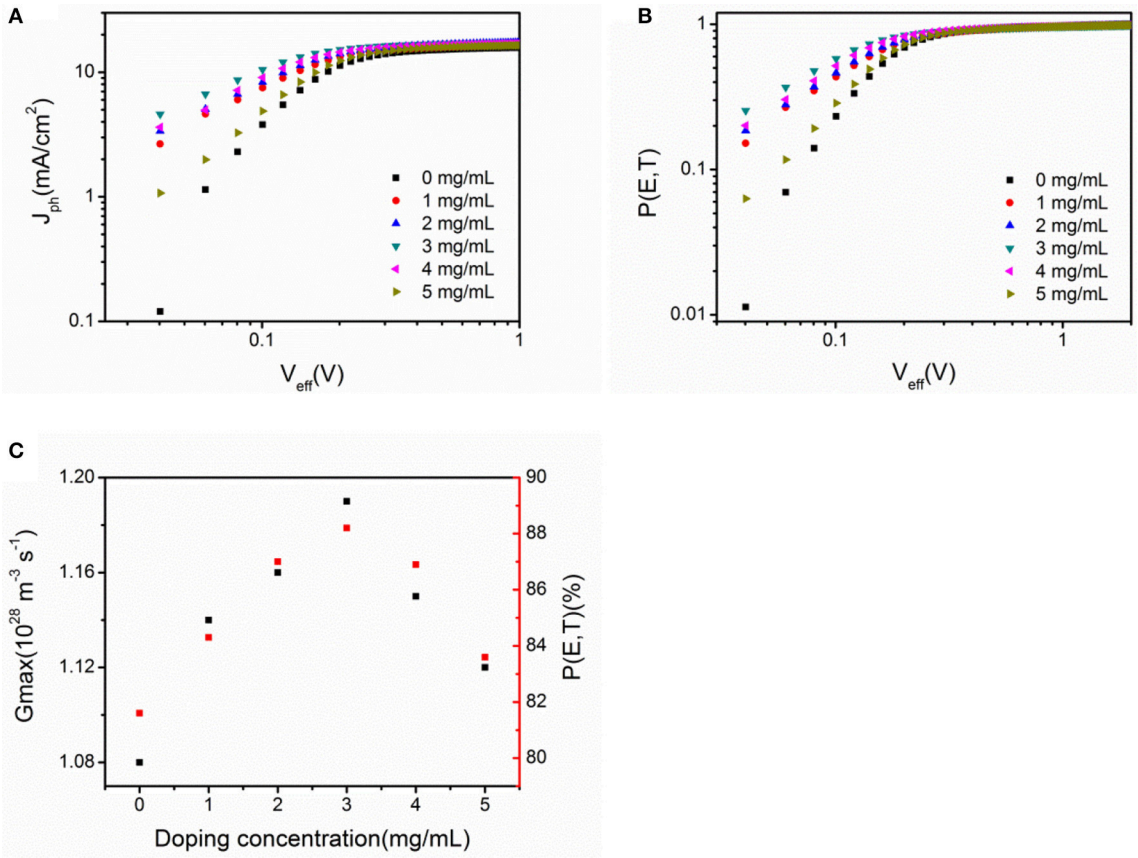

FIGURE 6 | (A) Photocurrent density (J_{ph}) as a function of the effective voltage (V_{eff}). **(B)** Exciton dissociation probability *P (E, T)* as a function of the effective voltage. **(C)** The values of G_{max} and *P (E, T)* obtained for inverted PSCs using U-ZnO as the ETL. All PSCs have an identical configuration of ITO/ETL(40 nm)/PTB7:PC_{71}BM(95 nm)/MoO_3(5 nm)/Al(80 nm).

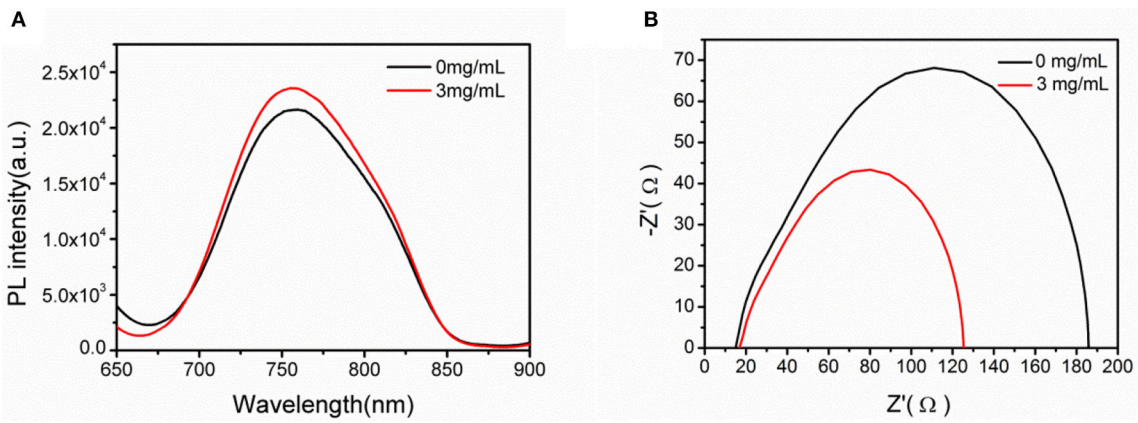

FIGURE 7 | (A) PL spectra measured for device with a geometry of ITO/ETL(40 nm)/PTB7 (50 nm)/MoO_3 (5 nm)/Al(10 nm) under photoexcitation of 600 nm at room temperature. **(B)** Impedance spectra (the Nyquist plot) of the devices with a structure of ITO/ETL(40 nm)/PTB7:PC_{71}BM (95 nm)/MoO_3 (5 nm)/Al (80 nm).

intensity was observed in the U-ZnO ETL based samples, which indicated suppressed exciton quenching at the interface of ETL and active layer. The suppressed exciton quenching is beneficial to the improvement of J_{sc}.

Electric impedance spectroscopy (EIS) is usually utilized to analyze the electrical behavior in PSCs (Zhang et al., 2018). Here, EIS spectrum is used to reveal the charge recombination inside of devices. The Nyquist plot of the impedance spectroscopy under

dark condition was plotted in **Figure 7B**. Shorter diameter was observed after introduction of urea, meaning a lower transport resistance in U-ZnO ETL based devices. The decreased transport resistance reflects better contact between U-ZnO ETL and active layer, resulting in an efficient charge transport probability. The EIS spectra analyses also prove the efficient charge transport and extraction in U-ZnO ETL based PSCs.

CONCLUSIONS

In summary, U-ZnO as the ETL was applied in PSCs. The advantages of U-ZnO ETL were analyzed in PTB7:$PC_{71}BM$ based inverted PSCs. The introduction of urea helps to passivate the defects of Sol-Gel processed ZnO ETL, polish the interface contact, and promote the exciton dissociation. In comparison with the devices using pure ZnO as the ETL, an impressive improvement was observed in PTB7:$PC_{71}BM$ based PSCs with the U-ZnO ETL. A champion efficiency of 9.15% was obtained with ∼15% enhancement compared to the efficiency of 7.76% in pure ZnO ETL based PSCs. Our results suggest that U-ZnO ETL have great potential in organic PSCs.

AUTHOR CONTRIBUTIONS

Device fabrication and photovoltaic performance studies were carried out by ZoW, RZ, and YW. ZhW, KG, HW, YH, and GC contributed to discussions. ZhW led the project, and prepared the manuscript. All authors contributed to the manuscript.

FUNDING

This study was supported by National Natural Science Foundation of China (NSFC) (Grant No. 61704118), Shanxi Provincial Natural Science Foundation of China (Grant No. 201601D021050). This study was also supported by the Qualified Personal Foundation of Taiyuan University of Technology (800101-02030017).

SUPPLEMENTARY MATERIAL

The Supplementary Material for this article can be found online at: https://www.frontiersin.org/articles/10.3389/fchem.2018.00398/full#supplementary-material

REFERENCES

Anger, P., Bharadwaj, P., and Novotny, L. (2006). Enhancement and quenching of single-molecule fluorescence. *Phys. Rev. Lett.* 96:113002. doi: 10.1103/PhysRevLett.96.113

Bi, P., Xiao, T., Yang, X., Niu, M., Wen, Z., Zhang, K., et al. (2018). Regulating the vertical phase distribution by fullerene-derivative in high performance ternary organic solar cells. *Nano Energy* 46, 81–90. doi: 10.1016/j.nanoen.2018.01.040

Cheng, J., Zhang, H., Zhao, Y., Mao, J., Li, C., Zhang, S., et al. (2018). Self-ssembled quasi-3d nanocomposite: a novel p-type hole transport layer for high performance inverted organic solar cells. *Adv. Funct. Mater.* 28:1706403. doi: 10.1002/adfm.201706403

Dai, T., Shino, T., Chen, X., Zhang, L., Li, J., Weis, M., et al. (2011). Analyzing carrier lifetime of double-layer organic solar cells by using optical electric-field-induced second-harmonic generation measurement. *Appl. Phys. Lett.* 98, 133507–1335013. doi: 10.1063/1.3574002

Gao, L., Zhang, Z. G., Xue, L., Min, J., Zhang, J., Wei, Z., et al. (2016). All-polymer solar cells based on absorption-complementary polymer donor and acceptor with high power conversion efficiency of 8.27%. *Adv. Mater.* 28, 1884–1890. doi: 10.1002/adma.201504629

Gu, C., Chen, Y., Zhang, Z., Xue, S., Sun, S., Zhong, C., et al. (2014). Achieving high efficiency of PTB7-based polymer solar cells via integrated optimization of both anode and cathode interlayers. *Adv. Funct. Mater.* 4, 1289–1295. doi: 10.1002/aenm.201301771

Gupta, M., Yan, D., Xu, J., Yao, J., and Zhan, C. (2018). Tetraphenylphosphonium bromide as cathode buffer layer material for highly efficient polymer solar cells. *ACS Appl. Mater. Interfaces* 10, 5569–5576. doi: 10.1021/acsami.7b17870

Han, C., Cheng, Y., Ling, C., Lei, Q., Yang, Z., Wei, X., et al. (2016). Enhanced performance of inverted polymer solar cells by combining ZnO nanoparticles and PFN as electron transport layer. *ACS Appl. Mater. Interfaces* 8, 3301–3307. doi: 10.1021/acsami.5b11140

Han, H., Seo, J., Song, M., Kim, H., and Kim, Y. (2018). Strong addition effect of n-type polymer with mid-energy level in polymer: fullerene solar cells with power conversion efficiency exceeding 10%. *J. Mater. Chem. A* 6, 7480–7487. doi: 10.1039/c8ta00147b

Hou, J., Inganäs, O., Friend, R. H., and Gao, F. (2018). Organic solar cells based on non-fullerene acceptors. *Nat. Mater.* 17, 119–128. doi: 10.1038/nmat5063

Huai, Z., Wang, L., Sun, Y., Fan, R., Huang, S., Zhao, X., et al. (2018). High-efficiency and stable organic solar cells enabled by dual cathode buffer layers. *ACS Appl. Mater. Interfaces* 10, 5682–5692. doi: 10.1021/acsami.7b15240

Huang, W., Cheng, P., Yang, Y. M., Li, G., and Yang, Y. (2018). High-performance organic bulk-heterojunction solar cells based on multiple-donor or multiple-acceptor components. *Adv. Mater.* 30:1705706. doi: 10.1002/adma.201705706

Jung, S., Lee, J., Seo, J., Kim, U., Choi, Y., and Park, H. (2018). Development of annealing-free, solution-processable inverted organic solar cells with n-doped graphene electrodes using zinc oxide nanoparticles. *Nano Lett.* 18, 1337–1343. doi: 10.1021/acs.nanolett.7b05026

Li, H., Zhao, Y., Fang, J., Zhu, X., Xia, B., Lu, K., et al. (2018). Improve the performance of the all-small-molecule nonfullerene organic solar cells through enhancing the crystallinity of acceptors. *Adv. Energy Mater.* 8:1702377. doi: 10.1002/aenm.201702377

Li, M., Gao, K., Wan, X., Zhang, Q., Kan, B., Xia, R., et al. (2017). Solution-processed organic tandem solar cells with power conversion efficiencies >12%. *Nat. Photon.* 11, 85–90. doi: 10.1038/nphoton.2016.240

Liu, D., Yang, B., Jang, B., Xu, B., Zhang, S., He, C., et al. (2017). Molecular design of a wide-band-gap conjugated polymer for efficient fullerene-free polymer solar cells. *Energy Environ. Sci.* 10, 546–551. doi: 10.1039/C6EE03489F

Liu, X., Li, X., Li, Y., Song, C., Zhu, L., Zhang, W., et al. (2016). High-performance polymer solar cells with PCE of 10.42% via Al-doped ZnO cathode interlayer. *Adv. Mater.* 28, 7405–7412. doi: 10.1002/adma.201601814

Liu, Z., Li, W., Peng, R., Jiang, W., Guan, Q., Lei, T., et al. (2017). Benzophenone-based small molecular cathode interlayers with various polar groups for efficient polymer solar cells. *J. Mater. Chem. A* 5, 10154–10160. doi: 10.1039/C7TA02427D

Peng, S., Huang, T., Gollavelli, G., and Hsu, C. (2017). Thiophene and diketopyrrolopyrrole based conjugated polymers as efficient alternatives to spiro-ometad in perovskite solar cells as hole transporting layers. *J. Mater. Chem. C* 5, 5193–5198. doi: 10.1039/c7tc00966f

Schilinsky, P., Waldauf, C., and Brabec, C. (2002). Recombination and loss analysis in polythiophene based bulk heterojunction photodetectors. *Appl. Phys. Lett.* 81, 3885–3887. doi: 10.1063/1.1521244

Sun, C., Wu, Z., Hu, Z., Xiao, J., Zhao, W., Li, H. W., et al. (2017). Interface design for high-efficiency non-fullerene polymer solar cells. *Energy Environ. Sci.* 10, 1784–1791. doi: 10.1039/c7ee00601b

Tozlu, C., Mutlu, A., Can, M., Havare, A. K., Demic, S., and Icli, S. (2017). Effect of TiO_2 modification with amino-based self-assembled monolayer on inverted organic solar cell. *Appl. Surf. Sci.* 422, 1129–1138. doi: 10.1016/j.apsusc.2017.06.128

Tran, V. H., Ambade, R. B., Ambade, S. B, Lee, S. H., and Lee, I. H. (2017). Low-temperature solution-processed SnO_2 nanoparticles as a cathode buffer layer for inverted organic solar cells. *ACS Appl. Mater. Interfaces* 9, 1645–1653. doi: 10.1021/acsami.6b10857

Vohra, V., Kawashima, K., Kakara, T., Koganezawa, T., Osaka, I., Takimiya, K., et al. (2015). Efficient inverted polymer solar cells employing favourable molecular orientation. *Nat. Photon.* 9, 403–408. doi: 10.1038/nphoton.2015.84

Wang, X., Zhao, X., Xu, G., Chen, Z., and Zhu, F. (2012). Degradation mechanisms in organic solar cells: localized moisture encroachment and cathode reaction. *Sol. Energy Mater. Sol. Cells* 104, 1–6. doi: 10.1016/j.solmat.2012.04.038

Wang, Y., Wu, B., Wu, Z., Lan, Z., Li, Y., Zhang, M., et al. (2017). Origin of efficient inverted nonfullerene organic solar cells: enhancement of charge extraction and suppression of bimolecular recombination enabled by augmented internal electric field. *J. Phys. Chem. Lett.* 8, 5264–5271. doi: 10.1021/acs.jpclett.7b02308

Wu, B., Wu, Z., Yang, Q., Zhu, F., Ng, T., Lee, C., et al. (2016). Improvement of charge collection and performance reproducibility in inverted organic solar cells by suppression of ZnO subgap states. *ACS Appl. Mater. Interfaces* 8, 14717–14724. doi: 10.1021/acsami.6b03619

Wu, Z., Sun, C., Dong, S., Jiang, X. F., Wu, S., Wu, H., et al. (2016). N-type water/alcohol-soluble naphthalene diimide-based conjugated polymers for high-performance polymer solar cells. *J. Am. Chem. Soc.* 138, 2004–2013. doi: 10.1021/jacs.5b12664

Xiao, J., Chen, Z., Zhang, G., Li, Q., Yin, Q., Jiang, X., et al. (2018). Efficient device engineering for inverted non-fullerene organic solar cells with low energy loss. *J. Mater. Chem. C* 6, 4457–4463. doi: 10.1039/c8tc00705e

Yang, Y., Qiu, B., Chen, S., Zhou, Q., Peng, Y., Zhang, Z., et al. (2018). High-efficiency organic solar cells based on a small-molecule donor and a low-bandgap polymer acceptor with strong absorption. *J. Mater. Chem. A* 6, 9613–9622. doi: 10.1039/c8ta01301b

Zhang, G., Zhang, K., Yin, Q., Jiang, X. F., Wang, Z., Xin, J., et al. (2017). High-performance ternary organic solar cell enabled by a thick active layer containing a liquid crystalline small molecule donor. *J. Am. Chem. Soc.* 139, 2387–2395. doi: 10.1021/jacs.6b11991

Zhang, K., Hu, Z., Sun, C., Wu, Z., Huang, F., and Cao, Y. (2016). Toward solution-processed high-performance polymer solar cells: from material design to device engineering. *Chem. Mater.* 29, 141–148. doi: 10.1021/acs.chemmater.6b02802

Zhang, R., Zhao, M., Wang, Z., Wang, Z., Zhao, B., Miao, Y., et al. (2018). Solution-processable ZnO/carbon quantum dots electron extraction layer for highly efficient polymer solar cells. *ACS Appl. Mater. Interfaces* 10, 4895–4903. doi: 10.1021/acsami.7b17969

Zisman, W. A. (2008). Relation of the equilibrium contact angle to liquid and solid constitution. *Adv. Chem.* 43, 1–51. doi: 10.1021/ba-1964-0043.ch001

Conflict of Interest Statement: The authors declare that the research was conducted in the absence of any commercial or financial relationships that could be construed as a potential conflict of interest.

frontiers in Chemistry

ORIGINAL RESEARCH
published: 04 September 2018
doi: 10.3389/fchem.2018.00328

Electron Acceptors With a Truxene Core and Perylene Diimide Branches for Organic Solar Cells: The Effect of Ring-Fusion

Kaiwen Lin†, Shiliang Wang†, Zhenfeng Wang, Qingwu Yin, Xi Liu, Jianchao Jia, Xiao'e Jia, Peng Luo, Xiaofang Jiang, Chunhui Duan, Fei Huang* and Yong Cao*

State Key Laboratory of Luminescent Materials and Devices, Institute of Polymer Optoelectronic Materials and Devices, South China University of Technology, Guangzhou, China

In this work, a star-shaped planar acceptor named FTr-3PDI was synthesized via ring-fusion between truxene core and three bay-linked perylene diimide (PDI) branches. Compared to the unfused non-planar acceptor Tr-3PDI, FTr-3PDI exhibits better structural rigidity and planarity, as well as more effective conjugation between truxene core and PDI branches. As a result, FTr-3PDI shows up-shifted energy levels, enhanced light absorption coefficient, increased electron mobility, and more favorable phase separation morphology in bulk-heterojunction (BHJ) blend films as compared to Tr-3PDI. Consequently, FTr-3PDI afforded higher power conversion efficiency (PCE) in BHJ solar cells when blended with a polymer donor PTB7-Th. This work demonstrates that ring-fusion is a promising molecular design strategy to combine the merits of truxene and PDI for non-fullerene acceptors used in organic solar cells.

Keywords: organic solar cells, star-shaped electron acceptors, truxene, perylene diimide, ring-fusion

OPEN ACCESS

Edited by:
Chuanlang Zhan,
Institute of Chemistry (CAS), China

Reviewed by:
Ling Teng Ye,
Harbin Institute of Technology, China
Gregory C. Welch,
University of Calgary, Canada

****Correspondence:***
Chunhui Duan
duanchunhui@scut.edu.cn
Fei Huang
msfhuang@scut.edu.cn

† These authors have contributed equally to this work

Specialty section:
This article was submitted to Organic Chemistry, a section of the journal Frontiers in Chemistry

Received: *26 April 2018*
Accepted: *12 July 2018*
Published: *04 September 2018*

Citation:
Lin K, Wang S, Wang Z, Yin Q, Liu X, Jia J, Jia X, Luo P, Jiang X, Duan C, Huang F and Cao Y (2018) Electron Acceptors With a Truxene Core and Perylene Diimide Branches for Organic Solar Cells: The Effect of Ring-Fusion. Front. Chem. 6:328. doi: 10.3389/fchem.2018.00328

INTRODUCTION

Recently, non-fullerene electron acceptors have received considerable attention in the community of organic solar cells (OSCs) due to their energy level tunability, intense optical absorption properties, and potential for low-cost and large-scale fabrication (Cheng et al., 2018; Hou et al., 2018; Yan et al., 2018). Among them, perylene diimide (PDI) derivatives are widely investigated in bulk-heterojunction (BHJ) OSCs because of their intense light absorption and high electron mobility (Zhan et al., 2007, 2011; Lin et al., 2014; Sun et al., 2015; Hendsbee et al., 2016; Liu J. et al., 2016; Liu Z. T. et al., 2016; Meng et al., 2016a). Despite these favorable properties, PDI monomer shows low device performance due to the formation of large aggregated nanostructure and undesired large crystalline domains caused by the large coplanar structure of PDI block, which hamper the exciton diffusion and separation process (Sharenko et al., 2013; Liu S. Y. et al., 2015). To overcome these drawbacks, an effective strategy is to develop non-coplanar PDI-based molecules via forming twisted intramolecular structures (Zhong et al., 2014, 2016; Lin et al., 2016; Zhang et al., 2016; Duan et al., 2017a; Liu X. et al., 2017; Liu et al., 2018). For example, a lot of star-shaped electron acceptors with PDI branches were reported recently based on this design guideline (Lin et al., 2014, 2016; Liu Y. H. et al., 2015; Lee et al., 2016; Duan et al., 2017a; Zhang A. D. et al., 2017). Although these star-shaped PDI electron acceptors can avoid forming large crystalline domains, their highly twisted architectures decrease the intermolecular contact and orbital overlapping between PDI π-planes, thus hampering electron hopping between molecules.

Therefore, the key point to develop high-performance PDI electron acceptors is to obtain a balance between highly twisted non-planar structures for forming proper phase separation in blend films and strong intermolecular interaction for supporting sufficient charge transport ability.

Recently, several studies showed that oxidative ring-fusion between the PDI branches and the central aromatic core of PDI-based molecules is an effective strategy to achieve such an exquisite balance (Hartnett et al., 2016; Meng et al., 2016b, 2017; Zhong et al., 2016; Wang B. et al., 2017; Zhang J. Q. et al., 2017). The resulting fused PDI molecules exhibit better structural rigidity and planarity, as well as more effective conjugation between the aromatic core and PDI branches. Meanwhile, the fused PDI molecules show stronger intermolecular π-π stacking and higher electron mobility. Moreover, these fused PDI acceptors can lead to desirable film morphology with proper domain size and high domain purity in BHJ blends when blended with donor polymers (Meng et al., 2016b, 2017; Wang B. et al., 2017; Zhang J. Q. et al., 2017). Therefore, the fused PDI acceptors display significantly improved photovoltaic performance compared to their carbon-carbon single bond connected counterparts (**Scheme 1**) (Li et al., 2016; Meng et al., 2016b, 2017; Liu X. F. et al., 2017; Wang B. et al., 2017; Zhang J. Q. et al., 2017). Actually, the best-performing OSCs based on PDI acceptors was achieved by a star-shaped fused PDI molecule named FTTB-PDI4, which afforded a power conversion efficiency (PCE) of 10.58% (Zhang J. Q. et al., 2017).

Among various central cores for star-shaped electron acceptors, truxene has been proved to be promising for constructing high-performance optoelectronic materials (Nielsen et al., 2013, 2014; Lin et al., 2018; Wu et al., 2018). The rigid coplanar structure and unique C_{3h} symmetry contribute to well-delocalized electronic structure in extended dimensionality for the resulting star-shaped conjugated molecules, which in turn result in strong light absorption and effective charge transport. Recently, Peng's group reported a state-of-the-art truxene-based electron acceptor for application in OSCs, which yielded impressive PCE exceeding 10% (Wu et al., 2018). These results suggested the promising prospect of truxene for constructing high-performance electron acceptors.

Inspired by these achievements, herein, we report the design and synthesis of two star-shaped acceptors named Tr-3PDI and FTr-3PDI, (**Scheme 2A**) where the truxene core and PDI branches are linked by carbon-carbon single bonds or via ring-fusion, respectively. We further evaluated their potential as electron acceptors in OSCs with poly[4,8-bis(5-(2-ethylhexyl)thiophen-2-yl)benzo[1,2-b;4,5-b]dithiophene-2,6-diyl-*alt*-(4-(2-ethylhexyl)-3-fluorothieno[3,4-b]thiophene)-2-carboxylate-2,6-diyl] (PTB7-Th) as the donor. The solar cells based on Tr-3PDI and FTr-3PDI exhibited a PCE of 2.2 and 3.8%, respectively. The better device performance of the fused acceptor FTr-3PDI is attributable to more favorable energy level alignment with the polymer donor PTB7-Th, more intense light absorption, stronger intermolecular packing, higher electron mobility, and more proper morphology in blend film. This work suggests the potential of ring-fusion strategy for constructing high performance PDI electron acceptors based on truxene core.

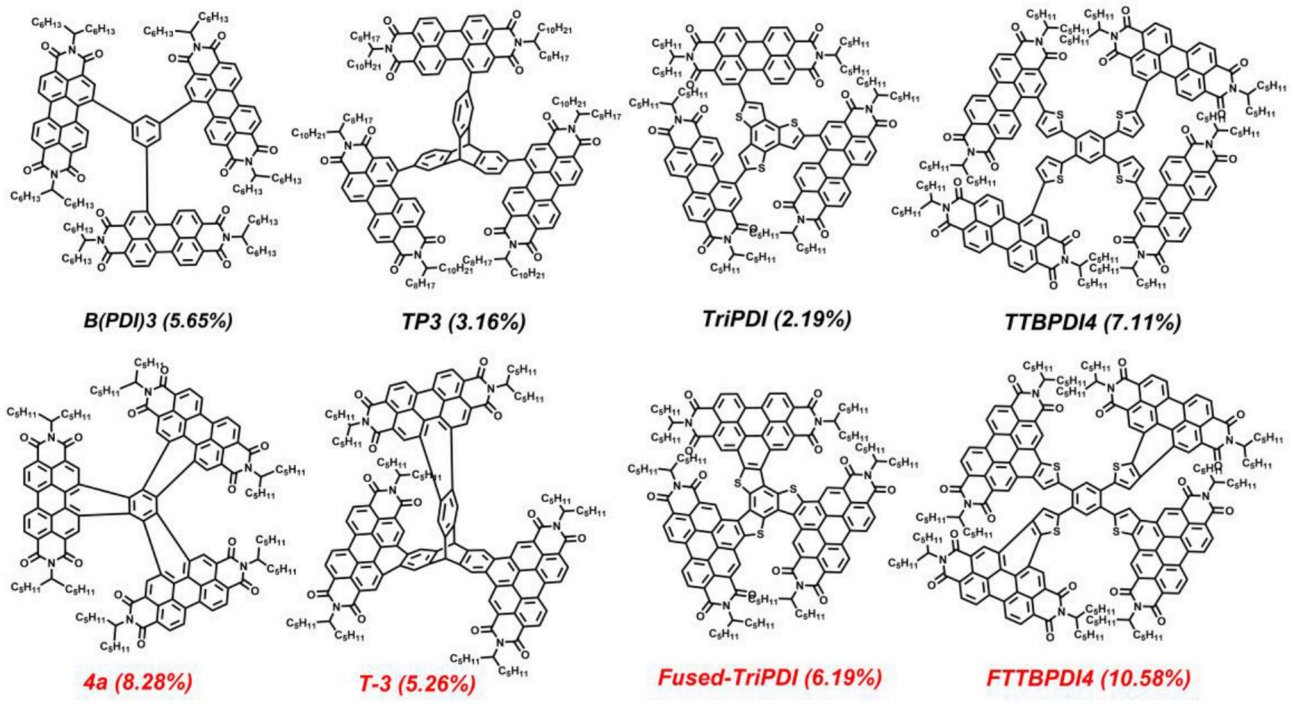

SCHEME 1 | The reported representative star-shaped electron acceptors with PDI branches linked by carbon-carbon single bonds and adjoin benzene rings.

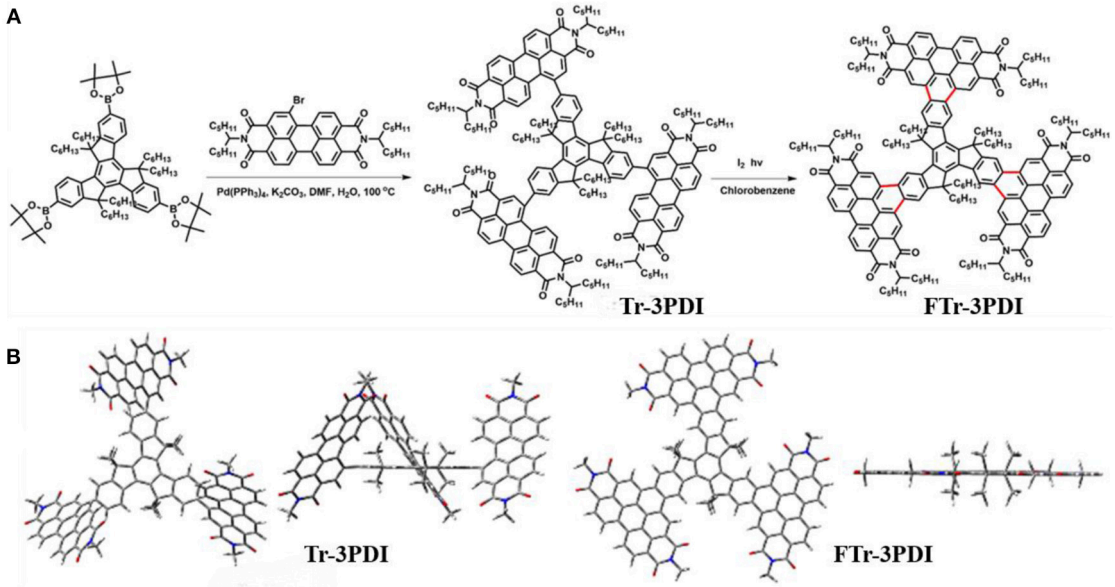

SCHEME 2 | (A) Synthetic routes and chemical structures of Tr-3PDI and Fused-Tr-3PDI; **(B)** views of the optimized geometries obtained using DFT calculations at the B3LYP/6-31G(d) level.

EXPERIMENTAL SECTION

Materials and Synthesis

All reagents were obtained from commercial sources and used without further purification, unless otherwise specified. **Scheme 2A** shows the synthetic routes of Tr-3PDI and FTr-3PDI. The detailed synthesis procedures are described as following.

Tr-3PDI

A mixture of 2,2′,2″-(5,5,10,10,15,15-hexahexyl-10,15-dihydro-5H-diindeno[1,2-a:1′,2′-c]fluorene-2,7,12-triyl)tris(4,4,5,5-tetramethyl-1,3,2-dioxaborolane (truxene boronic acid pinacol ester, 0.613 g, 0.5 mmol) and 5-Bromo-2,9-bis(1-pentylhexyl)anthra[2,1,9-def:6,5,10-d′e′f′]diisoquinoline-1,3,8, 10(2H,9H)-tetrone (monobromo-PDI, 1.746 g, 2.25 mmol) in anhydrous dimethylformamide (40 mL) was degassed for 30 min before $Pd(PPh_3)_4$ (58 mg, 0.05 mmol) and K_2CO_3 aqueous solution (2 M, 10 mL) was added. The solution was heated at 95°C for 48 h. Water and dichloromethane were added, and the organic layer was dried over $MgSO_4$. After removing the solvent, the crude product was chromatographically purified on silica gel column (eluted with ethyl acetate:petrolem ether = 1:20) to afford Tr-3PDI as a brownish-red solid (0.95 g, 65%). ^{1}H NMR (500 MHz, $CDCl_3$) δ: 8.74 (m, 18H), 8.60 (m, 6H), 7.62 (m, 6H), 5.25 (m, 6H), 3.04 (m, 6H), 2.17 (m, 30H), 1.29 (m, 112H), 0.86 (m, 72H). ^{13}C NMR (125MHz, $CDCl_3$) δ: 165.00, 163.91, 155.86, 155.72, 146.31, 142.03, 141.28, 140.62, 138.11, 135.10, 134.57, 132.77, 131.59, 129.98, 129.46, 128.77, 128.34, 127.78, 126.99, 126.80, 123.65, 122.84, 122.26, 56.45, 56.40, 54.95, 54.67, 37.20, 37.07, 32.52, 32.34, 31.91, 31.84, 31.83, 31.81, 31.59, 29.85, 29.80, 29.62, 29.39, 26.78, 26.69, 24.37, 24.13, 22.73, 22.66, 22.64, 22.60, 22.50, 22.43, 14.19,14.16, 14.14. MS (MALDI-TOF) calculated for $C_{201}H_{246}N_6O_{12}$, 2938.21; found, 2937.88.

FTr-3PDI

Tr-3PDI (293.7 mg, 0.1 mmol) was dissolved in 20 mL chlorobenzene before adding a catalytic amount of iodine (about 2 mg). The resultant mixture was stirred for 1 h under lab environment. After the reactivation process, kept the closed stand-up bottle exposing to irradiation of 500 W mercury lamp for 5 h at room temperature. The color of the solvent turned to brownish-yellow from brownish-red. After the reaction, the solvent was concentrated and the residue was purified by silica gel column chromatography (hexane:dichloromethane = 1:1) to afford a brownish-yellow solid (263.8 mg, 90%). ^{1}H NMR (500 MHz, $CDCl_3$) δ: 10.65 (m, 9H), 9.67 (s, 3H), 9.37 (m, 6H), 9.17 (m, 6H), 5.62 (m, 6H), 3.83 (m, 6H), 3.17 (m, 6H), 2.63 (m, 12H), 2.10 (m, 12H), 1.47 (m, 90H), 1.38 (m, 15H), 0.91 (m, 80H), 0.36 (m, 18H). ^{13}C NMR (125MHz, $CDCl_3$) δ: 165.06, 164.52, 155.41, 149.23, 141.71, 139.02, 134.27, 133.92, 129.76, 129.33, 128.73, 127.83, 127.71, 125.41, 125.27, 124.98, 123.50, 123.36, 119.83, 117.66, 57.60, 55.26, 38.26, 32.81, 32.03, 31.56, 29.57, 27.01, 24.91, 22.85, 22.81, 22.32, 14.30, 14.25, 13.84, 13.82. MS (MALDI-TOF) calculated for $C_{201}H_{240}N_6O_{12}$, 2932.16; found, 2931.94.

Instruments and Characterization

^{1}H and ^{13}C NMR spectra were tested on a Bruker AV-500 with tetramethylsilane (TMS) as an internal reference. MALDI-TOF-MS was performed by using a Bruker Agilent1290/maXis impact. UV-vis spectra were measured on a HP 8453 spectrophotometer. Thermogravimetric (TGA) analysis was measured on a

NETZSCH TG 209 at a heating rate of 10°C min^{-1} with a nitrogen flow rate of 20 mL min^{-1}. Cyclic voltammetry data were measured on a CHI600D electrochemical workstation with Bu_4NPF_6 (0.1 M) in acetonitrile as the electrolyte, a carbon electrode and a saturated calomel electrode as the working and reference electrodes, respectively. The thin films were coated on a glassy carbon working electrode. The scan rate was 100 mV s^{-1}. The geometry was optimized by Density Functional Theory (DFT) calculations performed at the B3LYP/6-31G(d) level to optimize the ground state geometries of the acceptor molecules using the Gaussian 09. The transient photocurrent of devices was measured by applying 500 nm laser pulses with a pulse width of 120 fs to the devices, which produced a transient voltage signal on a 50 Ω resistor and recorded by an oscilloscope (Tektronix EDS 3052C). The laser pulses were generated from optical parametric amplifier (TOPAS-Prime) pumped by a mode-locked Ti:sapphire oscillator seeded regenerative amplifier with a pulse energy of 1.3 mJ at 800 nm and a repetition rate of 1 KHz (Spectra Physics Spitfire Ace). The atom force microscopy (AFM) images were obtained from a NanoMan VS microscopy under tapping mode. The transmission electron microscopy (TEM) images were characterized with a JEM-2100F instrument.

Fabrication and Characterization of Solar Cells

The devices of indium tin oxide (ITO)/poly(3,4-ethylenedioxythiophene): poly(styrenesulfonate) (PEDOT:PSS)/PTB7-Th:acceptor/poly[(9,9-bis(3′-((N,N-dimethyl)-N-ethylammonium)-propyl)-2,7-fluorene)-*alt*-2,7-(9,9-dioctylfluorene)]dibromide (PFN-Br)/Al were fabricated through the following procedures. The ITO-coated glass substrate was cleaned in an ultrasonic bath with deionized water, acetone, and isopropanol, each process was approximately 15 min, and then dried under a stream of dry nitrogen. PEDOT:PSS (Heraeus Clevios PVPA 4083) was spin-coated on top of the above ITO and annealed in air at 150°C for 10 min. Subsequently, the blend solutions of PTB7-Th and truxene-PDI acceptors were prepared by simultaneously dissolving both materials with the optimized weight ratio in ortho-dichlorobenzene and spin-coated on the ITO/PEDOT:PSS electrode (at 1,600 rpm for 60 s) to form an active layer with thickness of about 100 nm. Then PFN-Br and Al layer were thermally deposited onto the active layer through a shadow mask at a vacuum of 5×10^{-5} Pa. During the test, an aperture with an area of 3.14 mm^2 was used. The current density–voltage (J–V) curves were measured on a computer-controlled Keithley 2400 source meter under 1 sun, the AM 1.5 G spectra came from a class solar simulator (Enlitech, Taiwan), and the light intensity was 100 mW cm^{-2} as calibrated by a China General Certification Center-certified reference monocrystal silicon cell (Enlitech). Before the J–V measurement, a physical mask with an aperture with precise area of 0.04 cm^2 was used to define the device area. The external quantum efficiency (EQE) spectra were measured on a commercial QE measurement system (QE-R3011, Enlitech).

Fabrication and Characterization of Single-Carrier Devices

The charge carrier mobilities of PTB7-Th:truxene-PDI acceptor blend films were determined from single-carrier devices with space-charge-limited current (SCLC) model. The device structures of the electron only and hole only devices are ITO/ZnO/PTB7-Th:acceptor/Ca/Al and ITO/PEDOT:PSS/PTB7-Th: acceptor/MoO_3/Ag respectively. The mobilities were determined by fitting the dark J–V current to the model of a single carrier SCLC using the equation: $J = 9\varepsilon_0\varepsilon_r\mu V^2/8d^3$, where J is the current density, d is the thickness of the blend films, ε_0 is the permittivity of free space, ε_r is the relative dielectric constant of the transport medium, and μ is the charge carrier mobility. $V = V_{app}$-V_{bi}, where V_{app} is the applied voltage and V_{bi} is the built-in voltage. The carrier mobility can be calculated from the slope of the $J^{1/2}$-V curves.

RESULTS AND DISCUSSION

Synthesis and Characterization

The synthetic routes to Tr-3PDI and FTr-3PDI are shown in **Scheme 2A**. Tr-3PDI was synthesized via Suzuki cross-coupling reaction between corresponding truxene boronic acid pinacol ester (Lin et al., 2018) and monobromo-PDI (Gao et al., 2017) using $Pd(PPh_3)_4$ as the catalyst. FTr-3PDI was obtained with an excellent yield (90%) from Tr-3PDI by dissolving in chlorobenzene containing a catalytic amount of iodine and exposed to irradiation. Tr-3PDI and FTr-3PDI are characterized by ^{1}H NMR, ^{13}C NMR, and mass spectra (Figures S1–S6). The optimized geometries of Tr-3PDI and FTr-3PDI are simulated using density functional theoretical (DFT) calculations at the B3LYP/6-31G(d) level (**Scheme 2B**). Clearly, Tr-3PDI exhibits higher twisted structure with a large dihedral angle over 50° owing to the steric hindrance effect. After the oxidative ring-fusion, each PDI moiety is tethered to truxene through benzene rings, resulting in an overall planarity structure because of the high rigidity and coplanarity of truxene core. Both acceptors are soluble in common organic solvents such as dichloromethane, chloroform, chlorobenzene, and ortho-dichlorobenzene at room temperature. The reason is that there are six hexyl chains on the truxene core, providing outstanding solubility for the resulting compounds.

The thermal properties of Tr-3PDI and FTr-3PDI were analyzed by thermogravimetric analysis (TGA) and differential scanning calorimetry (DSC). As shown in Figure S7, both truxene-PDI acceptors have decomposition temperature with 5% weight loss above 400°C. Moreover, there is no clear phase transition in DSC curves, which is indicative of the amorphous nature of Tr-3PDI and FTr-3PDI.

The UV-vis absorption spectra of the two acceptors in solutions and as thin films are shown in **Figure 1A**, Figure S8, and the relevant data are summarized in **Table 1**. Both Tr-3PDI and FTr-3PDI show two absorption bands with one in the short wavelength region of 300–400 nm and one in the longer wavelength region of 400–600 nm. The intense absorption in the short wavelength region is attributable to the large coplanar

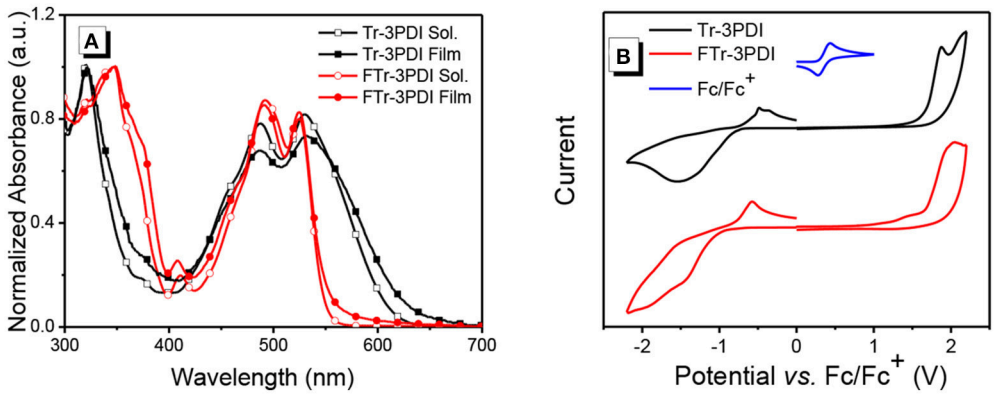

FIGURE 1 | (A) UV-vis absorption spectra of Tr-3PDI and FTr-3PDI in chloroform solutions and as thin films; **(B)** cyclic voltammograms of Tr-3PDI and FTr-3PDI.

TABLE 1 | Optical and electrochemical properties of Tr-3PDI and FTr-3PDI.

Acceptors	λ_{onset}^{film} (nm)	$E_g^{opt\ a}$ (eV)	E_{HOMO}^{b} (eV)	E_{LUMO}^{c} (eV)
Tr-3PDI	633	1.96	−6.09	−3.64
FTr-3PDI	556	2.23	−6.11	−3.44

[a]Calculated from $E_g^{opt} = 1240/\lambda_{onset}^{film}$ eV; [b]Calculated from $E_{HOMO} = -e(E_{ox}^{onse}$-$E_{Fc/Fc+}$+4.8) eV; [c]Calculated from $E_{LUMO} = -e(E_{red}^{onset}$-$E_{Fc/Fc+}$+4.8) eV.

core of truxene. FTr-3PDI shows little difference in normalized absorption spectra from the solution state to the film state, while the solid state Tr-3PDI has extended and redshifted absorption compared to the solution state. Notably, although the two compounds have very similar absorption maxima in both solution and solid state, FTr-3PDI shows considerably blue-shifted absorption onset as compared to Tr-3PDI, which could be related to the reduced conformational disorder via ring-fusion and then weakens the intramolecular charge transfer between truxene and PDI moieties. In addition, FTr-3PDI exhibits higher absorption coefficient than Tr-3PDI (Figure S8). The optical band gaps (E_g) are calculated to be 1.96 eV for Tr-3PDI, and 2.23 eV for FTr-3PDI (**Table 1**).

The energy levels of the acceptors were determined by cyclic voltammetry (CV) experiments. The half-wave potential of Fc/Fc^+ was measured to be 0.36 V, and the energy levels of the highest occupied molecular orbital (HOMO) and lowest unoccupied molecular orbital (LUMO) were estimated from the onset oxidation (E_{ox}^{onset}) and reduction (E_{red}^{onset}) potentials by equations: $E_{HOMO} = -e(E_{ox}^{onset}$-$E_{Fc/Fc+}$+4.8) and $E_{LUMO} = -e(E_{red}^{onset}$-$E_{Fc/Fc+}$+4.8), respectively (Li et al., 1999). The CV curves are shown in **Figure 1B**, and the relevant data are listed in **Table 1**. The HOMO/LUMO levels are −6.09/−3.64 eV for Tr-3PDI and −6.11/−3.44 eV for FTr-3PDI, respectively. The slightly up-shifted LUMO level of FTr-3PDI will help to offer a higher open-circuit voltage (V_{oc}), and the down-shifted HOMO level is favorable for hole transfer from excited acceptor phase to donor phase in BHJ OSCs (Duan et al., 2016a, 2017b, 2018; Jia et al., 2017).

Photovoltaic Properties

The photovoltaic properties of Tr-3PDI and FTr-3PDI were evaluated in OSCs under AM1.5G illumination at 100 mW cm^{-2} with a device structure of ITO/PEDOT:PSS/PTB7-Th:acceptor/PFN-Br/Ag (**Figure 2A**). PTB7-Th was used as the donor because of its strong optical absorption at long-wavelength region (Figure S9), which can achieve complementary absorption with our truxene-based acceptors (Zhang et al., 2015; McAfee et al., 2017; Welsh et al., 2018). The schematic energy diagram of individual components is displayed in **Figure 2B**, suggesting proper energy level alignment of each layer in the device. The devices were fully optimized in terms of host solvent, donor/acceptor weight ratios, active layer thickness, solvent additives, thermal annealing, and solvent annealing. The current density–voltage (J–V) curves of the optimized devices are shown in **Figure 2C**, and the photovoltaic parameters are summarized in **Table 1**. The device parameters under various conditions are collected in Tables S1–S8. The optimized device of Tr-3PDI afforded a PCE of 2.2% along with a V_{oc} of 0.92 V, a short-circuit current density (J_{sc}) of 6.5 mA cm^{-2}, and a fill factor (FF) of 0.37. The ring-fused acceptor FTr-3PDI produced a higher PCE of 3.8% along with a V_{oc} of 1.02 V, a J_{sc} of 8.1 mA cm^{-2}, and an FF of 0.46 (**Table 2**). The higher V_{oc} of FTr-3PDI is consistent with the up-shifted LUMO level. The difference in J_{sc} of the solar cells can be explained by their external quantum efficiency (EQE) spectra (**Figure 2D**) (Duan et al., 2016b; Wu et al., 2016). The PTB7-Th:FTr-3PDI blend film show higher EQE than PTB7-Th:Tr-3PDI almost in the whole spectral range of 300–800 nm, which is because of the enhanced light absorption of the former and more efficient charge generation. The PTB7-Th:FTr-3PDI device also shows higher FF than the PTB7-Th:Tr-3PDI device, suggesting improved charge transport, reduced charge recombination, and more optimal phase separated morphology (Duan et al., 2011; Xie et al., 2012).

Charge Transport and Recombination

The charge transport were investigated in single-carrier devices with a device structure of ITO/ZnO/ active layer /Ca/Al

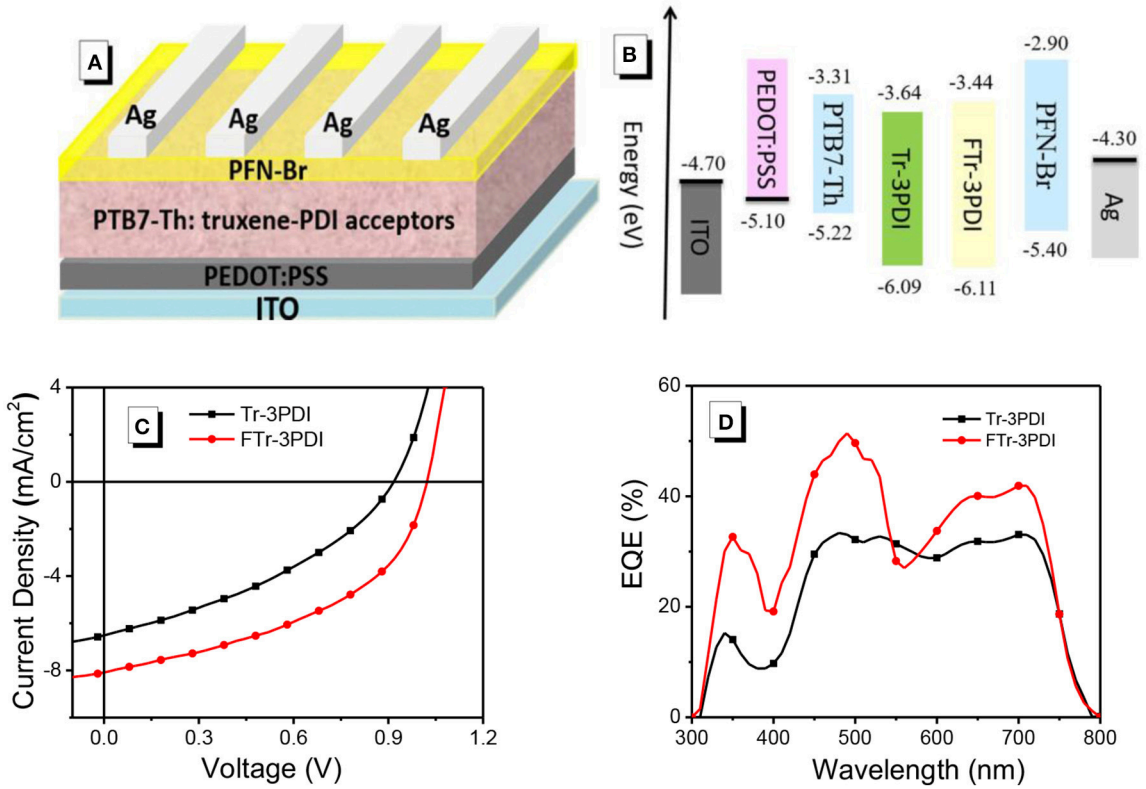

FIGURE 2 | (A) The device structure; **(B)** energy-level diagrams for all the materials used in this research; **(C)** *J–V* characteristics; and **(D)** EQE spectra of the OSCs based on PTB7-Th and truxene-PDI acceptors.

TABLE 2 | Photovoltaic parameters of OSCs based on PTB7-Th and truxene-PDI acceptors under AM1.5G illumination at 100 mW cm^{-2}.

Acceptor devices	V_{oc} (V)	J_{sc} (mA cm^{-2})	FF	PCE (%)
PTB7-Th: Tr-3PDI	0.92	6.5	0.37	2.2
PTB7-Th: FTr-3PDI	1.02	8.1	0.46	3.8

for electron only devices and ITO/PEDOT:PSS/ Active layer /MoO_3/Ag for hole only devices, respectively. The electron and hole mobilities were acquired by fitting the *J–V* with space-charge-limited current (SCLC) model. The *J–V* curves of the devices for pure acceptors and blend films are shown in Figures S10, S11. As shown in **Table 3**, the FTr-3PDI pure film exhibits higher electron mobility (μ_e) of 2.4 × 10^{-6} cm^2 V^{-1} s^{-1} than Tr-3PDI film (3.2 × 10^{-7} cm^2 V^{-1} s^{-1}), which support that the ring-fusion strategy is successful. As for blend films, the hole mobilities (μ_h) were estimated to be 1.2 × 10^{-3} cm^2 V^{-1} s^{-1} for PTB7-Th:Tr-3PDI and 8.2 × 10^{-3} cm^2 V^{-1} s^{-1} for PTB7-Th:FTr-3PDI, which are comparable with the value that obtained from PTB7-Th:fullerene devices (Huang et al., 2016). In contrast, theμ_e of the blend films of PTB7-Th:truxene-PDI acceptors were measured to be 5.8 × 10^{-6} cm^2 V^{-1} s^{-1} for PTB7-Th:Tr-3PDI and 1.3 × 10^{-5} cm^2 V^{-1} s^{-1} for PTB7-Th:FTr-3PDI, which are more than two orders of magnitude lower than that of PTB7-Th:fullerene film (Lin et al., 2015). The low electron mobility and highly imbalanced μ_e/μ_h seriously obstruct the charge transport and resulted in more bimolecular recombination, which in turn led to low FF and J_{sc}. For the solar cells with very imbalanced μ_e/μ_h, the device performance will be determined by the slower charge carrier, which is electron in these cases. The higher electron mobility in PTB7-Th:FTr-3PDI will thus result in better device performance.

To study the charge-recombination of these devices, we investigated the photocurrent (J_{sc}) as a function of light intensity (P_{in}, from 1 to 100 mW cm^{-2}), with the relevant characteristics plotted in **Figure 3A**. Generally, J_{sc} and P_{in} follow the relationship of $J_{sc} \propto P_{in}^{S}$. If all free carriers are swept out and collected at the electrodes prior to recombination, the slope (S) should be equal to 1, while $S<1$ indicates some extent of bimolecular recombination (Kyaw et al., 2013). The *S*-values of the two devices are 0.89 for PTB7-Th:FTr-3PDI and 0.88 for PTB7-Th:Tr-3PDI, respectively, which indicates the existence of some extent of bimolecular recombination. The charge recombination mechanism of the truxene-PDI-based OSCs are also investigated by estimating the slope (α) of V_{oc} vs. ln*P* (*P* is light intensity). In principle, the slope α approaching k_BT/q implies that the device has only bimolecular recombination, and the slope α approaching $2k_BT/q$

TABLE 3 | The relevant parameters related to charge transport and recombination of PTB7-Th: truxene-PDI acceptor devices.

Active layer	μ_h ($cm^2 V^{-1} s^{-1}$)	μ_e ($cm^2 V^{-1} s^{-1}$)	S	α	Charge-extraction time (μs)	Charge carrier lifetime (μs)
Tr-3PDI	–	3.2×10^{-7}	–	–	–	–
FTr-3PDI	–	2.4×10^{-6}	–	–	–	–
PTB7-Th:Tr-3PDI	1.2×10^{-3}	5.8×10^{-6}	0.88	2.1	0.15	9.72
PTB7-Th:FTr-3PDI	8.2×10^{-3}	1.3×10^{-5}	0.89	1.9	0.16	15.31

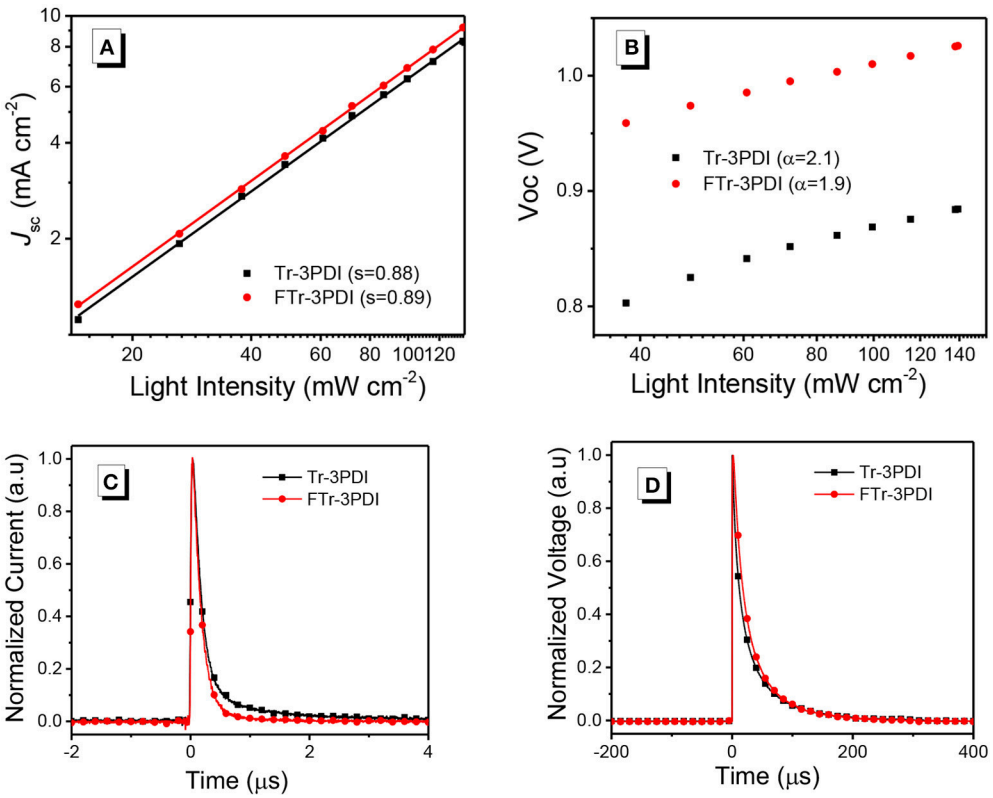

FIGURE 3 | (A) Current density vs. light intensity characteristics, and **(B)** open-circuit voltage vs. natural logarithm of light intensity characteristics for devices based on PTB7-Th and truxene-PDI acceptors; **(C)** transient photocurrent measurements; and **(D)** transient photovoltage of the relevant OSC devices.

suggests that the monomolecular recombination or trap-assisted recombination dominates in OSCs (where T, k_B, and q are the Kelvin temperature, Boltzmann constant, and elementary charge, respectively) (Koster et al., 2005; Lu et al., 2015). The α values for PTB7-Th:Tr-3PDI and PTB7-Th:FTr-3PDI are 2.1 and 1.9, respectively, which indicate considerable monomolecular recombination or trap-based recombination in these devices (**Figure 3B** and **Table 3**).

Transient photocurrent (TPC) and transient photovoltage (TPV) measurements were used to study the charge recombination dynamics and charge-extraction process in OSCs. From TPC analysis (**Figure 3C**), the charge-extraction time of the PTB7-Th:FTr-3PDI based device (0.15 μs) is slightly shorter than the PTB7-Th:Tr-3PDI based device (0.16 μs), suggesting increased charge extraction rate (Jin et al., 2016). From TPV analysis (**Figure 3D**), the charge carrier lifetime increased from 9.72 μs for the PTB7-Th:Tr-3PDI device to 15.31 μs for the PTB7-Th:FTr-3PDI device (**Table 3**), indicating reduced recombination loss for the PTB7-Th:FTr-3PDI device (Shuttle et al., 2008). The increased charge extraction rate and longer carrier lifetime thus explained the improved FF value and the higher PCE of the PTB7-Th:FTr-3PDI device.

Morphology Characterization

The morphology of the active layers was studied by atom force microscopy (AFM) and transmission electron microscopy (TEM). The AFM images and TEM images of the blend films are shown in **Figure 4**. The blend film of PTB7-Th:Tr-3PDI (**Figures 4A,C**) is homogeneous with a root-mean-square (RMS) surface roughness of 0.72 nm. The uniform film reveals intimately mixed blends without noteworthy phase

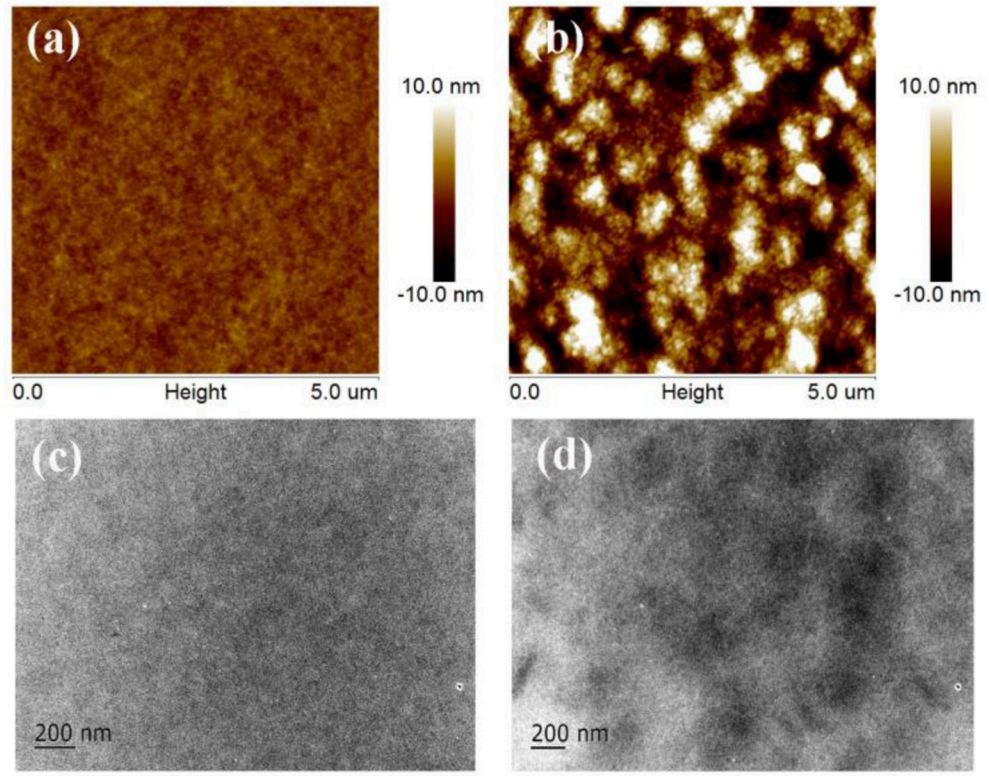

FIGURE 4 | AFM and TEM images of the blend films of PTB7-Th:truxene-PDI acceptor: **(A,C)** PTB7-Th:Tr-3PDI, **(B,D)** PTB7-Th:FTr-3PDI.

separation (Duan et al., 2017c; Wang J. Y. et al., 2017; Wen et al., 2018). With such a morphology, charge transport is impeded. The film of PTB7-Th:FTr-3PDI exhibits obvious phase separation with granulate features (**Figures 4B,D**), resulting in a relative coarse surface with a RMS surface roughness of 3.88 nm. The less phase-separated morphology of PTB7-Th:Tr-3PDI film could be a reason of the enhanced charge recombination and imbalanced hole/electron transport, which is in accordance with the analysis demonstrated above based on TPC, TPV, and charge carrier mobility measurements.

CONCLUSION

In summary, two electron acceptors with a truxene core and three PDIs branches linked by carbon-carbon single bonds (Tr-3PDI) or adjoin benzene ring (FTr-3PDI) are designed and developed. The FTr-3PDI shows up-shifted energy levels, enhanced absorption, improved charge mobility, and more favorable morphology as compared to Tr-3PDI. These merits further lead to higher V_{oc}, J_{sc}, and FF in resulting OSCs, respectively. The OSCs of PTB7-Th:FTr-3PDI blend shows a PCE of 3.8%, which is almost two times higher than that of PTB7-Th:Tr-3PDI blend. This work demonstrates a successful construction of star-shaped non-fullerene electron acceptor materials based on a truxene core and multiple PDI branches via ring-fusion to improve the performance of OSCs.

AUTHOR CONTRIBUTIONS

KL, FH and YC: Designed experiments; KL, SW, ZW, QY, XL, and XJ: Carried out experiments; JJ, XfJ, and PL: Analyzed experimental results; KL and CD: Wrote the manuscript.

FUNDING

This work was supported by the Ministry of Science and Technology (Nos. 2014CB643501, 2017YFA0206600). The research was also financially supported by the Recruitment Program of Global Youth Experts of China, the Natural Science Foundation of China (Nos. 21520102006 and 91633301).

SUPPLEMENTARY MATERIAL

The Supplementary Material for this article can be found online at: https://www.frontiersin.org/articles/10.3389/fchem.2018.00328/full#supplementary-material

REFERENCES

Cheng, P., Li, G., Zhan, X. W., and Yang, Y. (2018). Next-generation organic photovoltaics based on non-fullerene acceptors. *Nat. Photon*. 12, 131–142. doi: 10.1038/s41566-018-0104-9

Duan, C. H., Franeker, J. J., Wienk, M., and Janssen, R. A. J. (2016b). High open circuit voltage polymer solar cells enabled by employing thiazoles in semiconducting polymers. *Polym. Chem*. 7, 5730–5738. doi: 10.1039/c6py01083k

Duan, C. H., Gao, K., Colberts, F. J. M., Liu, F., Meskers, S. C. J., Janssen, R. A. J., et al. (2017b). Thiophene rings improve the device performance of conjugated polymers in polymer solar cells with thick active layers. *Adv. Energy Mater*. 7:1700519. doi: 10.1002/aenm.201700519

Duan, C. H., Guzmán, D., Colberts, F. J. M., Janssen, R. A. J., and Torres, T. (2018). Subnaphthalocyanines as electron acceptors in polymer solar cells: improving device performance by modifying peripheral and axial substituents. *Chem. Eur. J*. 24, 1–6. doi: 10.1002/chem.201800596

Duan, C. H., Wang, C. D., Liu, S. J., Huang, F., Choy, C. H. W., and Cao, Y. (2011). Two-dimensional like conjugated copolymers for high efficiency bulk-heterojunction solar cell application: band gap and energy level engineering. *Sci. China Chem*. 54, 685–694. doi: 10.1007/s11426-011-4257-3

Duan, C. H., Willems, R. E. M., Franeker, J. J., Bruijnaers, B. J., Wienk, M. M., and Janssen, R. A. J. (2016a). Effect of side chain length on the charge transport, morphology, and photovoltaic performance of conjugated polymers in bulk heterojunction solar cells. *J. Mater. Chem. A* 4, 1855–1866. doi: 10.1039/c5ta09483f

Duan, C. H., Zango, G., Iglesias, M. G., Martínez-Díaz, M. V., Janssen, R. A. J., Torres, T., et al. (2017c). The role of the axial substituent in subphthalocyanine acceptors for bulk-heterojunction solar cells. *Angew. Chem. Int. Ed*. 56, 148–152. doi: 10.1002/anie.201608644

Duan, Y. W., Xu, X. P., Yan, H., Wu, W. L., Li, Z. J., and Peng, Q. (2017a). Pronounced effects of a triazine core on photovoltaic performance-efficient organic solar cells enabled by a PDI trimer-based small molecular acceptor. *Adv. Mater*. 29:1605115. doi: 10.1002/adma.201605115

Gao, G. P., Liang, N. N., Geng, H., Jiang, W., Fu, H. T., Wang, Z. H., et al. (2017). Spiro-fused perylene diimide arrays. *J. Am. Chem. Soc*. 139, 15914–11592. doi: 10.1021/jacs.7b09140

Hartnett, P. E., Matte, H. S. S. R., Eastham, N. D., Jackson, N. E., Wasielewski, M. R., Marks, T. J., et al. (2016). Ring-fusion as a perylenediimide dimer design concept for high-performance non-fullerene organic photovoltaic acceptors. *Chem. Sci*. 7, 3543–3555. doi: 10.1039/c5sc04956c

Hendsbee, A. D., Sun, J. P., Law, W. K., Yan, H., Hill, I. G., and Welch, G., C. et al. (2016). Synthesis, self-assembly, and solar cell performance of N-annulated perylene diimide non-fullerene acceptors. *Chem. Mater*. 28, 7098–7109. doi: 10.1021/acs.chemmater.6b03292

Hou, J. H., Inganäs, O., Friend, R. H., and Gao, F. (2018). Organic solar cells based on non-fullerene acceptors. *Nat. Mater*. 17, 119–128. doi: 10.1038/NMAT5063

Huang, J., Carpenter, J. H., Li, C. Z., Yu, J. S., Ade, H., and Jen, A. K.-Y. (2016). Highly efficient organic solar cells with improved vertical donor–acceptor compositional gradient via an inverted off-center spinning method. *Adv. Mater*. 28, 967–974. doi: 10.1002/adma.201504014

Jia, J. C., Zheng, N. N., Wang, Z. F., Huang, Y. P., Duan, C. H., Huang, F., et al. (2017). The effect of end-capping groups in A-D-A type non-fullerene acceptors on device performance of organic solar cells. *Sci. China Chem*. 60, 1458–1467. doi: 10.1007/s11426-017-9102-1

Jin, Y. C., Chen, Z. M., Dong, S., Zheng, N. N., Ying, L., Huang, F., et al. (2016). A novel naphtho[1,2-c:5,6-c']Bis([1,2,5]Thiadiazole)-based narrow-bandgap π-conjugated polymer with power conversion efficiency over 10%. *Adv. Mater*. 28, 9811–9818. doi: 10.1002/adma.201603178

Koster, L. J. A., Mihailetchi, V. D., Ramaker, R., and Blom, P. W. M. (2005). Light intensity dependence of open-circuit voltage of polymer:fullerene solar cells. *Appl. Phys. Lett*. 86:123509. doi: 10.1063/1.1889240

Kyaw, A. K. K., Wang, D. H., Wynands, D., Zhang, J., Nguyen, T. Q., Bazan, G. C., et al. (2013). Improved light harvesting and improved efficiency by insertion of an optical spacer (ZnO) in solution-processed small-molecule solar cells. *Nano Lett*. 13, 3796–3801. doi: 10.1021/nl401758g

Lee, J., Singh, R., Sin, D. H., Kim, H. G., Song, K. C., and Cho, K. (2016). A nonfullerene small molecule acceptor with 3D interlocking geometry enabling efficient organic solar cells. *Adv. Mater*. 28, 69–76. doi: 10.1002/adma.201504010

Li, S. X., Liu, W. Q., Li, C. Z., Liu, F., Chen, H. Z., Russelld, T. P., et al. (2016). A simple perylene diimide derivative with a highly twisted geometry as an electron acceptor for efficient organic solar cells. *J. Mater. Chem. A* 4, 10659–10665. doi: 10.1039/c6ta04232e

Li, Y. F., Cao, Y., Gao, J., Wang, D. L., Yu, G., and Heeger, A. J. (1999). Electrochemical properties of luminescent polymers and polymer light-emitting electrochemical cells. *Synth. Met*. 99, 243–248. doi: 10.1016/S0379-6779(99)00007-7

Lin, H. R., Chen, S. S., Hu, H. W., Zhang, L., Ma, T. X., and Yan, H. (2016). Reduced intramolecular twisting improves the performance of 3D molecular acceptors in non-fullerene organic solar cells. *Adv. Mater*. 28, 8546–8551. doi: 10.1002/adma.201600997

Lin, K. W., Xie, B. M., Wang, Z. F., Duan, C. H., Huang, F., Cao, Y., et al. (2018). Star-shaped electron acceptors containing a truxene core for non-fullerene solar cells. *Org. Electron*. 52, 42–50. doi: 10.1016/j.orgel.2017.10.009

Lin, Y. Z., Wang, J. Y., Zhang, Z. G., Bai, H. T., Li, Y. F., Zhu, D. B., et al. (2015). An electron acceptor challenging fullerenes for efficient polymer solar cells. *Adv. Mater*. 27, 1170–1174. doi: 10.1002/adma.201404317

Lin, Y. Z., Wang, Y. F., Wang, J. Y., Hou, J. H., Li, Y. F., Zhu, D. B., et al. (2014). A star-shaped perylene diimide electron acceptor for high-performance organic solar cells. *Adv. Mater*. 26, 5137–5142. doi: 10.1002/adma.201400525

Liu, J., Chen, S. S., Qian, D. P., Gautam, B., Gundogdu, K., Gao, F., Yan, H., et al. (2016). Fast charge separation in a non-fullerene organic solar cell with a small driving force. *Nat. Energy* 1, 1–7. doi: 10.1038/NENERGY.2016.89

Liu, S. Y., Wu, C. H., Li, C. Z., Liu, S. Q., Wei, K. H., Chen, H. Z., et al. (2015). A tetraperylene diimides based 3D nonfullerene acceptor for efficient organic photovoltaics. *Adv. Sci*. 2:1500014. doi: 10.1002/advs.201500014

Liu, X., Liu, T., Duan, C. H., Sun, Y. M., Huang, F., Cao, Y., et al. (2017). Non-planar perylenediimide acceptors with different geometrical linker units for efficient nonfullerene organic solar cells. *J. Mater. Chem. A* 5, 1713–1723. doi: 10.1039/c6ta08739f

Liu, X. F., Cai, Y. H., Huang, X. B., Zhang, R. B., and Sun, X. B. (2017). A perylene diimide electron acceptor with a triptycene core for organic solar cells. *J. Mater. Chem. C* 5, 3188–3194. doi: 10.1039/c7tc00378a

Liu, Y. H., Mu, C., Jiang, K., Zhao, J. B., Li, Y. K., Yan, H., et al. (2015). A tetraphenylethylene core-based 3D structure small molecular acceptor enabling efficient non-fullerene organic solar cells. *Adv. Mater*. 27, 1015–1020. doi: 10.1002/adma.201404152

Liu, Z. T., Wu, Y., Zhang, Q., and Gao, X. (2016). Non-fullerene small molecule acceptors based on perylene diimides. *J. Mater. Chem. A* 4, 17604–17622. doi: 10.1039/c6ta06978a

Liu, Z. T., Zhang, L. H., Shao, M., Wu, Y., Zeng, D., Gao, X., et al. (2018). Fine-tuning the quasi-3D geometry: enabling efficient nonfullerene organic solar cells based on perylene diimides. *ACS Appl. Mater. Interfaces* 10, 762–768. doi: 10.1021/acsami.7b16406

Lu, L. Y., Chen, W., Xu, T., and Yu, L. P. (2015). High-performance ternary blend polymer solar cells involving both energy transfer and hole relay processes. *Nat. Commun*. 6:7327. doi: 10.1038/ncomms8327

McAfee, S. M., Dayneko, S. V., Josse, P., Blanchard, P., Cabanetos, C., and Welch, G. C. (2017). Simply complex: the efficient synthesis of an intricate molecular acceptor for high-performance air-processed and air-tested fullerene-free organic solar cells. *Chem. Mater*. 29, 1309–1314. doi: 10.1021/acs.chemmater.6b04862

Meng, D., Fu, H. T., Fan, B. B., Li, Y., Sun, Y. M., Wang, Z. H., et al. (2017). Rigid nonfullerene acceptors based on triptycene–perylene dye for organic solar cells. *Chem. Asian J*. 12, 1286–1290. doi: 10.1002/asia.201700440

Meng, D., Fu, H. T., Xiao, C. Y., Meng, X. Y., Sun, Y. M., Wang, Z. H., et al. (2016b). Three-bladed rylene propellers with three-dimensional network assembly for organic electronics. *J. Am. Chem. Soc*. 138, 10184–10190. doi: 10.1021/jacs.6b04368

Meng, D., Sun, D., Zhong, C. M., Sun, Y. M., Wang, Z. H., et al. (2016a). High-performance solution-processed non-fullerene organic solar cells based on selenophene-containing perylene bisimide acceptor. *J. Am. Chem. Soc*. 138, 375–380. doi: 10.1021/jacs.5b11149

Nielsen, C. B., Voroshazi, E., Holliday, S., Cnops, K., Cheyns, D., and McCulloch, I. (2014). Electron-deficient truxenone derivatives and their use in organic photovoltaics. *J. Mater. Chem. A* 2, 12348–12354. doi: 10.1039/c4ta01653j

Nielsen, C. B., Voroshazi, E., Holliday, S., Cnops, K., Randb, B. P., and McCulloch, I. (2013). Efficient truxenone-based acceptors for organic photovoltaics. *J. Mater. Chem. A* 1, 73–76. doi: 10.1039/c2ta00548d

Sharenko, A., Proctor, C. M., Poll, T. S. V., Henson, Z. B., Nguyen, T.-Q., and Bazan, G. C. (2013). A high-performing solution-processed small molecule: perylene diimide bulk heterojunction solar cell. *Adv. Mater*. 25, 4403–4406. doi: 10.1002/adma.201301167

Shuttle, C. G., O'Regan, B., Ballantyne, A. M., Nelson, J., Bradley, D. D. C., de Mello, J., et al. (2008). Experimental determination of the rate law for charge carrier decay in a polythiophene: fullerene solar cell. *Appl. Phys. Lett*. 92:093311. doi: 10.1063/1.2891871

Sun, D., Meng, D., Cai, Y. H., Huo, L. J., Sun, Y. M., Wang, Z. H., et al. (2015). Non-fullerene-acceptor-based bulk-heterojunction organic solar cells with efficiency over 7%. *J. Am. Chem. Soc*. 137, 11156–11162. doi: 10.1021/jacs.5b06414

Wang, B., Liu, W. Q., Li, H. B., Mai, J. Q., Li, C. Z., Chen, H. Z., et al. (2017). Electron acceptors with varied linkages between perylene diimide and benzotrithiophene for efficient fullerene-free solar cells. *J. Mater. Chem. A* 5, 9396–9401. doi: 10.1039/C7TA02582C

Wang, J. Y., Wang, S. L., Duan, C. H., Lu, X. H., Janssen, R. A. J., Huang, F., et al. (2017). Conjugated polymers based on difluorobenzoxadiazole toward practical application of polymer solar cells. *Adv. Energy Mater*. 7:1702033. doi: 10.1002/aenm.201702033

Welsh, T. A., Laventure, A., Baumgartner, T., and Welch, G. C. (2018). Dithienophosphole-based molecular electron acceptors constructed using direct (hetero)arylation cross-coupling methods. *J. Mater. Chem. C* 6, 2148–2154. doi: 10.1039/c7tc05631a

Wen, S. G., Wu, Y., Wang, Y. Y., Li, Y., Liu, Z. T., Yang, R. Q., et al. (2018). Pyran-bridged indacenodithiophene as a building block for constructing efficient A–D–A-type nonfullerene acceptors for polymer solar cells. *ChemSusChem* 11, 360–366. doi: 10.1002/cssc.201701917

Wu, W. L., Zhang, G. J., Xu, X. P., Wang, S. C., Li, Y., and Peng, Q. (2018). Wide bandgap molecular acceptors with a truxene core for efficient nonfullerene polymer solar cells: linkage position on molecular configuration and photovoltaic properties. *Adv. Funct. Mater*. 28, 1707493. doi: 10.1002/adfm.201707493

Wu, Z. H., Zhu, Y. X., Li, W., Huang, Y. P., Duan, C. H., Huang, F., et al. (2016). Design, synthesis and photovoltaic properties of a series of new acceptor-pended conjugated polymers. *Sci. China Chem*. 59, 1583–1592. doi: 10.1007/s11426-016-0203-5

Xie, H. M., Zhang, K., Duan, C. H., Liu, S. J., Huang, F., and Cao, Y. (2012). New acceptor-pended conjugated polymers based on 3,6- and 2,7-carbazole for polymer solar cells. *Polymer* 53, 5675–5683. doi: 10.1016/j.polymer.2012.10.008

Yan, C. Q., Barlow, S., Wang, Z. H., Yan, H., Jen, A. K.-Y., Marder, S. R., et al. (2018). Non-fullerene acceptors for organic solar cells. *Nat. Rev. Mater*. 3:18003. doi: 10.1038/natrevmats.2018.3

Zhan, X. W., Facchetti, A., Barlow, S., Marks, T. J., Ratner, M. A., Wasielewski, M. R., et al. (2011). Rylene and related diimides for organic electronics. *Adv. Mater*. 23, 268–284. doi: 10.1002/adma.201001402

Zhan, X. W., Tan, Z. A., Domercq, B., An, Z. S., Zhang, X., Barlow, S., et al. (2007). A high-mobility electron-transport polymer with broad absorption and its use in field-effect transistors and all-polymer solar cells. *J. Am. Chem. Soc*. 129, 7246–7247. doi: 10.1021/ja071760d

Zhang, A. D., Li, C., Yang, F., Zhang, J. Q., Wang, Z. H., Wei, Z. X., et al. (2017). An electron acceptor with porphyrin and perylene bisimides for efficient non-fullerene solar cells. *Angew. Chem. Int. Ed*. 56, 2694–2698. doi: 10.1002/anie.201612090

Zhang, J. Q., Li, Y. K., Huang, J. C., Hu, H. W., Zhang, G. Y., Yan, H.e., et al. (2017). Ring-fusion of perylene diimide acceptor enabling efficient nonfullerene organic solar cells with a small voltage loss. *J. Am. Chem. Soc*. 139, 16092–16095. doi: 10.1021/jacs.7b09998

Zhang, X., Yao, J. N., and Zhan, C. L. (2016). Synthesis and photovoltaic properties of low bandgap dimeric perylene diimide based non-fullerene acceptors. *Sci. China Chem*. 59, 209–217. doi: 10.1007/s11426-015-5485-8

Zhang, X., Zhan, C. L., and Yao, J. N. (2015). Non-fullerene organic solar cells with 6.1% efficiency through fine-tuning parameters of the film-forming process. *Chem. Mater*. 27, 166–173. doi: 10.1021/cm504140c

Zhong, H. L., Wu, C. H., Li, C. Z., Carpenter, J., Chueh, C.-C., Jen, A. K.-Y., et al. (2016). Rigidifying nonplanar perylene diimides by ring fusion toward geometry-tunable acceptors for high-performance fullerene-free solar cells. *Adv. Mater*. 28, 951–958. doi: 10.1002/adma.201504120

Zhong, Y. U., Trinh, M. T., Xiao, S. X., Ng, F., Zhu, X. Y., Nuckolls, C., et al. (2014). Efficient organic solar cells with helical perylene diimide electron acceptors. *J. Am. Chem. Soc*. 136, 15215–15221. doi: 10.1021/ja5092613

Conflict of Interest Statement: The authors declare that the research was conducted in the absence of any commercial or financial relationships that could be construed as a potential conflict of interest.

frontiers in Chemistry

ORIGINAL RESEARCH
published: 30 August 2018
doi: 10.3389/fchem.2018.00384

Fluorination Induced Donor to Acceptor Transformation in A1–D–A2–D–A1-Type Photovoltaic Small Molecules

Ruimin Zhou[1,2,3,4†], *Benzheng Xia*[1†], *Huan Li*[1], *Zhen Wang*[1], *Yang Yang*[1], *Jianqi Zhang*[1], *Bo W. Laursen*[4], *Kun Lu*[1*] and *Zhixiang Wei*[1*]

[1] CAS Key Laboratory of Nanosystem and Hierarchical Fabrication, CAS Center for Excellence in Nanoscience, National Center for Nanoscience and Technology, Beijing, China, [2] Sino-Danish College, University of Chinese Academy of Sciences, Beijing, China, [3] Sino-Danish Center for Education and Research, Beijing, China, [4] Nano-Science Center & Department of Chemistry, University of Copenhagen, Copenhagen, Denmark

With the development of diversity of non-fullerene acceptors, it is found that there is no clear boundary between electron donors and electron acceptors. Modulation of the electron donating and withdrawing properties of organic semiconductors is necessary for organic photovoltaics research. In this work, we designed and synthesized three A1–D–A2–D–A1-type (A represents acceptor unit and D represents donor unit) small molecules, named as M-0F, M-1F, and M-2F, respectively containing zero, one, and two fluorine atoms in the terminal acceptor segments (A1), respectively. Fluorination substitution was found to be able to downshift the HOMO and LUMO energy level, red-shift the absorption, and enhance the electron mobility. The M-0F exhibited the highest efficiency of 5.99% as a donor in fullerene-containing system and the lowest efficiency of 0.58% as an acceptor in fullerene-free system. While the M-2F performed the lowest efficiency of 0.97% as the donor and the highest efficiency of 2.65% as the acceptor. The electron-donating and electron-withdrawing property of M-1F are in-between that of M-0F and M-2F. Among the three molecules, the electron mobility is increased while the hole mobility is decreased with increasing fluorination. This work provides a typical example of tuning of the electron donating and withdrawing property without changes to the backbone of the conjugated molecules, which is important for further designing high performance solution processable small molecules.

Keywords: organic photovoltaics, small molecules, fluorination substitution, donors, acceptors

OPEN ACCESS

Edited by:
Chuanlang Zhan,
Institute of Chemistry (CAS), China

Reviewed by:
Yingping Zou,
Central South University, China
Hui Huang,
University of Chinese Academy of Sciences (UCAS), China

***Correspondence:**
Kun Lu
lvk@nanoctr.cn
Zhixiang Wei
weizx@nanoctr.cn

† These authors share joint first authorship

Specialty section:
This article was submitted to Organic Chemistry, a section of the journal Frontiers in Chemistry

Received: *12 June 2018*
Accepted: *09 August 2018*
Published: *30 August 2018*

Citation:
Zhou R, Xia B, Li H, Wang Z, Yang Y, Zhang J, Laursen BW, Lu K and Wei Z (2018) Fluorination Induced Donor to Acceptor Transformation in A1–D–A2–D–A1-Type Photovoltaic Small Molecules. Front. Chem. 6:384. doi: 10.3389/fchem.2018.00384

INTRODUCTION

The bulk-heterojunction (BHJ) organic solar cells (OSCs) show a promising prospect for low-cost and renewable energy technology because of their unique advantages of light weight, easy-fabrication, and the capability to be fabricated into large area flexible devices (Forrest, 2004; Brabec et al., 2010; Kumar and Chand, 2012). In a typical BHJ organic photovoltaic (OPV) device, the heterojunction usually consists of a p-type electron donor and an n-type electron acceptor, which is the photoactive part for converting solar light to electricity. The p-type electron donor can be polymers or organic small molecules. The n-type electron acceptors include fullerene derivatives,

such as [6, 6]-phenyl-C_{61}/C_{71}-butyric acid methyl ester ($PC_{61}BM$/$PC_{71}BM$) and non-fullerene electron acceptors. For a highly-efficient BHJ OPV, its active layer should possess the following features: (a) a broad absorption spectrum with a high extinction coefficient to utilize more solar photons; (b) a suitable molecular energy level alignment between the involved molecular orbitals on donor and acceptor to offer a sufficient driving force for efficient charge separation; (c) a bicontinuous network with nanoscale phase separation to facilitate exciton diffusion and charge separation; and (d) high charge mobility to facilitate charge transport (Scharber et al., 2006; Chen and Cao, 2009; Cheng et al., 2009; Beaujuge and Frechet, 2011; Henson et al., 2012; Li, 2012; Xu and Yu, 2014; Etxebarria et al., 2015; Zhang H. et al., 2015). Among these key features, the difference in LUMO energy of donor and acceptor is usually larger than 0.3 eV in fullerene system (Scharber and Sariciftci, 2013). However, with the development and application of non-fullerene electron acceptors, it is found that there is no clear boundary between electron donor and electron acceptor materials, and the difference of LUMO or HOMO energies in non-fullerene system could be very small. For instance, the polymer acceptor P-BNBP-fBT has a LUMO of −3.6 eV, and PTB7-Th donor has a LUMO level of −3.42 eV. The device based on PTB7-Th/P-BNBP-fBT showed a power conversation efficiency (PCE) as high as 6.26%, even though the difference in LUMO levels is only 0.18 eV (Long et al., 2016). However, polymer materials normally have a large polydispersity in molecular weight increasing the complexity of the materials. Thus, when it comes to fine tuning of the molecular levels, the use of solution processable small molecules is important to understand the relationship between molecular structures and their electron donating/withdrawing properties (Zhu et al., 2016; Wu et al., 2017).

At present, the small molecules could be designed as donor or acceptors based on different molecular architectures. For small molecule donors the conjugated skeleton is most often relatively planar. For example, oligothiophene-based small molecule donor DRCN7T exhibited an impressive optimized PCE of 9.30% using $PC_{71}BM$ acceptor (Zhang Q. et al., 2015). Our group synthesized

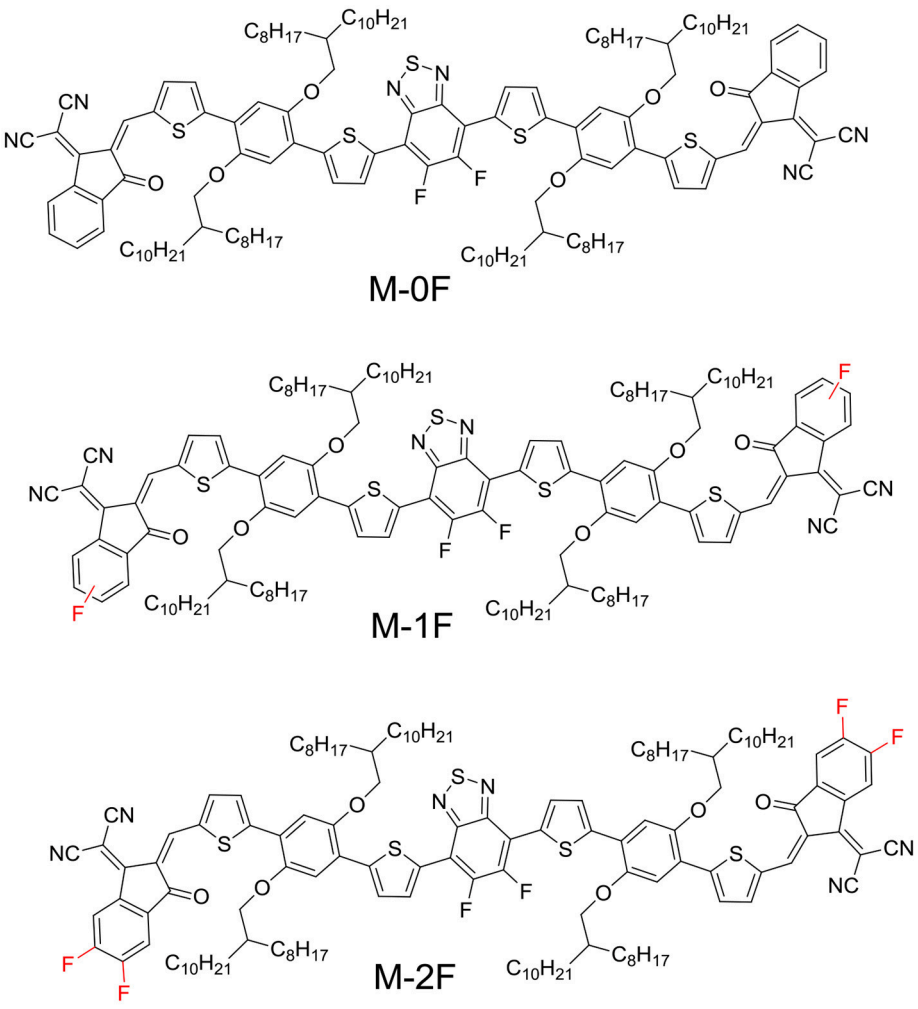

SCHEME 1 | Chemical structures of M-0F, M-1F, M-2F molecules.

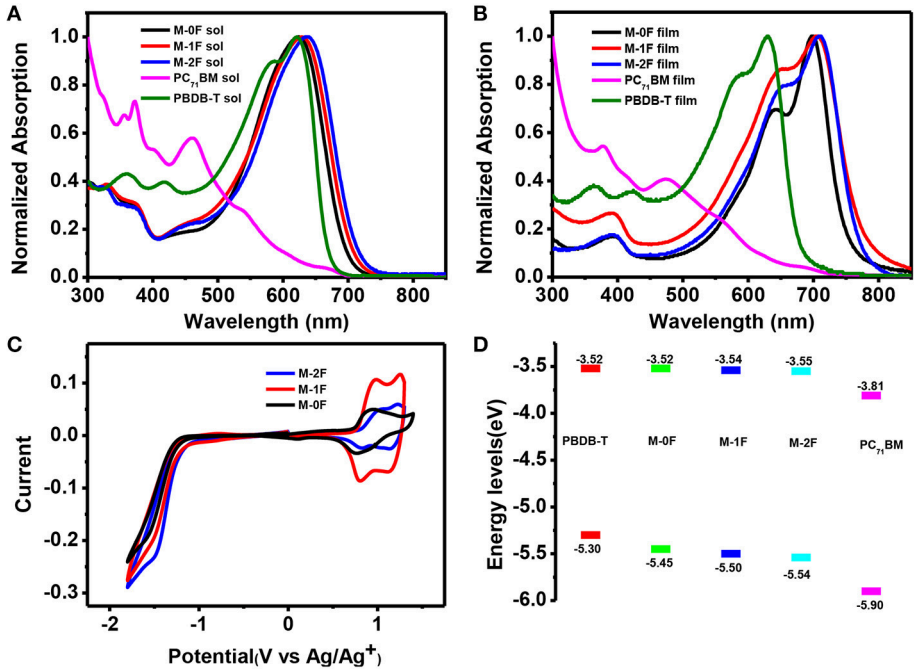

FIGURE 1 | (A) The normalized UV-vis absorption spectra of M-0F, M-1F, and M-2F, $PC_{71}BM$, PBDB-T in chloroform and **(B)** in thin film **(C)** Cyclic voltammograms of M-0F, M-1F, and M-2F **(D)** Energy level diagram of the related materials used in the device.

the A1–D–A2–D–A1 structure electron-donating small molecule with a PCE of more than 9% with enhanced molecular planarity and crystallinity (Yuan et al., 2016). On the other hand, currently non-fullerene acceptors are mainly concentrated on fused ring acceptors (Cheng et al., 2018; Hou et al., 2018). The acceptors based on perylene diimide (PDI) or naphthalene diimide (NDI) have shown relatively good performance in PSCs (Facchetti, 2013; Zhang et al., 2013; Hartnett et al., 2014; Li et al., 2014; Lin et al., 2014; Jung et al., 2015; Liu et al., 2015; Sun et al., 2015; Yang et al., 2016; Lei et al., 2018). Most of the high-performance PDI and NDI-based fullerene-free acceptors have twisted backbones to decrease the planarity, self-aggregation, and crystalline domains of simple rylene diimides. Besides the rylene-based fullerene-free electron acceptors, electron-donating extended fused rings, e.g., indacenodithiophene (IDT) and indacenodithieno[3,2-b]thiophene (IDTT), were widely used in small molecule acceptors because their LUMO levels can be readily tuned by flanking with different electron-withdrawing groups and the steric effect of tetrahexylphenyl substituents on the coplanar backbone can reduce the intermolecular interactions while weaken the stacking of donor units and promote the stacking of acceptor units (Lin et al., 2015; Wu et al., 2015; Lin and Zhan, 2016; Huang et al., 2017; Yu et al., 2017). Another example was present by Hou et al., the steric hindrance caused by side chains could convert two isomers to donors and acceptors separately (Liu et al., 2018). In this case, molecules with weak π-π stacking structure is more likely to work as acceptor materials. Although recent progress showed that small molecules based on the same backbone can be changed from donor to

TABLE 1 | Optical and electrochemical data of compounds M1-0F, M1-1F, and M1-2F.

Compound	$\lambda_{max}^{solution}$ (nm)	λ_{max}^{film} (nm)	$E_{g,\ film}^{opt}$ (eV)	$HOMO^{CV}$ (eV)	$LUMO^{CV}$ (eV)
M-0F	623	697	1.64	−5.45	−3.52
M-1F	630	705	1.59	−5.50	−3.54
M-2F	638	712	1.60	−5.54	−3.55

accepters by changing the side chain hindrance, it is still unclear whether one can slightly tune the energy levels of planer small molecules and charge mobility to realize the transformation from donor to acceptor.

Herein, we designed and synthesized three novel A1–D–A2–D–A1-type small molecules with dialkoxyphenyldithiophene (PDT) as D unit, difluorinated benzothiadiazole (2FBT) as A2 unit and strong electron-withdraw group 1, 1-dicyanomethylene-3-indanone (IC) substituted with 0–2 fluorine substituents as end-capped A1, namely M-0F, M-1F, and M-2F. All three molecules exhibit good planarity. The molecular structures are shown in **Scheme 1**. Fluorine is the most electronegative element with relatively small van der Waals radius. It can serve as an electron-withdrawing group without introducing undesirable steric hindrance. The introduction of fluorine onto the conjugated backbone of polymers or small molecules for BHJ solar cells could lower the LUMO and HOMO level (Price et al., 2011; Zhou et al., 2011; Zhang et al., 2017; Zhao et al., 2017). Fluorination IC also promotes intermolecular interactions

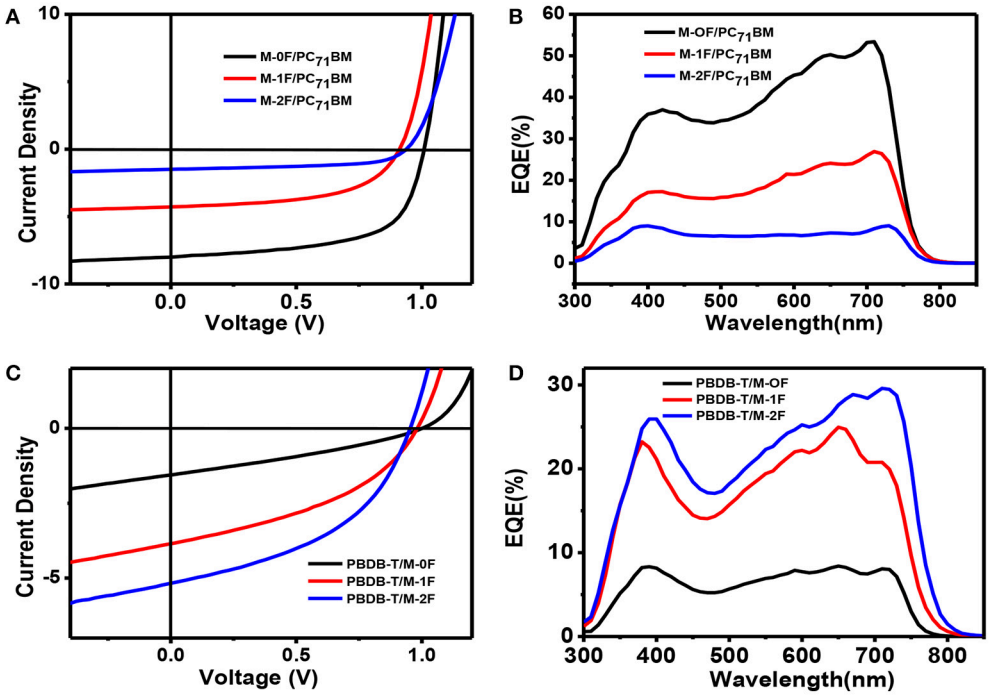

FIGURE 2 | (A,B) J–V curves and EQE curves of M-0F, M-1F, M-2F With $PC_{71}BM$ blends at the best performance condition. **(C,D)** J–V curves and EQE curves of M-0F, M-1F, M-2F with PBDB-T blends at the best performance condition.

through forming non-covalent F–S and F–H bonds, which can be favorable for charge transport (Sakamoto et al., 2001; Lei et al., 2014; Kim et al., 2015). The target molecules show red-shifted absorption spectrum and their LUMO and HOMO energies decreased with increasing fluorination. As donor, M-0F exhibited the highest PCE of 5.99%, M-1F performed a PCE of 2.60%, and M-2F showed the lowest PCE of 0.97% with $PC_{71}BM$ as acceptor. On the other hand, as acceptor, M-0F showed the lowest PCE of 0.58%, M-1F performed medium PCE of 1.85%, and M-2F achieved the highest PCE of 2.65% with polymer PBDB-T as donor. The energy level difference affects the performance of the molecule to a certain extent, M-0F exhibited the same LUMO level as PBDB-T, and cannot provide enough driving force for charge transfer and separation, but for M-2F, its lower LUMO is relatively better-match with PBDB-T although the LUMO difference is small. On the other hand, the hole and electron mobility also show that transition from hole transport to electron transport can be obtained via fluorination.

TABLE 2 | Device performance of M-0F, M-1F, and M-2F with $PC_{71}BM$ as acceptors.

Donor/Acceptor	V_{OC} (V)	J_{SC} (mAcm^{-2})	*FF* (%)	PCE (%)	Additive
M-0F/$PC_{71}BM$	1.01	9.54	62.41	5.99	1%DIO
M-1F/$PC_{71}BM$	0.91	5.14	55.71	2.60	1.5%DIO
M-2F/$PC_{71}BM$	0.93	1.80	57.65	0.97	1.5%DIO
PBDB-T/ M-0F	0.99	1.88	30.95	0.58	1%CN
PBDB-T/ M-1F	0.98	4.62	40.84	1.85	1%CN
PBDB-T/ M-2F	0.95	6.25	44.54	2.65	1%CN

RESULTS AND DISCUSSION

Molecular Synthesis and Properties

All three target molecules M-0F, M-1F, M-2F were synthesized according to the route shown in **Scheme 1**. To ensure the solubility of these three materials, the long branched side chain octyldodecyloxy was selected. Compound PDT2FBT-CHO was obtained through a Vilsmeier reaction from O-1. The three target molecules were synthesized by a Knoevenagel reaction. The synthetic routes, purification methods, and the nuclear magnetic resonance spectroscopy data are provided in the Supporting Information.

Figures 1A,B show the normalized UV–Vis absorption spectra of M-0F, M-1F, and M-2F measured in chloroform solution and in thin solid films. Detailed parameters are listed in **Table 1**. In solution, the three molecules show similar absorption spectra where the introduction of fluorine results in a red-shift of the absorption spectrum with the max absorption peak shifting from 623 to 630 and 638 nm. In thin films, all three molecules show more red-shifted and broader absorption spectra. The absorption peaks of these three compounds red-shift gradually from 697 to 705 nm and then to 712 nm in thin solid films. The strong shoulder peaks show that the three molecules have good π-π stacking in the film (Badgujar et al., 2016). The optical band gaps of M-0F, M-1F, and M-2F are calculated to be 1.64, 1.59, and 1.60 eV from the absorption edge, respectively.

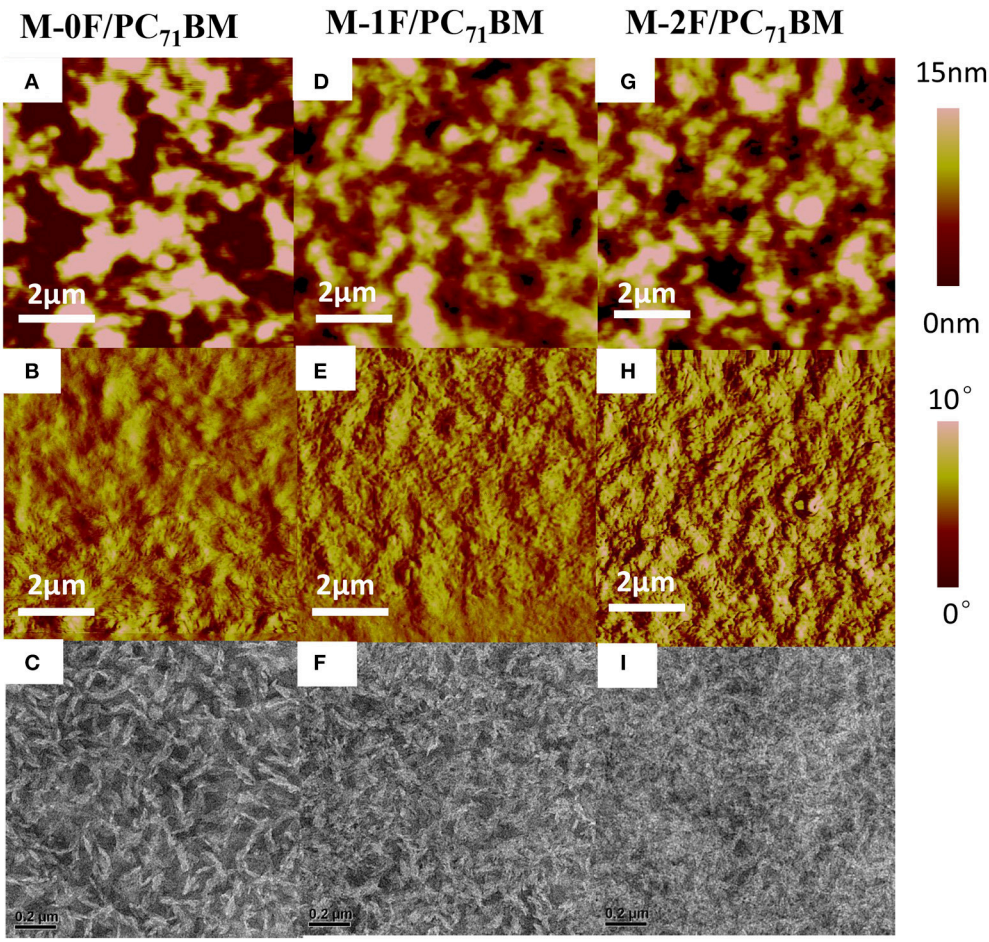

FIGURE 3 | Tapping-mode AFM **(A,D,G)** topography and **(B,E,H)** phase images and **(C,F,I)** TEM images of **(A–C)** M-0F/$PC_{71}BM$, **(D–F)** M-1F/$PC_{71}BM$, **(G–I)** M-2F/$PC_{71}BM$ blend films.

The cyclic voltammetry (CV) was used to evaluate the electrochemical properties of the three small molecules and the results are shown in **Figures 1C,D** with reversible reduction waves and quasi-reversible oxidation waves. The HOMO and LUMO energy levels are calculated from the onset oxidation and reduction potentials, assuming the absolute energy level of $FeCp_2^{+/0}$ to be 4.8 eV below vacuum. The equation of HOMO energy levels is $E_{HOMO} = -e\ (Eox + 4.8–E_{1/2,}\ (Fc/Fc^+))$ and the equation of the LUMO energy levels is $E_{LUMO} = -e\ (E_{RED} + 4.8–E_{1/2,}\ (Fc/Fc^+))$ (Li et al., 1999). Due to the strong electron withdraw ability of fluorine atom, the HOMO and LUMO of both M-1F, M-2F downshift. The HOMO levels of M-0F, M-1F, and M-2F are estimated to be −5.45, −5.50, and −5.54 eV and LUMO levels are −3.52, −3.54 to −3.55 eV (**Figure 1D**).

Photovoltaic Device Characterization

To investigate the photovoltaic behaviors of the three molecules as the electron donor and acceptor in OPV devices, we selected two materials, $PC_{71}BM$ as an acceptor (Wienk et al., 2003; Thompson and Fréchet, 2008) and PBDB-T as a donor polymer (Zhao et al., 2016) to blend with M-0F, M-1F, M-2F to fabricated conventional device structure: ITO/PEDOT:PSS/Donor:Acceptor/Ca/Al. We comparatively studied the photovoltaic performance of M-0F, M-1F, and M-2F as donor materials. The devices were made of blend of small molecule donor and $PC_{71}BM$ with chloroform as solvent by spin-coating. The photovoltaic properties of the devices were characterized under illumination of simulated solar light, AM1.5G (100 $mWcm^{-2}$). The optimized current density vs. voltage (J-V) curves and their corresponding external quantum efficiency (EQE) curves are displayed in **Figure 2**. The corresponding photovoltaic performance data is summarized in **Table 2**. The photovoltaic performance data of other condition is summarized in **Tables S1**, **S2**. The device based on M-0F: $PC_{71}BM$ exhibited a high V_{OC} of 1.01 V, a J_{SC} of 9.54 $mAcm^{-2}$ and a high FF of 62.41%, resulting in the highest optimal PCE of 5.99%. For device M-1F: $PC_{71}BM$, PCE was 2.60% with V_{OC} of 0.91 V, J_{SC} of 5.14 mA/cm^2 and FF 55.71%. However, for device M-2F: $PC_{71}BM$, the PCE was only 0.97% with a V_{OC} of 0.93 V, a J_{SC} of 1.80 $mAcm^{-2}$ and a FF of 57.65%. It can be concluded that as an electron donor in blends with $PC_{71}BM$, M-0F displays a superior photovoltaic performance compared

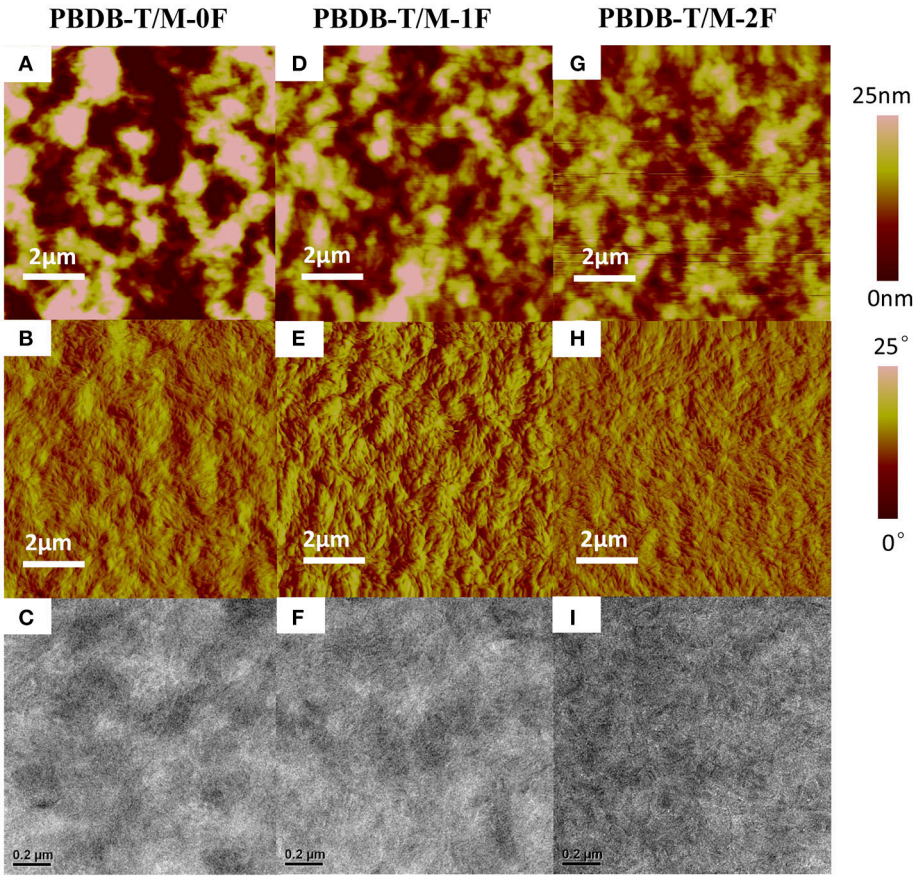

FIGURE 4 | Tapping-mode AFM **(A,D,G)** topography and **(B,E,H)** phase images and **(C,F,I)** TEM images of **(A–C)** PBDB-T/M-0F, **(D–F)** PBDB-T/M-1F, **(G–I)** PBDB-T/M-2F blend films.

to M-1F while M-1F has better photovoltaic performance than M-2F. The results show that the device performance based the three molecules as donors decreases with increased number of fluorine atoms attached to the terminal acceptor units (A1).

We also studied photovoltaic performance of M-0F, M-1F, and M-2F as electron acceptor material with PBDB-T as donor material. The blend of small molecule acceptor and PBDB-T was made with chlorobenzene as solvent by spin-coating. It was found that the PCE of a M-0F:PBDB-T device was only 0.58% with low J_{SC} and FF; the PCE of a device based on M-1F:PBDB-T was 1.85%; while the device based on M-2F:PBDB-T displayed a PCE as high as 2.65%, with a V_{OC} of 0.95, a J_{SC} of 6.25 $mAcm^{-2}$, and a FF of 44.54%. It can be concluded that, as electron acceptors after blending with PBDB-T, M-2F displays a superior photovoltaic performance compared to M-0F and M-1F. This means, that as acceptors and donors the series of small molecules display opposite trend in device performances. With increasing fluorination, the device performance as donor decreases while improves as acceptor.

Photoluminescence Quenching Effects

In order to investigate the donor property of M-0F, M-1F, and M-2F, the fluorescence spectra were measured in the range of 680–900 nm with exciting wavelength at 650 nm. As shown in **Figure S1A**, the photoluminescence (PL) of M-0F, M-1F can be partly quenched by $PC_{71}BM$, whereas the PL of M-2F almost can't be quenched by $PC_{71}BM$, indicating that the exciton dissociation in the blend of M-0F/$PC_{71}BM$, M-1F/$PC_{71}BM$ should be more efficient than that in the blend of M-2F/$PC_{71}BM$. For studying acceptor property of these three small molecules, the exciting wavelength at 740 nm was chosen as shown in **Figure S1B**. From the film of M-0F/ PBDB-T, M-1F/ PBDB-T to M-2F/ PBDB-T, the PL quenching effect is gradually stronger, indicating that the exciton dissociation is more efficient gradually. These results are in consistent with device performance.

Film Morphology and Microstructure

Using atomic force microscopy (AFM) and transmission electronic microscopy (TEM), the phase separation morphology of the blends for the two systems were investigated. As shown in **Figure 3**, the AFM images are consistent with the TEM images. For the $PC_{71}BM$ system, it can be seen that M-0F, M-1F, and M-2F have good compatibility with $PC_{71}BM$ and good phase separation. The surface roughness is 8.317, 4.236, and 4.617 nm for blend films M-0F:$PC_{71}BM$, M-1F:$PC_{71}BM$, and

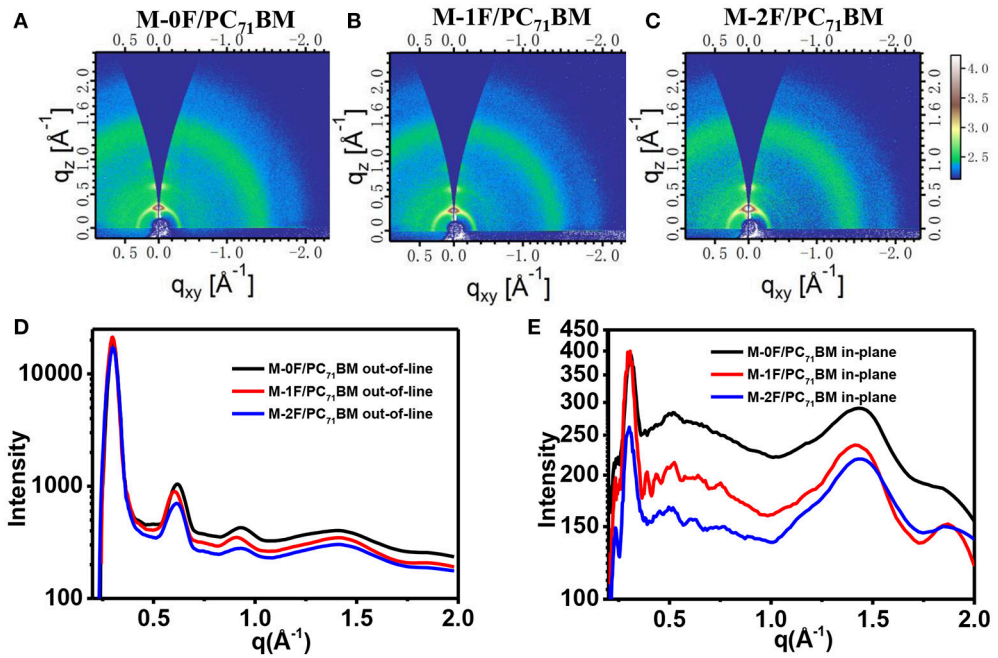

FIGURE 5 | 2D GIWAXS patterns of M-0F/$PC_{71}BM$ **(A)**, M-1F/$PC_{71}BM$ **(B),** and M-2F/$PC_{71}BM$ **(C)** blend film. Out-of-plane **(D)** and in-plane **(E)** cuts of the corresponding 2D GIWAXS patterns.

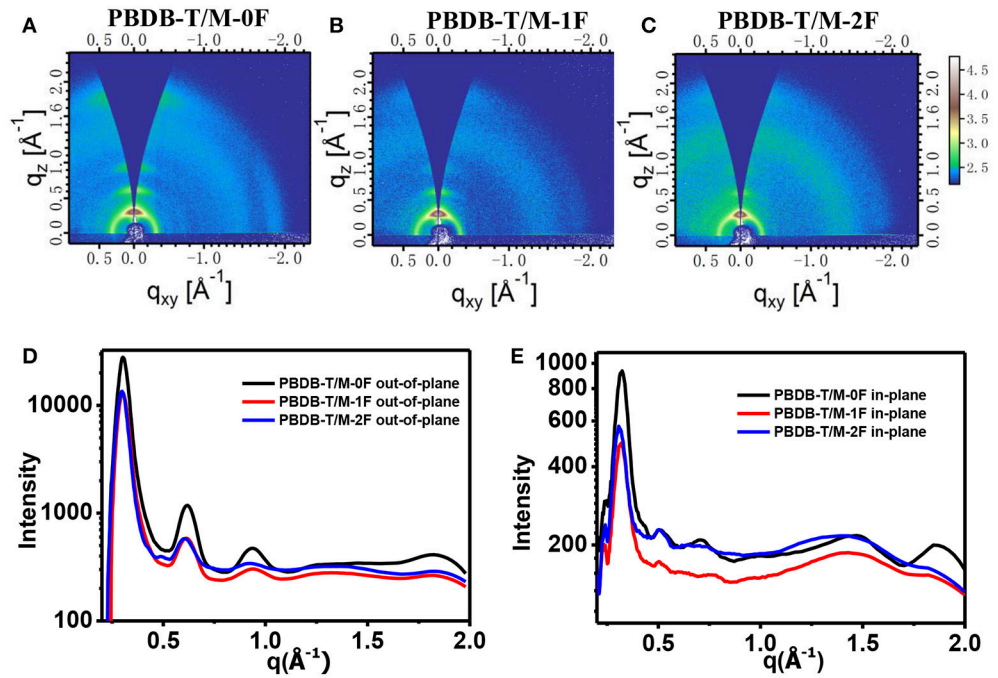

FIGURE 6 | 2D GIWAXS patterns of PBDB-T/ M-0F **(A)**, PBDB-T/ M-1F **(B),** and PBDB-T/ M-2F **(C)** blend film. Out-of-plane **(D)** and in-plane **(E)** cuts of the corresponding 2D GIWAXS patterns.

M-2F:$PC_{71}BM$, respectively. The M-0F:$PC_{71}BM$ blend has the larger size of aggregation phase region, and the proper domain size for efficient exciton diffusion and dissociation contributing to high J_{SC} and FF. For M-1F:$PC_{71}BM$ and M-2F:$PC_{71}BM$ blend film, the aggregation size is so small resulting in low J_{SC} and FF.

For the non-fullerene system shown in **Figure 4**, the surface roughness of PBDB-T:M-0F, PBDB-T:M-1F, and PBDB-T:M-2F

TABLE 3 | SCLC measured hole mobility and electron mobility for pure M-0F, M-1F, M-2F, and their $PC_{71}BM$ or PBDB-T blends.

	M-0F	M-1F	M-2F	M-0F /$PC_{71}BM$	M-1F /$PC_{71}BM$	M-2F /$PC_{71}BM$	PBDB-T /M-0F	PBDB-T /M-1F	PBDB-T /M-2F
Hole mobility (cm^2 V^{-1} S^{-1})	2.49×10^{-4}	1.78×10^{-5}	6.42×10^{-6}	9.26×10^{-5}	3.90×10^{-6}	1.74×10^{-6}	9.25×10^{-6}	1.47×10^{-5}	6.87×10^{-5}
Electron mobility (cm^2 V^{-1} S^{-1})	1.01×10^{-6}	3.03×10^{-6}	1.26×10^{-5}	5.20×10^{-5}	3.84×10^{-5}	1.52×10^{-5}	4.27×10^{-7}	2.07×10^{-6}	3.7×10^{-6}

blend film are 11.034, 6.672, and 4.356 nm. The surface of PBDB-T:M-2F is smoother. From TEM image, we can see that PBDB-T:M-2F formed a uniform nanoscale phase separation with nanofiber and continuous interpenetrating network structure, and the phase separation size is suitable, which facilitates the exciton diffusion and charge transfer and improve J_{SC} and FF. However, For the PBDB-T:M-0F and PBDB-T:M-1F blends large domain size can be seen, this is not conducive to the charge transfer, which cause a negative impact on the J_{SC} and FF.

In order to further study the molecular stacking and crystallization properties of the active layer, grazing incidence wide-angle X-ray scattering (GIWAXS) on the neat films and blend films was employed. The results of pristine M-0F, M-1F, M-2F, and PBDB-T films are shown in **Figure S2**. In-plane direction M-0F, M-1F, and M-2F all show π-π stacking peaks at 1.72 $Å^{-1}$ (d-spacing: 3.65 Å), 1.77$Å^{-1}$ (d-spacing: 3.55 Å), 1.78 $Å^{-1}$ (d-spacing: 3.53 Å), which indicates the higher crystallinity of M-1F, and M-2F compared with M-0F in the neat films. **Figure 5** shows the two-dimensional GIWAXS patterns and the one-dimensional GIWAXS cuts along in-plane and out-of-plane directions of M-0F:$PC_{71}BM$, M-1F:$PC_{71}BM$, and M-2F:$PC_{71}BM$ blended films. As can be seen from **Figure 5**, M-0F, M-1F, and M-2F all show very obvious diffraction peaks of (100), (200), (300), and (010), indicating the good crystallinity M-0F, M-1F, and M-2F with the orderly aggregation state structure. Besides, these corresponding peaks have almost the same location, which indicate the same d-spacing. The positions of (100) peak is ∼0.298 $Å^{-1}$ correspongding to a d-spacing of ∼21.08 Å. The positions of (010) q is ∼1.869 $Å^{-1}$, so the d-spacing is ∼3.36 Å. The π-π stacking of M-1F is stronger while the hole mobility is not the highest compared with M-0F, M-2F, indicating that the performance of the donor and acceptor has been changed.

Figure 6 shows the GIWAXS of PBDB-T:M-0F, PBDB-T:M-1F, and PBDB-T:M-2F blend films. Similar with $PC_{71}BM$ system, M-0F, M-1F, and M-2F all show very obvious diffraction peaks of (100) (200), (300), and (010), these corresponding peaks have almost the same location. The positions of (100) q is∼ 0.30 $Å^{-1}$, so the d-spacing is ∼20.94 Å. The positions of (010) q is ∼1.83 $Å^{-1}$, so the d-spacing is ∼3.43 Å. The GIWAXS results show the good crystallization of M-0F, M-1F, and M-2F.

Hole and Electron Mobility

In order to study the origin of the observed differences in photovoltaic properties of the three new materials, the hole and electron mobility of the three pure materials and blend films at the best performance condition were tested using space-limited charge (SCLC) method (Blom et al., 2005). The hole and electron mobility curves measured by the SCLC method are shown in Supplementary Information **Figure S3**. The data of hole and electron mobility under different conditions is summarized in **Table 3**. The hole and electron mobility for pristine M-0F are 2.49×10^{-4} and 1.01×10^{-6} cm^2 V^{-1} S^{-1}, respectively. For pristine M-1F, the hole and electron mobility are 1.78×10^{-5} and 3.03×10^{-6} cm^2 V^{-1} S^{-1}. For pristine M-2F, the hole and electron mobility are 6.42×10^{-6} and 1.26×10^{-5} cm^2 V^{-1} S^{-1}. This indicates the transition from hole transport to electron transport. Among M-1F and M-2F, the electron mobility of M-2F is higher than its hole mobility, so M-2F has better n-type semiconductor property than M-1F. At the corresponding best performance condition, from M-0F:$PC_{71}BM$, M-1F:$PC_{71}BM$ to M-2F:$PC_{71}BM$, both the hole and electron mobility decrease. From PBDB-T:M-0F, PBDB-T:M-1F to PBDB-T:M-2F, both the hole and electron mobility increase, which is consistent with photovoltaic performance results.

On the basis of above observations, we can conclude that M-0F has good donor property with better phase separation and higher hole mobility in fullerene system. while M-2F has the best acceptor properties with nanofiber interpenetrating network morphology and higher electron mobility in non-fullerene system.

CONCLUSION

In conclusion, we designed and synthesized three novel A1-D-A2-D-A1 small molecules (M-0F, M-1F, and M-2F) with the strong electron-withdraw group 1,1-dicyanomethylene-3-indanone (IC) substituted with varying number of fluorine atoms. With increasing number of fluorine atoms, the absorption spectra are red-shifted, and both the LUMO and HOMO energies are decreased. M-0F exhibited excellent electron-donating properties while M-2F showed excellent electron-accepting properties. Our work further proves that the definition of donor and acceptor is without clear boundaries, which offer wide potential for molecular design. The regulation of energy levels and carrier mobility is one of the effective ways to achieve this transformation. Also, the boundary between donor materials and acceptor materials is worth exploring for understanding the deep mechanism of exciton dissociation and charge transfer in BHJ active layers.

AUTHOR CONTRIBUTIONS

RZ designed the project, finished the synthesis, characterization, wrote the first draft of the manuscript; BX designed the

project, finished the device, and characterization of photovoltaic performance. BL, KL, and ZW guided the project and helped to revise the manuscript. The other authors gave the contribution in synthesis or data analysis.

ACKNOWLEDGMENTS

We acknowledge the Ministry of Science and Technology of China (Nos. 2016YFA0200700 and 2016YFF0203803), the National Natural Science Foundation of China (Grant Nos. 21474022, 21125420, 21603044, 51673049, and 21603044), the Beijing Nova Program, the Youth Innovation Promotion Association CAS, and the Chinese Academy of Sciences.

SUPPLEMENTARY MATERIAL

The Supplementary Material for this article can be found online at: https://www.frontiersin.org/articles/10.3389/fchem.2018.00384/full#supplementary-material

REFERENCES

Badgujar, S., Lee, G. Y., Park, T., Song, C. E., Park, S., Oh, S., et al. (2016). High-Performance small molecule via tailoring intermolecular interactions and its application in large-area organic photovoltaic modules. *Adv. Energy Mater.* 6:1600228. doi: 10.1002/aenm.201600228

Beaujuge, P. M., and Frechet, J. M. J. (2011). Molecular design and ordering effects in pi-functional materials for transistor and solar cell applications. *J. Am. Chem. Soc.* 133, 20009–20029. doi: 10.1021/ja2073643

Blom, P. W. M., Tanase, C., de Leeuw, D. M., and Coehoorn, R. (2005). Thickness scaling of the space-charge-limited current in poly(p-phenylene vinylene). *Appl. Phys. Lett.* 86:092105. doi: 10.1063/1.1868865

Brabec, C. J., Gowrisanker, S., Halls, J. J. M., Laird, D., Jia, S., and Williams, S. P. (2010). Polymer-fullerene bulk-heterojunction solar cells. *Adv. Mater.* 22, 3839–3856. doi: 10.1002/adma.200903697

Chen, J., and Cao, Y. (2009). Development of novel conjugated donor polymers for high-efficiency bulk-heterojunction photovoltaic devices. *Acc. Chem. Res.* 42, 1709–1718. doi: 10.1021/ar900061z

Cheng, P., Li, G., Zhan, X., and Yang, Y. (2018). Next-generation organic photovoltaics based on non-fullerene acceptors. *Nat. Photon.* 12, 131–142. doi: 10.1038/s41566-018-0104-9

Cheng, Y. J., Yang, S. H., and Hsu, C. S. (2009). Synthesis of conjugated polymers for organic solar cell applications. *Chem. Rev.* 109, 5868–5923. doi: 10.1021/cr900182s

Etxebarria, I., Ajuria, J., and Pacios, R. (2015). Solution-processable polymeric solar cells: a review on materials, strategies and cell architectures to overcome 10%. *Organ. Electron.* 19, 34–60. doi: 10.1016/j.orgel.2015.01.014

Facchetti, A. (2013). Polymer donor–polymer acceptor (all-polymer) solar cells. *Mater. Today* 16, 123–132. doi: 10.1016/j.mattod.2013.04.005

Forrest, S. R. (2004). The path to ubiquitous and low-cost organic electronic appliances on plastic. *Nature* 428, 911–918. doi: 10.1038/nature02498

Hartnett, P. E., Timalsina, A., Matte, H. S. S. R., Zhou, N., Guo, X., Zhao, W., et al. (2014). Slip-Stacked perylenediimides as an alternative strategy for high efficiency nonfullerene acceptors in organic photovoltaics. *J. Am. Chem. Soc.* 136, 16345–16356. doi: 10.1021/ja508814z

Henson, Z. B., Muellen, K., and Bazan, G. C. (2012). Design strategies for organic semiconductors beyond the molecular formula. *Nat. Chem.* 4, 699–704. doi: 10.1038/nchem.1422

Hou, J., Inganas, O., Friend, R. H., and Gao, F. (2018). Organic solar cells based on non-fullerene acceptors. *Nat. Mater.* 17, 119–128. doi: 10.1038/nmat5063

Huang, H., Yang, L., Facchetti, A., and Marks, T. J. (2017). Organic and polymeric semiconductors enhanced by noncovalent conformational locks. *Chem. Rev.* 117, 10291–10318. doi: 10.1021/acs.chemrev.7b00084

Jung, J. W., Jo, J. W., Chueh, C. C., Liu, F., Jo, W. H., Russell, T. P., et al. (2015). Fluoro-Substituted n-type conjugated polymers for additive-free all-polymer bulk heterojunction solar cells with high power conversion efficiency of 6.71%. *Adv. Mater.* 27, 3310–3317. doi: 10.1002/adma.201501214

Kim, H. G., Kang, B., Ko, H., Lee, J., Shin, J., and Cho, K. (2015). Synthetic tailoring of solid-state order in diketopyrrolopyrrole-based copolymers via intramolecular noncovalent interactions. *Chem. Mater.* 27, 829–838. doi: 10.1021/cm503864u

Kumar, P., and Chand, S. (2012). Recent progress and future aspects of organic solar cells. *Prog. Photovoltaics* 20, 377–415. doi: 10.1002/pip.1141

Lei, T., Xia, X., Wang, J. Y., Liu, C. J., and Pei, J. (2014). "Conformation locked" strong electron-deficient poly(p-phenylene vinylene) derivatives for ambient-stable n-type field-effect transistors: synthesis, properties, and effects of fluorine substitution position. *J. Am. Chem. Soc.* 136, 2135–2141. doi: 10.1021/ja412533d

Lei, Y., Wenxing, G., Lei, L., Yusheng, C., Yufei, Y., Pan, Y., et al. (2018). Triplet tellurophene-based acceptors for organic solar cells. *Angew. Chem.* 130, 1108–1114. doi: 10.1002/ange.201712011

Li, H., Earmme, T., Ren, G., Saeki, A., Yoshikawa, S., Murari, N. M., et al. (2014). Beyond fullerenes: design of nonfullerene acceptors for efficient organic photovoltaics. *J. Am. Chem. Soc.* 136, 14589–14597. doi: 10.1021/ja508472j

Li, Y. (2012). Molecular design of photovoltaic materials for polymer solar cells: toward suitable electronic energy levels and broad absorption. *Acc. Chem. Res.* 45, 723–733. doi: 10.1021/ar2002446

Li, Y., Cao, Y., Gao, J., Wang, D., Yu, G., and Heeger, A.J. (1999). Electrochemical properties of luminescent polymers and polymer light-emitting electrochemical cells. *Synthetic Metals* 99, 243–248. doi: 10.1016/S0379-6779(99)00007-7

Lin, Y., Wang, Y., Wang, J., Hou, J., Li, Y., Zhu, D., et al. (2014). A star-shaped perylene diimide electron acceptor for high-performance organic solar cells. *Adv. Mater.* 26, 5137–5142. doi: 10.1002/adma.201400525

Lin, Y., and Zhan, X. (2016). Oligomer molecules for efficient organic photovoltaics. *Acc. Chem. Res.* 49, 175–183. doi: 10.1021/acs.accounts.5b00363

Lin, Y., Zhang, Z.-G., Bai, H., Wang, J., Yao, Y., Li, Y., et al. (2015). High-performance fullerene-free polymer solar cells with 6.31% efficiency. *Energy Environ. Sci.* 8, 610–616. doi: 10.1039/C4EE03424D

Liu, D., Yang, L., Wu, Y., Wang, X., Zeng, Y., Han, G., et al. (2018). Tunable electron donating and accepting properties achieved by modulating the steric hindrance of side chains in a-d-a small-molecule photovoltaic materials. *Chem. Mater.* 30, 619–628. doi: 10.1021/acs.chemmater.7b03142

Liu, Y., Mu, C., Jiang, K., Zhao, J., Li, Y., Zhang, L., et al. (2015). Organic solar cells: a tetraphenylethylene core-based 3d structure small molecular acceptor enabling efficient non-fullerene organic solar cells. *Adv. Mater.* 27, 1014–1014. doi: 10.1002/adma.201570038

Long, X., Ding, Z., Dou, C., Zhang, J., Liu, J., and Wang, L. (2016). Polymer acceptor based on double B<-N bridged bipyridine (BNBP) unit for high-efficiency all-polymer solar cells. *Adv. Mater.* 28, 6504–6508. doi: 10.1002/adma.201601205

Price, S. C., Stuart, A. C., Yang, L., Zhou, H., and You, W. (2011). Fluorine substituted conjugated polymer of medium band gap yields 7% efficiency in polymer–fullerene solar cells. *J. Am. Chem. Soc.* 133, 4625–4631. doi: 10.1021/ja1112595

Sakamoto, Y., Komatsu, S., and Suzuki, T. (2001). Tetradecafluorosexithiophene: the first perfluorinated oligothiophene. *J. Am. Chem. Soc.* 123, 4643–4644. doi: 10.1021/ja015712j

Scharber, M. C., and Sariciftci, N. S. (2013). Efficiency of bulk-heterojunction organic solar cells. *Prog. Polym. Sci.* 38, 1929–1940. doi: 10.1016/j.progpolymsci.2013.05.001

Scharber, M. C., Wuhlbacher, D., Koppe, M., Denk, P., Waldauf, C., Heeger, A. J., et al. (2006). Design rules for donors in bulk-heterojunction solar cells - towards 10 % energy-conversion efficiency. *Adv. Mater.* 18, 789–794. doi: 10.1002/adma.200501717

Sun, D., Meng, D., Cai, Y., Fan, B., Li, Y., Jiang, W., et al. (2015). Non-fullerene-acceptor-based bulk-heterojunction organic solar cells with efficiency over 7%. *J. Am. Chem. Soc.* 137, 11156–11162. doi: 10.1021/jacs.5b06414

Thompson, B. C., and Fréchet, J. M. J. (2008). Polymer–fullerene composite solar cells. *Angew. Chem. Inter. Ed.* 47, 58–77. doi: 10.1002/anie.200702506

Wienk, M. M., Kroon, J. M., Verhees, W. J. H., Knol, J., Hummelen, J. C., van Hal, P. A., et al. (2003). efficient methano[70]fullerene/mdmo-ppv bulk heterojunction photovoltaic cells. *Angew. Chem.* 115, 3493–3497. doi: 10.1002/ange.200351647

Wu, Q., Deng, D., Lu, K., and Wei, Z. X. (2017). D-A structural protean small molecule donor materials for solution-processed organic solar cells. *Chin. Chem. Lett.* 28, 2065–2077. doi: 10.1016/j.cclet.2017.08.046

Wu, Y., Bai, H., Wang, Z., Cheng, P., Zhu, S., Wang, Y., et al. (2015). A planar electron acceptor for efficient polymer solar cells. *Energy Environ. Sci.* 8, 3215–3221. doi: 10.1039/C5EE02477C

Xu, T., and Yu, L. (2014). How to design low bandgap polymers for highly efficient organic solar cells. *Mater. Today* 17, 11–15. doi: 10.1016/j.mattod.2013.12.005

Yang, L., Chen, Y., Chen, S., Dong, T., Deng, W., Lv, L., et al. (2016). Achieving high performance non-fullerene organic solar cells through tuning the numbers of electron deficient building blocks of molecular acceptors. *J. Power Sour.* 324, 538–546. doi: 10.1016/j.jpowsour.2016.05.119

Yu, S., Chen, Y., Yang, L., Ye, P., Wu, J., Yu, J., et al. (2017). Significant enhancement of photovoltaic performance through introducing S?N conformational locks. *J. Mater. Chem. A* 5, 21674–21678. doi: 10.1039/C7TA05774A

Yuan, L., Lu, K., Xia, B., Zhang, J., Wang, Z., Wang, Z., et al. (2016). Acceptor end-capped oligomeric conjugated molecules with broadened absorption and enhanced extinction coefficients for high-efficiency organic solar cells. *Adv. Mater.* 28, 5980–5985. doi: 10.1002/adma.201600512

Zhang, H., Ye, L., and Hou, J. (2015). Molecular design strategies for voltage modulation in highly efficient polymer solar cells. *Polym. Int.* 64, 957–962. doi: 10.1002/pi.4895

Zhang, Q., Kan, B., Liu, F., Long, G., Wan, X., Chen, X., et al. (2015). Small-molecule solar cells with efficiency over 9%. *Nat. Photon.* 9, 35–41. doi: 10.1038/nphoton.2014.269

Zhang, Q., Kelly, M. A., Bauer, N., and You, W. (2017). The curious case of fluorination of conjugated polymers for solar cells. *Acc. Chem. Res.* 50, 2401–2409. doi: 10.1021/acs.accounts.7b00326

Zhang, X., Lu, Z., Ye, L., Zhan, C., Hou, J., Zhang, S., et al. (2013). A potential perylene diimide dimer-based acceptor material for highly efficient solution-processed non-fullerene organic solar cells with 4.03% efficiency. *Adv. Mater.* 25, 5791–5797. doi: 10.1002/adma.201300897

Zhao, W., Li, S., Yao, H., Zhang, S., Zhang, Y., Yang, B., et al. (2017). Molecular optimization enables over 13% efficiency in organic solar cells. *J. Am. Chem. Soc.* 139, 7148–7151. doi: 10.1021/jacs.7b02677

Zhao, W., Qian, D., Zhang, S., Li, S., Inganäs, O., Gao, F., et al. (2016). Fullerene-free polymer solar cells with over 11% efficiency and excellent thermal stability. *Adv. Mater.* 28, 4734–4739. doi: 10.1002/adma.201600281

Zhou, H., Yang, L., Stuart, A. C., Price, S. C., Liu, S., and You, W. (2011). Development of fluorinated benzothiadiazole as a structural unit for a polymer solar cell of 7 % efficiency. *Angew. Chem. Inter. Ed.* 50, 2995–2998. doi: 10.1002/anie.201005451

Zhu, X. W., Lu, K., Li, H., Zhou, R. M., and Wei, Z. X. (2016). Naphthodithiophene-based donor materials for solution processed organic solar cells. *Chin. Chem. Lett.* 27, 1271–1276. doi: 10.1016/j.cclet.2016.06.015

Conflict of Interest Statement: The authors declare that the research was conducted in the absence of any commercial or financial relationships that could be construed as a potential conflict of interest.

frontiers in Chemistry

ORIGINAL RESEARCH
published: 20 August 2018
doi: 10.3389/fchem.2018.00292

Constructing Desired Vertical Component Distribution Within a PBDB-T:ITIC-M Photoactive Layer via Fine-Tuning the Surface Free Energy of a Titanium Chelate Cathode Buffer Layer

Yiming Bai[1,2], *Bo Yang*[1], *Xiaohan Chen*[1], *Fuzhi Wang*[1,2], *Tasawar Hayat*[3,4], *Ahmed Alsaedi*[4] *and Zhan'ao Tan*[1,2*]

[1] State Key Laboratory of Alternate Electrical Power System with Renewable Energy Sources, North China Electric Power University, Beijing, China, [2] Beijing Key Laboratory of Energy Safety and Clean Utilization, North China Electric Power University, Beijing, China, [3] Department of Mathematics, Quiad-I-Azam University, Islamabad, Pakistan, [4] NAAM Research Group, Faculty of Science, King Abdulaziz University, Jeddah, Saudi Arabia

OPEN ACCESS

Edited by:
Chuanlang Zhan,
Institute of Chemistry (CAS), China

Reviewed by:
Xiaoyan Du,
i-MEET Institute Materials for Electronics and Energy Technology, Germany
Ziyi Ge,
Ningbo Institute of Industrial Technology (CAS), China
Zhixiang Wei,
National Center for Nanoscience and Technology (CAS), China

***Correspondence:**
Zhan'ao Tan
tanzhanao@ncepu.edu.cn

Specialty section:
This article was submitted to Organic Chemistry, a section of the journal Frontiers in Chemistry

Received: *26 April 2018*
Accepted: *25 June 2018*
Published: *20 August 2018*

Citation:
Bai Y, Yang B, Chen X, Wang F, Hayat T, Alsaedi A and Tan Z (2018) Constructing Desired Vertical Component Distribution Within a PBDB-T:ITIC-M Photoactive Layer via Fine-Tuning the Surface Free Energy of a Titanium Chelate Cathode Buffer Layer. Front. Chem. 6:292. doi: 10.3389/fchem.2018.00292

Rationally controlling the vertical component distribution within a photoactive layer is crucial for efficient polymer solar cells (PSCs). Herein, fine-tuning the surface free energy (SFE) of the titanium(IV) oxide bis(2,4-pentanedionate) (TOPD) cathode buffer layer is proposed to achieve a desired perpendicular component distribution for the PBDB-T:ITIC-M photoactive layer. The Owens-Wendt method is adopted to precisely calculate the SFE of TOPD film jointly based on the water contact angle and the diiodomethane contact angle. We find that the SFE of TOPD film increases as the annealing temperature rises, and the subtle SFE change causes the profound vertical component distribution within the bulk region of PBDB-T:ITIC-M. The results of secondary-ion mass spectroscopy visibly demonstrate that the TOPD film with an SFE of 48.71 mJ/cm^2, which is very close to that of the ITIC film (43.98 mJ/cm^2), tends to form desired vertical component distribution. Consequently, compared with conventional bulk heterojunction devices, the power conversion efficiency increases from 9.00 to 10.20% benefiting from the short circuit current density increase from 14.76 to 16.88 mA/cm^2. Our findings confirm that the SFE adjustment is an effective way of constructing the desired vertical component distribution and therefore achieving high-efficiency PSCs.

Keywords: polymer solar cells, vertical component distribution, surface free energy, cathode buffer layer, annealing temperature

INTRODUCTION

Stimulated by the need for a clean renewable energy source, there has been considerable interest in exploring polymer solar cells (PSCs) due to their unique properties of low cost, light weight, and flexibility (Krebs et al., 2010; Li G. et al., 2012; Zhao et al., 2017). The state-of-the-art device configuration is the sandwich bulk heterojunction (BHJ), blending the conjugated polymer donor

compactly with a fullerene or fullerene-free acceptor (Ouyang et al., 2015; Jiang et al., 2017; Peng et al., 2018). Very recently, the best power conversion efficiency (PCE) of single-junction PSCs based on the fullerene acceptor has exceeded 11.7% (Zhao et al., 2016), and that of fullerene-free PSCs has reached up to 14%. This can be attributed to the development of new electron donors and the matching acceptors, device structures and novel interfacial layers (Xiao et al., 2017).

The BHJ photoactive layer, as the main functional layer for light absorption, exciton generation, dissociation, and transportation, is commonly fabricated by spin-coating the mixed solution of electron donors and acceptors (Heriot and Jones, 2005; Lu et al., 2013; Xie et al., 2014; Bin et al., 2016). The mixed components will form a vertical phase separated photoactive layer during the film-drying process, which ensures a large interfacial area for efficient exciton dissociation and facilitates the charge transportation and selective collection via the formation of bi-continuous interpenetrating networks (Qiu et al., 2008; Xu et al., 2010; Meier et al., 2011). Hence, an in-depth understanding about the vertical component distribution within the photoactive layer is absolutely imperative for realizing efficient PSCs. However, its mechanism is complex and still vague, which involves thermodynamics, dynamics, free-surface, and interface effects during the blend formation process (Kim et al., 2017).

A number of studies on fullerene PSCs have illustrated that the perpendicular component distribution of photoactive blends is greatly influenced by the processing conditions, such as solvent soaking, solvent flush treatment, and solvent additives (Li C. Z. et al., 2012; Heo et al., 2014; Van Franeker et al., 2015). Li et al. introduced a mixed solvent-soaking approach to obtain an interpenetrating network composed of highly crystalline regioregular poly(3-hexylthiophene) (P3HT) and [6,6]-phenyl-C_{61}-butyric acid methyl ester ($PC_{61}BM$) nano-aggregates (Hui et al., 2011). The 2-chlorophenol flush treatment is also a simple and feasible way to acquire an optimal vertical composition profile of photoactive blends, leading to an increased PCE from 6.18 to 10.15% for inverted PSCs based on poly[4,8-bis(5-(2-ethylhexyl)thiophen-2-yl)benzo[1,2-b:4,5-b0]dithiophenealt-3-fluorothieno[3,4-b]thiophene-2-carboxylate] (PTB7-Th):[6,6]-phenyl-C_{71}-butyric acid methyl ester ($PC_{71}BM$) blends (Wang et al., 2016). The solvent additive 1,8-diiodooctane (DIO) with high boiling point, using the solubility of the different components to change and affect the donor and acceptor phase distributions, can selectively dissolve PCBM and facilitate long-range diffusion of PCBM to form a bicontinuous pathway for electron and hole transportation at the latter stage of the film-drying process (Xiao et al., 2014). However, few investigations have been conducted to elucidate the influence of processing parameters on the perpendicular component distribution of fullerene-free photoactive blends though it well exists, and this is an area warranting urgent exploration (Yan et al., 2017).

Evidence also shows that the free energy of electron donors and acceptors, and the substrate surface onto which they are deposited has a direct impact on the perpendicular component distribution (Jones et al., 1989; Jasieniak et al., 2016). Kim et al. found that P3HTs with hydroxyl-, ethyl-, perfluoro-, and bromo-end groups have different surface free energies (SFEs), and the vertical stratification in their blends with PCBM can be tuned as the surface energy difference between electron donors and acceptors (Kim et al., 2010). It is well-known that the system is the most stable if and only if the systematic energy is the minimum. Jones put forward that any surface energy difference between the pure components allows the photoactive blends to minimize its total free energy by increasing the surface concentration of the low-energy component (Jones et al., 1989). In contrast, Björström and Tillack believed that the variation of the substrate SFE affects the perpendicular component distribution within the bulk region rather than the air surface region (Björström et al., 2005; Tillack et al., 2011). Germack found that for the similar P3HT:PCBM blends (the surface energies for polymers P3HT and PCBM are about 23 and 45 mJ/m^2, respectively), their vertical component distributions are influenced by the substrates (Germack et al., 2009). Namely, if the P3HT:PCBM blends are deposited on poly(3,4-ethylenedioxythiophene):poly(styrenesulfonate) (PEDOT:PSS) with a surface energy of 45 mJ/m^2, the PCBM is enriched near the substrate surface, while the P3HT is enriched near the substrate interface as well as the free surface if the P3HT:PCBM blends are deposited on a poly(thienothiophene):Nafion substrate with a surface energy of 23 mJ/m^2 (Germack et al., 2010). The aforementioned reports are helpful for constructing ideal vertical morphology and further achieving efficient PSCs. However, most of the studies primarily focus on fullerene PSCs, and few works are available on fullerene-free PSCs, especially on finding modulation approaches to realize the desired vertical phase separation.

Hence, the present work is aimed at exploring the influence of processing parameters on the SFE of titanium(IV) oxide bis (2,4-pentanedionate) (TOPD) cathode buffer layer and further elucidating the impact of SFE on the vertical component distribution within the (poly[(2,6-(4,8-bis(5-(2-ethylhexyl)thiophen-2-yl)benzo[1,2-b:4,5-b′]dithiophene)-co-(1,3-bis(5-thiophene-2-yl)-5,7-bis(2-ethylhexyl)benzo[1,2-c:4,5-c]dithiophene-4,8-dione)] PBDB-T:ITIC-M (3,9-bis((Z)-1-(6-(dicyanomethylene)-2-methyl-5,6-dihydro-6H-cyclopenta[b]thiophen-6-one-5-yl) ethylene)-5,5,11,11-tetrakis(4-hexylphenyl)dithieno[2,3-d:2′,3′-d′]-sindaceno[1,2-b:5,6-b′]dithiophene) photoactive layer. Herein, the SFE of TOPD films annealed at different temperatures was quantified jointly from the water contact angle and the diiodomethane contact angle according to the Owens-Wendt (OW) method (Owens and Wendt, 1969). We found that the SFE of TOPD changes as the annealing temperature increases, and the PBDB-T:ITIC-M photoactive layer with the desired vertical component distribution is obtained via fine controlling the SFE of the TOPD layer, leading to a PCE high up to 10.20% for inverted PSCs. The results of time-of-flight secondary-ion mass spectroscopy (TOF-SIMS) visually present the optimized vertical concentration distribution, and the space-charge-limited current (SCLC) method elucidates that the rational vertical component distribution guarantees fully exciton dissociation and facilitates charge transportation.

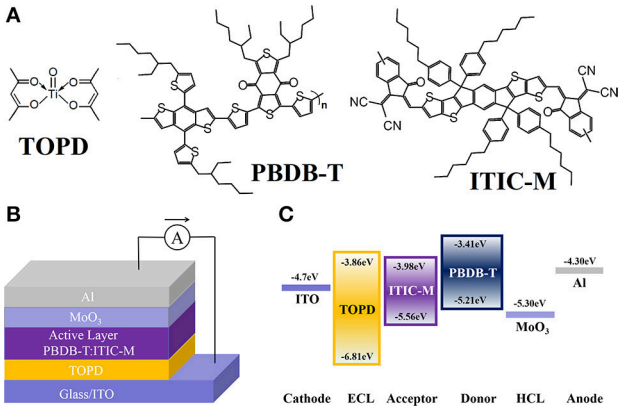

FIGURE 1 | (A) Molecular structures of TOPD, PBDB-T, and ITIC-M. **(B)** Architecture of i-PSCs. **(C)** The HOMO and LUMO energy levels of the materials involved in the i-PSCs.

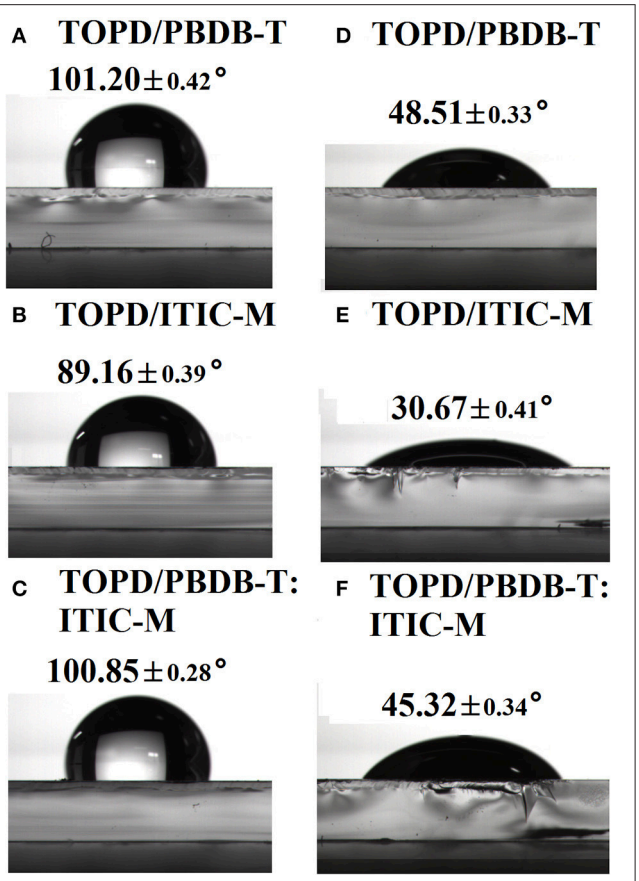

FIGURE 2 | Water contact angle images of **(A)** pure PBDB-T, **(B)** pure ITIC-M, and **(C)** PBDB-T:ITIC-M on the TOPD modified substrate; and diiodomethane contact angle images of **(D)** pure PBDB-T, **(E)** pure ITIC-M, and **(F)** PBDB-T:ITIC-M on the TOPD modified substrate.

EXPERIMENTAL SECTION

Materials and Instrumentations

Patterned indium tin oxide (ITO) glass with a sheet resistance of 10 Ω/sq was purchased from CSG HOLDING Co., Ltd. (Shenzhen, China). Both MoO_3 (purity > 99.0%) and DIO (purity > 98.0%) were purchased from Sigma Aldrich (St. Louis, MO). The TOPD was purchased from Alfa Aesar (Shanghai, China). PBDB-T and ITIC-M were purchased from Solarmer Materials Inc. (Beijing, China), and their molecular structures are displayed in **Figure 1A**. All these commercially available materials were used as received without further purification.

Ultraviolet–visible (UV-Vis) absorption spectra for TOPD films before and after annealing were measured by a Hitachi U-3010 UV-Vis spectrophotometer. X-ray diffraction (XRD) patterns were recorded on a Siemens D5005 diffractometer using CuKα radiation at 40 kV and 20 mA. The contact angle images were investigated using a profilometer of Dektak XT (Bruker) under ambient conditions. The perpendicular component distribution was analyzed using a TOF-SIMS from ION-TOF GmbH. The Ambios Technology XP-2 surface profilometer was employed to evaluate the film thicknesses involved in the device.

Device Design, Fabrication, and Characterization

A well-designed device architecture coupled with a desired perpendicular component distribution in photoactive blends is anticipated to prepare efficient PSCs. **Figure 1B** plots the inverted device structure, where PBDB-T:ITIC-M blend is sandwiched between the TOPD-coated ITO cathode and the high work function (WF) MoO_3 anode. **Figure 1C** demonstrates the energy levels of the materials involved in the devices. The PBDB-T:ITIC-M blend absorbs incident photons and produces excitons. The excitons diffuse toward and dissociate at the PBDB-T:ITIC-M interfaces to yield free electrons and holes. The free electrons can breezily transport from the active layer to the cathode through the TOPD layer due to the similar lowest unoccupied molecular orbital (LUMO) of TOPD (−3.86 eV) and ITIC-M (−3.98 eV). Meanwhile, the high up to 1.25 eV hole barrier between the highest occupied molecular orbital (HOMO) level of TOPD (−6.81 eV) and ITIC-M (−5.56 eV) can effectively block the transportation of the hole from PBDB-T to ITO, reducing carrier recombination losses at the interface (Bai et al., 2018). Furthermore, MoO_3 with WF of 5.30 eV facilitates hole transfer from the active layer to the Al anode (Bai et al., 2017).

All ITO substrates were successively ultrasonically cleaned twice by detergent, deionized water, acetone, and isopropanol. For the regular control device with the architecture of ITO/PEDOT:PSS/PBDB-T:ITIC-M/Ca/Al, the pre-cleaned and dried ITO substrates were treated under UV-ozone (UVO) exposure for 15 min to improve its surface smoothness and WF (Bai et al., 2018). Then a 30 nm PEDOT:PSS layer was deposited by spin-coating its aqueous solution at 2,000 rpm for 45 s, and baked at 150°C for 10 min in air. On the other hand, for the inverted PSCs with the structure of ITO/TOPD/PBDB-T:ITIC-M/Ca/Al, the clean ITO substrates without UVO treatment were transferred into the nitrogen-filled glovebox for the following process. After that, the isopropanol solution with optimized

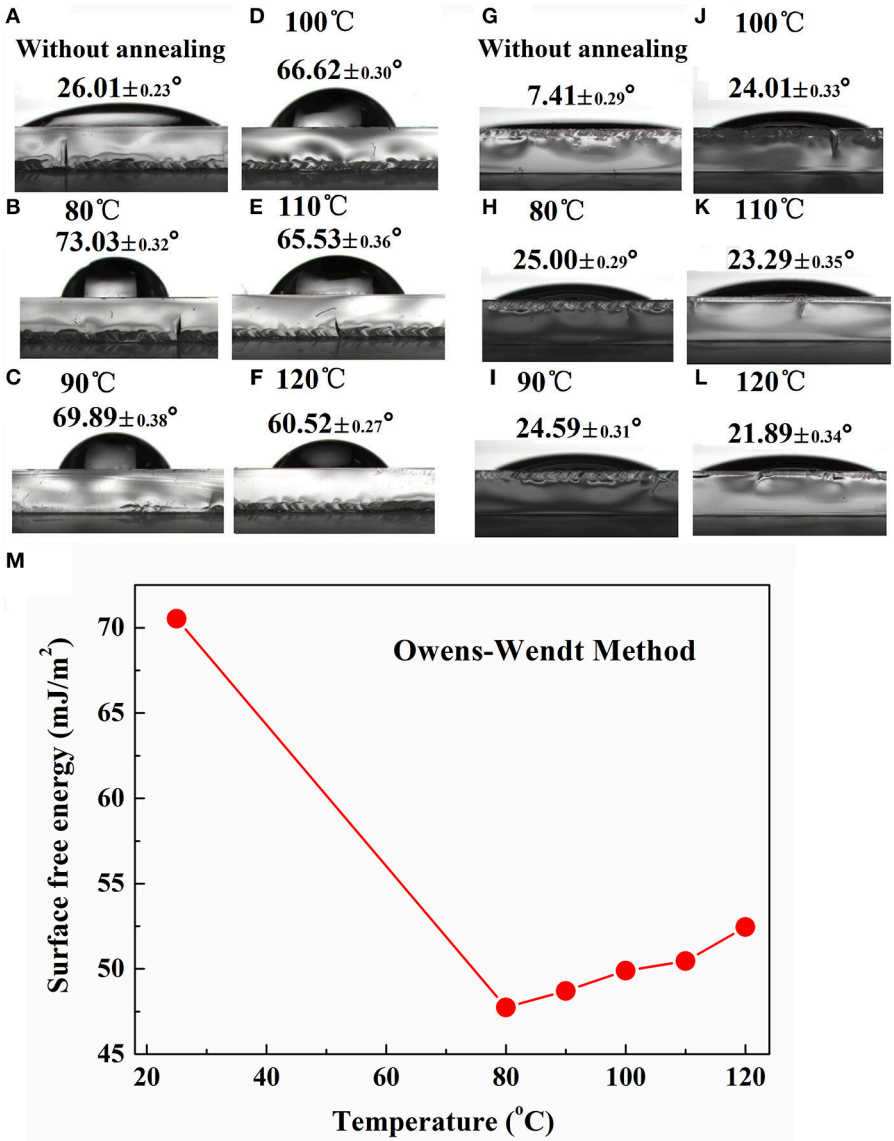

FIGURE 3 | Water contact angle images of TOPD film before **(A)** and after annealing at **(B)** 80°C, **(C)** 90°C, **(D)** 100°C, **(E)** 110°C, and **(F)** 120°C; and diiodomethane contact angle images of TOPD film before **(G)** and after annealing at **(H)** 80°C, **(I)** 90°C, **(J)** 100°C, **(K)** 110°C, and **(L)** 120°C; **(M)** surface free energy of TOPD films before and after annealing calculated from the OW method.

concentrations of TOPD (1,000 rpm/min, 12 mg/mL) were spin-coated on ITO, and finally annealed at different temperatures (80–120°C) for 5 min, and the 14-nm TOPD films with excellent robustness were obtained.

The photosensitive layer was prepared by spin-coating the PBDB-T:ITIC-M chlorobenzene solution (1:1 weight ratio, polymer concentration of 10 mg/mL) with 5% volume ratio of DIO additive on the ITO/PEDOT:PSS and ITO/TOPD substrates at optimized 1,900 rpm for 60 s. Subsequently, the samples were annealed at 100°C for 10 min to obtain the PBDB-T:ITIC-M layer with the thickness of ~100 nm (Bai et al., 2017). Finally, the anode of Ca(10 nm)/Al(100 nm) for the control devices or MoO_3(24 nm)/Al(100 nm) for the inverted PSCs was thermally deposited on the active layer under a base pressure of 5×10^{-5} Pa (Luo et al., 2018).

Device characterization of current density–voltage (*J-V*) performance was conducted in a nitrogen-filled glovebox using a Keithley 2400 Source Measure Unit under simulated AM1.5G solar irradiation with the light intensity of 100 mW/cm^2 (from SAN-EI LTD, AAA grade). The incident photon to electron conversion efficiency (IPCE) was measured using the QE-R system (Enli Tech., Kaohsiung, Taiwan) in air at room temperature. The intensity of each wavelength both in *J-V* and IPCE was calibrated with the standard single crystalline silicon photovoltaic device purchased from the national renewable energy laboratory. Electron mobility was

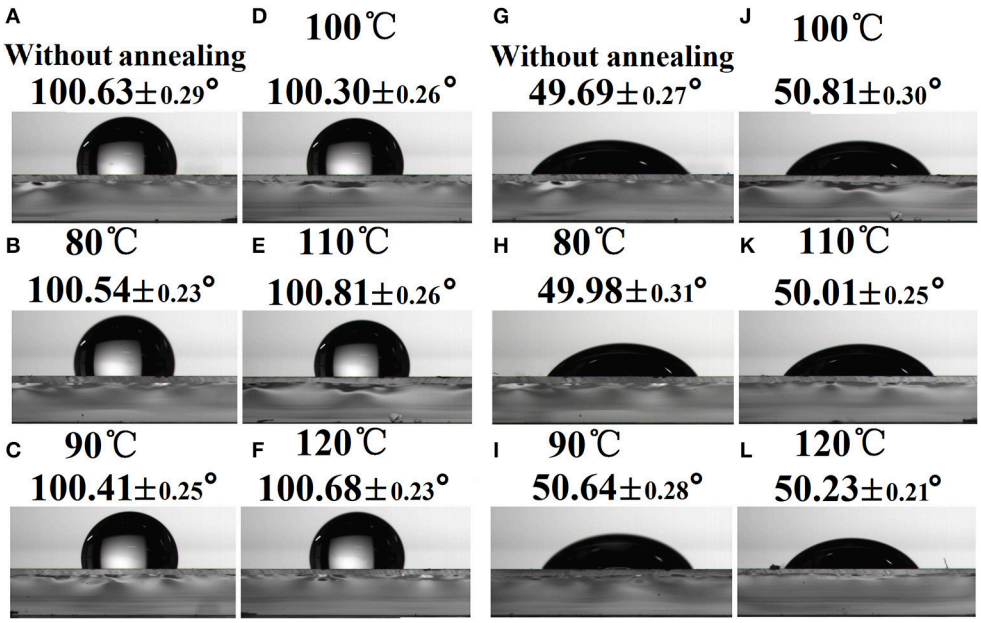

FIGURE 4 | Water contact angle images **(A–F)** and diiodomethane contact angle images **(G–L)** of PBDB-T:ITIC-M on TOPD film without or with annealing.

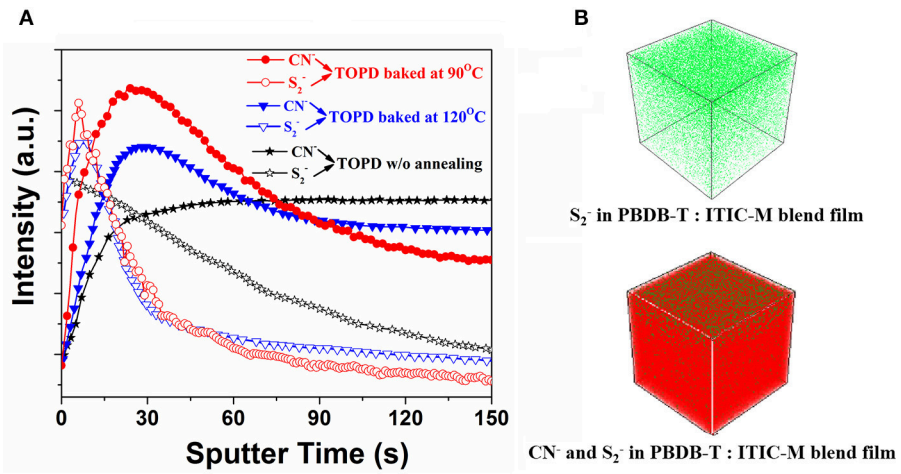

FIGURE 5 | (A) S_2^- and CN^- intensity as a function of sputter time. **(B)** Three-dimensional concentration profiles of S_2^- and CN^- in the PBDTBDD:ITIC-M blend films, and the TOPD layer is annealed at 90°C.

measured employing the SCLC method for devices with the structure of ITO/Al/TOPD/Al, ITO/Al/PBDB-T:ITIC-M/Al, and ITO/TOPD/PBDB-T:ITIC-M/Al. The results are plotted as $\ln(JL^3/V^2)$ vs. $(V/L)^{0.5}$. Electron mobility was calculated from the intercept of the corresponding lines on the axis of $\ln(JL^3/V^2)$ (Malliaras et al., 1998).

RESULTS AND DISCUSSION

OW Method for Determination the SFE of Solid Films

The measurement of the contact angle of sessile drops deposited on different film surfaces is one of the powerful approaches to evaluate the film SFEs and further modulate the vertical concentration distribution of the electron donor and acceptor (Clark et al., 2013). The OW method is the most common approach for polymeric materials so far, in which water and diiodomethane are used. According to OW principal assumptions, the SFE includes dispersion and polar two components. The former represents the dispersion interaction occurring on an interface and the latter is a sum of polar, hydrogen, inductive, and acid–base interactions. The SFE is evaluated with the OW method using the following set of equations (Żenkiewicz, 2007):

$$(\gamma_{Sd}\gamma_{Wd})^{\frac{1}{2}} + (\gamma_{Sp}\gamma_{Wp})^{\frac{1}{2}} = 0.5\gamma_W(1 + \cos\Theta_W) \quad (1)$$

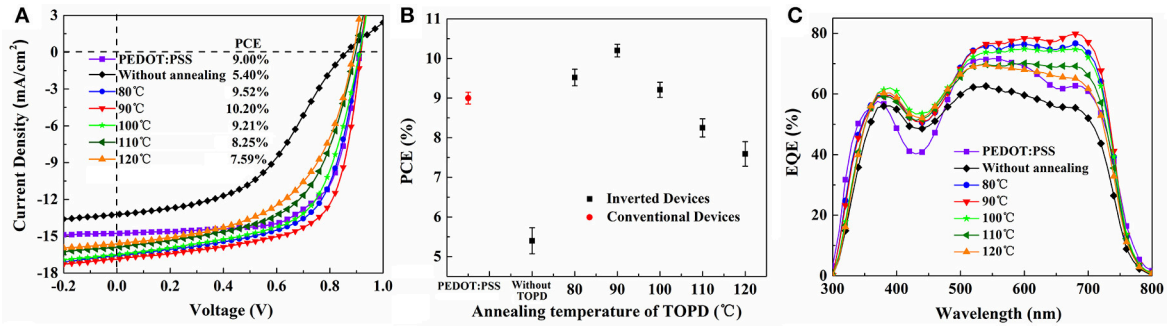

FIGURE 6 | (A) *J-V* curves, **(B)** PCE with error bars, and **(C)** IPCE spectra for conventional devices and inverted devices without and with TOPD. The *J-V* curves are measured under the illumination of AM 1.5G at 100 mW/cm^2.

TABLE 1 | Photovoltaic parameters (averaged over 12 individual devices) of the conventional devices and the i-PSCs with and without TOPD under 100 mW/cm^2.

Device	SFE of TOPD (mJ/cm^2)	V_{oc} (V)	J_{sc} (mA/cm^2)	*FF* (%)	PCE (%)	R_s^a (Ω cm^2)
Conventional device		0.913	14.76	66.78	9.00 ± 0.15	2.8
Without annealing	70.53	0.861	13.21	47.46	5.40 ± 0.33	6.5
80°C	47.74	0.911	16.57	63.09	9.52 ± 0.21	2.4
90°C	48.71	0.916	16.88	65.33	10.20 ± 0.16	2.1
100°C	49.90	0.912	16.51	61.15	9.21 ± 0.19	3.7
110°C	50.46	0.896	15.89	57.93	8.25 ± 0.23	4.6
120°C	52.46	0.889	15.60	54.67%	7.59 ± 0.31	5.2

[a] *Series resistance (R_s) for PSCs in the dark is obtained at 1 V.*

$$(\gamma_{Sd}\gamma_{Dd})^{\frac{1}{2}} + (\gamma_{Sp}\gamma_{Dp})^{\frac{1}{2}} = 0.5\gamma_D(1+\cos\Theta_D) \quad (2)$$

$$\gamma_S = \gamma_{Sd} + \gamma_{Sp} \quad (3)$$

where W, D, and S represent the polar liquid of water, the dispersion liquid diiodomethane, and the solid film; $\gamma_s, \gamma_{sd}, \gamma_{sp}$ are the SFE, the SFE dispersion component, and the SFE polar component of the solid film; $\gamma_{Wd}, \gamma_{Dd}, \gamma_{Wp}, \gamma_{Dp}$ are the dispersion component and the polar component of water and diiodomethane, and these values are extracted from Owens and Wendt (1969); Θ_W and Θ_D are the contact angles of water and diiodomethane, respectively.

Figures 2A–F demonstrate the average water contact angle (WCA) and the diiodomethane contact angle (DCA) of the pure ITIC-M, pure PBDB-T, and PBDB-T:ITIC-M blend films on TOPD-coated ITO. For pure PBDB-T, pure ITIC-M, and PBDB-T:ITIC-M blend film, the WCAs are 101.20° (**Figure 2A**), 89.16° (**Figure 2B**), and 100.85° (**Figure 2C**), respectively; the DCAs are 48.51° (**Figure 2D**), 30.67° (**Figure 2E**), and 45.32° (**Figure 2F**), respectively. Correspondingly, the SFEs for pure PBDB-T and pure ITIC-M are 35.67 and 43.98 mJ/cm^2 calculated by the OW method, respectively. Apparently, the SFE of PBDB-T is lower than that of ITIC-M, and we can foresee that a much higher proportion of PBDB-T will accumulate at the top surface of PBDB-T:ITIC-M blend film to lower the systematic SFE. As expected, the SFE of the PBDB-T:ITIC-M blend film is 37.56 mJ/m^2 calculated from the OW method, which visibly indicates that the blend film minimizes its total free energy by increasing the surface concentration of the low-energy component PBDB-T (Jasieniak et al., 2016).

To construct a desired vertical component distribution within PBDB-T:ITIC-M blend film, TOPD was annealed at different temperatures to change its SFE and further modulate the vertical concentration distribution of ITIC-M. **Figure 3** presents the WCA and DCA of TOPD films before and after annealing at different temperatures. The WCA and DCA for TOPD film without annealing are only 26.01° (**Figure 3A**) and 7.41° (**Figure 3G**), which indicates the high SFE of 70.53 mJ/cm^2. The WCA for TOPD film annealed at 80, 90 100, 110, and 120 °C are 73.03° (**Figure 3B**), 69.89° (**Figure 3C**), 66.62° (**Figure 3D**), 65.53° (**Figure 3E**), and 60.52° (**Figure 3F**); and their corresponding DCA are 25.00° (**Figure 3H**), 24.59° (**Figure 3I**), 24.01° (**Figure 3J**), 23.29° (**Figure 3K**), and 21.89° (**Figure 3L**), respectively. The SFEs are 47.74, 48.71, 49.9, 50.46, 52.46 mJ/cm^2 for TOPD film annealed at 80, 90 100, 110, and 120°C according to the OW method, as shown in **Figure 3**. Obviously, the SFE increases gradually with the rise in the annealing temperature, and these subtle changes certainly adjust the vertical concentration distribution of ITIC-M.

Component Distribution of PBDB-T:ITIC-M Blends at the Air Surface

To clarify the influence of substrate SFEs on the component distribution at the air surface, the WCA and DCA of PBDB-T:ITIC-M on TOPD film without or with annealing are illustrated in **Figures 4A-L**, respectively. As can be seen, both

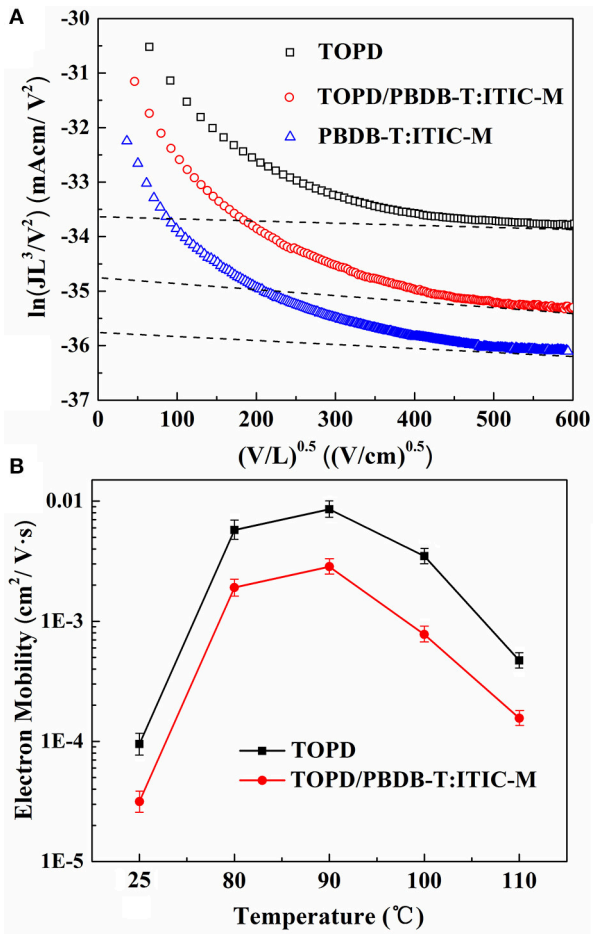

FIGURE 7 | (A) *J-V* curves of single-electron devices with the structure of ITO/Al/TOPD/Al, ITO/Al/PBDB-T:ITIC-M/Al, and ITO/TOPD/PBDB-T:ITIC-M/Al; **(B)** the electron mobility for TOPD and TOPD/PBDB-T:ITIC-M as a function of the annealing temperature of TOPD.

the WCA and DCA do not strongly depend on substrate SFEs, and their corresponding values remain almost the same whether TOPD is annealed or not. The WCAs change slightly around 100° and the DCAs alter around 50°, which suggests that there is no distinct difference about the component distribution of the electron donor and acceptor at the air surface. Hence, the changes of substrate SFEs hardly affect the component distribution at the top surface region (Björström et al., 2005; Tillack et al., 2011).

Vertical Component Distribution Within the PBDB-T:ITIC-M Photoactive Layer

The photoactive layers deposited on three typical TOPD cathode buffer layers (before annealing, annealed at 90 and 120°C) were selected to test the TOF-SIMS and further elucidate how SFEs affect the vertical component distribution. **Figure 5** plots the intensity change in the signals of S_2^- and CN^- with sputter time since they are characteristic species for PBDB-T and ITIC-M, respectively. As can be seen, the PBDB-T concentration located at the air surface is distinctly higher than that found in the bulk whether TOPD is annealed or not. However, the PBDB-T concentration distribution almost decreases linearly with sputter time for TOPD without annealing; the PBDB-T concentration distribution reaches a maximum value at 6 s for TOPD annealed at 90 and 120°C. When sputter time is beyond 55 s, in increasing order, the PBDB-T concentration distribution value for TOPD annealed at 120°C, next to TOPD baked at 90°C, is lower than that of TOPD before annealing. Obviously, the higher PBDB-T concentration distribution at the substrate interface has a detrimental effect on the collection of carriers for PSCs (Chen et al., 2009). Therefore, it is reasonable to postulate that the PSCs with TOPD baked at 90°C afford high performance.

The distributions of ITIC-M greatly rely on heat treatment. For TOPD film without annealing, the ITIC-M distribution in the blends increases rapidly during the first 30 s and remains constant after 30 s deviating away from the ideal distribution of the electron acceptor. For TOPD film baked at 90 and 120°C, their ITIC-M distributions reach a maximum value at 24 and 30 s, respectively, and the signal intensity of the former is stronger than that of the latter. There is no obvious change for signals of S_2^- and CN^- after the sputter time beyond 150 s. From the results obtained up till now, three aspects have to be addressed. The first is that the air surface is always enriched with a lower-surface-energy polymer component and the influence of substrate SFEs is negligible, which is in accordance with the contact angle measurement results (Tanaka et al., 2010). The second is that the substrate SFEs have a more direct and remarkable effect on the vertical component distribution within the active layer, both for the electron donor and acceptor. Lastly, the TOPD film baked at 90°C with the SFE of 48.71 mJ/cm^2, which is very close to that of the ITIC film with an SFE of 43.98 mJ/cm^2, tends to form a desired vertical component distribution facilitating carrier transportaion.

The mechanism of the vertical component distribution is complicated, including thermodynamics, kinetics, surface free energy, and selective dissolubility. In this work, we focus on the SFE of the TOPD layer, which roots from the kinetics of the molecular rearrangement in the blend films (Karagiannidis et al., 2011). As we know, the driving force for the lower SFE constituent accumulation to the high energy surface (air) is the lowering of the overall free energy of the system (Xu et al., 2010), leading to a larger concentration of PBDB-T at the surface. Theoretically, a complete demixing is expected to occur and the formation of a bilayer is thermodynamically possible if the thermal annealing above the polymer's glass transition temperature and the macromolecules obtain the appropriate mobility to rearrange (Klein et al., 2000). However, in the case of the PBDB-T:ITIC-M system, some ITIC-M molecules will probably diffuse into the PBDB-T layer driven by the different surface free energies of TOPD layers to achieve a more thermodynamically favorable component distribution, namely a phase separation will eventually come to a limit (Treat et al., 2011). Hence, the air–film interface is enriched with polymer, while the substrate–film interface is enriched with ITIC-M regardless of the annealing temperature. Films deposited on annealed TOPD show more ITIC-M close to the top surface (higher CN^- to S_2^- signal at around 30 s) induced by the different

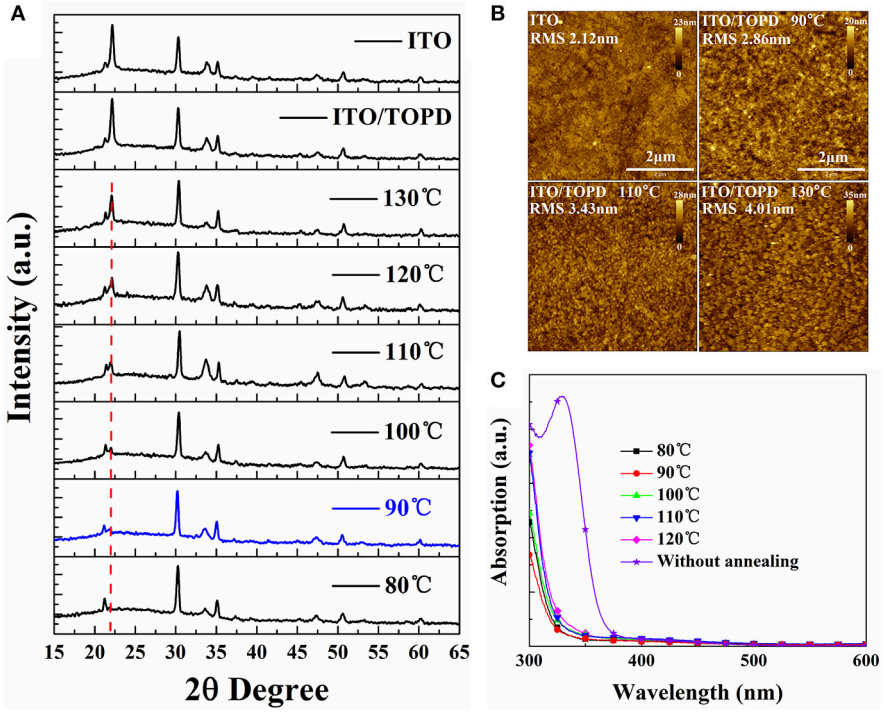

FIGURE 8 | (A) XRD patterns, **(B)** AFM images with 5 × 5 μm scan size, and **(C)** absorption spectra of TOPD films on ITO glasses before and after annealing at different temperatures in N_2 for 5 min.

SFEs of the TOPD layer. Nevertheless, the underlying mechanism of the vertical component distribution is still under way for all researchers, which is also the area warranting our further study.

Photovoltaic Performance and Electron Mobility

To further demonstrate the interplay between the vertical component distribution and device performance, *J-V* results, PCE with error bars and IPCE spectra of the control device and i-PSCs with TOPD cathode buffer layers are shown in **Figure 6**. The key parameters of PCE, short-circuit current density (J_{sc}), open-circuit voltage (V_{oc}), and fill factor (*FF*) under the illumination of AM1.5G, 100 mW/cm^2 (averaged over 12 individual devices), are compared in **Table 1**. The control device with PEDOT:PSS shows a PCE of 9.00%, with a V_{oc} of 0.913 V, a J_{sc} of 14.76 mA/cm^2, and an *FF* of 66.78%. The inverted device with an unannealed TOPD layer provides the lowest performance; the PCE, J_{sc}, V_{oc}, and *FF* are 5.40%, 13.21 mA/cm^2, 0.861 V, and 47.46%, respectivley. After annealing, the four parameters are all enhanced significantly, and the device with TOPD baked at 90°C affords the highest device metrics, with a PCE of 10.20%, a J_{sc} of 16.88 mA/cm^2, a V_{oc} of 0.916 V, and an *FF* of 65.33%. The improvement in J_{sc} and *FF* benefits from the vertical concentration distribution of PBDB-T and ITIC-M in the active layer, which fortify the charge separation and transportation (Ma et al., 2014). The five annealing temperatures affect PCEs in descending order as 90, 80, 100, 110, 120°C. The results of IPCE in **Figure 6B** are in agreement with the aforementioned results, which strongly confirm that the vertical concentration distribution of PBDB-T and ITIC-M within the blend film is affected by the substrate SFE greatly.

To illustrate how charge transportation and collection can be affected in the photoactive blends having different vertical component distributions, the *J-V* curves of single-electron devices (Ahmed and Nakazato, 1996) with the structure of ITO/Al/TOPD/Al, ITO/Al/PBDB-T:ITIC-M/Al, and ITO/TOPD/PBDB-T:ITIC-M/Al are displayed in **Figure 7A**, in which the TOPD film annealed at 90°C. The electron mobilities of TOPD, PBDB-T:ITIC-M, and TOPD/PBDB-T:ITIC-M are 8.56 × 10^{-3}, 1.04 × 10^{-3}, and 2.85 × 10^{-3} cm^2 V^{-1} s^{-1}, respectively. The change of the electron mobility as a function of the annealing temperature in **Figure 7B** shows that TOPD with heat treatment manifests higher charge mobility than that of TOPD film without annealing, and a maximum is passed through. Without annealing, the electron mobilities of TOPD and TOPD/PBDB-T:ITIC-M are 9.51 × 10^{-5} and 3.16 × 10^{-5} cm^2 V^{-1} s^{-1}, respectively. On the other hand, the electron mobilities of TOPD baked at 80, 90, 100, and 110°C are 5.74 × 10^{-3}, 8.56 × 10^{-3}, 3.48 × 10^{-3}, and 4.71 × 10^{-4} cm^2 V^{-1} s^{-1}, and the corresponding electron mobilities of TOPD/PBDB-T:ITIC-M are 1.91 × 10^{-3}, 2.85 × 10^{-3}, 7.77 × 10^{-4}, and 1.56 × 10^{-4} cm^2 V^{-1} s^{-1}, respectively. Therefore, the increased electron mobility for TOPD after heat treatment is in favor of charge transportation and collection. Our results confirm that 90°C is an appropriate annealing temperature for TOPD from the standpoint of charge transportation and collection, which can increase J_{sc} and *FF* of devices.

Other Structural and Optical Properties of TOPD Films

Other structural and optical information of TOPD film besides the SFE is explored to elaborate the device performance enhancements. **Figure 8A** shows the XRD patterns for TOPD films before and after annealing. Apparently, there does not appear to be any characteristic peak of TOPD except that of ITO, and all TOPD films are in the amorphous state whether they are annealed or not. But the peak of the glass substrate at $2\theta = 22^\circ$ illustrates obvious changes before and after annealing. Namely, the XRD curve of TOPD/ITO before annealing overlaps well with the bare ITO, and the peak intensity is very strong. On the other hand, there is no obvious peak at $2\theta = 22^\circ$ for TOPD annealed 80 or 90°C, and the peak intensity gradually increases as the annealing temperature increases from 100 to 130°C. This suggests that 80 and 90°C are the suitable temperatures for forming uniform and compact film on the surface of ITO. The different peak intensities for TOPD annealed at higher temperature are caused by different aggregation behaviors of TOPD films. The AFM images of TOPD annealed at different temperatures are shown in **Figure 8B**. Evidently, the root-mean-square (rms) roughness rises with the increase in the annealing temperature of TOPD, and they are 2.86, 3.43, and 4.01 nm for TOPD annealed at 90, 110, and 130°C, respectively. The suggests that fine and weak aggregation behaviors occur at lower annealing temperature, and the smooth and uniform film formed at lower temperature is favorable for effective charge transport and collection. This is in accordance with the result of the XRD results.

Figure 8C plots the absorption spectra of TOPD films before and after annealing at different temperatures. It is evident that the absorption of TOPD films decreases distinctly after annealing, which is caused by the organic residual solvents because there is no chemical component change before and after thermal annealing (Bai et al., 2018). The TOPD film baked at 90°C demonstrates the weakest absorption, which ensures more light harvesting in the photoactive layer. On the whole, the absorption first decreases slightly as the annealing temperature rises from 80 to 90°C, and then increases as the annealing temperature rises from 90 to 120°C. Therefore, TOPD film baked at 90°C shows superior structural and optical properties in addition to its appropriate SFE.

CONCLUSIONS

Fine-tuning the SFE of the TOPD cathode buffer layer has been explored in this work, with the aim of unraveling the underlying mechanism and rational controlling the vertical distribution of the electron donor and acceptor. Our studies confirm that the SFE of TOPD increases gradually with the rise in the annealing temperature, and these subtle changes certainly cause the profound vertical component distribution within the bulk region of the PBDB-T:ITIC-M. The results of TOF-SIMS visibly demonstrate that TOPD film baked at 90°C with the SFE of 48.71 mJ/cm^2, which is very close to that of the ITIC film with the SFE of 43.98 mJ/cm^2, tends to form a desired vertical component distribution facilitating charge transportation. Consequently, compared with conventional BHJ devices without tuning the donor and acceptor concentration, the PCE increases from 9.00 to 10.20% benefiting from the short circuit current density increase from 14.76 to 16.88 mA/cm^2. The results obtained in this work allow the conclusion that modulation of the SFE of the substrate is a feasible way to control the vertical component distribution of the electron donor and acceptor. This approach holds great potential for practical application of high-efficiency PSCs.

AUTHOR CONTRIBUTIONS

All authors listed have made a substantial, direct, and intellectual contribution to the work, and approved it for publication.

FUNDING

Financial support by the National Natural Science Foundation of China [grant numbers 61006050, 51573042], the Natural Science Foundation of Beijing [grant number 2151004], and the Fundamental Research Funds for the Central Universities [grant numbers 2016MS50, JB2015RCJ02, 2016YQ06] in China is gratefully acknowledged.

ACKNOWLEDGMENTS

Many thanks to Dr. Xingwang Zhang and Zhigang Yin for generous advice and help.

REFERENCES

Ahmed, H., and Nakazato, K. (1996). Single-electron devices. *Microelectron. Eng.* 32, 297–315. doi: 10.1016/0167-9317(95)00179-4

Bai, Y., Yang, B., Wang, F., Liu, H., Hayat, T., Alsaedi, A., et al. (2017). Bright prospect of using alcohol-soluble Nb_2O_5 as anode buffer layer for efficient polymer solar cells based on fullerene and non-fullerene acceptors. *Org. Electron.* 52, 323–328. doi: 10.1016/j.orgel.2017.11.010

Bai, Y., Yang, B., Zhao, C., Shi, Z., Hayat, T., Alsaedi, A., et al. (2018). Synergy of titanium chelate electron collection layer and vertical phase separated photoactive layer for efficient inverted polymer solar cells. *J. Mater. Chem. A* 6, 7257–7264. doi: 10.1039/c8ta01486h

Bin, H., Gao, L., Zhang, Z. G., Yang, Y., Zhang, Y., Zhang, C., et al. (2016). 11.4% efficiency non-fullerene polymer solar cells with trialkylsilyl substituted 2d-conjugated polymer as donor. *Nat. Commun.* 7:13651. doi: 10.1038/ncomms13651

Björström, C. M., Bernasik, A., Rysz, J., Budkowski, A., Nilsson, S., Svensson, M., et al. (2005). Multilayer formation in spin-coated thin films of low-bandgap polyfluorene:pcbm blends. *J. Phys. Condens. Matt.* 17:L529. doi: 10.1088/0953-8984/17/50/L01

Chen, L., Hong, Z., Li, G., and Yang, Y. (2009). Recent progress in polymer solar cells: manipulation of polymer:fullerene morphology and the formation of efficient inverted polymer solar cells. *Adv. Mater.* 21, 1434–1449. doi: 10.1002/adma.200802854

Clark, M. D., Jespersen, M. L., Patel, R. J., and Leever, B. J. (2013). Predicting vertical phase segregation in polymer-fullerene bulk heterojunction solar cells by free energy analysis. *ACS Appl. Mater. Int.* 5, 4799–4807. doi: 10.1021/am4003777

Germack, D. S., Chan, C. K., Hamadani, B. H., Richter, L. J., Fischer, D. A., Gundlach, D. J., et al. (2009). Substrate-dependent interface composition and charge transport in films for organic photovoltaics. *Appl. Phys. Lett.* 94:233303. doi: 10.1063/1.3149706

Germack, D. S., Chan, C. K., Kline, R. J., Fischer, D. A., Gundlach, D. J., Toney, M. F., et al. (2010). Interfacial segregation in polymer/fullerene blend films for photovoltaic devices. *Macromolecules* 43, 3828–3836. doi: 10.1021/ma100027b

Heo, S. W., Baek, K. H., Song, H. J., Lee, T. H., and Moon, D. K. (2014). Improved performance of P3HT:PCBM-based solar cells using nematic liquid crystals as a processing additive under low processing temperature conditions. *Macromol. Mater. Eng.* 299, 353–360. doi: 10.1002/mame.201300168

Heriot, S. Y., and Jones, R. A. (2005). An interfacial instability in a transient wetting layer leads to lateral phase separation in thin spin-cast polymer-blend films. *Nat. Mater.* 4, 782–786. doi: 10.1038/nmat1476

Hui, L., Tang, H., Li, L., Xu, W., Zhao, X., and Yang, X. (2011). Solvent-soaking treatment induced morphology evolution in P3HT:PCBM composite films. *J. Mater. Chem.* 21, 6563–6568. doi: 10.1039/C1JM10148J

Jasieniak, J. J., Treat, N. D., Mcneill, C. R., De Villers, B. J. T., Della Gaspera, E., and Chabinyc, M. L. (2016). Interfacial characteristics of efficient bulk heterojunction solar cells fabricated on moox anode interlayers. *Adv. Mater.* 28, 3944–3951. doi: 10.1002/adma.201503309

Jiang, W., Yu, R., Liu, Z., Peng, R., Mi, D., Hong, L., et al. (2017). Ternary nonfullerene polymer solar cells with 12.16% efficiency by introducing one acceptor with cascading energy level and complementary absorption. *Adv. Mater.* 30:1703005. doi: 10.1002/adma.201703005

Jones, R. A., Kramer, E. J., Rafailovich, M. H., Sokolov, J., and Schwarz, S. A. (1989). Surface enrichment in an isotopic polymer blend. *Phys. Rev. Lett.* 62, 280–283. doi: 10.1103/PhysRevLett.62.280

Karagiannidis, P. G., Georgiou, D., Pitsalidis, C., Laskarakis, A., and Logothetidis, S. (2011). Evolution of vertical phase separation in P3HT:PCBM thin films induced by thermal annealing. *Mater. Chem. Phys.* 129, 1207–1213. doi: 10.1016/j.matchemphys.2011.06.007

Kim, D. Y., Lee, S. A., Kim, S., Nah, C., Lee, S. H., and Jeong, K. U. (2017). Asymmetric fullerene nanosurfactant: interface engineering for automatic molecular alignments. *Small* 14:1702439. doi: 10.1002/smll.201702439

Kim, J. S., Lee, Y., Lee, J. H., Park, J. H., Kim, J. K., and Cho, K. (2010). High-efficiency organic solar cells based on end-functional-group-modified poly(3-hexylthiophene). *Adv. Mater.* 22, 1355–1360. doi: 10.1002/adma.200902803

Klein, J., Kerle, T., Zink, F., and Eiser, E. (2000). Segmental Interaction parameters of binary polymer mixtures evaluated from binodals and from surface-segregation profiles: comparison with small-angle neutron scattering. *Macromolecules* 33, 1298–1305. doi: 10.1021/ma990798a

Krebs, F. C., Nielsen, T. D., Fyenbo, J., Wadstrom, M., and Pedersen, M. S. (2010). Manufacture, integration and demonstration of polymer solar cells in a lamp for the "lighting africa" initiative. *Energy Environ. Sci.* 3, 512–525. doi: 10.1039/b918441d

Li, C. Z., Yip, H. L., and Jen, A. K. Y. (2012). Functional fullerenes for organic photovoltaics. *J. Mater. Chem.* 22, 4161–4177. doi: 10.1039/C2JM15126J

Li, G., Zhu, R., and Yang, Y. (2012). Polymer solar cell. *Nat. Photonics* 6, 153–161. doi: 10.1038/nphoton.2012.11

Lu, L., Luo, Z., Xu, T., and Yu, L. (2013). Cooperative plasmonic effect of Ag and Au nanoparticles on enhancing performance of polymer solar cells. *Nano Lett.* 13, 59–64. doi: 10.1021/nl3034398

Luo, Z., Yang, B., Bai, Y., Hayat, T., Alsaedi, A., Tan, Z., et al. (2018). Efficient polymer solar cells with alcohol-soluble zirconium(iv) isopropoxide cathode buffer layer. *Energies* 11:328. doi: 10.3390/en11020328

Ma, W., Tumbleston, J. R., Ye, L., Wang, C., Hou, J., and Ade, H. (2014). Quantification of nano- and mesoscale phase separation and relation to donor and acceptor quantum efficiency, Jsc, and FF in polymer:fullerene solar cells. *Adv. Mater.* 26, 4234–4241. doi: 10.1002/adma.201400216

Malliaras, G. G., Brock, P. J., Scott, C., and Salem, J. R. (1998). Electrical characteristics and efficiency of single-layer organic light-emitting diodes. *Phys. Rev. B* 581:10371. doi: 10.1103/PhysRevB.58.R13411

Meier, R., Ruderer, M. A., Diethert, A., Kaune, G., Körstgens, V., Roth, S. V., et al. (2011). Influence of film thickness on the phase separation mechanism in ultrathin conducting polymer blend films. *J. Phys. Chem. B* 115, 2899–2909. doi: 10.1021/jp200341u

Ouyang, X. H., Peng, R. X., Ai, L., Zhang, X. Y., and Ge, Z. Y. (2015). Efficient polymer solar cells employing a non-conjugated small-molecule electrolyte. *Nat. Photonics* 9, 520–525. doi: 10.1038/NPHOTON.2015.126

Owens, D. K., and Wendt, R. C. (1969). Estimation of the surface free energy of polymers. *J. Appl. Polym. Sci.* 13, 1741–1747. doi: 10.1002/app.1969.070130815

Peng, R., Liu, Z., Guan, Q., Hong, L., Song, W., Wei, Q., et al. (2018). Highly efficient non-fullerene polymer solar cells enabled by novel non-conjugated small-molecule cathode interlayers. *J. Mater. Chem. A* 6, 6327–6334. doi: 10.1039/C8TA00881G

Qiu, L., Lim, J. A., Wang, X., Lee, W. H., Hwang, M., and Cho, K. (2008). Versatile use of vertical-phase-separation-induced bilayer structures in organic thin-film transistors. *Adv. Mater.* 20, 1141–1145. doi: 10.1002/adma.200702505

Tanaka, T., Saitoh, M., Jyoyama, E., and Midorikawa, S. (2010). Surface free energy and ink transfer ratio. *Bull. Tech. Assoc. Graph. Arts Jpn* 38, 423–432. doi: 10.11413/nig1987.38.423

Tillack, A. F., Noone, K. M., Macleod, B. A., Nordlund, D., Nagle, K. P., Bradley, J. A., et al. (2011). Surface characterization of polythiophene:fullerene blends on different electrodes using near edge x-ray absorption fine structure. *ACS Appl. Mater. Int.* 3, 726–732. doi: 10.1021/am101055r

Treat, N. D., Brady, M. A., Smith, G., Toney, M. F., Kramer, E. J., Hawker, C. J., et al. (2011). Interdiffusion of PCBM and P3HT reveals miscibility in a photovoltaically active blend. *Adv. Energy Mater.* 1, 82–89. doi: 10.1002/aenm.201000023

Van Franeker, J. J., Turbiez, M., Li, W., Wienk, M. M., and Janssen, R. A. (2015). A real-time study of the benefits of co-solvents in polymer solar cell processing. *Nat. Commun.* 6:6229. doi: 10.1038/ncomms7229

Wang, Y., Zhu, H., Shi, Z., Wang, F., Zhang, B., Dai, S., et al. (2016). Engineering the vertical concentration distribution within the polymer:fullerene blends for high performance inverted polymer solar cells. *J. Mater. Chem. A* 5, 2319–2327. doi: 10.1039/C6TA10678A

Xiao, Z., Jia, X., and Ding, L. (2017). Ternary organic solar cells offer 14% power conversion efficiency. *Sci. Bull.* 62, 1562–1564. doi: 10.1016/j.scib.2017.11.003

Xiao, Z., Yuan, Y., Yang, B., Vanderslice, J., Chen, J., Dyck, O., et al. (2014). Universal formation of compositionally graded bulk heterojunction for efficiency enhancement in organic photovoltaics. *Adv. Mater.* 26, 3068–3075. doi: 10.1002/adma.201305196

Xie, F., Choy, W. C. H., Sha, W. E. I., Zhang, D., Zhang, S., Li, X., et al. (2014). Enhanced charge extraction in organic solar cells through electron accumulation effects induced by metal nanoparticles. *Energy Environ. Sci.* 6, 3372–3379. doi: 10.1039/C3EE42440E

Xu, Z., Chen, L., Yang, G., Huang, C., Hou, J., Wu, Y., et al. (2010). Vertical phase separation in poly(3-hexylthiophene): fullerene derivative blends and its advantage for inverted structure solar cells. *Adv. Funct. Mater.* 19, 1227–1234. doi: 10.1002/adfm.200801286

Yan, Y., Liu, X., and Wang, T. (2017). Conjugated-polymer blends for organic photovoltaics: rational control of vertical stratification for high performance. *Adv. Mater.* 29:1601674. doi: 10.1002/adma.201601674

Żenkiewicz, M. (2007). Comparative study on the surface free energy of a solid calculated by different methods. *Polym. Test.* 26, 14–19. doi: 10.1016/j.polymertesting.2006.08.005

Zhao, J., Li, Y., Yang, G., Jiang, K., Lin, H., Ade, H., et al. (2016). Efficient organic solar cells processed from hydrocarbon solvents. *Nat. Energy* 1:15027. doi: 10.1038/nenergy.2015.27

Zhao, W., Li, S., Yao, H., Zhang, S., and Zhang, Y. (2017). Molecular optimization enables over 13% efficiency in organic solar cells. *J. Am. Chem. Soc.* 139, 7148–7151. doi: 10.1021/jacs.7b02677

Conflict of Interest Statement: The authors declare that the research was conducted in the absence of any commercial or financial relationships that could be construed as a potential conflict of interest.

frontiers in Chemistry

REVIEW
published: 07 August 2018
doi: 10.3389/fchem.2018.00341

BN Embedded Polycyclic π-Conjugated Systems: Synthesis, Optoelectronic Properties, and Photovoltaic Applications

Jianhua Huang and Yuqing Li*

College of Materials Science and Engineering, Huaqiao University, Xiamen, China

OPEN ACCESS

Edited by:
Chuanlang Zhan,
Institute of Chemistry (CAS), China

Reviewed by:
Liu Jun,
Changchun Institute of Applied Chemistry (CAS), China
Guo Chen,
Shanghai University, China

****Correspondence:***
Jianhua Huang
huangjianhua@hqu.edu.cn

Specialty section:
This article was submitted to Organic Chemistry, a section of the journal Frontiers in Chemistry

Received: *18 June 2018*
Accepted: *19 July 2018*
Published: *07 August 2018*

Citation:
Huang J and Li Y (2018) BN Embedded Polycyclic π-Conjugated Systems: Synthesis, Optoelectronic Properties, and Photovoltaic Applications. Front. Chem. 6:341. doi: 10.3389/fchem.2018.00341

In the periodic table of elements, boron (B, atomic number, 5) and nitrogen (N, atomic number, 7) are neighboring to the carbon (C, atomic number, 6). Thus, the total electronic number of two carbons (12) is equal to the electronic sum of one boron (5) and one nitrogen (7). Accordingly, replacing two carbons with one boron and one nitrogen in a π-conjugated structure gives an isoelectronic system, i.e., the BN perturbed π-conjugated system, comparing to their all-carbon analogs. The BN embedded π-conjugated systems have unique properties, e.g., optical absorption, emission, energy levels, bandgaps, and packing order in contrast to their all-carbon analogs and have been intensively studied in terms of novel synthesis, photophysical characterizations, and electronic applications in recent years. In this review, we try to summarize the synthesis methods, optoelectronic properties, and progress in organic photovoltaic (OPV) applications of the representative BN embedded polycyclic π-conjugated systems. Firstly, the narrative will be commenced with a general introduction to the BN units, i.e., B←N coordination bond, B-N covalent bond, and N-B←N group. Then, the representative synthesis strategies toward π-conjugated systems containing B←N coordination bond, B-N covalent bond, and N-B←N group will be summarized. Afterwards, the frontier orbital energy levels, optical absorption, packing order in solid state, charge transportation ability, and photovoltaic performances of typical BN embedded π-conjugated systems will be discussed. Finally, a prospect will be proposed on the OPV materials of BN doped π-conjugated systems, especially their potential applications to the small molecules organic solar cells.

Keywords: BN-embedded unit, isoelectronic structure, π-conjugated material, organic solar cell, device performance

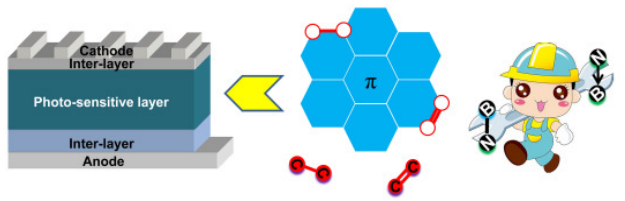

GRAPHICAL ABSTRACT | Design motif of BN embedded Pi-units for photovoltaic application.

INTRODUCTION

The past years have witnessed a fruitful advance of organic conjugated materials and great enthusiasm was fueled to develop novel π-molecules and judiciously apply them to organic electronic devices, e.g., organic field effect transistors (OFETs) (Gsänger et al., 2016; Li M. et al., 2018), organic light emitting diodes (OLEDs) (Grimsdale et al., 2009), organic solar cells (OSCs) (Lu et al., 2015; Zhan and Yao, 2016), organic thermoelectric devices (OTEDs) (Shi et al., 2015; Huang et al., 2016; Lim et al., 2018), and organic photodetectors (OTDs) (Wang et al., 2016a; Benavides et al., 2018; Murto et al., 2018). Especially, the bulk-heterojunction (BHJ)-type OSCs adopting organic semiconductors as photo-sensitive layers have been considered a promising candidate for the next generation of green energy due to solution processability, low cost, light weight, flexibility features of organic materials. The photo-sensitive layers of OSCs are blends of an electron-donor (p-type) and an electron-acceptor (n-type) with nano-phase separated morphology. Although the fullerene derivatives, e.g., phenyl-C_{61}-butyric acid methyl ester ($PC_{61}BM$) and phenyl-C_{71}-butyric acid methyl ester ($PC_{71}BM$) have been the dominant acceptor materials in a long time (Sariciftci et al., 1992), both the electron-donor and electron-acceptor materials have been extended to π-conjugated linear molecules, star molecules, oligomers, and polymers in recent years. To achieve satisfactory power conversion efficiency (PCE), the photo-sensitive materials should be featured by the following points (**Figure 1A**), (1) strong light-harvesting ability resulting from wide absorption band and strong absorption coefficients; (2) appropriate energy level alignment between the p-type and n-type materials to ensure efficient built-in field and driving force for exciton dissociation; (3) proper aggregation and crystallization ability for both of p-type and n-type materials to form well-defined blend film with desirable micro-morphology, e.g., domain sizes and molecular stacking order; (4) fairly well-charge carrier mobility, i.e., electron and hole mobility to facilitate the charge transportation and collection. These features are closely related to the material properties and device preparation technics. Thanks to the continuing devotion on material design and device optimization, the PCE of single junction photovoltaic devices based on organic semiconductors have been promoted from the initial 1% in 1986 (Tang, 1986) to 10–13% recently (Gupta et al., 2013; Chen et al., 2015; Zhang Z. G. et al., 2017; Li W. et al., 2018), illuminating the bright future of OSCs for low-cost and portable energy provision. However, in contrast to the inorganic and hybrid photovoltaics, for example, the silicon solar cells and perovskite solar cells, whose efficiencies are commonly on the magnitude of ca. 20% (Sun, 2015; Meng et al., 2016), the OSCs have a large offset to promotion. In fact, theoretical models based on Shockley–Queisser detailed balance approach predicted a reachable PCE of 20–24% for OSCs (Janssen and Nelson, 2013), Moreover, in the current stage, excellent photovoltaic materials capable of accomplishing efficiencies higher than 10% are limited. As such, large amount of fundamental explorations on developing novel photovoltaic materials are required to thrust the overall progress of OSCs.

The most popular strategy to construct the organic photovoltaic materials involves the covalently bonding of various conjugated units with electron-rich (D) or electron-deficient (A) nature to obtain D-A type linear molecules, star molecules, oligomers, and polymers. These D and A π-electronic units are basic building blockings that critically determine the optoelectronic properties and photovoltaic performances of the photovoltaic materials. Consequently, the design and structural tailoring of π-electronic units are essential for the construction of photovoltaic materials. To now, outstanding D units such as oligothiophene (OT), fluorene (Fl), cyclopentadithiophene (CPT), benzodithiophene, (BDT), and indacenodithiophene (IDT) and A units including perylene diimide (PDI), naphthalene diimide (NDI), diketopyrrolopyrrole (DPP), isoindigo (IID), thieno[3,4-c]pyrrole-4,6-dione (TPD), benzothiadiazole (BT), benzotriazole (BTz), benzo[1,2-c:4,5-c′]dithiophene-4,8-dione (BDD), rhodanine (Rh), cyano indone (IC), and N,N′-diethyl thiobarbituric acid (TBA) were revealed in literature (**Figure 1B**) (Lu et al., 2015; Zhan and Yao, 2016). Additionally, classic dye molecules such as phthalocyanine (Pc), porphyrin (Pr), and squaraine (SQ) are also frequently reported for construction of OPV materials (Chen et al., 2012, 2014; Chen G. et al., 2015). Developing novel D or A π-electronic units has being an energetic realm. A typical strategy of introducing heteroatoms including O, N, P, S, Se, Si, Ge, and B, etc. into the polycyclic aromatic hydrocarbons (PAH) backbone is widely used to tailor the properties of π-electronic units (Stepien et al., 2017).

When one gives a glance to the periodic table of elements, it's a cinch to perceive the neighbor elements of carbon (C, atomic number, 6), i.e., boron (B, atomic number, 5) and nitrogen (N, atomic number, 7). Thus, the total electronic number of two carbons (12) is equal to the electronic sum of one boron (5) and one nitrogen (7). Accordingly, replacing two carbons with one boron and one nitrogen in a π-conjugated structure gives an isoelectronic system, i.e., the BN embedded π-conjugated system, in contrast to its all-carbon analogs. The bonds between the B and N can be formed as coordinated bond (B←N) and covalent bond (B-N), corresponding to the isoelectronic units of C–C and C=C (**Figure 2A**), respectively. Replacing CC unit with BN unit in the conjugated skeleton is favorable for property adjustment. On the one hand, the BN would alter the electronic nature of the conjugated backbone due to the different electron-negativity of heteroatoms with that of carbon atom. On the other hand, the BN also enhances the dipolarity of hydrocarbon skeletons and thus boost the inter-molecular interactions. Additionally,

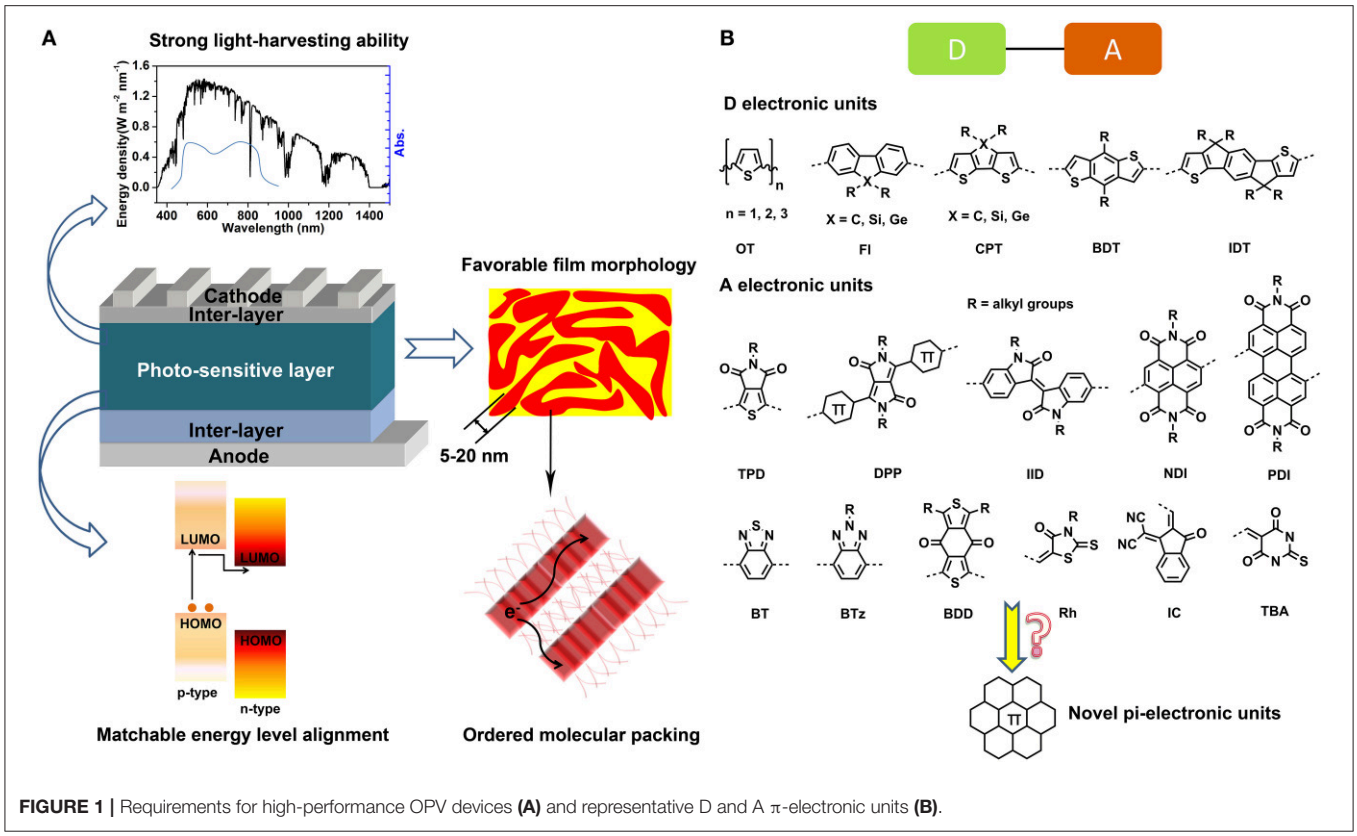

FIGURE 1 | Requirements for high-performance OPV devices **(A)** and representative D and A π-electronic units **(B)**.

replacing carbons with BN usually maintains the good co-planarity and rigidity of the backbones. All these features are desirable to design novel π-electronic units for photovoltaic materials construction. Taking the isoelectronic compounds of ethane and ammonia-borane (NH_3←BH_3, AB) for an example, ethane is gaseous at ambient temperature with a dipole moment of zero and weak inter-molecular interactions (Pritchard and Kern, 1969), whereas AB is a solid state at room temperature with a strong dipole moment of 5.2 D and inter-molecular BH…NH interactions (Leroy et al., 1993). For B←N embedded aromatic systems, the first report was in 1963 by Morrison et al. (Letsinger and MacLean, 1963). Recently, a series of conjugated materials containing B←N bonds have been revealed for OSCs application (Dou et al., 2015, 2017). For the B-N covalent bond embedded aromatic structures, the research history has been almost one century since the first synthesis of borazine in 1926 (Stock and Pohland, 1926). In 1950s and 1960s, Dewar and coworkers conducted pioneering work on synthesis of BN doped PAH (Dewar et al., 1958; Dewar and Dietz, 1959; Chissick et al., 1960; Davies et al., 1967). Since then, little progress in this field has been made due to limited characterization means at that time. Recently, the B-N embedded polycyclic aromatic systems are experiencing a renaissance with fast development of synthesis protocols and widely application to H_2 storage, OLEDs, and OFETs (Jaska et al., 2006, 2007; Bosdet et al., 2007a; Liu and Marder, 2008; Campbell et al., 2012; Hashimoto et al., 2014; Wang et al., 2015a,b, 2016b; Beniwal et al., 2017; Ishibashi et al., 2017). Additionally, N–B←N group, the comprehensive form of B←N coordination and B-N covalent bonds, also widely appears in the conjugated units, such as BODIPY (Loudet and Burgess, 2007). All of these BN perturbed structures have unique properties and are intensively interested in terms of synthesis routes, optoelectronic properties, and electronic device performances. However, studies on the photovoltaic applications of BN embedded π-electronic units are still in infancy. In this review, we are going to summarize the synthesis routes toward π-electronic units containing B←N coordination bond, B–N covalent bond, and N–B←N group (**Figures 2B–D**), and discuss their optoelectronic properties, as well as their applications in photovoltaic devices.

SYNTHESIS ROUTES

Synthesis of π-Electronic Units Containing B←N Coordination Bond

Alkyl Lithium (e.g., n-BuLi)/ Aryl Boron (e.g., BPh_3) System

In 2002, Erker et al. reported an intramolecular nucleophilic aromatic substitution reaction, using CH_3Li and $B(C_6F_5)_3$ to prepare the tricyclic fused structures containing B←N coordination (Dominik et al., 2002). As shown in **Figure 3**, the starting *N*-Methylimidazole **1** was coordinated with strong Lewis acid of $B(C_6F_5)_3$ to form adduct **2**. Deprotonation at the C-2 position of imidazole heterocycle was accomplished by treatment with CH_3Li, affording intermediate **3**, which experienced a rapid intramolecular nucleophilic aromatic substitution reaction with

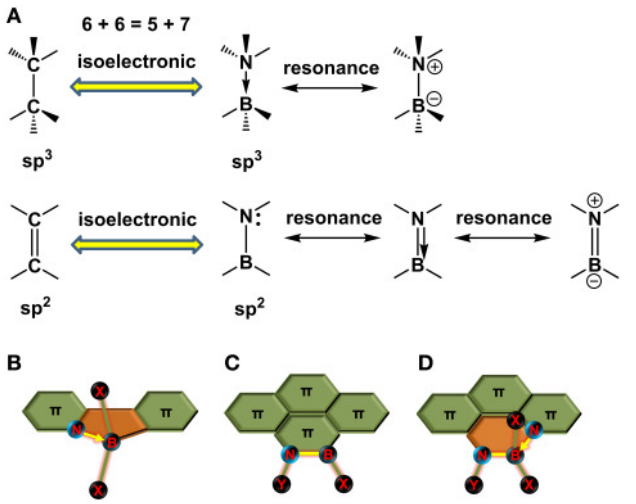

FIGURE 2 | Isoelectronic structures of CC and BN units **(A)** and schematic diagram of π-electronic units containing B←N coordination bond **(B),** B-N covalent bond **(C),** and N-B←N group **(D)**. X, Y, and Z represent the halogen atoms, alkyl chains, or phenyl groups.

one of the adjacent C_6F_5 groups to generate fused π-electron unit **4,** containing B←N coordination bond. One year later, they replaced the starting reactant with 1-methylbenzimidazole **5**. Using the same routes, larger conjugated π-electron unit **6** was obtained (Vagedes et al., 2003). Similarly, in 2010, B←N perturbed structures with further extended conjugation (**7** and **8**) were synthesized using the same strategy (Job et al., 2010). In 2006, Yamaguchi et al. reported the synthesis of π-electron systems **10** containing B←N coordination from **9** by n-BuLi and Mes_2BF (Mes_2 = 2, 4, 6-$Me_3C_6H_2$), whose mechanism involves the coordination between thiazole N and aryl B and consequent electrophilic attack of electron-deficient boron to the β-site of adjacent thiophene (Wakamiya et al., 2006). Recently, Liu et al. utilized this route to produce a stable electron-deficient unit **11**. By co-polymerizing with D or A units, they constructed a series of novel photovoltaic polymers with outstanding performances (Dou et al., 2015).

BX_3/Hindered Base System

This synthetic method can be traced back to 1963, when Maclean et al. passed BCl_3 into melts of 2-phenylbenzirnidazole (**12**) at 300°C and subsequently hydrolyzed in moisture air producing **13** (Letsinger and MacLean, 1963), as shown in **Figure 4**. The C-H borylation was considered to be reversible and the by-product HCl should be sequestered to improve the reaction yield. Accordingly, in 2010, Murakami et al. improved the method by adding a hindered base, $Et_2N(i\text{-Pr})$ to absorb the protic by-product (Ishida et al., 2010). They used **14** as starting reactant, by adding 3 eq BBr_3 and 1 eq $Et_2N(i\text{-Pr})$ at 0°C, achieving **15**. **15** was not stable in moisture due to the electron-drawing property of Br, endowing B atom strong electrophilic. Further functionalization at B atom can be realized by adding organometallic reagents to substitute the Br atoms, affording a series of stable ladder-type π-units containing B←N bonds (**16a**-**16f**). The reaction mechanism was proposed as follow: the Lewis acid-base coordination between **14** and BBr_3 provided **17**; then, another BBr_3 captured a Br^- from **17**, leading to trivalent cationic boron species **18**; finally, the cationic boron attacked the neighboring aromatic unit, generating the circular **16**. After that, several conjugated units containing B←N coordination with tunable emission and aggregating-induced emission properties were synthesized by this method (Wong et al., 2012, 2016; Zhao et al., 2013). Recently, based on this strategy, fused π-electronic units with good co-planarity, red-shifted absorption, and depressed energy levels of **21**, **23**, and **25** have been synthesized from **20**, **22**, and **24**, respectively (Yusuf et al., 2016; Zhu et al., 2016; Li Y. et al., 2018). These π-electronic units containing B←N coordination are potentially useful to construct organic semiconductors for electronic device applications. As this strategy involves the electrophilic attack on the aromatic units, the electron-rich nature of the aromatic cycles is critical to the C-H borylation. Ingleson and Turner et al. employed **26** as precursor to conduct the C-H borylation (Crossley et al., 2015). It's found that the C-H borylation occurred on the thiophene rather than the fluorene, presumably due to the more electronic-rich nature of thiophene than fluorene, facilitating electrophilic attack on the thiophene. Not only the small molecules, but also the polymers can undergo this reaction. Ingleson and Turner et al. also applied this method to modify the copolymer **28**, yielding near-infrared emitting polymer **29** (Crossley et al., 2017).

Although the BX_3/hindered base reaction condition has been demonstrated to be widely applicable to the C-H borylation, it's invalid in some cases. For example, Ingleson and Turner et al. found that precursor **30** can not afford **31** upon adding BX_3, e.g., BCl_3 or BBr_3 and the hindered base, e.g., $EtN(i\text{-Pr})_2$ or 2,4,6-tri-t-butylpyridine (TBP) (Crossley et al., 2015). Otherwise, the C-H borylation occurred by adding excess BCl_3 (ca. 4 eq), 2 eq of TBP and 4 eq of $AlCl_3$, yielding intermediate **32**, which was readily transformed to **31** by adding Bu_4NCl. The addition of 4 eq of $AlCl_3$ was regarded to be essential to ensure the fully conversion to intermediate **32**. The function of $AlCl_3$ herein is similar to its effect in the classic Friedel–Crafts reaction. It's worth to note although the structure units of **30** is the same to the repeating units of polymer **29**, the C-H borylation conditions were different for this two precursor, indicating the different reaction law in small molecules and polymers for C-H borylation. Recently, 2D conjugated units containing B←N coordination (**34** and **35**) were reported, also based on this method (Liu K. et al., 2017).

Synthesis of π-Electronic Units Containing B-N Covalent Bonds

Electrophilic Cyclization Between Boron and Aromatic Units

This method involves the Friedel-Crafts cyclization, in which BX_3 and Lewis acid are usually required to complete the cyclization (**Figure 5**). In 1958, Dewar et al. initially conducted the synthesis work from **36** by adding BCl_3 and $AlCl_3$ to obtain 9,10-azaboraphenanthrenes (**38**) (Dewar et al., 1958). Further modification on the B atom led to a series of BN-substituted

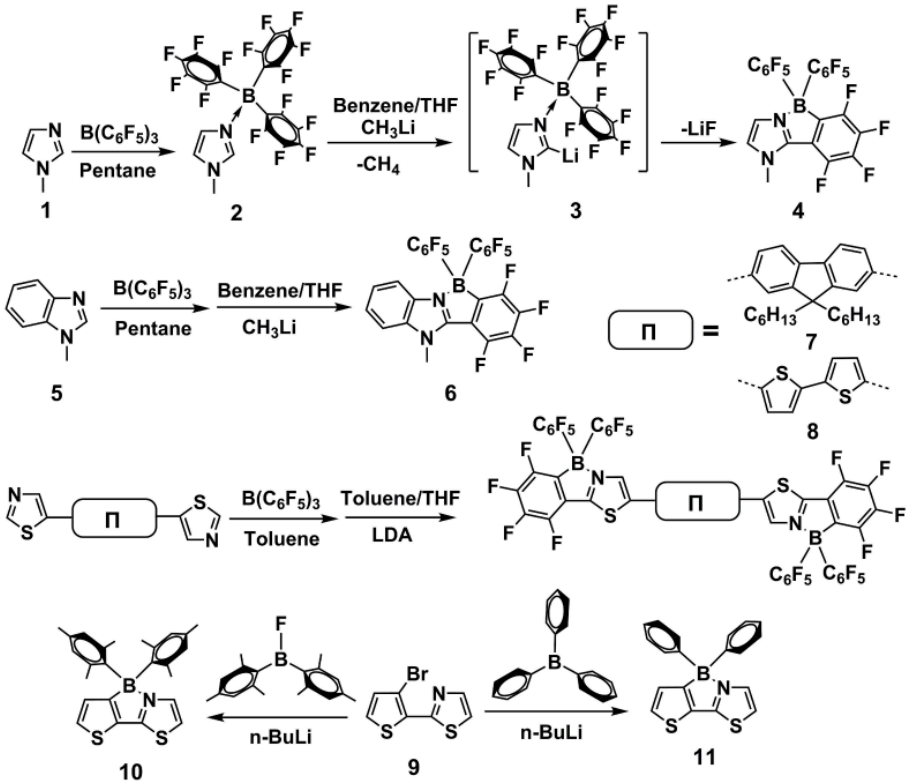

FIGURE 3 | Examples of synthesis routes toward B←N embedded units involving alkyl lithium / aryl boron reaction system.

phenanthrene derivatives (**39**). Consequently, a family of B-N embedded PAHs was synthesized via the similar strategies (Dewar and Dietz, 1959; Chissick et al., 1960; Dewar and Poesche, 1963, 1964). In 2013, Pei and coworkers reported BN-substituted tetrathienonaphthalene derivatives (**41**) (Wang X. Y. et al., 2013), starting from **40** by adding BBr_3 and Et_3N. BBr_3 attacked the imine and consequently electrophilic attacked the β-site of thiophene to finish the cyclization. Latterly, they revealed extended π-conjugated structure **43** with similar cyclization methods (Wang et al., 2014). It's worth to note that the conjugation of **42** is more extended than **40**, leading to weaker electron-rich of imine groups in **42**. Accordingly, the n-BuLi was required to facilitate the attack of BBr_3 to imine in **43**. Similarly, starting from **44**, Nakamura et al. utilized n-BuLi and BBr_3 to prepare the intermediate **45** (Hatakeyama et al., 2011). Due to weaker electron-rich properties of phenyl than thiophene, the Lewis acid such as $AlCl_3$ and hindered base TBP were required to complete the electrophilic cyclization to produce **46**. Liu et al. reported the synthesis of B-N embedded tetracene **48** and **49**, starting from **47** (Ishibashi et al., 2014, 2017). Pei et al. also reported synthesis of heterocoronene (**51**) by adding $PhBCl_2$ and Et_3N to **50** and heated to 180°C in *o*-DCB (Wang et al., 2015c). Based on similar methods, ladder-type conjugated units substituted by B-N covalent bonds were also synthesized (Wang X. et al., 2013; Zhou et al., 2016). Wang et al. revealed an electrophilic cyclization between B and methyl located on phenyl, obtaining unsaturated **53**, which was subjected to photoelimination, leading to **54** (Lu et al., 2013; Ko et al., 2014; Yang et al., 2015, 2016, 2017).

Chelation of Aromatic N and B Precursor

This method involves the chelation of B precursor and N Lewis base to eliminate a by-product (**Figure 6**). In 2003, Piers et al. reported the chelation of **55** with pyridazine and benzo[c]cinnoline, eliminating Me_3SiCl to obtain **56** and **57**, respectively (Emslie et al., 2003). Latterly in 2006, this method was applied to synthesize **58** (Jaska et al., 2006). In 2007, they further revealed synthesis of **61** by chelation of **59** with 2-ethynyl-pyridine, leading to intermediate **60**, which experienced smooth cyclization without any catalyst (Bosdet et al., 2007a). In another aspect, the chelation of **59** with 2, 5-diethynyl-pyridine afforded **62**, which required catalytic amount of $PdCl_2$ to complete the second cyclization of the ethynyl group to obtain the pyrene analog with internalized B-N substitution **63** (Bosdet et al., 2007b). The chelation and ethynyl-cyclization strategies were spread widely to prepare a series of PAHs embedded with B-N bonds (Jaska et al., 2007; Bosdet et al., 2010; Benedikt et al., 2013).

Synthesis of π-Electronic Units Containing N–B←N Groups

A family of conjugated molecules containing N–B←N groups has been intensively explored as fluorescence dyes with high

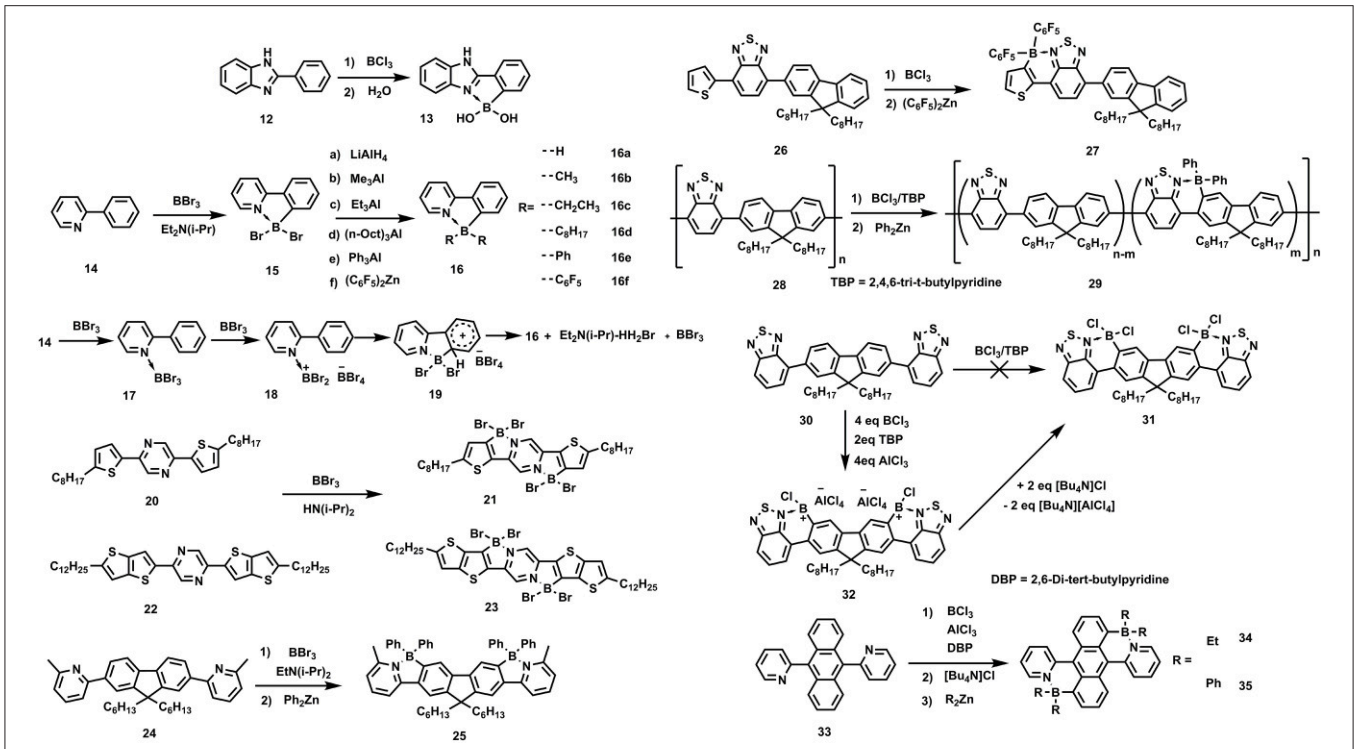

FIGURE 4 | Examples of synthesis routes toward B←N embedded units involving BX_3/ hindered base reaction system.

absorption coefficients and fluorescence quantum efficiency, which were widely utilized in OSCs, OLEDs, sensing, and imaging, etc (Li et al., 2013; Fu et al., 2015; Lin et al., 2015; Dou et al., 2017). The synthesis routes toward N–B←N groups usually require a precursor equipped with an amino group and an aromatic nitrogen at suitable position for chelation of the boron. BF_3•OEt_2/Et_3N is most widely used reaction condition (**Figure 7**). Taking the typical dye boron dipyrromethene (BODIPY) as an example, the precursor **64**, usually synthesized from pyrrole derivatives and aldehydes, is readily to obtain the BODIPY skeleton **65** by adding BF_3•OEt_2/Et_3N (Loudet and Burgess, 2007). This reaction condition is widely applicable to the precursors with the features of containing amino group and aromatic nitrogen atoms at appropriate positions, e.g., **66**, **67**, **68**, and **69** (Araneda et al., 2011; Nawn et al., 2013; Hao et al., 2014; Qiu et al., 2016).

OPTOELECTRONIC PROPERTIES AND OPV APPLICATIONS

π-Electronic Units Containing B←N Coordination Bonds

In a long time, the inter-molecular coordination between B and N has been well-demonstrated to adjust the optoelectronic properties of conjugated molecules. It's well-known that the B atom is an electron-deficient center (Lewis acid) due to the existence of an unoccupied orbital while the N atom is an electron-rich center (Lewis base) owing to the existence of un-bonded pair of electron. As such, typical Lewis acid-base coordination between B and N atoms occurs when molecules containing N and B atoms are mixed together (Maria and Gal, 1985; Piers, 2005). It's has been revealed that the optoelectronic properties of conjugated molecules containing N atoms can be readily amendable when mixed with boride Lewis acid, e.g., BF_3, BCl_3, BBr_3, and $B(C_6F_5)_3$ (BCF). In 2009, Bazan and co-workers reported the bandgap control of benzothiadiazole-based oligomers via Lewis acid of $B(C_6F_5)_3$ (Welch et al., 2009). As shown in **Figures 8A,B**, upon stoichiometric coordination with BCF, the absorption band of **74** red-shifted and the optical bandgap (E_g°pt) decreased from 2.15 to 1.60 eV. In 2011, they further implemented the method to a series of oligomers and polymers. The HOMO and LUMO, estimated from ultraviolet photoelectron spectroscopy (UPS) were found to synergetic lowering due to the introduction of electron-deficient center B to the conjugated backbone (**Figure 8C**) (Welch and Bazan, 2011). It's interpreted that the Lewis acid BCF pulled the electron density away from the conjugated backbone, altering the electron topology and leading to decreased HOMO/LUMO and optical bandgap. In 2017, the strategy was employed to the dye molecules of 7-azaisoindigo, by using BF_3 to amend the energy levels and optical absorption (Randell et al., 2017). Recently, we synthesized a series of pyridine end-capped diketopyrrolopyrrole (DPP) dye molecules and systematically explored the optical bandgap alteration upon coordinating with BCF (Huang et al., 2018). The effects of stoichiometry and equilibrium of the Lewis

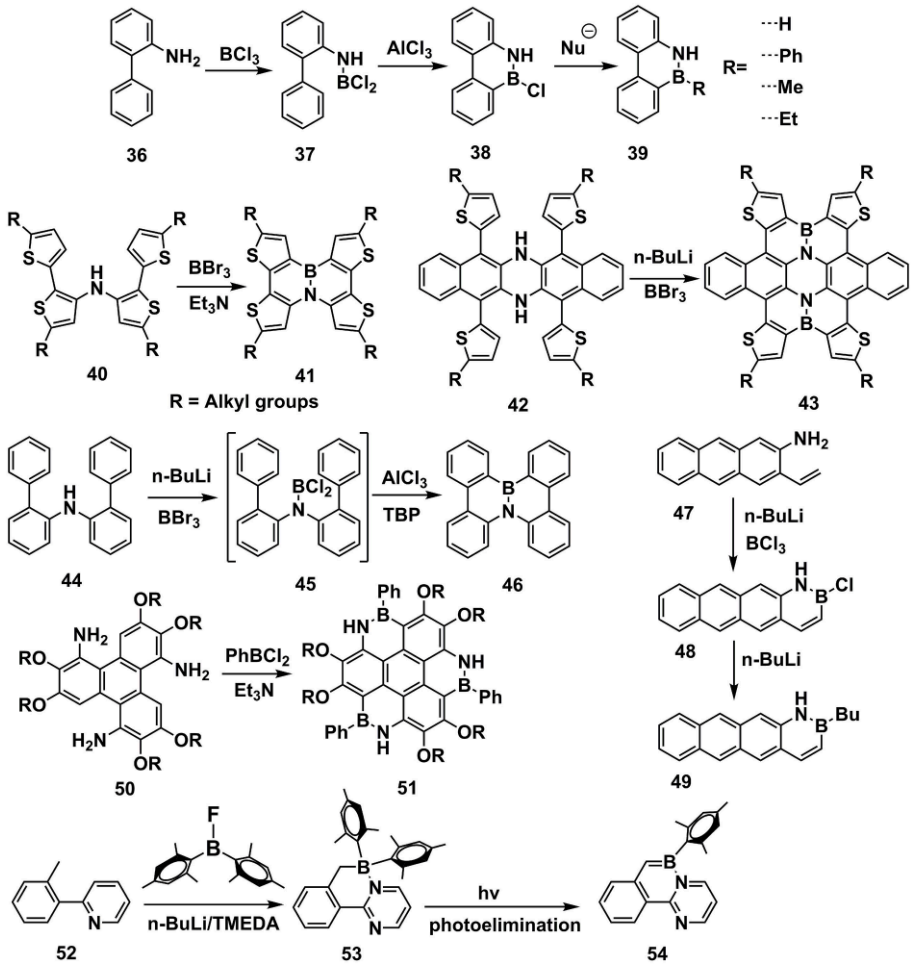

FIGURE 5 | Examples of synthesis routes toward B-N embedded units via electrophilic cyclization between boron and aromatic units.

acid-base interactions on the optical bandgaps were studied (**Figure 8D**).

Lewis acid-base complexation of conjugated polymers containing aromatic N atoms with BCF can also adjust the performances of OFET and OLED devices. Heeney et al. synthesized two indenopyrazine-based copolymers, with which the OFET devices were prepared. They explored the effects of doping BCF to the copolymers on the device performances (Han et al., 2016). It's found that by doping the polymers with BCF in a certain amount, e.g., 0.075 equiv, the hole mobility can be increased up to 11-fold along with the reduced threshold voltages. Otherwise, increased the amount of BCF to a critical amount, the OFET performances would be adversely affected. It's deduced by the authors that moderate amount of BCF leads to effective traps filling and positive effects on the device operation while the excess amount of BCF gives rise to defect formation and structural disorder, which negatively affects the device performances. Bazan and Nguyen et al. studied the color turning of OLED by BCF doping (Zalar et al., 2012). They selected a fluorescent copolymer of fluorene and pyridine. By doping the polymer with BCF, the OLED emission color red-shifted obviously.

Although the inter-molecular B←N interactions are effective to adjust the optoelectronic properties of conjugated molecules, this method are not applicable for OPV devices because the inter-molecular B←N complexation is unstable and the boride molecule dopants may lead to defect formation and hinder the molecular order packing. Consequently, incorporating B←N bonds into the molecular skeletons are more feasible for OPV applications. Recent development of synthesis protocols promoted the birth of several π-units containing B←N bonds (**Figure 9**). As the frontier orbital energy levels, i.e., HOMOs and LUMOs and optical absorption are critical parameters for the PCEs of OPV devices, we summarized these parameters of some B←N embedded π-units, as shown in **Table 1**. For **20** and **22** (**Figure 4**), after introducing the BBr_2 groups into the backbones, the LUMOs were decreased significantly by 0.96 and 0.53 eV, corresponding to **21** and **23**, respectively (Zhu et al., 2016). Moreover, remarkably red-shifted absorption band to near-infrared region occurred after introducing the BBr_2 groups

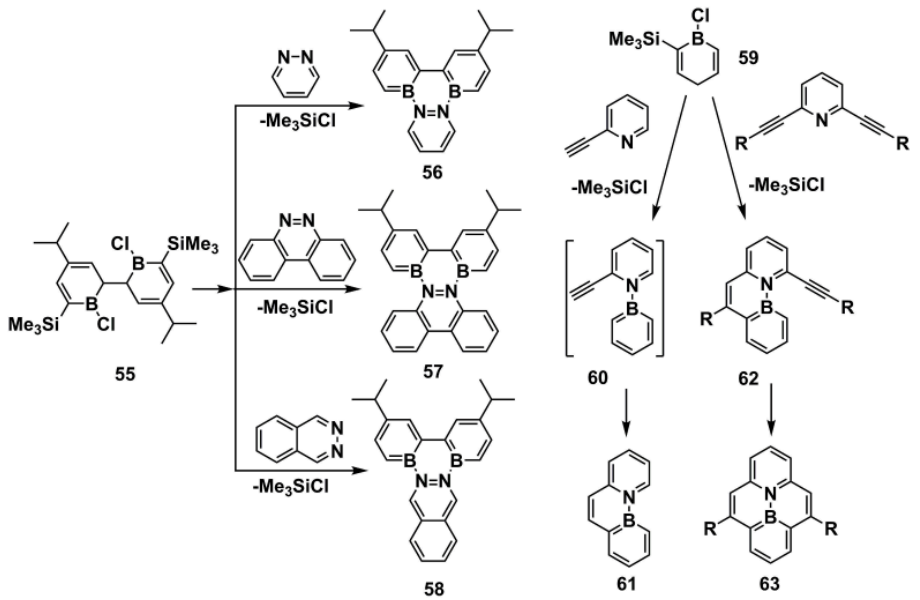

FIGURE 6 | Examples of synthesis routes toward B-N embedded units via chelation of aromatic N and B precursor.

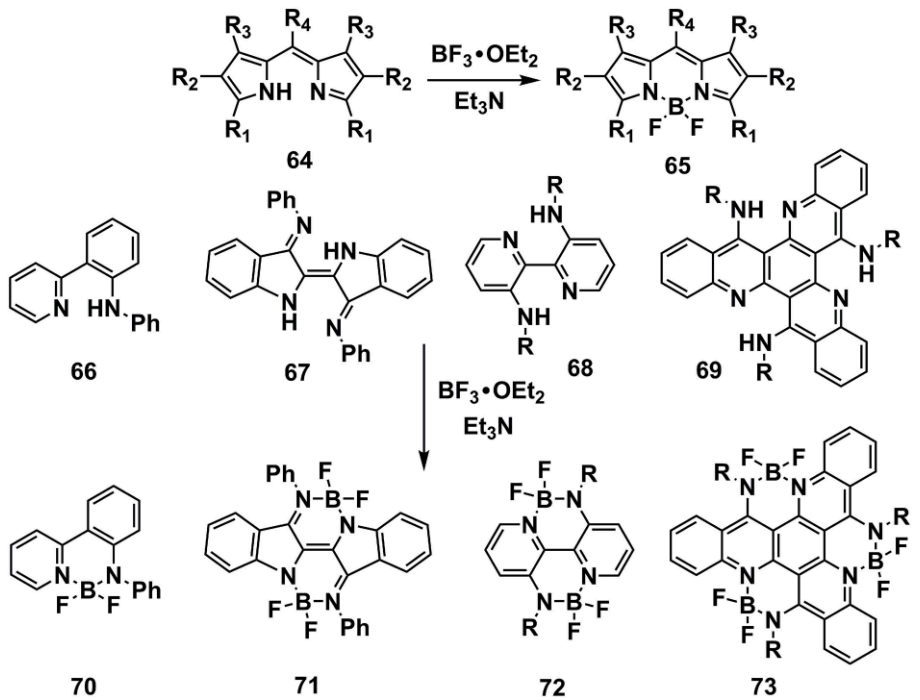

FIGURE 7 | Examples of synthesis routes toward π-units containing N-B←N groups via BF_3•OEt_2/Et_3N reaction condition.

into backbones (**Figure 10A**). Similarly, LUMOs of **79**, **81**, and **83** also lowered obviously in comparison to their precursors of **78**, **80**, and **82** (Crossley et al., 2015). It's worth to note that the LUMO depressed remarkably with the slightly changed HOMOs, leading to decreased bandgaps. An interesting comparison from precursor **84** (**86**), to inter-molecular B←N complex **85** (**87**), and to cyclization product **7** (**8**) further demonstrates the outstanding ability of B←N unit to depress the LUMO energy levels of π-units (Job et al., 2010). Not only compared to their precursors before cyclization, but also in contrast to the all-carbon analogs,

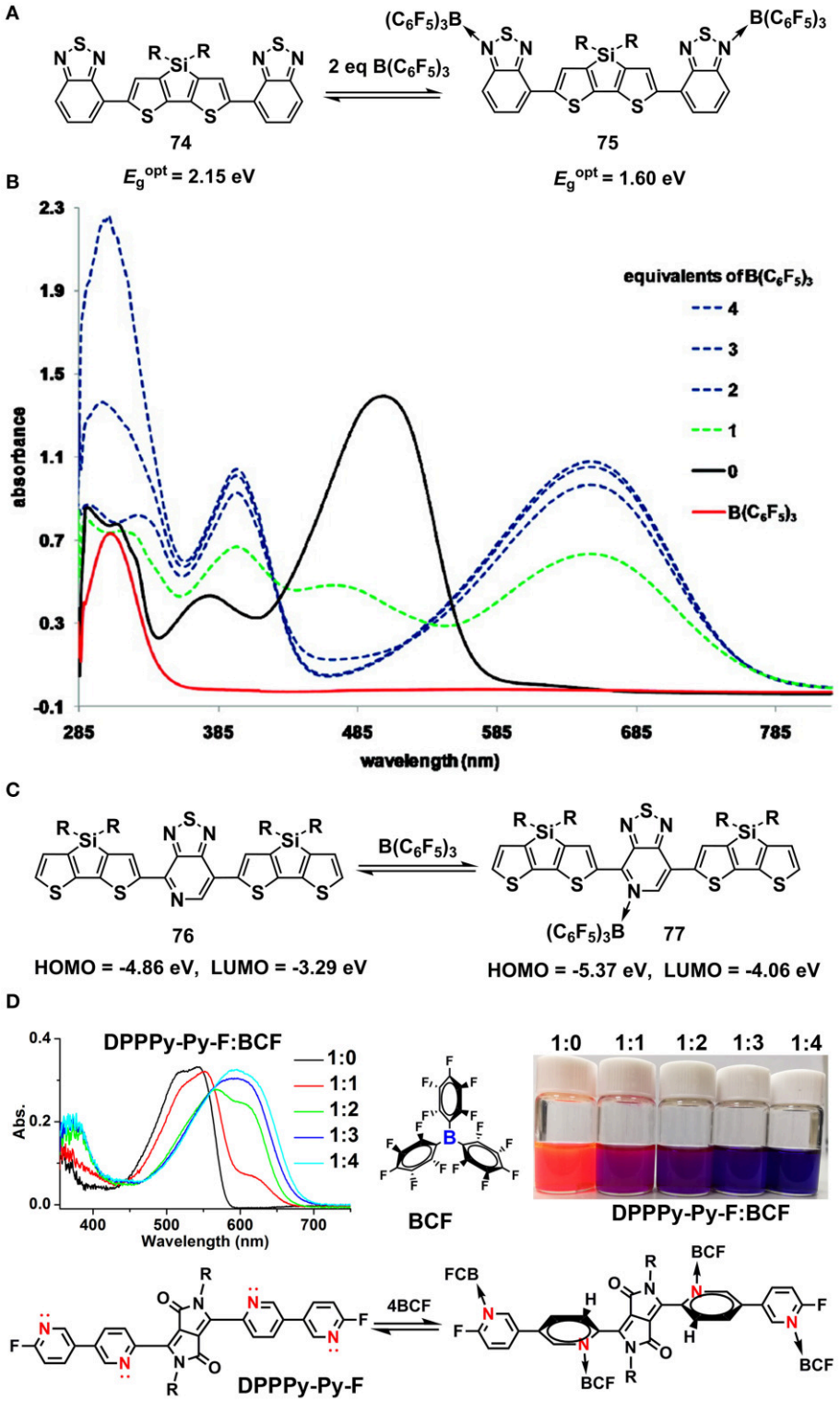

FIGURE 8 | Lewis acid-base coordination **(A–C)** and the variation of UV-Vis absorption spectra of **74** upon coordinating with BCF **(B),** Reprinted with permission from Welch et al. (2009). Copyright (2009) American Chemical Society. Manipulation of optical absorption spectra of DPP molecules upon coordinating with BCF **(D),** Reprinted with permission from Huang et al. (2018). Copyright (2018) Elsevier Ltd.

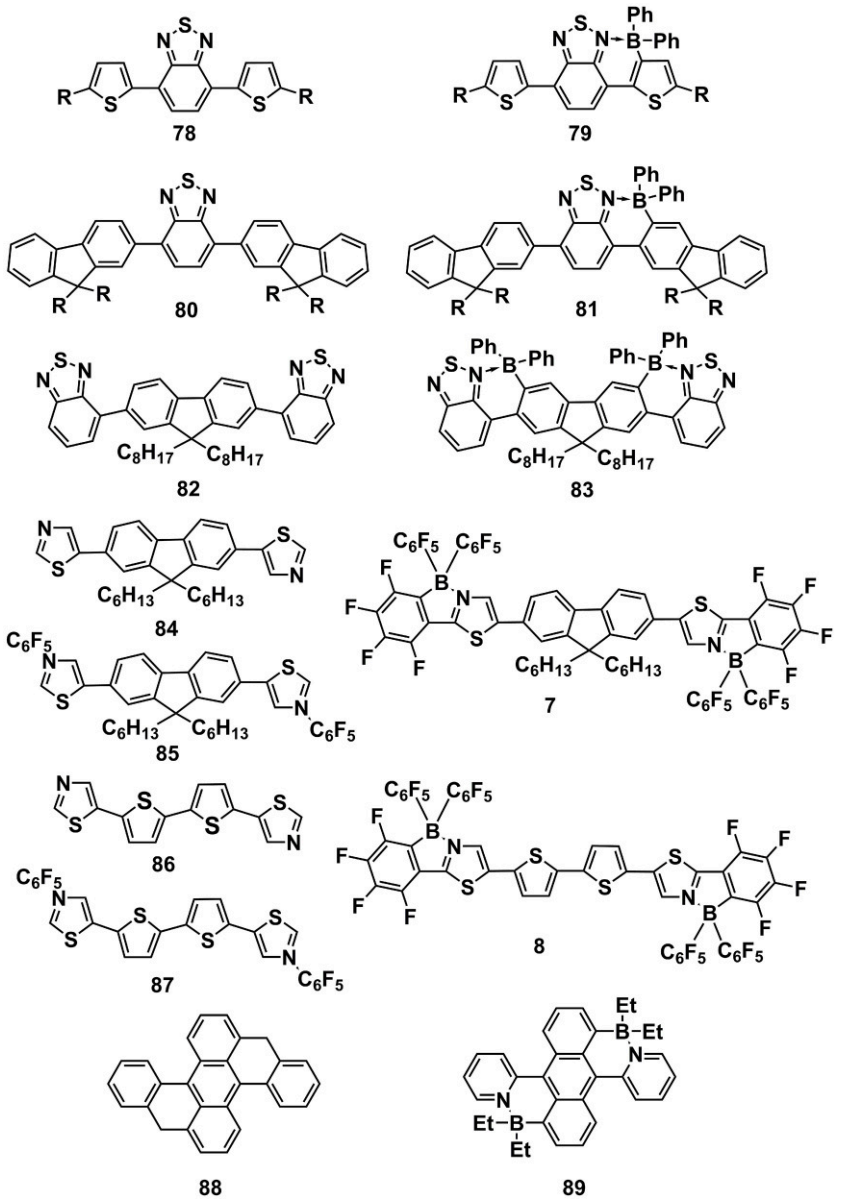

FIGURE 9 | Molecular structures of B←N embedded π-units and their precursors before cyclization.

the B←N embedded π-units also exhibit significantly lowered LUMOs, as illustrated by **88** and **89** (Liu K. et al., 2017). These results indicate that the B←N embedded π-units usually have depressed LUMOs and expanded absorption bands in contrast to their precursors and all-carbon analogs due to the introduction of electron-deficient center B.

Other properties that essentially affect the PCEs of OPV devices are the solid packing order and charge carrier mobility. Single crystal data indicate the B←N embedded π-units, e.g., **8** also have good co-planarity, rigidity, and ordered π-π packing, as shown in **Figure 10B** (Job et al., 2010). It's beneficial to the charge transport in solid state, which is critical to the OPV performances. These features of depressed LUMOs, namely, strong electron-affinity and good molecular planarity and π-π packing order make the B←N embedded π-units suitable for the electron-transporting materials. For example, the dimeric B←N embedded CPT showed electron mobility of 1.5×10^{-4} $cm^2/V\bullet s$ tested by time-off-light (TOF) carrier-mobility measurement (Wakamiya et al., 2006). Comprehensively, the B←N embedded π-units are excellent electron-deficient moieties with good co-planarity, depressed LUMOs, broadened absorption bands, and high electron mobility, which are promising for the application of photovoltaic materials, especially for acceptor materials. However, the contributions to exploit the potential

TABLE 1 | Frontier orbital energy levels and optical bandgaps of B←N embedded π-units.

Compounds	HOMO (eV)	LUMO (eV)	E_g^{opt}(eV)[b]
20	−5.66	−3.44	–
21	−5.72	−4.40	1.59
22	−5.54	−3.68	–
23	−5.40	−4.21	1.34
78	−6.00	−3.73	2.29
79	−5.96	−4.15	1.73
80	−6.27	−3.52	2.59
81	−6.19	−4.11	1.92
82	−6.34	−3.52	2.82
83	−6.11	−4.11	2.02
84	−5.52[a]	−1.78[a]	3.58
85	−6.68[a]	−2.88 [a]	3.52
7	−6.36[a]	−3.01[a]	3.11
86	−5.38[a]	−2.21[a]	3.25
87	−6.55[a]	−3.34[a]	3.19
8	−6.17[a]	−3.30 [a]	2.87
88	−4.54[a]	−1.81[a]	–
89	−4.76[a]	−2.44[a]	–

[a]*Obtained by theoretical calculations. Other HOMOs and LUMOs were estimated by electrochemistry method.* [b]*Calculated by 1240/λ_{onset}. λ_{onset} is the absorption onset of UV-Vis absorption spectra.*

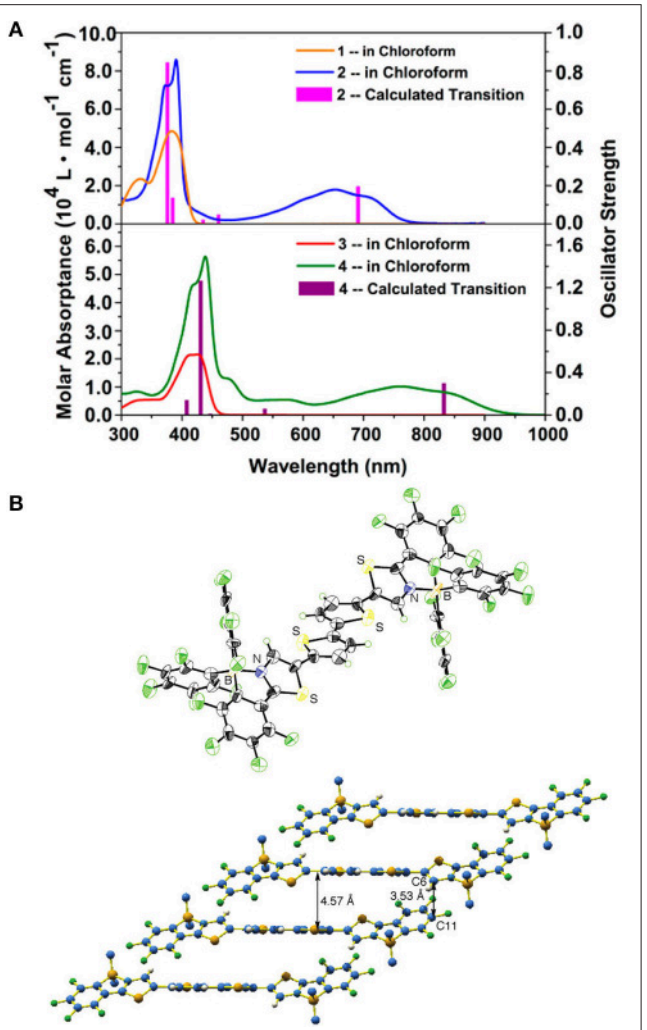

FIGURE 10 | Absorption spectra of **20**/**21** (upper) and **22**/**23** (bottom) in chloroform **(A)** and Single crystal structure of **8 (B)**. Reprinted with permission from Job et al. (2010) and Zhu et al. (2016). Copyright (2010, 2016) American Chemical Society.

of B←N embedded π-units for OPV application are scarcely revealed.

Until recently, Liu and co-workers' pioneering work demonstrated the great potential of B←N embedded π-units for the construction of OPV materials. They selected B←N embedded CPT (BNCPT), which was developed in 2006 by Yamaguchi et al. (Wakamiya et al., 2006), as co-monomer to copolymerize with thieno[3,4-c]pyrrole-4,6-dione-1,3-diyl (TPD) unit, obtaining a novel conjugated polymer P-BN (Dou et al., 2015). For comparison, the all-carbon analog CPT was also copolymerized with TPD, leading to P-CC. The HOMO and LUMO of P-BN were significantly depressed by 0.65 and 0.53 eV, respectively, in contrast to the values of P-CC (**Figure 11A**), indicating the electron acceptor property of P-BN, which was further confirmed by the fluorescence quenching of P-BN with P3HT in solutions. These results demonstrated the B←N based copolymers are suitable for electron acceptor in OPV devices. Then, they synthesized another copolymer by combining BNCPT with isoindigo (IID), affording P-BN-IID with HOMO = −3.80 eV and LUMO = −5.84 eV (Zhao et al., 2016). Using PTB7-Th as electron donor, the all-polymer solar cells based on P-BN-IID exhibited a competitive PCE of 5.04% (**Figure 11B**). On the other hand, the BNCPT was also adopted to construct electron donor polymers by copolymerizing with its all-carbon analog CPT. This polymer displayed suitable HOMO and LUMO levels and exhibited a PCE of 3.74% by using PC71BM as electron acceptor (Zhang et al., 2015). These pioneering studies on the application of B←N based units to the OPV materials open a new window for the design of novel and highly efficient photovoltaic materials, not only for the polymers, but also for the small molecules.

π-Electronic Units Containing B-N Bonds

As the B-N covalent bond is isosterism of C=C bond, replacing the C=C unit in a PAH with the isosteric B-N has emerged as a useful strategy to enlarge the library of π-conjugated units. The B-N embedded PAHs usually have similar geometric parameters but rather distinct electronic structures to its all-carbon analogs. As for the OPV materials, the energy levels, absorption spectra and solid state packing ability are extensively concerned. Herein, we summarized recent progress in some typical B-N embedded PAHs, emphasizing the comparison of B-N doped π-conjugated units to their all-carbon analogs in terms of frontier orbital energy levels, absorption spectra, bandgaps, as well as single crystal packing order. Liu et al.

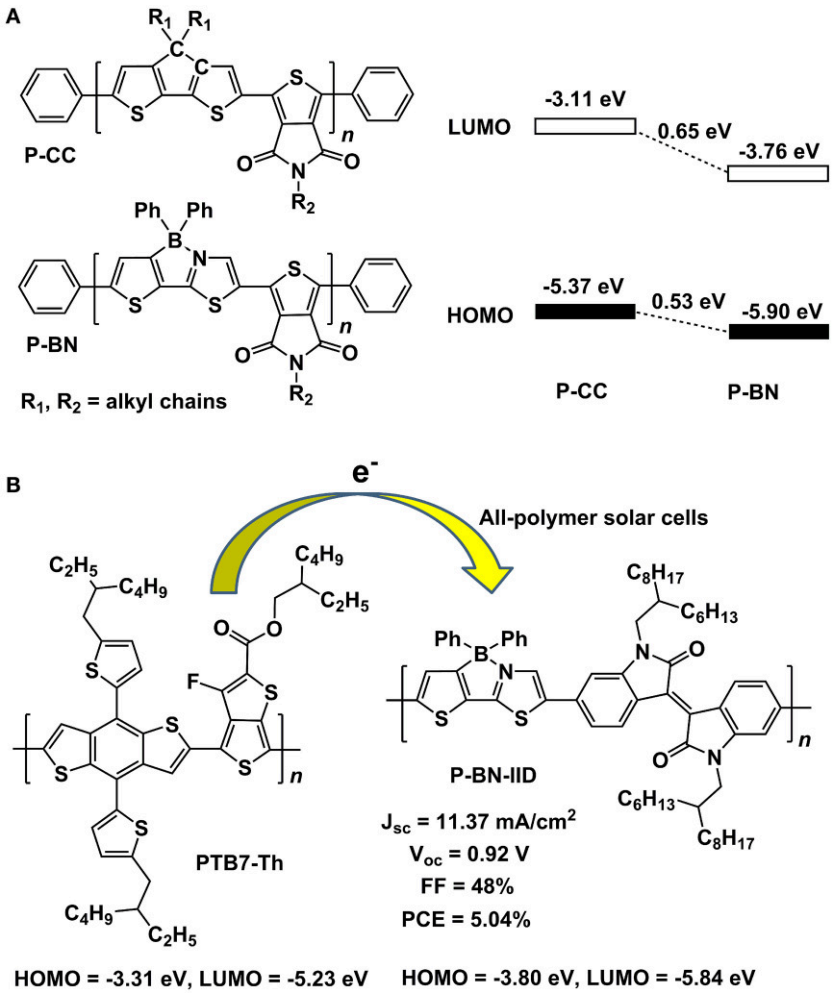

FIGURE 11 | Molecular structures of P-CC and P-BN and the alignment of frontier orbital energy levels **(A)** and parameters of all-polymer solar cells based on PTB7-Th and P-BN-IID **(B)**.

conducted systematic studies on the B-N embedded acenes, e.g., naphthalene, anthracene, and tetracene (Ishibashi et al., 2014, 2017; Liu Z. et al., 2017). In 2014, they revealed two B-N isosteres of anthracene, i.e., BN anthracene and bis-BN anthracene (**Figure 12A**) (Ishibashi et al., 2014). HOMO level tested from UV-photoelecton spectroscopy was −7.4, −7.7 eV, and −8.0 eV, respectively for anthrecene, BN anthracene, and bis-BN anthracene, indicating that the replacement of C=C with B-N gave rise to stabilized HOMO levels. Optical bandgaps estimated from the onset of the absorption spectra were similar for the three molecules. Comparing to anthracene, BN anthracene and bis-BN anthracene appeared a new absorption band at 310 nm, with relatively stronger oscillator strength, which mainly originated from the HOMO−1 to LUMO transition. Recently, they extended the reach of BN/CC isosterism to the tetracene, obtaining B-N perturbed tetracene (**Figure 12B**) (Ishibashi et al., 2017). In contrast to the all-carbon analog, the B-N perturbed tetracene showed slightly depressed HOMO and larger optical bandgap. Upon embedding B-N to tetracene, a blue-shift of HOMO to LUMO transition from 446 to 427 nm occurred and new absorption band originated from HOMO-1 to LUMO with stronger oscillator strength appeared around 380 nm. Very recently, they also disclosed that the orientation and location of B-N in the naphthalene exerted critical influence on the energy levels, bandgaps and absorption properties (Liu Z. et al., 2017).

The B-N embedded dibenzo[g,p]chrysene (BN-DBC) reported by Nakamura et al. showed negative-shifted redox potential in comparison to the all-carbon analog, dibenzo[g,p]chrysene (DCB) (**Figure 13A**) (Hatakeyama et al., 2011), indicating the synergistic depression of HOMO and LUMO levels and unchanged electrochemical bandgaps. X-ray crystallography data revealed the twisted conformations and offset face-to-face stacking style with π-π distances of 3.3–3.6 Å for both DCB and BN-DCB. Although the similar molecular stacking style for DCB and BN-DCB, the hole mobilities were distinct, with 0.07 and 0.007 $cm^2/V•s$, respectively for BN-DCB and DCB. The favorable hole mobility of BN-DCB are beneficial from the introduction of polar B-N unit into backbone

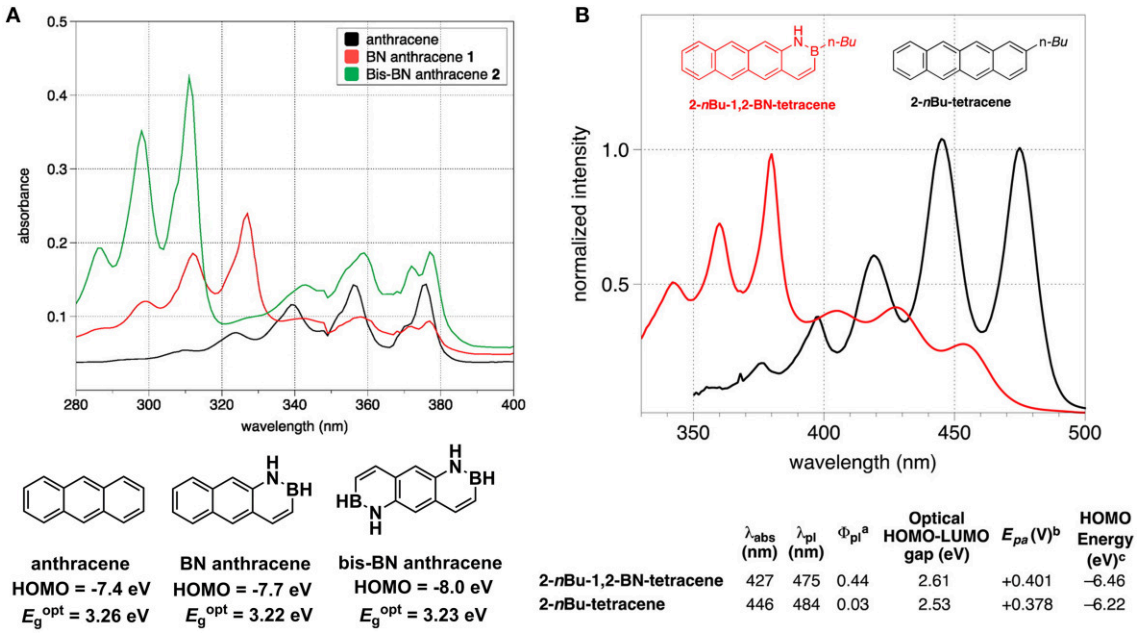

FIGURE 12 | Absorption and energy levels of anthracene and B-N embedded anthracene **(A)** and tetracene and B-N embedded tetracene **(B)**. Reprinted with permission from Ishibashi et al. (2014, 2017). Copyright (2014, 2017) American Chemical Society.

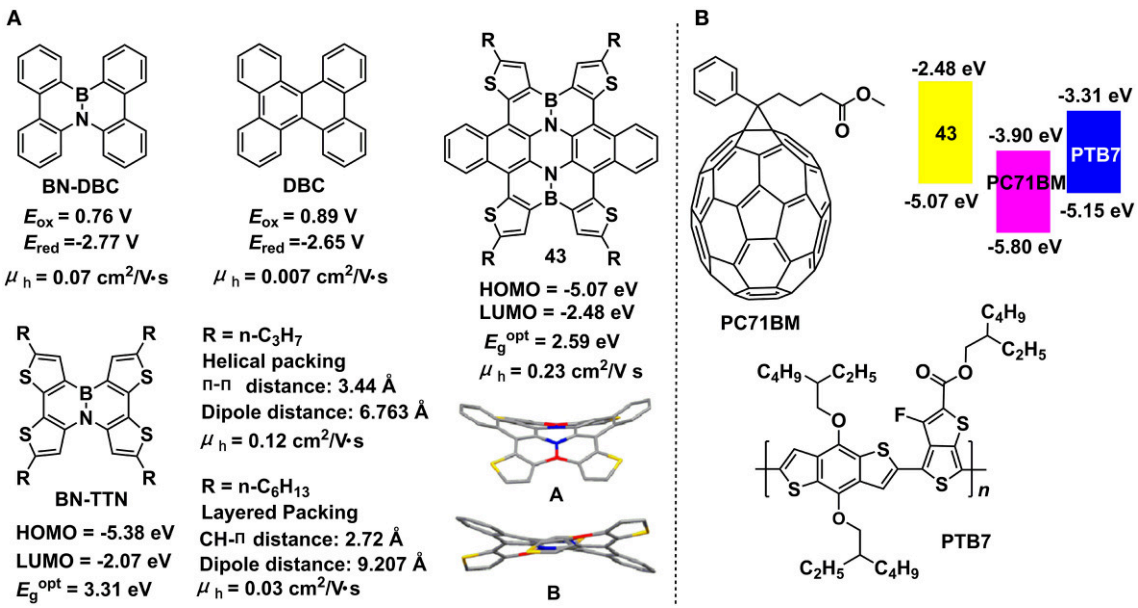

FIGURE 13 | Molecular structures, energy levels, and single crystal parameters for B-N embedded 2D π-conjugated units **(A)** and photovoltaic applications of compound 43 as an electron donor or additive **(B)**. Reprinted with permission from Wang et al. (2014). Copyright (2014) American Chemical Society.

leading to stronger electronic coupling between neighboring molecules. Pei and co-workers developed two BN-substituted tetrathienonaphthalene derivatives, i.e., BN-TTN-C3 and BN-TTN-C6 (Wang X. et al., 2013). Because of the different side chains, the two BN embedded units exhibited distinct packing mode, with helical and layered packing style for BN-TTN-C3 and BN-TTN-C6, respectively. BN-TTN-C3 displayed close π-π stacking (3.44 Å) in crystal state whereas BN-TTN-C6 showed CH-π interaction. Moreover, BN-TTN-C3 gave closer dipole-dipole interaction (6.763 Å) compared to that of BN-TTN-C6 (9.207 Å). Due to the higher ordered molecular packing, BN-TTN-C3 exhibited superior hole mobility of 0.12 $cm^2/V\bullet s$,

elevated by one magnitude than the value of BN-TTN-C3 (0.03 $cm^2/V\bullet s$). Recently, they copolymerized the BN-TTN with thiophene units to afford the conjugated polymers with lowered HOMO levels ($-5.46 \sim -5.67$ eV) and strong intermolecular interactions (Wang et al., 2015b). OFET devices prepared from these azaborine-based polymers exhibited a champion hole mobility of 0.38 $cm^2/V\bullet s$. By changing the co-monomers, a vast of novel copolymers based on this azaborine unit can be obtained, predicting a great potential of this unit for electronic device applications.

Furthermore, they developed a straightforward strategy to produce the largest BN embedded heteroaromatic (**43**) to date (Wang et al., 2014). Single crystal X-ray diffraction indicated the significant distorted conformation of **43** due to the steric hindrance among peripheral rings and two different conformations (A and B) were found in the same crystal. The single crystal showed a columnar stacking style along the 011 direction and one-dimensional micro-ribbons can be obtained feasibly due to the strong π-π interactions. OFET devices based on the micro-ribbons gave a hole mobility of 0.23 $cm^2/V\bullet s$, a low threshold of −3 V, and a current on/off ratio of $> 10^4$. Theoretical calculations indicated a depressed HOMO and unchanged LUMO of **43** in contrast to its all-carbon analog. HOMO estimated from electrochemistry and optical bandgap calculated from the absorption onset was −5.07 and −2.59 eV, respectively for **43**. OPV devices prepared with **43** as donor and PC71BM as acceptor gave a PCE of 3.12% and a V_{oc} of 0.96 eV (Zhong et al., 2016). Moreover, when it was added to PTB7/PC71BM system as additive, the ternary solar cells displayed improved PCE (4.75%) in comparison to the PCE of binary devices (3.91%) (**Figure 13B**). This is the first example of applying B-N embedded heteroaromatics to the OPV devices.

From the aforementioned discussion on the B-N embedded units, the following conclusions can be deduced. Different from the B←N bond, which amends the energy levels and optical absorption of π-units significantly, the B-N embedded π-units usually have similar or slightly different energy levels and optical bandgaps to their all-carbon analogs. Most of the B-N embedded units have large optical bandgaps and narrow absorption bands. Extending the conjugation of the B-N embedded π-units would broaden the absorption bands. Introducing the dipolar B-N bond into the conjugated backbone would enhance the intermolecular interaction, facilitating the ordered π-π stacking and enhancing the hole mobility in contrast to their all-carbon analogs. Accordingly, B-N embedded π-units are excellent electron-rich units and promising candidates for construction of OPV materials. Otherwise, to now, OPV applications involving the B-N embedded π-units are scarcely revealed. From my point of view, these B-N embedded PAHs are promising for OPV applications and will represent an important direction of OPV materials.

π-Electronic Units Containing N–B←N Groups

The typical π-electronic unit containing N–B←N group is the 4,4′-difluoro-4-bora-3a,4a-diaza-s-indacene (BODIPY), possessing unique optoelectronic properties, e.g., strong molar extinct coefficient ($10^5\ M^{-1}\bullet cm^{-1}$), low-lying HOMO (−5.5 eV) and LUMO (−3.5 eV), strong electron affinity, and high fluorescence quantum yield, which has drawn much attention in the field of labeling and chemical sensors (Sekiya et al., 2009; Lu et al., 2014). For OPVs, the BODIPY also plays an important role, either in the electron donor or acceptor materials. In general, α, β, and *meso*-positions are readily available for chemical modification to adjust the properties of BODIPY for OPV applications (**Figure 14**). **Table 2** summarizes the optoelectronic and photovoltaic parameters for BODIPY-based molecules. In 2009, Roncali et al. initially reported the BODIPY-based small molecules modified at α-position with styryl and *meso*-position with iodobenzene, i.e., **90a** and **90b** as electron donor materials, affording an optimum PCE of 1.17 and 1.34%, respectively, by using PC61BM as electron acceptor material (Rousseau et al., 2009a). Interestingly, ternary device prepared by blending **90a**, **90b**, and PC61BM as active layer showed a promoted PCE of 1.70% (Rousseau et al., 2009b). Then, the further modification of **90b** at *meso*-position with oligothiphene gave **90c**, leading to an improved PCE of 2.17% due to the enhanced hole mobility (Rousseau et al., 2010). In 2012, Ziessle et al. substituted the α-position of BODIPY with vinylthiophene to obtain **91a**, **91b**, **91c**, and **91d**, exhibiting a maximum PCE of 1.40, 4.70, 0.90, and 1.50%, respectively (Bura et al., 2012). The highest PCE for **91b** was interpreted by its depressed HOMO levels, broad and strong external quantum response and high hole mobility. Replacing at α and *meso*-positions with triphenylamine produced **92a** and **92b**, giving a moderate PCE of 1.50 and 0.51%, respectively (Kolemen et al., 2014). However, tailoring the *meso*-substituents with carbazole units along with device technique optimization by thermal annealing and solvent vapor annealing, **93a**, **93b**, and **93c** yielded a superior PCE of 5.05, 3.99, and 4.80%, respectively, by using PC71BM as electron acceptor material (Jadhav et al., 2015). Zhan and coworkers synthesized the dimeric BODIPY bridged with oligothiophene at the *meso*-positions (**94c**) (Liu et al., 2014). Compared with the single BODIPY cores **94a** and **94b**, the dimeric molecule **94c** showed improved packing order when blended with PC71BM and enhanced hole mobility, leading to a higher PCE of 3.13%. Mueller et al. revealed the BODIPY analogs of **95a** and **95b**, giving a PCE of 1.2 and 1.1% by using C60 as electron acceptor to prepare the vacuum-processed solar cells (Mueller et al., 2012). Similarly, Kraner et al. studied the influence of side groups on the OPV performance of BODIPY analogs, **95b**, **95c**, and **95d** (Kraner et al., 2015).

In order to further expand the absorption band of BODIPY, covalently combining it with other dye molecules emerged as an effective strategy. For example, the DPP unit was introduced to link with BODIPY, resulting into **96a** and **96b** (Cortizo-Lacalle et al., 2014). By using PC71BM as the acceptor, **96a** and **96b** showed a moderate PCE of 0.65 and 0.64%, respectively, due to the over-strong aggregating ability of these dye molecules, leading to poor film morphology. The porphyrin moiety was also selected to connect with BODIPY, producing **97**, which exhibited a competitive PCE of 5.29%

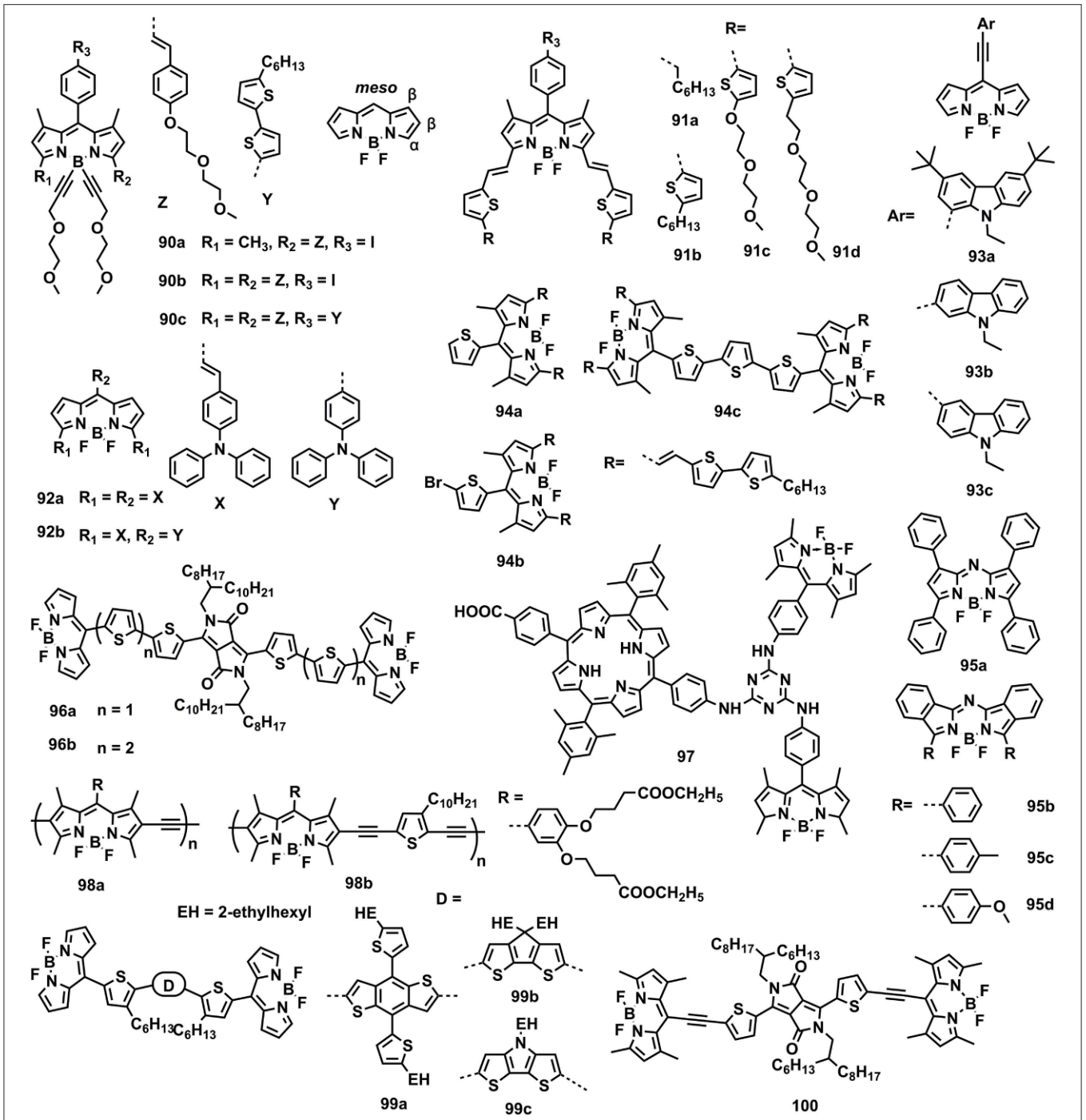

FIGURE 14 | Molecular structures of BODIPY-based photovoltaic materials.

(Sharma et al., 2015). Moreover, the BODIPY was also utilized as building block for construction of conjugated polymers. By copolymerizing with acetylene and thiophene, conjugated copolymers of **98a** and **98b** can be obtained, showing low bandgap of 1.61 and 1.65 eV, respectively. By using PC61BM as acceptor, moderated PCEs around 2.0% can be obtained (Kim et al., 2010).

Except for using as donor materials, the BODIPY-based molecules are also qualified for the acceptor materials due to its strong electron affinity. BODIPY dimers bridged with BDT (**99a**), CPDT (**99b**), and DTP (**99c**) were synthesized to be used as electron-acceptor materials. By selecting P3HT as electron-donor material, fullerene-free devices based on these BODIPY dimers showed PCEs from 1.18 to 1.51% (Poe

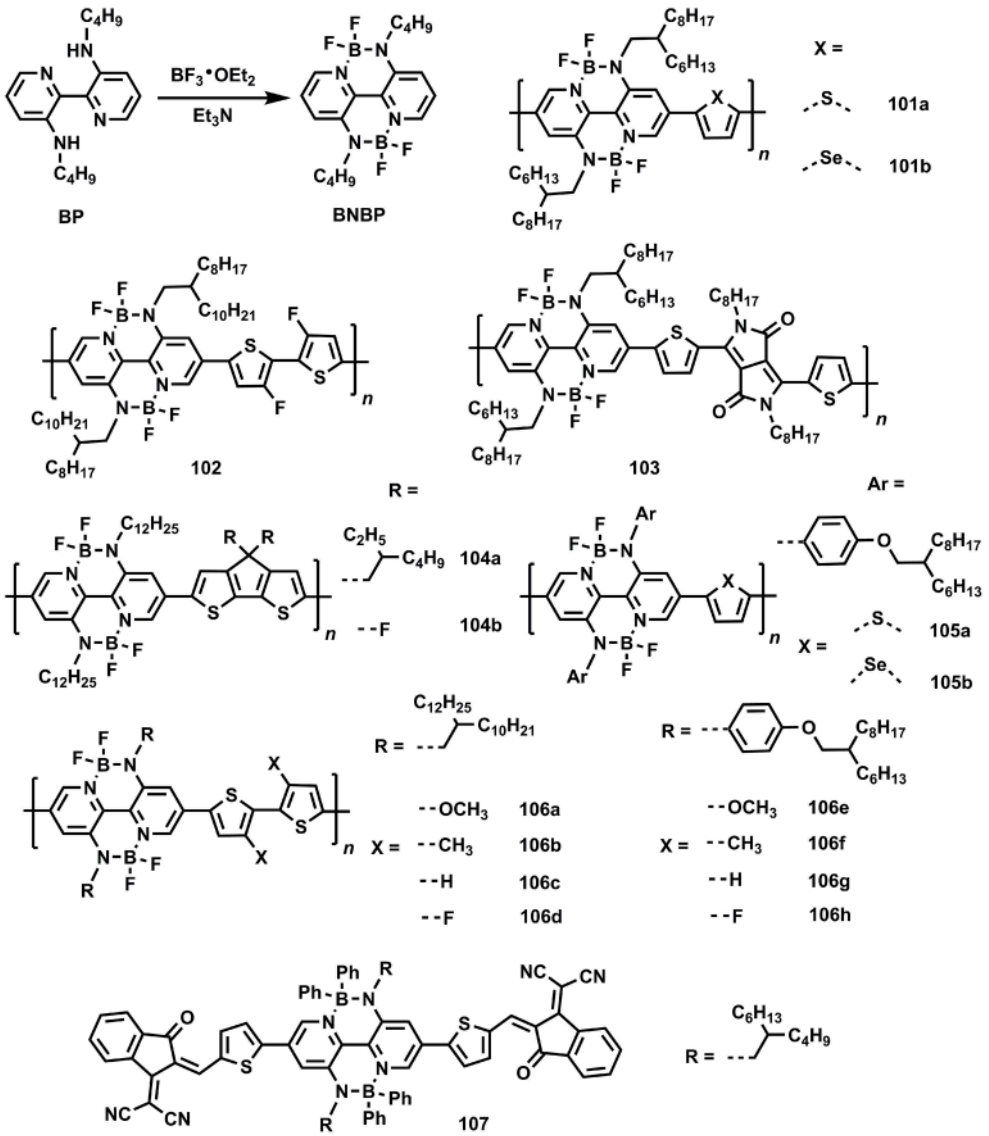

FIGURE 15 | Molecular structures of BNBP-based photovoltaic materials.

et al., 2014). Zhan et al. reported the DPP bridged BODIPY dimers (**100**), exhibiting an competitive PCE of 2.84% by using PTB7-Th/*p*-DTS(FBTTh$_2$)$_2$ (0.5:0.5) as donor (Liu W. et al., 2017).

Recently, a novel π-electronic unit containing N-B←N group, namely BNBP, with low-lying LUMO, bathochromic absorption, good co-planarity, and strong π-π interaction has been developed by Liu and coworkers. Owing to its strong electron-affinity, it's suitable to build conjugated copolymers for acceptor materials (**Figure 15**). **Table 3** summarizes the optoelectronic and photovoltaic parameters for BNBP-based materials. The primary attempt to copolymerize with thiophene produced a typical D-A copolymer **101a**, showing the HOMO and LUMO of −5.77 and −3.50 eV, respectively. By selecting PTB7 as donor materials, all-polymer solar cells were fabricated, affording a high V_{oc} of 1.09 V and an impressive PCE of 3.38% (Dou et al., 2016). The high V_{oc} was mainly originated from the large offset between HOMO of PTB7 and LUMO of **101a**. By selecting PCDTBT, a donor polymer with low-lying HOMO of −5.42 eV, to prepare all-polymer solar cells with **101a**, a recorded V_{oc} of 1.3 V can be obtained (Ding et al., 2017). Using small molecule donor *p*-DTS(FBTTh$_2$)$_2$ to match with **101a** also gave a V_{oc} of 1.08 V and a PCE of 3.5% (Zhang Z. et al., 2017). Replacing the co-monomer from thiophene to selenophene led to the copolymer **101b**, which displayed depressed HOMO (−5.77 eV) and LUMO (−3.66 eV) compared to the values of **101a**. By using PTB7-Th as donor material, the all-polymer solar cells gave an improved PCE of 4.26%, which were interpreted by the enhanced driving force for the charge dissociation between PTB7-Th and **101b**, resulting from

TABLE 2 | Optoelectronic and photovoltaic parameters for BODIPY-based materials.

BNBP	HOMO/LUMO(eV)	E_g^{opt}(eV)	Active layers	V_{oc} (V)	$J_{sc}(mA/cm^2)$	FF(%)	PCE(%)
90a	−5.69/−3.66	1.95	90a/PC61BM	0.80	4.43	34	1.17
90b	−5.56/−3.75	1.70	90b/PC61BM	0.75	4.14	44	1.34
90c	−5.61/−3.80	1.70	90c/PC61BM	0.75	7.00	38	2.17
91a	−5.46/−3.81	1.6	91a/PC61BM	0.76	5.84	31	1.40
91b	−5.34/−3.84	1.45	91b/PC61BM	0.70	14.3	47	4.70
91c	−5.30/−3.85	1.42	91c/PC61BM	0.56	5.10	30	0.90
91d	−5.32/−3.86	1.48	91d/PC61BM	0.55	8.50	32	1.50
92a	−5.00/−3.59	1.41	92a/PC61BM	0.68	7.00	31	1.50
92b	−4.96/−3.42	1.54	92b/PC61BM	0.43	3.59	32	0.51
93a	−5.48/−3.44	1.72	93a/PC71BM	0.90	10.2	55	5.05
93b	−5.62/−3.42	1.88	93b/PC71BM	0.90	9.24	48	3.99
93c	−5.54/−3.46	1.85	93c/PC71BM	0.96	9.64	52	4.80
94a	−5.02/−3.64	1.40	94a/PC71BM	0.67	6.80	34	1.56
94b	−5.06/−3.74	1.38	94b/PC71BM	0.72	7.62	36	1.96
94c	−5.06/−3.73	1.41	94c/PC71BM	0.74	11.28	38	3.13
95a	−5.68/−4.01	1.62	95a/C60	0.96	3.15	48	1.20
95b	−5.22/−3.65	1.48/(1.55)	95b/C60	0.65/(0.81)	2.40/(8.0)	65/(59)	1.1/(3.8)
95c	−5.27/−3.63	1.55	95c/C60	0.71	7.00	55	2.7
95d	−5.10/−3.60	1.52	95d/C60	0.61	5.40	52	1.7
96a	−5.13/−3.50	1.71	96a/PC71BM	0.71	3.39	27	0.65
96b	−5.10/−3.40	1.67	96b/PC71BM	0.53	4.55	26	0.64
97	−5.62/−3.52	1.84	97/PCBM	0.90	10.48	56	5.29
98a	−5.58/−3.73	1.61	98a/PC61BM	0.76	4.00	43	1.3
98b	−5.45/−3.71	1.65	98b/PC61BM	0.80	4.82	51	2.0
99a	−5.40/−3.79	1.73	P3HT/99a	0.65	3.09	0.60	1.21
99b	−5.16/−3.82	1.54	P3HT/99b	0.62	3.90	0.63	1.51
99c	−5.14/−3.74	1.47	P3HT/99c	0.57	3.28	0.63	1.18
100	−5.36/−3.79	1.50	PTB7-Th/*p*-DTS(FBTTh$_2$)$_2$/100	0.76	7.19	0.53	2.84

the deeper LUMO of **101b** in contrast to the value of **101a** (Ding et al., 2016). Furthermore, when the 3,3′-difluoro-2,2′-bithiophene (fBT) unit was utilized to copolymerize with BNBP, the resulting polymer **102** exhibited a high electron mobility of 2.4×10^{-4} cm^2/V•s due to the intra-molecular F…S interaction that locked the conformation, enhanced the co-planarity, and facilitate the ordered molecular packing. Therefore, all-polymer solar cells based on PTB7-Th/**102** afforded a recorded PCE of 6.26% for N-B←N based acceptor materials (Long et al., 2016a). In order to further broadened the absorption band to lower energy, the DPP unit was selected as co-monomer to obtain copolymer **103**, showing a small optical bandgap of 1.56 eV and high electron mobility of 2.1×10^{-4} cm^2/V•s. All-polymer solar cells based on PTB7/**103** gave a PCE of 2.69% (Long et al., 2016b).

Additionally, the electron-rich CPT unit was also copolymerized with BNBP leading to **104a**, showing the HOMO and LUMO of −5.64 and −3.45 eV, respectively, which was matched well with the energy levels of P3HT (HOMO/LUMO = −5.20/−3.20 eV). As such, all-polymer solar cells based on P3HT/**104a** were prepared, affording a moderate PCE of 1.76% with a high V_{oc} of 1.01 V (Long et al., 2017a). When the alkyl groups on the CPT were replaced by F atoms, a new electron-rich unit, namely, 4,4-Difluoro-4H-cyclopenta[2,1-b:3,4-b′]dithiophene (fCPT) can be obtained. By copolymerizing with BNBP, the novel polymer **104b** exhibited depressed HOMO and LUMO in comparison with the values of **104a**. PTB7-Th was selected as donor material to afford a competitive PCE of 3.76% (Zhao et al., 2017b). Moreover, conjugated side groups were introduced to BNBP unit and copolymer **105a** and **105b** were produced. The conjugated side chains were considered to improve the electron mobility and a good PCE of 3.77 and 4.46% were demonstrated for **105a** and **105b**, respectively (Zhao et al., 2017a). Recently, they revealed an effective method to finely tune the HOMO and LUMO of BNBP-based polymers by varying the side chains, as evident by **106a**—**106h**, whose LUMOs were decreased gradually. **106a** and **106e** were suitable for the donor materials due to their high-lying energy levels whereas **106d** and **106h** were applicable for acceptor materials owing to their low-lying energy levels (Long et al., 2017b).

In general, these BNBP-based copolymers are suitable for acceptor materials due to the strong electron-affinity properties. Although several polymers based on BNBP were reported for

TABLE 3 | Optoelectronic and photovoltaic parameters for BNBP-based materials.

BNBP	HOMO/LUMO(eV)	E_g^{opt}(eV)	Active layers	V_{oc} (V)	$J_{sc}(mA/cm^2)$	FF(%)	PCE(%)
101a	−5.77/−3.50	1.92	PTB7/101a	1.09	7.09	44	3.38
101b	−5.84/−3.66	1.87	PTB7-Th/101b	1.03	10.02	42	4.26
102	−5.87/−3.62	1.86	PTB7-Th/102	1.07	12.69	47	6.26
103	−5.45/−3.87	1.56	PTB7/103	0.88	7.54	41	2.69
104a	−5.64/−3.45	1.85	P3HT/104a	1.01	4.98	35	1.76
104b	−5.89/−3.60	1.82	PTB7-Th/104b	0.99	8.78	44	3.76
105a	−5.74/−3.72	1.97	PTB7-Th/105a	1.11	7.58	45	3.77
105b	−5.75/−3.73	1.87	PTB7-Th/105b	1.07	9.21	45	4.46
106a	−5.37/−3.39	1.72	106a/PC71BM	0.70	2.02	41	0.59
106b	−5.81/−3.32	1.83	–	–	–	–	–
106c	−5.92/−3.43	1.91	–	–	–	–	–
106d	−6.04/−3.62	1.90	PTB7-Ph/106d	1.09	10.13	47	5.16
106e	−5.46/−3.48	1.66	106e/PC71BM	0.76	7.59	51	2.92
106f	−5.84/−3.42	1.81	–	–	–	–	–
106g	−5.77/−3.51	1.85	–	–	–	–	–
106h	−5.85/−3.71	1.84	PTB7-Ph/106h	1.12	7.33	45	3.70
107	−5.34/−3.93	1.40	PTB7-Th/107	0.78	14.62	62	7.06

OPV applications, small molecules related to this unit are scarcely revealed to now. Very recently, a small-molecule acceptor (**107**) built by end-capping BNBP with IC unit was reported, exhibiting a low-lying LUMO of −3.93 eV and wide absorption band (Liu F. et al., 2017). By selecting PTB7-Th as donor material, OPV devices gave a J_{sc} of 14.62 mA/cm^2, a V_{oc} of 0.78 V, an FF of 62%, and a competitive PCE of 7.06%. This attempt points out the great potential of BNBP as a building block for small-molecule acceptor materials. We anticipate that the small molecules based on BNBP and its derivatives are also interesting and promising for non-fullerene acceptor materials. This field is blank to now and we strongly perceive that the small molecules based on novel π-electronic units containing N-B←N groups for OPV applications leave a large space and will be a research hot drawing great attention.

PROSPECT

In summary, the OPV applications of BN embedded π-conjugated electronic units are in infancy. From our point, the following aspects will presumably be the potential research interests concerning the BN perturbed π-conjugated units.

For B-N covalent bond embedded π-conjugated units, they are suitable to act as electron-rich units to construct electron-donor materials owing to their high-lying energy levels, good backbone co-planarity, and high hole mobility. However, their absorption bands should be further broadened to lower energy (600–800 nm) to enhance the light harvesting ability. On the one hand, novel π-units containing B-N bond with extended conjugation should be developed to further red-shift the absorption bands. On the other hand, linking the B-N embedded π-conjugated units with low bandgap electron-deficient units, e.g., PDI, NDI, DPP, IID, IC, TPD, and BT can be an effective method to decrease the optical bandgaps and shift the absorption bands to longer wavelength. To this end, fine-tuning the energy levels and optical absorption via D-A combination of B-N embedded π-units and electron-deficient units will be a systematical job.

For B←N and N-B←N embedded π-units, the low-lying energy levels, red-shifted absorption bands, and good electron mobility make them promising electron-deficient units for construction of acceptor materials. To now, most studies have been focusing on the BODIPY-based donor materials and a few novel units containing B←N or N-B←N, e.g., BNCTP and BNBP were used to construct polymer acceptor materials. However, the currently revealed structures are still limited in terms of electron affinity, conjugation degree and light absorption. Great research space remains in the development of novel fused π-units containing B←N or N-B←N groups with depressed energy levels and strong light-harvesting ability. Upon judicious molecular tailoring, these B←N or N-B←N embedded π-units possess high electron affinity and good rigidity, which may be comparable to those typical electron-deficient units, e.g., PDI, NDI, DPP, and IID. As such, small-molecule acceptors established with B←N or N-B←N embedded π-units will presumably be an important family of OPV materials, although few examples has been reported to now.

Challenges also exist in these structures, from synthesis routes, to material stability, and processability. The synthesis routes usually involve the usage of BX_3, which is strong Lewis acid, toxic, and easily subjected to hydrolysis. Similarly, some of the BN embedded units are unstable in moisture and cannot be purified by typical chromatographic methods due to the Lewis acid property of B atom (Crossley et al., 2015; Zhu et al., 2016). Moreover, how to introduce bulk substituents into the backbone to ensure sufficient solution processability without sacrificing the molecular co-planarity and packing order is also a challenge.

These challenges should be fully taken into account when designing BN embedded units for OPV applications. However, we expect that BN embedded units will draw great attention for the construction of OPV materials.

AUTHOR CONTRIBUTIONS

JH conceived, designed, and wrote the manuscript. YL retrieved the literature and edited sections of the manuscript. All authors approved it for publication.

ACKNOWLEDGMENTS

This work was financially supported by the National Natural Science Foundation of China (NSFC, No. 51603076) and Graphene Powder & Composite Research Center of Fujian Province (2017H2001). The Outstanding Youth Scientific Research Cultivation Plan of Colleges and Universities of Fujian Province and Promotion Program for Young and Middle-aged Teacher in Science and Technology Research of Huaqiao University (ZQN-PY405) were appreciated.

REFERENCES

Araneda, J. F., Piers, W. E., Heyne, B., Parvez, M., and McDonald, R. (2011). High stokes shift anilido-pyridine boron difluoride dyes. *Angew. Chem. Int. Ed. Engl.* 50, 12214–12217. doi: 10.1002/anie.201105228

Benavides, C. M., Murto, P., Chochos, C. L., Gregoriou, V. G., Avgeropoulos, A., Xu, X., et al. (2018). High-performance organic photodetectors from a high-bandgap indacenodithiophene-based π-conjugated donor-acceptor polymer. *ACS Appl. Mater. Interfaces* 10, 12937–12946. doi: 10.1021/acsami.8b03824

Benedikt, N., Araneda,. J., Piers, W., and Masood, P. (2013). BN-dibenzo[a,o]picenes: analogues of an unknown polycyclic aromatic hydrocarbon. *Angew. Chem. Int. Ed. Engl.* 52, 9966–9969. doi: 10.1002/anie.201302911

Beniwal, S., Hooper, J., Miller, D. P., Costa, P. S., Chen, G., Liu, S.-Y., et al. (2017). Graphene-like boron-carbon-nitrogen monolayers. *ACS Nano* 11, 2486–2493. doi: 10.1021/acsnano.6b08136

Bosdet, M. J. D., Jaska, C. A., Piers, W. E., Sorensen, T. S., and Parvez, M. (2007a). Blue fluorescent 4a-aza-4b-boraphenanthrenes. *Org. Lett.* 9, 1395–1398. doi: 10.1021/ol070328y

Bosdet, M. J. D., Piers, W. E., Sorensen, T. S., and Parvez, M. (2007b). 10a-aza-10b-borapyrenes: heterocyclic analogues of pyrene with internalized BN moieties. *Angew. Chem. Int. Ed. Engl.* 6, 4940–4943. doi: 10.1002/anie.200700591

Bosdet, M. J. D., Piers, W. E., Sorensen, T. S., and Parvez, M. (2010). 5b,7b-diaza-3b,9b-diborabenzo[ghi]perylenes. *Can. J. Chem.* 88, 426–433. doi: 10.1139/V10-009

Bura, T., Leclerc, N., Fall, S., Lévêque, P., Heiser, T., Retailleau, P., et al. (2012). High-performance solution-processed solar cells and ambipolar behavior in organic field-effect transistors with thienyl-BODIPY scaffoldings. *J. Am. Chem. Soc.* 134, 17404–17407. doi: 10.1021/ja3072513

Campbell, P. G., Marwitz, A. J., and Liu, S. Y. (2012). Recent advances in azaborine chemistry. *Angew. Chem. Int. Ed. Engl.* 51, 6074–6092. doi: 10.1002/anie.201200063

Chen, G., Sasabe, H., Igarashi, T., Hong, Z., and Kido, J. (2015). Squaraine dyes for organic photovoltaic cells. *J. Mater. Chem. A* 3, 14517–14534. doi: 10.1039/C5TA01879J

Chen, G., Sasabe, H., Sasaki, Y., Katagiri, H., Wang, X. F., Sano, T., et al. (2014). A series of squaraine dyes: effects of side chain and the number of hydroxyl groups on material properties and photovoltaic performance. *Chem. Mater.* 26, 1356–1364. doi: 10.1021/cm4034929

Chen, G., Sasabe, H., Wang, Z., Wang, X. F., Hong, Z., Yang, Y., et al. (2012). Co-evaporated bulk heterojunction solar cells with > 6.0% efficiency. *Adv. Mater.* 24, 2768–2773. doi: 10.1002/adma.201200234

Chen, J. D., Cui, C., Li, Y. Q., Zhou, L., Ou, Q. D., Li, C., et al. (2015). Single-junction polymer solar cells exceeding 10% power conversion efficiency. *Adv. Mater.* 27, 1035–1041. doi: 10.1002/adma.201404535

Chissick, S. S., Dewar, M. J. S., and Maitlis, P. M. (1960). New heteraromatic compounds containing two boron atoms. *Tetrahedron Lett.* 1, 8–10. doi: 10.1016/S0040-4039(00)70270-X

Cortizo-Lacalle, D., Howells, C. T., Pandey, U. K., Cameron, J., Findlay, N. J., Inigo, A. R., et al. (2014). Solution processable diketopyrrolopyrrole (DPP) cored small molecules with BODIPY end groups as novel donors for organic solar cells. *Beilstein J. Org. Chem.* 10, 2683–2695. doi: 10.3762/bjoc.10.283

Crossley, D. L., Cade, I. A., Clark, E. R., Escande, A., Humphries, M. J., King, S. M., et al. (2015). Enhancing electron affinity and tuning band gap in donor-acceptor organic semiconductors by benzothiadiazole directed C-H borylation. *Chem. Sci.* 6, 5144–5151. doi: 10.1039/C5SC01800E

Crossley, D. L., Urbano, L., Neumann, R., Bourke, S., Jones, J., Dailey, L. A., et al. (2017). Post-polymerization C-H borylation of donor-acceptor materials gives highly efficient solid state near-infrared emitters for near-IR-OLEDs and effective biological imaging. *ACS Appl. Mater. Interfaces* 9, 28243–28249. doi: 10.1021/acsami.7b08473

Davies, K. M., Dewar, M. J. S., and Rona, P. (1967). New heteroaromatic compounds. XXVI. synthesis of borazarenes. *J. Am. Chem. Soc.* 89, 6294–6297. doi: 10.1021/ja01000a054

Dewar, M. J. S., and Dietz, R. (1959). 546. New heteroaromatic compounds. Part, I. I. I. 2,1-borazaro-naphthalene (1,2-dihydro-1-aza-2-boranaphthalene). *J. Chem. Soc.* 2728–2730. doi: 10.1039/jr9590002728

Dewar, M. J. S., Kubba, V. P., and Pettit, R. (1958). 624. New heteroaromatic compounds. Part, I. 9-aza-10-boraphenanthrene. *J. Chem. Soc.* 3073–3076. doi: 10.1039/jr9580003073

Dewar, M. J. S., and Poesche, W. H. (1963). New heteroaromatic compounds. XVIII.1 boron-containing analogs of benz[a]anthracene. *J. Am. Chem. Soc.* 85, 2253–2256. doi: 10.1021/ja00898a014

Dewar, M. J. S., and Poesche, W. H. (1964). New heteroaromatic compounds. XXI. some tetracyclic systems. *J. Org. Chem.* 29, 1757–1762. doi: 10.1021/jo01030a023

Ding, Z., Long, X., Dou, C., Liu, J., and Wang, L. (2016). A polymer acceptor with an optimal LUMO energy level for all-polymer solar cells. *Chem. Sci.* 7, 6197–6202. doi: 10.1039/C6SC01756H

Ding, Z., Long, X., Meng, B., Bai, K., Dou, C., Liu, J., et al. (2017). Polymer solar cells with open-circuit voltage of 1.3 V using polymer electron acceptor with high LUMO level. *Nano Energy* 32, 216–224. doi: 10.1016/j.nanoen.2016.12.041

Dominik, V., Gerald, K., Dagmar, K., Katrin, W., Roland, F., Gerhard, E., et al. (2002). Formation of isomeric BAr_3 adducts of 2-lithio-N-methylimidazole. *Eur. J. Inorg. Chem.* 2002, 2015–2021. doi: 10.1002/1099-0682(200208)2002:8<2015::AID-EJIC2015>3.0.CO;2-8

Dou, C., Ding, Z., Zhang, Z., Xie, Z., Liu, J., and Wang, L. (2015). Developing conjugated polymers with high electron affinity by replacing a C-C unit with a B←N unit. *Angew. Chem. Int. Ed. Engl.* 54, 3648–3652. doi: 10.1002/anie.201411973

Dou, C., Liu, J., and Wang, L. (2017). Conjugated polymers containing B←N unit as electron acceptors for all-polymer solar cells. *Sci. China Chem.* 60, 450–459. doi: 10.1007/s11426-016-0503-x

Dou, C., Long, X., Ding, Z., Xie, Z., Liu, J., and Wang, L. (2016). An electron-deficient building block based on the B←N Unit: an electron acceptor for all-polymer solar cells. *Angew. Chem. Int. Ed. Engl.* 55, 1436–1440. doi: 10.1002/anie.201508482

Emslie, D. J. H., Piers, W., and Parvez, M. (2003). 2,2′-Diborabiphenyl: a lewis acid analogue of 2,2′-bipyridine. *Angew. Chem. Int. Ed. Engl.* 42, 1252–1255. doi: 10.1002/anie.200390320

Fu, Y., Qiu, F., Zhang, F., Mai, Y., Wang, Y., Fu, S., et al. (2015). A dual-boron-cored luminogen capable of sensing and imaging. *Chem. Commun.* 51, 5298–5301. doi: 10.1039/C4CC08551E

Grimsdale, A. C., Leok Chan, K., Martin, R. E., Jokisz, P. G., and Holmes, A. B. (2009). Synthesis of light-emitting conjugated polymers for applications in electroluminescent devices. *Chem. Rev.* 109, 897–1091. doi: 10.1021/cr000013v

Gsänger, M., Bialas, D., Huang, L., Stolte, M., and Würthner, F. (2016). Organic semiconductors based on dyes and color pigments. *Adv. Mater.* 28, 3615–3645. doi: 10.1002/adma.201505440

Gupta, V., Kyaw, A. K., Wang, D. H., Chand, S., Bazan, G. C., and Heeger, A. J. (2013). Barium: an efficient cathode layer for bulk-heterojunction solar cells. *Sci. Rep.* 3:1965. doi: 10.1038/srep01965

Han, Y., Barnes, G., Lin, Y.-H., Martin, J., Al-Hashimi, M., AlQaradawi, S. Y., et al. (2016). Doping of large ionization potential indenopyrazine polymers via lewis acid complexation with tris(pentafluorophenyl)borane: a simple method for improving the performance of organic thin-film transistors. *Chem. Mater.* 28, 8016–8024. doi: 10.1021/acs.chemmater.6b03761

Hao, Q., Yu, S., Li, S., Chen, J., Zeng, Y., Yu, T., et al. (2014). Locked planarity: a strategy for tailoring ladder-type pi-conjugated anilido-pyridine boron difluorides. *J. Org. Chem.* 79, 459–464. doi: 10.1021/jo402583y

Hashimoto, S., Ikuta, T., Shiren, K., Nakatsuka, S., Ni, J., Nakamura, M., et al. (2014). Triplet-energy control of polycyclic aromatic hydrocarbons by BN replacement: development of ambipolar host materials for phosphorescent organic light-emitting diodes. *Chem. Mater.* 26, 6265–6271. doi: 10.1021/cm503102d

Hatakeyama, T., Hashimoto, S., Seki, S., and Nakamura, M. (2011). Synthesis of BN-fused polycyclic aromatics via tandem intramolecular electrophilic arene borylation. *J. Am. Chem. Soc.* 133, 18614–18617. doi: 10.1021/ja208950c

Huang, D., Wang, C., Zou, Y., Shen, X., Zang, Y., Shen, H., et al. (2016). Bismuth interfacial doping of organic small molecules for high performance n-type thermoelectric materials. *Angew. Chem. Int. Ed. Engl.* 55, 10672–10675. doi: 10.1002/anie.201604478

Huang, J., Li, Y., Wang, Y., Meng, H., Yan, D., Jiang, B., et al. (2018). A lewis acid-base chemistry approach towards narrow bandgap dye molecules. *Dyes Pigm.* 153, 1–9. doi: 10.1016/j.dyepig.2018.02.003

Ishibashi, J. S. A., Dargelos, A., Darrigan, C., Chrostowska, A., and Liu, S.-Y. (2017). BN Tetracene: extending the reach of BN/CC isosterism in acenes. *Organometallics* 36, 2494–2497. doi: 10.1021/acs.organomet.7b00296

Ishibashi, J. S., Marshall, J. L., Maziere, A., Lovinger, G. J., Li, B., Zakharov, L. N., et al. (2014). Two BN isosteres of anthracene: synthesis and characterization. *J. Am. Chem. Soc.* 136, 15414–15421. doi: 10.1021/ja508813v

Ishida, N., Moriya, T., Goya, T., and Murakami, M. (2010). Synthesis of pyridine-borane complexes via electrophilic aromatic borylation. *J. Org. Chem.* 75, 8709–8712. doi: 10.1021/jo101920p

Jadhav, T., Misra, R., Biswas, S., and Sharma, G. D. (2015). Bulk heterojunction organic solar cells based on carbazole-BODIPY conjugate small molecules as donors with high open circuit voltage. *Phys. Chem. Chem. Phys.* 17, 26580–26588. doi: 10.1039/C5CP04807A

Janssen, R. A., and Nelson, J. (2013). Factors limiting device efficiency in organic photovoltaics. *Adv. Mater.* 25, 1847–1858. doi: 10.1002/adma.201202873

Jaska, C. A., Emslie, D. J. H., Bosdet, M. J. D., Piers, W. E., Sorensen, T. S., and Parvez, M. (2006). Triphenylene analogues with $B_2N_2C_2$ cores: synthesis, structure, redox behavior, and photophysical properties. *J. Am. Chem. Soc.* 128, 10885–10896. doi: 10.1021/ja063519p

Jaska, C. A., Piers, W. E., McDonald, R., and Parvez, M. (2007). Synthesis, characterization, and fluorescence behavior of twisted and planar B_2N_2-quaterphenyl analogues. *J. Org. Chem.* 72, 5234–5243. doi: 10.1021/jo0706574

Job, A., Wakamiya, A., Kehr, G., Erker, G., and Yamaguchi, S. (2010). Electronic tuning of thiazolyl-capped π-conjugated compounds via a coordination/cyclization protocol with $B(C_6F_5)_3$. *Org. Lett.* 12, 5470–5473. doi: 10.1021/ol102282x

Kim, B., Ma, B., Donuru, V. R., Liu, H., and Frechet, J. M. (2010). Bodipy-backboned polymers as electron donor in bulk heterojunction solar cells. *Chem. Commun.* 46, 4148–4150. doi: 10.1039/b927350f

Ko, S. B., Lu, J. S., and Wang, S. (2014). Chelation-assisted photoelimination of B,N-heterocycles. *Org. Lett.* 16, 616–619. doi: 10.1021/ol403550b

Kolemen, S., Cakmak, Y., Ozdemir, T., Erten-Ela, S., Buyuktemiz, M., Dede, Y., et al. (2014). Design and characterization of bodipy derivatives for bulk heterojunction solar cells. *Tetrahedron* 70, 6229–6234. doi: 10.1016/j.tet.2014.03.049

Kraner, S., Widmer, J., Benduhn, J., Hieckmann, E., Jägeler-Hoheisel, T., Ullbrich, S., et al. (2015). Influence of side groups on the performance of infrared absorbing aza-BODIPY organic solar cells. *Phys. Status Solidi A* 212, 2747–2753. doi: 10.1002/pssa.201532385

Leroy, G., Sana, M., and Wilante, C. (1993). Evaluation of the bond energy terms for the various types of boron-nitrogen bonds. *Theor. Chim. Acta* 85, 155–166. doi: 10.1007/BF01374585

Letsinger, R. L., and MacLean, D. B. (1963). Organoboron compounds. XVI. coöperative functional group effects in reactions of boronoarylbenzimidazoles. *J. Am. Chem. Soc.* 85, 2230–2236. doi: 10.1021/ja00898a009

Li, D., Zhang, H., and Wang, Y. (2013). Four-coordinate organoboron compounds for organic light-emitting diodes (OLEDs). *Chem. Soc. Rev.* 42, 8416–8433. doi: 10.1039/c3cs60170f

Li, M., An, C., Pisula, W., and Müllen, K. (2018). Cyclopentadithiophene-benzothiadiazole donor-acceptor polymers as prototypical semiconductors for high-performance field-effect transistors. *Acc. Chem. Res.* 51, 1196–1205. doi: 10.1021/acs.accounts.8b00025

Li, W., Ye, L., Li, S., Yao, H., Ade, H., and Hou, J. (2018). A high-efficiency organic solar cell enabled by the strong intramolecular electron push-pull effect of the nonfullerene acceptor. *Adv. Mater.* 30:1707170. doi: 10.1002/adma.201707170

Li, Y., Meng, H., Yan, D., Li, Y., Pang, B., Zhang, K., et al. (2018). Synthesis of B←N embedded indacenodithiophene chromophores and effects of bromine atoms on photophysical properties and energy levels. *Tetrahedron* 74, 4308–4314. doi: 10.1016/j.tet.2018.06.035

Lim, E., Peterson, K. A., Su, G. M., and Chabinyc, M. L. (2018). Thermoelectric properties of poly(3-hexylthiophene) (P3HT) doped with 2,3,5,6-tetrafluoro-7,7,8,8-tetracyanoquinodimethane (F4TCNQ) by vapor-phase infiltration. *Chem. Mater.* 30, 998–1010. doi: 10.1021/acs.chemmater.7b04849

Lin, S., Fan, Z., Xinyang, W., Feng, Q., Minzhao, X., Giulia, T., et al. (2015). Geometric and electronic structures of boron(III) -cored dyes tailored by incorporation of heteroatoms into ligands. *Chem. Asian J.* 10, 709–714. doi: 10.1002/asia.201403272

Liu, F., Ding, Z., Liu, J., and Wang, L. (2017). An organoboron compound with a wide absorption spectrum for solar cell applications. *Chem. Commun.* 53, 12213–12216. doi: 10.1039/C7CC07494H

Liu, K., Lalancette, R. A., and Jakle, F. (2017). B-N lewis pair functionalization of anthracene: structural dynamics, optoelectronic properties, and O_2 sensitization. *J. Am. Chem. Soc.* 139, 18170–18173. doi: 10.1021/jacs.7b11062

Liu, W., Tang, A., Chen, J., Wu, Y., Zhan, C., and Yao, J. (2014). Photocurrent enhancement of BODIPY-based solution-processed small-molecule solar cells by dimerization via the meso position. *ACS Appl. Mater. Interfaces* 6, 22496–22505. doi: 10.1021/am506585u

Liu, W., Yao, J., and Zhan, C. (2017). A novel BODIPY-based low-band-gap small-molecule acceptor for efficient non-fullerene polymer solar cells. *Chin. J. Chem.* 35, 1813–1823. doi: 10.1002/cjoc.201700542

Liu, Z., Ishibashi, J. S. A., Darrigan, C., Dargelos, A., Chrostowska, A., Li, B., et al. (2017). The least stable isomer of BN naphthalene: toward predictive trends for the optoelectronic properties of BN acenes. *J. Am. Chem. Soc.* 139, 6082–6085. doi: 10.1021/jacs.7b02661

Liu, Z., and Marder, T. B. (2008). B-N versus C-C: how similar are they? *Angew. Chem. Int. Ed. Engl.* 47, 242–244. doi: 10.1002/anie.200703535

Long, X., Ding, Z., Dou, C., Liu, J., and Wang, L. (2017a). A double B←N bridged bipyridine (BNBP)-based polymer electron acceptor: all-polymer solar cells with a high donor : acceptor blend ratio. *Mater. Chem. Front.* 1, 852–858. doi: 10.1039/C6QM00245E

Long, X., Ding, Z., Dou, C., Zhang, J., Liu, J., and Wang, L. (2016a). Polymer acceptor based on double B←N bridged bipyridine (BNBP) unit for high-efficiency all-polymer solar cells. *Adv. Mater.* 28, 6504–6508. doi: 10.1002/adma.201601205

Long, X., Dou, C., Liu, J., and Wang, L. (2017b). Fine-tuning LUMO energy levels of conjugated polymers containing a B←N Unit. *Macromolecules.* 50, 8521–8528. doi: 10.1021/acs.macromol.7b01986

Long, X., Wang, N., Ding, Z., Dou, C., Liu, J., and Wang, L. (2016b). Low-bandgap polymer electron acceptors based on double B←N bridged bipyridine (BNBP) and diketopyrrolopyrrole (DPP) units for all-polymer solar cells. *J. Mater. Chem. C* 4, 9961–9967. doi: 10.1039/C6TC03652J

Loudet, A., and Burgess, K. (2007). BODIPY dyes and their derivatives: syntheses and spectroscopic properties. *Chem. Rev.* 107, 4891–4932. doi: 10.1021/cr078381n

Lu, H., Mack, J., Yang, Y., and Shen, Z. (2014). Structural modification strategies for the rational design of red/NIR region BODIPYs. *Chem. Soc. Rev.* 43, 4778–4823. doi: 10.1039/C4CS00030G

Lu, J. S., Ko, S. B., Walters, N. R., Kang, Y., Sauriol, F., and Wang, S. (2013). Formation of azaborines by photoelimination of B,N-heterocyclic compounds. *Angew. Chem. Int. Ed. Engl.* 52, 4544–4548. doi: 10.1002/anie.201300873

Lu, L., Zheng, T., Wu, Q., Schneider, A. M., Zhao, D., and Yu, L. (2015). Recent advances in bulk heterojunction polymer solar cells. *Chem. Rev.* 115, 12666–12731. doi: 10.1021/acs.chemrev.5b00098

Maria, P. C., and Gal, J. F. (1985). A lewis basicity scale for nonprotogenic solvents: enthalpies of complex formation with boron trifluoride in dichloromethane. *J. Phys. Chem.* 89, 1296–1304. doi: 10.1021/j100253a048

Meng, L., You, J., Guo, T. F., and Yang, Y. (2016). Recent advances in the inverted planar structure of perovskite solar cells. *Acc. Chem. Res.* 49, 155–165. doi: 10.1021/acs.accounts.5b00404

Mueller, T., Gresser, R., Leo, K., and Riede, M. (2012). Organic solar cells based on a novel infrared absorbing aza-bodipy dye. *Sol. Energy Mater. Sol. Cells* 99, 176–181. doi: 10.1016/j.solmat.2011.11.006

Murto, P., Genene, Z., Benavides, C. M., Xu, X., Sharma, A., Pan, X., et al. (2018). High performance all-polymer photodetector comprising a donor-acceptor-acceptor structured indacenodithiophene-bithieno[3,4-c]pyrroletetrone copolymer. *ACS Macro Lett.* 7, 395–400. doi: 10.1021/acsmacrolett.8b00009

Nawn, G., Oakley, S. R., Majewski, M. B., McDonald, R., Patrick, B. O., and Hicks, R. G. (2013). Redox-active, near-infrared dyes based on 'Nindigo' (indigo-N,N′-diarylimine) boron chelate complexes. *Chem. Sci.* 4, 612–621. doi: 10.1039/C2SC21307A

Piers, W. E. (2005). The chemistry of perfluoroaryl boranes. *Cheminform* 36, 1–75. doi: 10.1002/chin.200518247

Poe, A. M., Della Pelle, A. M., Subrahmanyam, A. V., White, W., Wantz, G., and Thayumanavan, S. (2014). Small molecule BODIPY dyes as non-fullerene acceptors in bulk heterojunction organic photovoltaics. *Chem. Commun.* 50, 2913–2915. doi: 10.1039/C3CC49648A

Pritchard, R. H., and Kern, C. W. (1969). Bond moments in the two-carbon series ethane, ethylene, and acetylene. *J. Am. Chem. Soc.* 91, 1631–1635. doi: 10.1021/ja01035a008

Qiu, F., Zhang, F., Tang, R., Fu, Y., Wang, X., Han, S., et al. (2016). Triple boron-cored chromophores bearing discotic 5,11,17-triazatrinaphthylene-based ligands. *Org. Lett.* 18, 1398–1401. doi: 10.1021/acs.orglett.6b00335

Randell, N. M., Fransishyn, K. M., and Kelly, T. L. (2017). Lewis acid–base chemistry of 7-azaisoindigo-based organic semiconductors. *ACS Appl. Mater. Interfaces* 9, 24788–24796. doi: 10.1021/acsami.7b06335

Rousseau, T., Cravino, A., Bura, T., Ulrich, G., Ziessel, R., and Roncali, J. (2009a). BODIPY derivatives as donor materials for bulk heterojunction solar cells. *Chem. Commun.* 1673–1675. doi: 10.1039/B822770E

Rousseau, T., Cravino, A., Bura, T., Ulrich, G., Ziessel, R., and Roncali, J. (2009b). Multi-donor molecular bulk heterojunction solar cells: improving conversion efficiency by synergistic dye combinations. *J. Mater. Chem.* 19, 2298–2300. doi: 10.1039/B903189H

Rousseau, T., Cravino, A., Ripaud, E., Leriche, P., Rihn, S., De Nicola, A., et al. (2010). A tailored hybrid BODIPY-oligothiophene donor for molecular bulk heterojunction solar cells with improved performances. *Chem. Commun.* 46, 5082–5084. doi: 10.1039/c0cc01144d

Sariciftci, N. S., Smilowitz, L., Heeger, A. J., and Wudl, F. (1992). Photoinduced electron-transfer from a conducting polymer to buckminsterfullerene. *Science* 258, 1474–1476. doi: 10.1126/science.258.5087.1474

Sekiya, M., Umezawa, K., Sato, A., Citterio, D., and Suzuki, K. (2009). A novel luciferin-based bright chemiluminescent probe for the detection of reactive oxygen species. *Chem.Commun.* 3047–3049. doi: 10.1039/b903751a

Sharma, G. D., Siddiqui, S. A., Nikiforou, A., Zervaki, G. E., Georgakaki, I., Ladomenou, K., et al. (2015). A mono(carboxy)porphyrin-triazine-(bodipy)2 triad as a donor for bulk heterojunction organic solar cells. *J. Mater. Chem. C* 3, 6209–6217. doi: 10.1039/C5TC01076D

Shi, K., Zhang, F., Di, C. A., Yan, T. W., Zou, Y., Zhou, X., et al. (2015). Toward high performance n-type thermoelectric materials by rational modification of BDPPV backbones. *J. Am. Chem. Soc.* 137, 6979–6982. doi: 10.1021/jacs.5b00945

Stepien, M., Gonka, E., Zyła, M., and Sprutta, N. (2017). Heterocyclic nanographenes and other polycyclic heteroaromatic compounds: synthetic routes, properties, and applications. *Chem. Rev.* 117, 3479–3716. doi: 10.1021/acs.chemrev.6b00076

Stock, A., and Pohland, E. (1926). Borwasserstoffe, I. X.: B3N3H6. *Ber. Dtsch. Chem. Ges.* 59, 2215–2223.

Sun, L. (2015). Perovskite solar cells: crystal crosslinking. *Nat. Chem.* 7, 684–685. doi: 10.1038/nchem.2323

Tang, C. W. (1986). Two-layer organic photovoltaic cell. *Appl. Phys. Lett.* 48, 183–185. doi: 10.1063/1.96937

Vagedes, D., Erker, G., Kehr, G., Bergander, K., Kataeva, O., Frohlich, R., et al. (2003). Tris(pentafluorophenyl)borane adducts of substituted imidazoles: conformational features and chemical behavior upon deprotonation. *Dalton Trans.* 1337–1344. doi: 10.1039/b210030b

Wakamiya, A., Taniguchi, T., and Yamaguchi, S. (2006). Intramolecular B-N coordination as a scaffold for electron-transporting materials: synthesis and properties of boryl-substituted thienylthiazoles. *Angew. Chem. Int. Ed. Engl.* 45, 3170–3173. doi: 10.1002/anie.200504391

Wang, X., Lv, L., Li, L., Chen, Y., Zhang, K., Chen, H., et al. (2016a). High-performance all-polymer photoresponse devices based on acceptor-acceptor conjugated polymers. *Adv. Funct. Mater.* 26, 6306–6315. doi: 10.1002/adfm.201601745

Wang, X. Y., Lin, H. R., Lei, T., Yang, D. C., Zhuang, F. D., Wang, J. Y., et al. (2013). Azaborine compounds for organic field-effect transistors: efficient synthesis, remarkable stability, and BN dipole interactions. *Angew. Chem. Int. Ed.* 52, 3117–3120. doi: 10.1002/anie.201209706

Wang, X. Y., Wang, J. Y., and Pei, J. (2015a). BN heterosuperbenzenes: synthesis and properties. *Chem. Eur. J.* 21, 3528–3539. doi: 10.1002/chem.201405627

Wang, X.-Y., Zhuang, F.-D., Wang, J.-Y., and Pei, J. (2015b). Incorporation of polycyclic azaborine compounds into polythiophene-type conjugated polymers for organic field-effect transistors. *Chem. Commun.* 51, 17532–17535. doi: 10.1039/C5CC06927K

Wang, X. Y., Zhuang, F. D., Wang, R. B., Wang, X. C., Cao, X. Y., Wang, J. Y., et al. (2014). A straightforward strategy toward large BN-embedded pi-systems: synthesis, structure, and optoelectronic properties of extended BN heterosuperbenzenes. *J. Am. Chem. Soc.* 136, 3764–3767. doi: 10.1021/ja500117z

Wang, X.-Y., Zhuang, F.-D., Wang, X.-C., Cao, X.-Y., Wang, J.-Y., and Pei, J. (2015c). Synthesis, structure and properties of C3-symmetric heterosuperbenzene with three BN units. *Chem. Commun.* 51, 4368–4371. doi: 10.1039/c4cc10105g

Wang, X., Zhang, F., Liu, J., Tang, R., Fu, Y., Wu, D., et al. (2013). Ladder-type BN-embedded heteroacenes with blue emission. *Org. Lett.* 15, 5714–5717. doi: 10.1021/ol402745r

Wang, X., Zhang, F., Schellhammer, K. S., Machata, P., Ortmann, F., Cuniberti, G., et al. (2016b). Synthesis of NBN-type zigzag-edged polycyclic aromatic hydrocarbons: 1,9-diaza-9a-boraphenalene as a structural motif. *J. Am. Chem. Soc.* 138, 11606–11615. doi: 10.1021/jacs.6b04445

Welch, G. C., and Bazan, G. C. (2011). Lewis acid adducts of narrow band gap conjugated polymers. *J. Am. Chem. Soc.* 133, 4632–4644. doi: 10.1021/ja110968m

Welch, G. C., Coffin, R., Peet, J., and Bazan, G. C. (2009). Band gap control in conjugated oligomers via lewisacids. *J. Am. Chem. Soc.* 131, 10802–10803. doi: 10.1021/ja902789w

Wong, B. Y., Wong, H. L., Wong, Y. C., Chan, M. Y., and Yam, V. W. (2016). Air-stable spirofluorene-containing ladder-type Bis(alkynyl)borane compounds with readily tunable full color emission properties. *Chem. Eur. J.* 22, 15095–15106. doi: 10.1002/chem.201602829

Wong, H.-L., Wong, W.-T., and Yam, V. W.-W. (2012). Photochromic thienylpyridine–bis(alkynyl)borane complexes: toward readily tunable fluorescence dyes and photoswitchable materials. *Org. Lett.* 14, 1862–1865. doi: 10.1021/ol3004595

Yang, D. T., Mellerup, S. K., Peng, J. B., Wang, X., Li, Q. S., and Wang, S. (2016). Substituent directed phototransformations of BN-heterocycles: elimination vs isomerization via selective B-C bond cleavage. *J. Am. Chem. Soc.* 138, 11513–11516. doi: 10.1021/jacs.6b07899

Yang, D. T., Mellerup, S. K., Wang, X., Lu, J. S., and Wang, S. (2015). Reversible 1,1-hydroboration: boryl insertion into a C-N bond and competitive elimination of HBR2 or R-H. *Angew. Chem. Int. Ed.* 54, 5498–5501. doi: 10.1002/anie.201500487

Yang, D.-T., Shi, Y., Peng, T., and Wang, S. (2017). BN-heterocycles bearing two BN units: influence of the linker and the location of BN units on electronic properties and photoreactivity. *Organometallics* 36, 2654–2660. doi: 10.1021/acs.organomet.7b00261

Yusuf, M., Liu, K., Guo, F., Lalancette, R. A., and Jakle, F. (2016). Luminescent organoboron ladder compounds via directed electrophilic aromatic C-H borylation. *Dalton Trans.* 45, 4580–4587. doi: 10.1039/C5DT05077D

Zalar, P., Henson, Z. B., Welch, G. C., Bazan, G. C., and Nguyen, T. Q. (2012). Color tuning in polymer light-emitting diodes with Lewis acids. *Angew. Chem. Int. Ed.* 51, 7495–7498. doi: 10.1002/anie.201202570

Zhan, C., and Yao, J. (2016). More than conformational "Twisting" or "Coplanarity": molecular strategies for designing high-efficiency nonfullerene organic solar cells. *Chem. Mater.* 28, 1948–1964. doi: 10.1021/acs.chemmater.5b04339

Zhang, Z., Ding, Z., Dou, C., Liu, J., and Wang, L. (2015). Development of a donor polymer using a B←N unit for suitable LUMO/HOMO energy levels and improved photovoltaic performance. *Polym. Chem.* 6, 8029–8035. doi: 10.1039/C5PY01389E

Zhang, Z., Ding, Z., Long, X., Dou, C., Liu, J., and Wang, L. (2017). Organic solar cells based on a polymer acceptor and a small molecule donor with a high open-circuit voltage. *J. Mater.Chem. C* 5, 6812–6819. doi: 10.1039/C7TC01996C

Zhang, Z. G., Yang, Y., Yao, J., Xue, L., Chen, S., Li, X., et al. (2017). Constructing a strongly absorbing low-bandgap polymer acceptor for high-performance all-polymer solar cells. *Angew. Chem. Int. Ed.* 56, 13503–13507. doi: 10.1002/anie.201707678

Zhao, R., Bi, Z., Dou, C., Ma, W., Han, Y., Liu, J., et al. (2017a). Polymer electron acceptors with conjugated side chains for improved photovoltaic performance. *Macromolecules* 50, 3171–3178. doi: 10.1021/acs.macromol.7b00386

Zhao, R., Dou, C., Xie, Z., Liu, J., and Wang, L. (2016). Polymer acceptor based on B←N units with enhanced electron mobility for efficient all-polymer solar cells. *Angew. Chem. Int. Ed.* 55, 5313–5317. doi: 10.1002/anie.201601305

Zhao, R., Min, Y., Dou, C., Liu, J., and Wang, L. (2017b). A new electron-rich unit for polymer electron acceptors: 4,4-difluoro-4H-cyclopenta[2,1-b:3,4-b′]dithiophene. *Chem. Eur. J.* 23, 9486–9490. doi: 10.1002/chem.201702303.

Zhao, Z., Chang, Z., He, B., Chen, B., Deng, C., Lu, P., et al. (2013). Aggregation-induced emission and efficient solid-state fluorescence from tetraphenylethene-based N,C-chelate four-coordinate organoborons. *Chem. Eur. J.* 19, 11512–11517. doi: 10.1002/chem.201301815

Zhong, Z., Wang, X.-Y., Zhuang, F.-D., Ai, N., Wang, J., Wang, J.-Y., et al. (2016). Curved BN-embedded nanographene for application in organic solar cells. *J. Mater. Chem. A* 4, 15420–15425. doi: 10.1039/C6TA06523F

Zhou, J., Tang, R., Wang, X., Zhang, W., Zhuang, X., and Zhang, F. (2016). BN-heteroacene-cored luminogens with dual channel detection for fluoride anions. *J. Mater. Chem. C* 4, 1159–1164. doi: 10.1039/C5TC04139B

Zhu, C., Guo, Z. H., Mu, A. U., Liu, Y., Wheeler, S. E., and Fang, L. (2016). Low band gap coplanar conjugated molecules featuring dynamic intramolecular lewis acid-basecoordination. *J. Org. Chem.* 81, 4347–4352. doi: 10.1021/acs.joc.6b00238

Conflict of Interest Statement: The authors declare that the research was conducted in the absence of any commercial or financial relationships that could be construed as a potential conflict of interest.

frontiers in Chemistry

ORIGINAL RESEARCH
published: 26 July 2018
doi: 10.3389/fchem.2018.00303

Efficient Non-fullerene Organic Solar Cells Enabled by Sequential Fluorination of Small-Molecule Electron Acceptors

Ruihao Xie, Lei Ying, Hailong Liao, Zhongxin Chen, Fei Huang* and Yong Cao*

State Key Laboratory of Luminescent Materials and Devices, Institute of Polymer Optoelectronic Materials and Devices, South China University of Technology, Guangzhou, China

Three small-molecule non-fullerene electron acceptors containing different numbers of fluorine atoms in their end groups were designed and synthesized. All three acceptors were found to exhibit relatively narrow band gaps with absorption profiles extending into the near-infrared region. The fluorinated analog exhibited enhanced light-harvesting capabilities, which led to improved short-circuit current densities. Moreover, fluorination improved the blend film morphology and led to desirable phase separation that facilitated exciton dissociation and charge transport. As a result of these advantages, organic solar cells based on the non-fullerene acceptors exhibited clearly improved short-circuit current densities and power conversion efficiencies compared with the device based on the non-fluorinated acceptor. These results suggest that fluorination can be an effective approach for the molecular design of non-fullerene acceptors with near-infrared absorption for organic solar cells.

Keywords: organic solar cells, non-fullerene, small molecule electron acceptors, fluorination, near-infrared absorption

OPEN ACCESS

Edited by:
Chuanlang Zhan,
Institute of Chemistry (CAS), China

Reviewed by:
In Hwan Jung,
Kookmin University, South Korea
Chuluo Yang,
Wuhan University, China

****Correspondence:***
Lei Ying
msleiying@scut.edu.cn
Fei Huang
msfhuang@scut.edu.cn

Specialty section:
This article was submitted to Organic Chemistry, a section of the journal Frontiers in Chemistry

Received: *13 May 2018*
Accepted: *04 July 2018*
Published: *26 July 2018*

Citation:
Xie R, Ying L, Liao H, Chen Z, Huang F and Cao Y (2018) Efficient Non-fullerene Organic Solar Cells Enabled by Sequential Fluorination of Small-Molecule Electron Acceptors. Front. Chem. 6:303. doi: 10.3389/fchem.2018.00303

INTRODUCTION

Bulk heterojunction organic solar cells (OSCs) are a promising technology for solar energy collection and have attracted much interest owing to their unique advantages for the fabrication of lightweight and flexible devices (Li et al., 2016b, 2017a, 2018a,b; Zhao et al., 2016; Zhang et al., 2017b, 2018; Cheng et al., 2018; Hou et al., 2018; Zhang, 2018). Over the past several years, although fullerene derivatives have been extensively used as electron-acceptor materials for OSCs, their various intrinsic limitations, such as poor absorption in the visible-light region, a difficult-to-adjust molecular structure and morphological instability, have impeded the further development of OSCs (He and Li, 2011). To circumvent this constraint, considerable progress has been achieved recently due to the development of non-fullerene acceptors (NFAs) for high-performance non-fullerene OSCs, as NFAs have high absorption coefficients and suitable frontier molecular orbital energy levels that facilitate both the harvesting of solar photons and charge separation (Bin et al., 2016; Du et al., 2017; Fan et al., 2017; Kan et al., 2017b; Xu et al., 2017; Cui et al., 2018; Gao et al., 2018; Luo et al., 2018; Zhang et al., 2018; Zhu et al., 2018).

Typically, to achieve high photovoltaic performance of OSCs based on novel NFAs, much effort has been devoted to the use of advanced device structures and sophisticated film-processing

techniques (Li et al., 2016a, 2017c; Meng et al., 2016; Bao et al., 2017; Kan et al., 2017a; Zhang et al., 2017a; Wu et al., 2018). It is well established that the light-harvesting capability of OSCs plays a critical role in their photovoltaic performance, as their power conversion efficiencies can be enhanced by expanding the absorption spectrum of the photoactive layer in the near-infrared (NIR) region. Therefore, NFAs with absorption spectra extending into the NIR region have been explored, especially with respect to their potential applications in semi-transparent organic photovoltaics and tandem OSCs (Li et al., 2017b; Yao et al., 2017, 2018). Furthermore, the fluorination of conjugated semiconductors has proved to be an effective synthetic strategy for developing efficient photoactive-layer materials for OSC applications. The introduction of fluorine atoms into small molecules or polymers can not only optimize their optical and electrical properties but also promote intermolecular interactions via the formation of non-covalent F···S and F···H bonds, resulting in enhanced charge mobility (Wang et al., 2013; Jo et al., 2015; Dai et al., 2017). More importantly, fluorination can be used to fine-tune the hydrophobicity and polarity of conjugated semiconductors, thus permitting control over the interfacial interactions in blend films (Pagliaro and Ciriminna, 2005). The combination of these advantages leads to improved film morphology with appropriate phase domains and larger interfacial areas, which facilitates exciton dissociation and charge transport and thus enhances the overall photovoltaic performance of OSCs.

In this work, we designed and synthesized a series of non-fullerene electron acceptors (BT-IC, BT-F, and BT-2F) with different numbers of fluorine atoms on their end groups. The strong intramolecular charge transfer between the electron-rich cores and electron-deficient end groups of these acceptors was found to result in intense absorption in the NIR region. The sequential fluorination of the end groups not only enhanced the light-harvesting capabilities of BT-F and BT-2F but also simultaneously increased their electron mobilities, leading to a higher short-circuit current density (J_{SC}). More importantly, the fluorinated acceptors exhibited more favorable phase separation after blending with a medium-band-gap conjugated polymer. The combination of these phenomena led to improved short-circuit current density and thus enhanced the photovoltaic performance of the resulting devices.

EXPERIMENTAL

Instrumentation

^{1}H and ^{13}C NMR were characterized with Bruker-500 spectrometer in deuterated chloroform solution at 298 K. Chemical shifts were recorded as δ values (ppm) with the internal standard of tetramethylsilane (TMS). Mass spectra were collected on a MALDI Micro MX mass spectrometer, or an API QSTAR XL System. Number-average (M_n) and polydispersity index (PDI) were determined on a Polymer Laboratories PL-GPC 220 using 1,2,4-trichlorobenzene as eluent at 150°C vs. polystyrene standards. Thermogravimetric analyses (TGA) were performed on a Netzsch TG 209 under nitrogen at a heating rate of 10°C min^{-1}. Differential scanning calorimetry (DSC) was performed on a Netzsch DSC 204 under nitrogen flow at heating/cooling rates of 10/10°C min^{-1}. The absorption coefficients of films are calculated by dividing the film thickness with the maximum absorption peak. The thin films with thickness of about 100 nm (measured by the profilometer) is spin-coated from chloroform solution on the top of quartz. Then the absorption spectra of these films were recorded by a HP 8453 spectrophotometer. Cyclic voltammetry (CV) was performed on a CHI600D electrochemical workstation with a glassy carbon working electrode and a Pt wire counter electrode at a scanning rate of 50 mV s^{-1} against an Ag/Ag$^+$ reference electrode with a nitrogen saturated anhydrous solution of tetra-*n*-butylammonium hexafluorophosphate in acetonitrile (0.1 mol L^{-1}). Atomic force microscopy (AFM) measurements were carried out using a Digital Instrumental DI Multimode Nanoscope III in a taping mode. TEM images were characterized with a JEM-2100F instrument.

Photovoltaic Device Fabrication

The non-fullerene organic solar cells with a conventional device structure of ITO/PEDOT:PSS/active layer/PFN-Br/Ag were fabricated. Here PFN-Br represents poly[(9,9-bis(3′-((*N*,*N*-dimethyl)-*N*-ethylammonium)-propyl)-2,7-fluorene)-*alt*-2,7-(9,9-dioctylfluorene)] dibromide, which functioned as the cathode interlayer to facilitate electron extraction from the active layer. Before fabrication of the device, the indium tin oxide (ITO)-coated glass substrates were cleaned by ultrasonic treatment in deionized water, acetone, isopropyl alcohol, and dried in oven at 80°C for 12 h before used. After PEDOT:PSS (30 nm) layer was spin coated onto the substrate, and dried at 150°C for 15 min in air. Then, the ITO substrates were transferred into a nitrogen protected glovebox where the H_2O concentration is $\leq$ 0.5 ppm and O_2 concentration is $\leq$ 20 ppm. The thin film of active layer was spin-coated from a solution of PTZPF:non-fullerene acceptor blend in chlorobenzene. A thin PFN-Br layer (5 nm) was then spin coated onto the active layer as the cathode interface layer. The substrates were then transferred to a vacuum thermal evaporator, followed by deposition of the Ag cathode at a pressure of 2×10^{-7} Torr through a shadow mask. Before the *J-V* test, a physical mask with an aperture with precise area of 0.04 cm^2 was used to define the device area. The *J-V* curves were measured on a computer-controlled Keithley 2,400 source meter under 1 sun, the AM 1.5 G spectra came from a class solar simulator (Enlitech, Taiwan), and the light intensity was 100 mWcm^{-2} as calibrated by a China General Certification Center-certified reference monocrystal silicon cell (Enlitech). The external quantum efficiency (EQE) spectra measurements were performed on a commercial QE measurement system (QE-R3011, Enlitech).

Materials

The monomers of thieno[3′,2′:4,5] cyclopenta[1,2-*b*] thieno[2″, 3″:3′,4′] cyclopenta[1′,2′:4,5] thieno[2,3-*f*][1] benzothiophene-2,8-dicarboxaldehyde, 5,11-bis[(2-ethylhexyl)oxy] -4,4,10,10-tetrakis(4-hexylphenyl)-4,10-dihydro **(1)** were synthesized according to the reported procedures (Li et al., 2017b). And the

donor polymer PTZPF was synthesized via Stille polymerization (Scheme S1, supporting information, SI, with molecular structure shown in **Figure 1A**). 2-(3-Oxo-2,3-dihydro-1*H*-inden-1-ylidene)malononitrile (**2**), a mixture of 2-(5-fluoro-3-oxo-2,3-dihydro-1*H*-inden-1-ylidene)malononitrile and 2-(6-fluoro-3-oxo-2,3-dihydro-1*H*-inden-1-ylidene)malononitrile (**3**) and 2-(5,6-difluoro-3-oxo-2,3-dihydro-1*H*-inden-1-ylidene) malononitrile (**4**) were obtained from commercial sources and used without further purification. The small-molecule acceptors were prepared as the following procedures as below.

Synthesis of BT-IC

2-(3-Oxo-2,3-dihydro-1*H*-inden-1-ylidene)malononitrile (**2**) (194.2 mg, 1.0 mmol) was added into the mixture of thieno[3′,2′:4,5] cyclopenta[1,2-*b*] thieno[2″,3″:3′,4′] cyclopenta[1′,2′:4,5] thieno[2,3-*f*][1] benzothiophene-2,8-dicarboxaldehyde, 5,11-bis[(2-ethylhexyl)oxy] -4,4,10,10-tetrakis(4-hexylphenyl)-4,10-dihydro (**1**) (133.2 mg, 0.1 mmol) in chloroform (50 mL) with pyridine (1 mL). The reactant was refluxed for 6 h under nitrogen atmosphere. After cooling to room temperature, the reactant was poured into methanol and the precipitate was filtered off. The crude product was purified by silica gel using a mixture of hexane/dichloromethane as the eluent to give a blue black powder (121.2 mg, 73%). ^{1}H NMR (400 MHz, $CDCl_3$, δ): 8.79 (s, 2H), 8.64 (m, 2H), 7.87 (m, 2H), 7.70 (m, 4H), 7.48 (s, 2H), 7.31 (m, 8H), 7.08 (m, 8H), 3.48 (t, 4H), 2.57 (t, 8H), 1.60-1.53 (m, 2H), 1.35-1.28 (m, 48H), 0.96 (t, 6H), 0.87 (m, 18H). ^{13}C NMR (100 MHz, $CDCl_3$, δ): 188.56, 164.46, 160.31, 157.20, 153.89, 146.22, 142.16, 142.14, 140.67, 139.93, 138.69, 138.45, 138.23, 136.81, 135.89, 135.01, 134.30, 128.51, 128.50, 128.31, 125.25, 123.61, 121.32, 114.81, 68.40, 63.94, 39.38, 35.56, 31.71, 31.26, 31.24, 29.54, 29.21, 28.77, 23.34, 22.68, 22.59, 14.21, 14.10, 10.78. MS (MALDI-TOF) calcd for $C_{110}H_{114}N_4O_4S_4$, 1684.386; found, 1683.622.

Synthesis of BT-F

A similar procedure was followed as that described for **BT-IC**, a mixture of 2-(5-fluoro-3-oxo-2,3-dihydro-1*H*-inden-1-ylidene) malononitrile and 2-(6-fluoro-3-oxo-2,3-dihydro-1*H*-inden-1-ylidene)malononitrile (**3**) (212.2 mg, 1.0 mmol) and thieno [3′,2′:4,5] cyclopenta[1,2-*b*] thieno[2″,3″:3′,4′] cyclopenta[1′,2′:4,5] thieno[2,3-*f*] [1]benzothiophene-2,8-dicarboxaldehyde, 5,11-bis[(2-ethylhexyl)oxy] -4,4,10,10-tetrakis(4-hexylphenyl)-4,10-dihydro (**1**) (133.2 mg, 0.1 mmol) were used. **BT-F** was obtained as a blue black solid (149.2 mg, 88.0 %). ^{1}H NMR (400 MHz, $CDCl_3$, δ): 8.79 (s, 2H), 8.68 (m, 0.5H), 8.36 (m, 1.5H),7.88 (m, 1.5H), 7.52 (m, 2.5H), 7.40 (m, 2H), 7.30 (m, 8H), 7.08 (m, 8H), 3.48 (m, 4H), 2.53 (m, 8H), 1.60-1.54 (m, 2H), 1.35-1.28 (m, 48H), 0.96 (t, 6H), 0.87 (m, 18H). ^{13}C NMR (100 MHz, $CDCl_3$, δ): 187.10, 167.69, 165.65, 165.19, 164.64, 164.61, 159.23, 158.89, 157.55, 157.50, 154.55, 154.39, 146.29, 142.28, 142.22, 142.19, 140.66, 140.62, 139.94, 139.88, 138.74, 138.69, 138.42, 138.29, 135.97, 135.79, 133.01, 128.50, 128.48, 128.39, 128.33, 127.76, 125.75, 125.67, 122.13, 121.67, 121.48, 121.15, 121.08, 114.81, 114.65, 114.50, 114.36, 112.89, 112.68, 110.75, 76.77, 69.09, 68.18, 63.95, 39.37, 35.55, 31.70, 31.25, 31.23, 29.56, 29.22, 28.78, 23.38, 22.71, 22.60, 14.22, 14.11, 10.80. MS (MALDI-TOF) calcd for $C_{110}H_{112}F_2N_4O_4S_4$, 1720.367; found, 1719.595.

Synthesis of BT-2F

A similar procedure was followed as that described for **BT-IC**, 2-(5,6-difluoro-3-oxo-2,3-dihydro-1*H*-inden-1-ylidene) malononitrile (**4**) (230.2 mg, 1.0 mmol) and thieno[3′,2′:4,5] cyclopenta[1,2-*b*] thieno[2″,3″:3′,4′] cyclopenta[1′,2′:4,5] thieno [2,3-*f*][1] benzothiophene-2,8-dicarboxaldehyde, 5,11-bis[(2-ethylhexyl)oxy] -4,4,10,10-tetrakis(4-hexylphenyl)-4,10-dihydro (**1**) (133.2 mg, 0.1 mmol) were used. **BT-2F** was obtained as a black solid (138.6 mg, 80.0 %). ^{1}H NMR (400 MHz, $CDCl_3$, δ): 8.78 (s, 2H), 8.52 (m, 2H), 7.64 (t, 2H), 7.50 (s, 2H), 7.31 (dd, 8H), 7.08 (d, 8H), 3.49 (t, 4H), 2.57 (t, 8H), 1.60-1.54 (m, 2H), 1.36-1.28 (m, 48H), 0.96 (t, 6H), 0.86 (m, 18H). ^{13}C NMR (100 MHz, $CDCl_3$, δ): 186.22, 164.72, 160.58, 158.12, 155.49, 146.38, 142.47, 142.28, 140.62, 139.08, 138.95, 138.75, 138.35, 136.53, 136.03, 135.70, 134.62, 128.56, 128.48, 128.36, 120.53, 115.13, 114.39, 112.46, 68.67, 63.78, 39.40, 35.56, 31.72, 31.26, 31.24, 29.54, 29.21, 28.77, 23.34, 22.68, 22.59, 14.21, 14.10, 10.76. MS (MALDI-TOF) calcd for $C_{110}H_{110}F_4N_4O_4S_4$, 1756.348; found, 1755.581.

RESULTS AND DISCUSSION

Synthesis and Characterization

The synthesis of the target compounds BT-IC, BT-F, and BT-2F is outlined in **Scheme 1**. These small-molecule acceptors were prepared via Knoevenagel condensation between thieno[3′,2′:4,5] cyclopenta[1,2-*b*] thieno[2″,3″:3′,4′] cyclopenta[1′,2′:4,5] thieno[2,3-*f*][1] benzothiophene-2,8-dicarboxaldehyde, 5,11-bis [(2-ethylhexyl)oxy] -4,4,10,10-tetrakis(4-hexylphenyl)-4,10-dihydro (**1**) and 2-(3-oxo-2,3-dihydro-1*H*-inden-1-ylidene) malononitrile (**2**) or its fluorinated derivatives at 60°C in the presence of a catalytic amount of pyridine. It is worth noting that the monofluorinated compound **3** consisted of two regioisomers, namely, 2-(5-fluoro-3-oxo-2,3-dihydro-1*H*-inden-1-ylidene)malononitrile and 2-(6-fluoro-3-oxo-2,3-dihydro-1*H*-inden-1-ylidene)malononitrile. As these two isomers have very similar molecular structures and polarities, they could not be separated, and thus the resulting BT-F was obtained as a mixture of isomers. All three acceptors exhibited good solubility in typical organic solvents, such as chloroform, chlorobenzene and *ortho*-dichlorobenzene, at room temperature. The chemical structures of the three acceptors were confirmed by nuclear magnetic resonance spectroscopy and mass spectrometry (Figures S7–S12).

The thermal properties of these resulting NFAs were evaluated by thermogravimetric analysis and differential scanning calorimetry (DSC) under a nitrogen atmosphere (Figures S1, S2,). All of these NFAs exhibited excellent thermal stabilities with onset decomposition temperatures (T_d) higher than 310°C. The DSC curves were obtained by heating from 30 to 250°C in the second heating/cooling cycle. It was found that BT-IC exhibited a melting peak at 127°C, whereas no phase-transition signals were observed during the DSC measurements of the other two materials.

Optical, Electrochemical, and Electron-Transport Properties

Figure 1B shows the UV–vis absorption spectra of thin films of the donor polymer and acceptor molecules. All three NFAs showed similar absorption profile cut-offs in the NIR region (up to 866 nm) in the solid state. Such absorption profiles are complementary with a medium band gap conjugated polymer, namely PTZPF, which has the absorption onset of 620 nm (**Figure 1D**). Note that the complementary absorption is beneficial for the harvesting of solar photons to achieve a high

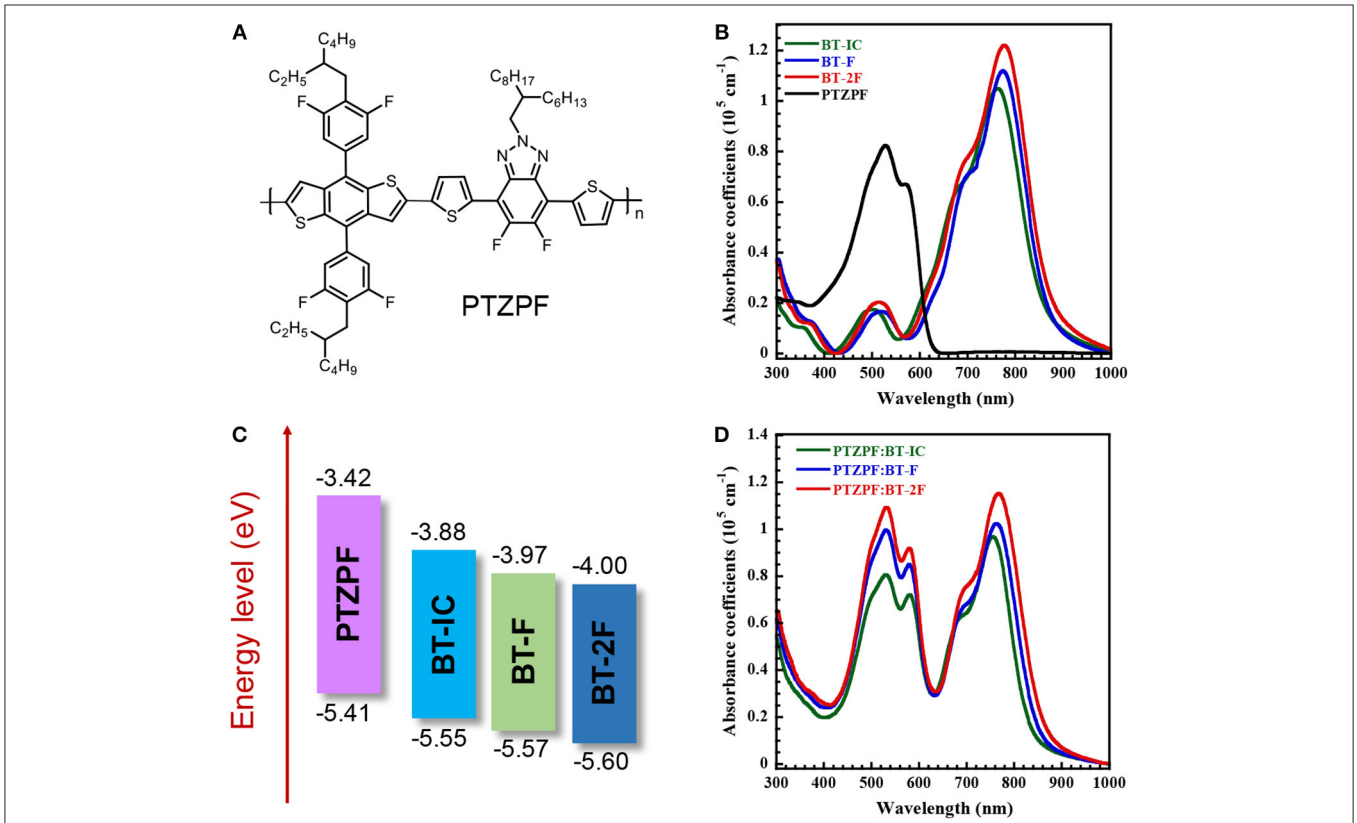

FIGURE 1 | (A) Chemical structure of PTZPF; **(B)** UV–vis absorption spectra and **(C)** energy level diagrams of BT-IC, BT-F, BT-2F, and PTZPF; **(D)** UV–vis spectra of PTZPF:NFA blend films.

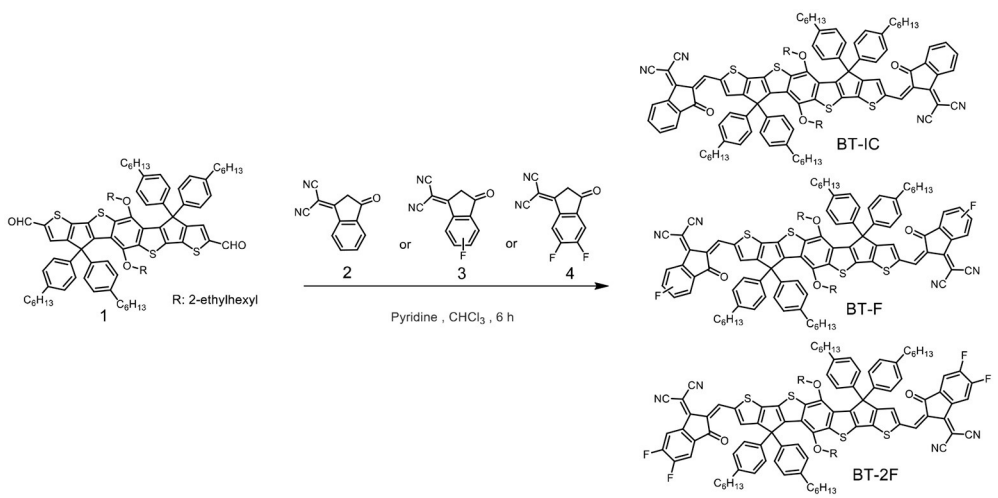

SCHEME 1 | Synthetic route of the small-molecule non-fullerene acceptors.

TABLE 1 | Optophysical and electrochemical properties of active layer materials.

Materials	λ_{abs} (nm) film	λ_{abs} (nm) onset	[a]E_g^{opt} (eV)	E_{ox} (V)	E_{red} (V)	[b]E_{HOMO} (eV)	[c]E_{LUMO} (eV)
BT-IC	760	866	1.43	1.05	−0.62	−5.55	−3.88
BT-F	774	872	1.42	1.07	−0.53	−5.57	−3.97
BT-2F	778	878	1.41	1.10	−0.50	−5.60	−4.00
PTZPF	528	620	2.00	0.91	−1.08	−5.41	−3.42

[a]*Calculated from the onset of UV-vis absorption as pristine thin films;* [b]$E_{HOMO} = -e\ (E_{ox} + 4.50)$ *(eV);* [c]$E_{LUMO} = -e\ (E_{red} + 4.50)$.

short-circuit current density. The fluorinated small molecules BT-F and BT-2F exhibited slightly red-shifted absorption edges compared with BT-IC. An optical band gap of 1.43 eV was obtained for BT-IC, which slightly decreased to 1.42 and 1.41 eV for BT-F and BT-2F, respectively. Importantly, the absorption coefficients were slightly enhanced from 1.05×10^5 cm^{-1} for BT-IC to 1.12×10^5 cm^{-1} and 1.22×10^5 cm^{-1} for BT-F and BT-2F, respectively (**Figure 1B**), indicating that the introduction of fluorine atoms into these acceptors enhanced their light-harvesting ability through improved intermolecular interactions (Yang et al., 2013; Wolf et al., 2015).

The electrochemical properties and energy levels of the polymer acceptors were investigated by cyclic voltammetry. Here we used the potential ferrocene/ferrocenium (Fc/Fc^+) redox couple as the standard. Under the current measurement conditions, the potential of Fc/Fc^+ couple was measured as 0.30 V regarding to the reference electrode. Assuming that the Fc/Fc^+ redox couple has an absolute potential of −4.80 V to vacuum, the highest occupied molecular orbital energy levels (E_{HOMO}) is calculated as $E_{HOMO} = -e\ (E_{ox} + 4.80 - 0.30)$ (eV), and the lowest unoccupied molecular orbital energy levels (E_{LUMO}) is calculated as $E_{LUMO} = -e\ (E_{red} + 4.80 - 0.30)$ (eV). The energy level diagrams of all of the materials are depicted in **Figure 1C** and the corresponding electrochemical data are summarized in **Table 1**. The calculated E_{LUMO}/E_{HOMO} values of BT-IC, BT-F and BT-2F were −3.88/−5.55 eV, −3.97/−5.57 eV and −4.00/−5.60 eV, respectively. Both the E_{LUMO} and E_{HOMO} levels of these acceptor molecules gradually decreased with the increasing number of fluorine atoms, indicating that fluorination of the end groups of small-molecule NFAs can effectively decrease the E_{LUMO} and E_{HOMO} levels owing to the strongly electron-withdrawing characteristics of fluorine atoms (Dutta et al., 2014). The E_{LUMO} and E_{HOMO} levels of the polymer donor PTZPF were −3.42 and −5.41 eV, respectively, which ensures an adequate driving force for efficient exciton dissociation (Scharber et al., 2010). The charge carrier mobilities of the pure films of acceptors were measured by the space-charge-limited current (SCLC) method using the Mott–Gurney equation (Figure S5). The measurements are carried out by fabricating electron-only devices with architecture of ITO/Ag/active layer/Ag structure. The pure film based on BT-2F exhibited the electron mobility (μ_e) of 9.64×10^{-5} $cm^2\ V^{-1}\ s^{-1}$, which is higher than those of BT-F ($\mu_e = 5.53 \times 10^{-5}$ $cm^2\ V^{-1}\ s^{-1}$) and BT-IC ($\mu_e = 2.28 \times 10^{-5}$ $cm^2\ V^{-1}\ s^{-1}$).

Photovoltaic Performances

To elucidate the effects of fluorination on the photovoltaic properties, OSC devices were fabricated using PTZPF as the electron-donor material and BT-IC, BT-F, or BT-2F as the electron-acceptor material. The devices were fabricated with the conventional configuration of ITO/PEDOT:PSS/active layer/PFN-Br/Ag, and the device performances were measured under simulated AM 1.5 G illumination at 100 mW cm^{-2}. Poly[(9,9-bis(3'-((*N*,*N*-dimethyl)-*N*-ethylammonium)propyl)-2,7-fluorene)-*alt*-2,7-(9,9-dioctylfluorene)] dibromide (PFN-Br) was used as the cathode interfacial layer to facilitate charge carrier collection (Zhang et al., 2017c). The initial optimisation of device performance was carried out by screening the weight ratios of the donor:acceptor (D:A) blend, film thickness of the photoactive layers and the effects of additives to the processing solvents (Figure S6 and Table S1). All of the photoactive layers of the devices were processed under the optimized conditions, which consisted of a D:A weight ratio of 1:1, spin casting of the films from chlorobenzene containing 0.5 v/v% of 1-chloronaphthalene (CN) as additive, and annealing of the fabricated films at 120°C for 10 min. The current density–voltage (J–V) curves are presented in **Figure 2A** and the corresponding data are summarized in **Table 2**.

Interestingly, the photovoltaic parameters of the resulting devices were strongly dependent on the number of fluorine substituents. The device based on BT-IC as the acceptor exhibited a moderate power conversion efficiency (PCE) of 5.63%, with an open-circuit voltage (V_{OC}) of 0.93 V, a J_{SC} of 12.27 mA cm^{-2} and a fill factor (FF) of 49.0%. In contrast, the devices based on the fluorinated acceptors BT-F and BT-2F exhibited clearly enhanced PCE values of 7.27% ($V_{OC} = 0.88$ V, $J_{SC} = 16.64$ mA cm^{-2} and FF = 49.0%) and 8.54% ($V_{OC} = 0.84$ V, $J_{SC} = 19.29$ mA cm^{-2} and FF = 53.0%), respectively. It should be noted that despite the decrease in the V_{OC} of the resulting devices upon the incorporation of fluorine substituents into the acceptors, which is consistent with the down-shifted E_{LUMO} levels observed for BT-F and BT-2F (Brabec et al., 2010; Kang et al., 2012), the J_{SC} values were dramatically enhanced. The combination of these effects led to the clearly enhanced PCE values of the devices based on the fluorinated acceptors.

To investigate the obvious enhancement of J_{SC}, we analyzed the absorption of PTZPF:BT-IC, PTZPF:BT-F and PTZPF:BT-2F blend films (**Figure 1D**). Similar to the absorption of neat films of BT-IC, BT-F, or BT-2F, the absorption coefficients of the PTZPF:BT-F and PTZPF:BT-2F blend films were both slightly

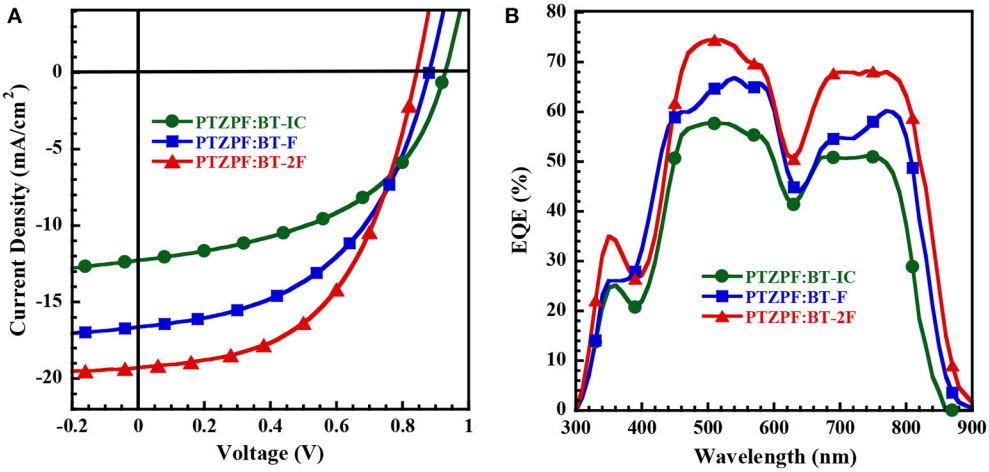

FIGURE 2 | (A) *J–V* curves and **(B)** EQE spectra of OSC devices measured under AM 1.5 G illumination at 100 mW cm^{-2}.

TABLE 2 | Photovoltaic parameters of OSCs measured under AM1.5 Illumination at 100 mW cm^{-2}.

Active layer[a]	V_{OC} (V)	J_{SC}[b] (mA cm^{-2})	$J_{SC,\ EQE}$[c] (mA cm^{-2})	FF (%)	PCE (%)
PTZPF:BT-IC	0.93	12.27	12.23	49.0	5.63 (5.45)[d]
PTZPF:BT-F	0.88	16.64	16.36	49.0	7.27 (7.00)
PTZPF:BT-2F	0.84	19.29	18.88	53.0	8.54 (8.50)

[a]*All of the blend films are processed by CB with 0.5 vol % CN and treated with 120°C for 10 min;* [b]*Obtained from J–V measurements;* [c]*Obtained from the integration of EQE spectra;* [d]*Average values across more than 6 devices. Device structure: ITO/PEDOT:PSS/active layer/PFN-Br/Ag.*

higher than that of the PTZPF:BT-IC blend film, which can be correlated to the improved J_{SC} of the devices based on fluorinated acceptors. Furthermore, to confirm the accuracy of the observed J_{SC}, we measured the external quantum efficiencies (EQEs) of the devices. It should be noted that the calculated J_{SC} values from the EQE spectra (**Figure 2B**) matched well with the J_{SC} values obtained from the *J–V* curves. The device based on BT-2F exhibited a stronger photocurrent response from 400 to 870 nm, with a maximum EQE of 75%, which was higher than those observed for the devices based on BT-F and BT-IC (**Figure 2B**).

Charge Generation, Transport, and Recombination

To study the charge generation process in the resulting bulk-heterojunction films, we measured the photoluminescence (PL) spectra of the neat and D:A blend films. The peak emission of the pure PTZPF film was located at 640 nm upon excitation at 500 nm, whereas the acceptor molecules BT-IC, BT-F, and BT-2F exhibited similar emission peaks at ∼845 nm upon excitation at 720 nm. As shown in **Figure 3A**, the strong emission peak of BT-IC was clearly observed in the PTZPF:BT-IC blend film, indicating the low charge separation efficiency of the device based on BT-IC. In contrast, the PL emission of the neat films was effectively quenched in the PTZPF:BT-F and PTZPF:BT-2F blend films, indicating that exciton dissociation and charge transfer were remarkably enhanced by the introduction of fluorine atoms into the acceptor moiety. A similar phenomenon can be observed in **Figure 3B**, where the PL of BT-2F was quenched by 92.7% in the blend film, which was more pronounced than the quenching observed for the blend films based on BT-F (90.9%) or BT-IT (86.4%).

The J_{SC} and V_{OC} values of the devices were measured as a function of the light intensity (P_{light}) to elucidate the charge recombination dynamics in the photoactive layer, as shown in **Figures 3C,D**, respectively. For organic solar cells, the power-law dependence of J_{SC} on the illumination intensity can generally be expressed as $J_{SC} \propto (P_{light})^S$, where S is the exponential factor, which is close to unity when the bimolecular recombination in the device is weak (Kyaw et al., 2013; Lu et al., 2015). The extracted values of S were 1.058, 1.060 and 1.043 for the devices based on BT-IC, BT-F, and BT-2F, respectively, all of which were close to unity, indicating the weak bimolecular recombination in these devices (Yang et al., 2016). Based on the V_{OC}-P_{light} plot, V_{OC} was plotted against the natural logarithm of P_{light} and the slope of nkT/q was calculated, where an n value of unity implies predominantly bimolecular recombination and an enhanced dependence of V_{OC} on P_{light} ($2kT/q$) indicates trap-assisted monomolecular recombination (Gasparini et al., 2016). The calculated slopes were 1.32, 1.23, and 1.21 kT/q for the devices based on BT-IC, BT-F and BT-2F, respectively. The smaller slope value for BT-2F than the others suggests less trap-assisted recombination, thus resulting in a higher FF value.

Film Morphology

Tapping-mode atomic force microscopy (AFM) and transmission electron microscopy (TEM) measurements were performed to determine the influence of fluorination on the film morphology. **Figures 4a–c** shows topographical AFM images of active layers of the different NFAs. The PTZPF:BT-IC blend film contained large granular aggregates across the entire film with

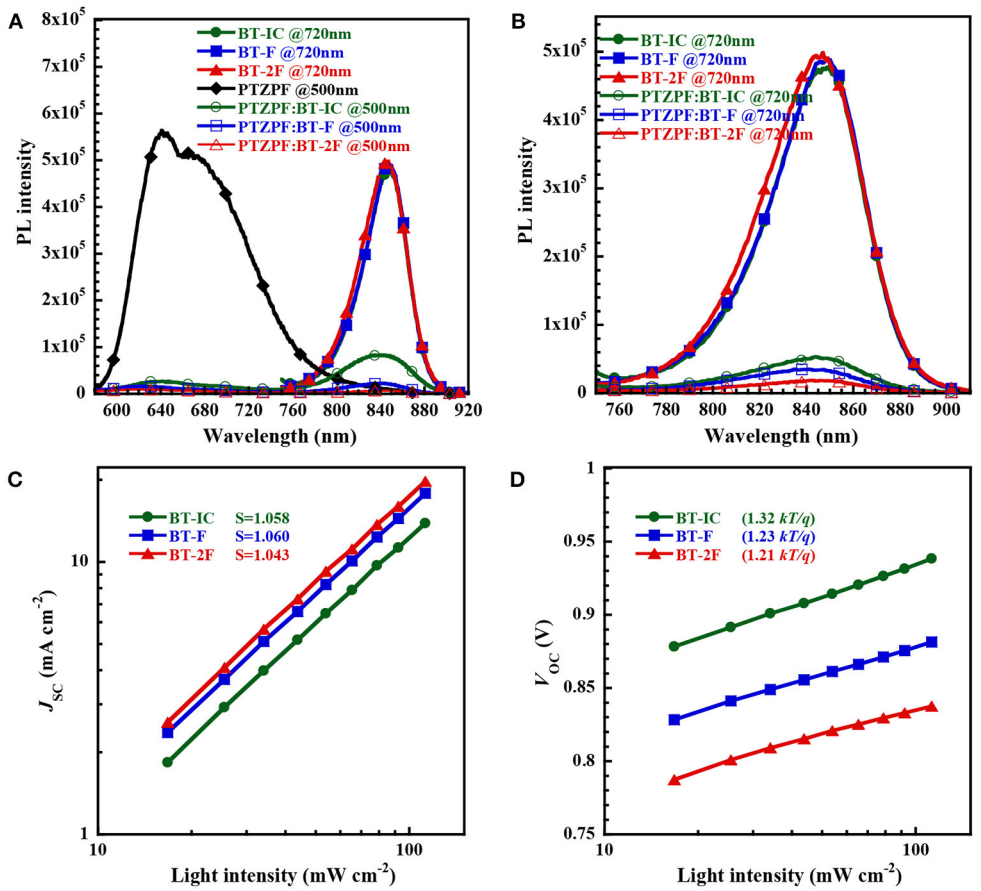

FIGURE 3 | (A,B) Photoluminescence spectra of pristine donor films (excited at 500 nm), pristine acceptor films (excited at 720 nm) and corresponding blend films (excited at both 500 and 720 nm) with a film thickness of about 100 nm; **(C,D)** plots of (c) J_{SC} and (d) V_{OC} vs. light intensity for devices based on PTZPF:NFA blend films.

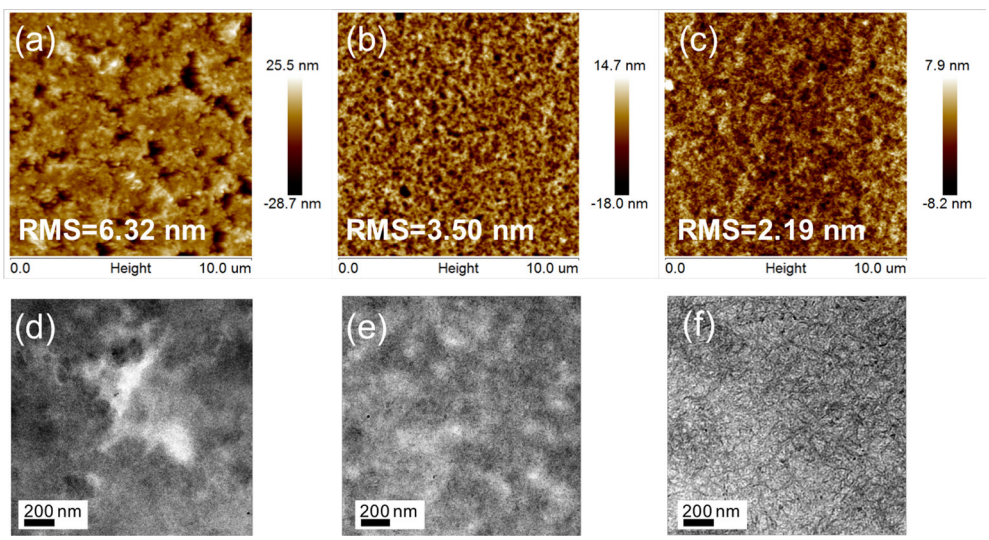

FIGURE 4 | AFM height images (10 μm × 10 μm) of **(a)** PTZPF:BT-IC, **(b)** PTZPF:BT-F, and **(c)** PTZPF:BT-2F; TEM images of **(d)** PTZPF:BT-IC, **(e)** PTZPF:BT-F, and **(f)** PTZPF:BT-2F.

a root-mean-square (RMS) roughness of 6.32 nm (**Figure 4a**), whereas the blend films gradually became smoother as the number of fluorine atoms increased, with RMS roughness values of 3.50 nm and 2.19 nm for BT-F and BT-2F, respectively, suggesting that the incorporation of fluorine atoms led to a smoother film morphology. The phase separation of the blend films with different electron acceptors was also readily apparent from the TEM images. **Figure 4d** shows that the PTZPF:BT-IC blend film exhibited large-scale phase-separation features across the entire film, which is unfavorable for charge transfer at the donor–acceptor interface. Interestingly, the degree of phase separation of the blend films gradually decreased as the number of fluorine atoms increased. Consequently, the PTZPF:BT-2F blend film exhibited a smoother surface morphology with favorable phase separation (**Figure 4f**), which induced desirable exciton dissociation and thus simultaneously enhanced the J_{SC} and FF values.

CONCLUSIONS

In summary, three NIR-absorbing electron acceptors containing different numbers of fluorine atoms were designed and synthesized. The results revealed that the fluorinated acceptors outperformed their non-fluorinated counterpart BT-IC. Sequentially increasing the number of fluorine atoms on the end groups of the acceptor molecules led to a dramatic improvement in the J_{SC} of the resulting photovoltaic devices. Non-fullerene OSCs based on the fluorinated acceptor BT-2F exhibited an improved PCE of 8.54% with a high J_{SC} of 19.29 mA cm^{-2}, regarding to the device based on BT-IC (PCE = 5.63%, J_{SC} = 12.27 mA cm^{-2}) that does not contain fluorine atom. The improved photovoltaic performances of devices based on fluorinated acceptors can be correlated to the broad absorption profile extending into the NIR region, favorable film morphology and efficient charge transfer. These results demonstrate that fluorination can be an effective technique in the design of efficient electron-acceptor materials.

AUTHOR CONTRIBUTIONS

RX, LY and FH conceived the ideas and coordinated the work. RX and LY designed the donor polymer and the acceptor molecules. RX synthesized the polymer PTZPF and conducted the DSC, TGA, UV-vis, PL and cyclic voltammetric measurements. HL performed the device fabrication, the light intensity-dependent *J-V* characterization, and analyzed the data. ZC synthesized the acceptor molecules of BT-IC, BT-F, and BT-2F. RX and HL conducted the AFM and TEM measurements. RX, LY, FH, and YC contributed to manuscript preparation. All authors commented on the manuscript and approved for submission.

FUNDING

This work was financially supported by the Ministry of Science and Technology (No. 2014CB643501), the National Natural Science Foundation of China (No. 91633301, 21490573, 51673069), the Natural Science Fund of Guangdong (No. 2017A030306011 and 2015A030313229), and the Science and Technology Program of Guangzhou, China (No. 201710010021, 201707020019 and 2017A050503002).

SUPPLEMENTARY MATERIAL

The Supplementary Material for this article can be found online at: https://www.frontiersin.org/articles/10.3389/fchem.2018.00303/full#supplementary-material

REFERENCES

Bao, X., Zhang, Y., Wang, J., Zhu, D., Yang, C., Li, Y., et al. (2017). High extinction coefficient thieno[3,4-b]thiophene-based copolymer for efficient fullerene-free solar cells with large current density. *Chem. Mater.* 29, 6766–6771. doi: 10.1021/acs.chemmater.7b01650

Bin, H., Gao, L., Zhang, Z. G., Yang, Y., Zhang, Y., Zhang, C., et al. (2016). 11.4% Efficiency non-fullerene polymer solar cells with trialkylsilyl substituted 2D-conjugated polymer as donor. *Nat. Commun.* 7:13651. doi: 10.1038/ncomms13651

Brabec, C. J., Cravino, A., Meissner, D., Sariciftci, N. S., Fromherz, T., Rispens, M. T., et al. (2010). Origin of the open circuit voltage of plastic solar cells. *Adv. Funct. Mater.* 11, 374–380. doi: 10.1002/1616-3028(200110)11:5<374::AID-ADFM374>3.0.CO;2-W

Cheng, P., Li, G., Zhan, X., and Yang, Y. (2018). Next-generation organic photovoltaics based on non-fullerene acceptors. *Nat. Photon.* 12, 131–142. doi: 10.1038/s41566-018-0104-9

Cui, Y., Yao, H. F., Yang, C. Y., Zhang, S. Q., and Hou, J. H. (2018). Organic solar cells with an efficiency approaching 15%. *Acta Polym. Sin.* 2, 223–230. doi: 10.11777/j.issn1000-3304.2018.17297

Dai, S., Zhao, F., Zhang, Q., Lau, T. K., Li, T., Liu, K., et al. (2017). Fused nonacyclic electron acceptors for efficient polymer solar cells. *J. Am. Chem. Soc.* 139, 1336–1343. doi: 10.1021/jacs.6b12755

Du, Z., Bao, X., Li, Y., Liu, D., Wang, J., Yang, C., et al. (2017). Balancing high open circuit voltage over 1.0 V and high short circuit current in benzodithiophene-based polymer solar cells with low energy loss: a synergistic effect of fluorination and alkylthiolation. *Adv. Energy Mater.* 8:1701471. doi: 10.1002/aenm.201701471

Dutta, G. K., Kim, T., Choi, H., Lee, J., Dong, S. K., Jin, Y. K., et al. (2014). Synthesis of fluorinated analogues of a practical polymer TQ for improved open-circuit voltages in polymer solar cells. *Polym. Chem.* 5, 2540–2547. doi: 10.1039/c3py01542d

Fan, B., Zhang, K., Jiang, X. F., Ying, L., Huang, F., and Cao, Y. (2017). High-Performance nonfullerene polymer solar cells based on imide-functionalized wide-bandgap polymers. *Adv. Mater. Weinheim.* 29:1606396. doi: 10.1002/adma.201606396

Gao, W., Zhang, M., Liu, T., Ming, R., An, Q., Wu, K., et al. (2018). Asymmetrical ladder-type donor-induced polar small molecule acceptor to promote fill factors approaching 77% for high-performance nonfullerene polymer solar cells. *Adv. Mater. Weinheim.* 30:1800052. doi: 10.1002/adma.201800052

Gasparini, N., Jiao, X., Heumueller, T., Baran, D., Matt, G. J., Fladischer, S., et al. (2016). Designing ternary blend bulk heterojunction solar cells with reduced carrier recombination and a fill factor of 77%. *Nat. Energy* 1:16118. doi: 10.1038/nenergy.2016.118

He, Y., and Li, Y. (2011). Fullerene derivative acceptors for high performance polymer solar cells. *Phys. Chem. Chem. Phys.* 13, 1970–1983. doi: 10.1039/C0CP01178A

Hou, J., Inganäs, O., Friend, R. H., and Gao, F. (2018). Organic solar cells based on non-fullerene acceptors. *Nat. Mater.* 17, 119–128. doi: 10.1038/nmat5063

Jo, J. W., Jung, J. W., Jung, E. H., Ahn, H. J., Shin, T., and Jo, W. H. (2015). Fluorination on both D and A Unit in D-A Type conjugated copolymer based on difluorobithiophene and benzothiadiazole for high efficient polymer solar cells. *Energy Environ. Sci.* 8, 2427–2434. doi: 10.1039/C5EE00855G

Kan, B., Feng, H., Wan, X., Liu, F., Ke, X., Wang, Y., et al. (2017a). Small-Molecule acceptor based on the heptacyclic benzodi(cyclopentadithiophene) unit for highly efficient nonfullerene organic solar cells. *J. Am. Chem. Soc.* 139, 4929–4934. doi: 10.1021/jacs.7b01170

Kan, B., Zhang, J., Liu, F., Wan, X., Li, C., Ke, X., et al. (2017b). Fine-tuning the energy levels of a nonfullerene small-molecule acceptor to achieve a high short-circuit current and a power conversion efficiency over 12% in organic solar cells. *Adv. Mater. Weinheim.* 30:1704904. doi: 10.1002/adma.201704904

Kang, H., Cho, C. H., Cho, H. H., Kang, T. E., Kim, H. J., Kim, K. H., et al. (2012). Controlling number of indene solubilizing groups in multiadduct fullerenes for tuning optoelectronic properties and open-circuit voltage in organic solar cells. *ACS Appl. Mater. Interfaces* 4, 110–116. doi: 10.1021/am201075y

Kyaw, A. K., Wang, D. H., Wynands, D., Zhang, J., Nguyen, T. Q., Bazan, G. C., et al. (2013). Improved light harvesting and improved efficiency by insertion of an optical spacer (ZnO) in solution-processed small-molecule solar cells. *Nano Lett.* 13, 3796–3801. doi: 10.1021/nl401758g

Li, K., Xie, R., Zhong, W., Lin, K., Lei, Y., Huang, F., et al. (2018a). 8.0% Efficient all-polymer solar cells based on novel starburst polymer acceptors. *Sci. China Chem.* 61, 576–583. doi: 10.1007/s11426-017-9197-0

Li, M., Gao, K., Wan, X., Zhang, Q., Kan, B., Xia, R., et al. (2017a). Solution-processed organic tandem solar cells with power conversion efficiencies >12%. *Nat. Photon.* 11, 85–90. doi: 10.1038/nphoton.2016.240

Li, Y., Qian, D., Zhong, L., Lin, J.-D., Jiang, Z.-Q., Zhang, Z.-G., et al. (2016a). A fused-ring based electron acceptor for efficient non-fullerene polymer solar cells with small HOMO offset. *Nano Energy* 27, 430–438. doi: 10.1016/j.nanoen.2016.07.019

Li, Y., Zhong, L., Gautam, B., Bin, H.-J., Lin, J.-D., Wu, F.-P., et al. (2017b). A near-infrared non-fullerene electron acceptor for high performance polymer solar cells. *Energy Environ. Sci.* 10, 1610–1620. doi: 10.1039/C7EE00844A

Li, Z., Fan, B., He, B., Ying, L., Zhong, W., Liu, F., et al. (2018b). Side-chain modification of polyethylene glycol on conjugated polymers for ternary blend all-polymer solar cells with efficiency up to 9.27%. *Sci. China Chem.* 61, 427–436. doi: 10.1007/s11426-017-9188-7

Li, Z., Xu, X., Zhang, W., Meng, X., Ma, W., Yartsev, A., et al. (2016b). High performance all-polymer solar cells by synergistic effects of fine-tuned crystallinity and solvent annealing. *J. Am. Chem. Soc.* 138, 10935–10944. doi: 10.1021/jacs.6b04822

Li, Z., Zhang, W., Xu, X., Genene, Z., Di Carlo Rasi, D., Mammo, W., et al. (2017c). High-performance and stable all-polymer solar cells using donor and acceptor polymers with complementary absorption. *Adv. Energy Mater.* 7:1602722. doi: 10.1002/aenm.201602722

Lu, L., Chen, W., Xu, T., and Yu, L. (2015). High-performance ternary blend polymer solar cells involving both energy transfer and hole relay processes. *Nat. Commun.* 6:7327. doi: 10.1038/ncomms8327

Luo, Z., Bin, H., Liu, T., Zhang, Z. G., Yang, Y., Zhong, C., et al. (2018). Fine-tuning of molecular packing and energy level through methyl substitution enabling excellent small molecule acceptors for nonfullerene polymer solar cells with efficiency up to 12.54%. *Adv. Mater. Weinheim.* 30:1706124. doi: 10.1002/adma.201706124

Meng, D., Fu, H., Xiao, C., Meng, X., Winands, T., Ma, W., et al. (2016). Three-bladed rylene propellers with three-dimensional network assembly for organic electronics. *J. Am. Chem. Soc.* 138, 10184–10190. doi: 10.1021/jacs.6b04368

Pagliaro, M., and Ciriminna, R. (2005). New fluorinated functional materials. *J. Mater. Chem.* 15, 4981–4991. doi: 10.1039/b507583c

Scharber, M. C., Mühlbacher, D., Koppe, M., Denk, P., Waldauf, C., Heeger, A. J., et al. (2010). Design rules for donors in bulk-heterojunction solar cells: towards 10% energy-conversion efficiency. *Adv. Mater.* 20, 579–583. doi: 10.1002/adma.200702337

Wang, N., Chen, Z., Wei, W., and Jiang, Z. (2013). Fluorinated benzothiadiazole-based conjugated polymers for high-performance polymer solar cells without any processing additives or post-treatments. *J. Am. Chem. Soc.* 135, 17060–17068. doi: 10.1021/ja409881g

Wolf, J., Cruciani, F., Labban, A. E., and Beaujuge, P. M. (2015). Wide band-gap 3,4-difluorothiophene-based polymer with 7% solar cell efficiency: an alternative to P3HT. *Chem. Mater.* 27, 4184–4187. doi: 10.1021/acs.chemmater.5b01520

Wu, W., Zhang, G., Xu, X., Wang, S., Li, Y., and Peng, Q. (2018). Wide bandgap molecular acceptors with a truxene core for efficient nonfullerene polymer solar cells: linkage position on molecular configuration and photovoltaic properties. *Adv. Funct. Mater.* 28:1707493. doi: 10.1002/adfm.201707493

Xu, S. J., Zhou, Z., Liu, W., Zhang, Z., Liu, F., Yan, H., et al. (2017). A twisted thieno[3,4-b]thiophene-based electron acceptor featuring a 14-pi-electron indenoindene core for high-performance organic photovoltaics. *Adv. Mater. Weinheim.* 29:1704510. doi: 10.1002/adma.201704510

Yang, L., Tumbleston, J. R., Zhou, H., Ade, H., and You, W. (2013). Disentangling the impact of side chains and fluorine substituents of conjugated donor polymers on the performance of photovoltaic blends. *Energy Environ. Sci.* 6, 316–326. doi: 10.1039/C2EE23235A

Yang, Y., Zhang, Z. G., Bin, H., Chen, S., Gao, L., Xue, L., et al. (2016). Side-chain isomerization on n-type organic semiconductor itic acceptor make 11.77% high efficiency polymer solar cells. *J. Am. Chem. Soc.* 138, 15011–15018. doi: 10.1021/jacs.6b09110

Yao, H., Cui, Y., Yu, R., Gao, B., Zhang, H., and Hou, J. (2017). Design, synthesis, and photovoltaic characterization of a small molecular acceptor with an ultra-narrow band gap. *Angew.Chem. Int. Educ.* 56, 3045–3049 doi: 10.1002/anie.201610944

Yao, Z., Liao, X., Ke, G., Lin, F., Xu, X., Shi, X., et al. (2018). Dithienopicenocarbazole-based acceptors for efficient organic solar cells with optoelectronic response over 1000 nm and an extremely low energy loss. *J. Am. Chem. Soc.* 140, 2054–2057. doi: 10.1021/jacs.7b13239

Zhang, J., Li, Y., Huang, J., Hu, H., Zhang, G., Ma, T., et al. (2017a). Ring-fusion of perylene diimide acceptor enabling efficient nonfullerene organic solar cells with a small voltage loss. *J. Am. Chem. Soc.* 139, 16092–16095. doi: 10.1021/jacs.7b09998

Zhang, J., Zhu, L., and Wei, Z. (2017b). Toward over 15% power conversion efficiency for organic solar cells: current status and perspectives. *Small Methods* 1:1700258. doi: 10.1002/smtd.201700258

Zhang, K., Huang, F., and Cao, Y. (2017c). Water/alcohol soluble conjugated polymer interlayer materials and their application in solution processed multilayer organic optoelectronic devices. *Acta Polym. Sin.* 9, 1400–1414. doi: 10.11777/j.issn1000-3304.2017.17075

Zhang, S., Qin, Y., Zhu, J., and Hou, J. (2018). Over 14% efficiency in polymer solar cells enabled by a chlorinated polymer donor. *Adv. Mater. Weinheim.* 30:1800868. doi: 10.1002/adma.201800868

Zhang, X. (2018). A tandem polymer solar cell based on non-fullerene-acceptors yields an efficiency approaching 15%. *Acta. Polym. Sin.* 2, 129–131. doi: 10.11777/j.issn1000-3304.2018.18019

Zhao, J., Li, Y., Yang, G., Jiang, K., Lin, H., Ade, H., et al. (2016). Efficient organic solar cells processed from hydrocarbon solvents. *Nat. Energy* 1:15027. doi: 10.1038/nenergy.2015.27

Zhu, J., Ke, Z., Zhang, Q., Wang, J., Dai, S., Wu, Y., et al. (2018). Naphthodithiophene-based nonfullerene acceptor for high-performance organic photovoltaics: effect of extended conjugation. *Adv. Mater. Weinheim.* 30:4312. doi: 10.1002/adma.201704713

Conflict of Interest Statement: The authors declare that the research was conducted in the absence of any commercial or financial relationships that could be construed as a potential conflict of interest.

frontiers in Chemistry

ORIGINAL RESEARCH
published: 02 July 2018
doi: 10.3389/fchem.2018.00260

Two Novel Small Molecule Donors and the Applications in Bulk-Heterojunction Solar Cells

Xin Qi[1], Yuan-Chih Lo[2], Yifan Zhao[1], Liyang Xuan[1], Hao-Chun Ting[2], Ken-Tsung Wong[2], Mostafizur Rahaman[3], Zhijian Chen[1,4], Lixin Xiao[1,4] and Bo Qu[1,4]**

[1] State Key Laboratory for Artificial Microstructures and Mesoscopic Physics, Department of Physics, Peking University, Beijing, China, [2] Department of Chemistry, National Taiwan University, Taipei, Taiwan, [3] Department of Chemistry, King Saud University, Riyadh, Saudi Arabia, [4] New Display Device and System Integration Collaborative Innovation Center of the West Coast of the Taiwan Strait, Fuzhou, China

Two novel small molecules **DTRDTQX** and **DTIDTQX**, based on ditolylaminothienyl group as donor moiety and quinoxaline as middle acceptor moiety with different terminal acceptor groups were synthesized and characterized in this work. In order to study the photovoltaic properties of **DTRDTQX** and **DTIDTQX**, bulk-heterojunction solar cells with the configuration of FTO/c-TiO_2/**DTRDTQX**(or **DTIDTQX**):C_{70}/MoO_3/Ag were fabricated, in which **DTRDTQX** and **DTIDTQX** acted as the donors and neat C_{70} as the acceptor. When the weight ratio of **DTRDTQX**:C_{70} reached 1:2 and the active layer was annealed at 100°C, the optimal device was realized with the power conversion efficiency (PCE) of 1.44%. As to **DTIDTQX**:C_{70}-based devices, the highest PCE of 1.70% was achieved with the optimal blend ratio (**DTIDTQX**:C_{70} = 1:2) and 100°C thermal annealing treatment. All the experimental data indicated that **DTRDTQX** and **DTIDTQX** could be employed as potential donor candidates for organic solar cell applications.

Keywords: bulk-heterojunction, small molecule, donor, solar cell, ditolylaminothienyl, quinoxaline

OPEN ACCESS

Edited by:
Chuanlang Zhan,
Institute of Chemistry (CAS), China

Reviewed by:
Xiaozhang Zhu,
Institute of Chemistry (CAS), China
Daniel Glossman-Mitnik,
Centro de Investigación en Materiales Avanzados, Mexico

****Correspondence:***
Ken-Tsung Wong
kenwong@ntu.edu.tw
Bo Qu
bqu@pku.edu.cn

Specialty section:
This article was submitted to Organic Chemistry, a section of the journal Frontiers in Chemistry

Received: *09 March 2018*
Accepted: *11 June 2018*
Published: *02 July 2018*

Citation:
Qi X, Lo Y-C, Zhao Y, Xuan L, Ting H-C, Wong K-T, Rahaman M, Chen Z, Xiao L and Qu B (2018) Two Novel Small Molecule Donors and the Applications in Bulk-Heterojunction Solar Cells. Front. Chem. 6:260. doi: 10.3389/fchem.2018.00260

INTRODUCTION

Recently, organic solar cells (OSCs) based on bulk-heterojunction structure have attracted much attention due to the distinctive characteristics of low cost, easy fabrication, flexibility and light weight, etc. (Gustafsson et al., 1992; Shaheen et al., 2001; Chen and Cao, 2009). Compared with polymers employed in solar cells, small molecule donors have the advantage of less batch-to-batch variation, well-defined molecular structure, easier purification, etc. (You et al., 2013; Chen et al., 2014, 2015; He et al., 2015; Zhou et al., 2015). Therefore, much work focused on small molecule donors and the photovoltaic performance of OSCs was improved accordingly (Sun et al., 2011; Liu et al., 2013; Love et al., 2013; Coughlin et al., 2014). In general, the active layers of the solar cells consisted of small molecule donors and fullerene/fullerene derivative acceptors (Chen et al., 2012; Huang et al., 2016). In order to optimize the photovoltaic characteristics of OSCs, narrow band-gap and deep highest occupied molecular orbital (HOMO) of small molecule donors should be considered, which resulted in broad absorption and high open-circuit voltage (V_{oc}) of devices. Then, various small molecules composed of electron rich moieties (donor, "D") and electron deficient moieties (acceptor, "A"), have been reported with the molecular configuration such as D-A (Roquet et al., 2006), A-D-A (Schulze et al., 2006), D-A-A (Lin et al., 2011) and D-A-D conjugated structures. In this regard, the HOMO and lowest unoccupied molecular orbital (LUMO) of the small molecules were effectively tuned, mainly due to the intramolecular charge transfer (ICT) between donors and acceptors (Zhang et al., 2011).

Herein, the photovoltaic properties of two novel small molecule donors (named **DTRDTQX** and **DTIDTQX**, **Figure 1**) based on D-A-A structure were studied in this work. **DTIDTQX** or **DTRDTQX** consisted of ditolylaminothienyl group as the donor moiety, quinoxaline as middle acceptor moiety with different terminal acceptor groups such as 1,3-indandione or 3-ethylrhodanine, respectively. To investigate the photovoltaic properties of the small molecules, bulk-heterojunction (BHJ) solar cells based on **DTRDTQX** or **DTIDTQX** as the donor together with C_{70} as the acceptor were fabricated and the optimal cells showed PCE of 1.44 and 1.70%, respectively.

EXPERIMENTAL

Materials and Characterization

All materials in this work were purchased commercially, except for the tailor made **DTRDTQX** and **DTIDTQX** donors. The commercial materials were used without further purification.

Scheme 1 depicts the synthesis of **DTIDTQX** and **DTRDTQX**. By following the protocols established by Krebs et al. (Jorgensen and Krebs, 2005) and Janssen et al. (Bijleveld et al., 2009), we could get 4-bromo-7-methyl-2,1,3-benzothiadiazole (**3**). Then the hetereocyclic **3** was converted to diamine intermediate **4** by treating Fe/HCl, which was then followed by condensation with glyoxal to afford 5-bromo-8-methylquinoxaline (**5**) without further purification. The 8-bromoquinoxaline-5-carbaldehyde (**7**) was synthesized by benzylic bromination with N-bromosuccinimide (NBS) initiated by azobisisobutyronitrile (AIBN) and followed by hydrolysis with $CaCO_3$ in H_2O/acetonitrile (Lin et al., 2011). Aldehyde **7** was reacted with N,N-di-p-tolyl-5-(tri-n-butylstannyl)-thiophen-2-amine (**8**) through Stille coupling reaction and gave key intermediate **9**. Finally, the condensation of **9** with 1,3-indandione and 3-ethylrhodanine via Knöevenagel reaction afforded **DTIDTQX** and **DTRDTQX**, respectively. The absorption spectra were measured with JASCO V-670 spectrophotometer. Themogravimetric analysis (TGA) was determined on a TA Instruments Model TGA Q500 V20.13 (build 39) with a heating rate of 10°C/min. Differential Scanning Calorimeter (DSC) was carried out at a heating rate of 10°C/min on a TA Instruments Model DSC Q100 V9.9 (build 303). The thickness of the films was evaluated using a surface profilometer. The electrochemical cyclic voltammetry (CV) was recorded by a CHI619B potentiostat with glassy carbon electrode, Pt wire and Ag/AgCl which were used as the working electrode, counter electrode, and reference electrode, respectively, further calibrated with the ferrocene/ferrocenium (Fc/Fc^+) redox couple. The oxidation waves were recorded in CH_2Cl_2 (for 1.0 mM) with 0.1 M tetrabutylammonium hexafluorophosphate ($^nBuNPF_6$) as supporting electrolyte, while reductive waves were recorded in THF (for 1.0 mM) with 0.1 M tetrabutylammonium perchlorate ($^nBuNClO_4$) as supporting electrolyte.

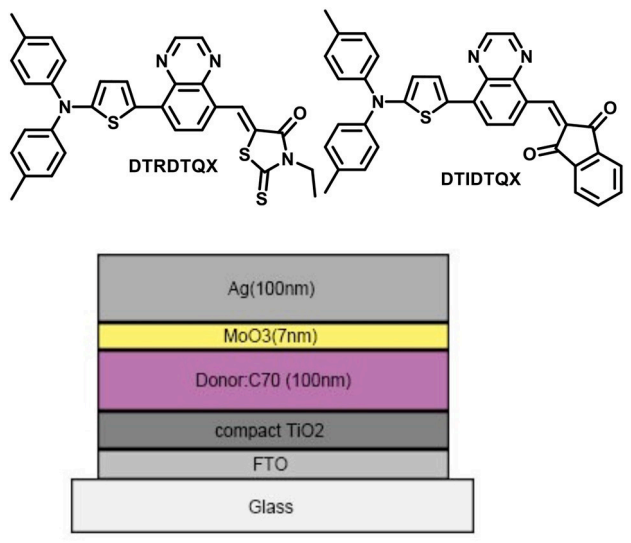

FIGURE 1 | Molecular structures of **DTRDTQX** and **DTIDTQX**, and the configuration of OSCs.

Solar Cell Fabrication and Characterization

In order to investigate the photovoltaic properties of **DTRDTQX** and **DTIDTQX**, the OSCs with the configuration of FTO/c-TiO_2/**DTRDTQX**(or **DTIDTQX**):C_{70}/MoO_3/Ag were fabricated as shown in **Figure 1**. The compact TiO_2 layer in OSCs acted as the electron transporting layer (Heo et al., 2015) and MoO_3 as the hole buffer layer. As to the photoactive layers, **DTRDTQX** and **DTIDTQX** served as the donors and C_{70} as the acceptor, respectively. The FTO cathode was pre-cleaned in an ultrasonic cleaner with deionized water, acetone and alcohol for 15 min respectively and then treated with oxygen plasma for 15 min. The TiO_2 films were fabricated according to the literatures (Kim et al., 2012; Zhang et al., 2016) and sintered at 500°C for 15 min in a muffle furnace. And then, the TiO_2 films were naturally cooled to room temperature. Blended solutions (total concentration: 20 mg/ml) of **DTRDTQX**(or **DTIDTQX**):C_{70} in *ortho*-dichlorobenzene (oDCB) were spin-coated (700 rpm, 18 s) onto FTO/TiO_2 substrates in a glove box and then thermal annealed at 100°C or 150°C. The effect of thermal annealing on the photovoltaic properties of the active layers was also studied in this work. Finally, 7 nm MoO_3 buffer layers and 100 nm Ag anodes were thermal evaporated successively below 10^{-6} Torr. The photovoltaic performance of the OSCs were evaluated by current density-bias voltage (J-V) measurement (using a Keithley 2400 source meter) under AM 1.5G simulated solar illumination (Newport model 94021A, 100 mW cm^{-2}).

RESULTS AND DISCUSSION

Thermal Property

Thermal properties of the two small molecules were investigated by TGA measurement as shown in **Figure 2** and the thermal decomposition temperatures (T_d, 5% weight loss) were evaluated to be 362°C and 312°C for DTRDTQX and DTIDTQX respectively, indicating the good thermal stability of the small molecules. According to the DSC plots shown in **Figure 3**, the melting temperatures (T_m) were evaluated to be 187.8°C and

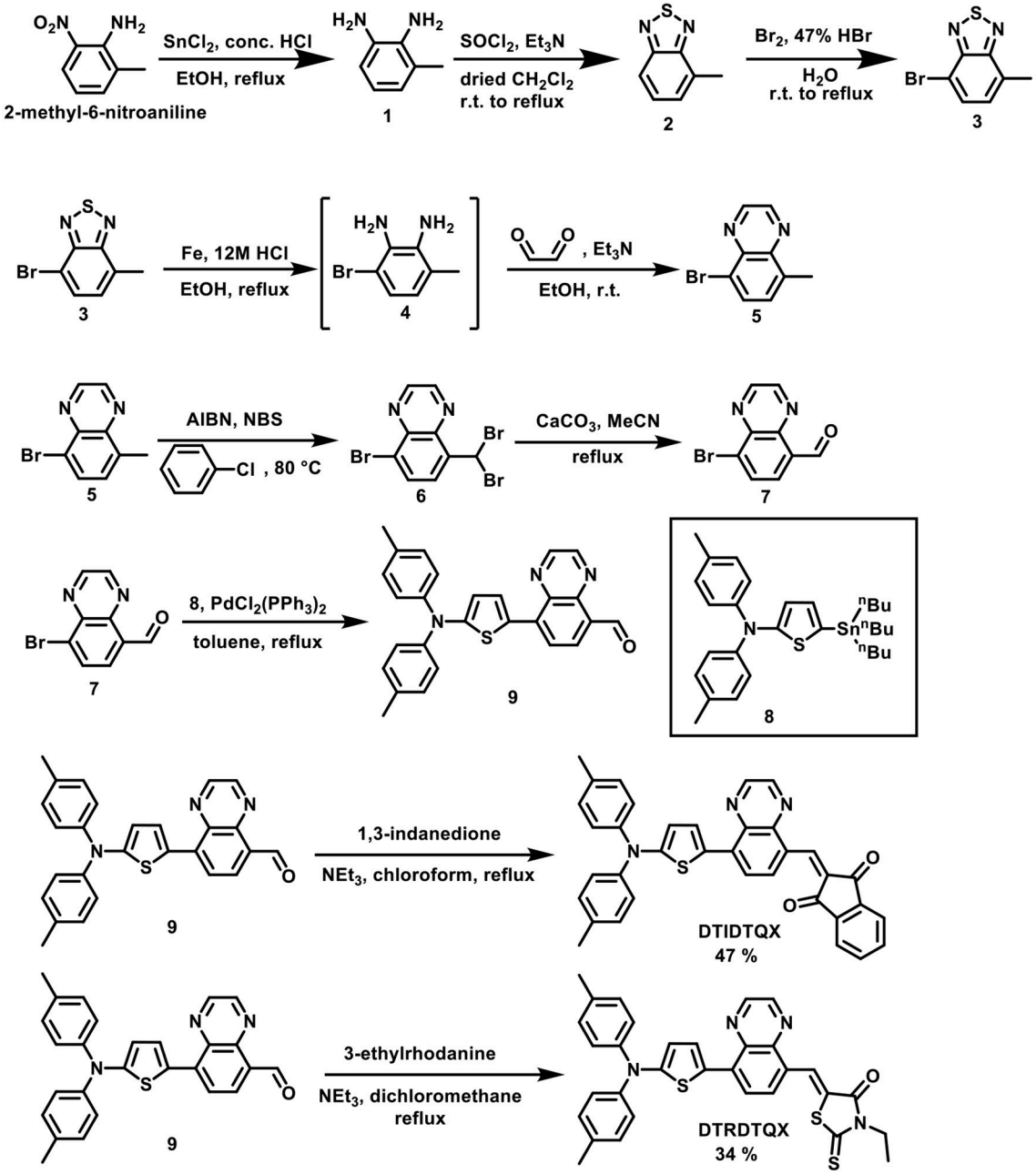

SCHEME 1 | Synthetic route of **DTIDTQX** and **DTRDTQX**.

263.3°C for DTRDTQX and DTIDTQX, respectively. Moreover, the glass transition temperatures (T_g) were measured to be 94.0°C and 149.7°C for DTRDTQX and DTIDTQX, respectively. Therefore, both DTRDTQX and DTIDTQX were stable donors for OSCs due to their decent thermal stability.

Absorption Properties

The UV-Vis absorption of **DTIDTQX** and **DTRDTQX** in CH_2Cl_2 were shown in **Figure 4** and the corresponding data were summarized in **Table 1**. The compounds showed broad band absorption from 480 to 750 nm with high extinction coefficient ($3.3–3.5 \times 10^4$ $M^{-1}cm^{-1}$) in the visible range (450–700 nm). **DTIDTQX** absorbed longer wavelength than **DTRDTQX** (631 vs. 588 nm), mainly due to the stronger electron withdrawing ability of 1,3-indanedione group than that of N-ethylrhodanine group.

Electrochemical Properties

The electrochemical properties of **DTRDTQX** and **DTIDTQX** were studied with cyclic voltammetry (CV) as shown in

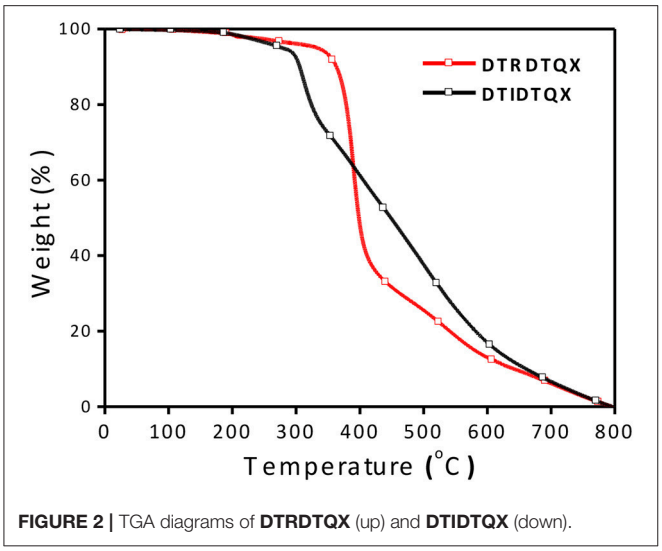

FIGURE 2 | TGA diagrams of **DTRDTQX** (up) and **DTIDTQX** (down).

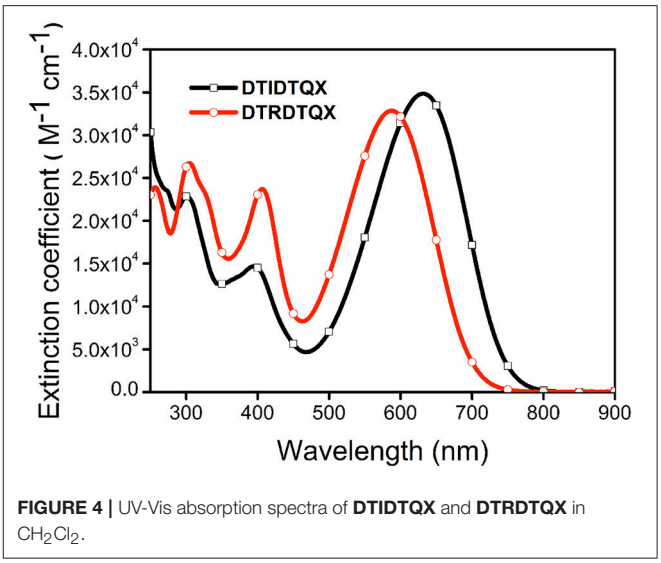

FIGURE 4 | UV-Vis absorption spectra of **DTIDTQX** and **DTRDTQX** in CH_2Cl_2.

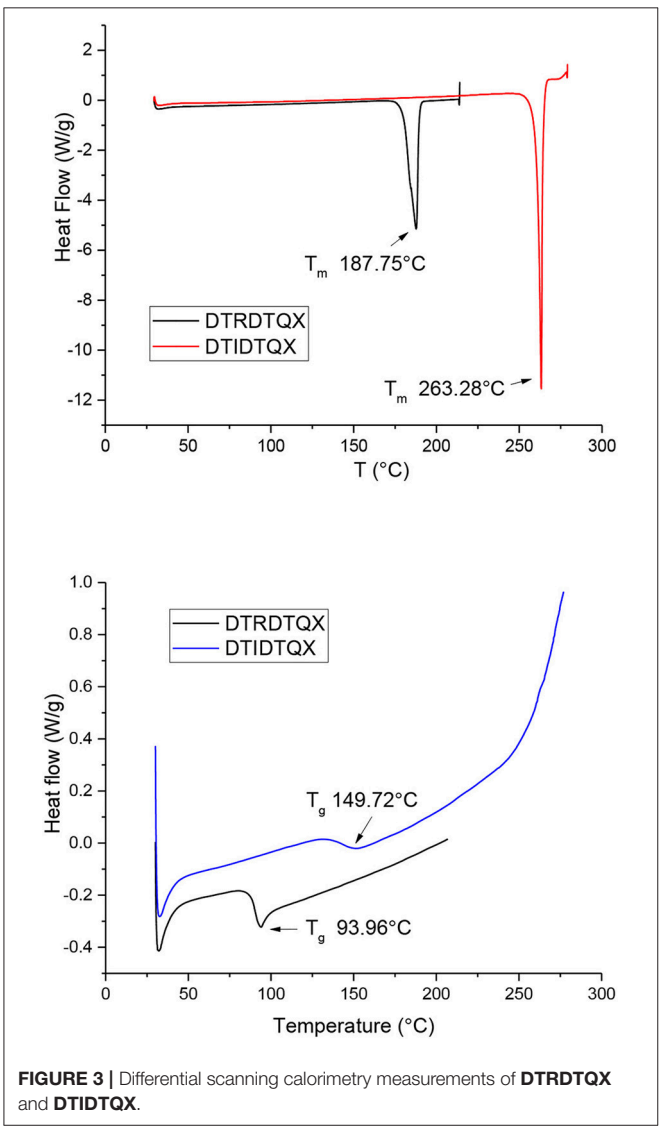

FIGURE 3 | Differential scanning calorimetry measurements of **DTRDTQX** and **DTIDTQX**.

Figure 5. In addition, the energy levels as well as the band gaps of **DTRDTQX** and **DTIDTQX** were summarized in **Table 1**. With the oxidation and reduction potentials recorded, the HOMO and LUMO levels of the two materials could be calculated (HOMO = −5.1 eV − E_{onset}^{ox}, LUMO = −5.1 eV − E_{onset}^{red}), which were −5.33 eV, −3.96 eV for **DTIDTQX** and −5.29 eV, −3.59 eV for **DTRDTQX** respectively. Interestingly, the HOMO and LUMO levels of **DTIDTQX** were both deeper than those of **DTRDTQX**. The phenomenon implied that the electron withdrawing ability of 1,3-indanedione group was stronger than that of N-ethylrhodanine group, which was consistent with the observation of UV-Vis absorption. The energy levels of the materials used in the OSCs were depicted in **Figure 6**. The large gap between the low-lying HOMO level (−5.33 eV) of **DTIDTQX** and LUMO (−4.20 eV) of C_{70} was evaluated to be 1.13 eV, which resulted in the large V_{oc} (0.71 V) of the optimal **DTIDTQX**-based OSCs in this work. Furthermore, the electrochemical energy band gap (ΔE^{CV}) of **DTIDTQX** was 0.33 eV lower than that of **DTRDTQX** and strong absorption of **DTIDTQX** active layer in red region could be realized, which was matched well with the UV-Vis absorption spectrum shown in **Figure 4**. Therefore, the light-harvesting capability as well as the photovoltaic performance of **DTIDTQX**-based devices could be superior to that of **DTRDTQX**-based counterparts, which will be discussed further in following.

Photovoltaic Properties

To study the photovoltaic properties of the small molecules, OSCs with the structure of FTO/c-TiO_2/donor:C_{70}/MoO_3/Ag were fabricated. The weight ratios of **DTRDTQX**:C_{70} and **DTIDTQX**:C_{70} varied from 1:1 to 1:3 and the corresponding J-V curves of the OSCs were shown in **Figures 7**, **8**. All the photovoltaic data of OSCs were summarized in **Table 2**. When the weight ratio of **DTRDTQX**:C_{70} reached 1:2 and the photoactive layer was thermal annealed at 100°C, the

TABLE 1 | Physical properties of **DTIDTQX** and **DTRDTQX**.

Compounds	λ_{abs} solution (nm)[a] (ε, $M^{-1}cm^{-1}$)	ΔE^{opt} sol. (eV)[a]	E^{ox}_{onset} (V)[b]	E^{red}_{onset} (V)[b]	ΔE^{CV} (eV)	HOMO (eV)[b]	LUMO (eV)[b]	Td (°C)
DTIDTQX	631 (34,900)	1.97	0.23	−1.14	1.37	−5.33	−3.96	312
DTRDTQX	588 (32,800)	2.11	0.19	−1.32	1.70	−5.29	−3.59	361

[a]*Measured in CH_2Cl_2 solution (10^{-5} M) and the value was estimated from the onset.* [b]*Estimated from the HOMO (−5.1 eV) (Cardona et al., 2011) of Fc^+/Fc as reference.* [c]*Temperature corresponding to 5% weight loss obtained from TGA analysis.*

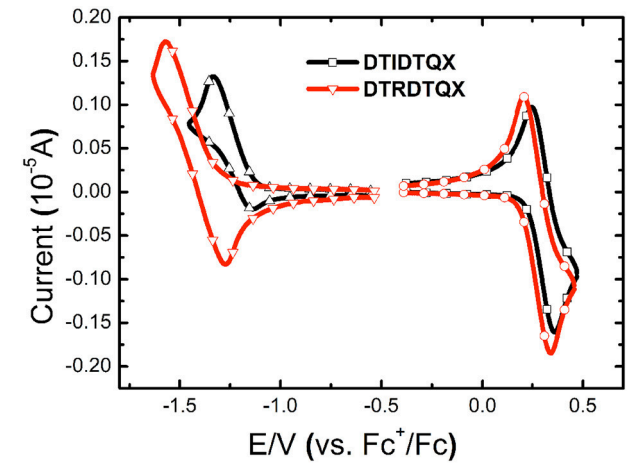

FIGURE 5 | Cyclic voltammograms of **DTIDTQX** and **DTRDTQX**.

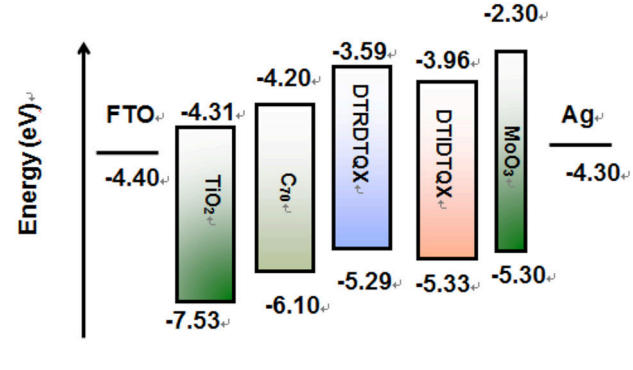

FIGURE 6 | The energy levels of the materials used in the OSCs (Lau et al., 2013; Zhang et al., 2013; Xiao et al., 2016).

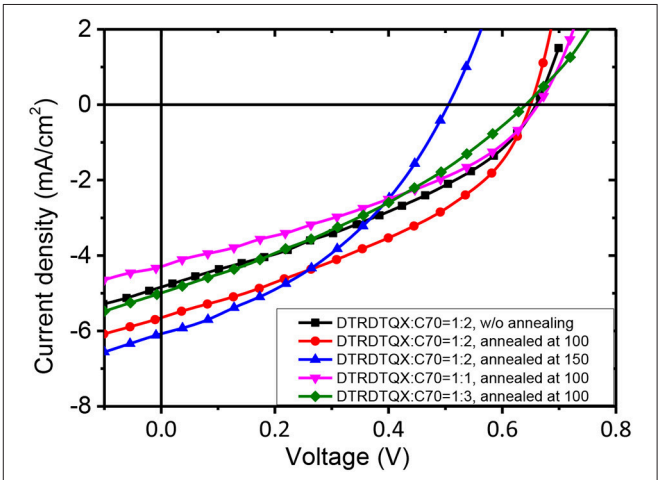

FIGURE 7 | The J-V curves of **DTRDTQX**-based devices.

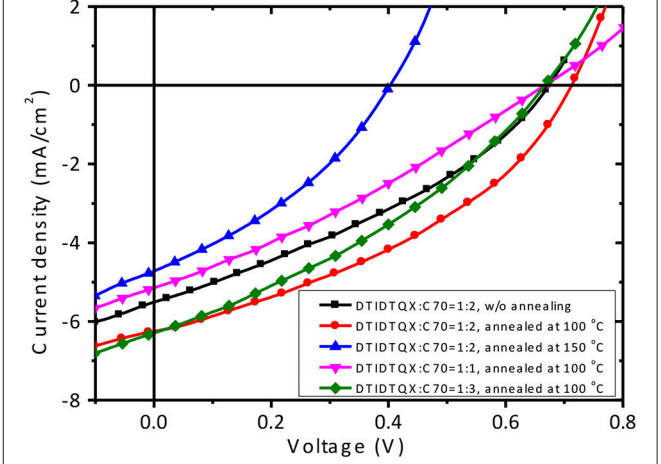

FIGURE 8 | The J-V curves of **DTIDTQX**-based devices.

best **DTRDTQX**-based OSC was realized with the short-circuit current density (J_{sc}) and PCE of 5.66 mA/cm^2 and 1.44%, respectively. The champion **DTRDTQX**-based OSC exhibited almost the same open-circuit voltage (V_{oc}) of ~0.65 V as other OSCs with different weight ratios (1:1 and 1:3) of **DTRDTQX**:C_{70}. Moreover, for the devices based on **DTRDTQX**:C_{70} with the weight ratios of 1:1 and 1:3, the decreased J_{sc} was mainly ascribed to the imbalanced electron and hole diffusion in the OSCs (Kim et al., 2009). The photovoltaic data in **Table 2** implied that the weight ratio (**DTRDTQX**:C_{70}) of 1:2 was advantageous to the photovoltaic performance of **DTRDTQX**:C_{70}-based OSCs. The photovoltaic properties of **DTRDTQX**:C_{70}(1:2)-based OSCs with 150°C thermal annealing and without thermal annealing were also studied and compared. The V_{oc} and PCE of the OSC with 150°C thermal annealing were decreased to 0.51 V and 1.19%, respectively. As to the OSC without thermal annealing, the PCE was decreased to 1.14% and V_{oc} (~0.66V) was almost unchanged compared with the champion **DTRDTQX**-based OSC. Therefore, 100°C

thermal annealing treatment was necessary for the reasonable photovoltaic performance of **DTRDTQX**:C_{70}(1:2)-based OSCs according to the experimental data.

As to **DTIDTQX**-based OSCs, the photovoltaic performance was modulated by the weight ratios of **DTIDTQX**:C_{70} from 1:1 to 1:3. When the blend ratio of **DTIDTQX**:C_{70} reached 1:2, the best **DTIDTQX**-based OSC was realized as shown in **Table 2**. The V_{oc}, J_{sc}, FF, and PCE of the champion device were 0.71V, 6.24 mA/cm^2, 0.38 and 1.70%, respectively. It was worthy to note that the V_{oc} of **DTIDTQX**:C_{70}(1:2)-OSC was 0.06 V higher than that of **DTRDTQX**:C_{70}(1:2)-OSC, mainly due to the low-lying HOMO (−5.33 eV) of **DTIDTQX** as shown in **Figure 6**. Moreover, the J_{sc} and PCE of **DTIDTQX**:C_{70}(1:2)-OSC were both higher than those of **DTRDTQX**:C_{70}(1:2)-OSC. Therefore, the photovoltaic properties of **DTIDTQX**-based devices were superior to those of **DTRDTQX**-based counterparts, which was mainly ascribed to the narrow band gap (∼1.37 eV) of **DTIDTQX** and the consequent effective absorption in solar spectrum. The photovoltaic performance of **DTIDTQX**:C_{70}(1:2)-OSC was deteriorated when the active layer was treated with 150°C thermal annealing as shown in **Table 2**. And when **DTIDTQX**:C_{70}(1:2)-OSC was fabricated without thermal annealing, the PCE decreased to 1.26%. Therefore, 100°C thermal annealing was favorable to **DTIDTQX**:C_{70}(1:2)-OSC and a decent PCE of 1.70% was obtained accordingly. However, the FF values of the OSCs were relatively low in this work and much work should be required to further increase FF as well as PCE of the OSCs, such as inserting buffer layers (Ji et al., 2016; Li et al., 2016; Mbuyise et al., 2016), introducing optical spacers (Ben Dkhil et al., 2014), employing solvent annealing (Sun et al., 2014; Li et al., 2015), chemical treatments (Bai et al., 2015), etc.

The morphology of **DTRDTQX**:C_{70}(1:2) and **DTIDTQX**:C_{70}(1:2) films was studied by atomic force microscopy (AFM) (Agilent Series 5500) as shown in **Figure 9**. The root-mean-square roughness (RMS) of **DTIDTQX**:C70

TABLE 2 | Photovoltaic data of the OSCs.

DTRDTQX: C_{70}	Thermal annealing	V_{oc} (V)	J_{sc} (mA/cm^2)	FF	PCE (%)
1:1	100°C	0.66	4.27	0.36	1.01
1:2	100°C	0.65	5.66	0.39	1.44
1:3	100°C	0.64	5.00	0.33	1.05
1:2	150°C	0.51	6.09	0.38	1.19
1:2	w/o	0.66	4.86	0.36	1.14
DTIDTQX: C_{70}					
1:1	100°C	0.67	5.13	0.30	1.02
1:2	100°C	0.71	6.24	0.38	1.70
1:3	100°C	0.67	6.31	0.34	1.43
1:2	150°C	0.40	4.71	0.35	0.66
1:2	w/o	0.67	5.51	0.34	1.26

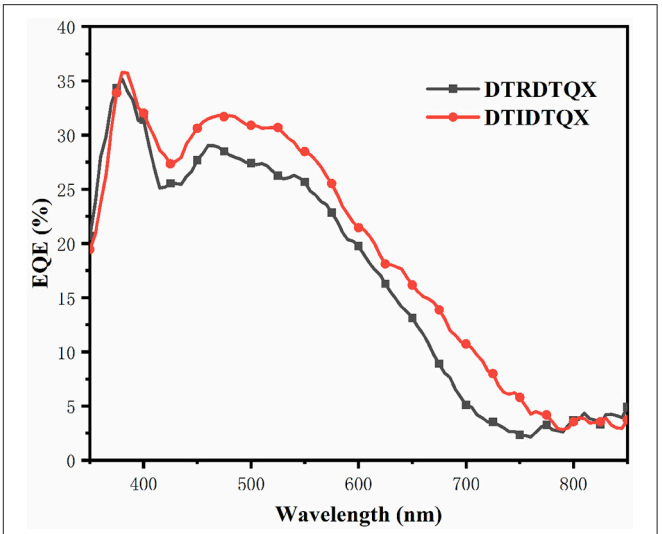

FIGURE 10 | The EQE spectra of **DTRDTQX** and **DTIDTQX**-based devices.

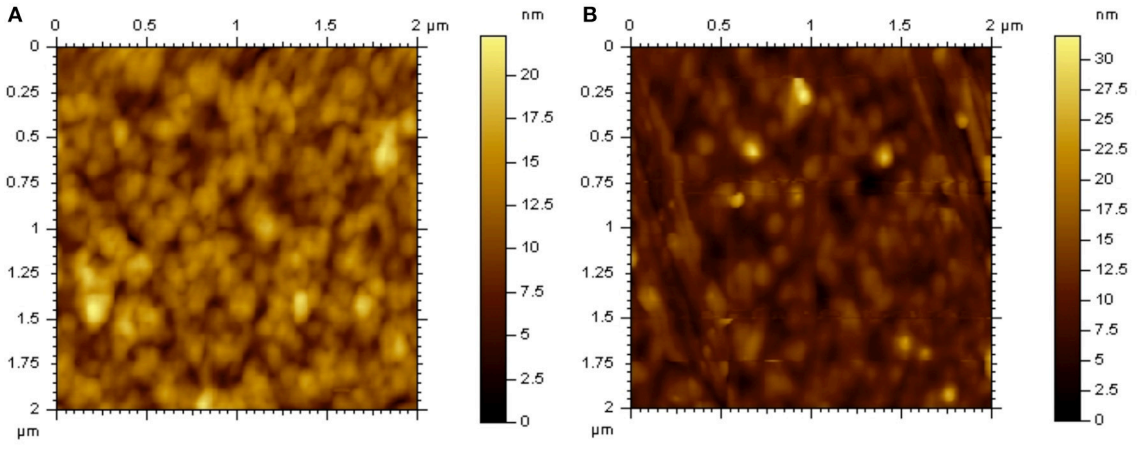

FIGURE 9 | AFM images of **(A) DTRDTQX**:C_{70}(1:2) and **(B) DTIDTQX**:C_{70}(1:2) films.

(1:2) film was 2.94 nm, which was a little higher than that of **DTRDTQX**:C70 (1:2) film (2.58 nm), The relatively low RMS of **DTRDTQX**:C_{70}(1:2) and **DTIDTQX**:C_{70}(1:2) facilitated the reasonable photovoltaic performance of the corresponding devices. Besides, the external quantum efficiency (EQE) spectra of the champion devices were measured with a lock-in amplifier (model SR830 DSP) as shown in **Figure 10**. The EQE of **DTIDTQX**-based device was higher than that of **DTRDTQX**-based counterpart and the integrated photocurrent was 5.47 and 4.71 mA/cm^2, respectively, which was consistent with the photovoltaic properties of the corresponding OSCs. In order to further study the charge transporting properties of the p-type small molecules, hole mobility was measured by using the space-charge-limited current (SCLC) method and the structure of the hole-only devices was ITO/PEDOT:PSS/donor/Au. The $J^{1/2}$-V curves were measured as shown in Supplementary Material. The relation of J and V could be described by $J = 9\varepsilon_0\varepsilon\mu(V_{app}\text{-}V_s\text{-}V_{bi})^2/8L^3$, where J was the current density, ε_0 was the permittivity of free space, ε was the relative permittivity of the p-type small molecules, μ was the hole mobility, V_{app} was the applied voltage, V_s was the voltage drop from series resistance of the substrate, V_{bi} was the built-in voltage and L was the thickness of the active layers (Qu et al., 2017). The hole mobilities were calculated with the fitted slope of the $J^{1/2}$-V curves, which were $3.62*10^{-6}$ cm^2 V^{-1} s^{-1} and $2.27*10^{-5}$ cm^2 V^{-1} s^{-1} for **DTRDTQX** and **DTIDTQX**, respectively. The hole mobility of **DTIDTQX** was higher than that of **DTRDTQX**, which contributed to the decent photovoltaic performance of **DTIDTQX**-based OSCs. All the experimental data showed that **DTIDTQX** and **DTRDTQX** were promising donor candidates for small molecule OSCs and improved photovoltaic performance of OSCs based on **DTIDTQX** and **DTRDTQX** would be foreseen in the future.

CONCLUSIONS

Two small molecules **DTRDTQX** and **DTIDTQX** with the D-A-A structure were studied in this work. **DTRDTQX** and **DTIDTQX** were used as the donors in bulk-heterojunction solar cells. The optimal OSCs based on **DTRDTQX**:C_{70}(1:2) and **DTIDTQX**:C_{70}(1:2) were achieved with the PCE of 1.44% and 1.70%, respectively. The photovoltaic properties of **DTIDTQX** were superior to those of **DTRDTQX**, which was attributed to the narrow band gap (1.37 eV) and the high hole mobility ($2.27*10^{-5}$ cm^2 V^{-1} s^{-1}) of **DTIDTQX.** Therefore, **DTRDTQX** and **DTIDTQX** would be promising donor materials for organic solar cells in future.

AUTHOR CONTRIBUTIONS

All authors listed have made a substantial, direct and intellectual contribution to the work, and approved it for publication.

FUNDING

This work was supported by the National Natural Science Foundation of China under grant Nos 11574013, U1605244, and 11527901, the National Fund for Fostering Talents of Basic Science (NFFTBS) with grant No. J1030310 and J1103205, the authors also extend their appreciation for the support from the International Scientific Partnership Program ISPP at King Saud University, ISPP#0112.

SUPPLEMENTARY MATERIAL

The Supplementary Material for this article can be found online at: https://www.frontiersin.org/articles/10.3389/fchem.2018.00260/full#supplementary-material

REFERENCES

Bai, S., Jin, Y. Z., Liang, X. Y., Ye, Z. Z., Wu, Z. W., Sun, B. Q., et al. (2015). Ethanedithiol treatment of solution-processed ZnO thin films: controlling the intragap states of electron transporting interlayers for efficient and stable inverted organic photovoltaics. *Adv. Energy Mater.* 5:1401606. doi: 10.1002/aenm.201401606

Ben Dkhil, S., Duche, D., Gaceur, M., Thakur, A. K., Aboura, F. B., Escoubas, L., et al. (2014). Interplay of optical, morphological, and electronic effects of ZnO optical spacers in highly efficient polymer solar cells. *Adv. Energy Mater.* 4:1400805. doi: 10.1002/aenm.201400805

Bijleveld, J. C., Shahid, M., Gilot, J., Wienk, M. M., and Janssen, R. A. J. (2009). Copolymers of cyclopentadithiophene and electron-deficient aromatic units designed for photovoltaic applications. *Adv. Funct. Mater.* 19, 3262–3270. doi: 10.1002/adfm.200900412

Cardona, C. M., Li, W., Kaifer, A. E., Stockdale, D., and Bazan, G. C. (2011). Electrochemical considerations for determining absolute frontier orbital energy levels of conjugated polymers for solar cell applications. *Adv. Mater.* 23, 2367–2371. doi: 10.1002/adma.201004554

Chen, C. C., Chang, W. H., Yoshimura, K., Ohya, K., You, J. B., Gao, J., et al. (2014). An efficient triple-junction polymer solar cell having a power conversion efficiency exceeding 11%. *Adv. Mater.* 26 5670–5677. doi: 10.1002/adma.201402072

Chen, J., and Cao, Y. (2009). Development of novel conjugated donor polymers for high-efficiency bulk-heterojunction photovoltaic devices. *Acc. Chem. Res.* 42, 1709–1718. doi: 10.1021/ar900061z

Chen, J. D., Cui, C., Li, Y. Q., Zhou, L., Ou, Q. D., Li, C., et al. (2015). Single-junction polymer solar cells exceeding 10% power conversion efficiency. *Adv. Mater.* 27, 1035–1041. doi: 10.1002/adma.201404535

Chen, Y. H., Lin, L. Y., Lu, C. W., Lin, F., Huang, Z. Y., Lin, H. W., et al. (2012). Vacuum-deposited small-molecule organic solar cells with high power conversion efficiencies by judicious molecular design and device optimization. *J. Am. Chem. Soc.* 134, 13616–13623. doi: 10.1021/ja301872s

Coughlin, J. E., Henson, Z. B., Welch, G. C., and Bazan, G. C. (2014). Design and synthesis of molecular donors for solution-processed high-efficiency organic solar cells. *Acc. Chem. Res.* 47, 257–270. doi: 10.1021/ar400136b

Gustafsson, G., Cao, Y., Treacy, G. M., Klavetter, F., Colaneri, N., and Heeger, A. J. (1992). Flexible light-emitting-diodes made from soluble conducting polymers. *Nature* 357, 477–479. doi: 10.1038/357477a0

He, Z. C., Xiao, B., Liu, F., Wu, H. B., Yang, Y. L., Xiao, S., et al. (2015). Single-junction polymer solar cells with high efficiency and photovoltage. *Nat. Photonics* 9, 174–179. doi: 10.1038/nphoton.2015.6

Heo, J. H., Song, D. H., Han, H. J., Kim, S. Y., Kim, J. H., Kim, D., et al. (2015). Planar CH3NH3PbI3 perovskite solar cells with constant 17.2% average power conversion efficiency irrespective of the scan rate. *Adv. Mater.* 27, 3424–3430. doi: 10.1002/adma.201500048

Huang, J., Zhang, S., Jiang, B., Chen, Y., Zhang, X., Fan, Z., et al. (2016). Terminal moiety-driven electrical performance of asymmetric small-molecule-based organic solar cells. *J. Mater. Chem. A* 4, 15688–15697. doi: 10.1039/C6TA07450B

Ji, C. H., Jang, J. M., and Oh, S. Y. (2016). Performance of organic photovoltaics using an ytterbium trifluoride n-type buffer layer. *Electr. Mater. Lett.* 12, 301–307. doi: 10.1007/s13391-016-5451-4

Jorgensen, M., and Krebs, F. C. (2005). Stepwise unidirectional synthesis of oligo phenylene vinylenes with a series of monomers. Use in plastic solar cells. *J. Org. Chem.* 70, 6004–6017. doi: 10.1021/jo0506783

Kim, B. J., Miyamoto, Y., Ma, B. W., and Frechet, J. M. J. (2009). Photocrosslinkable polythiophenes for efficient, thermally stable, organic photovoltaics. *Adv. Funct. Mater.* 19, 2273–2281. doi: 10.1002/adfm.200900043

Kim, H. S., Lee, C. R., Im, J. H., Lee, K. B., Moehl, T., Marchioro, A., et al. (2012). Lead iodide perovskite sensitized all-solid-state submicron thin film mesoscopic solar cell with efficiency exceeding 9%. *Sci. Rep.* 2:591. doi: 10.1038/srep00591

Lau, X. B. C., Wang, Z. Q., and Mitra, S. (2013). A C70-carbon nanotube complex for bulk heterojunction photovoltaic cells. *Appl. Phys. Lett.* 103:243108. doi: 10.1063/1.4847376

Li, J. S., Jiu, T. G., Li, B. R., Kuang, C. Y., Chen, Q. S., Ma, S. S., et al. (2016). Inverted polymer solar cells with enhanced fill factor by inserting the potassium stearate interfacial modification layer. *Appl. Phys. Lett.* 108:181602. doi: 10.1063/1.4948585

Li, M., Liu, F., Wan, X., Ni, W., Kan, B., Feng, H., et al. (2015). Subtle balance between length scale of phase separation and domain purification in small-molecule bulk-heterojunction blends under solvent vapor treatment. *Adv. Mater.* 27, 6296–6302. doi: 10.1002/adma.201502645

Lin, L. Y., Chen, Y. H., Huang, Z. Y., Lin, H. W., Chou, S. H., Lin, F., et al. (2011). A low-energy-gap organic dye for high-performance small-molecule organic solar cells. *J. Am. Chem. Soc.* 133, 15822–15825. doi: 10.1021/ja205126t

Liu, Y., Chen, C. C., Hong, Z., Gao, J., Yang, Y. M., Zhou, H., et al. (2013). Solution-processed small-molecule solar cells: breaking the 10% power conversion efficiency. *Sci. Rep.* 3:3356. doi: 10.1038/srep03356

Love, J. A., Proctor, C. M., Liu, J. H., Takacs, C. J., Sharenko, A., van der Poll, T. S., et al. (2013). Film morphology of high efficiency solution-processed small-molecule solar cells. *Adv. Funct. Mater.* 23, 5019–5026. doi: 10.1002/adfm.201300099

Mbuyise, X. G., Tonui, P., and Mola, G. T. (2016). The effect of interfacial layers on charge transport in organic solar cell. *Phys. B Condens. Matter* 496, 34–37. doi: 10.1016/j.physb.2016.05.021

Qu, B., Wu, H., Zhao, B., Liu, H., Gao, C., Qi, X., et al. (2017). An alternating polymer with fluorinated quinoxaline and 2,7-carbazole segments for photovoltaic devices. *RSC Adv.* 7, 16041–16048. doi: 10.1039/C6RA28128A

Roquet, S., Cravino, A., Leriche, P., Aleveque, O., Frere, P., and Roncali, J. (2006). Triphenylamine-thienylenevinylene hybrid systems with internal charge transfer as donor materials for heterojunction solar cells. *J. Am. Chem. Soc.* 128, 3459–3466. doi: 10.1021/ja058178e

Schulze, K., Uhrich, C., Schuppel, R., Leo, K., Pfeiffer, M., Brier, E., et al. (2006). Efficient vacuum-deposited organic solar cells based on a new low-bandgap oligothiophene and fullerene C-60. *Adv. Mater.* 18, 2872–2875. doi: 10.1002/adma.200600658

Shaheen, S. E., Radspinner, R., Peyghambarian, N., and Jabbour, G. E. (2001). Fabrication of bulk heterojunction plastic solar cells by screen printing. *Appl. Phys. Lett.* 79, 2996–2998. doi: 10.1063/1.1413501

Sun, K., Xiao, Z., Hanssen, E., Klein, M. F. G., Dam, H. H., Pfaff, M., et al. (2014). The role of solvent vapor annealing in highly efficient air-processed small molecule solar cells. *J. Mater. Chem. A* 2, 9048–9054. doi: 10.1039/c4ta01125b

Sun, Y., Welch, G. C., Leong, W. L., Takacs, C. J., Bazan, G. C., and Heeger, A. J. (2011). Solution-processed small-molecule solar cells with 6.7% efficiency. *Nat. Mater.* 11, 44–48. doi: 10.1038/nmat3160

Xiao, Y. M., Han, G. Y., Wu, J. H., and Lin, J. Y. (2016). Efficient bifacial perovskite solar cell based on a highly transparent poly(3,4-ethylenedioxythiophene) as the p-type hole-transporting material. *J. Pow. Sour.* 306, 171–177. doi: 10.1016/j.jpowsour.2015.12.003

You, J., Dou, L., Yoshimura, K., Kato, T., Ohya, K., Moriarty, T., et al. (2013). A polymer tandem solar cell with 10.6% power conversion efficiency. *Nat. Commun.* 4:1446. doi: 10.1038/ncomms2411

Zhang, H., Xu, M. F., Cui, R. L., Guo, X. H., Yang, S. Y., Liao, L. S., et al. (2013). Enhanced performance of inverted organic photovoltaic cells using CNTs-TiOX nanocomposites as electron injection layer. *Nanotechnology* 24:355401. doi: 10.1088/0957-4484/24/35/355401

Zhang, S. D., Lei, L., Yang, S. W., Li, X. M., Liu, Y., Gao, Q. Q., et al. (2016). Influence of TiO2 blocking layer morphology on planar heterojunction perovskite solar cells. *Chem. Lett.* 45, 592–594. doi: 10.1246/cl.160059

Zhang, Z. G., Yang, Y., Zhang, S. Y., Min, J., Zhang, J., Zhang, M. J., et al. (2011). Effect of acceptor substituents on photophysical and photovoltaic properties of triphenylamine-carbazole alternating copolymers. *Synth. Met.* 161, 1383–1389. doi: 10.1016/j.synthmet.2011.05.005

Zhou, H., Zhang, Y., Mai, C. K., Collins, S. D., Bazan, G. C., Nguyen, T. Q., et al. (2015). Polymer homo-tandem solar cells with best efficiency of 11.3%. *Adv. Mater.* 27, 1767–1773. doi: 10.1002/adma.201404220

Conflict of Interest Statement: The authors declare that the research was conducted in the absence of any commercial or financial relationships that could be construed as a potential conflict of interest.

The reviewer XZ and handling Editor declared their shared affiliation.

frontiers in Chemistry

ORIGINAL RESEARCH
published: 05 June 2018
doi: 10.3389/fchem.2018.00198

Insight Into the Role of $PC_{71}BM$ on Enhancing the Photovoltaic Performance of Ternary Organic Solar Cells

*Bei Wang[1,2], Yingying Fu[1], Chi Yan[1,3], Rui Zhang[1,3], Qingqing Yang[1], Yanchun Han[1] and Zhiyuan Xie[1]**

[1] State Key Laboratory of Polymer Physics and Chemistry, Changchun Institute of Applied Chemistry, Chinese Academy of Sciences, Changchun, China, [2] University of Science and Technology of China, Hefei, China, [3] University of Chinese Academy of Sciences, Beijing, China

The development of non-fullerene acceptor molecules have remarkably boosted power conversion efficiency (PCE) of polymer solar cells (PSCs) due to the improved spectral coverage and reduced energy loss. An introduction of fullerene molecules into the non-fullerene acceptor-based blend may further improve the photovoltaic performance of the resultant ternary PSCs. However, the underlying mechanism is still debatable. Herein, the ternary PSCs based on PBDB-T:ITIC:$PC_{71}BM$ blend were fabricated and its PCE was increased to 10.2% compared to 9.2% for the binary PBDB-T:ITIC devices and 8.1% for the PBDB-T:$PC_{71}BM$ PSCs. Systematic investigation was carried out to disclose the effect of $PC_{71}BM$ on the blend morphology and charge transport behavior. It is found that the $PC_{71}BM$ tends to intermix with the PBDB-T donor compared to the ITIC counterpart. A small amount of $PC_{71}BM$ in the ternary blend is helpful for ITIC to aggregate and form efficient electron-transport pathways. Accordingly, the electron mobility is increased and the density of electron traps is decreased in the ternary blend in comparison with the PBDB-T:ITIC blend. Finally, the suppressed bimolecular recombination and enhanced charge collection lead to high PCE for the ternary solar cells.

Keywords: ternary organic solar cells, morphology, aggregation, charge transport, trap density

OPEN ACCESS

Edited by:
Donghong Yu,
Aalborg University, Denmark

Reviewed by:
Junwu Chen,
South China University of Technology, China
Zhishan Bo,
Beijing Normal University, China

***Correspondence:**
Zhiyuan Xie
xiezy_n@ciac.ac.cn

Specialty section:
This article was submitted to Organic Chemistry, a section of the journal Frontiers in Chemistry

Received: *09 April 2018*
Accepted: *15 May 2018*
Published: *05 June 2018*

Citation:
Wang B, Fu Y, Yan C, Zhang R, Yang Q, Han Y and Xie Z (2018) Insight Into the Role of $PC_{71}BM$ on Enhancing the Photovoltaic Performance of Ternary Organic Solar Cells. Front. Chem. 6:198. doi: 10.3389/fchem.2018.00198

INTRODUCTION

Non-fullerene acceptors have drawn great research interests in the community of polymer solar cells (PSCs) in recent years. The power conversion efficiencies (PCE) of PSCs employing non-fullerene acceptors have increased rapidly as compared to the PSCs using fullerene derivatives as acceptors (Lin et al., 2015; Cao et al., 2017; Fan et al., 2017; Li et al., 2017; Xiao et al., 2017; Dai et al., 2018). Non-fullerene acceptors possess some advantages such as strong absorption in the visible region and tunable energy levels with regard to fullerene derivatives, and thus allows for suitable combination of donor/acceptor blend to improve the spectral coverage and reduce the energy loss (Holliday et al., 2016; Li et al., 2016, 2018; Qiu et al., 2017). In addition to the strong and complementary absorption and the matched energy levels of the donor/acceptor combination, the donor/acceptor morphology with a suitable phase separation is equally important for realizing a high PCE. More recently, addition of another type of donor or acceptor in the binary non-fullerene PSCs to fabricate so-called ternary PSCs have drawn great interests. This kind of ternary strategy

is to some extent powerful to enhance the photovoltaic performance of the devices (Cheng et al., 2014; Gasparini et al., 2016). As it is argued, ternary PSCs possess some features such as more complementary absorption (Jiang et al., 2018) and more appropriate microstructure relative to the binary counterparts (Wang et al., 2017) and easier fabrication compared with tandem solar cells. With these superiorities, ternary PSCs have developed very quickly and become a research focus in the field (Yu et al., 2017; Zhang G. et al., 2017; Zhao et al., 2017; Wang et al., 2018). Nonetheless, the morphology of ternary blends is more complex resulting in the underlying mechanism debatable. It is proposed that the ternary morphology can be divided into four types according to the relative position of third component to the donor phases and acceptor phases, namely the third component embedded in one phase, located at the interfaces, formed alloy structure with either the donor or acceptor material and parallel-like bulk heterojunction structure with the donor or acceptor (Lu et al., 2015). In fact, the ternary morphology is too complicated to be clearly identified using the current technology. Typical electron acceptor fullerene derivatives, such as $PC_{71}BM$ and Bis-$PC_{71}BM$ have been used as additives in non-fullerene PSCs. For example, Bo et al. have reported high-performance ternary PSCs employing non-fullerene and fullerene acceptors simultaneously for the first time, in which they found that a small amount of fullerene is in favor of boosting the photovoltaic performance of the devices (Lu et al., 2016). Hou et al. also reported the high-efficiency ternary PSCs using Bis-$PC_{71}BM$ as the third component (Zhao et al., 2017). They proposed that Bis-$PC_{71}BM$ mainly exists in the upper surface of active layer and promotes electron transport in their ternary blend PSCs. For the ternary PSCs, the third component such as $PC_{71}BM$ may have strong effect on the resultant ternary morphology and hence its photovoltaic properties. Although some researches on the function of third component were carried out (Yu et al., 2017; Zhang J. et al., 2017; Wang et al., 2018), the underlying mechanism is still debatable.

Herein, a reported wide bandgap polymer poly[(2,6-(4,8-bis(5-(2-ethylhexyl)thiophen-2-yl)-benzo[1,2-b:4,5-b′] dithiophene))-alt-(5,5-(1′,3′-di-2-thienyl-5′,7′-bis(2-ethylhexyl) benzo[1′,2′-c:4′,5′-c′]dithiophene-4,8-dione))] (PBDB-T) is used as the donor, organic molecule (3,9-bis(2-methylene-(3-(1,1-dicyanomethylene)-indanone))- 5,5,11,11-tetrakis(4-hexylphenyl)-dithieno[2,3-d:2′,3′-d′]-s-indaceno[1,2-b:5,6-b′] dithiophene) (ITIC) is used as the acceptor and [6,6]-phenyl-C71-butyric acid methyl ester ($PC_{71}BM$) is used as the third component to prepare the ternary PSCs. The optimized PSCs based on ternary PBDB-T:ITIC:$PC_{71}BM$ blend demonstrate a higher PCE of 10.2% than 9.2% of the binary PBDB-T:ITIC devices and 8.1% of the PBDB-T:$PC_{71}BM$ PSCs. Further studies are mainly focused on the effect of $PC_{71}BM$ on the blend morphology and charge transport behavior. It is found that the $PC_{71}BM$ tends to intermix with the PBDB-T donor compared to the ITIC counterpart. A small amount of $PC_{71}BM$ in the ternary blend is helpful for ITIC to aggregate and form efficient electron-transport pathways. Accordingly, the electron mobility is increased and the density of electron traps is decreased in the ternary blend in comparison with the PBDB-T:ITIC blend. Finally, the suppressed bimolecular recombination and enhanced charge collection lead to an enhanced PCE for the ternary solar cells.

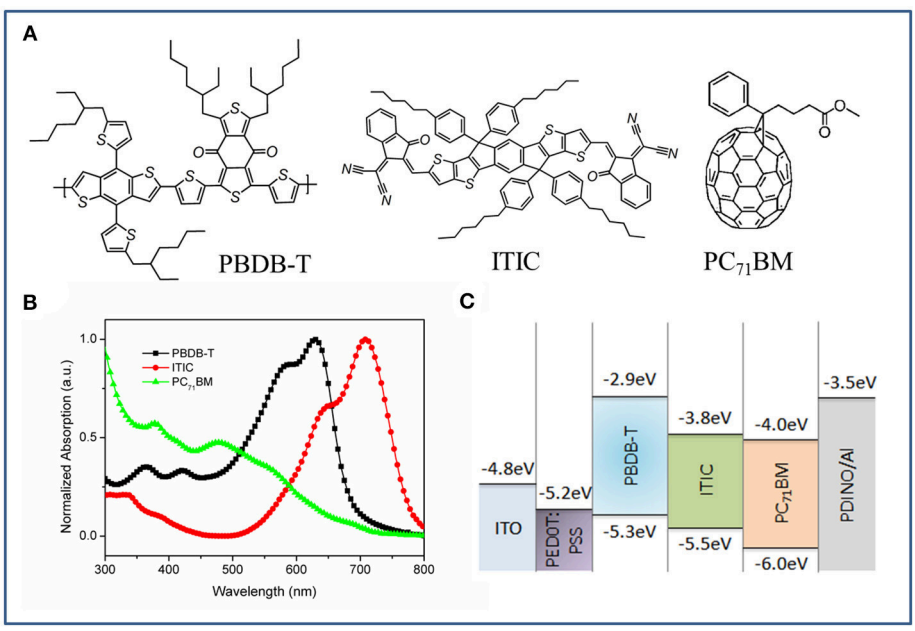

FIGURE 1 | (A) Chemical structures of PBDB-T, ITIC, and $PC_{71}BM$. **(B)** Normalized absorption of pure PBDB-T, ITIC, and $PC_{71}BM$ films. **(C)** Energy level diagram of solar cells.

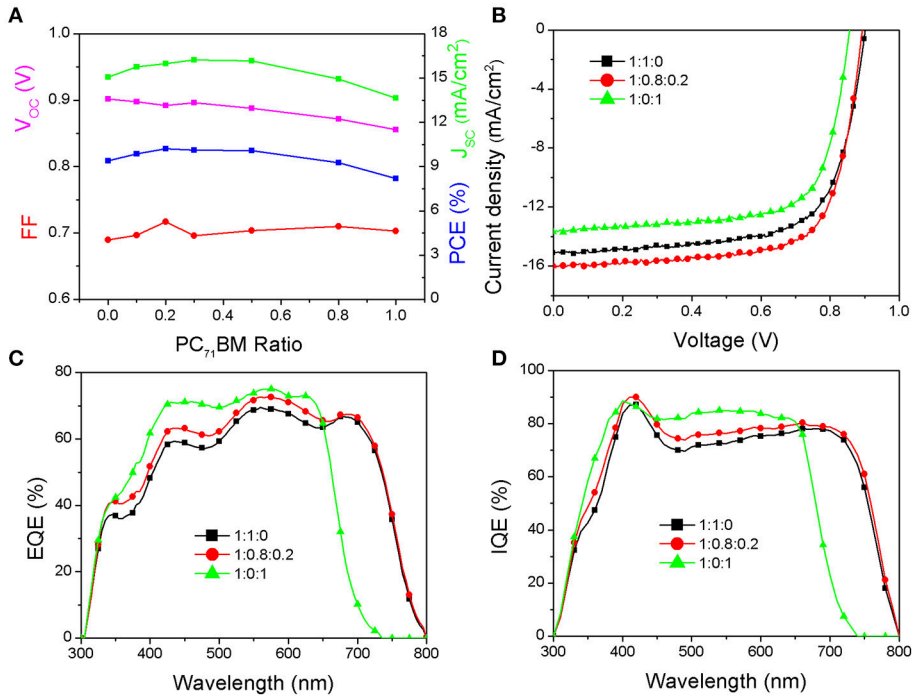

FIGURE 2 | (A) The photovoltaic parameters of the PBDB-T:ITIC:$PC_{71}BM$ (1:1-x:x) PSCs. The J-V **(B)**, EQE **(C),** and IQE **(D)** curves of PSCs based on PBDB-T:ITIC (1:1), PBDB-T:ITIC:$PC_{71}BM$ (1:0.8:0.2), and PBDB-T:$PC_{71}BM$ (1:1) blend films, respectively.

EXPERIMENTAL SECTION

Both the polymer PBDB-T donor and small molecule ITIC acceptor were bought from Solarmer Ltd. The PBDB-T has a molecular weight Mn of 21.5 kDa and a PDI of 1.9. $PC_{71}BM$ was bought from American Dye Source. The interfacial material PDINO was provided by Dr. Zhiguo Zhang in Institute of Chemistry, Chinese Academy of Sciences. All materials were used as received without further purification.

Polymer solar cells were fabricated with a structure of ITO/PEDOT: PSS/active layer/PDINO/Al. The ITO substrates were subject to routine cleaning procedure of detergent, acetone and deionized water. After drying in an oven for 30 min, the ITO substrates were treated with UV-ozone for 25 min. The PEDOT:PSS layer was first deposited via spin-coating and dried at 140°C for 30 min in air. The subsequent active layer and buffer layer were spin-coated in a glove box. The active layers consisting of PBDB-T:$PC_{71}BM$, PBDB-T:ITIC, or ternary PBDB-T:ITIC:$PC_{71}BM$ were spin-coated from their respective solutions in CB containing 0.5% DIO with a total concentration of 20 mg/mL. The spin-coating rate for the active layers was kept at 2,500 rpm for 1 min. The samples were annealed at 160°C for 10 min. A cathode buffer layer of PDINO was spin-coated on the active layer from its methanol solution with a concentration of 1 mg/mL at 3,000 rpm for 30 s. Finally, the Al cathode with a thickness of 100 nm was thermally deposited in a vacuum chamber. The electron—and hole-only devices were fabricated under the same procedure with a structure of ITO/PEIE/active layer/PDINO/Al and ITO/PEDOT:PSS/active layer/MoO_3/Al, respectively.

The current density-voltage (J-V) curves of the PSCs were traced by a computer-controlled Keithley 2400 Source Meter under simulated solar light illumination (AM 1.5G, 100 mW/cm^2). The EQE data were measured by solar cell spectral response measurement system (QE-R 3011, Enli Tech. Co.). The film absorption and fluorescence spectra were recorded on Agilent Cary 60UV-Vis spectrophotometer and Perkin-Elmer LS 55 spectrofluorometer, respectively. The thicknesses of individual layers were measured with a surface profilometer. The 2D-GIXD data were acquired at station 14B in Shanghai Synchrotron Radiation Facility.

RESULTS AND DISCUSSION

The chemical structures of PBDB-T, ITIC and $PC_{71}BM$ are shown in **Figure 1A**. The normalized UV-vis absorption spectra of neat PBDB-T, ITIC and $PC_{71}BM$ films are plotted in **Figure 1B**. It is clearly seen from **Figure 1B** that the main peaks of PBDB-T and ITIC are located at 625 and 710 nm, respectively, and their complementary absorption can strongly improve the spectral coverage in the visible region. $PC_{71}BM$ exhibits absorption in short wavelength region but its absorption capability is relatively weak. In this study, the PSCs with a conventional device structure of ITO/PEDOT:PSS/active layer/PDINO/Al were fabricated, and their energy levels were plotted in **Figure 1C**. The polymer PDINO was used as cathode buffer layer referenced to the

literature (Zhang Z. et al., 2014). The total ratio of donor component to acceptor component is kept at a fixed ratio of 1:1 (w/w). The ratio of PBDB-T:ITIC:$PC_{71}BM$ is marked as the D:A1:A2.

The photovoltaic performance of the PSCs based on the PBDB-T:ITIC:$PC_{71}BM$ (1:1-x:x) blend were firstly evaluated. The ratio of A1:A2 is varied from 1:0 to 0:1 while the ratio of D:(A1+A2) is fixed at 1:1 in order to keep a constant active layer thickness. The detailed photovoltaic parameters of the resultant PSCs with different ratio of two acceptors are listed in Table S1 in Supplementary Information. The dependence of V_{OC}, J_{SC}, FF, and PCE on the $PC_{71}BM$ content for the resultant PSCs are plotted in **Figure 2A**. In the case of V_{OC}, it undergoes gradually decrease from 0.902 V for the binary PBDB-T:ITIC PSCs to 0.856 V for the binary PBDB-T: $PC_{71}BM$ PSCs with increasing $PC_{71}BM$ content from 0 to 1 in the ternary blend PSCs. The change is reasonable since the LUMO of ITIC is higher than that of $PC_{71}BM$, and the electron transport and collection will occur in $PC_{71}BM$ phases when the $PC_{71}BM$ amount is larger. The interesting thing is that the J_{SC} are initially increased and then decreased with the increase of $PC_{71}BM$ contents for the resultant ternary PSCs. The FF shows similar trend. Considering the intrinsic absorption properties between ITIC and $PC_{71}BM$, the substitution of small amount of ITIC by $PC_{71}BM$ would decrease the total absorption of the ternary PBDB-T:ITIC:$PC_{71}BM$ blend active layer. Thus, the improved J_{SC} and FF for the ternary PBDB-T:ITIC:$PC_{71}BM$ PSCs may imply that both the exciton dissociation and charge-collection efficiencies are enhanced in comparison to the binary PBDB-T:ITIC PSCs. It is plotted the illuminated J-V curves of the PBDB-T:ITIC PSCs, the PBDB-T:$PC_{71}BM$ PSCs and the optimized ternary PBDB-T:ITIC:$PC_{71}BM$ PSCs in **Figure 2B**, respectively. The non-fullerene PSCs based on binary PBDB-T:ITIC blend demonstrate a V_{OC} of 0.902 V, a J_{SC} of 15.06 mA/cm^2, a FF of 0.69, respectively, leading to a PCE of 9.38%. Due to the limited spectral coverage, the PBDB-T:$PC_{71}BM$ PSCs show a lower J_{SC} of 13.64 mA/cm^2, and finally result in a PCE of 8.21% together with a V_{OC} of 0.856 V and a FF of 0.703. The ternary PBDB-T:ITIC:$PC_{71}BM$ (1:0.8:0.2) PSCs demonstrate a V_{OC} of 0.892 V, a J_{SC} of 15.98 mA/cm^2, a FF of 0.717 and an overall PCE of 10.22%. Although the V_{OC} is a little lowered in comparison to the binary PBDB-T:ITIC PSCs, the increased J_{SC} and FF boost the PCE enhancement of the ternary PSCs. The external quantum efficiency (EQE) curves of the three devices are shown in **Figure 2C**. The spectral response of the PBDB-T:$PC_{71}BM$ PSCs cover at a range of 300–700 nm with EQE higher than 70% at 450–650 nm. The PBDB-T:ITIC PSCs show extended spectral coverage of 300–800 nm due to the narrow bandgap of ITIC. The ternary PBDB-T:ITIC:$PC_{71}BM$ PSCs show similar spectral response profile but high EQE compared to the PBDB-T:ITIC PSCs. The internal quantum efficiency (IQE) of these devices are also measured to clarify the absolute quantum efficiency in these devices and the curves are plotted in **Figure 2D**. It indicates that the photon-to-electron conversion efficiency is really improved by adding some amount of $PC_{71}BM$ into the PBDB-T:ITIC blend. The absorption spectra of the active layers in three kinds of PSCs are plotted in **Figure 3A**.

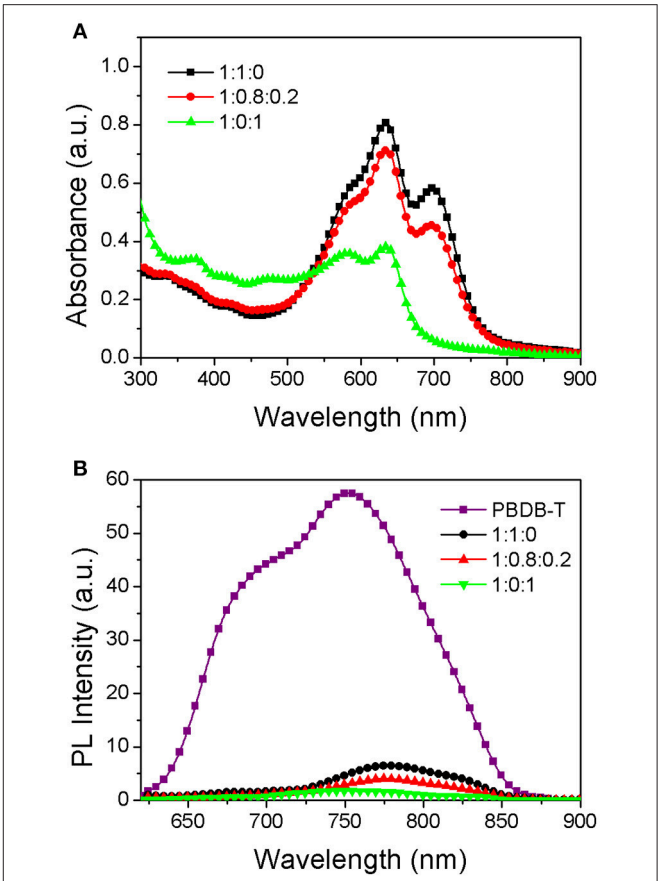

FIGURE 3 | (A) Absolute absorption spectra of PBDB-T:ITIC (1:1), PBDB-T:ITIC:$PC_{71}BM$ (1:0.8:0.2), and PBDB-T:$PC_{71}BM$ (1:1) blend films. **(B)** Photoluminescent spectra of pure PBDB-T, PBDB-T:ITIC (1:1), PBDB-T:ITIC:$PC_{71}BM$ (1:0.8:0.2), and PBDB-T:$PC_{71}BM$ (1:1) films.

The PBDB-T:ITIC:$PC_{71}BM$ (1:0.8:0.2) active layer shows a little low absorption at 550–750 nm due to decreased ITIC content compared to the PBDB-T:ITIC (1:1) film. Although the PBDB-T:$PC_{71}BM$ (1:1) film demonstrates enhanced absorption at 300–500 nm, its absorption at 550–700 nm is remarkably decreased. Photoluminescence (PL) quenching experiments were carried out to check the charge transfer status in these films. As shown in **Figure 3B**, the introduction of $PC_{71}BM$ favors to quench the excitons dominated on the PBDB-T donor.

The relationship between photocurrent (J_{ph}) and effective voltage (V_{eff}) is investigated to judge the charge generation and collection status in the PSCs based on the PBDB-T:ITIC (1:1), PBDB-T:ITIC:$PC_{71}BM$ (1:0.8:0.2), and PBDB-T:$PC_{71}BM$ (1:1) blends (Yuan et al., 2017; Zhang G. et al., 2017). As shown in **Figure 4A**, J_{ph} is given by $J_{ph} = J_L - J_D$, where J_L & J_D are the current density under illumination and in the dark, respectively. V_{eff} is defined as $V_0 - V_{appl}$, V_0 is the voltage when $J_{ph} = 0$ and V_{appl} is the applied voltage during the measurement. The J_{ph} is supposed to be saturated at a V_{eff} of 3 V, which are 16.55 mA/cm^2, 17.40 mA/cm^2 and 14.45 mA/cm^2, respectively, for the PSCs based on the PBDB-T:ITIC

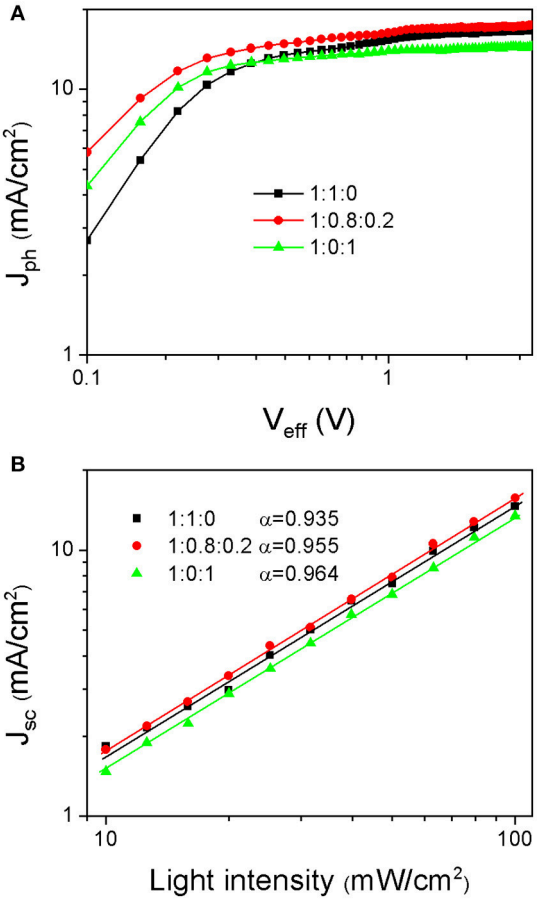

FIGURE 4 | (A) J_{ph} – V_{eff} curves and **(B)** J_{SC} dependence on the illuminated light intensity of PSCs based on PBDB-T:ITIC (1:1), PBDB-T:ITIC:$PC_{71}BM$ (1:0.8:0.2), and PBDB-T:$PC_{71}BM$ (1:1) blend films, respectively.

(1:1), PBDB-T:ITIC:$PC_{71}BM$ (1:0.8:0.2), and PBDB-T:$PC_{71}BM$ (1:1) blends. The device based on ternary PBDB-T:ITIC:$PC_{71}BM$ (1:0.8:0.2) blend demonstrates the highest saturation current, indicating its highest charge-generation capability. Charge dissociation probability P(E,T) is defined as J_{ph}/J_{sat}. When a high bias is applied, the charge recombination is suppressed and most of photo-generated charges are extracted, leading to P(E,T) close to100%. It is calculated that the P(E,T) values under short-circuit condition ($V_{appl} = 0$ V) are 90.6, 91.9, and 94.9%, respectively, for the PSCs based on the PBDB-T:ITIC (1:1), PBDB-T:ITIC:$PC_{71}BM$ (1:0.8:0.2), and PBDB-T:$PC_{71}BM$ (1:1) blends. The PBDB-T:$PC_{71}BM$ (1:1) device shows the best charge-extraction capability, whereas the charge-extraction ability is a little poor for the PBDB-T:ITIC (1:1) device. The ternary PBDB-T:ITIC:$PC_{71}BM$ (1:0.8:0.2) shows improved exciton dissociation and charge extraction compared to the PBDB-T:ITIC (1:1) device. The charge recombination status in these devices is also investigated via the dependence of J_{SC} on the incident light intensity as shown in **Figure 4B**. J_{SC} is dependent on the incident light intensity with $J_{SC} \propto I^{\alpha}$, in which exponential factor α would be close to unity without bimolecular recombination (Gao et al., 2016; Xu et al., 2017, 2018). The PBDB-T:$PC_{71}BM$ (1:1) device has the highest α value of 0.964, whereas α value of the PBDB-T:ITIC (1:1) device is merely 0.935 implying severe bimolecular recombination within the film. Such kind of bimolecular recombination in the PBDB-T:ITIC (1:1) device is to some extent suppressed with α value of 0.955 in ternary PBDB-T:ITIC:$PC_{71}BM$ (1:0.8:0.2) device.

As discussed above, with the introduction of $PC_{71}BM$ into the PBDB-T:ITIC blend, the resultant ternary PSCs demonstrate an enhanced exciton-dissociating and charge-extracting property, leading to improved PCE compared to the PBDB-T:ITIC PSCs. The detailed mechanism accounting for the enhancement is further investigated. The electron and hole transport properties of the various blend films were firstly measured via space-charge limited current (SCLC) method (Bin et al., 2016). The J-V curves of the devices were plotted as in Figure S1 and the calculated electron and hole mobility are listed in Table S2. The PBDB-T:$PC_{71}BM$ (1:1) blend film shows relatively high electron and hole mobility of 8.45×10^{-4} and 5.30×10^{-4} $cm^2V^{-1}s^{-1}$, respectively. However, the electron and hole mobility of the PBDB-T:ITIC (1:1) film is 3.05×10^{-4} and 2.70×10^{-4} $cm^2V^{-1}s^{-1}$. After incorporating $PC_{71}BM$, the electron and hole mobility of the resultant PBDB-T:ITIC:$PC_{71}BM$ (1:0.8:0.2) film is increased to 4.55×10^{-4} and 3.37×10^{-4} $cm^2V^{-1}s^{-1}$. As it is known, the high and balanced charge transport may help to efficient charge extraction and hence low charge recombination. This is in agreement with the recombination status in these PSCs. It is speculated that the incorporation of $PC_{71}BM$ improves the PBDB-T and ITIC interpenetrating networks and thus the photovoltaic performance.

The morphology of the PBDB-T:ITIC (1:1), PBDB-T:ITIC:$PC_{71}BM$ (1:0.8:0.2), and PBDB-T:$PC_{71}BM$ (1:1) blend films are investigated and their AFM and TEM images are shown in Figures S2, S3. All the blend films are smooth with a root mean square (RMS) roughness of <2 nm. However, the morphology of the ternary blend is not changed obviously compared to the PBDB-T:ITIC (1:1) blend film. The structural information of the blended films are further investigated by grazing incidence X-ray diffraction (GIXD). The 2D-GIXD images of the pure PBDB-T and ITIC films are plotted in Figure S4. The pure PBDB-T film shows dominant peak at $q_{xy} = 0.29$ Å^{-1} in the in-plane direction, attributing to its strong (100) diffraction. The pure ITIC film demonstrates two featured peaks at $q_z = 0.26$ Å^{-1} and $q_z = 0.53$ Å^{-1} in out-of-plane direction and one peak in in-plane direction at $q_{xy} = 0.36$ Å^{-1}. 2D-GIXD patterns and line-cut profiles of the PBDB-T:ITIC (1:1), PBDB-T:ITIC:$PC_{71}BM$ (1:0.8:0.2) and PBDB-T:$PC_{71}BM$ (1:1) films are shown in **Figure 5**. The diffractions originated from PBDB-T aggregation is observed both in PBDB-T:ITIC (1:1) and PBDB-T:$PC_{71}BM$ (1:1) films in contrast to the pure PBDB-T film. However, the diffraction signal originated from the ITIC component is not obviously presented in PBDB-T:ITIC blend film, implying its poor aggregation. In the PBDB-T:ITIC:$PC_{71}BM$ (1:0.8:0.2) blend film, the diffraction signal from PBDB-T is still presented but weakened. More importantly, two additional peaks marked 1 and 2 are presented in the ternary blend film compared to the PBDB-T:ITIC (1:1)

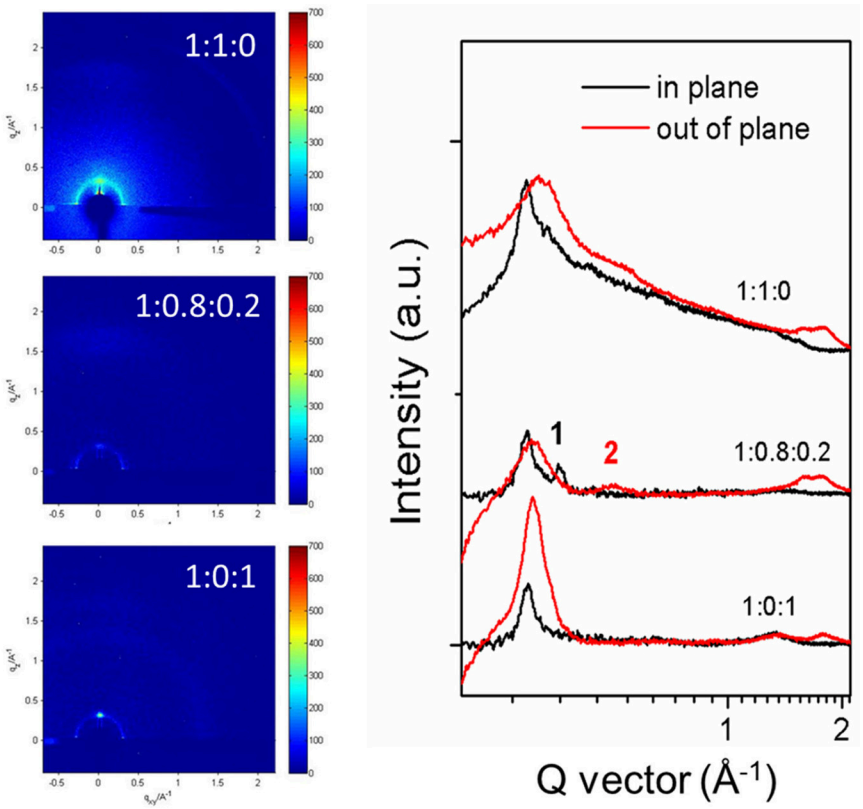

FIGURE 5 | 2D-GIXD images of PBDB-T:ITIC (1:1), PBDB-T:ITIC:$PC_{71}BM$ (1:0.8:0.2), and PBDB-T:$PC_{71}BM$ (1:1) blend films **(Left)**. The in-plane and out-of-plane line profiles of the films **(Right)**.

counterpart, which corresponds to the featured diffraction from ITIC in the in-plane and out-of-plane directions. Bo et al. observed similar phenomenon in their work (Lu et al., 2016). This indicates that the ITIC aggregation is enhanced in the PBDB-T:ITIC:$PC_{71}BM$ (1:0.8:0.2) blend film though the ITIC content is decreased. In other words, the small amount of $PC_{71}BM$ may serve as "lubricant" to favor ITIC molecules to aggregate out of the polymer PBDB-T matrix.

The prerequisite to get such a conclusion is that the compatibility between PBDB-T and $PC_{71}BM$ should be better than that between PBDB-T and ITIC. The electron mobility of the PBDB-T:ITIC (1:x) and PBDB-T:$PC_{71}BM$ (1:x) blend films are measured and its dependence on the acceptor ratio is plotted in **Figure 6**. It is supposed that the acceptor phase forms continuous tunnels when the electron mobility of the blend films exceeds 10^{-5} $cm^2V^{-1}s^{-1}$. Both the as-prepared film deposited in CB solution and the annealed film deposited in CB:DIO (0.5%, v/v) solution are tested. The results show that the continuous electron-transport tunnels is formed in the PBDB-T:ITIC film with the ITIC/PBDB-T ratio <20%. The DIO additive and thermal annealing donot change the electron transport remarkably. For the as-prepared PBDB-T:$PC_{71}BM$ film, the critical $PC_{71}BM$ content is increased to 25%. The DIO additive and thermal annealing lowers the critical $PC_{71}BM$ content. This indicates that the PBDB-T is inclined to intermix with $PC_{71}BM$ better than with ITIC. In the ternary PBDB-T:ITIC:$PC_{71}BM$ (1:0.8:0.2) blend film, the small amount of $PC_{71}BM$ may mix with PBDB-T and does not form networks.

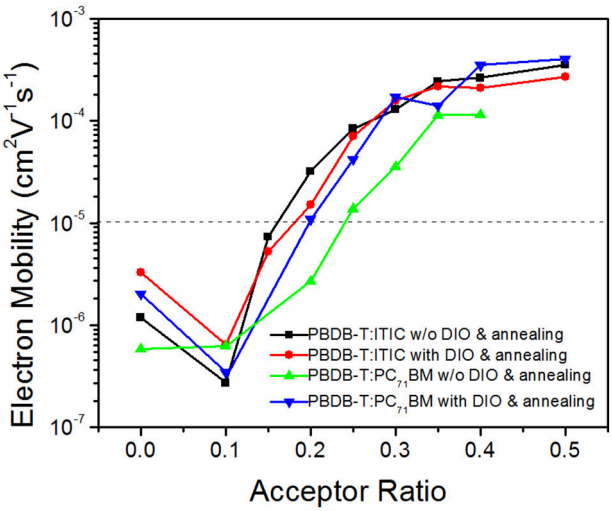

FIGURE 6 | The measured electron mobility in the PBDB-T:ITIC (1:x) and PBDB-T:$PC_{71}BM$ (1:x) films.

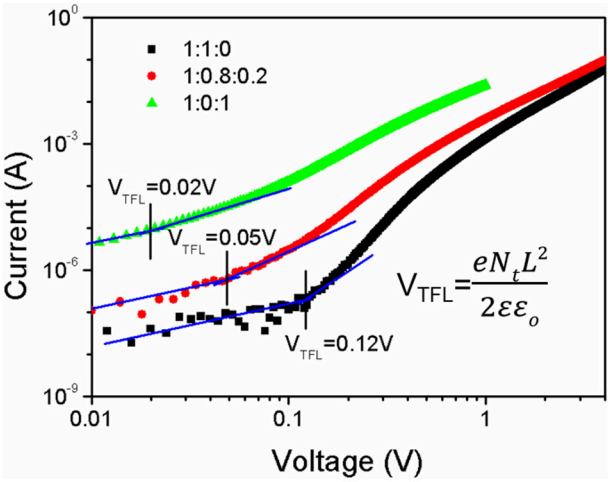

FIGURE 7 | The current-voltage curves of the electron-only devices based on the PBDB-T:ITIC (1:1), PBDB-T:ITIC:$PC_{71}BM$ (1:0.8:0.2), and PBDB-T:$PC_{71}BM$ (1:1) blend films.

Moreover, the existence of $PC_{71}BM$ favors ITIC aggregating to form electron-transporting networks. This is confirmed by the increased electron mobility and the XRD results compared to the PBDB-T:ITIC (1:1) film.

The electron trap-state density in these blend films is further investigated. From the I–V curves of the electron-only devices based on the PBDB-T:ITIC (1:1), PBDB-T:ITIC:$PC_{71}BM$ (1:0.8:0.2) and PBDB-T:$PC_{71}BM$ (1:1) blend shown in **Figure 7**, the electron trap density N is calculated by the equation as below (Yang et al., 2016):

$$V_{TFL} = \frac{eNL^2}{2\varepsilon_0\varepsilon_r} \quad (1)$$

where V_{TFL} is the trap-filled limit voltage, e is the elementary charge of electron, L is the thickness of film, ϵ_0 is the vacuum permittivity, and ϵ_r is the relative dielectric constant ($\epsilon_r = 3$). The V_{TFL} of three devices is 0.12, 0.05, and 0.02 V. The calculated deep trap density is 3.3×10^{15}, 1.5×10^{15}, and 7.3×10^{14} cm^{-3}, respectively. It confirms that the incorporation of $PC_{71}BM$ is helpful for ITIC molecules to move out of PBDB-T phases and thus the density of electron traps is reduced. The increased electron mobility and the decreased electron traps are helpful to enhance the photovoltaic performance of the PBDB-T:ITIC:$PC_{71}BM$ (1:0.8:0.2).

CONCLUSION

In summary, the ternary PSCs based on PBDB-T:ITIC:$PC_{71}BM$ (1:0.8:0.2) blend were fabricated and its PCE was increased to 10.2% compared to 9.2% for the PBDB-T:ITIC (1:1) devices. The mechanism accounting for the enhanced photovoltaic performance is discussed in detail. It is found that the $PC_{71}BM$ tends to intermix with the PBDB-T donor compared to the ITIC counterpart. A small amount of $PC_{71}BM$ in the ternary blend is helpful for ITIC to aggregate and form efficient electron-transport pathways. The electron mobility is increased and the density of electron traps is decreased in the ternary PBDB-T:ITIC:$PC_{71}BM$ (1:0.8:0.2) blend in comparison with the PBDB-T:ITIC blend. Finally, the suppressed bimolecular recombination and enhanced charge collection lead to a high PCE for the ternary solar cells.

AUTHOR CONTRIBUTIONS

BW and CY conceived and designed the experiments. BW performed the experiments. RZ performed 2D-GIXD measurements. QY performed the absorption and PL experiments. BW and YF analyzed data. BW wrote the manuscript. All authors discussed and commented on the paper.

ACKNOWLEDGMENTS

This work is supported by the National Key Basic Research and Development Program of China (Nos. 2014CB643504, 2015CB655001) and the National Natural Science Foundation of China (nos.21774122, 21334006, 51611530705, 51773195, 51703222). The financial support of the Strategic Priority Research Program of the Chinese Academy of Sciences (XDB12030200) is also acknowledged. We also thank Shanghai Synchrotron Radiation Facility (SSRF) beamline 14B for the grazing X-ray measurements.

SUPPLEMENTARY MATERIAL

The Supplementary Material for this article can be found online at: https://www.frontiersin.org/articles/10.3389/fchem.2018.00198/full#supplementary-material

REFERENCES

Bin, H., Zhang, Z. G., Gao, L., Chen, S., Zhong, L., Xue, L., et al. (2016). Non-fullerene polymer solar cells based on alkylthio and fluorine substituted 2D-conjugated polymers reach 9.5% efficiency. *J. Am. Chem. Soc.* 138, 4657–4664. doi: 10.1021/jacs.6b01744

Cao, Q., Xiong, W., Chen, H., Cai, G., Wang, G., Zheng, L., et al. (2017). Design, synthesis, and structural characterization of the first dithienocyclopentacarbazole-based ntype organic semiconductor and its application in non-fullerene polymer solar cells. *J. Mater. Chem. A* 5, 7451–7461. doi: 10.1039/C7TA01143A

Cheng, P., Li, Y., and Zhan, X. (2014). Efficient ternary blend polymer solar cells with indene-C60 bisadduct as an electron-cascadeacceptor. *Energy Environ. Sci.* 7, 2005–2011. doi: 10.1039/c3ee44202k

Dai, S., Li, T., Wang, W., Xiao, Y., Lau, T. K., Li, Z., et al. (2018). Enhancing the performance of polymer solar cells via core engineering of nir-absorbing electron acceptors. *Adv. Mater.* 30:e1706571. doi: 10.1002/adma.201706571

Fan, Q., Su, W., Guo, X., Wang, Y., Chen, J., Ye, C., et al. (2017). Side-chain engineering for efficient non-fullerene polymer solar cells based on a wide-bandgap polymer donor. *J. Mater. Chem. A* 5, 9204–9209. doi: 10.1039/C7TA02075A

Gao, L., Zhang, Z. G., Bin, H., Xue, L., Yang, Y., Wang, C., et al. (2016). High-efficiency nonfullerene polymer solar cells with medium bandgap polymer donor and narrow bandgap organic semiconductor acceptor. *Adv. Mater.* 28, 8288–8295. doi: 10.1002/adma.201601595

Gasparini, N., Jiao, X., Heumueller, T., Baran, D., Matt, G., Fladischer, S., et al. (2016). Designing ternary blend bulk heterojunction solar cells with reduced carrier recombination and a fill factor of 77%. *Nat. Energy* 1:16118. doi: 10.1038/nenergy.2016.118

Holliday, S., Ashraf, R. S., Wadsworth, A., Baran, D., Yousaf, S. A., Nielsen, C. B., et al. (2016). High-efficiency and air-stable P3HT-based polymer solar cells with a new non-fullerene acceptor. *Nat. Commun.* 7:11585. doi: 10.1038/ncomms11585

Jiang, W., Yu, R., Liu, Z., Peng, R., Mi, D., Hong, L., et al. (2018). Ternary nonfullerene polymer solar cells with 12.16% efficiency by introducing one acceptor with cascading energy level and complementary absorption. *Adv. Mater.* 30:1703005. doi: 10.1002/adma.201703005

Li, S., Ye, L., Zhao, W., Zhang, S., Ade, H., and Hou, J. (2017). Signifcant influence of the methoxyl substitution position on optoelectronic properties and molecular packing of small-molecule electron acceptors for photovoltaic cells. *Adv. Energy Mater.* 7:1700183. doi: 10.1002/aenm.201700183

Li, S., Ye, L., Zhao, W., Zhang, S., Mukherjee, S., Ade, H., et al. (2016). Energy-level modulation of small-molecule electron acceptors to achieve over 12% effciency in polymer solar cells. *Adv. Mater.* 28, 9423–9429. doi: 10.1002/adma.201602776

Li, S., Zhan, L., Liu, F., Ren, J., Shi, M., Li, C. Z., et al. (2018). An unfused-core-based nonfullerene acceptor enables high-efficiency organic solar cells with excellent morphological stability at high temperatures. *Adv. Mater.* 30:1705208. doi: 10.1002/adma.201705208

Lin, Y., Wang, J., Zhang, Z. G., Bai, H., Li, Y., Zhu, D., et al. (2015). An electron acceptor challenging fullerenes for efficient polymer solar cells. *Adv. Mater.* 27, 1170–1174. doi: 10.1002/adma.201404317

Lu, H., Zhang, J., Chen, J., Liu, Q., Gong, X., Feng, S., et al. (2016). Ternary-blend polymer solar cells combining fullerene and nonfullerene acceptors to synergistically boost the photovoltaic performance. *Adv. Mater.* 28, 9559–9566. doi: 10.1002/adma.201603588

Lu, L., Kelly, M., You, W., and Yu, L. (2015). Status and prospects for ternary organic photovoltaics. *Nat. Photonics* 9, 491–500. doi: 10.1038/nphoton.2015.128

Qiu, N., Zhang, H., Wan, X., Li, C., Ke, X., Feng, H., et al. (2017). A new nonfullerene electron acceptor with a ladder type backbone for high-performance organic solar cells. *Adv. Mater.* 29:1604964. doi: 10.1002/adma.201604964

Wang, J., Peng, J., Liu, X., and Liang, Z. (2017). Efficient and stable ternary organic solar cells based on two planar nonfullerene acceptors with tunable crystallinity and phase miscibility. *ACS Appl. Mater. Interfaces* 9, 20704–20710. doi: 10.1021/acsami.7b03757

Wang, Z., Zhu, X., Zhang, J., Lu, K., Fang, J., Zhang, Y., et al. (2018). From alloy-like to cascade blended structure: designing high-performance all small molecule ternary solar cells. *J. Am. Chem. Soc.* 140, 1549–1556. doi: 10.1021/jacs.7b13054

Xiao, Z., Jia, X., Li, D., Wang, S., Geng, X., Liu, F., et al. (2017). 26 mA cm−2 Jsc from organic solar cells with a low-bandgap nonfullerene acceptor. *Sci. Bull.* 62, 1494–1497. doi: 10.1016/j.scib.2017.10.017

Xu, S., Wang, X., Feng, L., He, Z., Peng, H., Cimrová, V., et al. (2018). Optimizing the conjugated side chains of quinoxaline based polymers for nonfullerene solar cells with 10.5% efficiency. *J. Mater. Chem. A* 6, 3074–3083. doi: 10.1039/C7TA10262C

Xu, X., Bi, Z., Ma, W., Wang, Z., Choy, W. C. H., Wu, W., et al. (2017). Highly efficient ternary-blend polymer solar cells enabled by a nonfullerene acceptor and two polymer donors with a broad composition tolerance. *Adv. Mater.* 29:1704271. doi: 10.1002/adma.201704271

Yang, D., Yang, R., Ren, X., Zhu, X., Yang, Z., Li, C., et al. (2016). Hysteresis-suppressed high-efficiency flexible perovskite solar cells using solid-state ionic-liquids for effective electron transport. *Adv. Mater.* 28, 5206–5213. doi: 10.1002/adma.201600446

Yu, R., Zhang, S., Yao, H., Guo, B., Li, S., Zhang, H., et al. (2017). Two well-miscible acceptors work as one for efficient fullerene-free organic solar cells. *Adv. Mater.* 29:1700437. doi: 10.1002/adma.201700437

Yuan, J., Guo, W., Xia, Y., Ford, M. J., Jin, F., Liu, D., et al. (2017). Comparing the device physics, dynamics and morphology of polymer solar cells employing conventional PCBM and non-fullerene polymer acceptor N2200. *Nano Energy* 35, 251–262. doi: 10.1016/j.nanoen.2017.03.050

Zhang, G., Zhang, K., Yin, Q., Jiang, X. F., Wang, Z., Xin, J., et al. (2017). High-performance ternary organic solar cell enabled by a thick active layer containing a liquid crystalline small molecule donor. *J. Am. Chem. Soc.* 139, 2387–2395. doi: 10.1021/jacs.6b11991

Zhang, J., Zhao, Y., Fang, J., Yuan, L., Xia, B., Wang, G., et al. (2017). Enhancing performance of large-area organic solar cells with thick film via ternary strategy. *Small* 13:1700388. doi: 10.1002/smll.201700388

Zhang, Z., Qi, B., Jin, Z., Chi, D., Qi, Z., Li, Y., et al. (2014). Perylene diimides: a thickness-insensitive cathode interlayer for high performance polymer solar cells. *Energy Environ. Sci.* 7, 1966–1973. doi: 10.1039/c4ee00022f

Zhao, W., Li, S., Zhang, S., Liu, X., and Hou, J. (2017). Ternary polymer solar cells based on two acceptors and one donor for achieving 12.2% effciency. *Adv. Mater.* 29:1604059. doi: 10.1002/adma.201604059

Conflict of Interest Statement: The authors declare that the research was conducted in the absence of any commercial or financial relationships that could be construed as a potential conflict of interest.

frontiers in Chemistry

ORIGINAL RESEARCH
published: 01 May 2018
doi: 10.3389/fchem.2018.00147

Utilizing Benzotriazole and Indacenodithiophene Units to Construct Both Polymeric Donor and Small Molecular Acceptors to Realize Organic Solar Cells With High Open-Circuit Voltages Beyond 1.2 V

Ailing Tang[1], *Fan Chen*[1,2], *Bo Xiao*[1,2], *Jing Yang*[1,2], *Jianfeng Li*[1,2], *Xiaochen Wang*[1] *and Erjun Zhou*[1]*

[1] CAS Key Laboratory of Nanosystem and Hierarchical Fabrication, CAS Center for Excellence in Nanoscience, National Center for Nanoscience and Technology, Beijing, China, [2] University of Chinese Academy of Sciences, Beijing, China

OPEN ACCESS

Edited by:
Chuanlang Zhan,
Institute of Chemistry (CAS), China

Reviewed by:
Qiang Peng,
Sichuan University, China
Zhan'Ao Tan,
North China Electric Power University, China

***Correspondence:**
Erjun Zhou
zhouej@nanoctr.cn

Specialty section:
This article was submitted to Organic Chemistry, a section of the journal Frontiers in Chemistry

Received: 11 March 2018
Accepted: 16 April 2018
Published: 01 May 2018

Citation:
Tang A, Chen F, Xiao B, Yang J, Li J, Wang X and Zhou E (2018) Utilizing Benzotriazole and Indacenodithiophene Units to Construct Both Polymeric Donor and Small Molecular Acceptors to Realize Organic Solar Cells With High Open-Circuit Voltages Beyond 1.2 V. Front. Chem. 6:147. doi: 10.3389/fchem.2018.00147

Devolopment of organic solar cells with high open-circuit voltage (V_{OC}) and power conversion efficiency (PCE) simutaniously plays a significant role, but there is no guideline how to choose the suitable photovoltaic material combinations. In our previous work, we developed "the Same-Acceptor-Strategy" (SAS), by utilizing the same electron-accepting segment to construct both polymeric donor and small molecular acceptor. In this study, we further expend SAS to use both the same electron-accepting and electron-donating units to design the material combination. The p-type polymer of PIDT-DTffBTA is designed by inserting conjugated bridge between indacenodithiophene (IDT) and fluorinated benzotriazole (BTA), while the n-type small molecules of BTA*x* (x = 1, 2, 3) are obtained by introducing different end-capped groups to BTA-IDT-BTA backbone. PIDT-DTffBTA: BTA*x* (x = 1–3) based photovolatic devices can realize high V_{OC} of 1.21–1.37 V with the very small voltage loss (0.55–0.60 V), while only the PIDT-DTffBTA: BTA3 based device possesses the enough driving force for efficient hole and electron transfer and yields the optimal PCE of 5.67%, which is among the highest value for organic solar cells (OSCs) with a V_{OC} beyond 1.20 V reported so far. Our results provide a simple and effective method to obtain fullerene-free OSCs with a high V_{OC} and PCE.

Keywords: benzotriazole, indacenodithiophene, fullerene-free organic solar cells, high open-circuit voltage, non-fullerene acceptor

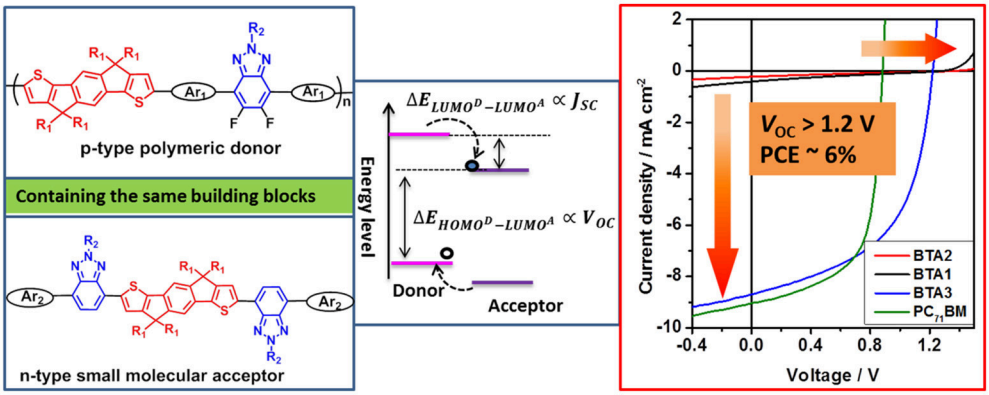

Graphical abstract |We applied a simple design concept to realize organic solar cells with ultrahigh open-circuit voltage beyond 1.2 V and power conversion efficiency of 5.67%, by utilizing the same building blocks of indacenodithiophene and benzotriazole to design both p-type polymeric donor and n-type small molecular acceptors.

INTRODUCTION

As one of the most promising technique in photoelectric conversion, bulk-heterojunction (BHJ) organic solar cells (OSCs) have been extensively studied. For a long time, fullerene derivatives have taken up the major part of the acceptor materials, benefited from their high electron affinity and electron mobility, as well as isotropic charge transport. (Guldi, 2000; von Hauff et al., 2005; Anthony et al., 2010; Eftaiha et al., 2014) It's not until the recent 2 years that non-fullerene small molecular acceptors (NFSMAs) with strong sunlight harvesting capability and tunable energy levels have drawn considerable attention and hundreds of novel NFSMAs have been developed (Hwang et al., 2015; Lin et al., 2015, 2016a,b; Zhong et al., 2015; Guo et al., 2016; Holliday et al., 2016; Li et al., 2016b, 2017; Wu et al., 2016; Duan et al., 2017a,b; Fan et al., 2017; Liu et al., 2017; Sun et al., 2017; Wang et al., 2017; Xiao B. et al., 2017a,b; Xu S. J. et al., 2017; Xu X. et al., 2017; Yang et al., 2017; Zhang G. et al., 2017; Zhang Z. G et al., 2017) To date, the power conversion efficiencies (PCEs) of the fullerene-free OSCs have reached up to 13%. (Xiao Z. et al., 2017a; Zhao et al., 2017). The short circuit current (J_{SC}) and fill factor (FF) in these efficient fullerene-free OSCs could arrive as high as 18–25 mA cm^{-2} and 60–70%, respectively. However, the open-circuit voltage (V_{OC}) values remain relatively low (<1.0 V), because of the large energy loss (E_{loss}) (Xiao Z. et al., 2017b).

Recently, by developing novel NFSMAs with high LUMO levels and choosing suitable p-type polymers, the resulted solar cells could realize high V_{OC} values of beyond 1.0 V (Yang et al., 2014; Yu et al., 2014; Zhang et al., 2015, 2016; Baran et al., 2016; Fu et al., 2016; Li et al., 2016a; Liu et al., 2016; Ni et al., 2016; Chen et al., 2017; Ding et al., 2017; Xiao B. et al., 2017a; Zhan et al., 2017; Zhang Y. et al., 2017). In fact, there is always a problematic trade-off between J_{SC} and V_{OC}. Thus, very limited devices could simultaneously realize a high V_{OC} of beyond 1.2 V and a high PCE (As shown in **Figure 1**) (Fu et al., 2016; Xiao B. et al., 2017a; Zhan et al., 2017; Zhang Y. et al., 2017). For example, Xie et al. reported that the OSCs containing poly(3-hexylthiophene) (P3HT) as electron donor and the oligomer F4TBT4 with four repeated fluorene and di-2-thienyl benzothiadiazole units as electron acceptor can output a high V_{OC} above 1.2 V and a PCE of 4.12% (Fu et al., 2016). Our group synthesized a novel benzotriazole based acceptor, BTA2, which showed a high V_{OC} of 1.22 V with an acceptable PCE of 4.5% with P3HT as donor (Xiao B. et al., 2017a). Recently, a pyrene-fused perylene diimide acceptor synthesized by Li and Sun et al. can achieve a high V_{OC} of 1.21 V with a PCE of 5.10%, with the wide-bandgap polymer PBT1-EH as the donor (Zhan et al., 2017). Zhang et al. reported a combination of perylene monoimide (PMI)-based electron acceptor and a wide-bandgap polymer of PTZ1, which demonstrated a very high V_{OC} of 1.3 V with a PCE of 6% (Zhang Y. et al., 2017). However, in the above-cases, they used a trial-and-error procedure and there is no guideline how to choose suitable p-type polymer and n-type NFSMA combination to realize such a high V_{OC} and PCE simultaneously. Thus, finding a promising strategy to achieve a high V_{OC} without sacrificing the other impact factors is essential for practical application. Furthermore, this kind of OSCs with a high V_{OC} can also be used as a sub cell in the tandem devices to offer opportunities to realize a high V_{OC} beyond 2.0 V (Xu et al., 2018), which will supply high enough voltage for solar-energy-driven water splitting (Walter et al., 2010; Luo et al., 2014).

Based on the molecular orbital theory, for donor-acceptor (D-A)-type conjugated materials, the highest occupied molecular orbital (HOMO) and the lowest unoccupied molecular orbital (LUMO) energy level are mainly decided by the electron-donating and electron-withdrawing segments respectively. Thus, it may realize the close molecular energy levels by utilizing the same building blocks to build both donor and acceptor materials. By further slightly modulating the chemical structures, the enough LUMO-LUMO and HOMO-HOMO offsets could be realized to guarantee sufficient driving force for efficient hole and electron transfer and simultaneously result in an ultra-large Voc. In our previous work, we used "the Same-Acceptor-Strategy" (SAS), both p-type polymer of J61 and n-type small molecule of

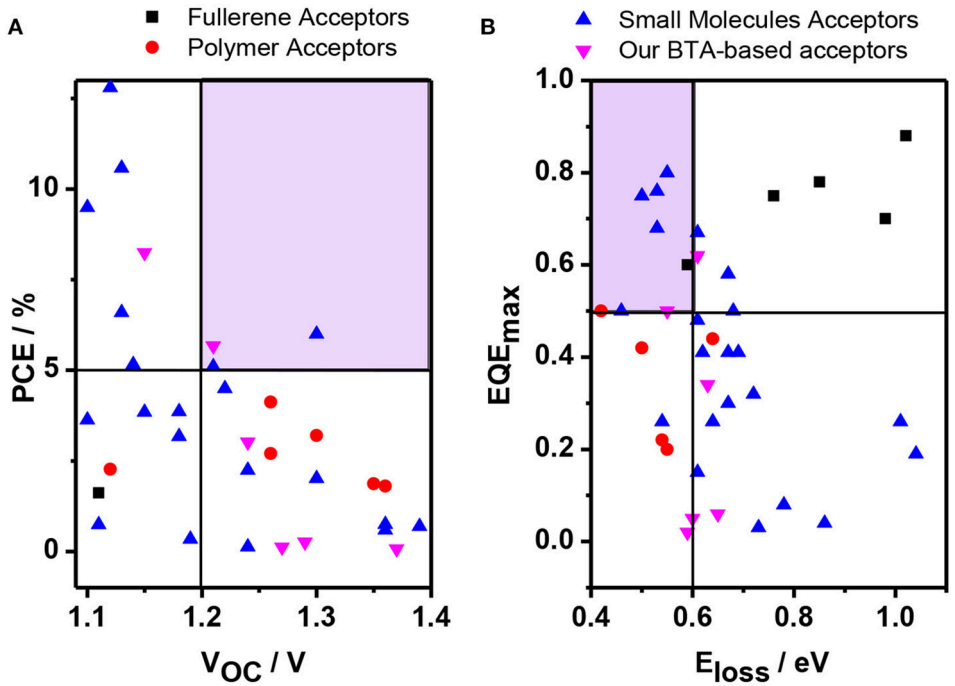

FIGURE 1 | (A) Plots of PCE against V_{OC} as well as **(B)** EQE_{max} against E_{loss} in various OSCs with fullerene and non-fullerene acceptors with the V_{OC} > 1.1 V. The according references were shown in Supporting Information.

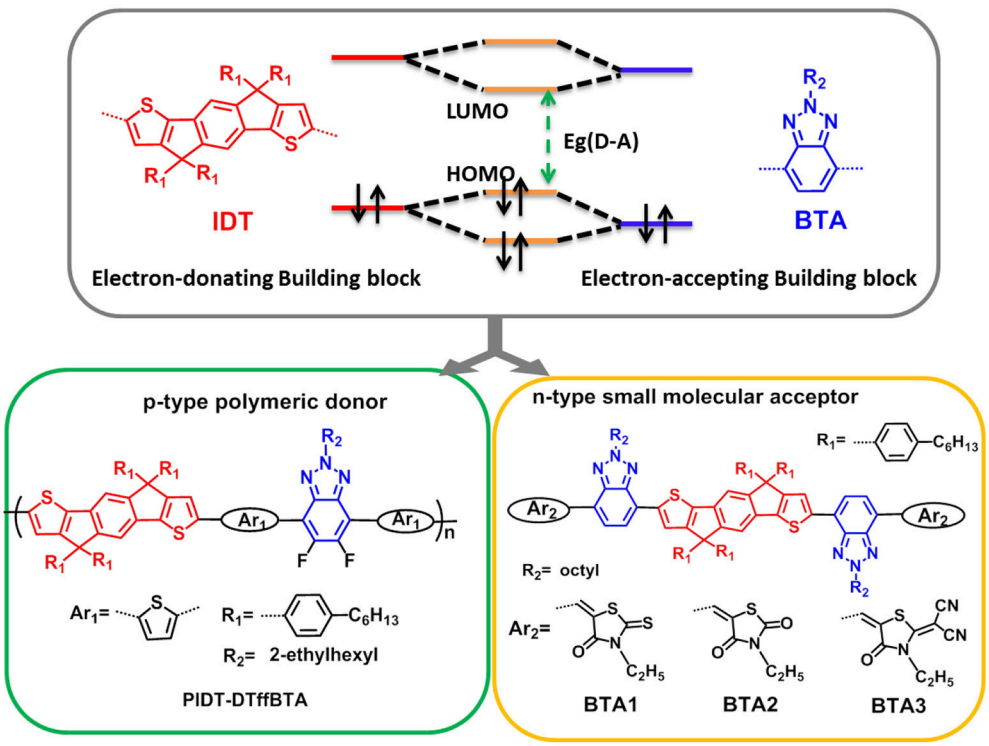

FIGURE 2 | The basic design strategy of the photovoltaic materials containing the same electron-donating and accepting building blocks.

BTA3 contain the same electron-accepting unit of BTA, which could realize a high *Voc* of 1.15 V (Tang et al., 2017). In this paper, we further adopted this feasible strategy and chose the classic electron-donating unit of indacenodithiophene (IDT) and electron-accepting segment of benzotriazole (BTA) to construct the polymer donor and small molecular acceptors. The donor-acceptor (D-A) type copolymer of PIDT-DTffBTA, as shown in **Figure 2**, containing IDT as the donor unit and difluoro-substituted BTA as the acceptor unit and thiophene as π-bridge, was designed as the polymer donor. In addition, we utilized IDT and BTA to construct the conjugated backbone of the small molecular acceptors and fine-tuned the electron-withdrawing end-capped units to adjust their energy levels. In our previous work, we have proved that the energy levels of BTA-based small molecules could be fine-tuned and OSCs based P3HT: BTA1 (Xiao B. et al., 2017b), P3HT: BTA2 (Xiao B. et al., 2017a), and J61: BTA3 (Tang et al., 2017) could realize relatively higher V_{OC} of 1.02, 1.22, and 1.15 V, respectively.

Here, as expected, these devices based on PIDT-DTffBTA: BTA*x* (x = 1–3) as acceptors exhibited the reduced energy loss below 0.60 eV and the according V_{OC} in the range of 1.21–1.37 V were higher by nearly 0.3–0.5 V than that of [6,6]-phenyl-C_{71}-butyric acid methyl ester ($PC_{71}BM$) based device. Differently, the BTA2 and BTA1 based devices showed poor J_{SC} below 0.4 mA cm^{-2} while BTA3 gave a dramatically increased J_{SC} of 8.68 mA cm^{-2}. It is remarkable that the achieved PCE of 5.67% in BTA3 based device is among the highest values for OSCs with a V_{OC} beyond 1.20 V reported so far. Our results provide a simple and feasible method to design both p-type and n-type photovoltaic materials for OSCs with high V_{OC} and PCE.

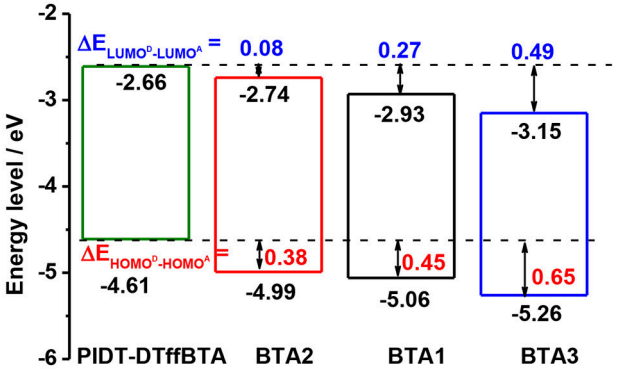

FIGURE 3 | The simulated frontier molecular orbitals obtained by DFT calculation at B3LYP/6-31G(d) level.

RESULTS AND DISCUSSION

Theoretical Calculation

Calculations with density functional theory (DFT) at the B3LYP/6-31G(d) level are firstly performed to compare the energy levels of these photovoltaic molecules. The polymers were replaced with the dimers of the repeating units and the long alkyls were replaced with methyl groups to simplify the calculations. As shown in **Figure 3**, the calculted LUMO/HOMO levels of PIDT-DTffBTA and BTA*x* (x = 1, 2, 3) are −2.66/−4.61, −2.93/−5.06, −2.74/−4.99, and −3.15/−5.26 eV, respectively. The LUMO offsets between PITD-DTffBTA and three acceptors (BTA2, BTA1 and BTA3) ($\Delta E_{LUMO^D-LUMO^A}$) are calculated to be 0.08, 0.27, and 0.49 eV, respectively, and the according HOMO offsets ($\Delta E_{HOMO^D-HOMO^A}$) are 0.38, 0.45, 0.65 eV, respectively. These results reveal that utilizing the same building blocks to construct both p-type polymeric donor and n-type small molecular acceptors has the potential to realize similar LUMO levels and give rise to high voltage. Modulating the end-capped units can help optimize the energy offsets to achieve the enough driving force for charge transfer and produce high photocurrent.

Synthesis

The synthetic routes of the photovoltaic materials are depicted in Scheme S1. PIDT-DTffBTA was synthesized by Stille-coupling reaction between 4,7-bis-(5-bromothiophen-2-yl)-5,6-difluoro-2-octyl-2H-benzotriazole and (4,4,9,9-tetrakis(4-hexylphenyl)-4,9-dihydro-s-indaceno [1,2-b:5,6-b']dithiophene-2,7-diyl)bis(trimethylstannane). BTA*x* were synthesized by Stille-coupling reaction and a Knoevenagel condensation with a yield of 70–80%. The number-average molecular weight (M_n) and polydispersity index (PDI) value of PIDT-DTffBTA are 62.8 kDa and 1.55, respectively, determined by gelpermeation chromatography (GPC) (see Figure S1). The temperature with the 5% weight loss (T_d) of BTA*x* (x = 1–3) are 386, 405, and 396°C, respectively, measured with thermogravimetric analysis (TGA) (Figure S2). All the materials are soluble in common organic solvents, such as chloroform (CF), chlorobenzene (CB), and *o*-dichlorobenzene (*o*-DCB).

Optical Properties

The UV–vis absorption spectra of the donor and acceptors in solution and films are shown in Figure S3 and **Figure 4A**, respectively, and their absorption characteristics are summarized in Table S1. The absorption of the BTA2 overlaps with that of PIDT-DTffBTA. The maximum absorption peaks red-shifts as the increase of the electron-withdrawing properties of the end-capped units. As a result, the absorption of BTA1 and BTA3 become more and more complementary to that of PITD-DTBTA, which would allow for an improved J_{SC} compared to BTA2 based devices. The optical band gaps (E_g^{opt}) of PIDT-DTffBTA and BTA*x* (x = 2, 1, 3) calculated from the film absorption onsets are ca. 1.96, 2.00, 1.87, 1.76 eV, respectively.

The molecular energy levels of these four materials are determined by electrochemical cyclic voltammetry (CV, **Figure 4B**). The according results are listed in Table S1. Calculated with their onset oxidation potentials, the HOMO levels of PIDT-DTffBTA and BTA*x* (x = 2, 1, 3) are −5.34, −5.43, −5.46, and −5.49 eV, respectively. The LUMO levels are estimated to be −3.38, −3.43, −3.59, and −3.73 eV, respectively, by adding the optical bandgap to their HOMO levels. $\Delta E_{HOMO^D-HOMO^A}$ between the donor and the acceptors (BTA2, 1, 3) are 0.09, 0.12, 0.15 eV, respectively, and $\Delta E_{LUMO^D-LUMO^A}$ are respectively 0.05, 0.21, 0.35 eV. As expected, the very small $\Delta E_{LUMO^D-LUMO^A}$ produce the ultar-high offsets between the

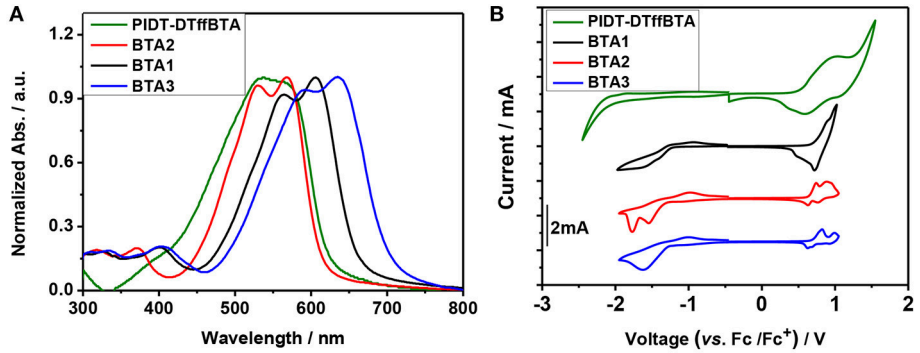

FIGURE 4 | (A) The UV–vis absorption spectra of the pure films. **(B)** The CV curves of the four materials.

HOMO level of the donor and the LUMO level of the acceptor, giving a chance to achieve the ultra-hight V_{OC} (Armstrong et al., 2009).

Photovoltaic Device Performance

To investigate the photovoltaic properties, photovoltaic devices are fabricated with a conventional device configuration of indium tin oxide (ITO)/ poly(3,4-ethylenedioxythiophene): poly(styrenesulfonate)(PEDOT:PSS)/PIDT-DTffBTA: BTAx (x = 1–3)/Ca/Al. The optimized photovoltaic characteristics are listed in **Table 1** and the optimal current density–voltage (J–V) curves and the corresponding external quantum efficiency (EQE) spectra are displayed in **Figure 5**. The detail optimization conditions are shown in Tables S2–S7. The device using the PIDT-DTffBTA: BTA1 and PIDT-DTffBTA: BTA2 blend (1:1 in wt %) with thermal annealing show nearly no performance with a PCE of 0.12 and 0.07%, respectively, which is likely due to their very high-lying LUMO, resulting in insufficient charge transfer from polymer to acceptor. Under the same conditions, the BTA3-based device (1:3 in wt %) exhibits improved solar cell performance with a PCE of 2.61%, which may be attributed to the decreased LUMO level. After solvent annealing, the devices using PIDT-DTffBTA: BTA3 show the highest PCE of 5.67% with the increased FF and J_{SC}. It has been seen that after solvent annealing, the strong aggregation (Figure S4) can enhance domain purity and further improve charge transport in the active layer (see farther below), giving rise to the improved J_{SC} and FF.

As expected, all of the three devices show high V_{OC} (> 1.2 V), which are much higher than that of PIDT-DTffBTA: $PC_{71}BM$ ([6,6]-phenyl C_{71} butyric acid methyl ester) based device (V_{OC} = 0.88 V) and PIDT-DTffBTA: ITIC based device (V_{OC} = 0.94 V). The V_{OC} of the devices increase from 1.21, 1.27 to 1.37 V in the order of BTA3, BTA1, and BTA2. The energy loss values for the OSCs of PIDT-DTffBTA: BTAx (x = 2, 1, 3) are calculated to be 0.59, 0.60, and 0.55 eV, respectively, which is a result of the high V_{OC}. Interestingly, the J_{SC} for PIDT-DTffBTA: BTA2 and PIDT-DTffBTA: BTA1 based devices are very low (<0.5 mA cm^2), while the one for PIDT-DTffBTA:BTA3 based device dramatically reaches up to 8.68 mA cm^{-2}, close to the value in PIDT-DTffBTA: $PC_{71}BM$ based device (9.06 mA cm^{-2}). Accordingly, the maximum EQE values of PIDT-DTffBTA: BTA2 and PIDT-DTffBTA: BTA1 based devices are below 5%, while the one of PIDT-DTffBTA: BTA3 based device reaches up to 50%. The according current density obtained by the integration of the EQE curves are 0.24, 0.54, 8.85 mA cm^{-2}, respectively, which are consistent with the J_{SC} values from the J–V curves within 5% error. Therefore, the OSCs based on PIDT-DTffBTA: BTA3 exhibits the best performance with a maximal PCE of 5.67%, which is among the highest values reported in the literature to date for NF OSCs with V_{OC} >1.20V.

To study the cause of the different J_{SC}, we first investigate the exciton generation and separation by measuring the photoluminescence (PL) in these blends. As shown in **Figure 6A**, at the excitation wavelength of 480 nm, emission from the blend with BTA2 is close to the emission of the pristine PIDT-DTffBTA film and the PL quenching efficiency is only 16% (Li Z. et al., 2016). The inefficient quenching of PL indicates the excitons quick recombination rather than efficient separation. The shape of PL from the blend with BTA1 is close to the emission of the pristine BTA1 film but the polymer PL quenching efficiency significantly raises up to 88%, indicating that excitons initially generated on the PIDT-DTffBTA can transfer to BTA1 in high yield but they are inefficiently quenched by the heterojunction (Hoke et al., 2013). Considering the fine film morphology (as shown in **Figure 7**), the inefficient quenching of PL in PIDT-DTffBTA:BTA2 and PIDT-DTffBTA:BTA1 is owing to the too small $\Delta E_{LUMO^D-LUMO^A}$ (0.05 eV) and $\Delta E_{HOMO^D-HOMO^A}$ (0.12 eV), respectively. The too small energy offsets could reduce the overall exciton dissociation efficiency and create exergonic pathways for charge recombination of holes in PIDT-DTffBTA or electrons in BTA1, obviously increasing the voltage loss. As the increase of $\Delta E_{LUMO^D-LUMO^A}$ and $\Delta E_{HOMO^D-HOMO^A}$, the driving force for the hole and electron tranfer are obviously improved. Hence, BTA1 shows similar results with BTA2 but BTA3 can completely quench the PL of PIDT-DTffBTA with a quenching efficiency of ~100% and the luminous efficiency of BTA3 in the blend is as low as 25%, as shown in **Figures 6B,C**. The high PL quenching efficiency of both PIDT-DTffBTA and BTA3 suggests the improved electron and hole transfer in BTA3-based devices, which can partially explain its high photocurrent. Though J_{SC} and FF can be improved, they still below 9 mA/cm^2 and 0.60, respectively, which may be attributed to

TABLE 1 | The photovoltaic characteristics of the PIDT-DTffBTA based OSCs.

Acceptors	V_{OC} [V]	J_{SC} [mA cm^{-2}]	FF	PCE [%]	μ_h [cm^2 V^{-1} s^{-1}]	μ_e [cm^2 V^{-1} s^{-1}]
BTA2	1.37 1.34 ± 0.02	0.21 0.21 ± 0.03	0.23 0.23 ± 0.02	0.07 0.065 ± 0.01	3.50×10^{-5}	2.43×10^{-7}
BTA1	1.27 1.27 ± 0.02	0.43 0.42 ± 0.00	0.22 0.22 ± 0.001	0.12 0.12 ± 0.00	4.96×10^{-5}	4.21×10^{-7}
BTA3	1.21 1.21 ± 0.00	8.68 8.69 ± 0.09	0.54 0.53 ± 0.01	5.67 5.63 ± 0.02	1.21×10^{-4}	1.12×10^{-5}
$PC_{71}BM$	0.88 0.88 ± 0.01	9.04 8.88 ± 0.12	0.63 0.63 ± 0.01	5.01 4.93 ± 0.06	–	–
ITIC	0.94 0.945 ± 0.01	9.96 9.67 ± 0.06	54.04 53.65 ± 0.24	5.06 4.90 ± 0.03	–	–

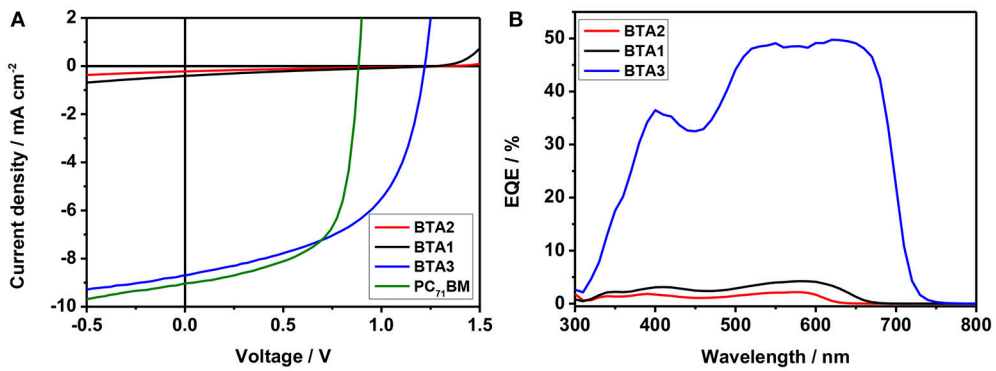

FIGURE 5 | (A) *J-V* curves and **(B)** EQE curves of the optimal devices under the illumination of AM 1.5 G, 100 mW cm^{-2}.

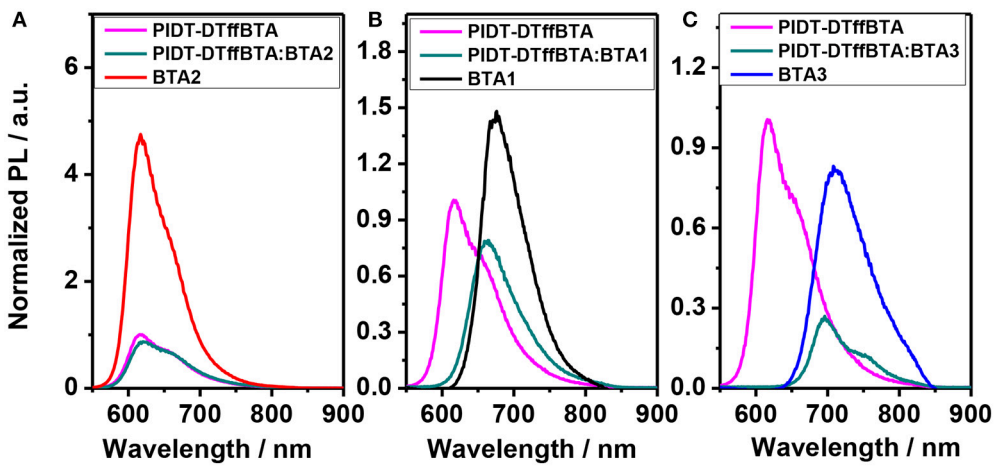

FIGURE 6 | The photoluminescence spectra of neat PIDT-DTffBTA, acceptor films and BHJ blend films with the D/A ratio of 1:1: **(A)** BTA2; **(B)** BTA1; **(C)** BTA3. Note: all the films are excited at 480 nm.

its incomplete fluorescence quenching of BTA3, resulting in the modest hole transfer from BTA3 to polymer. Besides, time resolved photoluminescence measurements were also performed on neat and blended films with the same excited wavelength (Figure S5). All the time-resolved PL (TRPL) lifetime data fitted with bi-exponential decay model are summarized in **Table 2**. The fast decay is related to the exciton dissociation due to charge transfer at the donor/acceptor interfaces. The little changes in τ and f for the PIDT-DTffBTA:BTA2 and PIDT-DTffBTA:BTA1 blend films can be attributed to the poor exciton separation arising from the limitation of the small driving force. Moreover, the exciton lifetimes of PIDT-DTffBTA:BTA3 based blend film

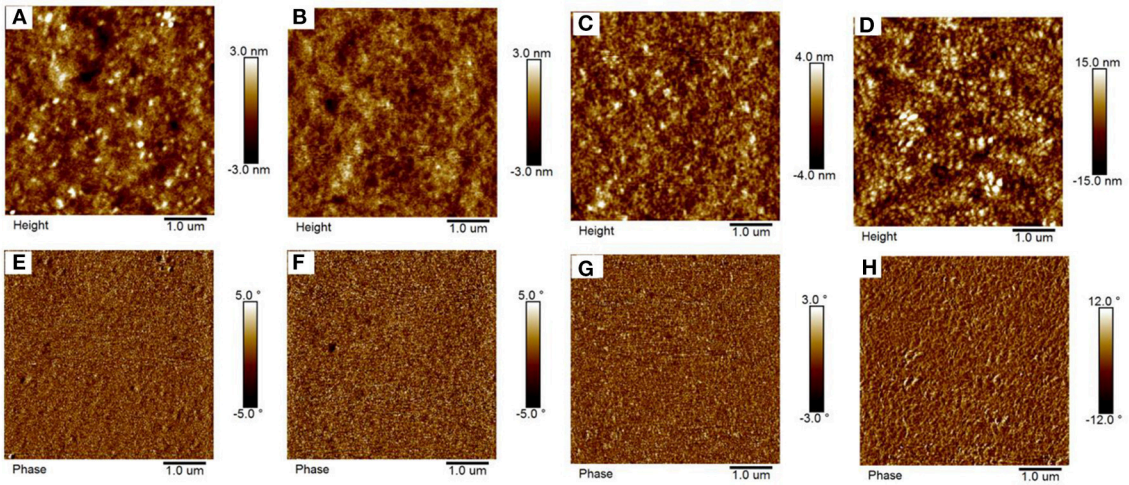

FIGURE 7 | (A–C) The height images for the PIDT-DTffBTA:BTA2, PIDT-DTffBTA:BTA1, and PIDT-DTffBTA:BTA3 blend films without solvent annealing, respectively; **(E–G)** The phase images for the PIDT-DTffBTA:BTA2, PIDT-DTffBTA:BTA1, and PIDT-DTffBTA:BTA3 blend films without solvent annealing, respectively; **(D,H)** Is the height and phase images for the PIDT-DTffBTA:BTA3 blend films with solvent annealing, respectively.

TABLE 2 | Fitting parameters of PL decay dynamics of the various films with excitation at 450 nm.

Films	τ_1 [ps]	f_1 [%]	τ_2 [ns]	f_2 [%]
PIDT-DTffBTA	402	98.84	6.01	1.16
BTA1	565	98.66	5.69	1.34
BTA2	432	96.13	2.53	3.87
BTA3	807	94.94	4.26	5.06
PIDT-DTffBTA:BTA1	432	95.60	3.28	4.40
PIDT-DTffBTA:BTA2	426	97.83	4.92	2.17
PIDT-DTffBTA:BTA3	317	93.44	3.16	6.56

is clearly quenched as compared to neat films, suggesting both efficient hole and electron transfer at the donor/acceptor interface. Compared to the other two control device, the well improved exciton dissociation efficiency may explain part of the remarkably increased J_{SC} in the PIDT-DTffBTA:BTA3 based device. The PL quenching behavior of the TRPL measurements agrees well with the steady-state PL measurements discussed above.

Atom force microscope (AFM) is performed to investigate if the surface morphologies of the blend films play a role in the different J_{SC} and FF. As shown in the height images (**Figures 7A–C**), the PIDT-DTffBTA:BTA2, PIDT-DTffBTA: BTA1, and PIDT-DTffBTA: BTA3 based films without solvent annealing exhibit smooth and uniform surface morphologies with small root-mean-square roughness (RMS) of 0.95, 0.79, and 0.87 nm, respectively. Interestingly, the RMS in PIDT-DTffBTA: BTA3 based film increases up to 5.29 nm after solvent annealing (**Figure 7D**), which may be a result of the enhanced intermolecular aggregation effect (Figure S4) (Zhong et al., 2017) and increased crystallinity of BTA3 in the blend films (Figure S6) (Li et al., 2013). As shown in the phase images (**Figures 7E–G**), it is clear that all of the blend films exhibit interpenetrating networks with different domain sizes. The three blends of PIDT-DTffBTA: BTAx ($x = 1$–3) without solvent annealing show thinner domain sizes below 10 nm. While the blend of PIDT-DTffBTA and BTA3 shows the sufficient phase separation behavior with the domain size of 40–50 nm after solvent annealing (**Figure 7H**), which is beneficial to the efficient charge separation and transport, giving rise to the reduced recombination loss and improved J_{SC} and FF.

At last, the space charge limited current (SCLC) method is applied to measure the carriers mobilities (Figure S7). As listed in **Table 1**, the carriers mobilities observed in both PIDT-DTffBTA: BTA2 and PIDT-DTffBTA: BTA1 based devices are very low, on the order of only 10^{-5} cm^2 V^{-1} s^{-1} for hole mobility (μ_h) and 10^{-7} cm^2 V^{-1} s^{-1} for electron mobility (μ_e). These low and imbalance mobilities could result in the low FF observed in these devices (Earmme et al., 2013; Meng et al., 2015). The μ_h of BTA3 based device is 3–6 times higher than that of two other devices while the μ_e is higher about 2 order of magnitude, which is attributed to the dominant face-on orientation (Figure S6). As a result, the transport of holes and electrons in the PIDT-DTffBTA: BTA3 based device is faster and more balanced, which can effectively prevent the accumulation of charge and achieve higher FF and J_{SC}.

CONCLUSIONS

In this work, we applied a new design concept to construct the OSCs with ultrahigh V_{OC}, utilizing the same building blocks (indacenodithiophene and benzotriazole) to design both p-type polymeric donor and n-type small molecular acceptors. The resulted non-fullerene acceptors showed high-lying LUMO levels, close to that of the donor polymer. With small voltage loss

(0.55–0.60 V), all of the three devices show ultra-high V_{OC} (1.21–1.37 V). With the increase of the ability of attracting electron of acceptor, PIDT-DTffBTA: BTA3 device possesses the large driving force for efficient electron and hole transfer and yields a dramatically increased J_{SC}. The achieved PCE of 5.67% is among the highest values for NF OSCs with a V_{OC} >1.20 V reported so far (as shown in Table S8). The results here offer a new method to construct the promising OSCs with ultra-high V_{OC}, which could contribute to further improve the performance of the OSCs.

AUTHOR CONTRIBUTIONS

Device fabrication and photovoltaic performance studies were carried out by AT and JY. Materials synthesis was carried out by BX and JL. EZ, FC, and XW contributed to project planning and discussions. EZ had the idea, led the project, and prepared the manuscript. All authors contributed to the manuscript preparation.

ACKNOWLEDGMENTS

This work is supported by the National Natural Science Foundation of China (Nos. 21602040, 51473040, 51673048, 21504019, 51773046), the National Natural Science Foundation of Beijing (No. 2162045), the Chinese Academy of Sciences (QYZDB-SSW-SLH033) and the National Key Research and Development Program of China (2017YFA0206600).

SUPPLEMENTARY MATERIAL

The Supplementary Material for this article can be found online at: https://www.frontiersin.org/articles/10.3389/fchem.2018.00147/full#supplementary-material

REFERENCES

Anthony, J. E., Facchetti, A., Heeney, M., Marder, S. R., and Zhan, X. (2010). N-type organic semiconductors in organic electronics. *Adv. Mater.* 22, 3876–3892. doi: 10.1002/adma.200903628

Armstrong, N. R., Veneman, P. A., Ratcliff, E., Placencia, D., and Brumbach, M. (2009). Oxide contacts in organic photovoltaics: characterization and control of near-surface composition in indium– tin oxide (Ito) electrodes. *Acc. Chem. Res.* 42, 1748–1757. doi: 10.1021/ar900096f

Baran, D., Kirchartz, T., Wheeler, S., Dimitrov, S., Abdelsamie, M., Gorman, J., et al. (2016). Reduced voltage losses yield 10% and >1v fullerene free organic solar cells. *Energy Environ. Sci.* 9, 3783–3793. doi: 10.1039/C6EE02598F

Chen, S., Liu, Y., Zhang, L., Chow, P. C. Y., Wang, Z., Zhang, G., et al. (2017). A wide-bandgap donor polymer for highly efficient non-fullerene organic solar cells with a small voltage loss. *J. Am. Chem. Soc.* 139, 6298–6301. doi: 10.1021/jacs.7b01606

Ding, Z., Long, X., Meng, B., Bai, K., Dou, C., Liu, J., et al. (2017). Polymer solar cells with open-circuit voltage of 1.3 V using polymer electron acceptor with high lumo level. *Nano Energy* 32, 216–224. doi: 10.1016/j.nanoen.2016.12.041

Duan, Y., Xu, X., Li, Y., Li, Z., and Peng, Q. (2017a). Chalcogen-atom-annulated perylene diimide trimers for highly efficient nonfullerene polymer solar cells. *Macromol. Rapid Commun.* 38:1700405. doi: 10.1002/marc.201700405

Duan, Y., Xu, X., Yan, H., Wu, W., Li, Z., and Peng, Q. (2017b). Pronounced effects of a triazine core on photovoltaic performance-efficient organic solar cells enabled by a Pdi trimer-based small molecular acceptor. *Adv. Mater.* 29:1605115. doi: 10.1002/adma.201605115

Earmme, T., Hwang, Y.-J., Murari, N. M., Subramaniyan, S., and Jenekhe, S. A. (2013). All-polymer solar cells with 3.3% efficiency based on naphthalene diimide-selenophene copolymer acceptor. *J. Am. Chem. Soc.* 135, 14960–14963. doi: 10.1021/ja4085429

Eftaiha, A. F., Sun, J. P., Hill, I. G., and Welch, G. C. (2014). Recent advances of non-fullerene, small molecular acceptors for solution processed bulkheterojunction solar cells. *J. Mater. Chem. A* 2, 1201–1213. doi: 10.1039/C3TA14236A

Fan, B., Ying, L., Wang, Z., He, B., Jiang, X.-F., Huang, F., et al. (2017). Optimisation of processing solvent and molecular weight for the production of green-solvent-processed all-polymer solar cells with a power conversion efficiency over 9%. *Energy Environ. Sci.* 10, 1243–1251. doi: 10.1039/C7EE00619E

Fu, Y., Wang, B., Qu, J., Wu, Y., Ma, W., Geng, Y., et al. (2016). Fullerene-free polymer solar cells with open-circuit voltage above 1.2 V: tuning phase separation behavior with oligomer to replace polymer acceptor. *Adv. Funct. Mater.* 26, 5922–5929. doi: 10.1002/adfm.201601880

Guldi, D. M. (2000). Fullerenes: three dimensional electron acceptor materials. *Chem. Commun.* 33, 321–327. doi: 10.1039/a907807j

Guo, Y., Li, Y., Awartani, O., Zhao, J., Han, H., Ade, H., et al. (2016). A vinylene-bridged perylenediimide-based polymeric acceptor enabling efficient all-polymer solar cells processed under ambient conditions. *Adv. Mater.* 28, 8483–8489. doi: 10.1002/adma.201602387

Hoke, E. T., Vandewal, K., Bartelt, J. A., Mateker, W. R., Douglas, J. D., Noriega, R., et al. (2013). Recombination in polymer:fullerene solar cells with open-circuit voltages approaching and exceeding 1.0 V. *Adv. Energy Mater.* 3, 220–230. doi: 10.1002/aenm.201200474

Holliday, S., Ashraf, R. S., Wadsworth, A., Baran, D., Yousaf, S. A., Nielsen, C. B., et al. (2016). High-efficiency and air-stable P3ht-based polymer solar cells with a new non-fullerene acceptor. *Nat. Commun.* 7:11585. doi: 10.1038/ncomms11585

Hwang, Y.-J., Courtright, B. A., Ferreira, A. S., Tolbert, S. H., and Jenekhe, S. A. (2015). 7.7% efficient all-polymer solar cells. *Adv. Mater.* 27, 4578–4584. doi: 10.1002/adma.201501604

Li, S., Liu, W., Shi, M., Mai, J., Lau, T.-K., Wan, J., et al. (2016a). A spirobifluorene and diketopyrrolopyrrole moieties based non-fullerene acceptor for efficient and thermally stable polymer solar cells with high open-circuit voltage. *Energy Environ. Sci.* 9, 604–610. doi: 10.1039/C5EE03481G

Li, S., Ye, L., Zhao, W., Zhang, S., Mukherjee, S., Ade, H., et al. (2016b). Energy-level modulation of small-molecule electron acceptors to achieve over 12% efficiency in polymer solar cells. *Adv. Mater.* 28, 9423–9429. doi: 10.1002/adma.201602776

Li, W., Hendriks, K. H., Furlan, A., Roelofs, W. S., Wienk, M. M., and Janssen, R. A. (2013). Universal correlation between fibril width and quantum efficiency in diketopyrrolopyrrole-based polymer solar cells. *J. Am. Chem. Soc.* 135, 18942–18948. doi: 10.1021/ja4101003

Li, X., Yan, T., Bin, H., Han, G., Xue, L., Liu, F., et al. (2017). Insertion of double bond π-bridges of A-D-A acceptor for high performance near-infrared polymer solar cells. *J. Mater. Chem. A* 5, 22588–22597. doi: 10.1039/C7TA07049G

Li, Z., Xu, X., Zhang, W., Meng, X., Ma, W., Yartsev, A., et al. (2016). High performance all-polymer solar cells by synergistic effects of fine-tuned crystallinity and solvent annealing. *J. Am. Chem. Soc.* 138, 10935–10944. doi: 10.1021/jacs.6b04822

Lin, Y., He, Q., Zhao, F., Huo, L., Mai, J., Lu, X., et al. (2016a). A facile planar fused-ring electron acceptor for as-cast polymer solar cells with 8.71% efficiency. *J. Am. Chem. Soc.* 138, 2973–2976. doi: 10.1021/jacs.6b00853

Lin, Y., Wang, J., Zhang, Z. G., Bai, H., Li, Y., Zhu, D., et al. (2015). An electron acceptor challenging fullerenes for efficient polymer solar cells. *Adv. Mater.* 27, 1170–1174. doi: 10.1002/adma.201404317

Lin, Y., Zhao, F., He, Q., Huo, L., Wu, Y., Parker, T. C., et al. (2016b). High-performance electron acceptor with thienyl side chains for organic photovoltaics. *J. Am. Chem. Soc.* 138, 4955–4961. doi: 10.1021/jacs.6b02004

Liu, J., Chen, S., Qian, D., Gautam, B., Yang, G., Zhao, J., et al. (2016). Fast charge separation in a non-fullerene organic solar cell with a small driving force. *Nat. Energy* 1:16089. doi: 10.1038/nenergy.2016.89

Liu, Y., Zhang, Z., Feng, S., Li, M., Wu, L., Hou, R., et al. (2017). Exploiting noncovalently conformational locking as a design strategy for high performance fused-ring electron acceptor used in polymer solar cells. *J. Am. Chem. Soc.* 139, 3356–3359. doi: 10.1021/jacs.7b00566

Luo, J., Im, J.-H., Mayer, M. T., Schreier, M., Nazeeruddin, M. K., Park, N.-G., et al. (2014). Water photolysis at 12.3% efficiency via perovskite photovoltaics and earth-abundant catalysts. *Science* 345, 1593–1596. doi: 10.1126/science.1258307

Meng, D., Sun, D., Zhong, C., Liu, T., Fan, B., Huo, L., et al. (2015). High-performance solution-processed non-fullerene organic solar cells based on selenophene-containing perylene bisimide acceptor. *J. Am. Chem. Soc.* 138, 375–380. doi: 10.1021/jacs.5b11149

Ni, W., Li, M., Kan, B., Liu, F., Wan, X., Zhang, Q., et al. (2016). Fullerene-free small molecule organic solar cells with a high open circuit voltage of 1.15 V. *Chem. Commun.* 52, 465–468. doi: 10.1039/C5CC07973J

Sun, H., Song, X., Xie, J., Sun, P., Gu, P., Liu, C., et al. (2017). Pdi derivative through fine-tuning the molecular structure for fullerene-free organic solar cells. *ACS Appl. Mater. Interfaces* 9, 29924–29931. doi: 10.1021/acsami.7b08282

Tang, A., Xiao, B., Wang, Y., Gao, F., Tajima, K., Bin, H., et al. (2017). Simultaneously achieved high open-circuit voltage and efficient charge generation by fine-tuning charge-transfer driving force in non-fullerene polymer solar cells. *Adv. Func. Mater.* 28:1704507. doi: 10.1002/adfm.201704507

von Hauff, E., Dyakonov, V., and Parisi, J. (2005). Study of field effect mobility in pcbm films and P3ht:Pcbm blends. *Sol. Energy Mater. Sol. Cells* 87, 149–156. doi: 10.1016/j.solmat.2004.06.014

Walter, M. G., Warren, E. L., McKone, J. R., Boettcher, S. W., Mi, Q., Santori, E. A., et al. (2010). Solar water splitting cells. *Chem. Rev.* 110, 6446–6473. doi: 10.1021/cr1002326

Wang, W., Yan, C., Lau, T. K., Wang, J., Liu, K., Fan, Y., et al. (2017). Fused hexacyclic nonfullerene acceptor with strong near-infrared absorption for semitransparent organic solar cells with 9.77% efficiency. *Adv. Mater.* 29:1701308. doi: 10.1002/adma.201701308

Wu, Q., Zhao, D., Schneider, A. M., Chen, W., and Yu, L. (2016). Covalently bound clusters of alpha-substituted PDI—rival electron acceptors to fullerene for organic solar cells. *J. Am. Chem. Soc.* 138, 7248–7251. doi: 10.1021/jacs.6b03562

Xiao, B., Tang, A., Yang, J., Wei, Z., and Zhou, E. (2017a). P3ht-based photovoltaic cells with a high Voc of 1.22 V by using a benzotriazole-containing nonfullerene acceptor end-capped with thiazolidine-2,4-dione. *ACS Macro Lett.* 6, 410–414. doi: 10.1021/acsmacrolett.7b00097

Xiao, B., Tang, A., Zhang, J., Mahmood, A., Wei, Z., and Zhou, E. (2017b). Achievement of high Voc of 1.02 V for P3ht-based organic solar cell using a benzotriazole-containing non-fullerene acceptor. *Adv. Energy Mater.* 7:1602269. doi: 10.1002/aenm.201602269

Xiao, Z., Jia, X., and Ding, L. (2017a). Ternary organic solar cells offer 14% power conversion efficiency. *Sci. Bull.* 62, 1562–1564. doi: 10.1016/j.scib.2017.11.003

Xiao, Z., Jia, X., Li, D., Wang, S., Geng, X., Liu, F., et al. (2017b). 26 mA Cm^{-2} Jsc from organic solar cells with a low-bandgap nonfullerene acceptor. *Sci. Bull.* 62, 1494–1496. doi: 10.1016/j.scib.2017.10.017

Xu, S. J., Zhou, Z., Liu, W., Zhang, Z., Liu, F., Yan, H., et al. (2017). A twisted Thieno[3,4-B]thiophene-based electron acceptor featuring a 14-Pi-electron indenoindene core for high-performance organic photovoltaics. *Adv. Mater.* 29:1704510. doi: 10.1002/adma.201704510

Xu, X., Bi, Z., Ma, W., Wang, Z., Choy, W. C. H., Wu, W., et al. (2017). Highly efficient ternary-blend polymer solar cells enabled by a nonfullerene acceptor and two polymer donors with a broad composition tolerance. *Adv. Mater.* 29:1704271. doi: 10.1002/adma.201704271

Xu, X., Yu, T., Bi, Z., Ma, W., Li, Y., and Peng, Q. (2018). Realizing over 13% efficiency in green-solvent-processed nonfullerene organic solar cells enabled by 1,3,4-thiadiazole-based wide-bandgap copolymers. *Adv. Mater.* 30:1703973. doi: 10.1002/adma.201703973

Yang, J., Xiao, B., Tajima, K., Nakano, M., Takimiya, K., Tang, A., et al. (2017). Comparison among Perylene Diimide (Pdi), Naphthalene Diimide (Ndi), and Naphthodithiophene Diimide (Ndti) based N-type polymers for all-polymer solar cells application. *Macromolecules* 50, 3179–3185. doi: 10.1021/acs.macromol.7b00414

Yang, Q., Song, H., Gao, B., Wang, Y., Fu, Y., Yang, J., et al. (2014). High open-circuit voltage polymer/polymer blend solar cells with a polyfluorene copolymer as the electron acceptor. *RSC Adv.* 4, 12579–12585. doi: 10.1039/c3ra47512c

Yu, W., Yang, D., Zhu, X., Wang, X., Tu, G., Fan, D., et al. (2014). Control of nanomorphology in all-polymer solar cells via assembling nanoaggregation in a mixed solution. *ACS Appl. Mater. Interfaces* 6, 2350–2355. doi: 10.1021/am404483g

Zhan, X., Xiong, W., Gong, Y., Liu, T., Xie, Y., Peng, Q., et al. (2017). Pyrene-fused perylene diimides: new building blocks to construct non-fullerene acceptors with extremely high open-circuit voltages up to 1.26 V. *Solar RRL* 1:1700123. doi: 10.1002/solr.201700123

Zhang, G., Yang, G., Yan, H., Kim, J.-H., Ade, H., Wu, W., et al. (2017). Efficient nonfullerene polymer solar cells enabled by a novel wide bandgap small molecular acceptor. *Adv. Mater.* 29:1606054. doi: 10.1002/adma.201606054

Zhang, J., Zhang, X., Xiao, H., Li, G., Liu, Y., Li, C., et al. (2016). 1,8-Naphthalimide-based planar small molecular acceptor for organic solar cells. *ACS Appl. Mater. Interfaces* 8, 5475–5483. doi: 10.1021/acsami.5b10211

Zhang, X., Zhang, J., Lu, H., Wu, J., Li, G., Li, C., et al. (2015). A 1,8-naphthalimide based small molecular acceptor for polymer solar cells with high open circuit voltage. *J. Mater. Chem. C* 3, 6979–6985. doi: 10.1039/C5TC01148E

Zhang, Y., Guo, X., Guo, B., Su, W., Zhang, M., and Li, Y. (2017). Nonfullerene polymer solar cells based on a perylene monoimide acceptor with a high open-circuit voltage of 1.3 V. *Adv. Funct. Mater.* 27:1603892. doi: 10.1002/adfm.201603892

Zhang, Z. G., Yang, Y., Yao, J., Xue, L., Chen, S., and Li, X. (2017). Constructing a strongly absorbing low-bandgap polymer acceptor for high-performance all-polymer solar cells. *Angew. Chem. Int. Ed Engl.* 56, 13503–13507. doi: 10.1002/anie.201707678

Zhao, W., Li, S., Yao, H., Zhang, S., Zhang, Y., Yang, B., et al. (2017). Molecular optimization enables over 13% efficiency in organic solar cells. *J. Am. Chem. Soc.* 139, 7148–7151. doi: 10.1021/jacs.7b02677

Zhong, W., Li, K., Cui, J., Gu, T., Ying, L., Huang, F., et al. (2017). Efficient all-polymer solar cells based on conjugated polymer containing an alkoxylated imide-functionalized benzotriazole unit. *Macromolecules* 50, 8149–8157. doi: 10.1021/acs.macromol.7b01432

Zhong, Y., Trinh, M. T., Chen, R., Purdum, G. E., Khlyabich, P. P., Sezen, M., et al. (2015). Molecular helices as electron acceptors in high-performance bulk heterojunction solar cells. *Nat. Commun.* 6:8242. doi: 10.1038/ncomms9242

Conflict of Interest Statement: The authors declare that the research was conducted in the absence of any commercial or financial relationships that could be construed as a potential conflict of interest.

Advantages of publishing in Frontiers

OPEN ACCESS
Articles are free to read for greatest visibility and readership

FAST PUBLICATION
Around 90 days from submission to decision

HIGH QUALITY PEER-REVIEW
Rigorous, collaborative, and constructive peer-review

TRANSPARENT PEER-REVIEW
Editors and reviewers acknowledged by name on published articles

Frontiers
Avenue du Tribunal-Fédéral 34
1005 Lausanne | Switzerland

Visit us: www.frontiersin.org
Contact us: info@frontiersin.org | +41 21 510 17 00

REPRODUCIBILITY OF RESEARCH
Support open data and methods to enhance research reproducibility

DIGITAL PUBLISHING
Articles designed for optimal readership across devices

FOLLOW US
@frontiersin

IMPACT METRICS
Advanced article metrics track visibility across digital media

EXTENSIVE PROMOTION
Marketing and promotion of impactful research

LOOP RESEARCH NETWORK
Our network increases your article's readership